CNF

Cornell NanoScale Science and Technology Facility

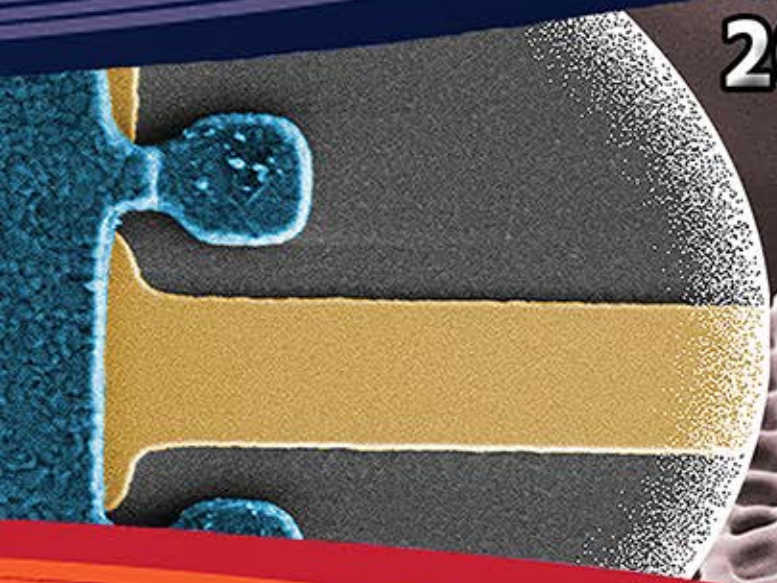

2021-2022 Research Accomplishments

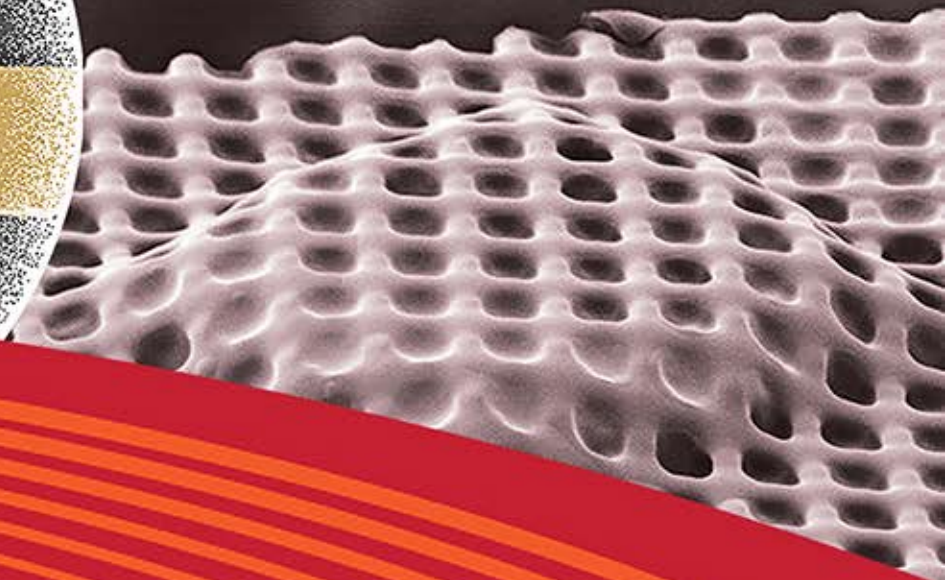

CELEBRATING

45 *years* 1977 – 2022

250 Duffield Hall • 343 Campus Road • Ithaca NY 14853-2700
Phone: 607.255.2329 • Fax: 607.255.8601 •
Email: information@cnf.cornell.edu • Website: www.cnf.cornell.edu

Cornell NanoScale Facility 2021-2022 Research Accomplishments

CNF Lester B. Knight Director:
Christopher Kemper Ober

CNF Director of Operations:
Ronald Olson

Cornell NanoScale Facility (CNF) is a member of the
National Nanotechnology Coordinated Infrastructure *(www.nnci.net)*
and is supported by the National Science Foundation under Grant No. NNCI-2025233,
the New York State Office of Science, Technology and Academic Research,
Cornell University, Industry, and our Users.

The 2021-2022 CNF Research Accomplishments are also available on the web in full color:
http://cnf.cornell.edu/publications/research_accomplishments

Table of Contents

Biological Applications, pages 2-41

Chemistry, pages 42-49

Electronics, pages 50-65

Materials, pages 66-97

Mechanical Devices, pages 98-111

Optics & Opto-Electronics, pages 112-149

Optics, continued

Physics & Nano-Structure Physics, pages 150-181

Process & Characterization, pages 182-191

Index, pages 192-194

Directors' Welcome

The Cornell NanoScale Science & Technology Facility presents the 2021-2022 CNF Research Accomplishments!

*"**First steps are always the hardest** but until they are taken the notion of progress remains only a **notion** and not an achievement."*

*– **Aberjhani***

Gratitude and Continued Thanks

This year marks the 45th Anniversary of the Cornell Nanoscale Facility. Since 1977 CNF has been proudly recognized as a national and international facility dedicated to serving the needs of its diverse community of users and research groups. The extensive resources offered at the CNF, including an expansive collection of equipment capabilities and a staff dedicated to excellence have allowed the CNF to command a strong, influential presence in emerging, state-of-the-art nanotechnology research that is second to none. We remain thankful to the users for their contributions to this publication and for the trust they have placed in the CNF to help them successfully achieve results. We would also like to acknowledge all the companies, groups and people who have supported and contributed to the success of the CNF over the last 45 years, we could not have done it without you! Forty-five years is quite the milestone and we look forward to continuing to evolve and grow with the continued dedication and support of our diverse research community. You are all appreciated.

Progress and Commitment Through the Years

The CNF has grown tremendously since 1977 when Cornell won a national competition to become the first NSF funded, "microfabrication" user facility. Originally referred to as the National Research and Resource Facility for Submicron Structures (NRRFSS), the CNF evolved through six rounds of NSF facility funding. This transformation timeline includes the National Nanofab Facility (NNF) in 1987, The Cornell Nanofab Facility (CNF) in 1993, the Cornell Node of the National Nanotechnology Users Network (NNUN) in 1994, the National Nanotechnology Infrastructure Network (NNIN) in 2004, to its present membership in the National Nanotechnology Coordinated Infrastructure (NNCI) since September 2015. One thing that has remained constant during the CNF's history is its proven commitment to the advancement of science and technology through continued support of academic, industrial, and government research communities. CNF prides itself on its seasoned staff who work diligently to serve and address the needs of the user community. Their extensive expertise enables high equipment uptime, thorough training, and provision of valuable technical advice that is paramount to successful user outcomes.

What We Have Been Up To and Future Plans

The CNF is excited to continue its membership in the National Nanotechnology Coordinated Infrastructure (NNCI) with support provided by the National Science Foundation (NSF) and the NYSTAR/ESD Matching Grant Program from New York State. This support is critical to CNF and its position in the vanguard of the nanofabrication industry. Cornell is one of 16 sites working collaboratively as a national user consortium committed to providing cutting edge fabrication and characterization tools to users from industry

and academia. Earlier this year the CNF submitted "The Year 7 Annual Report" and participated in a successful, virtual, reverse site visit as part of the cooperative agreement with the NNCI.

In May the CNF hosted the first New York State Nanotechnology Network (NNN) symposium and workshop to identify initiatives aimed at bridging the workforce gap. The CNF is pleased to have assumed a leadership role in the establishment of the NNN. The overall mission of the NNN is to help build regional relationships, solve common problems, and grow awareness of the state's nanotechnology capabilities while providing more synergistic opportunities for workforce development within the state. The 2023 meeting will be hosted by SUNY Albany.

August presented the CNF with the opportunity to host the 2022 NNCI Nanoscale Internet-of-Things (Nano-IoT) Research Community Workshop. The meeting was hybrid allowing attendees to participate in-person or virtually via Zoom. The workshop assisted the NNCI network in planning the future of nanotechnology as well as the identification and exploration of goals for the Nano-IoT.

Considering CNF is midway through the second half of its grant period, it is crucial to begin planning the strategic focus of activities and equipment acquisitions for the next 5 -10 year period. Following the 2022 Annual Meeting key experts in nanotechnology will gather for an exclusive strategic planning workshop that will define the CNF's future strategic direction.

As we enter the final months of the year the CNF is thrilled to be hosting the 2022 National Nanotechnology Coordinated Infrastructure (NNCI) Annual Conference on October 19 -21st at Cornell University. In this closed meeting, we look forward to engaging in discussions, updates, and idea exchanges with the leadership of the other NNCI sites. It is sure to be a valuable, energizing in-person exchange!

Comments, feedback, and suggestions about CNF are always welcome. Feel free to use our online User Comment Form at https://www.cnfusers.cornell.edu/user_feedback

Warm Welcomes and Recent Additions

We are thrilled to extend a warm welcome to two, new Advanced Lithography Research Associates; Dr. Roberto Panepucci who began in June, and Dr. Giovanni Sartorello joined us in September. Their knowledge and expertise will further enhance the CNF and we look forward to their contributions.

Dr. Roberto Panepucci received his Master's (1990) and Bachelor's (1989) in Applied Physics from the University of São Paulo (USP), São Carlos, and his Ph.D. from the University of Illinois at Urbana-Champaign, Illinois in 1996. He was a postdoctoral fellow at the Device Research Laboratory at Unicamp, Brazil, working on III-V devices. Dr. Panepucci joined the Cornell Nanofabrication Facility (CNF) in 1999 as a Senior Researcher. He joined startup Galayor Networks in 2000 and led the MEMS R&D team in developing suspended waveguide silicon photonic devices. In 2002 he joined the Nanophotonics Group at Cornell where he led the nanofabrication of key novel silicon photonic devices in SOI technology. From 2003 to 2008 he was an Assistant Professor at FIU developing photonic devices in silicon and polymers and received tenure with promotion to Associate Professor at FIU in 2009. He took a leave of absence to join CTI, a national research center in Brazil, as a Senior Researcher where he served as General Coordinator and Deputy Director. Dr. Panepucci headed the Hardware Systems Design Division and coordinated projects in the area of photonic integrated circuits in silicon and the fabrication of micro and nano systems. He has been an associated researcher with the Brazilian Neuroscience and Neurotechnology Institute (BRAINN) since 2013, coordinating research in neural probes and micro-electrode arrays. He was vice-coordinator of the CTINano, of the Strategic Laboratories of the Brazilian initiative in Nanotechnology prior to joining CNF as Research Associate.

Dr. Giovanni Sartorello, obtained his BSc and MSc in Physics from the University of Padua in Italy, graduating in 2013. He studied for his PhD at King's College London in the UK, where he worked on light-controllable plasmonic meta surfaces in Anatoly Zayats's group. He graduated in 2018 and moved to Cornell in 2019, where he worked in Gennady Shvets's group on the control of nonlinear generation with dielectric meta surfaces. Part of his work as a CNF user has focused mainly on

meta surface fabrication via Ebeam lithography (EBL), chromium or resist masks, and reactive-ion etching. He's also conducted extensive metrology and microscopy and has hands on photolithography experience.

In November of 2021 we welcomed James Crawford to the CNF family after previously working at Ithaca College. James has already established himself as a key staff member responsible for maintaining CNF mechanical facilities, process gas supplies, and research equipment critical to lab operation.

Outreach and Recognition

2022 marked the return to in-person learning for CNF's short course, "Technology and Characterization at the Nanoscale (TCN)" as well as education and community outreach events. Given the success of the virtual TCN short course, CNF will be offering the course virtually each January and in- person each June. By continuing this important educational initiative, the CNF will be able to reach an even more expansive audience. The course is open to participants from academia, industry and government and will include lectures and key demonstrations of the concepts involved in micro and nanoscale device fabrication. The most recently held TCN course opened with daily guest lectures from CNF investigators that aligned with the day's educational content. The guest presenters were very well received and will be a permanent part of our TCN program.

The education and outreach program also had a very successful year with CNF hosting nearly 400 students for tours and activities at our facility in Duffield Hall. The largest event was the Tompkins County Expanding Your Horizons Conference that welcomed over 200 budding, young scientists to the facility to explore nanoscience and watch a live, virtual tour of the cleanroom. In addition, the CNF continues to maintain a partnership with the 4-H Club, through participation in their multi-day Career Explorations event each June.

In recognition of our 45th anniversary celebration the CNF worked with the ScienCenter to bring the Nano Mini-Exhibition to Ithaca. As part of this collaboration, Tom Pennell worked to expand the exhibit by including content on plasma and biomimetics. Tom was instrumental in planning and building an interactive plasma globe exhibit for visitors to enjoy and installing a Nanooze magazine rack that provided distribution of several hundred issues to the local community.

The Education and Outreach program is always working to develop new and exciting educational content to spark greater interest in the field of science. To discuss how your research might translate into a fun, educational experience or to schedule an outreach event, please contact Tom Pennell (pennell@cnf.cornell.edu).

NNCI Awards

Congratulations to Melanie-Claire Mallison and Aaron Windsor who were recently honored with national awards from the NNCI. Annually, the NNCI acknowledges the efforts of NNCI staff who provide exceptional service and support to network users in the categories of Technical Staff, Education and Outreach, and User Support. This year Aaron was a recipient of the NNCI Staff Award in the User Support category and Melanie-Claire was granted the NNCI Staff Award for Education and Outreach. Melanie-Claire and Aaron will receive a plaque and acknowledgement at the NNCI Annual Conference. The exceptional staff at the CNF have been consistently recognized with NNCI Outstanding Staff Member Awards. Past award recipients include Chris Alpha – Technical Staff (2018), Tom Pennell – Education and Outreach (2020), Phil infante – Technical staff (2021) and Mike Skvarla – User Support (2021).

Reflecting on the history of the CNF and where it stands today, we are proud of our achievements and look forward future progress. Thank you for being a part of the CNF's success over the past four and a half decades. We greatly appreciate and value everyone who has contributed to the continued growth and success of the Cornell NanoScale Science & Technology Facility. The dedication and commitment you have all demonstrated was integral in making the CNF what it is today, a leader in the national and international nanoscale communities. Happy 45th Anniversary!

Christopher Ober, Lester B. Knight Director, CNF
director@cnf.cornell.edu

Claudia Fischbach-Teschl, CNF Associate Director
cf99@cornell.edu

Ron Olson, CNF Director of Operations
olson@cnf.cornell.edu

A Selection of 2021 CNF-Research-Related Patents, Presentations, and Publications

Henderson, A.R.; Ilan, I.S.; Lee, E.; "A Bioengineered Lymphatic Vessel Model for Studying Lymphatic Endothelial Cell-Cell Junction and Barrier Function"; Microcirculation; Vol. 28, Issue 8, November 2021, e12730; https://doi.org/10.1111/micc.12730 (2021).

Liu, Q.; Zhang, Y.; Liu, W.; Wang, L.-H.; Choi, Y.W.; Fulton, M.; Fuchs, S.; Shariati, K.; Qiao, M.; Bernat, V.; Ma, M.; "A Broad-Spectrum Antimicrobial and Antiviral Membrane Inactivates SARS-CoV-2 in Minutes"; Advanced Functional Materials, Vol. 31, Issue 47, Page(s) 2103477; Publisher: Wiley Online Library (2021).

Giloteaux, L.; J.K. Chia, S.M. Levine, G.E. Moore, B. Keller, and M.R. Hanson; "A Cardiopulmonary Exercise Challenge Changes the Extracellular Vesicles Proteome in ME/CFS"; 2021 International Association for Chronic Fatigue Syndrome/Myalgic Encephalomyelitis Virtual Conference, Oral Presentation, August 19-21, 2021 (2021).

Smith, V.M.; Nguyen, H.; Rumsey, J.W.; Long, C.J.; Shuler, M.L.; Hickman, J.J.; "A Functional Human-on-a-Chip Autoimmune Disease Model of Myasthenia Gravis for Development of Therapeutics"; Frontiers in Cell and Developmental Biology, 22 Nov 2021, 9:745897, DOI: 10.3389/fcell.2021.745897 (2021).

Adeoye, S.; Anatoly, P.; Peles, Y.; "A Micro Impinging Jet with Supercritical Carbon Dioxide"; International Journal of Heat and Mass Transfer, Volume 170, May 2021, 121028; https://doi.org/10.1016/j.ijheatmasstransfer.2021.121028 (2021).

Jain, P.; Liu, W.; Zhu, S.; Chang, C. Y.-Y.; Melkonian, J.; Rockwell, F.E.; Pauli, D.; Sun, Y.; Zipfel, W.R.; Holbrook, N.M.; "A Minimally Disruptive Method for Measuring Water Potential in Planta Using Hydrogel Nanoreporters"; National Academy of Sciences; Proceedings Vol. 118, Issue 23; June 8, 2021; e2008276118; https://doi.org/10.1073/pnas.2008276118 (2021).

Miles, D.; "A Reflection-Grating Spectrometer for Extended-Source Soft-X-Ray Astronomy"; The Pennsylvania State University Ph.D. Thesis, July 19, 2021 (2021).

Saraswat, D.; "A Study of Large Barrier Height Schottky Barrier Diodes using Noble Metal Oxide Contacts on β-Ga2O3"; Cornell University Ph.D. Thesis (2021-12) (2021).

Domínguez, S., L.Ma, H.Yu, G.Pouchelon, C. Mayer, G.D.Spyropoulos, C.Cea, G.Buzsáki, G.Fishell, D.Khodagholy, J.N.Gelinas; "A Transient Postnatal Quiescent Period Precedes Emergence of Mature Cortical Dynamics"; bioRxiv preprint doi: https://doi.org/10.1101/2021.02.17.430487; this version posted February 17, 2021 (2021).

Liu, Q.; Wang, X.; Chiu, A.; Liu, W.; Fuchs, S.; Wang, B.; Wang, L.-H.; Flanders, J.; Zhang, Y.; Wang, K.; Melero-Martin, J.M.; Ma, M.; "A Zwitterionic Polyurethane Nanoporous Device with Low Foreign-Body Response for Islet Encapsulation"; Advanced Materials; Vol. 33, Issue 39, Page(s) 2102852; Publisher: Wiley Online Library (2021).

Suyolcu, Y.E.; Sun, J.; Goodge, B.H.; Park, J.; Schubert, J.; Kourkoutis, L.F.; Schlom, D.G.; "a-axis YBa2Cu3O7-x/PrBa2Cu3O7-x/YBa2Cu3O7-x Trilayers with Subnanometer RMS Roughness"; APL Materials; Vol. 9, Issue 2, Page(s) 21117; Publisher: AIP Publishing LLC; https://doi.org/10.1063/5.0034648 (2021).

Zhu, L.; R.A. Buhrman; "Absence of Significant Spin-Current Generation in Ti/Fe-Co-B Bilayers with Strong Interfacial Spin-Orbit Coupling"; Physical Review Applied 15, L031001 – Published 10 March 2021, DOI: https://doi.org/10.1103/PhysRevApplied.15.L031001 (2021).

Fuchs, G.D.; "Acoustically-Driven Quantum Spin Sensor"; Patent application # PCT/US21/14733. (2021) (2021).

Tiwari-Heckler, S.; Yee, E.U.; Yalcin, Y.; Park, J.; Nguyen, D.-H.T.; Gao, W.; Csizmadia, E.; Afdhal, N.; Mukamal, K.J.; Robson, S.C.; "Adenosine Deaminase 2 Produced by Infiltrative Monocytes Promotes Liver Fibrosis in Nonalcoholic Fatty Liver Disease"; Cell reports; Vol. 37, Issue 4, Page(s) 109897; Publisher: Elsevier (2021).

Vogt, P., F.V.E.Hensling, K.Azizie, C.S.Chang, D.Turner, J.Park, J.P.McCandless, H.Paik, B.J.Bocklund, G.Hoffman, O.Bierwagen, D.Jena, H.G.Xing, S.Mou, D.A.Muller, S.-L.Shang, Z.-K.Liu, and D.G.Schlom; "Adsorption-Controlled Growth of Ga2O3 by Suboxide Molecular-Beam Epitaxy"; APL Materials; Vol. 9, 031101 (2021); https://doi.org/10.1063/5.0035469 (2021).

Li, W.; D.Jena and H.G.Xing; "Advanced Concepts in Ga2O3 Power and RF Devices (Chapter)"; Semiconductors and Semimetals, Elsevier, 2021 (2021).

Wan, G.; Freeland, J.W.; Kloppenburg, J.; Petretto, G.; Nelson, J.N.; Kuo, D.-Y.; Sun, C.-J.; Wen, J.; Diulus, J.T.; Herman, G.S.; Dong, Y.; Kou, R.; Sun, J.; Chen, S.; Shen, K.M.; Schlom, D.G.; Rignanese, G.-M.; Hautier, G.; Fong. D.D.; Feng, Z.; Zhou, H.; Suntivich, J.; "Amorphization Mechanism of SrIrO3 Electrocatalyst: How Oxygen Redox Initiates Ionic Diffusion and Structural Reorganization"; Science Advances; Vol. 7, Issue 2, Page(s) eabc7323; Publisher: American Association for the Advancement of Science (2021).

Palmer, D., and Molnar, A.C.; "An Autonomous, Optically-Powered, Direct-to-Digital Sun-Angle Recorder for Honey Bee Flight Tracking"; IEEE Transactions on Circuits and Systems II: Express Briefs, vol. 68, no. 5, pp. 1680-1684, May 2021, doi: 10.1109/TCSII.2021.3067033 (2021).

Javid, U. A.; J. Ling, J. Staffa, M. Li, Y. He, and Q. Lin; "An Efficient Nanophotonic Source of Ultra-Broadband Entangled Photons"; Conference on Lasers and Electro-Optics (CLEO), OSA Technical Digest (Optica Publishing Group, 2021), paper JM3F.2. https://doi.org/10.1364/CLEO_AT.2021.JM3F.2 (2021).

Huang, H. , G.Kelp, G.Shvets; "An Integrated Microfluid Device for Capture and Spectroscopic Characterization of Live Cells Under Various Treatment Conditions"; Patent Application, United States (2021).

Li, R.; Li, P.; Yi, D.; Riddiford, L.; Chai, Y.; Suzuki, Y.; Ralph, D.C.; Nan, T.; "Anisotropic Magnon Spin Transport in Ultra-Thin Spinel Ferrite Thin Films; Evidence for Anisotropy in Exchange Stiffness"; arXiv:2105.13943 [cond-mat.mtrl-sci] [Submitted on 28 May 2021] (2021).

Azizi, M.; Nguyen, A.V.; Dogan, B.; Zhang, S.; Simpson, K.W.; Abbaspourrad, A.; "Antimicrobial Susceptibility Testing in a Rapid Single Test via an Egg-Like Multivolume Microchamber-Based Microfluidic Platform"; ACS Appl. Mater. Interfaces 2021, 13, 17, 19581-19592, April 22, 2021, https://doi.org/10.1021/acsami.0c23096 (2021).

Gao, H., M.Guimaraes, K.Kang, J.Park, D.Ralph, S.Xie; "Apparatuses with Atomically-Thin Ohmic Edge Contacts Between Two-Dimensional Materials, Methods of Making Same, and Devices Comprising Same"; Issued Patent, 2021-02-02 Publication of US10910473B2 (2021).

Sanghvi, R.; Ni, D.; Gund, V.; Ji, Q.; Schenkel, T.; Afridi, K.K.; Lal, A.; Petro, E.; "Application of Microelectromechanical-System Based RF Linear Accelerators for Ultra-High Specific Impulse Ion Micropropulsion"; AIAA Propulsion and Energy 2021 Forum, Vol. 6, Issue 16, Page(s) e0252961 (2021).

Marohn, J.A.; Nathan, S.R.; Dwyer, R.P. ; "Atomic Force Microscopy Apparatus, Methods, and Applications"; U. S. Patent 11,175,306; November 16, 2021 (2021).

Abbaspourrad, A., A. Mokhtare, G. Palermo; "Automated Microfluidic Oocyte Denudation Module"; Patent Application (PCT App) (2021).

Ament, S.; Amsler, M.; Sutherland, D.R.; Chang, M.-C.; Guevarra, D.; Connolly, A.B.; Gregoire, J.M.; Thompson, M.O.; Gomes, C.P.; van Dover, R.B.; "Autonomous Materials Synthesis via Hierarchical Active Learning of Nonequilibrium Phase Diagrams"; Science Advances; Vol. 7, Issue 51, Page(s) eabg4930; Publisher: American Association for the Advancement of Science (2021).

Ament, S.; Amsler, M.; Sutherland, D.R.; Chang, M.-C.; Guevarra, D.; Connolly, A.B.; Gregoire, J.M.; Thompson, M.O.; Gomes, C.P.; van Dover, R.B.; "Autonomous Synthesis of Metastable Materials"; arXiv:2101.07385 [cond-mat.mtrl-sci] [Submitted on 19 Jan 2021] (2021).

Ortiz, J.D.; Baena, J.D.; Marqués, R.; Enemuo, A.N.; Gollub, J.; Akhmechet, R.; Penkov, B.; Sarantos, C.; Crouse, D.T.; "Babinet's Principle and Saturation of the Resonance Frequency of Scaled-Down Complementary Metasurfaces"; Applied Physics Letters; Vol. 118, Issue 22, Page(s) 221901; Publisher: AIP Publishing LLC (2021).

Ji, Q.; Afridi, K.K.; Bauer, T.; Giesbrecht, G.; Hou, Y.; Lal, A.; Ni, D.; Persaud, A.; Qin, Z.; Seidl, P.; Sinha, S.; Schenkel, T. [AS Cornell Nano Fabrication (CNF)]; "Beam Power Scale-Up in Micro-Electromechanical Systems Based Multi-Beam Ion Accelerators"; Review of Scientific Instruments, Vol. 10, Issue 92, Page(s) 103301 (2021).

Long, Y.; "Beta-Gallium Oxide Lateral Field-Effect Transistors: Fabrication and Performance"; Cornell Ph.D. Thesis, 2021 (2021).

Pan, Z.; Tao, Y.; Zhao, Y.; Fitzgerald, M.L.; McBride, J.R.; Zhu, L.; Li, D.; "Bidirectional Modulation of Contact Thermal Resistance between Boron Nitride Nanotubes from a Polymer Interlayer"; Nano Letters 2021, Vol. 21, Issue 17, Page(s) 7317-7324; Publisher: ACS Publications (2021).

Abbaspourrad, A., M. Azizi; "Biological Small-Molecule Assays Using Gradient-Based Microfluidics"; Patent Application (PCT App) (2021).

Azizi, M.; Davaji, B.; Nguyen, A.V.; Mokhtare, A.; Zhang, S.; Dogan, B.; Gibney, P.A.; Simpson, K.W.; Abbaspourrad, A.; "Biological Small-Molecule Assays Using Gradient-Based Microfluidics"; Biosensors and Bioelectronics, Vol. 178, 15 April 2021, 113038, https://doi.org/10.1016/j.bios.2021.113038 (2021).

Luo, T.; Wu, M. (NOTE: Tao's works was featured on the back cover of Lab on a Chip. https://pubs-rsc-org.proxy.library.cornell.edu/en/content/articlepdf/2021/lc/d1lc90112e?page=search); "Biologically Inspired Micro-Robotic Swimmers Remotely Controlled by Ultrasound Waves"; Lab on a Chip; Vol. 21, Issue 21, Page(s) 4095-4103; Publisher: Royal Society of Chemistry (2021).

Shuler, M.; "Body-on-a-Chip: A Transformative Approach to Improve Drug Development"; SelectBio, Boston, MA, March 21-22. (Virtual Talk) (2021).

Shuler, M.; "Body-on-a-Chip: Human Microscale Models for Drug Development"; SelectBio, San Diego, CA. Dec 13-15. (Virtual Talk). (2021).

Chlipala, M., D.Jena, K.Nomoto, V.Protasenko, H.Turski, L.van Deurzen, H.G.Xing; "Bottom Tunnel Junction Laser Diode Field-Effect Transistors"; Invention Disclosure, Center for Technology Licensing - Cornell University (2021).

Bharadwaj, S., A.Hickman, D.Jena, K.Lee, K.Nomoto, V.Protasenko, L.van Deurzen, H.G.Xing; "Bottom Tunnel Junction Light-Emitting Field-Effect Transistors"; Patent Application, United States (PCT App) (2021).

Moule, T.; S.Dalcanale; A.S.Kumar; M.J.Uren; W.Li; K.Nomoto; D.Jena; H.G.Xing; M.Kuball; "Breakdown Mechanisms in β-Ga2O3 Trench-MOS Schottky-Barrier Diodes"; IEEE Transactions on Electron Devices, vol. 69, no. 1, pp. 75-81, Jan. 2022, doi: 10.1109/TED.2021.3130861 (2021).

Javid, U.A.; Rogers, S.D.; Graf, A.; Lin, Q.; "Cavity Optomechanical Sensing in the Nonlinear Saturation Limit"; Laser & Photonics Reviews; Vol. 15, Issue 9, Page(s) 2100166; Publisher: Wiley Online Library (2021).

Poudel, S.; Zou, A.; Maroo, S.C.; "CFD Simulation of Wicking in Nanochannels"; ASME Summer Heat Transfer Conference, SHTC 2021 70362, June 16 18, 2021 (2021).

Ralph, D.C.; "Challenges and Opportunities in Spintronics"; NSF Future of Semiconductors and Beyond Workshop: Materials, Devices, and Integration, March 1, 2021 (2021).

Sun, Z. ; Liepe, M. ; Oseroff, T.E.; Deng, X. ; "Characterization of Atomic-Layer-Deposited NbTiN and NbTiN/AlN Films for SIS Multilayer Structures"; International Conference on RF Superconductivity, 2021 Proceedings (2021).

Sun, Z. ; Liepe, M. ; Oseroff, T.E.; Deng, X. ; "Characterization of Atomic-Layer-Deposited NbTiN and NbTiN/AlN Films for SIS Multilayer Structures"; International Conference on RF Superconductivity (SRF'21), virtual, June 2021, WEBTEV012 (Poster) (2021).

Li, T.; J. Zhu, Y. Tang, K. Watanabe, T. Taniguchi, V. Elser, J. Shan, and K. F. Mak; "Charge-Order-Enhanced Capacitance in Semiconductor Moiré Superlattices"; Nature Nanotechnology, Volume 16, Issue 10, p.1068-1072, August 2021, DOI: 10.1038/s41565-021-00955-8 (2021).

Cohen, I.; "Cilia Metasurfaces for Electronically Programmable Microfluidic Manipulation"; Invention Disclosure, Center for Technology Licensing - Cornell University (2021).

Abbaspourrad, A., M. Azizi, A. Nguyen, M. Yaghoobi ; "Circuit Ladder Microfluidic Platform (CLAMP) for Rapid Antimicrobial Susceptibility Testing (AST)"; Invention Disclosure, Center for Technology Licensing - Cornell University (2021).

Plourde, B.; "Circuit QED with Superconducting Metamaterials and Artificial Atoms"; 15th International Congress on Artificial Materials for Novel Wave Phenomena invited talk (virtual due to COVID), September 21, 2021 (2021).

Buhrman, R., M.-H.Nguyen, C.-F.Pai, D.Ralph; "Circuits and Devices Based on Enhanced Spin Hall Effect for Efficient Spin Transfer Torque"; Issued Patent, China (2021).

Mohamed, Z.; Shin, J.-H.; Ghosh, S.; Sharma, A.K.; Pinnock, F.; Bint E Naser Farnush, S.; Dorr, T.; Daniel, S.; "Clinically Relevant Bacterial Outer Membrane Models for Antibiotic Screening Applications"; ACS Infectious Diseases; Vol. 7, Issue 9, Page(s) 2707-2722; Publisher: ACS Publications (2021).

Szoka, E.C.; Werth, J.C.; Cleland, T.A.; Fried, S.; Molnar, A.; "CMOS Neural Probe with Multi-Turn Micro-Coil Magnetic Stimulation"; 2021 IEEE Biomedical Circuits and Systems Conference (BioCAS), 7-9 Oct. 2021, 10.1109/BioCAS49922.2021.9644971 (2021).

Sempertegui, N.; S.Lux, M.Whitman, S.Choi and C.Fischbach; "Collagen Mineralization and Breast Cancer-Derived Factors Synergistically Regulate MSC Behavior"; BMES 2021 Annual Meeting on October 6-9, 2021, in Orlando, Florida (2021).

Fischbach, C.; "Collagen Mineralization and Its Role in Breast Cancer Bone Metastasis "; AACR Virtual Special Conference on The Evolving Tumor Microenvironment, Cancer Progression; Mechanisms and Emerging Therapeutic Opportunities, January 11-12, 2021 (2021).

Miskin, M., McEuen, P., Cohen I., Liu, Q.; "Compact Actuators, Electrically Programmable Microscale Surface Oxide Memory Actuators and Related Robotic Devices"; PCT patent, WO2021178978A1, 2021-09-10 (2021).

Skye, R.; Dshemuchadse, J.; "Competing Structural Motifs in Confined Assemblies of Hard Tetrahedral Particles"; 2021 AIChE Annual Meeting (Fall 2021 Nov 9) (2021).

Gasparini, F.; "Confined 4He Near Tλ: Scaling and Giant Proximity Effects"; Journal of Low Temperature Physics volume 205, pages 183–199 (2021), https://doi.org/10.1007/s10909-021-02637-0 (2021).

Hsia, C.-R., J.McAllister, O.Hasan, J.Judd, S.Lee, R.Agrawal, C.-Y. Chang, P.Soloway, J.Lammerding; "Confined Migration Induces Heterochromatin Formation and Alters Chromatin Accessibility"; bioRxiv, Posted September 23, 2021, doi: https://doi.org/10.1101/2021.09.22.461293 (2021).

Fitzgerald, M.L.; Zhao, Y.; Pan, Z.; Yang, L.; Lin, S.; Sauti, G.; Li, D.; "Contact Thermal Resistance between Silver Nanowires with Poly(vinylpyrrolidone) Interlayers"; Nano Letters 2021, 21, 10, 4388-4393, May 6, 2021, https://doi.org/10.1021/acs.nanolett.1c01034 (2021).

Abbaspourrad, A., A. Mokhtare, G. Palermo; "Contactless Acoustofluidic Sample Agitator and Uses Thereof"; Patent Application, United States (2021).

Li, T.; S.Jiang, L.Li, Y.Zhang, K.Kang, J.Zhu, K.Watanabe, T.Taniguchi, D.Chowdhury, L.Fu, J.Shan & K.F.Mak; "Continuous Mott Transition in Semiconductor Moiré Superlattices"; Nature, volume 597, pages 350-354 (2021) (2021).

Bagheri, M.H.; Loibl, R.T.; Schiffres, S.N.; "Control of Water Adsorption via Electrically Doped Graphene: Effect of Fermi Level on Uptake and H2O Orientation"; Advanced Materials Interfaces; Vol. 8, Issue 18, Page(s) 2100445; Publisher: Wiley Online Library (2021).

Fuchs, G.D.; "Controlling Quantum Emission in 2D Materials with Strain"; SPIE Photonics West (virtual) 2021 (2021).

Jang, J.K.; Okawachi, Y.; Zhao, Y.; Ji, X.; Joshi, C.; Lipson, M.; Gaeta, A.L.; "Conversion Efficiency of Soliton Kerr Combs"; Optics Letters; Vol. 46, Issue 15, Page(s) 3657-3660; Publisher: Optical Society of America (2021).

Cothard, N.F.; "Cryogenic Optics and Detectors for Next-Generation Microwave Cosmology and Astrophysics Observatories"; Cornell University Ph.D. Thesis (2021-08) (2021).

Yu, F.; Zhang, Q.; Wiesner, U.; "Crystalline Inorganic Nanomaterials Templated from Block Copolymers: Non-Equilibrium Processing and Unique Topology from Reduced Symmetry"; ACS Spring 2021 (2021).

Gulinatti, A.; Ceccarelli, F.; Ghioni, M.; Rech, I.; "Custom Silicon Technology for SPAD-Arrays with Red-Enhanced Sensitivity and Low Timing Jitter"; Optics Express; Vol. 29, Issue 3, Page(s) 4559-4581; Publisher: Optical Society of America (2021).

Ament, S.; Amsler, M.; Sutherland, D.R.; Chang, M.-C.; Guevarra, D.; Connolly, A.B.; Gregoire, J.M.; Thompson, M.O.; Gomes, C.P.; van Dover, R.B.; "Data from: Autonomous Synthesis of Metastable Materials"; eCommons, Cornell University, https://doi.org/10.7298/h63q-9r54 (2021).

Chen, W.-H., C.Shang, S.Zhu, K.Haldeman, M.Santiago, A.D.Stroock, and F.You; "Data-Driven Robust Model Predictive Control Framework for Stem Water Potential Regulation and Irrigation in Water Management"; Control Engineering Practice, Vol. 113, August 2021, 104841, https://doi.org/10.1016/j.conengprac.2021.104841 (2021).

Lemasters, R.; Shcherbakov, M.R.; Yang, G.; Song, J.; Lian, T.; Harutyunyan, H.; Shvets, G.; "Deep Optical Switching on Subpicosecond Timescales in an Amorphous Ge Metamaterial"; Advanced Optical Materials, Vol. 9, Issue 15, August 4, 2021, 2100240, https://doi.org/10.1002/adom.202100240 (2021).

Fuchs, G.D.; "Defect Centers in Hexagonal Boron Nitride: Optical, Spin Properties and Applications"; 49th International School and Conference on the Physics of Semiconductors "Jaszowiec 2021", (online only) 2021 (2021).

Jayasuriya, S., A.Molnar, S.Sivaramakrishnan; "Depth Field Imaging Apparatus, Methods, and Applications"; Issued Patent, 2021-04-20 Publication of US10983216B2 (2021).

Hickman, A.; "Design, Fabrication, and Characterization of AlN/GaN/AlN High-Electron-Mobility Transistors "; Cornell University Ph.D. Thesis (2021-08) (2021).

Bint E Naser Farnush, S.; Su, H.; Liu, H.-Y.; Manzer, Z.A.; Chao, Z.; Roy, A.; Pappa, A.-M.; Salleo, A.; Owens, R.M.; Daniel, S.; "Detection of Ganglioside-Specific Toxin Binding with Biomembrane-Based Bioelectronic Sensors"; ACS Applied Bio Materials; Vol. 4, Issue 11, Page(s) 7942-7950; Publisher: ACS Publications (2021).

Gaitan, G., et al.; "Development of a System for Coating SRF Cavities Using Remote Plasma Chemical Vapor Deposition"; International Conference on RF Superconductivity (SRF'21), virtual, June 2021 (2021).

An, H., M.Daniel, X.Liu, R.Shepherd; "Devices and Methods for Data Communications and Sensing"; Patent Application (PCT App) (2021).

Sun, R.; Xu, W.; van Dover, R. B.; "Dielectric Properties of Amorphous Bi-Ti-O Thin Films"; Journal of Advanced Dielectrics, Volume 11, Issue 2, id. 2150009-103 (2021).

Sun, R.; "Dielectric Properties of Thin Film Composition Spreads"; Cornell University Ph.D. Thesis (2021-08) (2021).

Barone, M., M.Jeong, K.Lee, D.Schlom; "Dielectric Thin Film Comprising Perovskite Material, Capacitor Comprising the Dielectric Thin Film and Electronic Device Including the Capacitor"; Invention Disclosure, 12/6/21, Center for Technology Licensing - Cornell University (2021).

Barone, M., M.Jeong, K.Lee, D.Schlom; "Dielectric Thin Film Comprising Perovskite Material, Capacitor Comprising the Dielectric Thin Film and Electronic Device Including the Capacitor"; Patent Application, 12/2/21, United States (2021).

Nguyen, A.V.; Azizi, M.; Yaghoobi, M.; Dogan, B.; Zhang, S.; Simpson, K.W.; Abbaspourrad, A.; "Diffusion–Convection Hybrid Microfluidic Platform for Rapid Antibiotic Susceptibility Testing"; Analytical Chemistry; Vol. 93, Issue 14, Page(s) 5789-5796; Publisher: ACS Publications (2021).

Li, S., H.Bai, Z.Liu, X.Zhang, C.Huang, L.W.Wiesner, M.Silberstein, R.F.Shepherd ; "Digital Light Processing of Liquid Crystal Elastomers for Self-Sensing Artificial Muscles"; Science Advances, Vol. 7, No. 30, 23 Jul 2021, DOI: 10.1126/sciadv.abg3677 (2021).

Holtz, M.E.; Padgett, E.S.; Steinhardt, R.; Brooks, C.M.; Meier, D.; Schlom, D.G.; Muller, D.A.; Mundy, J.A.; "Dimensionality-Induced Change in Topological Order in Multiferroic Oxide Superlattices"; Physical Review Letters; Vol. 126, Issue 15, Page(s) 157601; Publisher: APS (2021).

Sato, Y.; Joshi, A.; Packard, R.; "Direct Measurement of Quantum Phase Gradients in Superfluid â He Flow"; academia.edu (2021).

Zou, A.; Poudel, S.; Gupta, M.; Maroo, S.C.; "Disjoining Pressure of Water in Nanochannels"; Nano Letters 2021, 21, 18, 7769-7774, August 30, 2021; https://doi.org/10.1021/acs.nanolett.1c02726 (2021).

van Deurzen, L.; Ruiz, M.G.; Lee, K.; Turski, H.; Bharadwaj, S.; Page, R.; Protasenko, V.; Xing, H.G.; Lähnemann, J.; Jena, D.; "Dislocation and Indium Droplet Related Emission Inhomogeneities in InGaN LEDs"; Journal of Physics D: Applied Physics; Vol. 54, Issue 49, Page(s) 495106; Publisher: IOP Publishing (2021).

Li, M.; T. Leonard; W. Herzog; "Do Relaxed Sarcomeres Return to Their Original Length Following Repeated Activations?"; Canadian Society for Biomechanics Meeting; Montreal, Canada, May 25-28, 2021 (2021).

Poudel, Sajag; Zou, An; Maroo, Shalabh C.; "Droplet Evaporation on Porous Nanochannels for High Heat Flux Dissipation"; ACS Appl. Mater. Interfaces 2021, 13, 1, 1853–1860, https://doi.org/10.1021/acsami.0c17625 (2021).

Uribe, J.; Traberg, W.C.; Hama, A.; Druet, V.; Mohamed, Z.; Ooi, A.; Pappa, A.; Huerta, M.; Inal, S.; Owens, R.M.; Daniel, S.; "Dual Mode Sensing of Binding and Blocking of Cancer Exosomes to Biomimetic Human Primary Stem Cell Surfaces"; ACS Biomater. Sci. Eng. 2021, 7, 12, 5585–5597, November 21, 2021, https://doi.org/10.1021/acsbiomaterials.1c01056 (2021).

Steinhardt, R.A.; Brooks, C.M.; Correa, G.C.; Holtz, M.E.; Ramesh, R.; Muller, D.A.; Mundy, J.A.; Schlom, D.G.; "DyFe2O4: A New Trigonal Rare-Earth Ferrite Grown by Molecular-Beam Epitaxy"; APL Materials; Vol. 9, Issue 4, Page(s) 41106; Publisher: AIP Publishing LLC (2021).

Abbaspourrad, A., M. Azizi; "Egg-Like Multi-Volume Microchamber-Based Microfluidic (EL-MVM2) Platform for Bacterial Antimicrobial Susceptibility Testing"; Patent Application (PCT App) (2021).

Janicki, Ł., R.Chaudhuri, S.J.Bader, H.G.Xing, D.Jena, and R.Kudrawiec; "Electric Fields and Surface Fermi Level in Undoped GaN/AlN Two-Dimensional Hole Gas Heterostructures"; physica status solidi (RRL)-

Rapid Research Letters, Vol. 15, Issue 4, 18 February 2021, https://doi.org/10.1002/pssr.202000573 (2021).

Marohn, J.A., R. Cohn, A. M. Tirmzi, R. P. Dwyer, and L. E. Harrell; "Electric Force Microscopy of Photoactive Samples: Achieving Nanosecond Time Resolution Using Phase Kicks and Getting the Tip-Sample Interaction Right Using Lagrangian Mechanics"; American Vacuum Society 68th International Symposium & Exhibition (virtual and in person); Charlotte, North Carolina; October 24 – 29, 202 (2021).

Wang, W., Liu, Q., Reynolds, M., Miskin, M., McEuen, P. and Cohen, I.; "Electrically Actuated Artificial Cilia for Microfluidic Applications"; Bulletin of the American Physical Society, 2021 (2021).

Bosch, M.; Shcherbakov, M.R.; Won, K.; Lee, H.-S.; Shvets, G.; "Electrically Actuated Varifocal Lens Based on a Liquid-Crystal-Encapsulated Semiconductor Metasurface"; Conference on Lasers and Electro-Optics (CLEO): QELS_Fundamental Science (FTu4H. 2). Optical Society of America (2021).

Bosch, M.; Shcherbakov, M.R.; Won, K.; Lee, H.-S.; Shvets, G.; "Electrically Actuated Varifocal Lens Based on a Liquid-Crystal-Encapsulated Semiconductor Metasurface"; Flat Optics: Components to Systems; Page(s) FW2C-3; Optical Society of America (2021).

Bosch, M.; Shcherbakov, M.R.; Won, K.; Lee, H.-S.; Kim, Y.; Shvets, G.; "Electrically Actuated Varifocal Lens Based on Liquid-Crystal-Embedded Dielectric Metasurfaces"; Nano Letters 2021, 21, 9, 3849-3856, April 26, 2021, https://doi.org/10.1021/acs.nanolett.1c00356 (2021).

Liu, Q., Wang, W., Sinhmar, H., Cortese, A., Griniasty, I., Reynolds, M., Taghavi, M., Apsel, A., Kress-Gazit, H., McEuen, P. and Cohen, I.; "Electrically Programmable Micro-Scale Morphing Robots Based on Mechanical Metamaterials"; Bulletin of the American Physical Society, 2021 (2021).

Cohen, I.; "Electronically Integrated Microscopic Robots"; Israel Physical Society Conference, 2021 (2021).

Cohen, I.; "Electronically Integrated Self-Assembling Microscopic Robots"; Self-Organization under Confinement, online seminar, March, 2021 (2021).

Hur, Y.H.; Feng, S.; Wilson, K.F.; Cerione, R.A.; Antonyak, M.A.; "Embryonic Stem Cell-Derived Extracellular Vesicles Maintain ESC Stemness by Activating FAK"; Developmental cell; Vol. 56, Issue 3, Page(s) 277-291; Publisher: Elsevier (2021).

Ober, C.K.; "Enabling the Fastest Electronics: Advances in Polymer Photoresists for sub-10 nm Pattern Formation"; Macromex 2021, invited talk, Riviera Maya, MX, Nov. 1 – 4, 2021 (2021).

Shimpi, A.A.; Fischbach, C.; "Engineered ECM Models: Opportunities to Advance Understanding of Tumor Heterogeneity"; Current Opinion in Cell Biology, Vol. 72, October 2021, Pages 1-9, https://doi.org/10.1016/j.ceb.2021.04.001 (2021).

Fischbach, C.; "Engineered Extracellular Matrix Models to Study Tumor Heterogeneity"; NIH Biomedical Engineering Special Interest Group (BME-SIG), December 9, 2021 (2021).

Kim, S. ; "Engineering Materials for Immunomodulation"; Cornell University Ph.D. Thesis (2021-05) (2021).

Fischbach, C.; "Engineering Models to Analyze Tumor-Stroma Interactions and Their Relevance to Cancer Progression and Therapy"; University of Cambridge, IRC Seminar, EPSRC IRC in Targeted Delivery for Hard-to-Treat Cancers, January 7, 2021 (2021).

Meisenheimer, P.; R.Steinhardt, S.Sung, L.Williams, S.Zhuang, M.Nowakowski, S.Novakov, M.Torunbalci, B.Prasad, C.Zollner, Z.Wang, N.Dawley, J.Schubert, A.Hunter, S.Manipatruni, D.Nikonov, I.Young, L.Chen, J.Bokor, S.Bhave, R.Ramesh, J.Hu, E.Kioupakis, R.Hovden, D.Schlom & J.Heron ; "Engineering New Limits to Magnetostriction Through Metastability in Iron-Gallium Alloys"; Nature Communications V12, Issue 1, Article number: 2757 (2021) (2021).

Tan, M.L., L.Ling, C.Fischbach; "Engineering Strategies to Capture the Biological and Biophysical Tumor Microenvironment in vitro"; Advanced Drug Delivery Rev, Vol. 176, Sept 2021, 113852 (2021).

van Deurzen, L.; Bharadwaj, S.; Lee, K.; Protasenko, V.; Turski, H.; Xing, H.G.; Jena, D.; "Enhanced Efficiency in Bottom Tunnel Junction Blue InGaN LEDs"; SPIE Light-Emitting Devices, Materials, and Applications XXV; Vol. 11706, Page(s) 117060F; International Society for Optics and Photonics (2021).

Bhargava, A.; Elbaz, Y.; Sam, Q.; Smeaton, M.A.; Kourkoutis, L.F.; Caspary Toroker, M.; Robinson, R.D.; "Enhanced Li-Ion Diffusion and Electrochemical Performance in Strained-Manganese–Iron Oxide Core–Shell Nanoparticles"; Journal of Chemical Physics; Vol. 155, Issue 14, Page(s) 144702; Publisher: AIP Publishing LLC (2021).

Song, M.; Steinmetz, J.; Zhang, Y.; Nauriyal, J.; Lyons, K.; Jordan, A.N.; Cardenas, J.; "Enhanced On-Chip Phase Measurement by Inverse Weak Value Amplification"; Nature Communications Vol. 12, Issue 1, Page(s) 1-7; Publisher: Nature Publishing Group (2021).

Casamento, J., B.Davaji, V.Gund, D.Jena, A.Lal, H.Lee, H.G.Xing ; "Epitaxial Ferroelectric/Semiconductor Heterostructure Devices"; Invention Disclosure, Center for Technology Licensing - Cornell University (2021).

Sun, J.; "Epitaxial Growth of Palladates and Related Oxides for Oxide Electronics by Molecular-Beam Epitaxy"; Cornell University Ph.D. Thesis (2021-12) (2021).

Casamento, J., D.Jena, H.Lee, T.Maeda, H.G.Xing ; "Epitaxial High K Dielectric-Semiconductor Heterostructures"; Invention Disclosure, Center for Technology Licensing - Cornell University (2021).

Casamento, J.; Lee, H.; Maeda, T.; Gund, V.; Nomoto, K.; van Deurzen, L.; Lal, A.; Jena, D.; "Epitaxial ScxAl1-xN on GaN is a High K Dielectric"; arXiv preprint arXiv:2110.14679, Vol. 2, Issue 15, Page(s) 24059 [Submitted on 27 Oct 2021] (2021).

Dang, P.; "Epitaxial Spin-Orbit and Magnetic Materials for Integration onto a Semiconductor Platform"; Cornell University Ph.D. Thesis (2021-12) (2021).

Hensling, F.V.E., D.Dahliah, P.Dulal, P.Singleton, J.Sun, J.Schubert, H.aik, I.Subedi, B.Subedi, G.-M.Rignanese, N.J.Podraza, G.Hautier, and D.G.Schlom; "Epitaxial Stannate Pyrochlore Thin Films: Limitations of Cation Stoichiometry and Electron Doping"; APL Materials 9, 051113 (2021); https://doi.org/10.1063/5.0049334 (2021).

Mathur, N.; Mukherjee, A.; Gao, X.; Luo, J.; McCullian, B.A.; Li, T.; Vamivakas, A.N.; Fuchs, G.D.; "Excited-State Spin-Resonance Spectroscopy of V/B Defect Centers in Hexagonal Boron Nitride"; arXiv preprint arXiv:2111.10855 (2021).

Koksal, O.; "Exciton-Trion-Polaritons in Two-Dimensional Transition-Metal Dichalcogenides "; Cornell University Ph.D. Thesis (2021-08) (2021).

Ji, X.; Jang, J.K.; Dave, U.D.; Corato-Zanarella, M.; Joshi, C.; Gaeta, A.L.; Lipson, M.; "Exploiting Ultralow Loss Multimode Waveguides for Broadband Frequency Combs"; Laser & Photonics Reviews; Vol. 15, Issue 1, Page(s) 2000353; Publisher: Wiley Online Library (2021).

Vogt, P.; Hensling, F.V.E.; Azizie, K.; McCandless, J.P.; Park, P.; DeLello, K.; Muller, D.A.; Xing, H.G.; Jena, D.; Schlom, D.G.; "Extending the Kinetic and Thermodynamic Limits of Molecular-Beam Epitaxy Utilizing Suboxide Sources or Metal-Oxide Catalyzed Epitaxy"; arXiv:2112.05022 [cond-mat.mtrl-sci] [Submitted on 9 Dec 2021 (v1), last revised 10 Dec 2021 (this version, v2)] (2021).

Fischbach, C.; "Extracellular Matrix as a Microenvironmental Regulator of Cancer"; Berlin-Brandenburg School for Regenerative Therapies (BSRT) Symposium, Berlin, Germany – November 29-December 3rd, 2021 (2021).

Fischbach, C.; "Extracellular Matrix as a Microenvironmental Regulator of Cancer"; Biomedical Engineering, University of Arkansas, November 8th, 2021, https://news.uark.edu/articles/58185/aimrc-seminar-on-the-extracellular-matrix-as-a-microenvironmental-regulator-of-cancer (2021).

Fischbach, C.; "Extracellular Matrix as a Microenvironmental Regulator of Cancer"; University of Massachusetts Amherst, UMass Medical School, January 25th, 2021 (2021).

Fischbach, C.; "Extracellular Matrix as a Microenvironmental Regulator of Cancer"; Weill Cornell Medicine, Metastasis Working Group – Oct 27, 2021 (2021).

Hur, Y.H.; "Extracellular Vesicles in Stem Cell Biology"; Cornell University Ph.D. Thesis, 2021 (2021).

Held, R.; J. A. Mundy, M. E. Holtz, D. Hodash, T. Mairoser, D. A. Muller, and D. G. Schlom; "Fabrication of Chemically and Structurally Abrupt Eu1−xLaxO/SrO/Si Interfaces and Their Analysis by STEM-EELS"; Physical Review Materials 5, 124419 – Published 30 December 2021 (2021).

McDermott, R. (U. Wisconsin); Plourde, B.; "Fabrication of Normal Conducting or Low-Gap Islands for Downconversion of Pair-Breaking Phonons in Superconducting Quantum Circuits"; U. S. Patent Application 17/469,380, 2021 (2021).

Alam, T.; Li, W.; Chang, W.; Yang, F.; Khan, J.; Li, C.; "Favourably Regulating Two-Phase Flow Regime of Flow Boiling HFE-7100 in Microchannels Using Silicon Nanowires"; Scientific Reports; Vol. 11, Issue 1, Page(s) 1-16; Publisher: Nature Publishing Group (2021).

Casamento, J.; Gund, V.; Lee, H.; Nomoto, K.; Maeda, T.; Davaji, B.; Asadi, M.J.; Wright, J.; Shao, Y.-T.; Muller, D.A.; "Ferroelectricity in Polar ScAlN/GaN Epitaxial Semiconductor Heterostructures"; arXiv preprint arXiv:2105.10114, Vol. 10, Issue 126, Page(s) 107204 (2021).

Hwang, J.; Davaji, B.; Kuo, J.; Lal, A.; "Focusing Profiles of Planar Si-SiO2 Metamaterial GHz Frequency Ultrasonic Lens"; 2021 IEEE International Ultrasonics Symposium (IUS); Page(s) 1-4; IEEE (2021).

Heikkinen, P.J.; Casey, A.; Levitin, L.V.; Rojas, X.; Vorontsov, A.; Sharma, P.; Zhelev, N.; Parpia, J.M.; Saunders, J.; "Fragility of Surface States in Topological Superfluid 3He"; Nature Communications Vol. 1, Issue 12, Page(s) 1-8 (2021).

Zhu, L.; Zhu, L.; Buhrman, R.A.; "Fully Spin-Transparent Magnetic Interfaces Enabled by the Insertion of a Thin Paramagnetic NiO Layer"; Physical Review Letters, Vol. 1, Issue 50, Page(s) 80-84 (2021).

Green, A., D. Jena, W.Li, Y.Long, K.Nomoto, K.Smith, H.Xing; "Gallium Oxide (Ga2O3) Lateral MOSFET with Fin Geometry"; Patent Application, United States (2021).

Wang, H.; Alarcón, C.N.; Liu, B.; Watson, F.; Searles, S.; Lee, C.K.; Keys, J.; Pi, W.; Allen, D.; Lammerding, J.; Bui, J.D.; Klemke, R.L.; "Genetically Engineered and Enucleated Human Mesenchymal Stromal Cells for the Targeted Delivery of Therapeutics to Diseased Tissue"; Nature Biomedical Engineering (20 December 2021), https://doi.org/10.1038/s41551-021-00815-9 (2021).

Kuo, J.; Baskota, A.; Zimmerman, S.; Hay, F.; Pethybridge, S.; Lal, A.; "Gigahertz Ultrasonic Imaging of Nematodes in Liquids, Soil, and Air"; 2021 IEEE International Ultrasonics Symposium (IUS); Page(s) 1-4; IEEE (2021).

Aquino, A.; Manzer, Z.; Daniel, S.; DeLisa, M.P.; "Glycosylation-on-a-Chip: A Flow-Based Microfluidic System for Cell-Free Glycoprotein Biosynthesis"; Front. Mol. Biosci. 2021, 8 (December), 1–13. https://doi.org/10.3389/fmolb.2021.782905 (2021).

Azizi, M.; Davaji, B.; Nguyen, A.V.; Zhang, S.; Dogan, B.; Simpson, K.W.; Abbaspourrad, A.; "Gradient-Based Microfluidic Platform for One Single Rapid Antimicrobial Susceptibility Testing"; ACS sensors; Vol. 6, Issue 4, Page(s) 1560-1571; Publisher: ACS Publications (2021).

Schaefer, B.T.; "Graphene Devices for Sensing and Electrical Control of Magnetic Phenomena"; Cornell University Ph.D. Thesis, 2021 (2021).

Gund, V.; Lal, A.; "Graphene-On-Polymer Flexible Vaporizable Sensor"; 2021 IEEE 34th International Conference on Micro Electro Mechanical Systems (MEMS), pp. 521-524. IEEE, 2021 (2021).

Gund, V.; Lal, A.; "Graphene-On-Polymer Flexible Vaporizable Sensor"; 2021 IEEE 34th International Conference on Micro Electro Mechanical Systems (MEMS), DOI: 10.1109/MEMS51782.2021, 25-29 Jan. 2021 (2021).

Parahovnik, A.; Peles, Y.; "Heat Transfer Mode Shift to Adiabatic Thermalization in Near-Critical Carbon Dioxide Under Terrestrial Conditions"; Research Square, DOI: https://doi.org/10.21203/rs.3.rs-199789/v1 (2021).

Hu, Z., D.Jena, W.Li, K.Nomoto, H.G.Xing; "High Voltage Group III Trioxide Trench MOS Barrier Schottky and Methods of Fabricating Same"; Patent Application, United States (2021).

Chaudhuri, R.; Chen, Z.; Muller, D.A.; Xing, H.G.; Jena, D.; "High-Conductivity Polarization-Induced 2D Hole Gases in Undoped GaN/AlN Heterojunctions Enabled by Impurity Blocking Layers"; Journal of Applied Physics 130, 025703 (2021); https://doi.org/10.1063/5.0054321 (2021).

Hilfiker, M.; U.Kilic, M.Stokey, R.Jinno, Y.Cho, H.G.Xing, D.Jena, R.Korlacki, and M.Schubert; "High-Frequency and Below Bandgap Anisotropic Dielectric Constants In Alpha-(AlxGa1-x)2O3(0≤□≤1)"; Applied Physics Letters 119 092103 (2021) (2021).

Xiong, K., G.Qiu, Y.Wang, L.Li, A.Göritz, M.Lisker, M.Wietstruck, M.Kaynak, W.Wu, P.D.Ye, A.Madjar, J.C.M.Hwang; "High-Frequency Tellurene MOSFETs with Biased Contacts"; 2021 IEEE MTT-S International Microwave Symposium (IMS), 2021, pp. 319-322, doi: 10.1109/IMS19712.2021.9574853 (2021).

Rai, D.K.; Gillilan, R.E.; Huang, Q.; Miller, R.; Ting, E.; Lazarev, A.; Tate, M.W.; Gruner, S.M.; "High-Pressure Small-Angle X-Ray Scattering Cell for Biological Solutions and Soft Materials"; Journal of Applied Crystallography; Vol. 54, Issue 1; Publisher: International Union of Crystallography (2021).

Huang, Y.; Tran, H.; Ober, C.K.; "High-Resolution Nanopatterning of Free-Standing, Self-Supported Helical Polypeptide Rod Brushes via Electron Beam Lithography"; ACS Macro Lett. 2021, 10, 6, 755-759, May 31, 2021, https://doi.org/10.1021/acsmacrolett.1c00187 (Featured as Supplementary Cover) (2021).

Huang, Y.; Tran, H.; Ober, C.K.; "High-Resolution Nanopatterning of Mixed Rod-Coil Polymer Brushes Via Electron Beam Lithography"; ACS Meeting Fall 2021. doi: 10.1021/scimeetings.1c01253 POSTER (2021).

Cestarollo, L.; El-Ghazaly, A.; "High-Resolution Reconfigurable Haptic Displays"; Invention Disclosure, Center for Technology Licensing - Cornell University (2021).

Delco, M.; "Human Mesenchymal Stem Cells Release Functional Mitochondria in Extracellular Vesicles"; Osteoarthritis Research Society International 2021, Thu, 04/29/-Mon, 05/03/2021 (2021).

Pinrod, V.; Gupta, S.K.; Nadig, S.; Ruyack, A.; Davaji, B.; Lal, A.; "Hybrid PZT Lateral Bimorphs and 3D-Printed Spring-Mass Resonators for Battery-Less RF Transmission and Vibration Identification"; IEEE Internet of Things Journal, vol. 8, no. 6, pp. 5009-5022, 15 March 2021, doi: 10.1109/JIOT.2020.3036872 (2021).

Sourtiji, E.; Peles, Y.; "Hydrodynamic Characteristics of an Evaporation-Based Micro-Synthetic Jet for Micro-Propulsion"; Journal of Micromechanics and Microengineering; Vol. 31, Issue 10, Page(s) 105001; Publisher: IOP Publishing (2021).

Crouse, D.T.; Bendoym, I.; and Lepak, L.A.; "Hyperspectral Filters with Reduced Angle-of-Incidence Dependence"; USPTO Provisional Patent Application No. 63251884, file date October 4, 2021 (2021).

Latifkar, A., F. Wang, J.J. Mullmann, I.R. Fernandez, L. Ling, C. Fischbach, R.S. Weiss, H. Lin, R.A. Cerione, M.A. Antonyak; "IGF2BP2 Promotes Cancer Progression by Degrading the RNA Transcript Encoding a v-ATPase Subunit"; bioRxiv, Posted April 01, 2021, doi: https://doi.org/10.1101/2021.04.01.438101 (2021).

Liu, Y.; Kuo, J.; Cox, K.; Heuvel, J.V.; Petersen, K.; Lal, A.; "Imaging and Detection of Botrytis Cinerea with Gigahertz Ultrasonic Imager"; 2021 IEEE International Ultrasonics Symposium (IUS); Page(s) 1-4; IEEE (2021).

Lai, Kristine; "Immune Organoids to Study Antigen Presentation"; Cornell University Ph.D. Thesis (2021-12) (2021).

Moille, G.; Westly, D.; Simelgor, G.; Srinivasan, K.; "Impact of Stoichiometric Silicon Nitride Growth Conditions on Dispersion"; Gas, 2021 Nov 3;3(5):7 (2021).

Moille, G.; Westly, D.; Simelgor, G.; Srinivasan, K.; "Impact of the Precursor Gas Ratio on Dispersion Engineering of Broadband Silicon Nitride Microresonator Frequency Combs"; Optics Letters; Vol. 46, Issue 23, Page(s) 5970-5973; Publisher: Optical Society of America (2021).

Plourde, B.; "Implementation of Protected Qubits with Pi-Periodic Josephson Elements"; American Physical Society March Meeting invited talk (virtual due to COVID), March 19, 2021 (2021).

Barone, M.R.; Dawley, N.M.; Nair, H.P.; Goodge, B.H.; Holtz, M.E.; Soukiassian, A.; Fleck, E.E.; Lee, K.; Jia, Y.; Heeg, T.; Gatt, R.; Nie, Y.; Muller, D.A.; Kourkoutis, L.F.; Schlom, D.G.; "Improved Control of Atomic Layering in Perovskite-Related Homologous Series"; APL Materials; Vol. 9, Issue 2, Page(s) 21118; Publisher: AIP Publishing LLC (2021).

Hedderick, K.; "in situ AFM Observation of Surface-Induced Coacervation Facilitating Localized Precipitation of Mineral Precursors from Dilute Solutions"; VC3OC Virtual Conference on Solid State Organic Chemistry: May 24th, 2021 (2021).

Chaudhuri, R.; Hickman, A.; Singhal, J.; Casamento, J.; Xing, H.G.; Jena, D.; "in situ Crystalline AlN Passivation for Reduced RF Dispersion in Strained-Channel AlN/GaN/AlN High-Electron-Mobility Transistors"; physica status solidi (a); Page(s) 2100452; https://doi.org/10.1002/pssa.202100452 (2021).

Faeth, B.D.; Yang, S.-L.; Kawasaki, J.K.; Nelson, J.N.; Mishra, P.; Parzyck, C.T.; Li, C.; Schlom, D.G.; Shen, K.M.; "Incoherent Cooper Pairing and Pseudogap Behavior in Single-Layer FeSe/SrTiO3"; Physical Review X; Vol. 11, Issue 2, Page(s) 21054; Publisher: APS (2021).

Muneer, S., Bakan, G., Gokirmak, A., and H.Silva; "Incorporation of GTR (Generation–Transport–Recombination) in Semiconductor Simulations"; Journal of Applied Physics 129, 055702 (2021); https://doi.org/10.1063/5.0037411 (2021).

Encomendero, J.; Protasenko, V.; Jena, D.; Xing, H.G.; "Influence of Collector Doping Setback in the Quantum Transport Characteristics of GaN/AlN Resonant Tunneling Diodes"; Applied Physics Express, Vol. 14, Number 12, Page(s) 3246 (2021).

Balazs, D.M.; Erkan, N.D.; Quien, M.; Hanrath, T.; "Inkjet Printing of Epitaxially Connected Nanocrystal Superlattices"; Nano Research (2021). https://doi.org/10.1007/s12274-021-4022-7 (2021).

Chaudhuri, R.; "Integrated Electronics on Aluminum Nitride: Materials and Devices"; Cornell University Ph.D. Thesis (2021-12) (2021).

Chaudhuri, R., A.Hickman, J.Hwang, D.Jena, H.G.Xing; "Integrated Electronics on the Aluminum Nitride Platform"; Patent Application, United States (2021).

Rizzo, A.; A.Novick, V.Gopal, B.Y.Kim, X.Ji, S.Daudlin, Y.Okawachi, Q.Cheng, M.Lipson, A.L. Gaeta, K.Bergman; "Integrated Kerr Frequency Comb-Driven Silicon Photonic Transmitter"; arXiv:2109.10297 [physics.app-ph] [Submitted on 8 Sep 2021] (2021).

Dang, P., D.Jena, G.Khalsa, J.Wright, H.G.Xing; "Integrated Quantum Computing with Epitaxial Materials"; Invention Disclosure, Center for Technology Licensing - Cornell University (2021).

Dang, P., D.Jena, G.Khalsa, J.Wright, H.G.Xing; "Integrated Quantum Computing with Epitaxial Materials"; Patent Application, United States (2021).

Dutta, S.; Bose, A.; Tulapurkar, A.A.; Buhrman, R.A.; Ralph, D.C.; "Interfacial and Bulk Spin Hall Contributions to Fieldlike Spin-Orbit Torque Generated by Iridium"; Physical Review B; Vol. 103, Issue 18, Page(s) 184416; Publisher: APS (2021).

Faeth, B.D.; Xie, S.; Yang, S.; Kawasaki, J.K.; Nelson, J.N.; Zhang, S.; Parzyck, C.; Mishra, P.; Li, C.; Jozwiak, C.; Bostwick, A.; Rotenberg, E.; Schlom, D. G.; Shen, K.M.; "Interfacial Electron-Phonon Coupling Constants Extracted from Intrinsic Replica Bands in Monolayer FeSe/SrTiO3"; Physical Review Letters; Vol. 127, Issue 1, Page(s) 16803; Publisher: APS (2021).

Choi, S.; M. Whitman, A. Shimpi, A. Chiou, J. Druso, A. Verma, O. Elemento, LA. Estroff, C. Fischbach ; "Intrafibrillar, Bone-Mimetic Collagen Mineralization as a Model System to Study Breast Cancer Bone Metastasis"; BioInterface Workshop & Symposium, Virtual on September 2021 (2021).

Kelly, C.M.; "Intrinsic and Extrinsic Regulatory Mechanisms of the Dynamin-Related G Protein Atlastin: Implications in Cellular Function and Human Health"; Cornell University Ph.D. Thesis (2021-05) (2021).

McEwen, B.; Mahaboob, I.; Rocco, E.; Hogan, K.; Meyers, V.; Green, R.; Nouketcha, F.; Murray, T.; Kaushik, V.; Lelis, A.; Shahedipour-Sandvik, F.; "Investigation of the Effects of Forming Gas Annealing on Al2O3/GaN Interface"; Journal of Electronic Materials, Vol. 50, pages 80-84 (2021), https://doi.org/10.1007/s11664-020-08532-w (2021).

Wang, F.; Cerione, R.A.; Antonyak, M.A.; "Isolation and Characterization of Extracellular Vesicles Produced by Cell Lines"; STAR protocols, Vol. 1, Issue 2, Page(s) 100295 (2021).

Sahoo, S.; "ISS Microgravity Experiments on Flat and Perforated Capillary Plates"; Cornell University Ph.D. Thesis, 2021 (2021).

Louge, M.; "ISS: Inertial Spreading and Imbibition of a Liquid Drop Through a Porous Surface"; NSF/CASIS Transport Phenomena Program Day, Friday, January 14, 2022, credited NSF-NNCI-2025233 (2021).

Davaji, B., A.Hira, A.Lal, C.Lee ; "Kirigami Acoustic Transducers: Miniaturized Ribbon Microphones"; Invention Disclosure, Center for Technology Licensing - Cornell University (2021).

Chang, W.-H.; Nguyen, T.-T.T.; Hsu, C.-H.; Bryant, K.L.; Kim, H.J.; Ying, H.; Erickson, J.W.; Der, C. J.; Cerione, R.A.; Antonyak, M.A.; "KRAS-Dependent Cancer Cells Promote Survival by Producing Exosomes Enriched in Survivin"; Cancer Letters, Vol. 517, 1 October 2021, Pages 66-77, https://doi.org/10.1016/j.canlet.2021.05.031 (2021).

Zhu, L.; Ralph, D.C.; Buhrman, R.A.; "Lack of Simple Correlation between Switching Current Density and Spin-Orbit-Torque Efficiency of Perpendicularly Magnetized Spin-Current-Generator–Ferromagnet Heterostructures"; Physical Review Applied, 15, 024059, Published 24 February 2021 (2021).

Hickman, A.; Chaudhuri, R.; Moser, N.; Elliott, M.; Nomoto, K.; Li, L.; Hwang, J.C.M.; Xing, H.G.; Jena, D.; "Large Signal Response of AlN/GaN/AlN HEMTs at 30 GHz"; 2021 IEEE Device Research Conference (DRC); Page(s) 1-2; IEEE (2021).

Shcherbakov, M.R.; Sartorello, G.; Tripepi, M.; AlShafey, A.; Bosch, M.; Talisa, N.; Chowdhury, E.; Shvets, G.; "Laser Nanostructuring by Tailored Free Carrier Generation in Designer Semiconductor Metasurfaces"; Conference on Lasers and Electro-Optics (CLEO): Science and Innovations; Page(s) SM3B-1; Optical Society of America (2021).

Bhaskar, A.; Walth, M.; Rand, R.H.; Zehnder, A.T. ; "Laser-Induced Bistability in Coupled Micromechanical Oscillators"; arXiv:2112.15213 [nlin.PS] [Submitted on 30 Dec 2021] (2021).

Islam, S.M., D.Jena, V.Protasenko, H.G.Xing; "Light Emitting Diodes Using Ultra-Thin Quantum Heterostructures"; Issued Patent, 2021-06-22 Publication of US11043612B2 (2021).

Molnar, A.; Wang, A.; "Light Field Image Sensor, Method and Applications"; Issued Patent 1/27/21; Europe, France, Germany, and United Kingdom (2021).

Marohn, J.A.; A.M. Tirmzi, R.P. Dwyer, F. Jiang; "Light-Dependent Impedance Spectra and Transient Photoconductivity in a Ruddlesden–Popper 2D Lead-Halide Perovskite Revealed by Electrical Scanned Probe Microscopy"; Materials Research Society Spring Meeting (virtual); Seattle, Washington; April 18 – 23, 2021 (2021).

Cao, Xiangkun (Elvis); "Light, Fluidics and Their Applications in Global Sustainability and Health"; Cornell University Ph.D. Thesis (2021-12) (2021).

Klaassen, C.; "Lithium-Air Battery Cathodes: A Study on the Effects of Fabrication Method and Active Material Properties on Battery Performance"; Cornell University Ph.D. Thesis (2021-08) (2021).

Jarjour, A.; Ferguson, G.; Schaefer, B.; Lee, M.; Chowdhury, D.; Nowack, K.; "Local Magnetic Measurements of a Few-Layer van der Waals Superconductor"; Bulletin of the American Physical Society, Abstract: F47.00005, APS March Meeting 2021 (2021).

Bell, E.S., P. Shah, N. Zuela-Sopilniak, D. Kim, A.L. McGregor, P. Isermann, P.M. Davidson, J.J. Elacqua, J.N. Lakins, L. Vahdat, V.M. Weaver, M.B. Smolka, P.N. Span, J.Lammerding; "Low Lamin A Levels Enhance Confined Cell Migration and Metastatic Capacity in Breast Cancer"; bioRxiv, Posted July 12, 2021, doi: https://doi.org/10.1101/2021.07.12.451842 (2021).

Marohn, J.A.; "Magnetic Resonance Force Microscopy Tutorial"; Nano-MRI: The next generation (virtual and in person); Leiden, the Netherlands; June 28 – July 2, 2021 (2021).

Fuchs, G.D.; "Magneto-Thermal and Single-Spin Microscopy of Magnetic Quantum Materials"; NSF Workshop on Emerging Opportunities at the Intersection of Quantum and Thermal Sciences, 2021 (2021).

Zaferani, M.; Suarez, S.S.; Abbaspourrad, A.; "Mammalian Sperm Hyperactivation Regulates Navigation via Physical Boundaries and Promotes Pseudo-Chemotaxis"; National Academy of Sciences; Proceedings Vol. 118, Issue 44; Publisher: National Acad Sciences (2021).

Zaferani, M.; "Mammalian Sperm Navigation within the Female Reproductive Tract"; Cornell University Ph.D. Thesis (2021-12) (2021).

Chen, P., X.Mao; "Materials and Methods Enabling Two-Dimensional Junctions on Three-Dimensional Particles"; Patent Application, 1/13/21, United States (2021).

Roberts, S.; Ji, X.; Cardenas, J.; Corato-Zanarella, M.; Lipson, M.; "Measurements and Modeling of Atomic-Scale Sidewall Roughness and Losses in Integrated Photonic Devices"; arXiv:2105.11477 [physics.optics] [Submitted on 24 May 2021] (2021).

Baraissov, Z., et al; "Measuring Composition Variation and Lattice Strain in Nb3Sn Films"; International Conference on RF Superconductivity (SRF'21), virtual, June 2021 (2021).

Harper, C.; W.hang, J.-H.Shin, P.Chen, T.Doerr, C.J.Hernandez; "Mechanical Stress Activates VxrAB Signaling in Vibrio Cholerae"; EMBO/EMBL Symposium: Life at the Periphery: Mechanobiology of the Cell Surface Virtual Conference. 3/2/2021-3/3/2021. Poster (2021).

Thedford, R. P.; Gruner, S.; Wiesner, U.; "Mesostructured Metal Superconductors via Block Copolymer Nanocomposites: Quantum Metamaterials from Soft Matter"; Bulletin of the American Physical Society, 2021, Abstract: F03.00011 (2021).

Thedford, R. P.; Gruner, S.; Wiesner, U.; "Mesostructured Metal Superconductors via Block Copolymer Nanocomposites: Quantum Metamaterials from Soft Matter"; APS Spring 2021, Tuesday, March 16, 2021, Session F03: Polymer Nanocomposites: Structure and Property (2021).

Bosch, M., H.Lee, M.Shcherbakov, G.Shvets, K.Won; "Meta Optical Device with Variable Performance and Electronic Apparatus Including the Same"; Patent Application; Europe 12/8/21, United States 12/15/21 (2021).

Bosch, M.; Shcherbakov, M. R.; Won, K.; Lee, H. S.; Shvets, G; "Meta-Optical Device Having Variable Performance and Electronic Device Including the Same"; Korean Patent Application No. 10-2021-0091853, filed July 2021 (2021).

Tan, M.L.; Shimpi, A.A.; Vilkhovoy, M.; Dai, D.; Roberts, L.D.M.; Kuo, J.; Huang, L.T.; Varner, J.D.; Paszek, M.J.; Fischbach C.; "Metabolism-Dependent Hyaluronic Acid Production Promotes a Breast Cancer Stem-like Cell Phenotype"; Biomedical Engineering Society Annual Meeting, Orlando FL, October 2021 (2021).

Jeong, J., K.Kim, Y.Ko, K.Lee, H.Lee, C.Lin, C.Ober; "Metal Etchant Compositions and Methods of Fabricating a Semiconductor Device Using the Same"; Patent Application, South Korea (2021).

LaHaye, M.; Plourde, B.; "Metamaterial-Boosted Quantum Electromechanical Transducer for Microwave-Optical Interfacing"; U. S. Patent No.: 11,163,209 B2, Nov. 2, 2021 (2021).

Shire, D.B.; Ayton, L.N.; Wong, P.I.; Gingerich, M.D.; "Method and Apparatus for Minimally-Invasive Implantation of Electrodes and Flexible, Thin-Film Substrates into Cortical or Sub-Cortical Structures of the Brain "; U. S. Patent 10,967,172, April 6, 2021 (2021).

Hines, M. A., and W. J. I. DeBenedetti; "Method for Protecting Reactive Materials with Atomically Thin Film"; U. S. Patent Application 63/185,407 (2021) (2021).

Cohen, I., I.Griniasty, C.Mostajeran; "Methods for Designing Three-Dimensional (3D) Shapes from Surfaces and Surfaces for Same"; Patent Application, United States (2021).

Butcher, J., P.Cheung, L.Hockaday, K.Kang, K.Yeh; "Methods for Specifying and Fabrication an Object, Associated Apparatus, and Applications"; Issued Patent, 2021-01-19 Publication of US10894362B2 (2021).

Jia, X., Roberts, S., Corato-Zanarella, M., Lipson, M.; "Methods to Achieve Ultra-High Quality Factor Silicon Nitride Resonators"; APL Photonics 6, 071101 (2021); https://doi.org/10.1063/5.0057881 (2021).

Abbaspourrad, A., M. Davachi, T. Deisenroth, A. Mokhtare, H. Torabi ; "Microfludic Devices for Screening of Polymer Degradation"; Invention Disclosure, Center for Technology Licensing - Cornell University (2021).

Abbaspourrad, A., M. Azizi, M. Yaghoobi; "Microfluidic Device for Analysis of Sperm Motility, and Methods of Use"; Patent Application (PCT App) (2021).

Craighead, H.; H.Tian, J.Topolancik, C.Wallin; "Microfluidic Device for Extracting, Isolating, and Analyzing DNA from Cells"; Issued Patent, 2021-06-24 Publication of US20210189381A1 (2021).

Tan, M.L., Jenkins-Johnston, N., Fischbach, C.; "Microfluidics to Study the Metabolic Regulation of Breast Cancer Cells in the Perivascular Niche"; Cornell NanoScale Facility Annual Meeting, Ithaca NY, September 2021 (2021).

Liu, Q.; Wang, W.; Reynolds, M.F.; Cao, M.C.; Miskin, M.Z.; Arias, T.A.; Muller, D.A.; McEuen, P.L.; Cohen, I.; "Micrometer-Sized Electrically Programmable Shape-Memory Actuators for Low-Power Microrobotics"; Science Robotics [COVER], 17 Mar 2021, Vol. 6, Issue 52, eabe6663, DOI: 10.1126/scirobotics.abe6663 (2021).

Mon, K.J.Y.; Zhu, H.; Daly, C.W.P.; Vu, L.T.; Smith, N.L.; Patel, R.; Topham, D.J.; Scheible, K.; Jambo, K.; Le, M.T.N.; Rudd, B.; Grimson, A.; "MicroRNA-29 Specifies Age-Related Differences in the CD8+ T Cell Immune Response"; Cell Reports; Vol. 37, Issue 6, Page(s) 109969; Publisher: Elsevier (2021).

Ji, X., D. Mojahed, Y. Okawachi, A. L. Gaeta, C. P. Hendon and M. Lipson; "Millimeter-Scale Chip-Based Supercontinuum Generation for Optical Coherence Tomography"; 2021 Conference on Lasers and Electro-Optics (CLEO), pp. 1-2 (2021).

Ji, X., D. Mojahed, Y. Okawachi, A. L. Gaeta, C. P. Hendon and M. Lipson; "Millimeter-Scale Chip-Based Supercontinuum Generation for Optical Coherence Tomography"; Science Advances 2021 Sep; 7(38): eabg8869, 2021 Sep 17. doi: 10.1126/sciadv.abg8869 (2021).

Hufziger, K. A.; Farquharson, E. L.; Goddard, J. M.; Nugen, S. R.; "Modification of Bacteriophage Capsids to Improve Bacteria Separation and Detection in Complex Food and Water Samples"; Materials Research Society Fall Meeting, Virtual, December 8, 2021 (2021).

Encomendero, J.; Islam, S..M.; Jena, D.; Xing, H.G.; "Molecular Beam Epitaxy of Polar III-Nitride Resonant Tunneling Diodes"; Journal of Vacuum Science & Technology A: Vacuum, Surfaces, and Films, Vol. 2, Issue 39, Page(s) 23409 (2021).

Yu, T.; J.Wright; G.Khalsa; B.Pamuk; C.S.Chang; Y.Matveyev; X.Wang; T.Schmitt; D.Feng; D.A.Muller; H.G.Xing; D.Jena; V.N.Strocov; "Momentum-Resolved Electronic Structure and Band Offsets in an Epitaxial NbN/GaN Superconductor/Semiconductor Heterojunction";

Science Advances, 22 Dec 2021, Vol 7, Issue 52, DOI: 10.1126/sciadv.abi5833 (2021).

Huang, S.H.; Li, J.; Fan, Z.; Delgado, R.; Shvets, G.; "Monitoring the Effects of Chemical Stimuli on Live Cells with Metasurface-Enhanced Infrared Reflection Spectroscopy"; Lab on a Chip; Vol. 21, Issue 20, Page(s) 3991-4004; Publisher: Royal Society of Chemistry (2021).

Jena, D., G.Muziol, M.Siekacz, C.Skierbiszewski, H.Turski, H.G.Xing; "Monolithically Inverted III-V Laser Diode Realized using Buried Tunnel Junction"; Patent Application, United States (2021).

Cohen, I., I.Griniasty, C.Mostajeran ; "Multi-Valued Inverse Design: Multiple 3D Surfaces from One Flat Sheet"; Invention Disclosure, Center for Technology Licensing - Cornell University (2021).

Indrajeet; "Multimode Circuit Quantum Electrodynamics with Superconducting Metamaterial Resonators"; Syracuse University Ph.D. Thesis, Aug. 2021 (2021).

Bisogni, A., H.Craighead, D.Lin, H.Tian; "Multiomic Analysis of Cell Analytes using Microfluidic Systems"; Patent Application, USA (2021).

Molnar, A.C.; Lee, S.; Cortese, A.; McEuen, P.; Sadeghi, S.; Ghajari, S.; "Nanoliter-Scale Autonomous Electronics: Advances, Challenges, and Opportunities"; 2021 IEEE Custom Integrated Circuits Conference (CICC); Page(s) 1-6; IEEE (2021).

Alden, J.; A.Cortese, A.Barnard, and P.McEuen; "Nanopore-Containing Substrates with Aligned Nanoscale Electronic Elements and Methods of Making and Using Same"; U. S. US11009498B2, filed December 1, 2015, and issued May 18, 2021. https://patents.google.com/patent/US11009498B2/en (2021).

Kim, S., B.Rudd, A.Singh; "Nanoprojection Devices as Well as Methods of Making and Using Such Devices"; Patent Application, United States (2021).

Liu, E.T. ; "Nanoscale Hot-Wire Anemometer Probes for Turbulence Measurements: From Design to Fabrication"; Cornell University Ph.D. Thesis (2021-12) (2021).

Zhang, C.; Bartell, J.M.; Karsch, J.C.; Gray, I.; Fuchs, G.D.; "Nanoscale Magnetization and Current Imaging Using Time-Resolved Scanning-Probe Magneto-Thermal Microscopy"; Nano Letters 2021, 21, 12, 4966-4972, June 8, 2021, https://doi.org/10.1021/acs.nanolett.1c00704 (2021).

Zhang, C.; Bartell, J.M.; Karsch, J.C.; Gray, I.; Fuchs, G.D.; "Nanoscale Magnetization and Microwave Current Imaging Using Scanning-Probe Magneto-Thermal Microscopy"; APS March Meeting 2021, March 15-19, 2021, Abstract: V36.00008, https://meetings.aps.org/Meeting/MAR21/Session/V36.8 (2021).

Szoka, E.C.; Werth, J.C.; Lee, S.; Lee, J.-I.; Cortese, A.J.; Cleland, T.A.; Fried, S.y; Molnar, A.; "Neural Probe Utilizing Programmable Micro-Coil Magnetic Stimulation"; 2021 10th International IEEE/EMBS Conference on Neural Engineering (NER), 4-6 May 2021, DOI: 10.1109/NER49283.2021.9441227 (2021).

Ober, C.K.; "New Approaches to EUV Photoresists: Expanding the Polymer Toolbox"; 38th International Conference of Photopolymer Science and Technology 2021, invited talk, Online Meeting, June 15 to July 14, 2021 (2021).

Deng, J.; Kaefer, F.; Bailey, S.; Otsubo, Y.; Meng, Z.; Segalman, R.; Ober, C.K.; "New Approaches to EUV Photoresists: Studies of Polyacetals and Polypeptoids to Expand the Photopolymer Toolbox"; Journal of Photopolymer Science and Technology, 34(1-6) (2021) (2021).

Hickman, A.L.; Chaudhuri, R.; Bader, S.J.; Nomoto, K.; Li, L.; Hwang, J.C.M.; Xing, H.G.; Jena, D.; "Next Generation Electronics on the Ultrawide-Bandgap Aluminum Nitride Platform"; Semiconductor Science and Technology; Vol. 36, Issue 4, Page(s) 44001; Publisher: IOP Publishing (2021).

Lidon, P.; Perrot, E.; Stroock, A.D.; "Nonisothermal Effects on Water Potential Measurement in a Simple Geometry"; Physical Review Fluids; Vol. 6, Issue 2, Page(s) 23801; Publisher: APS (2021).

Graf, A.; Rogers, S.D.; Staffa, J.; Javid, U.A.; Griffith, D.H.; Lin, Q.; "Nonreciprocity in Photon Pair Correlations"; arXiv preprint arXiv:2107.10203 (2021).

Rafson, J. ; "Novel Extractions of Trace-Level Compounds Using PDMS Sorbent Polymers for High-Throughput Analyses and Mass Spectral Imaging"; Cornell University Ph.D. Thesis, 2021 (2021).

Huang, X.; S.Sayed, J.Mittelstaedt, S.Susarla, S.Karimeddiny, L.Caretta, H.Zhang, V.A. Stoica, T.Gosavi, F.Mahfouzi, Q.Sun, P.Ercius, N. Kioussis, S.Salahuddin, D.C. Ralph, and R.Ramesh; "Novel Spin–Orbit Torque Generation at Room Temperature in an All-Oxide Epitaxial La0.7Sr 0.3MnO3/SrIrO3 System"; Advanced Materials 33, 2008269, https://doi.org/10.1002/adma.202008269 (2021) (2021).

Shah, P.; Hobson, C.M.; Cheng, S.; Colville, M.J.; Paszek, M.J.; Superfine, R.; Lammerding, J.; "Nuclear Deformation Causes DNA Damage by Increasing Replication Stress"; Current Biology, Vol. 31, Issue 4, 22 February 2021, Pages 753-765.e6, https://doi.org/10.1016/j.cub.2020.11.037 (2021).

Poudel, S.; "Numerical Simulation of Bubble Nucleation in Nanochannel"; ASME Summer Heat Transfer Conference, SHTC 2021 69682, June 16 18, 2021 (2021).

Stephenson, R.; B. Hopkins, Y.Shah, A. Verma, O. Elemento, C. Leifer, C. Fischbach; "Obesity-Associated Collagen Regulates Macrophage Polarization-Dependent Tumor Development"; Biomedical Engineering Society Annual Meeting, Orlando, FL, October 7th, 2021 (2021).

Yang, L.; Tao, Y.; Zhu, Y.; Akter, M.; Wang, K.; Pan, Z.; Zhao, Y.; Zhang, Q.; Xu, Y.-Q.; Chen, R.; Xu, T.T.; Chen, Y.; Mao, Z.; Li, D.; "Observation of Superdiffusive Phonon Transport in Aligned Atomic Chains"; Nature Nanotechnology Vol. 16, pages 764-768 (2021). https://doi.org/10.1038/s41565-021-00884-6 (2021).

Huang, M.; Dorta-Quiñones, C.I.; Minch, B.A.; Lindau, M.; "On-Chip Cyclic Voltammetry Measurements Using a Compact 1024-Electrode CMOS IC"; Analytical Chemistry, 93, 22, 8027-8034, May 26, 2021, https://doi.org/10.1021/acs.analchem.1c01132 (2021).

Li, W.; Nomoto, K.; Hu, Z.; Jena, D.; Xing, H.G.; "ON-Resistance of Ga2O3 Trench-MOS Schottky Barrier Diodes: Role of Sidewall Interface Trapping"; IEEE Transactions on Electron Devices; Vol. 68, Issue 5, Page(s) 2420-2426; Publisher: IEEE (2021).

Fuchs, G.D.; "Optical Properties of Quantum Emitters Hosted by van der Waals Materials"; APS March Meeting 2021 (2021).

Luo, Y.K.; Gupta, V.; Karimeddiny, S.; Cham, T.M.J.; Mak, K.F.; Shan, J.; Ralph, D.; "Optical Readout of Spin-Orbit Torque Acting on Magnetic Thin Films"; Bulletin of the American Physical Society, APS March Meeting 2021, Vol. 66, Number 1 (2021).

Frazer, T.D.; Zhu, Y.; Cai, Z.; Walko, D.A.; Adamo, C.; Schlom, D.G.; Fullerton, E.E.; Evans, P.G.; Hruszkewycz, S.O.; Cao, Y.; Wen, H.; "Optical Transient Grating Pumped X-Ray Diffraction Microscopy for Studying Mesoscale Structural Dynamics"; Scientific Reports; Vol. 11, Issue 1, Page(s) 1-8; Publisher: Nature Publishing Group (2021).

van Deurzen, L.; Page, R.; Protasenko, V.; Jena, D.; "Optically Pumped AlGaN Double Heterostructure Deep-UV Laser by Molecular Beam Homoepitaxy: Mirror Imperfections and Cavity Loss"; arXiv preprint arXiv:2109.10515 (2021).

Vargo, E.; Evans, K.M.; Wang, Q.; Sattler, A.; Qian, Y.; Yao, J.; Xu, T.; "Orbital Angular Momentum from Self-Assembled Concentric Nanoparticle Rings"; Advanced Materials; Vol. 33, Issue 40, Page(s) 2103563; Publisher: Wiley Online Library (2021).

Tran, H.; "Organization and Orientation of Rod-Type Polymer Brushes in Different Brush Architectures Under Solvent Treatments"; Cornell University Ph.D. Thesis (2021-05) (2021).

Erickson, D.; Wang, R.; "Paper-Based Sample Testing Devices and Methods Thereof"; Patent Application (PCT App) (2021).

Domeneguetti, R.R.; Zhao, Y.; Ji, X.; Martinelli, M.; Lipson, M.; Gaeta, A.L.; Nussenzveig, P.; "Parametric Sideband Generation in CMOS-Compatible Oscillators from Visible to Telecom Wavelengths"; Optica, Vol. 8, Issue 3, pp. 316-322 (2021), https://doi.org/10.1364/OPTICA.404755 (2021).

Lotnyk, D.; Eyal, A.; Zhelev, N.; Sebastian, A.; Tian, Y.; Chavez, A.; Smith, E.; Saunders, J.; Mueller, E.; Parpia, J.; "Path-Dependent Supercooling of the 3He Superfluid A-B Transition"; Physical Review Letters; Vol. 126 Issue 21, 215301 – Published 25 May 2021 (2021).

Sakai, K.; Kosma, V.; Ober, C.K.; Giannelis, E.P.; "Pattern-Forming Method and Radiation-Sensitive Composition"; Patent Application number: 20210181627 (2021).

Yu, F.; Thedford, R. P.; Wiesner, U.; "Patternable Mesoporous Superconducting Thin Films Self-Assembled from Block Copolymers and Niobia Sol"; ACS Fall 2021 (2021).

Yu, F.; Thedford, R.P.; Hedderick, K.R.; Freychet, G.; Zhernenkov, M.; Estroff, L.A.; Nowack, K.C.; Gruner, S.M.; Wiesner, U.B.; "Patternable Mesoporous Thin Film Quantum Materials via Block Copolymer Self-Assembly: An Emergent Technology?"; ACS Applied Materials & Interfaces; Vol. 13, Issue 29, Page(s) 34732-34741; Publisher: ACS Publications (2021).

Ni, D., V.Gund, and A.Lal; "PCB Integrated Linbo3 Pyroelectric High Voltage Supply with Electrostatic Switch Regulator"; 2021 21st International Conference on Solid-State Sensors, Actuators and Microsystems (Transducers), pp. 968-971. IEEE, 2021 (2021).

Ni, D., V.Gund, and A.Lal; "PCB Integrated Linbo3 Pyroelectric High Voltage Supply with Electrostatic Switch Regulator"; 2021 21st International Conference on Solid-State Sensors, Actuators and Microsystems (Transducers), 20-25 June 2021 (2021).

Cohn, R.; Marohn, J.A.; "Photo-Induced Resistance and Capacitance Measurements in Organic Solar Cell Materials using Broadband Local Dielectric Spectroscopy and Phase-Kick Electric Force Microscopy with Nanosecond Time Resolution"; 2021 ISPM + Scanning Probe Microscopy on Soft & Polymeric Materials (SPMonSPM) = I(SPM)3 (virtual); June 28 – July 2, 2021 (2021).

Barreiros Flores, J.A.; "Physical Intelligence Enabled by Soft Robotic Systems"; Cornell University Ph.D. Thesis (2021-08) (2021).

Choi, S.; M. Whitman, A. Shimpi, A. Chiou, J. Druso, A. Verma, O. Elemento, LA. Estroff, C. Fischbach; "Physiological Mineralization of Collagen Promotes Breast Cancer Stem-like Properties and Resistance to Doxorubicin"; Biointerfaces International Conference on August 18-19, 2021, in Zurich, Switzerland (2021).

Islam, S.M., D.Jena, V.Protasenko, H.G.Xing; "Polarization Field Assisted Heterostructure Design for Efficient Deep Ultra-Violet Light Emitting Diodes"; Issued Patent, 2021-03-23 Publication of US10957817B2 (2021).

Bader, S., R.Chaudhuri, D.Jena, H.G.Xing; "Polarization-Induced 2D Hole Gases for High-Voltage p-Channel Transistors"; Issued Patent, United States US11158709B2, 2021-10-26 Application granted (2021).

Zhang, Z.; J.Encomendero, R.Chaudhuri, Y.Cho, V.Protasenko, K.Nomoto, K.Lee, M.Toita, H.G.Xing and D.Jena; "Polarization-Induced 2D Hole Gases in Pseudomorphic Undoped GaN/AlN Heterostructures on Single-Crystal AlN Substrates"; Applied Physics Letters 119 162104 (2021) (2021).

Huang, Y.; Ober, C.K.; "Preparation of Immobilized Sub-50nm Polymer Nanostructures on Surfaces"; Invention Disclosure, Center for Technology Licensing - Cornell University (2021).

Lopez Baltazar, J.M.; "Probing the Fundamental Forces of Gold Nanoparticles Interacting through Non-Covalent Quadruple Hydrogen Bonding"; Cornell University Ph.D. Thesis (2021-08) (2021).

Ondera, T., and Stein, M.; "Programmable Photonic Planar Waveguides Using Optical Images"; Disclosed to the Center for Technology Licensing at Cornell University (CTL) on October 1st, 2021 (2021).

Yaghoobi, M.; Azizi, M.; Mokhtare, A.; Abbaspourrad, A.; "Progressive Sperm Separation Using Parallelized, High-Throughput, and Efficient Microchamber-Based Microfluidics"; Lab on a Chip; Issue 14, 2021, DOI https://doi.org/10.1039/D1LC00091H (2021).

Dodge, K., et al.; "Protected C-Parity Qubits Part 1: Characterization and Protection"; American Physical Society March Meeting contributed talk (virtual due to COVID), March 19, 2021 (2021).

LaValley, D.J.; Miller, P.G.; Shuler, M.L.; "Pumpless, Unidirectional Microphysiological System for Testing Metabolism-Dependent Chemotherapeutic Toxicity"; Biotechnology Progress; Vol. 37, Issue 2, Page(s) e3105; Publisher: Wiley Online Library (2021).

Vinayakumar, K.B.; V.Gund, A.Lal; "Pyroelectric Lithium Niobate Electron Emission-Based Ion-Pump"; Journal of Vacuum Science & Technology B, Nanotechnology and Microelectronics: Materials, Processing, Measurement, and Phenomena 39, no. 2 (2021): 024202 (2021).

Li, T.; S.Jiang, B.Shen, Y.Zhang, L.Li, Z.Tao, T.Devakul, K.Watanabe, T.Taniguchi, L.Fu, J.Shan & K.F.Mak; "Quantum Anomalous Hall Effect from Intertwined Moiré Bands"; Nature, volume 600, pages 641–646 (22 December 2021) (2021).

Fuchs, G.D.; "Quantum Control of Spin and Orbital States with a Diamond Acoustic Resonator"; QNEXT/ANL SUF Workshop, (Online only) 2021 (2021).

Fuchs, G.D.; "Quantum Control of Spin and Orbital States with a Diamond MEMS Resonator"; Transducers Online Virtual Conference 2021 (2021).

Fang, Y.; Nair, H.P.; Miao, L.; Goodge, B.; Schreiber, N.J.; Ruf, J. P.; Kourkoutis, L.F.; Shen, K.M.; Schlom, D.G.; Ramshaw, B.J.; "Quantum Oscillations and the Quasiparticle Properties of Thin Film Sr2RuO4"; arXiv preprint arXiv:2103.00723 arXiv:2103.00723 [cond-mat.supr-con] [Submitted on 1 Mar 2021] (2021).

Cheung, H.F.H.; Chilcote, M.; Yusuf, H.; Cormode, D.S.; Shi, Y.; Kurfman, S.; Franson, A.; Flatte, M.E.; Johnston-Halperin, E.; Fuchs, G.D.; "Raman Spectroscopy and Aging of the Low-Loss Ferrimagnet Vanadium Tetracyanoethylene"; Journal of Physical Chemistry C; Vol. 125, Issue 37, Page(s) 20380-20388; Publisher: ACS Publications (2021).

Rafson, J.; Sacks, G.L.; "Rapid Analysis of Volatile Phenols from Grape Juice by Immersive Sorbent Sheet Extraction Prior to Direct Analysis in Real-Time Mass Spectrometry (DART-MS)"; Journal of Agricultural and Food Chemistry; Vol. 69, Issue 41, Page(s) 12344-12353; Publisher: ACS Publications (2021).

Farhangdoust, F.; Cheng, F.; Liang, W.; Liu, Y.; Wanunu, M.; "Rapid Identification of DNA Fragments through Direct Sequencing with Electro-Optical Zero-Mode Waveguides"; Advanced Materials, 29 December 2021, https://doi.org/10.1002/adma.202108479 (2021).

Bell, R.T.; Beaucage, P.A.; Murphy, M.J.; Connolly, A.B.; Wiesner, U.B.; Ginley, D.; van Dover, R.B.; Thompson, M.O.; "Rapid Identification of Synthetic Routes to Functional Metastable Phases Using X-Ray Probed Laser Anneal Mapping (XPLAM) Time–Temperature Quench Maps"; Chemistry of Materials; 2021, 33, 12, 4328-4336, https://doi.org/10.1021/acs.chemmater.0c04926 (2021).

Rafson, J.; Sacks, G.L.; "Rapid Quantitation of Volatile Phenols by Immersive Sorbent Sheet Extraction Prior to Direct Analysis in Real Time Mass Spectrometry (DART-MS)"; Journal of Agricultural and Food Chemistry 69(41), 12344–12353 2021 (2021).

Jena, D., J.McCandless, V.Protasenko, H.G.Xing ; "Reduction of Surface Oxidation in Molecular Beam Epitaxy (MBE) Sources"; Invention Disclosure, Center for Technology Licensing - Cornell University (2021).

Li, C.; Ma, H.; Li, T.; Dai, J.; Rasel, M.A.J.; Mattoni, A.; Alatas, A.; Thomas, M.G.; Rouse, Z.W.; Shragai, A.; "Remarkably Weak Anisotropy in Thermal Conductivity of Two-Dimensional Hybrid Perovskite Butylammonium Lead Iodide Crystals"; Nano Letters 2021, Vol. 21, Issue 9, Page(s) 3708-3714, May 3, 2021, https://doi.org/10.1021/acs.nanolett.0c04550 (2021).

Davaji, B., V.Gund, S.Jadhav, D.Jena, A.Lal, H.G.Xing; "Resistive Electrodes on Ferroelectric Devices for Linear Piezoelectric Programming: Applied to NEMS Multiply/Add Unit, and Resonator Tuning"; Invention Disclosure, Center for Technology Licensing - Cornell University (2021).

Davaji, B., V.Gund, S.Jadhav, D.Jena, A.Lal, H.G.Xing; "Resistive Electrodes on Ferroelectric Devices for Linear Piezoelectric Programming: Applied to NEMS Multiply/Add Unit, and Resonator Tuning"; Patent Application, United States (2021).

Karimeddiny, S.; Ralph, D.C.; "Resolving Discrepancies in Spin-Torque Ferromagnetic Resonance Measurements: Lineshape vs. Linewidth Analyses"; Physical Review Applied; Vol. 15, Issue 6, Page(s) 64017; Published 7 June 2021 (2021).

Mittelstaedt, J.A.; Ralph, D.C.; "Resonant Measurement of Non-Reorientable Spin-Orbit Torque from a Ferromagnetic Source Layer Accounting for Dynamic Spin Pumping"; Physical Review Applied, Volume 16, Issue 2, article id.024035, August 2021, DOI: 10.1103/PhysRevApplied.16.024035 (2021).

Liang, G.; H.Huang, A.Mohanty, M.C.Shin, X.Ji, M.J.Carter, S.Shrestha, M.Lipson & N.Yu ; "Robust, Efficient, Micrometre-Scale Phase Modulators at Visible Wavelengths"; Nature Photonics, volume 15, pages 908–913 (22 November 2021) (2021).

Zaferani, M.; Javi, F.; Mokhtare, A.; Li, P.; Abbaspourrad, A.; "Rolling Controls Sperm Navigation in Response to the Dynamic Rheological Properties of the Environment"; eLife Aug 4, 2021;10:e68693 doi: 10.7554/eLife.68693 (2021).

Karimeddiny, S.; Cham, T.M.; Ralph, D.C.; Luo, Y.K.; "Sagnac Interferometry for High-Sensitivity Optical Measurements of Spin-Orbit Torque"; arXiv preprint arXiv:2109.13759 (2021).

Bircan, B.; "Self-Folding Microsystems Based on Atomic Layer Deposition Nanofilms"; Cornell University Ph.D. Thesis (2021-08) (2021).

Wang, Y.; Nair, H.P.; Schreiber, N.J.; Ruf, J.P.; Cheng, B.; Schlom, D. G.; Shen, K.M.; Armitage, N.P.; "Separated Transport Relaxation Scales and Interband Scattering in Thin Films of SrRuO3, CaRuO3, and Sr2RuO4"; Physical Review B; Vol. 103, Issue 20, Page(s) 205109; Publisher: APS (2021).

Cham, T.M.; Karimeddiny, S.; Gupta, V.; Mittelstaedt, J.A.; Ralph, D.C.; "Separation of Artifacts from Spin-Torque Ferromagnetic Resonance Measurements of Spin-Orbit Torque for the Low-Symmetry van der Waals Semi-Metal ZrTe3"; Advanced Quantum Technologies; Page(s) 2100111; Publisher: Wiley Online Library (2021).

Asadi, M.J.; L.Li; W.Zhao; K.Nomoto; P.Fay; H.G.Xing; D.Jena; J.C.M.Hwang; "SiC Substrate-Integrated Waveguides for High-Power Monolithic Integrated Circuits Above 110 GHz"; 2021 IEEE MTT-S International Microwave Symposium (IMS), 7-25 June 2021, DOI: 10.1109/IMS19712.2021.9574845 (2021).

Ballard, A., et al.; "Single Flux Quantum-Based Superconducting Qubit Control and Quasiparticle Mitigation: Part 1"; American Physical Society March Meeting contributed talk (virtual due to COVID), March 17, 2021 (2021).

Reynolds, M.F.; "Smart Microscopic Robots: From 2D Materials to Actuators to CMOS-Integrated Robots"; Cornell University Ph.D. Thesis, 2021 (2021).

Oliver, R.; Okawachi, Y.; Ji, X.; Johnson, A.R.; Klenner, A.; Lipson, M.; Gaeta, A.L.; "Soliton-Effect Compression of Picosecond Pulses on a Photonic Chip"; Optics Letters; Vol. 46, Issue 18, Page(s) 4706-4709; Publisher: Optical Society of America (2021).

Jain, R.; Bose, A.; Richardella, A.; Pillsbury, T.; Ou, Y.; Samarth, N.; Buhrman, R.A.; Ralph, D.C.; "Spin Nernst Effect in a Topological Insulator Bi2Se3"; Bulletin of the American Physical Society, APS March Meeting 2021, Abstract: L36.00003 (2021).

Castelletto, S.; C.You, D.L.Gater, A.F.Isakovic (Used the correct grant number but called us the "Cornell University Center for Nanofabrication" HA!); "Spin Relaxation in Quasi-1D GaAs Mesowires: Control via Electric Field and Aspect Ratio"; arXiv:2111.08884 [cond-mat.mes-hall] [Submitted on 17 Nov 2021] (2021).

Li, Xiang; "Spin-Orbit Torque Field-Effect Transistor (SOTFET): A Memory Device Proposal, Modelling, and Experiments"; Cornell University Ph.D. Thesis (2021-08) (2021).

Cham, T.M.J.; Gupta, V.; Vareskic, B.; Jain, R.; Bose, A.; Ralph, D.C.; "Spin-Orbit Torques Generated by Low-Symmetry ZrTe3"; Bulletin of the American Physical Society, APS March Meeting 2021, Vol. 66, Number 1 (2021).

Ruf, J.P.; Paik, H.; Schreiber, N.J.; Nair, H.P.; Miao, L.; Kawasaki, J.K.; Nelson, J.N.; Faeth, B.D.; Lee, Y.; Goodge, B.H.; Pamuk, B.; Fennie, C.J.; Kourkoutis, L.F.; Schlom, D.G.; Shen, K.M.; "Strain-Stabilized Superconductivity"; Nature Communications Vol. 12, Issue 1, Article number: 59 (2021) (2021).

Casamento, J.; Lee, H.; Chang, C.S.; Besser, M.F.; Maeda, T.; Muller, D.A.; Xing, H.G.; Jena, D.; "Strong Effect of Scandium Source Purity on Chemical and Electronic Properties of Epitaxial ScxAl1- xN/GaN Heterostructures"; APL Materials, Vol. 9, Issue 9, Page(s) 91106 (2021).

Bose, A.; Schreiber, N.; Nair, H.; Zhang, X.; Jain, R.; Cham, T.M.J.; Sun, J.; Muller, D.; Buhrman, R.A.; Schlom, D.G.; "Strong, Anisotropic In-Plane and Out-Of-Plane Damping-Like Spin-Orbit Torque in Epitaxial RuO2"; Bulletin of the American Physical Society, APS March Meeting 2021, Abstract: E38.00005 (2021).

Ma, L.; P. X. Nguyen, Z. Wang, Y. Zeng, K. Watanbe, T. Taniguchi, A.H. MacDonald, K.F. Mak, and J. Shan; "Strongly Correlated Excitonic Insulator in Atomic Double Layers"; Nature, Volume 598, Issue 7882, p.585-589 (October 2021), DOI: 10.1038/s41586-021-03947-9 (2021).

Páez Fajardo, G.J.; Howard, S.A.; Evlyukhin, E.; Wahila, M.J.; Mondal, W.R.; Zuba, M.; Boschker, J.E.; Paik, H.; Schlom, D.G.; Sadowski, J.T.; "Structural Phase Transitions of NbO2: Bulk versus Surface"; Chemistry of Materials; Vol. 33, Issue 4, Page(s) 1416-1425; Publisher: ACS Publications (2021).

Sun, Z.; T. Oseroff, K. Howard, R. Porter, Z. Baraissov, N. Sitaraman, M. Kelly, K. D. Dobson, X. Deng, A. Connolly, M. O. Thompson, J. Sethna, T. Arias, D. Muller, M. Liepe; "Study of Alternative Materials for Next Generation SRF Cavities at Cornell University"; 9th International Workshop on Thin Films and New Ideas for Pushing the Limits of RF Superconductivity, virtual, March 2021 (Invited talk) (2021).

Beaucage, P. A.; van Dover, R. B.; DiSalvo, F. J.; Gruner, S. M.; Wiesner, U.; "Superconducting Quantum Metamaterials from Convergence of Soft and Hard Condensed Matter Science"; Adv Materials 2021, 33 (26), 2006975. https://doi.org/10.1002/adma.202006975 (2021).

Thedford, R.P.; Beaucage, P.A.; Susca, E.M.; Chao, C.A.; Nowack, K.C.; van Dover, R.B.; Gruner, S.M.; Wiesner, U.; "Superconducting Quantum Metamaterials from High Pressure Melt Infiltration of Metals into Block Copolymer Double Gyroid Derived Ceramic Templates"; Advanced Functional Materials, Vol. 31, Issue 23, 22 March 2021, https://doi.org/10.1002/adfm.202100469 (2021).

Felix, N.; Tsuchiya, K.; Luk, C.M.Y.; Ober, C.K.; "Supercritical CO2 for High-Resolution Photoresist Development"; SPIE Proceedings Vol. 6153, Page(s) 61534B-1 (2021).

McBroom, T., et al.; "Superstrong Coupling Between a Transmon and a Metamaterial Resonator"; American Physical Society March Meeting contributed talk (virtual due to COVID), March 18, 2021 (2021).

Uribe, J. ; "Supported Biomimetic Membranes to Study the Surface Interactions Between Cancer Extracellular Vesicles and Human Primary Stem Cells"; Cornell Ph.D. Thesis (2021-12) (2021).

Daniel, S., H.-Y.Liu, M.Stuebler; "Supported Plant Plasma Lipid Bilayer-on-a-Chip"; Patent Application, United States (2021).

Sun, Z.; M. U. Liepe, T. Oseroff, R. D. Porter; T. Arias, Z. Baraissov, D. Muller, N. Sitaraman; D. Johnson-McDaniel, M. Salim; C. Dukes; "Surface Oxides on Nb and Nb3Sn Surfaces: Toward a Deeper Understanding"; International Conference on RF Superconductivity, June 2021, Proceedings (2021).

Sun, Z.; M. U. Liepe, T. Oseroff, R. D. Porter; T. Arias, Z. Baraissov, D. Muller, N. Sitaraman; D. Johnson-McDaniel, M. Salim; C. Dukes; "Surface Oxides on Nb and Nb3Sn Surfaces: Toward a Deeper Understanding"; International Conference on RF Superconductivity, virtual, June 2021. (Poster) (2021).

Sun, Z.; M. Ge; M. U. Liepe; T. Oseroff; R. D. Porter; A. Connolly; M. O. Thompson; "Surface Roughness Reduction of Nb3Sn Thin Films via Laser Annealing for Superconducting Radio-Frequency Cavities"; International Particle Accelerator Conference (SRF'21), Jun. 2021, Proceedings (2021).

Sun, Z.; M. Ge; M. U. Liepe; T. Oseroff; R. D. Porter; A. Connolly; M. O. Thompson; "Surface Roughness Reduction of Nb3Sn Thin Films via Laser Annealing for Superconducting Radio-Frequency Cavities"; International Particle Accelerator Conference (SRF'21), virtual, June 2021 (Poster) (2021).

Krounbi, L.; Hedderick, K.; Eyal, Z; Aram, L.; Shimoni, E.; Estroff, L.A.; Gal, A.; "Surface-Induced Coacervation Facilitates Localized Precipitation of Mineral Precursors from Dilute Solutions"; Chem. Mater. 2021, 33, 10, 35343542 (2021).

Kim, B.Y.; Jang, J.K.; Okawachi, Y.; Ji, X.; Lipson, M.; Gaeta, A.L.; "Synchronization of Non-Solitonic Kerr Combs"; arXiv preprint arXiv:2104.15141 (2021).

Liu, F.; Yazdani, M.; Wagner, N.; Ahner, B.; Wu, M.; "Synergistic Effects of Nitrogen and Phosphorous on the Growth of Algal Cells Reveled by a Microfluidic Platform"; Bulletin of the American Physical Society, Issue 11687, Page(s) 116870E (2021).

Craighead, H.; Tian, H.; "Systems and Methods for On-Chip Analysis of Nucleic Acids and for Multiplexed Analysis of Cells"; Patent Application 6/28/21, Europe (2021).

Gund, V.; B.Davaji; H.Lee; M.J.Asadi; J.Casamento; H.G.Xing; D.Jena; A.Lal; "Temperature-Dependent Lowering of Coercive Field in 300 nm Sputtered Ferroelectric Al0.70Sc0.30N"; 2021 IEEE International Symposium on Applications of Ferroelectrics (ISAF), pp. 1-3. IEEE, 2021 (2021).

Gund, V.; B.Davaji; H.Lee; M.J.Asadi; J.Casamento; H.G.Xing; D.Jena; A.Lal; "Temperature-Dependent Lowering of Coercive Field in 300 nm Sputtered Ferroelectric Al0.70Sc0.30N"; 2021 IEEE International Symposium on Applications of Ferroelectrics (ISAF), 16-21 May 2021, DOI: 10.1109/ISAF51943.2021.9477328 (2021).

Moore, E.S.; Tan, M.L., Shimpi, A.., Fischbach, C.; "The Impact of Cell-Matrix Interactions on the DNA Damage Response and Stemness of Breast Cancer Cells"; Cold Spring Harbor Laboratory "Biology of Cancer: Microenvironment and Metastasis", 2021 (2021).

Moore, E.S.; Tan, M.L., Shimpi, A.., Fischbach, C.; "The Impact of Cell-Matrix Interactions on the DNA Damage Response and Stemness of Breast Cancer Cells"; Cornell Stem Cell Symposium, 2021 (2021).

Howard, K., Sun, Z.; "Thermal Annealing of Sputtered Nb3Sn and V3Si Thin Films for Superconducting RF Cavities"; International Conference on RF Superconductivity (SRF'21), virtual, June 2021 (2021).

Dawley, N.M.; Pek, E.K.; Lee, C.-H.; Ragasa, E.J.; Xiong, X.; Lee, K.; Phillpot, S.R.; Chernatynskiy, A.V.; Cahill, D.G.; Schlom, D.G.; "Thermal Conductivity of the n = 1-5 and 10 Members of the (SrTiO3)nSrO Ruddlesden-Popper Superlattices"; Applied Physics Letters; Vol. 118, Issue 9, Page(s) 91904 (2021); https://doi.org/10.1063/5.0037765 (2021).

Chatterjee, B.; Li, W.; Nomoto, K.; Xing, H.G.; Choi, S.; "Thermal Design of Multi-Fin Ga2O3 Vertical Transistors"; Applied Physics Letters, Vol. 10, Issue 119, Page(s) 103502 (2021).

Wang, Z.; "Thermal Measurements Using Laser Flash Analysis and Frequency-Domain Thermoreflectance"; Cornell University Ph.D. Thesis (2021-08) (2021).

McCandless, J.P.; C. S. Chang, K. Nomoto, J. Casamento, V. Protasenko, P. Vogt, D. Rowe, K. Gann, S.T. Ho, W. Li, R. Jinno, Y. Cho, A. Green, K. Chabak, D. Schlom, M. O. Thompson, D. A. Muller, H. G. Xing and D. Jena; "Thermal Stability of Epitaxial Alpha-Ga2O3 and (Al,Ga)2O3 Layers on m-Plane Sapphire"; Applied Physics Letters 119 062102 (2021) Editor's Pick (2021).

Dawley, N., C.Fennie, G.Olsen, D.Schlom, Z.Wang; "Thin-Film Structure and Method of Manufacturing the Same"; Issued Patent, 2021-09-28 Publication of US11133179B2 (2021).

Barbalas, D.; Chatterjee, S.; Schlom, D.G.; Shen, K.M.; Armitage, N.P.; "THz Electrodynamics of Mixed-Valent YbAl3 and LuAl3 Thin Films"; European Physical Journal B; Vol. 94, Issue 9, Page(s) 1-8; Publisher: Springer (2021).

Bose, A.; Schreiber, N.J.; Jain, R.; Shao, D.-F.; Nair, H.P.; Sun, J.; Zhang, X.S.; Muller, D.A.; Tsymbal, E.Y.; Schlom, D.G.; Ralph, D.C.; "Tilted Spin Current Generated by the Collinear Antiferromagnet RuO2"; arXiv preprint arXiv:2108.09150 (2021).

Bartell, J., G.Fuchs, J.Karsch, C.Zhang ; "Time-Resolved Near-Field Gigahertz-Frequency Current Microscope (Combined into D10143)"; Invention Disclosure, Center for Technology Licensing - Cornell University (2021).

Bartell, J., G.Fuchs, J.Karsch, C.Zhang ; "Time-Resolved Near-Field Magneto-Thermal Microscope (D10144 combined herein)"; Invention Disclosure, Center for Technology Licensing - Cornell (2021).

Sempertegui, N.; Fischbach, C.; "Tissue Engineered Models of Metastasis: Focus on Bone Metastasis"; Biomaterial-Based Approaches to Study the Tumour Microenvironment; Royal Society of Chemistry. Accepted 2021, Jessica Winter, Shreyas Rao eds (2021).

Gao, X.; Hong, Y.; Ye, F.; Inman, J.T.; Wang, M.D.; "Torsional Stiffness of Extended and Plectonemic DNA"; Physical Review Letters; Vol. 127 Issue 2, 028101 – Published 7 July 2021 (2021).

Sun, Z.; G. Gaitan, M. Ge, K. Howard, M. U. Liepe, R. D. Porter, T. Oseroff; T. Arias, Z. Baraissov, M. Kelly, D. Muller, J. Sethna, N. Sitaraman; K. D. Dobson; "Toward Stoichiometric and Low-Surface-Roughness Nb3Sn Thin Films via Direct Electrochemical Deposition"; International Conference on RF Superconductivity, 2021, Proceedings (2021).

Sun, Z.; G. Gaitan, M. Ge, K. Howard, M. U. Liepe, R. D. Porter, T. Oseroff; T. Arias, Z. Baraissov, M. Kelly, D. Muller, J. Sethna, N. Sitaraman; K. D. Dobson; "Toward Stoichiometric and Low-Surface-Roughness Nb3Sn Thin Films via Direct Electrochemical Deposition"; International Conference on RF Superconductivity (SRF'21), virtual, June 2021 (Invited talk) (2021).

Balasubramanian, P.S.; "Towards High Resolution in Stimulation, Sensing, and Characterization of Neural Tissue – Applications in Gigahertz Ultrasonic Neural Interfaces and Magnetic Resonance Imaging of Brain Tissue for Quantitative Susceptibility Mapping"; Cornell University Ph.D. Thesis (2021-12) (2021).

Gund, V.; Davaji, B.; Lee, H.; Casamento, J.; Xing, H.G.; Jena, D.; Lal, A.; "Towards Realizing the Low-Coercive Field Operation of Sputtered Ferroelectric ScxAl1-xN"; 2021 21st International Conference on Solid-State Sensors, Actuators and Microsystems (Transducers); Page(s) 1064-1067; IEEE (2021).

Gund, V.; Davaji, B.; Lee, H.; Casamento, J.; Xing, H.G.; Jena, D.; Lal, A.; "Towards Realizing the Low-Coercive Field Operation of Sputtered Ferroelectric ScxAl1-xN"; 2021 21st International Conference on Solid-State Sensors, Actuators and Microsystems (Transducers), 20-25 June 2021 (2021).

Yu, F.; Zhang, Q.; Wiesner, U.; "Transient Laser Heating Enabled Nanocomposite Structures from Block Copolymers Toward Photonic & Phononic Quantum Materials"; Bulletin of the American Physical Society, 2021 (2021).

De Santi, C.; Fabris, E.; Caria, A.; Buffolo, M.; Li, W.; Nomoto, K.; Hu, Z.; Jena, D.; Xing, H.G.; Meneghesso, G.; "Trapping Processes and Band Discontinuities in Ga2O3 FinFETs Investigated by Dynamic Characterization and Optically-Assisted Measurements"; SPIE proceedings of the 11687 conference March 2021; Oxide-based Materials and Devices XII; Volume 11687, 116870E (2021) https://doi.org/10.1117/12.2579478 (2021).

Xie, H.; Jiang, S.; Rhodes, D.A.; Hone, J.C.; Shan, J.; Mak, K.F.; "Tunable Exciton-Optomechanical Coupling in Suspended Monolayer MoSe2"; Nano Letters 2021, 21, 6, 2538-2543, March 15, 2021, https://doi.org/10.1021/acs.nanolett.0c05089 (2021).

Javid, U.A.; Ling, J.; Staffa, J.; Li, M.; He, Y.; Lin, Q.; "Ultra-Broadband Entangled Photons on a Nanophotonic Chip"; Physical Review Letters, Volume 127, Issue 18, article id.183601, October 2021, DOI: 10.1103/PhysRevLett.127.183601 (2021).

Jiang, W.C.; Li, K.; Gai, X.; Nolan, D.A.; Dainese, P.; "Ultra-Low-Power Four-Wave Mixing Wavelength Conversion in High-Q Chalcogenide Microring Resonators"; Optics Letters; Vol. 46, Issue 12, Page(s) 2912-2915; Publisher: Optical Society of America (2021).

Lal, A.; "Ultrasonic Fourier Computation Hardware for Convolutional Neural Network Computing"; Patent Application, United States (2021).

Ye, F.; Islam, A.; Zhang, T.; Feng, P.X.-L.; "Ultrawide Frequency Tuning of Atomic Layer van der Waals Heterostructure Electromechanical Resonators"; Nano Letters 2021, 21, 13, 5508–5515, June 18, 2021, https://doi.org/10.1021/acs.nanolett.1c00610 (2021).

Wright, J.; Chang, C.; Waters, D.; Lüpke, F.; Feenstra, R.; Raymond, L.; Koscica, R.; Khalsa, G.; Muller, D.; Xing, H.G.; "Unexplored MBE Growth Mode Reveals New Properties of Superconducting NbN"; Physical Review Materials, Vol. 2, Issue 5, Page(s) 24802 (2021).

Zhu, L.; Ralph, D.C.; Buhrman, R.A.; "Unveiling the Mechanism of Bulk Spin-Orbit Torques Within Chemically Disordered FexPt1-x Single Layers"; Advanced Functional Materials, 2103898 (2021); doi:10.1002/adfm.202103898 (2021).

Lawlor, C.; "Use of a Custom Quartz Crystal Microbalance Vacuum Chamber to Investigate Area-Selective Atomic Layer Deposition"; Cornell University Ph.D. Thesis (2021-12) (2021).

Tsuei, M.; Tran, H.; Roh, S.; Ober, C.K.; Abbott, N.L.; "Using Liquid Crystals to Probe the Organization of Helical Polypeptide Brushes Induced by Solvent Pretreatment"; Macromolecules; Vol. 54, Issue 17, Page(s) 7786-7795; Publisher: ACS Publications (2021).

Slaughter, V.L; Rumsey,J.W.; Boone,R.; Malik,D; Cai,Y.; Sriram, N. N; Long, C.L.; McAleer,C.W. ; Lambert, S.; Shuler, M.L.; Hickman,J.; "Validation of an Adipose-Liver Human-on-a-Chip Model of NAFLD for Preclinical Therapeutic Efficacy Evaluation"; Scientific Reports (2021)11:13159 (2021).

Oeschger, T.M.; Erickson, D.C.; "Visible Colorimetric Growth Indicators of Neisseria Gonorrhoeae for Low-Cost Diagnostic Applications"; PLOS ONE, June 17, 2021, https://doi.org/10.1371/journal.pone.0252961 (2021).

Ardanuc, S., V.K.K.Basavarajappa, Q.Ji, A.Lal, A.Persaud, T.Schenkel, P.Seidl, W.Waldron; "Wafer-Based Charged Particle Accelerator, Wafer Components, Methods and Applications"; Issued Patent 2021-02-02 Publication of US10912184B2 (2021).

Bai, H., R.Huang, S.Li, R.Shepherd, H.Zhao; "Waveguides for Use in Sensors or Displays"; Patent Aplication China (2021).

Corato-Zanarella, M.; Gil-Molina, A.; Ji, X.; Shin, M.C.l; Mohanty, A.; Lipson, M.; "Widely Tunable and Narrow Linewidth Chip-Scale Lasers from Deep Visible to Near-IR"; arXiv preprint arXiv:2109.08337 (2021).

Sheng, H.; Jiang, Y.; Rahmati, M.; Chia, J.-C.; Dokuchayeva, T.; Kavulych, Y.; Zavodna, T.-O.; Mendoza, P.N.; Huang, R.; Smieshka, L.M.; "YSL3-Mediated Copper Distribution is Required for Fertility, Seed Size and Protein Accumulation in Brachypodium"; Plant Physiology, Vol. 186, Issue 1, May 2021, Pages 655-676, https://doi.org/10.1093/plphys/kiab054 (2021).

Photography Credits

The 2021-2022 Cornell NanoScale Facility Research Accomplishments are online in full color PDFs,
http://cnf.cornell.edu/publications/research_accomplishments

Common Abbreviations & Meanings

µl. . . . . microliter
µm. . . . . micron, micrometer
µN. . . . . micro-Newtons
µs . . . . . microsecond
Ω. . . . . Ohm
<. . . . . is less than
>. . . . . is greater than
~. . . . . approximately
1D. . . . . one-dimensional
2D. . . . . two-dimensional
2DEG. . . . . two-dimensional electron gas
3D. . . . . three-dimensional
^{3}He helium-3
a-Al_2O_3. . . . . sapphire
a-Si . . . . . amorphous silicon
AC. . . . . alternating current
AFM. . . . . atomic force microscopy/microscope
AFOSR. . . . . Air Force Office of Scientific Research
Ag. . . . . silver
Al . . . . . aluminum
Al_2O_3 . . . . . aluminum oxide
ALD. . . . . atomic layer deposition
AlGaAs. . . . . aluminum gallium arsenide
AlGaN. . . . . aluminum gallium nitride
Ar . . . . . argon
ARC. . . . . anti-reflective coating
ArF . . . . . argon fluoride
As . . . . . arsenic
atm . . . . . standard atmosphere (as a unit of pressure)
Au. . . . . gold
AuNPs . . . . . gold nanoparticles
B. . . . . boron
B. subtilis. . . . . *Bacillus subtilis*
Bi . . . . . bismuth
BOE. . . . . buffered oxide etch
Br . . . . . bromine
C. . . . . carbon
C. . . . . centigrade
C-V. . . . . capacitance-voltage
C_3N_4. . . . . carbon nitride
$CaCl_2$ . . . . . calcium chloride
$CaCO_3$. . . . . calcium carbonate
CAD. . . . . computer-aided design
CaF_2. . . . . calcium fluoride
CCMR. . . . . Cornell Center for Materials Research
Cd. . . . . cadmium
CdS . . . . . cadmium sulfide
CdSe. . . . . cadmium selenide
CDW . . . . . charge-density-wave
Ce . . . . . cerium
CF_4. . . . . carbon tetrafluoride or tetrafluoromethane
CFD. . . . . computational fluid dynamics
CH_4 . . . . . methane
CHESS . . . . . Cornell High Energy Synchrotron Source
CHF_3. . . . . trifluoromethane
Cl. . . . . chlorine
Cl_2. . . . . chlorine gas
Cl_2/SF_6. . . . . chlorine sulfur hexafluoride
cm. . . . . centimeter
CMOS. . . . . complementary metal oxide semiconductor
CMP. . . . . chemical mechanical polishing
CNF. . . . . Cornell NanoScale Science & Technology Facility
Co. . . . . cobalt
CO_2 . . . . . carbon dioxide
Co_3O_4. . . . . cobalt oxide
CoFeAl. . . . . cobalt iron aluminum
CoFeB. . . . . cobalt iron boron
CoP . . . . . cobalt porphyrin
CPC. . . . . colloidal photonic crystal
CPD. . . . . contact potential difference
CpG. . . . . cytosine-phosphate-guanine
Cr . . . . . chromium
CRDS. . . . . cavity ring-down spectrometer
cryoSAXS . . . . cryogenic small angle x-ray scattering
CTE. . . . . coefficients of thermal expansion
CTL. . . . . confinement tuning layer
Cu. . . . . copper
CVD. . . . . cardiovascular disease
CVD. . . . . chemical vapor deposition
CW . . . . . continuous wave
CXRF. . . . . confocal x-ray fluorescence microscopy
DARPA. . . . . Defense Advanced Research Projects Agency
DC. . . . . direct current
DCB. . . . . double cantilever beam
DCE. 1,2-dichloroethane
DCM. . . . . dichloromethane
DEP. . . . . dielectrophoresis
DFT. . . . . density functional theory
DFT. . . . . discrete Fourier transform
DI . . . . . de-ionized
DMF. . . . . dimethyl formamide
DNA. . . . . deoxyribonucleic acid
DNP. . . . . dynamic nuclear polarization
DOE. . . . . United States Department of Energy
DPPC. 1,2-dipalmatoyl-sn-glycero-3-phosphocholine
DRAM. . . . . dynamic random access memory
DRIE . . . . . deep reactive ion etch
DSA. . . . . directed self assembly
dsDNA . . . . . double-stranded DNA
DUV. . . . . deep ultraviolet
e-beam . . . . . electron beam lithography
E. coli. . . . . *Escherichia coli*
EBL. . . . . electron-beam lithography
EDS. . . . . energy dispersive spectroscopy
EELS . . . . . electron energy loss spectroscopy
EG. . . . . ethylene glycol
EIS. . . . . electrochemical impedance spectroscopy
ELISA. . . . . enzyme-linked immunosorbent assays
EO. . . . . electro-optic
EOT. . . . . equivalent oxide thickness
EPICs. . . . . electronic photonic integrated circuits
Er . . . . . erbium
ErAs. . . . . erbium arsenide
ESM. . . . . effective screening medium
EUV. . . . . extreme ultraviolet
ex situ. . . . . Latin phrase which translated literally as 'off-site' -- to examine the phenomenon in another setting than where it naturally occurs
ex vivo . . . . . Latin for "out of the living" -- that which takes place outside an organism
F. . . . . fluorine
FDA. . . . . United States Food & Drug Administration
FDMA. . . . . fluorinated perfluorodecyl methacrylate
Fe . . . . . iron
Fe_2O_3 . . . . . iron oxide
$FeCl_3$ . . . . . iron(III) chloride, aka ferric chloride
FeGe. . . . . iron germanium
FEM. . . . . finite element method
FET . . . . . field-effect transistor
FFTs. . . . . fast Fourier transforms
fg. . . . . femto gram
FIB. . . . . focused ion beam
FIR . . . . . far infrared
fJ. . . . . femto Joules
FM. . . . . frequency modulation
FMR. . . . . ferromagnetic resonance
FOTS . . . . . fluorosilane, tridecafluoro-1,1,2,2-tetrahydrooctyltrichlorosilane

FTIR. . . . . Fourier transform infrared spectroscopy
Ga . . . . . gallium
Ga_2O_3 . . . . . gallium(III) trioxide
GaAs . . . . . gallium arsenide
GaAsN . . . . . gallium arsenide nitride
GaInNAs. . . . . gallium indium nitride arsenide
GaN. . . . . gallium nitride
GaP . . . . . gallium phosphide
GaSb . . . . . gallium antimonide
Gd. . . . . gadolinium
Ge . . . . . germanium
GFET . . . . . graphene field effect transistor
GHz. . . . . gigahertz
GI . . . . . gastrointestinal
GMR. . . . . giant magnetoresistance
GPa . . . . . gigapascal
GPS . . . . . global positioning system
h. . . . . hours
H . . . . . hydrogen
H_2O_2. . . . . hydrogen peroxide
HBAR. . . . . high-overtone bulk acoustic resonator
hBN. . . . . hexagonal boron nitride
HBr . . . . . hydrogen bromide
hcp . . . . . hexagonal close packing
He. . . . . helium
HEMTs. . . . . high electron mobility transistors
Hf . . . . . hafnium
HF. . . . . hydrofluoric acid
HfB_2 . . . . . hafnium diboride
HFEs . . . . . hydrofluoroethers
HfO_2 . . . . . hafnium dioxide
Hg. . . . . mercury
high-k. . . . . high dielectric constant
HMDS. . . . . hexamethyldisilazane
HRS. . . . . high resistance state
HSQ. . . . . hydrogen silsesquioxane
HSQ/FOx. . . . negative electron beam resist hydrogen silsesquioxane
Hz. . . . . Hertz
I-V. . . . . current-voltage
I/O. . . . . input/output
IARPA. . . . . Intelligence Advanced Research Projects Activity
IC . . . . . integrated circuit
ICP. . . . . inductively coupled plasma
ICP-MS. . . . . inductively coupled plasma mass spectroscopy
ICP-RIE. . . . . inductively coupled plasma reactive ion etcher
IFVD . . . . . impurity free vacancy diffusion
IID . . . . . impurity induced disordering
IIEI . . . . . ion implant enhanced interdiffusion
In . . . . . indium
in situ . . . . . Latin phrase which translated literally as 'in position' -- to examine the phenomenon exactly in place where it occurs
in vitro . . . . . Latin for "within glass" -- refers to studies in experimental biology that are conducted using components of an organism that have been isolated from their usual biological context in order to permit a more detailed or more convenient analysis than can be done with whole organisms
in vivo. . . . . Latin for "within the living" -- experimentation using a whole, living organism
InAlN. . . . . indium aluminum nitride
InAs . . . . . indium arsenide
InAs NWs . . . . indium arsenide nanowires
INDEX . . . . . Institute for Nanoelectronics Discovery and Exploration
InGaAsN. . . . . indium gallium arsenide nitride
$InGaZnO_4$ . . . indium gallium zinc oxide
InP. . . . . indium phosphide
IPA. . . . . isopropyl alcohol
IR . . . . . infrared
IrO_2 or IrO_x . . iridium oxide
ITO . . . . . indium tin oxide
JP-8 . . . . . Jet Propellant 8

k. . . . . dielectric constant
K. . . . . Kelvin (a unit of measurement for temperature)
K. . . . . potassium
KFM . . . . . Kelvin force microscopy
kg . . . . . kilogram
kHz . . . . . kilohertz
KOH . . . . . potassium hydroxide
La . . . . . lanthanum
LED . . . . . light-emitting diode
LER . . . . . line edge roughness
Li. . . . . lithium
low-k. . . . . low dielectric constant
LPCVD . . . . . low pressure chemical vapor deposition
lpm . . . . . liter per minute
LRS . . . . . low resistance state
Lu . . . . . lutetium
LWR. . . . . line width roughness
MBE. . . . . molecular beam epitaxy
MEMs. . . . . microelectromechanical systems
MFMR . . . . . microfabricated micro-reactors
MgO . . . . . magnesium oxide
MGs. . . . . molecular glasses
MHz. . . . . megahertz
micron. . . . . micrometer, aka μm
min . . . . . minutes
ml . . . . . milliliter
mm . . . . . millimeter
mM . . . . . millimolar
Mo . . . . . molybdenum
MOCVD. . . . . metal oxide chemical vapor deposition
MOS . . . . . metal oxide semiconductor
MoS_2 . . . . . molybdenum disulfide
$MoSe_2$. . . . . molybdenum diselenide
MOSFET. . . . . metal oxide semiconductor field effect transistor
MRAM . . . . . magnetic random access memory
MRFM . . . . . magnetic resonance force microscopy
MRI . . . . . magnetic resonance imaging
ms. . . . . millisecond
MSM . . . . . metal-semiconductor-metal
mTorr. . . . . millitorr
mV. . . . . millivolt
MVD. . . . . molecular vapor deposition
MΩ . . . . . megaohms
N . . . . . nitrogen
N_2 . . . . . nitrous oxide
nA. . . . . nanoAmperes
NaCl. . . . . sodium chloride
NASA . . . . . National Aeronautics & Space Administration
Nb. . . . . niobium
Nb_3Sn . . . . . triniobium-tin
NCs . . . . . nanocrystals
Nd. . . . . neodymium
NEMs. . . . . nanoelectromechanical systems
NH_4F . . . . . ammonium fluoride
Ni . . . . . nickel
NIH . . . . . National Institutes of Health
NIR . . . . . near-infrared
nL . . . . . nanoliter
nm. . . . . nanometer
NMP. n-methyl-2-pyrrolidone
NNCI . . . . . National Nanotechnology Coordinated Infrastructure
NPs . . . . . nanoparticles
NPs . . . . . nanopores
ns . . . . . nanosecond
NSF . . . . . National Science Foundation
NV . . . . . nitrogen-vacancy
NVM. . . . . non-volatile memory
NW FETs. . . . . nanowire field-effect transistors
O . . . . . oxygen
O_3 . . . . . trioxygen
OFET . . . . . organic field effect transistor
OLED. . . . . organic light-emitting diode

ONO . . . . . oxide/nitride/oxide
ONR-MURI . . Office of Naval Research Multidisciplinary University Research Initiative
OPV. . . . . organic photovoltaic cells
OTFT . . . . . organic thin-film transistor
Pa . . . . . Pascals
PAB . . . . . post-apply bake
PaC . . . . . Parylene-C
PAG . . . . . photoacid generator
Pb . . . . . lead
PBG. . . . . photonic bandgap
PbS . . . . . lead sulfide
PBS . . . . . phosphate-buffered saline
PbSe. . . . . lead selenide
PC. . . . . persistent current
PC. . . . . photocurrent
PCN. . . . . photonic crystal nanocavity
Pd . . . . . palladium
PD. . . . . photodetector
PDMS . . . . . polydimethylsiloxane
PEB . . . . . post-exposure bake
PEC . . . . . photoelectrochemical
PECVD . . . . . plasma enhanced chemical vapor deposition
PEDOT:PSS . . poly(3,4-ethylenedioxythiophene): poly(styrenesulfonate)
PEG . . . . . polyethylene glycol
PEI. . . . . polyethyleneimine
pFET . . . . . p-channel field-effect transistor
PFM . . . . . piezo-response force microscopy
PGMA. . . . . poly(glycidyl methacrylate)
pH. . . . . a measure of the activity of hydrogen ions (H+) in a solution and, therefore, its acidity
Ph.D. . . . . doctorate of philosophy
PhC . . . . . photonic crystal
PL. . . . . photoluminescence
pL . . . . . picoliter
PLD . . . . . pulsed laser deposition
PMMA . . . . . poly(methyl methacrylate)
poly-Si . . . . . polycrystalline silicon
PS . . . . . polystyrene
PS-*b*-PMMA . . polystyrene-*block*-poly(methyl methacrylate)
Pt . . . . . platinum
Pt/Ir . . . . . platinum/iridium
$PtSe_2$ . . . . . platinum diselenide
PV. . . . . photovoltaic
PVD. . . . . physical vapor deposition
Py . . . . . permalloy, $Ni_{81}Fe_{19}$
Q. . . . . quality factor
QD . . . . . quantum dots
QW . . . . . quantum well
RA. . . . . resistance-area
REU. . . . . Research Experiences for Undergraduates Program
RF. . . . . radio frequency
RF MEMS . . . . radio frequency microelectromechanical systems
RIE . . . . . reactive ion etch
RMS or rms. . root mean square
RNA . . . . . ribonucleic acid
RTA . . . . . rapid thermal anneal
RTD. . . . . resistance temperature device
RTD. . . . . resonant tunneling diodes
Ru. . . . . ruthenium
s . . . . . seconds
S . . . . . sulfur
SAMs . . . . . self-assembled monolayers
SAXS . . . . . small angle x-ray scattering
Sb . . . . . antimony
Sc . . . . . scandium
sccm . . . . . standard cubic centimeters per minute
$scCO_2$ . . . . . supercritical carbon dioxide
SDS . . . . . sodium dodecyl sulfate
Se . . . . . selenium
sec . . . . . seconds
SEM. . . . . scanning electron microscopy/microscope
SERS . . . . . surface enhanced Raman spectroscopy
SF_6 . . . . . sulfur hexafluoride
Si. . . . . silicon
Si_3N_4. . . . . silicon nitride
SiC . . . . . silicon carbide
SiH_4 . . . . . silane
SiN. . . . . silicon nitride
SiO_2 . . . . . silicon dioxide, silica
Sn . . . . . tin
SnO_2. . . . . tin oxide
$SnSe_2$ . . . . . tin selenide or stannous selenide
SOI. . . . . silicon-on-insulator
SPR . . . . . surface plasmon resonance
SQUID . . . . . superconducting quantum interference device
Sr_2RuO_4. . . . . strontium ruthenate
SRC . . . . . Semiconductor Research Corporation
$SrTiO_3$ . . . . . strontium titanate
STEM. . . . . scanning transmission electron microscopy/microscope
t-BOC. . . . . *tert*-butoxycarbonyl
Ta . . . . . tantalum
Ta_2O_5 . . . . . tantalum pentoxide
TaN . . . . . tantalum nitride
TAO_x. . . . . tantalum oxide
Te . . . . . tellurium
TEM . . . . . transmission electron microscopy/microscope
TFET . . . . . tunnel field effect transistor
TFT . . . . . thin-film transistor
Tg . . . . . glass transition temperature
THz . . . . . terahertz
Ti . . . . . titanium
TiN . . . . . titanium nitride
TiO_2. . . . . titanium dioxide
TM. . . . . transverse magnetic
TXM . . . . . transmission x-ray microscopy
UHV . . . . . ultra-high vacuum
USDA. . . . . United States Department of Agriculture
UV. . . . . ultraviolet
UV-Vis . . . . . ultraviolet-visible
V. . . . . vanadium
V. . . . . voltage
vdW . . . . . van der Waals
VLS . . . . . vapor-liquid-solid
VRMs. . . . . voltage regulator modules
VSM. . . . . vibrating sample magnetometry
W . . . . . tungsten
WDM. . . . . wavelength-division multiplexing
WSe_2 . . . . . tungsten diselenide
XeF_2. . . . . xenon difluoride
XPM . . . . . cross-phase modulation
XPS . . . . . x-ray photoelectron spectroscopy
XRD. . . . . x-ray diffraction
XRR. . . . . x-ray reflectivity
ZMW . . . . . zero-mode waveguide
Zn . . . . . zinc
$ZnCl_2$ . . . . . zinc chloride
ZnO . . . . . zinc oxide
ZnO:Al . . . . . zinc aluminum oxide
ZnS . . . . . zinc sulfide or zinc-blende
Zr . . . . . zirconium
ZrO_2 . . . . . zirconium dioxide
ZTO. . . . . zinc tin oxide

Cornell NanoScale Science & Technology Facility (CNF)

2021-2022 Research Accomplishments

Microfluidic Handling of DNA for Spatial Genome Research

2022 CNF REU Intern: Eryka Kairo

Intern Affiliation: Physics Department, Seton Hall University

CNF REU Principal Investigator: Dr. Warren Zipfel, Meinig School of Biomedical Engineering, Cornell
CNF REU Mentor: Jack Crowley, Meinig School of Biomedical Engineering, Cornell University
CNF REU Project and Primary Source(s) of Research Funding: 2022 Cornell NanoScale Science & Technology Facility Research Experiences for Undergraduates (CNF REU) Program via the National Science Foundation under Grant No. NNCI-2025233
Contact: eryka.kairo@gmail.com, wrz2@cornell.edu, jcc453@cornell.edu
Website: https://cnf.cornell.edu/education/reu/2022
Primary CNF Tools Used: ABM Contact Aligner, Class II Photoresist Room, P7 Profilometer

Abstract:

Nuclear envelope invaginations that contain endoplasmic reticulum (ER), mitochondria and other cytosolic organelles have been linked to cancer, and can be used as tumor biomarkers. To gain a better understanding of how this occurs, the organization and composition of chromatin near nuclear invaginations needs to be examined. Assuming that these invaginations are involved in cell signaling and transcription, they may control disease-specific phenotypes through spatial gene regulation.

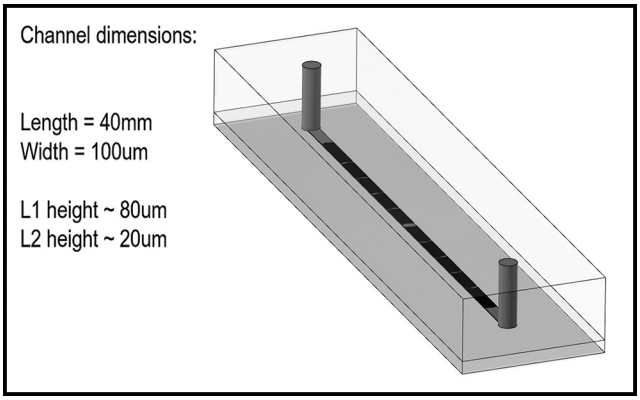

Figure 1: Schematic design of microfluidic device.

To explore spatial control of gene regulation, we have developed a method that enables chromatin isolation from small (femtoliter scale) targeted volumes within the nucleus. The method, we call Femto-seq, uses localized nonlinear excitation to photo-biotinylate small nuclear volumes so that chromatin can be obtained using affinity purification, and then sequenced. To improve the throughput and efficacy of Femto-seq, here we demonstrate a microfluidic purification device utilizing a single fluidic channel with a functionalized surface and mixing elements that improve sample yield and the level of purification. When validated and employed, our microfluidic devices will enhance the capacity of Femto-seq to elucidate spatial gene regulation patterns associated with nuclear invaginations.

The device was fabricated using multilayer SU-8 photolithography. Herringbone structures were added along the fluidic channel to encourage "chaos" in flow patterns of our sample through the channel, increasing the capture efficiency and improve our purification yield. We utilized a negative resist and our design was cast into PDMS and bonded to a glass surface. Our device was characterized through fluorescence microscopy and biochemical assays to first, validate that a streptavidin-biotin complex is formed using a glass functionalization protocol, and then to optimize an elution protocol suitable for our device and quantify our yield and purity of biotinylated deoxyribonucleic acid (DNA).

Summary of Research:

Our project goal for this summer was to fabricate and optimize a microfluidic device that can immobilize biotinylated DNA. The device design was already determined by mentor Jack Crowley, which was a single fluidic channel that had added mixing elements called herringbones on the top of the channel, both embedded in a layer of polydimethylsiloxane (PDMS) as shown in Figure 1.

The PDMS is then binded onto a glass slide to close the channel. To achieve this goal, the project had three main parts. The first part was the wafer fabrication and the device construction, and our methodology for this part was to use multi-layer SU-8 soft photolithography because the design required the fluidic channel to be treated as one layer during photolithography, and the herringbones to be treated as another; the second part was to functionalize the device surface in order to immobilize streptavidin on to the glass substrate and take advantage of the very strong affinity between streptavidin and biotin; the final part was validation and characterization of the device, and to set up an engineering system to optimally operate the device.

The first portion of the project took the longest because we were in unfamiliar territory working with multi-layer photolithography — so there was a lot of trial and error. Issues arose when we weren't able to achieve proper contact between our silicon wafer and our photomasks, but by talking to Aaron Windsor and Chris Alpha from the CNF staff, we were able to gather some tips and tweak our fabrication process, which yielded better results.

Upon being able to consistently acquire usable channels from this process we were able to move on to the functionalizing portion of the project. This portion involved functionalizing fully constructed devices and validating the protocol worked as intended.

To do this we used fluorescent microscopy and flowed fluorescent biotin through functionalized devices, to image and search for bright sports which correlate to immobilzed biotin. We were able to see that we were immobilizing some biotin, so the next step was to set up an experiment to characterize our device. We chose to use DNA gel electrophoresis to do this as we are able to quantify the DNA bands in the agarose gel after the process, so we would be able to get quantitive data.

We set up the experiment by using DNA gel extraction on a DNA ladder to biotinylate a single length of DNA, and then flowing the ladder and the biotinylated DNA through our device and collecting the flow through. The flow through was run through the gel alongside some baseline samples to learn as much as we could about our device.

Conclusions and Final Steps:

Our next steps begin with completing an engineering system to operate the microfluidic chip. This includes setting up a system that adds an oscillatory washing step within the fluidic channel to increase our purification yield, and would also include adding washing and buffer steps. After this system has been set up, a DNA gel electrophoresis experiment can be run on the device flow-through to validate that biotinylated DNA can be captured using our microfluidic device design and the surface functionalization protocol used works as expected.

Once these have been validated the next step would be to quantify the devices performance, and compare the amount of cells needed to provide a sufficient DNA sample via Femto-seq, and determine the reduction of cells needed for this process from the beginning of the summer, which was 30,000 cells, to now. Next, elution steps to break the strepatavidin-biotin complex formed in this device should be tested and optimized.

The goal is to find a protocol that does minimal damage to the device itself to encourage longevity of the materials used. Part of this elution step would be to develop a flow-through collection protocol that leads to minimal loss of the DNA we worked so hard to affinity capture in the channel. Furthermore, ideally after the steps to optimize this device's function have been established, the system to control the device itself should become programmable, to make device operation as automatic as possible.

References:

[1] Ma, S., et al. 2018. Sci. Adv. 4(4).

[2] Stroock, A.D., et al. 2002. Science 295, 647-51.

A Nanotool for Phase Equilibrium and Water Potential Measurements in Living and Synthetic Systems

CNF Project Number: 1119-03

Principal Investigator(s): Abraham D. Stroock

User(s): Piyush Jain

Affiliation(s): Chemical Engineering, Cornell University

Primary Source(s) of Research Funding: National Science Foundation
Science and Technology Centers (STC);
Air Force Office of Scientific Research

Contact: abe.stroock@cornell.edu, pj248@cornell.edu

Primary CNF Tools Used: Zeta-Sizer

Abstract:

The multiphases water transport in unsaturated porous media has been investigated for a long period yet remains unknown fundamental questions for exploration. In this report, our group developed a nanotool, AquaDust, to measure the local water potential in both living and synthetic unsaturated porous media. In leaves, the disequilibrium in water potential between symplast and apoplast points out a large hydraulic resistance at the plasma membrane of mesophyll cells. In synthetic porous media, a water potential distribution of the wetting front in an imbibition process can enhance the understanding of the capillary properties and the dynamic of the process.

Summary of Research:

The mesophyll in leaves operates as an unsaturated porous medium, with vapor-filled spaces interspersed within a matrix that is wetted by the condensed liquid phase. The undersaturated state introduced a local coupling between phase equilibrium and transport processes in the two phases, and resulted in the strong global coupling of heat and mass transfer. The physic and mathematical model developed by Rockwell et al. shows the competition between these two phases in mesophyll through modeling in Figure 1 [1]. This model strengthened the understanding of the fundamental questions in transport processes, and open a new route for the experimental exploration in both living and synthetic systems.

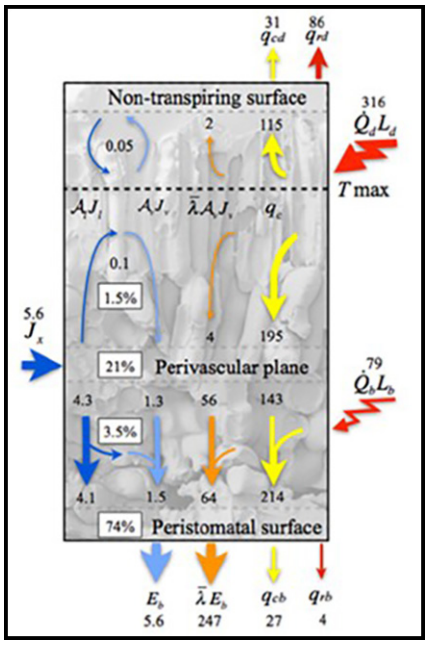

Figure 1: Model prediction of heat and mass flux within a transpiring leaf [1].

In a previous study by our group, a new hydrogel nanoreporter, AquaDust, was developed to report local water potential (Ψ) for *in planta* measurements [2]. Figure 2a shows the mechanism that the gel matrix responds to water potential by shrinking and swelling under dry and wet environments, respectively. The volumetric changes of the matrix will lead to the distance changes between donor and acceptor dyes. Accordingly, the emission spectrum via Förster Resonance Energy Transfer (FRET) between donor and acceptor dyes provides quantitative measurement of water potential in Figure 2b.

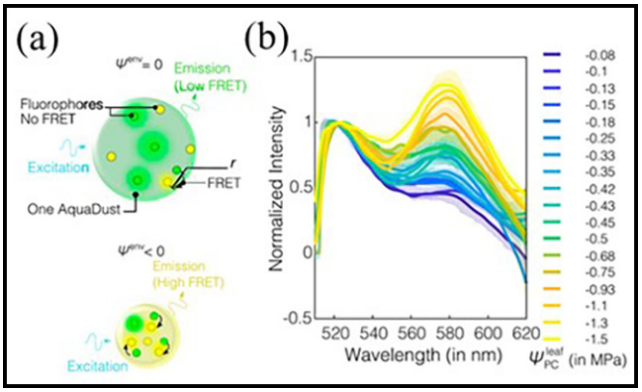

Figure 2: (a) Mechanism of AquaDust responses under wet and dry environments. (b) Spectra of AquaDust in maize leaves at different water potentials. (Jain, et al., 2021.)

The *in planta* measurement of AquaDust provided local water potential in mesophyll. The gradient in water potential of through-thickness section of a maize leaf are depicted in Figure 3a. The inset highlights the disequilibrium in water potential between the symplast

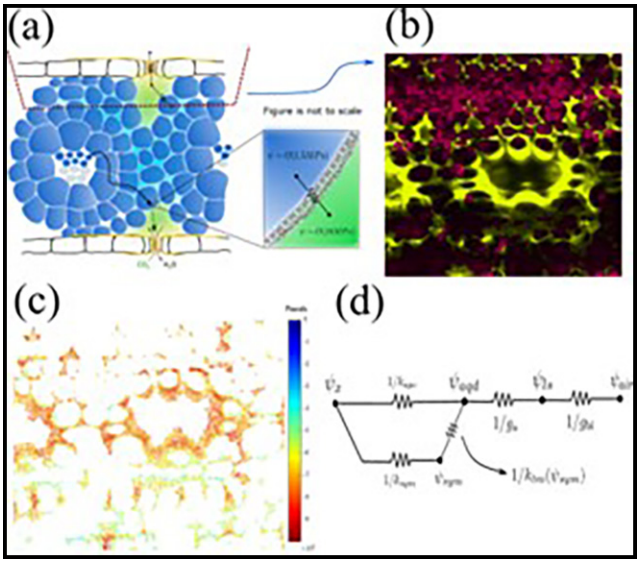

Figure 3: (a) Through-thickness section of a maize leaf depicting the gradient in water potential from xylem to stomates. (b) Confocal microscope image of a horizontal section in a maize leaf. (c) Spatial distribution water potential for the location shown in (b). (d) A model of hydraulic resistances in a maize leaf.

and apoplast. In Figure 3b, the confocal image shows turgid mesophyll cells, with chloroplasts (pink) pushing against cell boundaries (in turgid state), having their cell walls coated with AquaDust (yellow). In Figure 3c, the AquaDust response shows that water potentials in the vapor phase as low as -9 MPa are observed adjacent to turgid cells.

To explain this disequilibrium, we invoke a large hydraulic resistance at the plasma membrane of mesophyll cells, and a model of hydraulic resistances in a maize leaf is shown in Figure 3d. The xylem (Ψ_x) and AquaDust/mesophyll-apoplast (Ψ_{AQD}) nodes are connected by an apoplasmic resistance ($1/k_{apo}$) in parallel with a transmembrane resistance ($1/k_{tm}(\Psi_{sym})$), with the latter assumed to be a variable function of the symplastic water potential; this 'outside-xylem' part of the network is in series with the stomatal resistance ($1/g_s$) and boundary-layer resistance ($1/g_{bl}$).

In the synthetic system, we developed an experimental method to measure water potential distribution in synthetic porous media. First, the relationship between relative FRET efficiency and water potential in Figure 4a was built through measuring relative FRET efficiency under control relative humidity. The relative humidities were converted into water potentials through Kelvin equation [3] and the results were anastomotic with the theory presented in Jain, et al. [2].

Then, an imbibition process was performed in an AquaDust-filled cellulose acetate filter paper to investigate water potential distribution in capillary-driven process. The results before and after imbibition are shown in Figure 4b-c. Within the imbibition area, lower relative FRET efficiency and transition area of wetting front are observed. The detailed water potential

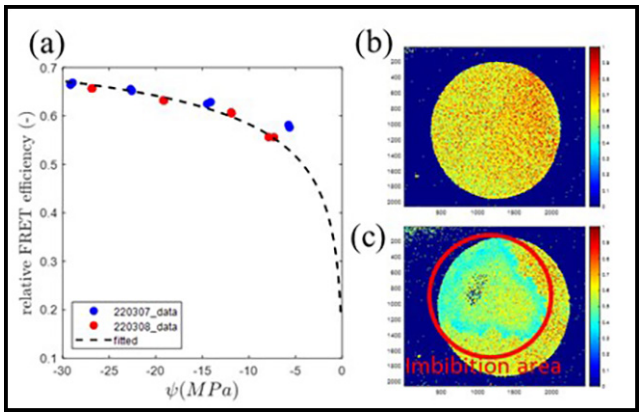

Figure 4: (a) The relative FRET efficiency to water potential data. Dashed line is the theoretical prediction as obtained from the Flory–Rehner theory and dipole-plane FRET model presented in Jain, et al., 2021. (b-c) The relative FRET efficiency (b) before and (c) after imbibition.

distribution in synthetic porous media can enable investigations on capillary properties and dynamic processes.

Conclusions and Next Steps:

AquaDust can provide an outstanding and reliable tool to measure water potential in both living and synthetic systems. For living system, water potential measured by AquaDust shows the disequilibrium in water potential between the symplast and apoplast, indicating a large hydraulic resistance at the plasma membrane of mesophyll cells. In synthetic system, the transition area of water potential in an imbibition process can be clearly recorded by AquaDust.

The next steps of *in planta* experiments presented in Figure 3 should include understanding the molecular mechanism regulating outside-xylem hydraulic conductance (K_{ox}) using tools from genetics such as aquaporin mutants, transcriptomic analysis and treatments using abscisic acid (ABA) and blue light responses [4]. The next steps of synthetic system will be to investigate the coupled heat and mass transport in the thermally loaded unsaturated porous medium by measuring the spatiotemporal water potential.

References:

[1] Rockwell, F.E., N.M. Holbrook, and A.D. Stroock, The competition between liquid and vapor transport in transpiring leaves. Plant Physiol, 2014. 164(4): p. 1741-58.

[2] Jain, P., et al., A minimally disruptive method for measuring water potential in planta using hydrogel nanoreporters. Proc Natl Acad Sci U S A, 2021. 118(23).

[3] Skinner, L. and J. Sambles, The Kelvin equation—a review. Journal of Aerosol Science, 1972. 3(3): p. 199-210.

[4] Shatil-Cohen, A., Z. Attia, and M. Moshelion, Bundle-sheath cell regulation of xylem-mesophyll water transport via aquaporins under drought stress: a target of xylem-borne ABA? The Plant Journal, 2011. 67(1): p. 72-80.

Development of a Biomembrane Platform for the Study of Virus Infection

CNF Project Number: 1686-08
Principal Investigator(s): Susan Daniel
User(s): Zhongmou Chao

Affiliation(s): Smith School of Chemical and Biomolecular Engineering, Cornell University
Primary Source(s) of Research Funding: Defense Threat Reduction Agency
Contact: sd386@cornell.edu, zc83@cornell.edu
Primary CNF Tools Used: Heidelberg Mask Writer - DWL2000, ABM Contact Aligner, Odd-Hour E-beam Evaporator, Oxford PECVD, PT 740 Etcher, DISCO Dicing Saw, Bruker AFM

Abstract:

As a "label-free" alternative to optical sensing, electrical sensing represents a more feasible, reproducible, and scalable detection method [1,2]. Among various electrical sensing techniques, the non-invasive electrochemical impedance spectroscopy (EIS) technique is especially suitable for accurately quantifying the bio-recognition events occurring at a variety of biointerfaces, such as bacterial, viral, cellular and synthetic lipid membranes [3,4]. Our group aims to design a microelectrode system that will support the self-assemble of supported lipid bilayers (SLBs) on the electrode surfaces, and their electrical properties (resistance, capacitance) can be extracted by applying an alternating voltage and recording the current response [4-7]. Since the electrode dimensions and the local environment are readily controlled via photolithography, this system gives us a edge to easily mimic and manipulate the local environment to support the assembly of various SLBs of interest. Future work will focus on the incorporation of the microfluidic system into the microelectrode system.

Summary of Research:

To fabricate the microelectrode devices, photomasks were created using the Heidelberg Mask Writer - DWL2000, and used with the ABM contact aligner to pattern photoresist that was spun onto a fused silica wafer. A first layer of gold contact pad was patterned following the developing of SPR220 3.0 photoresist and the deposition of Au thin film. A thin layer of SiO_2 insulating layer is then deposited directly on top of the Au contact pad using Oxford PECVD.

Electrode area was then patterned on SiO_2 following the spin-coating and developing of the second layer of photoresist. PT-740 etched was then used to etch the exposed SiO_2 until Au contact pad has been exposed. A conductive polymer, PEDOT:PSS was then spun over the fused silica wafer followed by the deposition of a germanium (Ge) hard mask (odd-hour evaporator). A third layer of photolithography was performed on a layer of negative photoresist spun on top of Ge, where all resists above Ge at areas outside active electrode surface have been developed.

Unprotected Ge and PEDOT:PSS underneath were then etched using PT-740. Ge on top of active electrode area was then etched in water bath overnight.

Once the microelectrode device was fabricated, a PDMS well was stamped directly on top to create a reservoir for SLB self-assembling and allow EIS measurement.

References:

[1] Berggren, M., and A. Richter-Dahlfors. "Organic bioelectronics." Advanced Materials 19.20 (2007): 3201-3213.

[2] Chalklen, T., Q. Jing, and S. Kar-Narayan. "Biosensors based on mechanical and electrical detection techniques." Sensors 20.19 (2020): 5605.

[3] Magar, H.S., R.Y.A. Hassan, and A.Mulchandani. "Electrochemical Impedance Spectroscopy (EIS): Principles, Construction, and Biosensing Applications." Sensors 21.19 (2021): 6578.

[4] Lisdat, F., and D. Schäfer. "The use of electrochemical impedance spectroscopy for biosensing." Analytical and Bioanalytical Chemistry 391.5 (2008): 1555-1567.

[5] Tang, T., et al. "Functional infectious nanoparticle detector: Finding viruses by detecting their host entry functions using organic bioelectronic devices." ACS Nano 15.11 (2021) 18142-52.

[6] B.E. Naser, et al. "Detection of Ganglioside-Specific Toxin Binding with Biomembrane-Based Bioelectronic Sensors." ACS Applied Bio Materials 4.11 (2021): 7942-7950.

[7] Pappa, A., et al. "Optical and electronic ion channel monitoring from native human membranes." ACS Nano 14.10 (2020): 12538-12545.

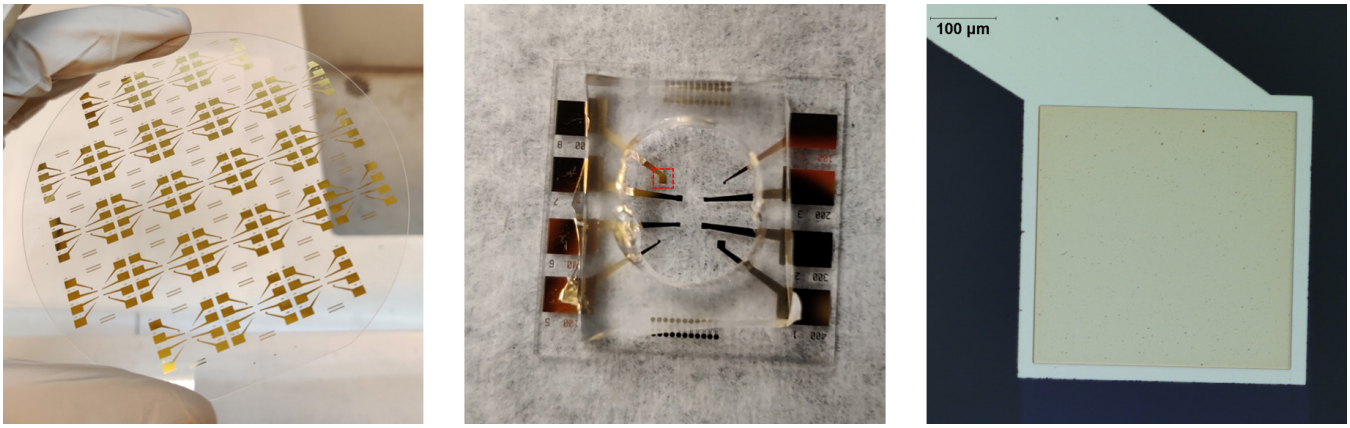

Figure 1: Microelectrode devices on a fused silica wafer (left); PDMS well stamped on a single device to enable self-assembling of SLB and EIS measurement (middle) and zoomed in figure to show PEDOT:PSS electrode on Au contact pad (right).

Resonator Nanophotonic Standing-Wave Array Trap for Single-Molecule Measurements

CNF Project Number: 1738-08

Principal Investigator(s): Michelle D. Wang

User(s): Yifeng Hong

Affiliation(s): a) Department of Electrical and Computer Engineering, Cornell University; b) Department of Physics, Cornell University; c) Howard Hughes Medical Institute

Primary Source(s) of Research Funding: Howard Hughes Medical Institute

Contact: mdw17@cornell.edu, yh874@cornell.edu

Website: http://wanglab.lassp.cornell.edu/

Primary CNF Tools Used: ASML Deep Ultraviolet Stepper, Oxford 100 Plasma Etcher, Oxford 81 Etcher, Oxford 82 Etcher, Unaxis 770 Deep Si Etcher, Heidelberg Mask Writer - DWL2000, SÜSS MA6-BA6 Contact Aligner, Gamma Automatic Coat-Develop Tool, LPCVD Nitride - B4 furnace, Wet/Dry Oxide - B2 furnace, AJA Sputter Deposition, Oxford PECVD, SC4500 Odd-Hour Evaporator, SC4500 Even-Hour Evaporator, Zeiss Supra SEM, Zeiss Ultra SEM

Abstract:

Optical trapping force has been the greatest limitation of the nanophototic tweezer platform. To overcome this obstacle, we designed and fabricated a resonator nanophotonic standing-wave trap (RnSWAT) device that supports significant force enhancement. As a result, the maximum force is no longer a limiting factor for standard single-molecule experiments, such as DNA stretching and unzipping. We experimentally demonstrated bound protein localization through unzipping a DNA molecule on the RnSWAT and achieved a maximum trapping force of 20 pN with sub-pN and sub-nm resolution. The RnSWAT is the first reported nanophotonic platform realizing standard table top single-molecule measurements.

Summary of Research:

Our lab developed the nanophotonic standing-wave array trap (nSWAT) device. The nSWAT makes use of two counter-propagating modes to form multiple trapping spots along waveguides [1-7]. The first demonstration of the nSWAT device used a silicon (Si) waveguide (Figure 1) [1]. However, due to the strong non-linear absorption, the laser power cannot be efficiently delivered to the Si waveguide at the trapping region.

To resolve this problem, we developed an Si_3N_4 device coupled with 1064 nm laser for the second generation of the nSWAT (Figure 1) [2]. To generate more force, we designed the waveguide path so that the force would be doubled at the trapping region, which we termed as the double-force nSWAT (Figure 1) [3]. However, these nSWAT devices still could not achieve sufficient force for high-force single-molecule experiments, which typically require at least 15 pN.

Last year, our lab finalized the latest generation of nSWAT. We can now generate ~ 20 pN force using a resonator waveguide loop (Figure 1) [7]. The resonator nSWAT wavegudies were patterned with deep ultraviolet

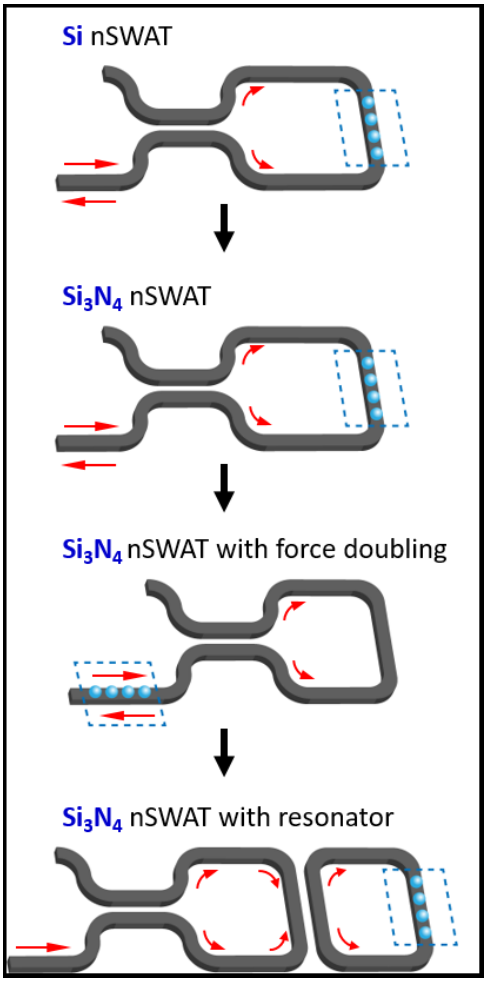

Figure 1: Development progression of the nSWAT platform. Gray structures denote waveguides, and red arrows indicate light propagation [7].

(DUV) lithography. Multiple heaters were deposited on the waveguides (isolated with SiO_2 protection layers) to realize the control of the standing-wave position as well as the resonance condition.

A 15-μm tall and 100-μm wide SU-8 flow channel was patterned to allow the biological sample injection to the waveguides at the trapping region (Figure 2). The resonator nSWAT was then used for single-molecule measurements.

We demonstrated simultaneous unzipping of five DNA molecules [7]. The capability of unzipping through DNA molecules opened up the opportunity of more advanced single-molecule measurements, such as protein localization. We also demonstrated high-throughput ZraI/dCAS9 localization at base-pair resolution with the DNA unzipping mapper technique on the resonator nSWAT [7]. We believe the resonator nSWAT can be a fundamental platform for a broader range of single-molecule applications.

Figure 2: SEM of the fluid pool containing waveguides of the trapping region. The scattering gratings of the four light intensity samplers from the two resonators are clearly visible. Scale bar is 20 μm [7].

References:

[1] M. Soltani, J. Lin, R. A. Forties, J. T. Inman, S. N. Saraf, R. M. Fulbright, M. Lipson, and M. D. Wang, "Nanophotonic trapping for precise manipulation of biomolecular arrays" Nature Nanotechnology 9(6), 448-452 (2014).

[2] F. Ye, R. P. Badman, J. T. Inman, M. Soltani, J. L. Killian, and M. D. Wang, "Biocompatible and high stiffness nanophotonic trap array for precise and versatile manipulation" Nano Letters 16(10), 6661-6667 (2016).

[3] F. Ye, M. Soltani, J. T. Inman, and M. D. Wang, "Tunable nanophotonic array traps with enhanced force and stability" Optics Express 25 (7) 7907-7918 (2017).

[4] J. E. Baker, R. P. Badman, and M. D. Wang, "Nanophotonic trapping: precise manipulation and measurement of biomolecular arrays" WIREs Nanomed Nanobiotechnol. e1477 (2017).

[5] R. Badman, F. Ye, W. Caravan, and M. D. Wang, "High Trap Stiffness Microcylinders for Nanophotonic Trapping" ACS Appl. Mater. Interfaces 11(28), 25074-25080 (2019).

[6] R. Badman, F. Ye, and M. D. Wang, "Towards biological applications of nanophotonic tweezers", Current Opinion in Chemical Biology, 53, 158-166 (2019).

[7] F. Ye, J. T. Inman, Y. Hong, P. M. Hall, M. D. Wang, Resonator nanophotonic standing-wave array trap for single-molecule manipulation and measurement. Nat. Commun. 13, 77 (2022).

Building Microfluidics Devices to Study Zinc Metal Homeostasis in *E. Coli*

CNF Project Number: 1844-09
Principal Investigator(s): Peng Chen
User(s): Felix Alfonso

Affiliation(s): Department of Chemistry and Chemical Biology, Cornell University
Primary Source(s) of Research Funding: National Institutes of Health, National Institute of General Medical Sciences
Contact: pc252@cornelll.edu, fsa33@cornell.edu
Website: http://chen.chem.cornell.edu/
Primary CNF Tools Used: Heidelberg Mask Writer - DWL2000, SÜSS MA6-BA6 Contact Aligner, Oxford Cobra ICP Etcher, Plasma-Therm Deep Silicon Etcher, P7 Profilometer

Abstract:

Microbial life has evolved a set of molecular tools to import the necessary nutrients for survival from their environment and efflux the excess to avoid toxicity. The aim of this study is to elucidate the role individual bacterial cells play in achieving metal homeostasis at the community level. Hence, we constructed a custom-made microfluidic device for the controlled growth of *Escherichia coli* (*E. coli*) colonies in microchambers. The confinement of the cells is achieved by matching the height of the microchambers with the diameter of the *E. coli* cells. Using molecular biology, *E. coli* strains were constructed with fluorescent protein reporters to quantify the gene expression of the influx and efflux ion channels specific to zinc. The dynamic environmental control in microfluidic devices allows us to probe how the community of bacteria achieves zinc metal homeostasis.

Summary of Research:

Zinc is an essential micronutrient for all living organisms [1]. It plays a vital role in protein folding, catalysis, and gene regulation [2,3]. Zinc deficiency or excess is associated with drastic changes in the gut microbiome, which results in poor health [4,5]. Microbial life has evolved a set of molecular tools to import nutrients from their environment and efflux excess nutrients to avoid toxicity. To regulate the efflux pumps, bacterial cells control the transcription of the protein pumps by using metal-responsive transcription regulators that sense the cellular concentration of metal ions to achieve a state of metal homeostasis.

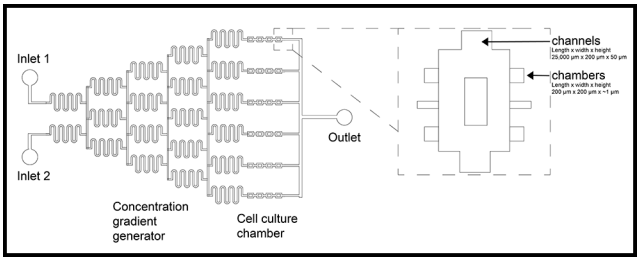

Figure 1: Schematic of the microfluidic device design of the gradient generator, microchannels, and microchambers with the desired dimensions.

The aim of this project is to quantify the management of Zn^{2+} in a microbiome and determine the role individual cells play in achieving metal homeostasis as a community. As a model system, *Escherichia coli* (*E. coli*) will be used to study the community-derived zinc metal regulation. *E. coli* cell's motility and poor adherence to a substrate make it difficult to conduct imaging studies with long time scales. Microfluidics technology is a widely accepted method to study bacterial communities in a controlled environment [6]. A microfluidic platform permits tight control of the nutrients influx and has been successfully used for long-timescale imaging studies [7].

The microfluidic device used in this study consist of three necessary components: a gradient generator, channels, and microchambers (Figure 1). The depth of the microchamber has been chosen to match the diameter of an *E. coli* cell (~1μm) thus facilitating the confinement of the colonies [8]. The microfluidics devices are constructed using well-established silicon nanofabrication technology.

The fabrication scheme is summarized in Figure 2. Briefly, silicon wafers were cleaned with piranha solution from the Hamatech wafer processor. Afterward, they

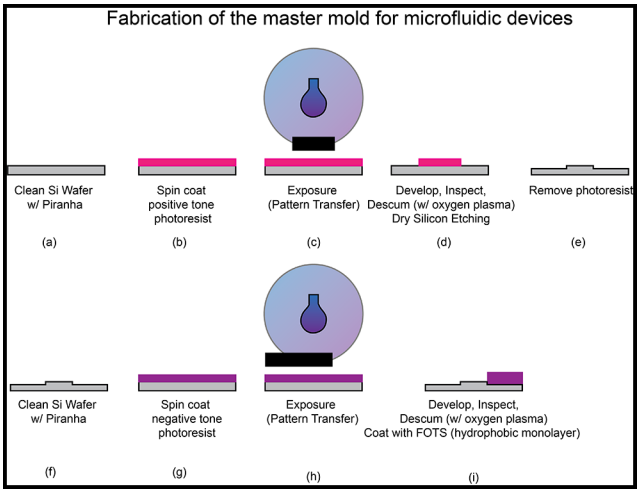

Figure 2: Fabrication of microfluidic devices combining dry etching to construct the chambers and SU-8 lithography to construct the channels.

were spin-coated with photoresists. The photoresist was removed 2 mm from the edge of the wafer using the edge bead removal system. The substrate was patterned using a pre-patterned photomask made using the Heidelberg Mask Writer - DWL2000. The SÜSS MA6-BA6 contact aligner was used for the UV light exposure of the wafer. After developing the wafer and cleaning it with a brief oxygen plasma. The chamber was created by etching about ~ 1 µm of silicon using the Oxford Cobra ICP Etcher. The photoresist was removed using the photoresist stripper bath. The height of the chamber was measured using a profilometer. The channels were constructed using SU-8 lithography.

Briefly, SU-8 was spin-coated onto the substrate and pattern using the SÜSS MA6-BA6 contact aligner. The SU-8 was cured on a hot plate at 95°C. The unpolymerized SU-8 was removed with the developer and the resulting structure was hard baked for 10 minutes at 200°C.

The final step was coating the silicon mold with a hydrophobic molecular monolayer such as tridecafluoro-1,1,2,2-tetrahydrooctyl trichlorosilane (FOTS) to facilitate PDMS removal. After casting PDMS on the silicon mold, the microfluidic devices were bonded to coverslips and inspected using a microscope.

The cells were loaded into the chambers and imaged using a microscope equipped with the appropriate laser line and filters. The composite image shown in Figure 3 shows an example of a chamber loaded with *E. coli*. The cells colored in green are bacterial cells expressing the zinc efflux channels while the cell colored in red indicates the expression of the zinc influx channels.

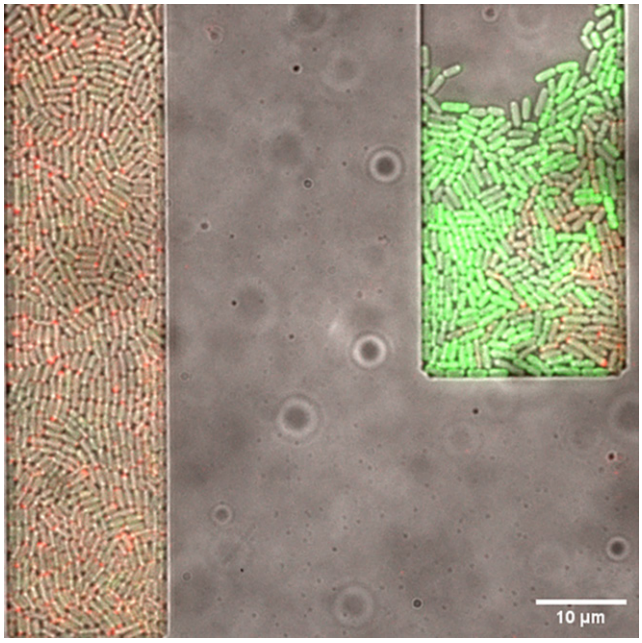

Figure 3: A composite image of E. coli *cells residing in the microchambers expressing influx ion channels (red) and efflux ion channels (green).*

References:

[1] R. R. Robert, B. Saper, Zinc: An Essential Micronutrient. Am. Fam. Physician. 79, 768 (2009).

[2] S. Tan, D. Guschin, A. Davalos, Y.-L. Lee, A. W. Snowden, Y. Jouvenot, H. S. Zhang, K. Howes, A. R. McNamara, A. Lai, C. Ullman, L. Reynolds, M. Moore, M. Isalan, L.-P. Berg, B. Campos, H. Qi, S. K. Spratt, C. C. Case, C. O. Pabo, J. Campisi, P. D. Gregory, Zinc-finger protein-targeted gene regulation: genome wide single-gene specificity. Proc. Natl. Acad. Sci. U. S. A. 100, 11997-12002 (2003).

[3] C. Andreini, I. Bertini, in Encyclopedia of Metalloproteins (Springer, New York, NY, 2013), pp. 2549-2554.

[4] S. R. Gordon, S. Vaishnava, Zinc supplementation modulates T helper 17 cells via its effect on gut microbiome. The Journal of Immunology. 204, 83.18-83.18 (2020).

[5] O. Koren, E. Tako, Chronic Dietary Zinc Deficiency Alters Gut Microbiota Composition and Function. Proc. AMIA Annu. Fall Symp. 61, 16 (2020).

[6] F. Wu, C. Dekker, Nanofabricated structures and microfluidic devices for bacteria: from techniques to biology. Chem. Soc. Rev. 45, 268-280 (2016).

[7] D. Binder, C. Probst, A. Grünberger, F. Hilgers, A. Loeschcke, K.-E. Jaeger, D. Kohlheyer, T. Drepper, Comparative Single-Cell Analysis of Different *E. coli* Expression Systems during Microfluidic Cultivation. PLoS One. 11, e0160711 (2016).

[8] A. Groisman, C. Lobo, H. Cho, J. K. Campbell, Y. S. Dufour, A. M. Stevens, A. Levchenko, A microfluidic chemostat for experiments with bacterial and yeast cells. Nat. Methods. 2, 685-689 (2005).

Biomechanics of Bacteria

CNF Project Number: 1970-10

Principal Investigator(s): Christopher J. Hernandez

User(s): Christine Harper, Junsung Lee, Ellen van Wjingaarden, C.J. Hernandez

Affiliation(s): Sibley School of Mechanical and Aerospace Engineering, Biomedical Engineering Department; Cornell University

Primary Source(s) of Research Funding: NSF 2055214, 2135586, 2125491

Contact: cjh275@cornell.edu, ceh272@cornell.edu, jl3939@cornell.edu, ewv8@cornell.edu

Website: hernandezresearch.com

Primary CNF Tools Used: Deep UV Photolithography, AJA Sputter Deposition, ASML, PT 770, Oxford 100, MOS Clean Anneal

Abstract:

In this project we seek to understand the biomechanical properties of individual bacteria as well as bacterial mechanobiology (the response of living bacteria to mechanical stimuli). We have two goals in this project: 1) to understand how physical forces influence bacterial resistance and tolerance to antibiotics; and 2) to understand how to embed and maintain viable bacteria within rigid materials, the so-called "engineered living material."

Summary of Research:

We have designed microfluidic systems that allow us to apply mechanical loads to individual bacteria and observe the cellular response. We manufacture our devices on silica glass wafers using DUV photolithography to achieve nanoscale features (250 nm smallest dimension, Figure 1). We have demonstrated that mechanical stimuli applied to individual bacteria interrupt the assembly of the tripartite efflux pump responsible for removing copper and silver from the bacteria, CusCBA [1].

We recently demonstrated that mechanical stresses within the bacterial cell envelope also interrupt the function of the MacAB-TolC efflux pump which is used by bacteria remove aminoglycoside antibiotics. Additionally, we have developed mechanical modelling methods that allow us to use the results of our experiments as a measure of the elastic modulus of the bacterial cell envelope [2].

In our most recent work, we have demonstrated that mechanical stress within the cell envelope of the pathogen *Vibrio cholerae* stimulates cell wall repair mechanisms through the VxrAB two-component regulatory system [3].

This finding is exciting in that it suggests that mechanical stress and strain regulate maintenance of the bacterial cell envelope, which is the primary load carrying component of bacteria and the primary target of bacteriocidal antibiotics.

We were recently awarded two grants from the National Science Foundation to explore methods of populating rigid materials with living bacteria and the effects of mechanical stimuli on bacterial biomineralization.

References:

[1] Genova, L.A., Roberts, M.F., Wong, Y-C, Harper, C.E., Santiago, A.G., Fu, B., Srivastava, A., Jung, W., Kreminski, L., Mao, X., Sun, X., Yang, F., Hui, C-Y, Chen, P, Hernandez, C.J.. (2019) "Mechanical Stress Compromises Bacterial Toxin Efflux." Proc Natl Acad Sci U S A. 116 (51) 25462-25467, https://www.pnas.org/content/early/2019/11/25/1909562116.

[2] Lee, J., Harper, C.E., Zhang, W., Ramsukh, M., Bouklas, N., Chen, P., Hernandez, C.J. (2022) "Determining the Young's Modulus of the Bacterial Cell Envelope Using Microfluidic-based Extrusion Loading." Submitted.

[3] Harper, C.E., Zhang, W., Shin, J., van Wjingaarden, E., Chou, E., Lee, J., Wang, Z., Dörr, T., Chen, P., Hernandez, C.J. (2023) "Mechanical stimuli activate gene expression for bacterial cell-wall synthesis." In preparation.

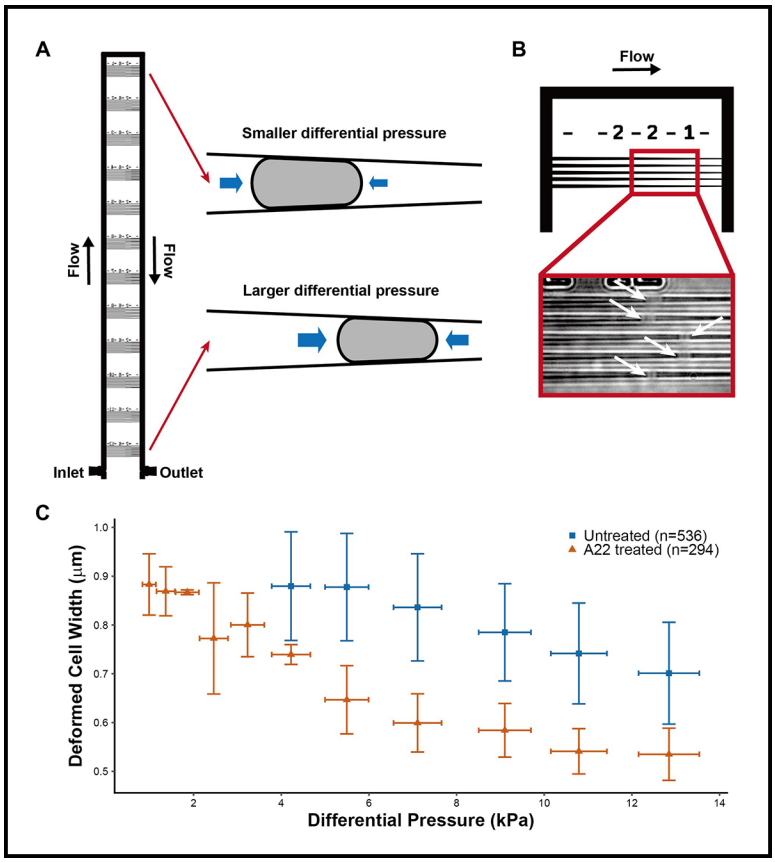

Figure 1: (A) The microfluidic device is shown. Bacteria in liquid media flow through the large bypass channel or become trapped by fluid pressure within the nanoscale tapered channels. The tapered channels are in sets of five, each set providing a different magnitude of differential pressure. (B) E. coli *trapped within the tapered channels are shown. (C) The results of an experiment in which* E. coli *are placed within the device untreated or after treatment with the small molecule A22 that depolymerizes the structural protein MreB, resulting in a less stiff cell as seen from the smaller cell width at each applied differential pressure.*

Design and Application of Microfluidic Devices to Study Cell Migration in Confined Environments

CNF Project Number: 2065-11

Principal Investigator(s): Jan Lammerding

User(s): Richa Agrawal, Maggie Elpers, Julie Heffler

Affiliation(s): Meinig School of Biomedical Engineering, CNF, Weill Institute; Cornell University

Primary Source(s) of Research Funding: National Institutes of Health award R01 HL082792, National Institutes of Health award R01 GM137605, National Institutes of Health award 1U54 CA210184

Contact: jan.lammerding@cornell.edu, ra664@cornell.edu, mae228@cornell.edu, jh2347@cornell.edu

Website: http://lammerding.wicmb.cornell.edu/

Primary CNF Tools Used: PT 770 Deep Silicon Etcher, Oxford Cobra Etcher, Heidelberg Mask Writer - DWL2000, SÜSS MA6 Contact Aligner, Anatech SCE-110-RF Resist Stripper, P-7 Profilometer, MVD 100, SU-8 Lithography Room (Spinners, Hot Plates, etc.)

Abstract:

The ability of cells to migrate through tissues is an essential factor during development, tissue homeostasis, and immune cell mobility. At the same time, it enables cancer cells to invade surrounding tissues and metastasize. We have created microfluidic devices that mimic the narrow, heterogeneous interstitial spaces and that can be used to study nuclear mechanobiology during confined migration. Using these devices in combination with fluorescent imaging, we have developed a method to assess the confined migration fitness of varying cell types.

Research Summary:

During *in vivo* migration, cells such as immune cells, fibroblasts, or metastatic tumor cells traverse interstitial spaces as small as 1-2 μm in diameter. This 'confined migration' requires the deformation not only of the soft cell body but also the rate-limiting step of deforming the large (5-10 μm diameter) and relatively rigid nucleus [1]. To study these processes in more detail, we have previously designed and fabricated polydimethyl siloxane (PDMS) microfluidic devices to model the tight three-dimensional constrictions that metastatic cancer cells may encounter during the metastatic process [2]. These devices support a wide range of cell lines and enable high-quality fluorescence imaging of nuclear lamina bucking, chromatin strain, DNA damage and nuclear rupture/blebbing and repair [2-4]. However, these devices require time-consuming single-cell analysis, do not fully mimic the heterogeneously confining nature of interstitial spaces, and do not allow use of sufficient cell numbers for biological and genomic analyses of cells that have migrated through the confined spaces due to their relatively small constriction areas (Figure 1).

To overcome these limitations, we have designed novel migration devices that mimic the intermittent confinement of interstitial environments using a precisely controlled but heterogeneous "field of pillars" with variable spacing [5] (Figures 1,2). We have created two different geometries of these devices optimized for (1) rapid, easy assessment of migratory fitness as a function of distance traveled, and (2) collection of cells that have successfully completed confined migration through precisely defined constrictions.

One type of device (Figure 2a) features a large constriction area that is compatible with time-lapse microscopy and also enables assessment of migratory fitness from single images captured on multiple consecutive days (Figure 3). Another device design (Figure 2b) features a shorter pillared distance (i.e., fewer constrictions) and is well suited for easy collection of large numbers of cells following confined migration. In ongoing studies, we are combining these devices with the use of the LEGO-optical barcoding system, which utilizes combinations of red, green, and blue fluorescent markers to monitor individual cells based on their distinguishable and heritable colors. This enables us to track cells and their progeny over days and weeks and to quantify the varying abilities of different cells to perform confined migration and to tolerate the associated physical stress. This experimental pipeline presents a high-throughput method for observing the short- and longer-term effects

of mechanically induced nuclear deformation and rupture on cancer cell function and survival.

In order to microfabricate the constriction layer of these designs, we etch silicon using hydrogen bromide in the Oxford Cobra etcher, which has proven to be a highly efficient, reliable method to achieve vertical sidewalls necessary for PDMS devices (Figure 4). We have found this to be advantageous over other etching methods or SU-8 lithography because it provides sufficient resolution of the fine (1 µm) features, and is more reliable and practical than using the photonics etch on the Unaxis 770 and seasoning/re-seasoning the chamber. We continue to use SU-8 photolithography for rapid prototyping and versions of the device which do not require very closely spaced features. Eventually, we will transition this process to a stepper, which will enable us to create "taller" constrictions to serve as a vertically "unconfined control" (>10 µm), which cannot currently be performed using HBr etching. Taken together, these examples illustrate new uses of the available nanofabrication technologies to create improved *in vitro* models to study cancer cell migration.

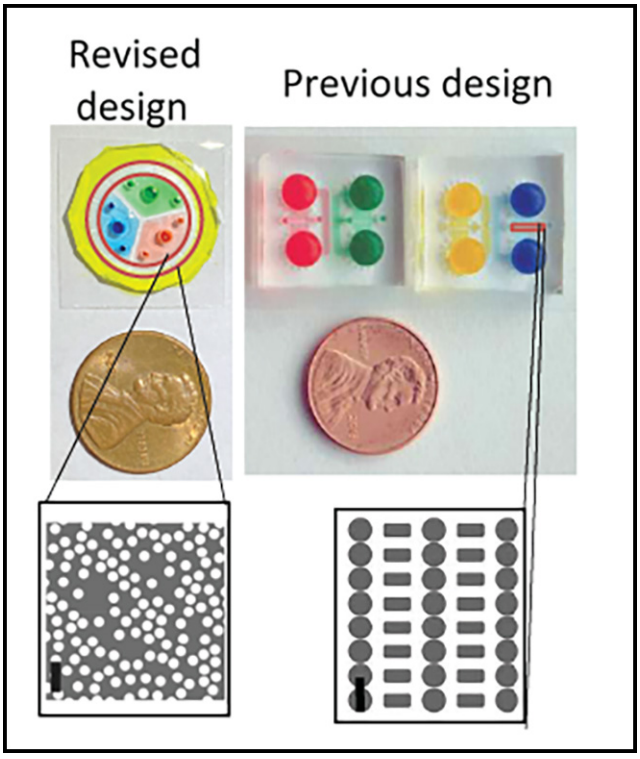

Figure 1: Overview of cancer cell migration device. Top: Partial figure reproduced from Davidson, et al. [2]. Previous PDMS microfluidic devices bonded on glass coverslips and filled with food coloring dye. Bottom: New design of "random pillar" microfluidic devices also bonded to glass coverslip and filled with food coloring. CAD for constriction areas of each design shown (outlined in red on left). Scale bars: 30 µm. All devices have migration areas with 5 µm height. Figure adapted from manuscript submitted to Methods in Molecular Biology.

References:

[1] Davidson, P. M., et al. Nuclear deformability constitutes a rate-limiting step during cell migration in 3-D environments. Cell. Mol. Bioeng. 7, 293-306 (2014).

[2] Davidson, P. M., et al. Design of a microfluidic device to quantify dynamic intra-nuclear deformation during cell migration through confining environments.

[3] Shah, P., et al. Nuclear Deformation Causes DNA Damage by Increasing Replication Stress. Curr. Biol. 31, 753-765.e6 (2021).

[4] Denais, C. M., et al. Nuclear envelope rupture and repair during cancer cell migration. Science (80-.). 352, 353-358 (2016).

[5] Agrawal, R., et al. Assembly and Use of a Microfluidic Device to Study Nuclear Mechanobiology During Confined Migration. Methods Mol Biol. 329-349 (2022).

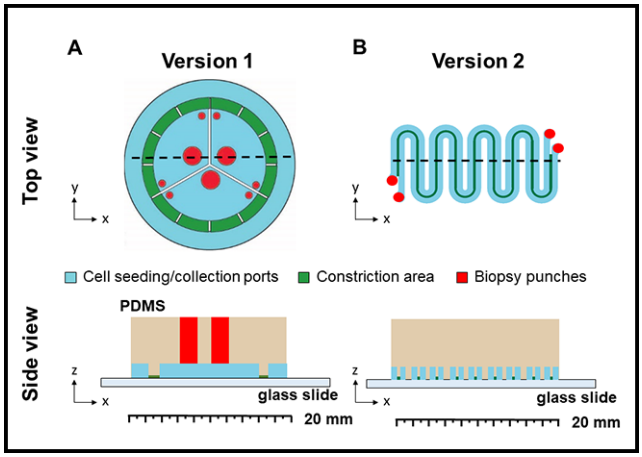

Figure 2: Schematic overview of PDMS migration device geometries. (A) Device optimized for long-term imaging and easy analysis of confined migration efficiency. (B) Device optimized for collection of cells that have completed confined migration. Devices are created by casting PDMS (tan) from wafer and bonded to glass slide to create a confined environment for cancer cell migration (green), after which cells are seeded through biopsy punches (red).

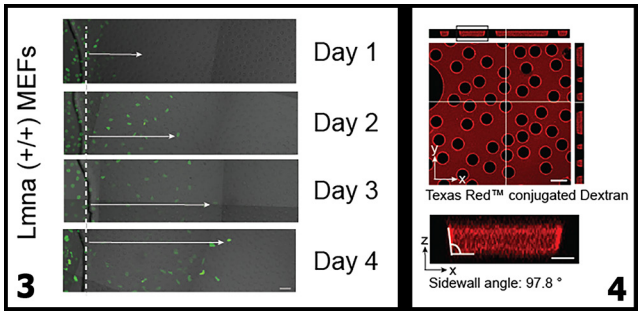

Figure 3, left: Cell migration in microfluidic device. Representative image series to show usage of microfluidic devices to determine migratory fitness as a function of distance traveled from seeding port into constriction area (white arrows) over four days. Figure adapted from manuscript submitted to Methods in Molecular Biology. Figure 4, right: Confocal 3D reconstruction of confined migration area. The PDMS microfluidic device was bonded to a glass coverslip, filled with fluorescent TexasRed-conjugated Dextran, and imaged by confocal microscopy to create a 3D image stacks. Orthogonal projection used to measure sidewall angle, α, of 97.8°. Scale bars: 4 µm. Figure adapted from manuscript submitted to Methods in Molecular Biology.

Development of a 3D Microfluidic Platform for Dynamic Compression of Tumor Spheroids

CNF Project Number: 2068-11

Principal Investigator(s): Dr. Mingming Wu

User(s): Young Joon Suh

Affiliation(s): Department of Biological and Environmental Engineering, Cornell University

Primary Source(s) of Research Funding: NIH Grant R01CA22136, Cornell Center on the Microenvironment and Metastasis (National Center Institute Grant U54CA143876)

Contact: mw272@cornell.edu, ys668@cornell.edu

Website: biofluidics.bee.cornell.edu

Primary CNF Tools Used: Heidelberg Mask Writer – DWL2000, ABM Contact Aligner, P7 Profilometer, MVD100, SUEX Laminator, DISCO Dicing Saw, YES EcoClean Asher, Unaxis 770 Deep Si Etcher, Plasma-Therm Deep Si Etcher, Oxford 81 Etcher, Oxford PECVD, YES Polyimide Oven, Hamatech Hot Piranha

Abstract:

Solid tumor stress caused by rapid growth of tumor cells and abnormality of vascular vessels has long been associated with a poor prognosis of cancer. However, understanding of tumor mechanics has been limited largely to single cells under static compressive loads. In this study, we have developed a high-throughput microfluidic platform providing well-controlled dynamic compression to tumor spheroids.

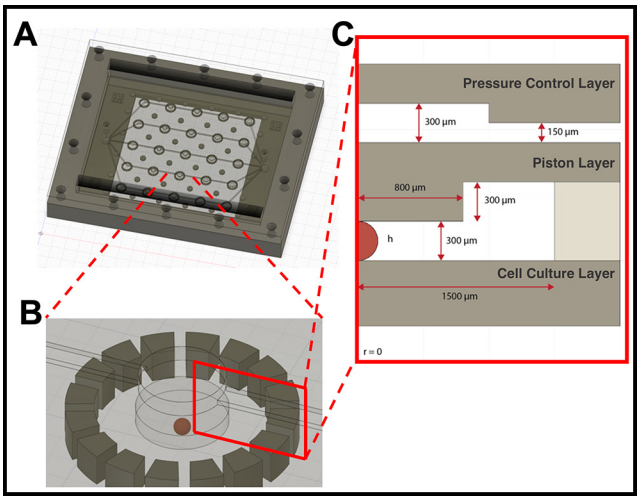

Figure 1: A 3D microfluidic platform for controlled compression of tumor spheroids. (A) An array of 5 × 5 microfluidic compression units. A schematic of an assembled device. Tumor spheroids embedded ECM is loaded into the lower cell culture layer, and pressure regulation media is introduced into the top compression layer. Each column provides five repeats of the same compression magnitude while each row provides five different compression magnitudes. (B) A close-up view of one compression unit. (C) Cross-section view of one compression unit with the dimensions. The PDMS piston is 1600 µm in diameter and the initial distance between the piston and the bottom of the well, h, is 300 µm. The diameters of the five pressure control chambers are 0, 1500, 2000, 2500 to 3000 µm.

Summary of Research:

A 5 × 5 array microfluidic compression device for tumor mechanics studies was designed (see Figure 1). The device consists of three layers: (1) cell culture layer, where the tumor spheroids embedded in extracellular matrices (ECM) are loaded; (2) PDMS piston layer, which is a PDMS membrane that has a top hat shape; and (3) a pressure control layer, which can push the PDMS piston down to apply compressive forces on the tumor spheroids. The three layers are then sandwiched between a Plexiglass® top cover and a stainless-steel frame to provide a good seal. COMSOL modeling has been used to calculate the displacement of the PDMS piston and the force applied on the tumor spheroids at pressure ranging from 0 to 7000 Pa (Figure 2). When pressure is applied in the pressure control chamber, the PDMS piston moves down a distance of Δh, applying a force on the tumor spheroids underneath, and leads to a well-controlled compressive strain, Δh/h, on the spheroids. This device can accommodate tumor spheroids of Young's modulus of about 1250 Pa, that are 100-600 µm in diameter for up to compressive strain (Δh/h) of 0.5.

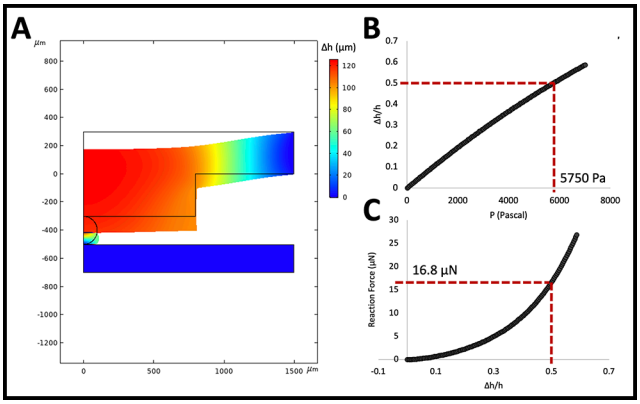

Figure 2: COMSOL computation of a microfluidic compression unit with a tumor spheroid. (A) A colored rendition of COMSOL calculation result of Δh at 7000 Pa of pressure applied. Here, Δh/h = 0.5 at the location of spheroids. The Young's modulus of spheroid and PDMS is 1250 Pa and 2 MPa, respectively. (B) Compressive strain versus applied pressure with spheroid in place. (C) Compression force on spheroid versus compression strain, Δh/h.

Fabrication:

Three layers of the device were fabricated separately. *The cell culture layer* consists of SU-8 wells 600 μm in depth on a 500 μm thick glass (Borofloat®). To fabricate this layer, SU-8 100 was spun on a Borofloat wafer at 475 rpm and soft baked at 95°C for 30 hours. The SU-8 was then exposed to 2310mJ/cm^2 of UV light through a 365 nm filter using an ABM contact aligner. The resist was then post-exposure-baked and developed in the SU-8 developer, followed by a hard bake at 200°C.

The main challenge was to fabricate the height of the wells uniform at 600 μm across the wafer. Keeping the wafer leveled at all steps was found to be crucial.

The piston layer consists of PDMS pistons that are 300 μm in height and 1600 μm in diameter and the PDMS membrane is 300 μm thick. To fabricate the master for this layer, 300 μm wells were etched into a Si wafer. Briefly, 4.5 μm of SPR-220-4.5 was spun on an Si wafer. The resist was then baked at 115°C for 2 mins on a proximity hot plate. Then, it was exposed to the pattern of the pistons at 120 mJ/cm^2 on the ABM contact aligner. After leaving it in room temperature for 30 mins for the post exposure reaction, it was baked at 115°C for 2 mins on a proximity hot plate for the post exposure bake. It was then developed in 726MIF for 120 sec. Then, a mild descum procedure was completed using the Oxford 81 for 90 sec.

Finally, the Si wafer was loaded on the Unaxis 770 Deep Si etcher and a total of 567 loops (200 + 200 + 167) of Bosch process were performed to etch 300 μm into the Si wafer. To remove any excess resist, the wafer was exposed to a strong plasma in a EcoClean Asher. The wafer was then coated with FOTS using the MVD-100 to make the surface hydrophobic. The depth of the piston wells was then measured using the P-7 profilometer.

The pressure control layer is a PDMS membrane with five parallel channels of 200 μm depth. The master is fabricated in a similar way as that for cell culture layer, except that a Si wafer is used instead of a Borofloat wafer.

A 10:1 PDMS was poured and cured on the master molds of the piston and the pressure control layer. After curing the PDMS in a 65°C oven overnight, these two layers were bonded together after plasma treatment and placed in a 90°C oven for 20 mins. Then, these two layers were placed on top of the cell culture layer and sandwiched between a metal frame and a Plexiglass top and connected to a pressure controller.

The compression (Δh) was measured using the defocused particle imaging velocimetry, which was originally developed in our lab [1]. Tumor spheroids were embedded in collagen, which was then introduced into the cell culture chamber. The pressure control chamber is pressurized with a pressure controller. We were able to precisely control the tumor compression with a precision of 1 μm.

References:

[1] Wu, et al., Three-dimensional fluorescent particle tracking at micron-scale using a single camera, Experiments in Fluids, 38, 461 (2005).

Microfabrication of Sample Holders for Cryogenic Small Angle X-Ray Scattering and Flow Cells for Fluorescence Measurements of Ligand Diffusion in Protein Crystals

CNF Project Number: 2157-12

Principal Investigator(s): Robert Thorne

User(s): John Indergaard, Jonathan Clinger, Liam Barnes

Affiliation(s): Laboratory of Atomic and Solid State Physics, Cornell University
Primary Source(s) of Research Funding: National Institutes of Health
Contact: ret6@cornell.edu, jai55@cornell.edu, jac762@cornell.edu, lnb49@cornell.edu
Website: https://www.lassp.cornell.edu/Thorne/
Primary CNF Tools Used: Heidelberg Mask Writer - DWL2000, SÜSS MA6-BA6 Contact Aligner, Oxford 81 / 82 PlasmaLab, VersaLaser Engraver/Cutter, YES Polyimide Curing Oven, SUEX Laminator, Harrick Plasma Generator, Hamatech Wafer Processor, LPCVD CMOS Nitride - E4, Filmetrics Reflectometer, Class II Resist Room

Abstract:

We use microfabrication in our development of methods for probing the structure and dynamics of proteins and other biomolecules. We have fabricated sample cell arrays for high-throughput small-angle X-ray scattering of biomolecules that allow samples to be "immortalized" by cooling to cryogenic temperatures. We are also fabricating crystal trap flow cells for quantitative fluorescence measurements of diffusion coefficients of small molecules inside protein crystals, critical parameters for design and interpretation of time-resolved X-ray crystallography experiments probing enzyme function.

Summary of Research:

CryoSAXS Sample Holders. Small-angle X-ray scattering on biomolecules in solution at room temperature is a workhorse tool for determining biomolecular size, shape, and changes in these due to interactions with other molecules or environmental changes. Our goal is to enable SAXS measurements on samples cooled to (and stored and shipped at) cryogenic temperature. This will allow sample preparation in the home lab as soon as protein is purified, long-term storage, and mail-in, remote data collection at synchrotrons, while dramatically reducing radiation damage and required sample volumes [1].

We have developed and have been evaluating and evolving sample cell arrays for cryoSAXS, shown in Figure 1. The cell arrays consist of pairs of 300 μm thick double-side polished Si pieces, coated on one side with 500 nm of silicon nitride, and KOH-etched to form X-ray transparent nitride windows. Before KOH etching, SUEX sheet is bonded to the nitride-coated side and patterned to form alignment and sealing rings. Thin-wall polyimide tubes are bonded to the rings on one piece, and quartz spacers bonded to fix the X-ray path length through the tubes between windows. X-ray

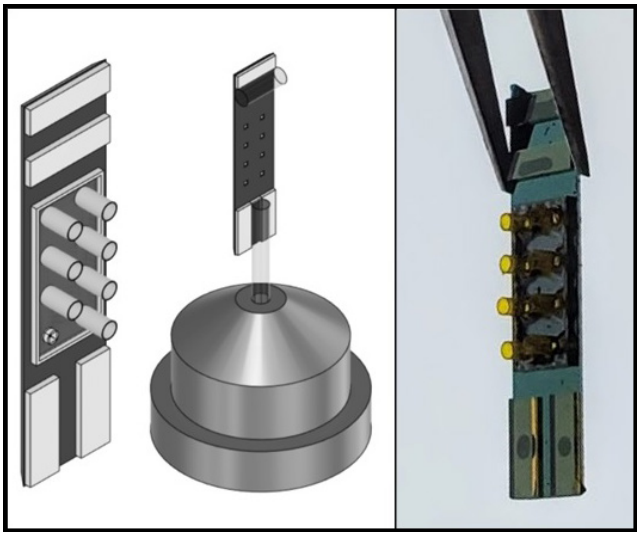

Figure 1: CAD image and photograph of cryoSAXS sample cell arrays. Each sample is held within a polyimide tube between two silicon nitride X-ray windows. The X-ray beam passes axially through the tube. Measurements from two cells in the array, one containing protein+buffer solution and one protein-free buffer solution, must be subtracted to obtain information about the biomolecular structure. As the subtracted diffraction may be 10^{-3} of the total, the cells must be identical.

experiments at CHESS and NSLS-II show that these cells allow rapid cooling of biomolecular samples without ice nucleation and without cracking seen due to differential contraction of sample and cell components (seen in previous cells [2]). However, experiments in the last 18 months identified issues with parasitic upstream X-ray scatter and how this scatter interacts with the sample cells that lead to unacceptable irreproducibility. We are currently addressing this issue, which we believe to be the final major obstacle to obtaining high-quality cryoSAXS data, through changes in cell design and in the experimental configuration at the X-ray beamline. We are also pursuing a simplified, all-microfabricated cell array design in which the polyimide tubes are replaced with high aspect ratio SUEX tubes.

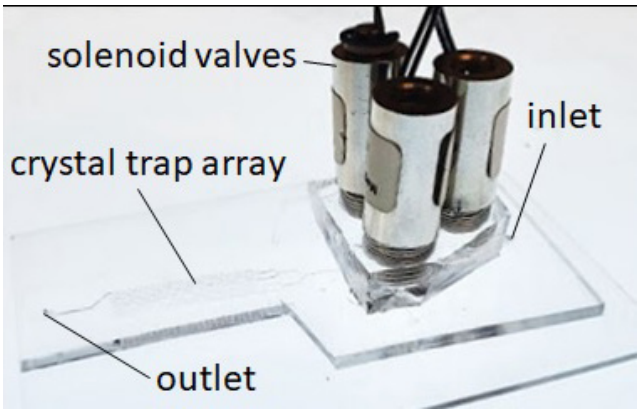

Figure 2: Microcrystal trap array formed by molded PDMS on a glass slide, for measurement of fluorophore diffusion in protein crystals. Solenoid valves control flow of protein crystal-and fluorophore-containing solutions.

Crystal Trap Array Flow Cells. Studying enzymes in action with atomic resolution has been a holy grail in structural enzymology. The most promising methods involve mixing enzyme microcrystals with reactant solution, allowing the reactant to diffuse into the crystal, and then measuring X-ray diffraction at different time delays after mixing [3]. Experiments so far have assumed that diffusion coefficients of reactants in protein crystals are the same as in bulk solution, but theoretical analysis of related problems suggest they may be as much as 10 to 100 times smaller, with major consequences for interpretation of time resolved diffraction experiments.

We are attempting to measure diffusion coefficients of small molecules in protein crystals using either fluorophores or molecules with distinctive intrinsic fluorescence / absorption. To do so, we have fabricated a microcrystal trap array (Figure 2), based on the design and fabrication protocol described in [4]. The traps are loaded by flowing a microcrystal-containing solution through the array. Then a solution containing the small molecule fluorophore is sent through the array, and fluorescence monitored both inside the crystal (using laser scanned microscopy) and in the surrounding solution. The trap array is fabricated from PDMS, and flows are controlled by solenoids.

A master is fabricated by laminating a 100 μm thick SUEX sheet to a silicon wafer, which is then exposed using a mask to define the features of the trap array, and developed. PDMS is poured onto the master with a target thickness of 2 mm, cured, removed, and then bonded to a glass slide. A second, 5 mm thick PDMS layer is then fabricated with screws, centered over the location of input flow channels of the first layer, cast within it. These screws are removed, the second layer bonded to the first, and solenoid valves threaded into the holes. When activated, each solenoid presses down on the first layer of PDMS and collapses the inlet channel over which it is situated.

We successfully tested a valve-free version of the trap array, obtaining fluorescence data from 50 μm crystals and credible diffusion coefficients. The valved version will simplify data collection and improve time resolution.

References:

[1] Meisburger, S. P., et al., (2013) Biophys. J., 104, 227-236.

[2] Hopkins, J. B., et al., (2015) J. Appl. Cryst. 48, 227-237.

[3] Clinger, J. A. et al., (2021). IUCrJ 8, 784-792 (2021).

[4] Lyubimov, A. Y. et al., Acta Cryst. D 71, 928-940 (2015).

Array Microhabitat Platform for Microalgae Growth

CNF Project Number: 2262-13
Principal Investigator(s): Dr. Mingming Wu
User(s): Fangchen Liu

Affiliation(s): Department of Biological and Environmental Engineering, Cornell University
Primary Source(s) of Research Funding: United State Department of Agriculture – National Institute of Food and Agriculture
Contact: mw272@cornell.edu, fl373@cornell.edu
Website: biofluidics.bee.cornell.edu
Primary CNF Tools Used: Heidelberg Mask Writer – DWL2000, ABM Contact Aligner, P10 Profilometer, MVD100, VersaLaser Engraver/Cutter Tool

Abstract:

The occurrence of harmful algal blooms (HABs) is increasing at an alarming rate worldwide, threatening water resources and aquatic ecosystems. Nutrients are known to trigger the onset of HABs and systematic investigation at cellular level is lacking. To study the combination effects of multiple nutrients on microalgae growth in a high throughput way, we built a dual-gradient microhabitat device and a micro-scale light gradient generation platform. Using these platforms, the effect of chemical and physical microenvironment on the growth of model microalgal *Chlamydomonas reinhardtii* was revealed.

Summary of Research:

Harmful algal blooms, or HABs, are serious environmental problems, where a sudden growth of algae or cyanobacteria poses threat to freshwater and marine ecosystems. HABs deteriorate drinking water quality and have huge environmental and economic costs. Nutrient enrichment is believed to be the fundamental cause of HABs, and climate change may further intensity the problem [1]. However, there lacks a quantitative/mechanistic understanding of the roles of environmental factors in the onset of HABs at cellular level. The goal of this project is to investigate the synergistic roles of multiple environmental factors in the growth of cyanobacteria.

Environmental conditions known to affect algae growth include nutrients, mainly nitrogen (N) and phosphorous (P), light intensity and temperature. These conditions are hard to control in nature, and also cannot be quantified in a high throughput way in flasks and chemostats. To address the need for quantitative, systematic, and high-throughput screening of environmental factors, we first developed a high throughput array microhabitat platform, capable of generating stable dual nutrient gradients, and used it for monitoring growth of photosynthetic microbes [2]. The device consists of 64 microhabitats in the form of an 8 × 8 array and each habitat is 100 μm × 100 μm × 100 μm. The microhabitat array is surrounded by two sets of side channels each with the width of 400 μm and height of 200 μm. The device design is shown in Figure 1.

The silicon master was fabricated using two-layer SU-8 negative resist photolithography, and pattern was transferred to a thin agarose membrane later used for cell seeding via soft lithography. Applying this platform, we discovered that nutrients N and P synergistically promoted the growth of *Chlamydomonas reinhardtii* (*C. reinhardtii*) (see Figure 2).

In addition to controlling the chemical environment in the microfluidic device, we developed microscope-based light gradient generation platform, compatible with the array microhabitats, for the investigation of the impact of light intensity on algal growth [3]. The controlled light gradient was generated by modifying the transmitted light path of a commercially available inverted microscope (see Figure 3). A piece of 45 mm half-moon mask, made of optical resin, was fabricated using the CO_2 laser cutter, and customized for a half-dark, half-bright gradient. Light gradient was characterized by grayscale values of bright field images and photosynthetically active radiation (PAR) meter measurements. Growth of algal cells under the controlled light gradient was monitored by fluorescence imaging for five days, and the growth curves and growth rates were obtained (see Figure 4). Results showed that the growth of the microalgae was significantly regulated by the light intensity and a Monod kinetics model fit revealed the half saturation constant of light to be 1.9 $\mu mol \cdot m^{-2} \cdot s^{-1}$ for *C. reinhardtii*.

Our results provided the enabling capability of creating multiple controlled environmental parameters, nutrients and light intensity within one platform, which is suitable for growth studies of all photosynthetic micro-organisms. Future study will move a step further to combine the chemical and physical cues and actively working towards incorporating microbial communities in the HAB-on-a-chip platform.

References:

[1] Paerl, Hans W., et al. Environmental Science and Technology (2018): 5519-5529.

[2] Liu, Fangchen, et al. Lab on a Chip 20.4 (2020): 798-805.

[3] Liu, Fangchen and Larissa Gaul, et al. Lab on a Chip (2022) Advance Article.

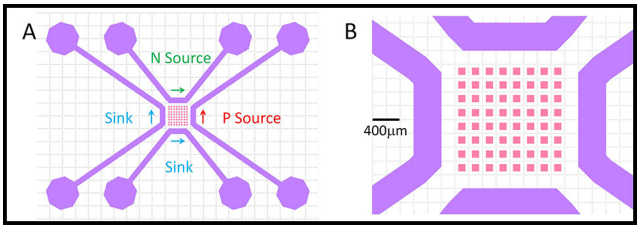

Figure 1: Dual-gradient microfluidic platform design. A. Top view of a device. B. A zoomed-in view of microhabitats and channel. The 8 × 8 array of 100 μm cubic habitats are separated by 100 μm from each other. These habitats are surrounded by four channels with width of 400 μm and height of 200 μm. N source and P source runs through the top and right channel respectively, and the other channels are sink channels. A gradient is generated for each chemical species in the microhabitat array region through molecular diffusion.

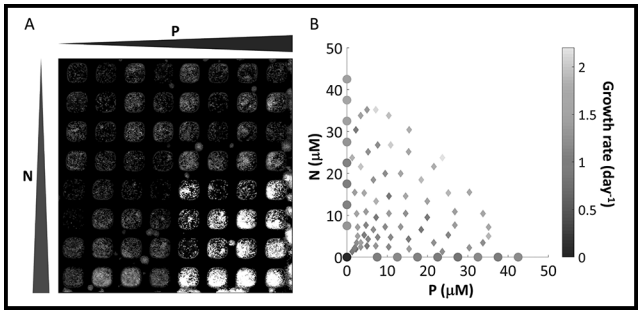

Figure 2: Growth of C. reinhardtii *under nutrients (N, P) gradient. A. Fluorescence images of nutrients co-limited cells growing under N and P dual gradients at day 4. B. The growth rate of* C. reinhardtii *under: control condition, no N or P (dot at the origin), single P gradient (dots on x axis), single N gradient (dots on y axis), and dual-gradient (all the diamonds). Shade is coded for the value of the growth rate.*

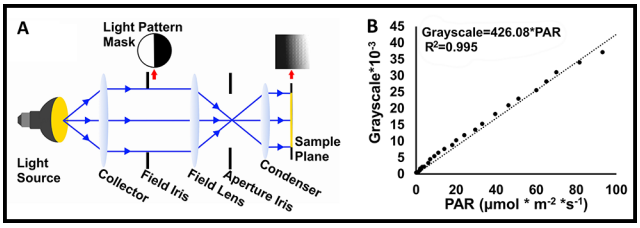

Figure 3: Experimental setup for micrometer-scale light intensity gradient generation and characterization. A. Modifying the light path of a microscope for light gradient generation. Light comes from a halogen lamp. A half-moon light pattern mask was placed directly below the field iris to create the light gradient. Both field and aperture irises were fully open throughout all experiments for optimal, reproducible light gradient generation. (B) Calibration curve of grayscale value from the CCD camera as a function of the light intensity measured by the PAR (photosynthetic active radiation) meter. Dots are the adjusted grayscale values, and the line is a fit to a linear function.

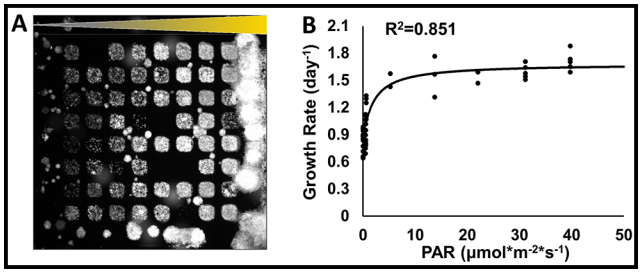

Figure 4: Growth response of C. reinhardtii *to light intensity gradient in an array microhabitat. A. Fluorescence images of cells growing in the array microhabitats under a light intensity gradient at day 5, with approximately 0 PAR on the left side and about 47.7 PAR on the right. B. Growth rate as a function of PAR. Dots are experimental values and line is a fit to Monod model. The fitted coefficients with 95% confidence bounds are μ_0 = 0.823±0.07 day^{-1} μmax' = 0.860±0.099 day^{-1}, and K_s = 1.9±1.18 μmol/(m^2*s), with an R-squared value of 0.851. This data is collected from one of three replicates.*

Metasurface-Enhanced Infrared Spectroscopy for the Measurement of Live Cells

CNF Project Number: 2472-16

Principal Investigator(s): Gennady Shvets

User(s): Steven He Huang, Po-Ting Shen, Aditya Mahalanabish

Affiliation(s): Applied and Engineering Physics, Cornell University

Primary Source(s) of Research Funding: National Cancer Institute of the National Institutes of Health award number R21 CA251052, National Institute of General Medical Sciences of the National Institutes of Health award number R21 GM138947

Contact: gs656@cornell.edu, hh623@cornell.edu, ps944@cornell.edu, am2952@cornell.edu

Website: http://shvets.aep.cornell.edu

Primary CNF Tools Used: JEOL 9500, SC4500 Evaporator, Zeiss Supra SEM, PDMS Casting Station, Anatech Resist Strip, Glen 1000 Resist Strip, Oxford PECVD, Oxford ALD FlexAL, Plasma-Therm 740, DISCO Dicing Saw

Abstract:

We have developed Metasurface-Enhanced Infrared Spectroscopy (MEIRS) as a novel tool to perform spectral analysis of live cells. In MEIRS, cells are cultured on plasmonic nanoantennas (metasurface), which enhances infrared absorption through the plasmonic hotspots. Various cellular responses can be observed from the IR absorption spectra collected in real-time. Our current work focuses on expanding the application of MEIRS through the integration of metasurface with multi-well cell culture chambers for high-throughput measurements, exploring the use of MEIRS to measure cellular response from chemotherapeutics, as well as combining plasmonic metasurfaces with nano-topography to study cell-nanostructure interactions.

Summary of Research:

Infrared (IR) spectroscopy is widely used to identify chemical compounds through their molecular vibration fingerprints and has recently found many applications in biological analysis. We have developed a novel technique called Metasurface-Enhanced Infrared Spectroscopy (MEIRS) to measure live cells in physiological conditions. In MEIRS, cells are grown on an array of plasmonic nanoantennas called metasurfaces. These resonant nanoantennas support plasmonic hot spots, enhancing the light-matter interaction and IR absorption. In the past, we have used MEIRS to detect spectroscopic changes in response to cellular dissociation and cholesterol depletion [1]. Our current work focuses on expanding the application of MEIRS through the integration of metasurface with multi-well cell culture chambers for high-throughput measurement, exploring the use of MEIRS to measure cellular response from chemotherapeutics, as well as combining plasmonic metasurfaces with nano-topography to study cell-nanostructure interactions.

Figure 1 shows a schematic drawing of the MEIRS measurement setup for live cells.

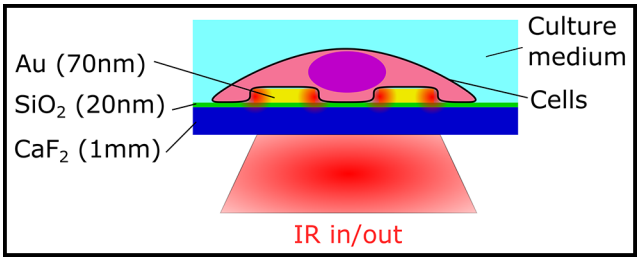

Figure 1: Schematic drawing of the metasurface-enhanced infrared spectroscopy setup for live cell measurement.

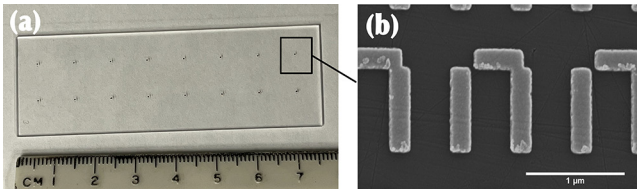

Figure 2: Metasurface integration with multi-well cell culture chamber. (a) 16 metasurface patterns fabricated on 1" × 3" CaF_2 slide, to be attached to a cell culture chamber superstructure (not shown). (b) SEM images of the metasurface. Scale bar: 1 µm.

In order to make metasurface compatible with standard cell culture in multi-well format, metasurface devices are fabricated as repeating patterns on top of a $1^2 \times 3^2$ infrared transparent CaF_2 substrate (Figure 2). The fabrication starts with a 4-inch diameter CaF_2 window, which is coated with 20 nm of SiO_2 using Oxford PECVD as a protection layer.

Metasurface patterns are defined using electron-beam lithography with the JEOL 9500 system and poly(methyl methacrylate) (PMMA) as the resist.

Then, 5 nm Cr and 70 nm Au are deposited using SC4500 evaporator. The 4-inch CaF_2 window is cut into $1^2 \times 3^2$ pieces using the DISCO dicing saw.

As the final step, Anatech or Glen 1000 Resist Strip is used to clean the metasurface sample. Commercial superstructures for multi-well cell culture chambers are attached to this metasurface for cell culture.

We used MEIRS to measure the response of live cancer cells to a novel chemotherapeutic metal complex: tricarbonyl rhenium isonitrile polypyridyl (TRIP) [2]. This drug is an endoplasmic reticulum (ER) stress inducer and regulates important biological functions such as protein synthesis. By analyzing the measured infrared spectra using linear regression, we extract the temporal changes in proteins and lipids IR absorption and local refractive index changes from the shift of metasurface plasmonic resonance. In addition, the local concentration of TRIP can be observed through its intrinsic IR absorption at the carbonyl stretching modes and is useful in monitoring the precise drug delivery time. Figure 3 shows the protein IR absorption signal of the cells in response to TRIP treatment.

We have observed an increase in protein signal in the short-term (tens of minutes) and a reduction in protein signal in the long-term (several hours). This result demonstrates that MEIRS is an effective label-free real-time cellular assay capable of detecting and interpreting the early phenotypic responses of cells to chemotherapeutics.

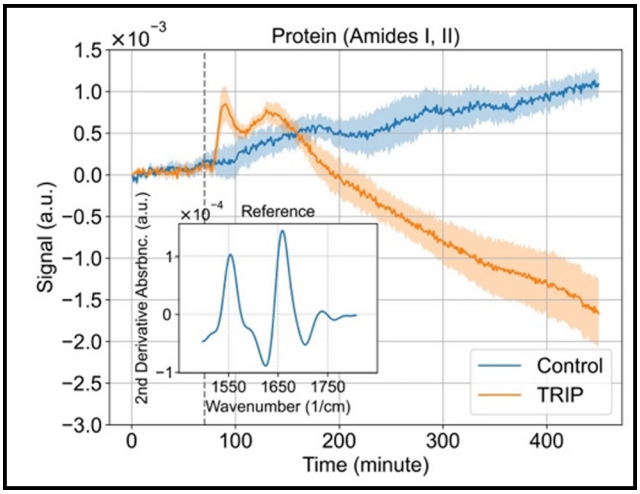

Figure 3: Cellular response to TRIP treatment. Inset: reference spectra of amide I and amide II bands attributed to proteins, used for linear regression. Dashed black line shows the timing of TRIP arrival.

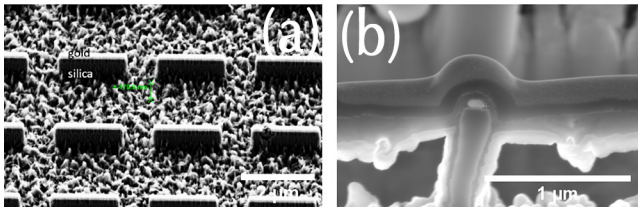

Figure 4: Nanoantenna-on-nanopillar structure. (a) SEM image of the nanoantenna-on-nanopillar structure without cells. Scale bar: 2 μm. (b) Cross section SEM image of one nanoantenna, with a cell adhered on top. Cell membrane can be seen curved around the nanoantenna-on-nanopillar. Scale bar: 1 μm.

Another direction in this project is the combination of metasurfaces with nano-topography to study cell-nanostructure interactions. Current research in surface nano-projections has shown that they can be used as effective tools to manipulate cellular attachment. We use nanopillars to incite physical and chemical responses in cells, which are then monitored through MEIRS.

We have fabricated gold nanoantennas on top of silica nanopillars (Figure 4(a)). The fabrication process starts with growing a layer of silica (~1μm) on top of CaF_2 substrate using the Oxford PECVD. Next, metasurface patterns are defined using electron-beam lithography (JEOL 9500). Gold is deposited in the patterned region using the CVC SC4500 even/odd hour evaporator. We also deposit a thin layer of chromium above the gold nanoantenna and use it as a mask to chemically etch the silica using the Plasma-Therm 740. When cells attach to such nanopillar structures, cell membrane curves around these nanopillars (Figure 4(b)), increasing the overlap between the metasurface hotspots and the cells and also increasing the concentration of certain proteins (actin, clathrin) in the metasurface hotspots.

Spectroscopically, we have observed that IR absorption from these cells on the nano-contoured metasurfaces is enhanced and shows different spectral features compared with cells on flat metasurfaces, likely related to protein secondary structures.

References:

[1] Huang, S. H., Li, J., Fan, Z., Delgado, R. and Shvets, G. Monitoring the effects of chemical stimuli on live cells with metasurface-enhanced infrared reflection spectroscopy. Lab Chip 21, 3991-4004 (2021).

[2] Shen, P.-T., et al. Probing the Drug Dynamics of Chemotherapeutics Using Metasurface-Enhanced Infrared Reflection Spectroscopy of Live Cells. Cells 11, (2022).

Arrays of Elliptical Pillars for Optical Detection of Bacteria

CNF Project Number: 2472-16
Principal Investigator(s): Gennady Shvets
User(s): Giovanni Sartorello

Affiliation(s): School of Applied and Engineering Physics, Cornell University
Primary Source(s) of Research Funding: National Cancer Institute (award number R21 CA251052), National Institute of General Medical Sciences (award number R21 GM138947) of the National Institutes of Health
Contact: gs656@cornell.edu, gs664@cornell.edu
Primary CNF Tools Used: Oxford 100 PECVD, JEOL JBX 9500FS, Oxford Cobra ICP Etcher

Abstract:

We fabricate prototype arrays of amorphous silicon nanopillars to be used for sensing bacterial binding.

Summary of Research:

Metasurfaces have been widely used for biosensing applications [1]. Organic matter, from proteins to cells, interacts with metasurfaces and changes their optical behavior, allowing detection by one of several optical techniques. In our case, we aim to use arrays of elliptical amorphous silicon nanopillars, spaced 1.2 μm in both directions, 1.2 μm tall, and in various sizes around 0.7 μm times 0.5 μm for the elliptical axes. They are intended to be used in immersion, with bacteria adhering to them. When the metasurface is illuminated in transmittance, there is a change in birefringence induced by the presence of the bound bacteria, allowing for their detection and localization.

We fabricated a prototype array by coating a glass wafer with amorphous silicon on the Oxford PECVD tool, followed by coating with a negative resist (HSQ) and EBL exposure on the JEOL 9500. After development, we used the Oxford Cobra etcher to transfer the pattern to the silicon. Timing the etching correctly was critical, because there is limited selectivity for silicon etching when using HSQ as the mask, requiring a rate measurement about midway through. Our arrays (Figure 1) match the design specifications.

Conclusions and Future Steps:

Fabrication was successful, proving the usefulness of HSQ as etching mask even with structures with relatively high aspect ratios, if etching is carefully monitored. The sample turned out not to work as hoped in the wavelength range of interest, but this can be fixed by tweaking the dimensional parameters of the metasurface. This procedure can also be applied to other devices, suited to this and many other detection techniques, by changing the design and/or materials of the metasurface.

References:

[1] Zhang, S., Wong, C. L., Zeng, S., Bi, R., Tai, K., Dholakia, K., and Olivo, M. (2021). Metasurfaces for biomedical applications: Imaging and sensing from a nanophotonics perspective. Frontiers in Optics and Photonics, 10(1), 265-299. https://doi.org/10.1515/9783110710687-023.

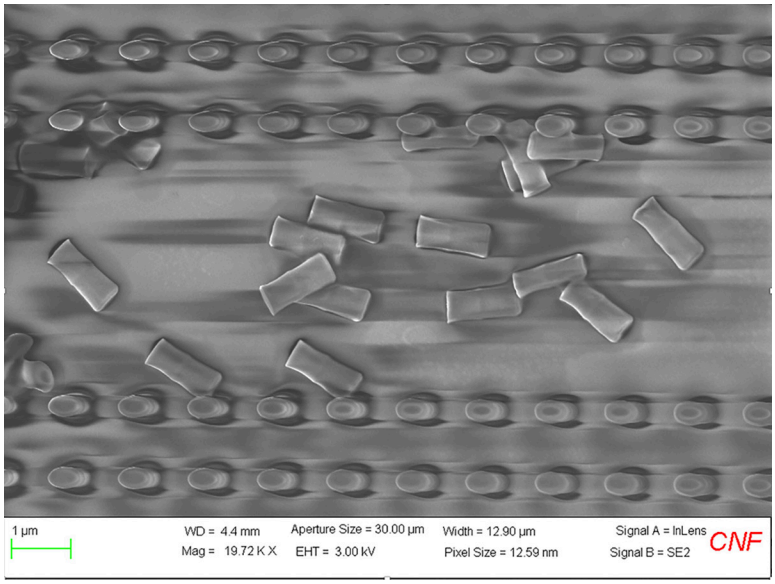

Figure 1: SEM image of one of the fabricated arrays. The pillars stand and are seen from above, except for those in the middle, which have been knocked down by the profilometer, which allows their height to be measured and shows a slight enlargement where the etching was interrupted for the rate measurement.

Studying Viral Binding and Fusion Mechanisms with Host Cell Membranes

CNF Project Number: 2575-17
Principal Investigator(s): Susan Daniel
User(s): Ambika Pachaury, Annie Chien

Affiliation(s): Smith School of Chemical and Biomolecular Engineering, Cornell University
Primary Source(s) of Research Funding: National Science Foundation, National Institutes of Health
Contact: sd386@cornell.edu, ap2387@cornell.edu, yc2499@cornell.edu
Primary CNF Tools Used: Malvern NS300 NanoSight

Abstract:

The current COVID-19 pandemic caused by the SARS-CoV-2 virus led to millions of deaths worldwide [1]. This virus is not the first of its kind; the SARS and MERS outbreaks in 2003 and 2012, respectively, were also caused by coronaviruses [1]. Additionally, the flu that we experience every year caused by the influenza virus continues to spread and we have yet to come up with a permanent solution for this viral infection [2]. Given the continuing threat these viruses pose to human health, our lab is focused on understanding the mechanisms of viral entry to determine antiviral targets. One such target is the viral fusion mechanism mediated by the spike protein in the case of coronaviruses and hemagglutinin (HA) in the case of influenza virus [1,2]. By fluorescently labelling these viruses or pseudoparticles, safer surrogates to live virus particles, we can study how they fuse with synthetic liposomes that contain receptors for the spike and HA proteins [3]. Additionally, the Daniel lab uses a chemical method to make blebs or vesicles that bud off cell membranes and can better mimic the cell membrane composition and be used for such fusion experiments [4]. These methods and experiments will provide a fundamental understanding of these viral entry events that in turn will enable us to be better prepared for future pandemics.

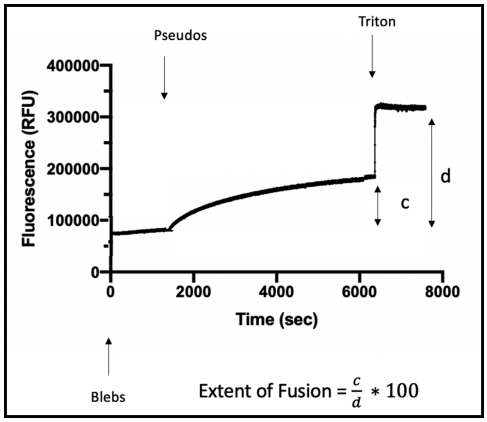

Summary of Research:

In order to test fusion between virus or viral like pseudoparticles with liposomes or cell membrane blebs, we use a method known as Ensemble Fluorescence Assay or bulk fusion assay. We label the membrane of either virus or host-cell mimic with a lipophilic dye that is self-quenched at high concentrations and then dequenches once fusion occurs. This helps us measure the extent of fusion when all the fluorescent dye is released on adding a detergent. However, in order to optimize the ratio between virus and membrane-mimic particles we rely heaving on dynamic light scattering and the NanoSight, which gives us information regarding the size, homogeneity and concentration of these particles. This concentration is critical in ensuring that we are able to get the best possible fluorescence signal and measure fusion events.

References:

[1] Tang T, Bidon M, Jaimes JA, Whittaker GR, Daniel S. Coronavirus membrane fusion mechanism offers a potential target for antiviral development. Antiviral Res. 2020 Jun;178:104792. doi: 10.1016/j.antiviral.2020.104792. Epub 2020 Apr 6. PMID: 32272173; PMCID: PMC7194977.

[2] Sriwilaijaroen N, Suzuki Y. Molecular basis of the structure and function of H1 hemagglutinin of influenza virus. Proc Jpn Acad Ser B Phys Biol Sci. 2012;88(6):226-49. doi: 10.2183/pjab.88.226. PMID: 22728439; PMCID: PMC3410141.

[3] Millet JK, Tang T, Nathan L, Jaimes JA, Hsu HL, Daniel S, Whittaker GR. Production of Pseudotyped Particles to Study Highly Pathogenic Coronaviruses in a Biosafety Level 2 Setting. J Vis Exp. 2019 Mar 1;(145):10.3791/59010. doi: 10.3791/59010. PMID: 30882796; PMCID: PMC6677141.

[4] M.J. Richards, C.-Y. Hsia, R.R. Singh, H. Haider, J. Kumpf, T. Kawate, and S. Daniel. Membrane Protein Mobility and Orientation Preserved in Supported Bilayers Created Directly from Cell Plasma Membrane Blebs. Langmuir 2016 32 (12), 2963-2974. DOI: 10.1021/acs.langmuir.5b03415.

Selective Single-Beam Acoustic Tweezers for Cell Manipulation

CNF Project Number: 2690-18
Principal Investigator(s): Alireza Abbaspourrad
User(s): Amir Mokhtare

Affiliation(s): Food Science and Technology, Cornell University
Primary Source(s) of Research Funding:
Contact: alireza@cornell.edu, am2964@cornell.edu
Primary CNF Tools Used: ABM Contact Aligner, Heidelberg Mask Writer - DWL2000, SC4500 Even-Hour Evaporator

Abstract:

Structured sound waves, mechanical waves carrying energy and momentum flux, are frontiers in advancing our understanding of cell mechanobiology. The acoustical tweezers enable biocamplatical, contact and label free manipulation of single cells and microorganisms. Focused sound beams can exert acoustic radiation force and torque that can be used for mechanical property probing and mechanosensitive ion channel activation at powers much lower than their optical counterpart. The external actuation of the mechanosensitive ion channel can act as switches for manipulation of specific cell activities in an electrical-to-chemical mediator manner.

Summary of Research:

We developed a vortex-based acoustic tweezer that can be operated from a single transparent piezoelectric transducer and can be fully integrated to a standard microscopy environment [1,2].

These vortices-based tweezers enable spatially selective manipulation of cells at single cell resolution. Furthermore, we have also developed and fabricated conventional ultrasound focusing lenses but on transparent transducers that are also easily integrated on top of the microscope objective to monitor the sound effects on biological cells [3]. (Figure 1)

To examine the feasibility of vortex-based and focused acoustic tweezers, we have built a fully integrated acoustic tweezer platform on a Nikon Ti microscope (Figure 2) and successfully performed single cell manipulation, positioning (Figure 4) and characterized it in terms of cell viability and exerted force (Figure 3). Figure 4.a shows the capability of the device in manipulating a single 7-micron diameter particle inside a microfluidic device. Figure 4.b shows the selective manipulation of a 15 μm particle using an acoustic tweezer in a microfluidic chamber observed through a standard microscope. As shown, the selected particle marked with a red circle is moved among the other particles marked in yellow, blue and green which do not move. And Figure 4.c is a representation of single budding yeast manipulation and rotation over the course of 0.3 seconds.

Conclusions and Future Steps:

Single beam acoustic tweezers that operate at biomedical ultrasound frequencies have the potential to be integrated into current conventional optical setups. Such level of integration significantly alleviates the tedious single cell manipulation procedures and lets young researchers work more efficiently on analyzing data instead of mastering working with complicated tools. It is also important to study and understand the new mechanotransduction pathways, cell reaction to stress, stress communication between cells, electromagnetic radiation consequences of mechanical stimuli, among many others that these new techniques make possible.

For the future steps, our hypothesis is that, by engineering a reliable mechanotransduction pathway that is responsible for actuating a specific signal pathway, we will be able to realize an efficient non-invasive and remote interface for on demand communication with biological entities at cellular level. Engineering focalized structured sound waves and sensitive impedance measuring sensors are the key technologies for a reversible mechanotransduction based interface between cell and electronics.

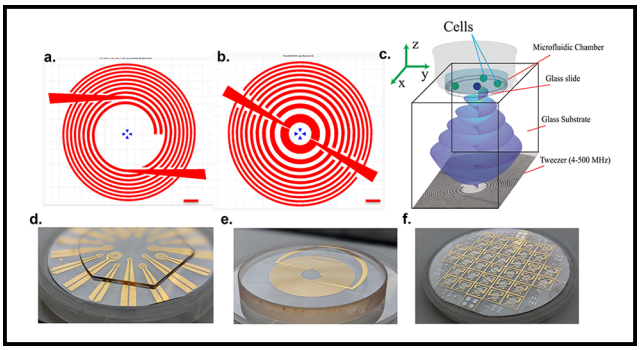

Figure 1: The acoustic tweezer and lens design. a. The intertwined spiral electrode pattern obtained from the approximate equations for frequency of 100 MHz and focal distance of 1235 µm. b. The Fresnel pattern of electrodes for acoustic focusing for f = 100 MHz and focal length of 1000 µm. Scale bar is 50 µm. c. The schematic showing the composition of the acoustic tweezer. The electrode patterns on the active piezo substrate creates a spherical vortex that propagates into the glass medium and focalizes it before it reaches the cover glass and PDMS chamber that holds the cells. The fluidic chamber on top of the acoustic tweezers is held in place by applying silicone oil as a coupler. d-f. Representative images of acoustic tweezers for manipulation of eukaryotic cells at ~ 50 MHz, embryonic female cells at ~ 5 MHz and yeast cells at ~ 200 MHz frequency.

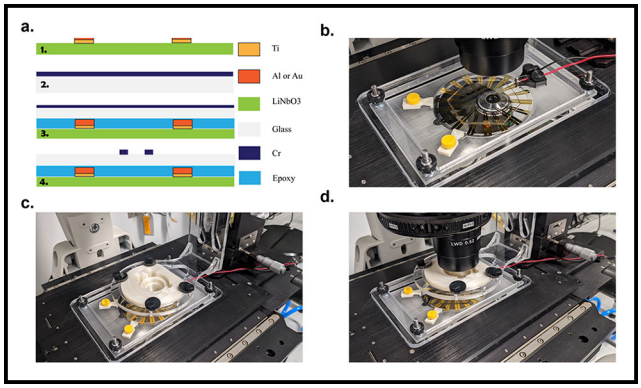

Figure 2: Acoustix tweezer fabrication and integration. a. Shows the fabrication steps. b-d. Shows the integration of the acoustic tweezer to a Nikon TE-300 microscope and 3D manipulator position that controls the fluidic chamber.

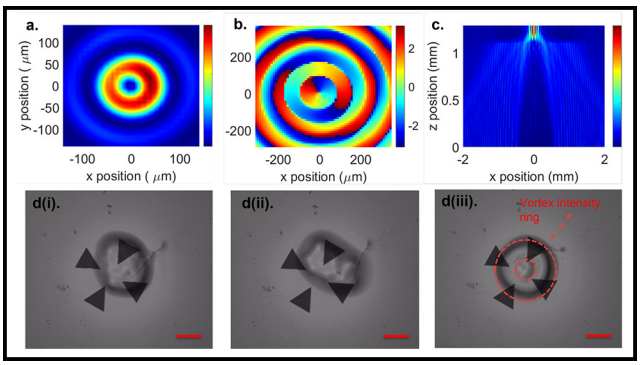

Figure 3: Numerical simulation and experimental observations. a. Intensity and b. phase prediction using angular spectrum method in the xy plane. c. intensity prediction using angular spectrum method in the xz plane. d(i)-(iii) observation of intensity profile variation during a frequency sweep to identify the acoustic tweezer resonant frequency. Scale bar is 40 µm.

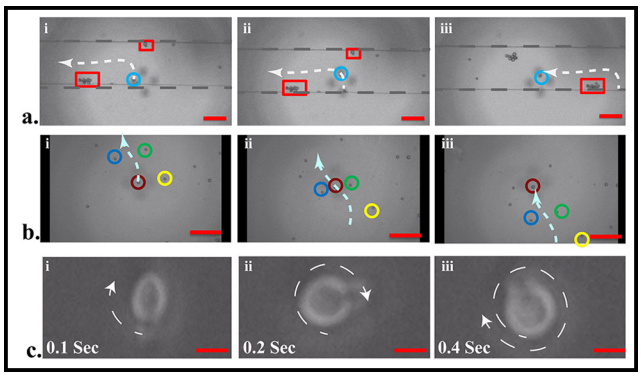

Figure 4: a. Selective manipulation of a 7 µm particle inside a microfluidic device. b. Isolation and manipulation of a 15 µm particle inside a microfluidic chamber. c. Single yeast manipulation and rotation in a microfluidic channel.

References:

[1] M. Baudoin, J.-C. Gerbedoen, A. Riaud, O. B. Matar, N. Smagin and J.-L. Thomas, Sci Adv, 2019, 5, eaav1967.

[2] M. Baudoin, J.-L. Thomas, R. A. Sahely, J.-C. Gerbedoen, Z. Gong, A. Sivery, O. B. Matar, N. Smagin, P. Favreau and A. Vlandas, Nat. Commun., 2020, 11, 4244.

[3] P. S. Balasubramanian, A. Singh, C. Xu and A. Lal, Sci. Rep., 2020, 10, 3075.

Engineering Surfaces to Investigate Cell-Material Interactions

CNF Project Number: 2748-18
Principal Investigator(s): Dacheng Ren
User(s): Yikang Xu

Affiliation(s): Biochemical and Chemical Engineering, Syracuse University
Primary Source(s) of Research Funding: National Institutes of Health
Contact: dren@syr.edu, yxu138@syr.edu
Website: https://renlab.syr.edu/
Primary CNF Tools Used: Heidelberg Mask Writer - DWL2000, ABM High Resolution Mask Aligner, Hamatech-Steag Wafer Processors, Hamatech-Steag HMP900 Mask Processing System, Unaxis SLR 770 Etcher, SC4500 Cryopumped Evaporator, DISCO Dicing Saw, MVD-100 Molecular Vapor Deposition System, Westbond 7400A Ultrasonic Wire Bonder

Abstract:

Microscale fabrication technique was employed to create master wafers for polydimethylsiloxane devices including microfluidic devices, micropillar arrays, and micro patterning. These devices were used to study bacterial response to active topography with micropillar arrays loaded with magnetic nanoparticles. The microfluidic devices were used to construct a model to simulate protein aggregation in kidney arterioles that is superior to traditional models. A valid protocol to produce a Giant Magnetoimpedance (GMI) sensor was also explored. Several iterations of the protocol were performed to troubleshoot and find a valid protocol. These platforms are useful for understanding the mechanism of cell-material interactions and complex biological processes.

Summary of Research:

Several fluid transport microfluidic devices with smallest feature size of 20 μm were fabricated by writing patterns onto masks with 1 to 1 feature ratio. The patterns were then transferred onto wafers by contact aligning and exposing photoresist coated silicon wafers, which were subsequently etched to create master wafers for soft lithography peel off process. The final microfluidic devices have channels from tens of microns to as large as millimeters in diameter mimicking capillary structure in typical human kidney vascular system. The implementation of microfluidic devices eliminates air liquid interface and intense fluidic shear force present in current laboratory protein aggregation protocols, which involves aggressive stirring of protein solution by magnetic stir bar in beakers.

Micropillar array has also been fabricated according to previously published protocol [1], where briefly, patterns of different sizes and spacing between patterns were exposed onto silicon wafer with photoresist, and etched to create high aspect ratio pillars (50:1) micro hole arrays with hole diameter as small as 2 μm. The master wafer was then used in soft lithography to create micropillar arrays with magnetic nanoparticle loaded polydimethylsiloxane. The pillars are finally placed under actuated magnetic field at different field densities for either biofilm removal or biofilm formation prevention.

A protocol for the fabrication of a GMI sensor is currently under development. This sensor consists of a sandwich structure with multiple sub-micron thick metal layers on a fused-silica wafer. The thin films were deposited with electron beam deposition and exposed several times using different masks to create three layers of different patterns on top of the substrate. A final lift-off process was done to remove photoresist and preserve the sensor structure. This sensor can be used to study cell-material interactions.

Conclusions and Future Steps:

Both microfluidic device and micropillar array master wafers were successfully fabricated with desired polydimethylsiloxane structures and excellent performance in experimental setups. For the micropillar arrays, the 50:1 aspect ratio pillar was fully achieved

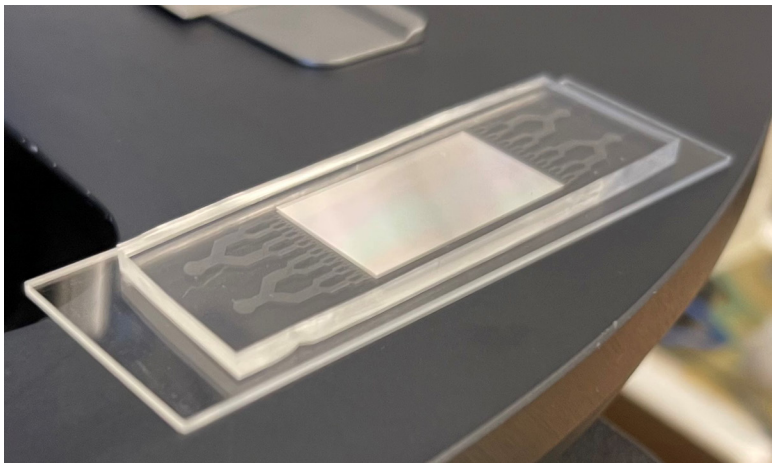

Figure 1: A picture of a microfluidic device plasma bonded to glass slide, with the channels visualized by artificial red dye.

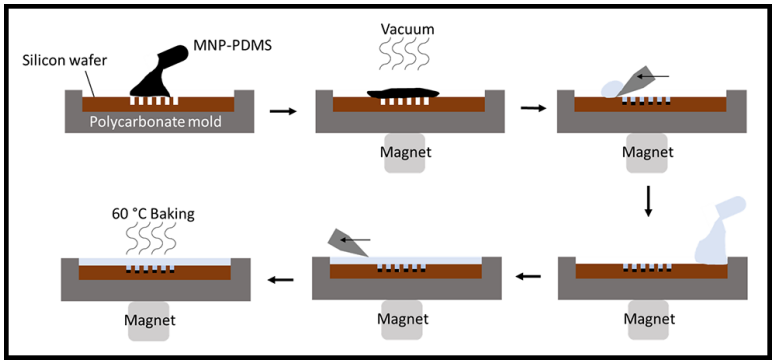

Figure 2: Illustration of fabrication process for micropillar array loaded with magnetic nanoparticles, using the master wafers.

even at the theoretical lower limit of soft lithography process (2 μm features). Future plan for these devices includes varying the dimensions or design, as well as fabricating extra master wafers for higher throughput device fabrication.

For the GMI sensor protocol, several challenges were met in the lift-off process, where the edge of the metal layers have a tendency to peel off when stripping the photoresist, resulting in partially incomplete or completely destroyed patterns. The future plan for this protocol includes optimization of pattern design to protect the layers.

References:

[1] Gu, H.; Lee, S. W.; Carnicelli, J.; Zhang, T.; Ren, D., Magnetically driven active topography for long-term biofilm control. Nature Communications 2020, 11 (1), 2211.

Fabrication of Microchip Devices for Organ-on-a-Chip and Lab-on-a-Chip

CNF Project Number: 2857-19
Principal Investigator(s): Esak (Isaac) Lee, Ph.D.
User(s): Renhao Lu, Yansong Peng

Affiliation(s): Meinig School of Biomedical Engineering, Cornell University
Primary Source(s) of Research Funding:
Contact: el767@cornell.edu, rl839@cornell.edu, yp255@cornell.edu
Primary CNF Tools Used: Heidelberg Mask Writer - DWL2000, ABM Contact Aligner, MVD 100

Abstract:

Organ-on-a-chip is a microfluidic cell culture platform, integrated circuit (chip) that simulates the activities, mechanics, and physiological response of an entire organ or an organ system. Our lab aims to create organ-on-a-chip devices to study the mechanism of various diseases. In the past year, we mainly focused on two projects: glaucoma-on-a-chip study and Micropatterned traction force microscopy for blood and lymphatic endothelial monolayer in pancreatic ductal adenocarcinoma (PDAC).

Summary of Research, Project 1: Glaucoma-on-a-Chip Model

Fluid homeostasis in the human eyes is maintained by the eye-specific fluid drainage system comprised of Trabecular meshwork (TM) and Schlemm's canal (SC). Structural and functional defects in TM and SC may impede ocular fluid drainage, elevating intraocular pressure (IOP) and damaging retinal ganglion cells, which initiates glaucoma pathogenesis. Here, we developed a dual-layer microfluidic chip system that allows coculture of TM and SC cells, recreating a three-dimensional (3D) SC channel surrounded by TM cells, mimicking the eye-specific fluid drainage system.

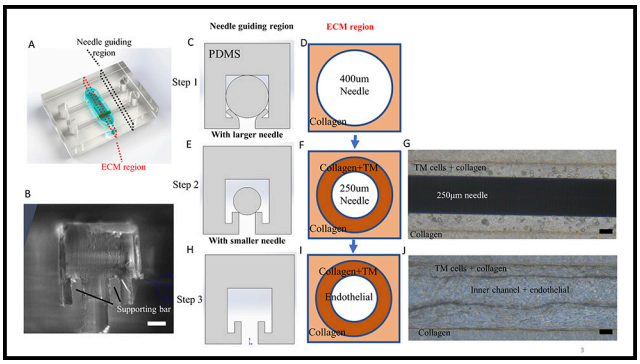

Figure 1: Fabrication of the glaucoma-on-a-chip model. (A) Schematic image of the microfluidic device. (B) The cross-section of the needle guiding region. (C-G) Three steps for fabricating the dual layer structure of TM cells and SC endothelial cells. Scale bar: (B, G, J) 50 μm.

The glaucoma-on-a-chip device design is shown in Figure 1A. In order to achieve the bilayer structure, we designed the cross-section of the needle guiding region as Figure 1B, and the function of this needle guiding region is shown in Figure 1C-J. In the first step, the larger needle was inserted into the needle guiding region, bending the supporting bar, and creating a larger cylinder channel in the ECM region (Figure 1C, D). In the second step, we filled the channel with TM cells suspended in collagen solution and inserted a smaller needle. The supporting bar kept standing to keep the smaller needle in the center of the larger channel (Figure 1E-G). In the last step, the smaller needle was withdrawn and a monolayer of endothelial cells was seeded onto the inner channel, forming a dual layer of TM and SC cells (Figure 1H-J).

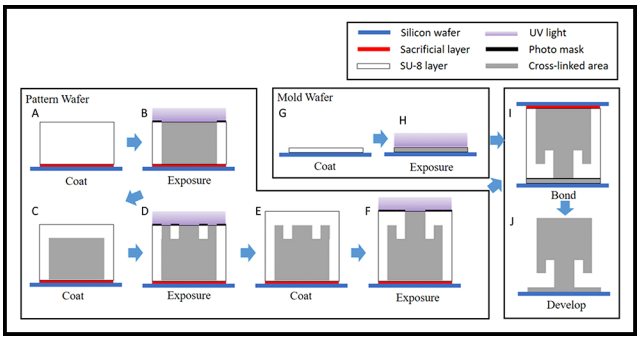

Figure 2: Modified "sandwich" method for fabricating the SU-8 needle guiding region. (A-F) One layer of OmniCoat and three layers of SU-8 were coated and exposed on the pattern wafer. (G-H) One single layer of SU-8 50 was coated and exposed on the model wafer. (I-J) The two wafers were joined before the final PEB, and the final needle guiding layer with two supporting bars was fabricated as designed.

In order to fabricate the needle guiding region with a supporting bar as shown in Figure 1B, we modified the "sandwich" fabrication method which was reported previously [1]. The microfabrication photolithography for the PDMS mold needs to combine two 100 mm

silicon wafer substrates, one was fabricated as a 'pattern wafer' (Figures 2A-F), and another was fabricated as a 'mold wafer' (Figure 2G, H).

Based on the dual layer glaucoma-on-a-chip model, we found that the coculture of SC and TM could better model the development of glaucoma compared with the monoculture of TM or SC Further, Based on NicheNet and angiogenesis reverse western arrays, we further identified VEGF-C and TGFβ as potential targets that may play a role in glaucoma development. Our finding suggests targeting VEGF-C and TGFβ pathways for the development of future glaucoma therapeutic methods.

Summary of Research, Project 2: Micropatterned TFM for Blood and Lymphatic Endothelial Monolayer in PDAC

Pancreatic ductal adenocarcinoma (PDAC) is the most common type of pancreatic cancer and one of the deadliest neoplastic malignancies in humans. It is characterized by desmoplastic stroma, paucity of tumor blood vessels, colonization of tumor-associated immunosuppressive cells, dysfunctional lymphatic vessels, and highly elevated solid stress and interstitial fluid pressure (IFP) [2]. The efficacy of immunotherapy relies on the infiltration of T cells in the tumor microenvironment (TME), but T cell infiltration is difficult under high IFP and with dysfunctional vasculature [3,4].

By combining anti-angiogenic therapy to normalize blood vessels with checkpoint blockade therapy targeting PD-L1, many mechanisms have been described for blood vascular normalization enhancement of immunotherapy in mouse tumor models [5-7]. More recent reports indicate that lymphatic vessels may play an equally significant role in the efficacy of cancer immunotherapies, previously overshadowed by harmful metastasis [8,9].

As a result of these recent findings, lymphatic vessels are now being investigated as targets to alter the TME and response to immunotherapy.

In order to understand the correlation among the intratumoral IFP, blood vessels, and lymphatic vessels, we need to investigate the relationship between vascular endothelial cadherin (VE-cad) junction and biophysical properties (i.e., traction force, intercellular force, and permeability) of endothelium with or without tumor. By creating a patterned endothelial cell monolayer on a force sensing platform, we were able to quantify and characterize the traction and intercellular force of endothelial cells in a control or tumor condition.

A microstamp mimicking the cannula shape of a vessel was fabricated using the soft lithography method (Figure 3A). The surface of a polyacrylamide gel (PAG) based substrate was preprocessed and stamped with cell adhesion molecules (e.g., fibronectin) for cell attachment (Figure 3B). Traction maps were then generated by measuring the displacement of the microbeads embedded in the gel substrate using fluorescent microscopy and Matlab processing (Figure 3C). Results were shown in Figure 4.

References:

[1] Kwak, T.J., and E. Lee. Biofabrication 13.1 (2020): 015002

[2] Osuna de la Pena, D., et al., Nat Commun, 2021. 12(1): p. 5623.

[3] Bellone, M. and A. Calcinotto, Frontiers in Oncology, 2013. 3(231).

[4] Huang, Y., et al., Nature Reviews Immunology, 2018. 18(3): p. 195-203.

[5] Mpekris, F., et al., Proceedings of the National Academy of Sciences, 2020. 117(7): p. 3728-3737.

[6] Shigeta, K., et al., Hepatology, 2020. 71(4): p. 1247-1261.

[7] Huang, Y., et al., Proceedings of the National Academy of Sciences, 2012. 109(43): p. 17561.

[8] Lund, A.W., Trends in Cancer, 2016. 2(10): p. 548-551.

[9] Vaahtomeri, K. and K. Alitalo, Cancer Res, 2020.

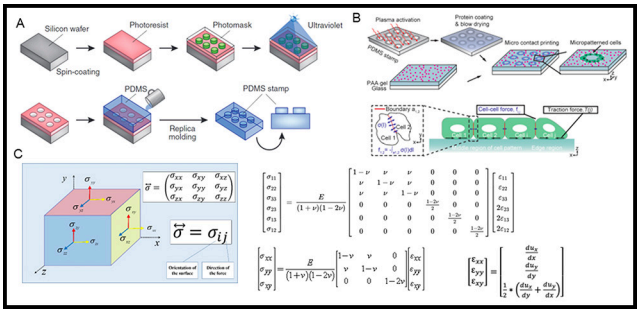

Figure 3: Schematic for micropatterned TFM. (A) Microfabrication process of PDMS stamps for micro-contact printing. Adapted from Bhatia et al., Nat. Biotech., 2014. (B) Fabrication of polyacrylamide gel based substrates with embedded fluorescent microbeads for force detection. (C) Computational modeling of traction force between the cell and the force detection substrate. (B) and (C) are both adapted from Cui, et al., Biophysical Jour., 2020.

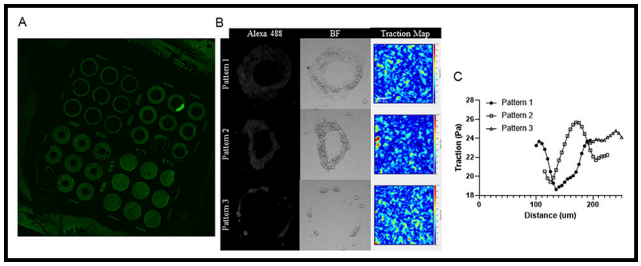

Figure 4: Micropatterned TFM for cancer cell mechanophenotyping. (A) Micropatterned surface of the force detection substrate. (B) Traction map of patterned cancer cells generated from the force detection substrate. (C) Quantification of the traction force in (B).

Human MSCs Release Multiple EV Populations Containing Mitochondria

CNF Project Number: 2864-20
Principal Investigator(s): Dr. Michelle L. Delco, DVM, PhD, DACVS
User(s): Matthew Thomas

Affiliation(s): College of Veterinary Medicine, Department of Clinical Sciences; Cornell University
Primary Source(s) of Research Funding: Harry M. Zweig Fund for Equine Research National Institute of Health-National Institute of Arthritis and Musculoskeletal and Skin Diseases
Contact: mld12@cornell.edu, mt826@cornell.edu
Primary CNF Tools Used: Malvern Nano ZS Zetasizer, Malvern NS300 NanoSight

Abstract:

A growing body of evidence supports intracellular mitochondrial (MT) transfer as an important intercellular signaling mechanism. Further, increasing evidence suggests that Mesenchymal Stromal Cells (MSCs) can rescue injured and dysfunctional cells by donating whole mitochondria, and this phenomenon may explain the beneficial effects of therapeutically implanted MSCs. One possible mechanism for MT transfer involves packaging mitochondria into extracellular vesicles (EVs). This would open the possibility of cell-free MT-targeted regenerative therapies. Confirming that this is possible would be an important step toward therapeutic development. As demonstrated here, human MSCs produce EVs containing MT. We have used the CNF facilities to further characterize these 'mitovesicles' and found that there are multiple populations of different sizes, indicating different modes of biogenesis and/or distinct bio-signaling functions.

Summary of Research:

The phenomenon of intercellular mitochondrial transfer, by which mesenchymal stromal cells donate whole mitochondria (MT) to other cell types undergoing MT dysfunction, is a promising avenue for therapeutic intervention in degenerative disease [1]. Mitochondrial donation has been demonstrated in multiple cell types, including neurons and myocytes. It has been shown to improve MT function and prevent apoptosis *in vitro*, as well as improve tissue repair *in vivo* [2–4].

Our lab studies MSC MT donation in the context of orthopedic disease, using *in vitro* chondrocyte cultures and explanted cartilage tissue as models. Using confocal imaging, we have identified several possible modes of MSC-chondrocyte MT transfer, including direct cell-cell contact (e.g., nanotubule-medial filipodial transfer, gap junction-mediated transfer) and what appears to be non-contact transfer, whereby MSCs release mitochondria into the extracellular space, which are then taken up by chondrocytes. We hypothesize that these are MT are packaged inside of extracellular vesicles (EVs) as so-called 'mitovesicles'.

This strategy of loading MT into EVs has precedent in literature. Phinney, et al., showed that MSCs can use mitovesicles, to outsource mitophagy of depolarized MT to macrophages, boosting bioenergetics for both the donating MSC and the recipient macrophage [5]. Furthermore, Morrison, et al., used cellular staining and flow cytometry to demonstrate that distressed lung epithelial cells can take up MT through EV-mediated transfer, and this ameliorates lung injury *in vivo* [6].

Our goal was to characterize the EVs produced by human MSCs. EVs are an inherently heterogenous population, making specific categorization difficult. However, it is widely recognized that they fall into three size categories: small (15-100 nm, exosomes), medium (150-1000, microvesicles), and large (1 μm+, apoptotic bodies). We isolated EVs from human bone marrow derived MSCs and used dynamic light scattering (DLS) to analyze their size distribution (Figure 1). As expected, we found the three categories supported by previous work [7] (Figure 1).

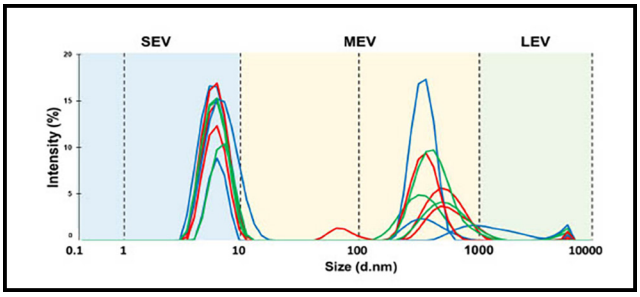

Figure 1: Dynamic Light Scattering of human MSC-derived extracellular vesicles (EVs) reveals three sub-populations of EVs based on size: small, (SEV; ~5-10nm) medium, (MEV; ~100-1000nm) and large (LEV; 5,000-10,000nm). N =3.

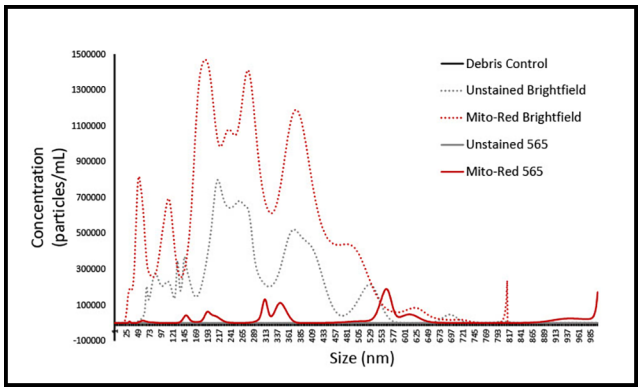

Figure 2: NTA supports trend of larger EVs containing MT. EVs were stained with Mitotracker Red and run with either a non-fluorescent (brightfield) filter, or with fluorescence exciting at 565 nm. These groups were compared to non-stained EVs and a double filtered PBS control. Unstained particles were undetectable using the 565 filter. Mitotracker positive EVs seemed to show a trend towards a larger size, with nearly all of the smallest population disappearing altogether. N = 1.

Next, we used the Malvern NS300 NanoSight to identify which, if any of these categories contain MT. We stained hMSC EVs with Mitotracker Red, then performed nanoparticle tracking analysis using the NanoSight's 565 nm fluorescent filter. We were able to validate that this method allows us to track exclusively EVs that contain mitochondrial content (Figure 2). Further, we found that mitovesicles make up around 20% of the total EV's released and appear to trend slightly larger than the general population (Figure 2). The significance of these findings is not yet clear, but likely reflects distinct modes of biogenesis and cargos for different sub-populations of mitovesicles.

Conclusions and Future Steps:

Our work thus far has confirmed our ability to isolate EVs from MSCs and identify mitovesicles within that population. Our next step is to identify and separate the EVs that contain functional and non-functional MT. This will allow us to begin identifying the role that these particles play in intercellular signaling and to further investigate MSC-EV mediated MT transfer.

This work has contributed to a poster, "MitoEVs Containing CX43 Transfer Mitochondria to Chondrocytes" that was presented at the International Gap Junction Conference 2022 and a manuscript, "Human Mesenchymal Stromal Cells Release Functional Mitochondria in Extracellular Vesicles" that is currently being proofed for publication in Frontiers in Bioengineering and Biotechnology.

References:

[1] Delco, M. L., Bonnevie, E. D., Bonassar, L. J., and Fortier, L. A. Mitochondrial dysfunction is an acute response of articular chondrocytes to mechanical injury. J. Orthop. Res. 36, (2018).

[2] Jiang, D., et al. Mitochondrial transfer of mesenchymal stem cells effectively protects corneal epithelial cells from mitochondrial damage. Cell Death Dis. 7, (2016).

[3] Konari, N., Nagaishi, K., Kikuchi, S., and Fujimiya, M. Mitochondria transfer from mesenchymal stem cells structurally and functionally repairs renal proximal tubular epithelial cells in diabetic nephropathy *in vivo*. Sci. Rep. 9, (2019).

[4] Spees, J. L., Olson, S. D., Whitney, M. J., and Prockop, D. J. Mitochondrial transfer between cells can rescue aerobic respiration. Proc. Natl. Acad. Sci. U. S. A. 103, (2006).

[5] Phinney, D. G., et al. Mesenchymal stem cells use extracellular vesicles to outsource mitophagy and shuttle microRNAs. Nat. Commun. 6, (2015).

[6] Morrison, T. J., et al. Mesenchymal stromal cells modulate macrophages in clinically relevant lung injury models by extracellular vesicle mitochondrial transfer. Am. J. Respir. Crit. Care Med. 196, (2017).

[7] Zhang, X., Hubal, M. J., and Kraus, V. B. Immune cell extracellular vesicles and their mitochondrial content decline with ageing. Immun. Ageing 17, (2020).

Scalable Continuous Flow Electroporation Platform

CNF Project Number: 2900-20
Principal Investigator(s): Thomas Corso
User(s): Jacob VanderBurgh

Affiliation(s): CyteQuest
Primary Source(s) of Research Funding: Investor funding
Contact: tcorso@cytequest.com, jvanderburgh@cytequest.com
Website: https://cytequest.com/
Primary CNF Tools Used: Odd-Hour Evaporator

Abstract:

Viral vectors are a bottleneck in the manufacturing of cell therapies. To bypass viral vectors, electroporation has emerged as a non-viral transfection method for primary cells. However, standard cuvette-style approaches are limited by difficult optimization and incompatibility with large-scale cell manufacturing. Here, we present and fabricate a novel electroporation platform that can efficiently transfect small volumes of cells for research and process optimization and scale to volumes required for applications in cellular therapy. We demonstrate of messenger ribonucleic acid (mRNA) to primary human T cells with high efficiency and viability at research scale and we demonstrate seamless scaling of delivery by increasing experimental throughput by a factor of five.

Report:

To address limitations associated with cuvette-style electroporation, CyteQuest has developed a scalable electroporation platform to optimize transfection parameters and deliver cargo efficiently and reproducibly at high throughput. Our approach incorporates a single use, continuous-flow fluidic system designed to integrate with automated cell processing approaches.

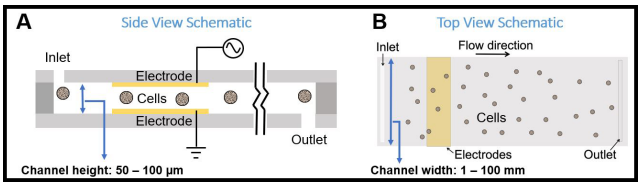

Figure 1: (A) Side view schematic of the flow cell (not to scale). (B) Top view schematic of the flow cell (not to scale).

The prototype electroporation flow cell consists of a planar flow chip with a thin slab geometry. It contains a single fluid inlet/outlet that receives cells suspended in electroporation buffer containing the cargo to be delivered. Electrodes are patterned on the top and bottom flow cell surfaces in order to apply a uniform electric field perpendicular to the flow direction (Figure 1A). The thin slab geometry of the device ensures that each cell is subject to the same electric field and the same chemical environment enabling reproducible electroporation. The shallow height (50 -100 µm) also means that we can achieve the necessary electric field strength to open pores in the cellular and nuclear membranes by applying relatively low voltages (~15 V) compared to the high voltage of traditional commercial systems. The width (1-100 mm) of the device is much larger than its depth to allow for rapid and continuous flow of the cells through the chip (Figure 1B). Importantly, the width of the device can be varied to match the desired experimental throughput without changing the electric field experienced by the cells. As such, our planar geometry enables us to seamlessly scale from small volumes of precious sample to determine optimal transfection parameters to large volumes for delivery at clinical scales.

Electroporation flow chips are constructed from a three-layer stack of polymer substrates. All three layers are laser cut with a small beam spot, high resolution carbon dioxide laser. The top and bottom layers, cut from 1 mm thick acrylic slabs, create the floor and sealing channel

surfaces. The middle layer is a spacer that defines the channel depth and width and is composed of a thin pressure sensitive adhesive tape. To fabricate the chip, the bottom and top acrylic layers are laser-cut into 1" × 2" pieces. The pieces are then laser-cut to add fluid inlet/outlet ports and alignment holes for use during the assembly process. Afterwards, a thin film electrode of gold is deposited by physical vapor deposition on the inside surface of each acrylic piece at the CNF using the odd-hour evaporator. The middle layer is cut to shape and also receives the corresponding alignment holes via the laser cutting process. The three-piece (acrylic, spacer, acrylic) sandwich assembly is then compression bonded in a press.

Cells with the cargo to be transfected are loaded into a syringe and injected through tubing into the flow cell by a syringe pump. As cells flow through the electrode pair, they experience a spatially uniform electrical field produced by a computer-controlled function generator and amplifier. The applied voltage waveform and resultant current are monitored via an oscilloscope. The electroporated cells then exit the flow cell and are dispensed into wells of a well-plate by a robotic fraction collector. Computer-controlled waveform selection and robotic sampling enable rapid sweeping of waveform parameters such as the voltage amplitude or waveform shape.

Using this system, CyteQuest has delivered mRNA encoding green fluorescent protein (GFP) to primary human T cells with high efficiency and high viability, observing > 95% transfection efficiency with < 2% loss of cell viability compared to control cells (Figure 2). To demonstrate the ability of our device to scale experimental throughput, we increased the width of the device from 2 to 10 mm and the volumetric flow rate from 320 µL/min to 1.6 mL/min (Figure 3A-B). Scaling both the channel width and flow rate by a factor of five produced identical GFP expression and viability values in both channel widths for Jurkat cells transfected with mRNA encoding GFP (Figure 3B). Overall, these data demonstrate the ability of our platform to efficiently deliver mRNA to cells and seamlessly scale-up delivery without changing delivery performance.

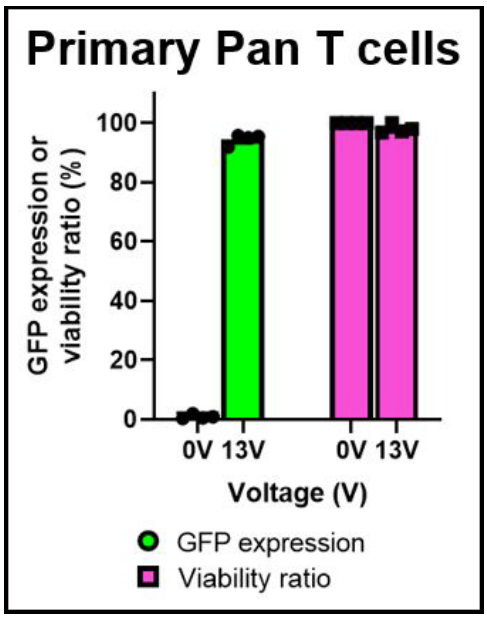

Figure 2: Delivery of mRNA to primary human T cells. Data from primary T cells from four healthy donors (n = 4). Data shown as mean ± standard deviation.

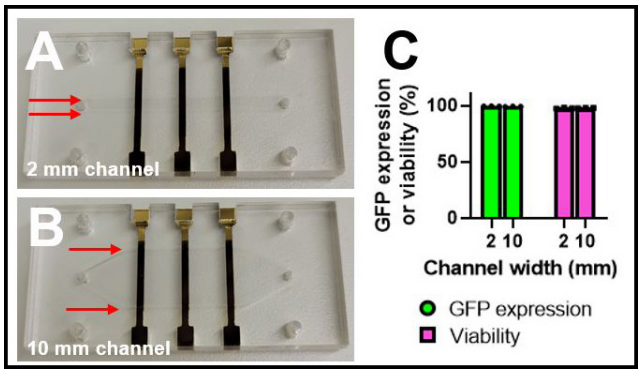

Figure 3: Scaled-up delivery of mRNA to Jurkat cells. (A) Photograph of a 2 mm and (B) 10 mm electroporation flow cell. Red arrows highlight the channel width. (C) Plot of GFP expression and viability values from Jurkat cells transfected with mRNA encoding GFP in either the 2- or 10-mm channels (n = 3). Data shown as mean ± standard deviation.

Plant Membrane Bioelectronic Devices for the Study of a Membrane Transporter

CNF Project Number: 2908-20
Principal Investigator(s): Susan Daniel
User(s): Barituziga Banuna, Miriam Huerta

Affiliation(s): Smith School of Chemical and Biomolecular Engineering, Cornell University
Primary Source(s) of Research Funding: NSF EAGER GRANT
Contact: sd386@cornell.edu, bb675@cornell.edu, gh437@cornell.edu
Primary CNF Tools Used: Malvern NS300 NanoSight

Abstract:

As a "label-free" alternative to optical sensing, electrical sensing represents a more feasible, reproducible, and scalable detection method [1,2]. Among various electrical sensing techniques, the non-invasive electrochemical impedance spectroscopy (EIS) technique is especially suitable for accurately quantifying the bio-recognition events occurring at a variety of biointerfaces, such as bacterial, viral, cellular and synthetic lipid membranes [3,4]. Our group aims to design a microelectrode system that will support the self-assemble of supported lipid bilayers (SLBs) on the electrode surfaces, and their electrical properties (resistance, capacitance) can be extracted by applying an alternating voltage and recording the current response [4-7]. Since the electrode dimensions and the local environment are readily controlled via photolithography, this system gives us a edge to easily mimic and manipulate the local environment to support the assembly of various SLBs of interest. Future work will focus on the incorporation of the microfluidic system into the microelectrode system.

Summary of Research:

Lipid vesicle nanoparticles were induced to form via chemical induction of cell-wall free Arabidopsis Thaliana plant protoplast. These vesicles or blebs composed of the native membrane materials were collected and then the size, distribution and concentration were characterized via NTA with Malvern NS300 NanoSight. Following characterization, blebs were used to form SLBs on microelectrodes and the resulting device was used with electrical sensing techniques such as EIS.

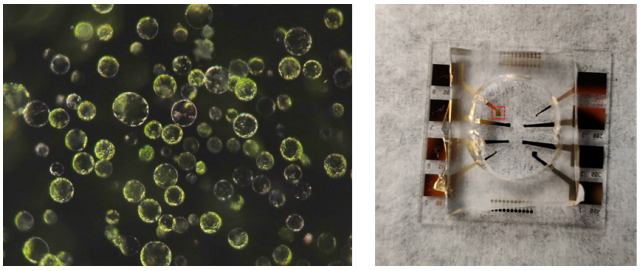

Figure 1: Arabidopsis Thaliana *derived protoplast (left); PDMS well stamped on a single device to enable self-assembling of SLB and EIS measurement (right).*

References:

[1] Berggren, Magnus, and Agneta Richter-Dahlfors. "Organic bioelectronics." Advanced Materials 19.20 (2007): 3201-3213.

[2] Chalklen, Thomas, Qingshen Jing, and Sohini Kar-Narayan. "Biosensors based on mechanical and electrical detection techniques." Sensors 20.19 (2020): 5605.

[3] Magar, Hend S., Rabeay YA Hassan, and Ashok Mulchandani. "Electrochemical Impedance Spectroscopy (EIS): Principles, Construction, and Biosensing Applications." Sensors 21.19 (2021): 6578.

[4] Lisdat, F., and D. Schäfer. "The use of electrochemical impedance spectroscopy for biosensing." Analytical and Bioanalytical Chemistry 391.5 (2008): 1555-1567.

[5] Tang, Tiffany, et al. "Functional infectious nanoparticle detector: Finding viruses by detecting their host entry functions using organic bioelectronic devices." ACS Nano 15.11 (2021): 18142-18152.

[6] Bint E Naser, Samavi Farnush, et al. "Detection of Ganglioside-Specific Toxin Binding with Biomembrane-Based Bioelectronic Sensors." ACS Applied Bio Materials 4.11 (2021): 7942-7950.

[7] Pappa, Anna-Maria, et al. "Optical and electronic ion channel monitoring from native human membranes." ACS Nano 14.10 (2020): 12538-12545.

Investigating the Effect of the Tumor Microenvironment on Metastatic Progression using Micro and Nano-Scale Tools

CNF Project Number: 2912-20

Principal Investigator(s): Claudia Fischbach

User(s): Matthew Tan, Niaa Jenkins-Johnston, Nicole Sempertegui

Affiliation(s): Biomedical Engineering, Cornell University

Primary Source(s) of Research Funding: 2021 Cornell NanoScale Facility REU Program National Science Foundation Grant No. NNCI-2025233, Stem Cell Research Training Fellowship Stem Cell Program of Cornell University, the Center on the Physics of Cancer Metabolism National Cancer Institute Award Number 1U54CA210184-01

Contact: cf99@cornell.edu, mlt239@cornell.edu, noj4@cornell.edu, nds68@cornell.edu

Primary CNF Tools Used: ABM Contact Aligner, Heidelberg Mask Writer - DWL2000, Hamatech 9000, Malvern NS300 NanoSight

Abstract:

Breast cancer mortality is driven by metastasis, where cancer cells disseminate from the primary tumor to seed distant tissues. During the metastatic cascade, cancer cells interact with their microenvironment consisting of extracellular matrix including collagen and other cell types including endothelial cells in blood vessels and mesenchymal stromal cells (MSCs) in the bone. Cancer cells may interact locally or from distant sites through mechanisms such as soluble factor and extracellular vesicle (EV) signaling. In this study, CNF tools were used to investigate the two stages in metastasis: early invasion towards blood vessels and EV-mediated formation of a pre-metastatic niche. For the former, we developed a microfluidic model of the perivascular niche and found that ECs stimulate breast cancer invasion into collagen, and that an EC-coated micro channel exhibits a distinct diffusion profile from a channel without ECs. For the latter, we've been able to isolate and characterize EVs from two breast cancer cell lines. Future work will continue to use the microfluidic model to investigate the mechanisms by which ECs influence cancer invasion and apply EVs to MSCs on a bone-mimetic model system to investigate how cancer cells can influence the formation of a pre-metastatic niche.

Summary of Research:

Introduction. Breast cancer is the second leading cause of cancer-related death for women in the United States [1]. Mortality in breast cancer is driven by metastasis, where tumor cells disseminate from the primary tumor and spread to distant tissues. During this process, tumor cells become invasive and move towards blood vessels, where they will enter the circulation and seed onto distance sites such as the bones. Tumor cells that proceed through the metastatic cascade encounter a changing microenvironment consisting of extracellular matrix (ECM) such as collagen and other cell types, including endothelial cells (ECs) and mesenchymal stromal cells (MSCs) [2]. These cells are known to participate in reciprocal signaling with tumor cells to influence tumorigenesis through the exchange of soluble factors [2,3].

Incidentally, tumor cells may even be able to prime future metastatic sites through the release of extracellular vesicles (EVs) that enable long distance transport of cell-derived cargo [4]. However, the mechanisms by which soluble factor and EV signaling influence tumor cell invasion and the development of a pro-tumorigenic microenvironment remain unclear due to the lack of models that enable systematic study. To this end, we have used the expertise at the CNF to investigate two key steps in the metastatic cascade: initial invasion towards ECs in blood vessels, and EV-mediated formation of the pre-metastatic niche.

Regulation of Breast Cancer Invasion Using a Microfluidic Model of the Perivascular Niche. In early invasion, tumor cells initially invade towards blood vessels, responding to metabolic gradients from the vessels and signaling gradients from ECs. Using SU-8 photolithography in conjunction with the ABM Contact Aligner and a photomask generated by the Heidelberg DWL2000, we have created a dual-channel microfluidic devices that enables co-culture of breast cancer cells and ECs encapsulated in a 3D collagen matrix. In this system,

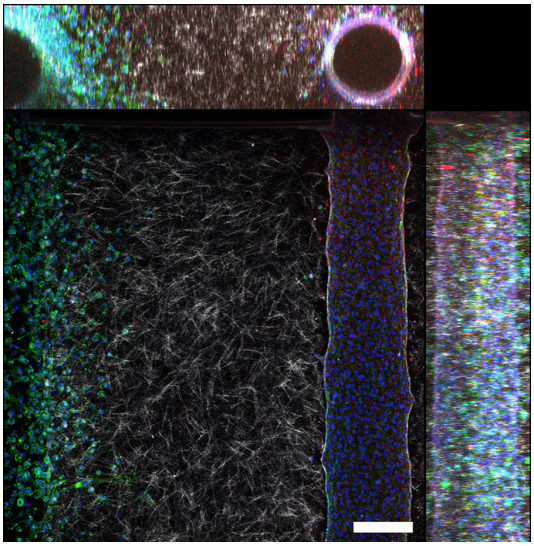

Figure 1: Confocal microscopy projection of breast cancer cells stained with invading into collagen in response to an endothelial cell channel stained with CD31 (red). DAPI was used to stain nuclei (blue), phalloidin was used to stain f-actin (green), and confocal reflectance was used to visualize collagen fibers (white). Scale bar: 200 µm.

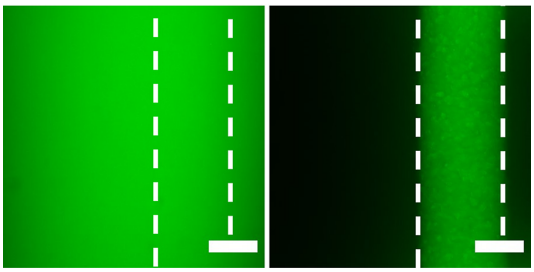

Figure 2: Diffusion of fluorescein (FITC) from a non-human umbilical vein endothelial cell (HUVEC) channel and a HUVEC coated channel. Scale bar: 200 µm.

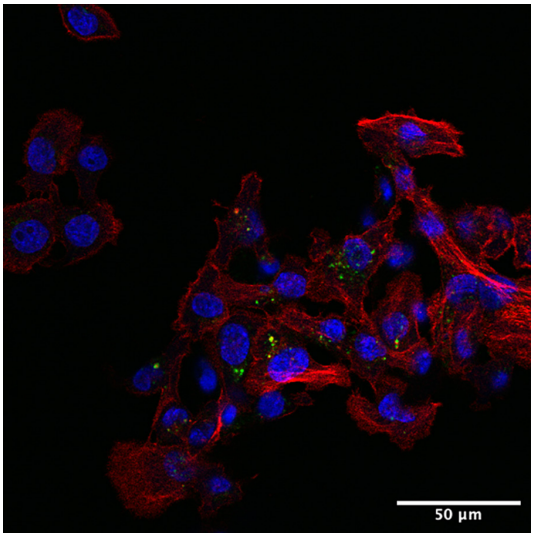

Figure 3: Extracellular vesicles labeled with a DiO lipophilic dye (green), MCF10ACA1a cells labeled with DAPI for nuclei (blue) and phalloidin for f-actin (red). Scale bar: 50 µm.

we found that the presence of ECs stimulated cancer invasion into a collagen hydrogel (Figure 1). Additionally, using fluorescent molecule diffusion studies, we found that an EC-coated channel restricted diffusion of molecules within in the channel compared to a channel without ECs (Figure 2).

Isolation and Characterization of Breast Cancer-Derived Extracellular Vesicles. Prior to arriving at distant metastatic sites, tumor cells can release soluble factors and extracellular vesicles (EVs) into the circulation to prime the microenvironment of distant target organs for subsequent development of organotropic metastasis. While soluble factor signaling plays a demonstrated role in cancer, EVs are gaining appreciation as stable vehicles of cell-derived cargo contributing to tumorigenesis and pre-metastatic niche (PMN) formation. Thus far, we have successfully isolated and characterized EVs from MDA-MB-231s and MCF10CA1a breast cancer cells using the Malvern NS300 NanoSight (Figure 3). Additionally, we have started to investigate differences in cell adhesion between MSCs cultured in the presence or absence of EVs that bind to the bone matrix.

Conclusions and Future Steps:

In this project we were able to develop tools and pipelines to study the breast cancer metastatic cascade. We were able to successfully fabricate and culture a 3D microfluidic tumor-perivascular niche model. Future work using this device will be to uncover the metabolic and mechanical mechanisms by which ECs influence breast cancer invasion. We were also able to isolate and characterize breast cancer derived ECs. Future work will assess markers of MSC behavior in the presence of EVs in a biomimetic mineralized bone scaffold. This will include investigating differences in differentiation fate, proliferation and cytokine secretion. Finally, we will examine whether these changes in MSC phenotype in turn affect metastatic breast cancer cell outgrowth.

Acknowledgements:

The work described was supported by the Center on the Physics of Cancer Metabolism through Award Number 1U54CA210184-01 from the National Cancer Institute. The content is solely the responsibility of the authors and does not necessarily represent the official views of the National Cancer Institute or the National Institutes of Health.

References:

[1] Siegel, R. L., Miller, K. D., Fuchs, H. E., and Jemal, A. Cancer Statistics, 2021. CA. Cancer J. Clin. 71, 7-33 (2021).

[2] Tan, M. L., Ling, L., and Fischbach, C. Engineering strategies to capture the biological and biophysical tumor microenvironment *in vitro*. Adv. Drug Deliv. Rev. 176, 113852 (2021).

[3] Zheng, P., and Li, W. Crosstalk Between Mesenchymal Stromal Cells and Tumor-Associated Macrophages in Gastric Cancer. Front. Oncol. 10, 1-9 (2020).

[4] Peinado, H., et al. Pre-metastatic niches: organ-specific homes for metastases. Nat. Rev. Cancer 17, 302-317 (2017).

Sample Preparation for Study of Space Charge Limited Current

CNF Project Number: 863-00
Principal Investigator(s): John Marohn
User(s): Rachael Cohn, Virginia McGhee

Affiliation(s): Department of Chemistry and Chemical Biology, Cornell University
Primary Source(s) of Research Funding: National Science Foundation
Contact: jam99@cornell.edu, rc784@cornell.edu, vem26@cornell.edu
Website: http://marohn.chem.cornell.edu/
Primary CNF Tools Used: Heidelberg Mask Writer - DWL2000,
ABM Contact Aligner, Odd Hour Evaporator

Abstract:

Scanning probe microscopy is used to study charge injection from a metal to a pi-conjugated system. Unique capabilities of a custom-built electric force microscope will be utilized to reproduce data collected in Ref. [1]. This report discusses substrate preparation conducted at the Cornell NanoScale Science & Technology Facility (CNF) to enable the study space charge limited current.

Summary of Research:

Organic photovoltaics have been steadily growing in both efficiency and functionality [2]. To design and operate organic electronic devices, it is essential to understand how charge is injected from a metal to a pi-conjugated organic system. Typically, there is an assumption that the electric field is uniform between the source and drain gap. However, studies done by Ng, Silveira, and Marohn, show that the electric field varies with both temperature and source-drain voltage [3]. Furthermore, at the injection site, the electric field differs greatly from the bulk, possibly due to the addition of space charge. The previous assumption has an error that propagates through the calculation of electron mobility and concentrations of free charge carriers [1]. To correct for these errors, space charge limited current in an organic photovoltaic film will be studied.

N,N'-diphenyl-N-N'-bis(3-methylphenyl)-(1,1'-biphenyl)-4,4'-diamine (TPD) / polystyrene (PS) films will be spin-coated on quartz substrates. The quartz substrates contain gold interdigitated electrodes prepared at the CNF. The preparation is based on Ref. [1]. The source-drain gap varies in length at 2, 5, 12, 16, and 20 μm, and the channel width varies at 1.5, 2, and 2.5 mm. There are a total of 68 electrodes per substrate and 15 different substrates with the various source-drain gaps and channel widths that can be made on one wafer.

A mask was designed in L-edit and printed using the Heidelberg mask writer. The substrate making process was begun by cleaning quartz wafers with hot piranha, spin coating resist, and exposing the wafer. An exposure matrix using the ABM contact aligner was done to determine the optimal exposure time.

Conclusions and Future Steps:

Users will expose a wafer using the determined exposure time, deposit a 50 Å Cr adhesion layer and 500 Å Au using the odd hour evaporator, lift off to remove excess Au, and dice the wafer to make 1 cm × 1 cm substrates. Once the substrates are completed, users will deposit TPD:PS films and study space charge limited current.

References:

[1] W. R. Silveira and J. A. Marohn, Microscopic view of charge injection in an organic semiconductor, Phys. Rev. Lett., 2004, 93, 116104, URL http://dx.doi.org/10.1103/PhysRevLett.93.116104.

[2] Q. Liu, Y. Jiang, K. Jin, J. Qin, J. Xu, W. Li, J. Xiong, J. Liu, Z. Xiao, K. Sun, S. Yang, X. Zhang, and L. Ding, 18% efficiency organic solar cells, Science Bulletin, 2020, 65, 272–275, URL http://dx.doi.org/10.1016/j.scib.2020.01.001.

[3] T. N. Ng, W. R. Silveira, and J. A. Marohn, Dependence of charge injection on temperature, electric field, and energetic disorder in an organic semiconductor, Phys. Rev. Lett., 2007, 98, 066101, URL http://dx.doi.org/10.1103/PhysRevLett.98.066101.

Nanopatterned Polymer Brushes with Localized Surface Functionalities

CNF Project Number: 1757-09

Principal Investigator(s): Christopher Kemper Ober

User(s): Yuming Huang

Affiliation(s): Department of Materials Science and Engineering, Cornell University
Primary Source(s) of Research Funding: National Science Foundation
Contact: cko3@cornell.edu, yh839@cornell.edu
Website: https://ober.mse.cornell.edu/index.html
Primary CNF Tools Used: E-beam Resist Spinners, JEOL 9500, FilMetrics F50-EXR, Oxford 81 Etcher, Zeiss Ultra SEM, Optical Microscope

Abstract:

It was previously reported that the arrangement of polymer brushes could be organized via an integrated process of electron-beam lithography, surface-initiated synthesis, and post-processing treatments. In this work, the customizability of such polymer nanostructure was further enhanced by chemically functionalizing the chain-ends of these nanopatterned brushes. It was later found that the distribution of these active endpoints was strongly correlated with the polymer chain alignments as characterized by florescence microscopes.

Summary of Research:

Introduction. Polymer brushes are polymer chains with one end covalently anchored to a surface. The development of surface-initiated polymerization enabled the fabrication of polymer brushes with high grafting density. Due to the unusual molecular arrangements and surface attachments, these densely grafted polymer brushes have exhibited unique mechanochemical properties and thus has gained wide interest from the polymer science community [1]. Potential applications of such thin film could be biosensors [2], photovoltaic devices [3], organic electronics [4], and biomimicry surfaces [5].

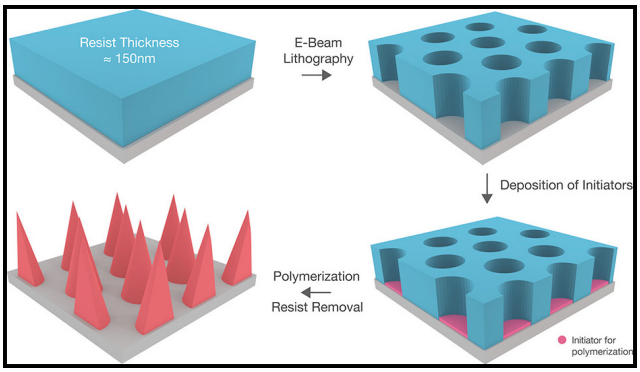

Figure 1: Schematic illustration of the fabrication process of nano-patterned brushes.

Previously we reported a nanopatterning process of making "spiky" nanoarrays of polypeptide rod brushes on silicon substrates, which has resulted in interesting "bridging" morphology governed by the localized chain-chain interactions (Figure 1) [6].

In this work, we further improved the customizability of these nanopatterned polymer brushes by developing end-point modification methods to chemically attach active compounds, such as florescent dyes, to the chain-ends.

Fabrication. The localized growth of polymer brushes was achieved via a sequential fabrication process of area-selective deposition of surface-immobilized initiators and surface-initiated polymerizations.

E-Beam Resist Mask Preparation. E-beam resist was patterned via JEOL 9500, which was later used as the mask for the vapor deposition of aminosilane initiators. Prior to the deposition, the substrate was descummed via the Oxford 81 etcher to remove residual debris in the unmasked area.

Synthesis of the Rod Brushes. The vapor deposition of the silane initiators was carried out in a closed chamber at 1 torr and 70°C for 18 hours. Afterward, the resist mask was removed by sonication in organic solvents. Subsequently, surface-initiated ring-opening

polymerization of poly-b-benzyl-L-glutamate (PBLG), a rod-like polymer, was carried out under continuous vacuum and 105°C for two hours.

End-Point Functionalization. 5 mg of rhodamine B isothiocyanate was dissolved in 2 ml of an hydrous dimethylformamide (DMF) together with a piece of PBLG brush sample. Then 0.8 ml of triethylamine was added to the solution. The reaction was allowed to proceed for 48 hours and the substrate was taken out, rinsed and sonicated in DMF for one minute and dried with nitrogen gas.

Characterization and Results. The thickness of the thin film was measured by FilMetrics F50-EXR. The patterned e-beam resist (Figure 2) and the patterned PBLG brushes (Figure 3) were characterized using Zeiss Ultra Scanning Electron Microscopy (SEM) and Veeco Icon Atomic Force Microscope (AFM) for topological analysis. The florescence behavior of the modified brushes was characterized using Zeiss LSM 710 confocal microscope (Figure 4).

Conclusions and Future Steps:

In addition to nanolithography and post-processing treatment, we have demonstrated that polymer nanostructures can be further customized by chemical modification of the chain-ends. The distribution and molecular arrangements of these active chain-ends can be examined by the behavior of the attached florescence molecules. In the near future, we plan to explore the possibility of functionalizing these nanostructures with bio-active compounds for biomimicry surface and modeling study. We also plan to introduce mixed rod-coil brushes in the same system for binary and stimuli-responsive surface functionalities.

References:

[1] W. L. Chen, M. Menzel, T. Watanabe, O. Prucker, J. Ruhe, and C. K. Ober, "Reduced Lateral Confinement and Its Effect on Stability in Patterned Strong Polyelectrolyte Brushes," Langmuir, vol. 33, no. 13, pp. 3296-3303, 2017, doi: 10.1021/acs.langmuir.7b00165.

[2] M. Welch, A. Rastogi, and C. Ober, "Polymer brushes for electrochemical biosensors," Soft Matter, vol. 7, pp. 297-302, 2011, doi: 10.1039/c0sm00035c.

[3] S. Saha and G. L. Baker, "Surface-tethered conjugated polymers created via the grafting-from approach," J Appl Polym Sci, vol. 132, no. 4, p. n/a-n/a, 2015, doi: 10.1002/app.41363.

[4] N. Doubina, et al., "Surface-initiated synthesis of poly(3-methylthiophene) from indium tin oxide and its electrochemical properties," Langmuir, vol. 28, pp. 1900-8, 2012, doi: 10.1021/la204117u.

[5] Z. Zhou, P. Yu, H. M. Geller, and C. K. Ober, "Biomimetic polymer brushes containing tethered acetylcholine analogs for protein and hippocampal neuronal cell patterning," Biomacromolecules, vol. 14, pp. 529-37, 2013, doi: 10.1021/bm301785b.

[6] Y. Huang, H. Tran, and C. K. Ober, "High-Resolution Nanopatterning of Free-Standing, Self-Supported Helical Polypeptide Rod Brushes via Electron Beam Lithography," ACS Macro Lett, vol. 10, no. 6, pp. 755-759, 2021, doi: 10.1021/acsmacrolett.1c00187.

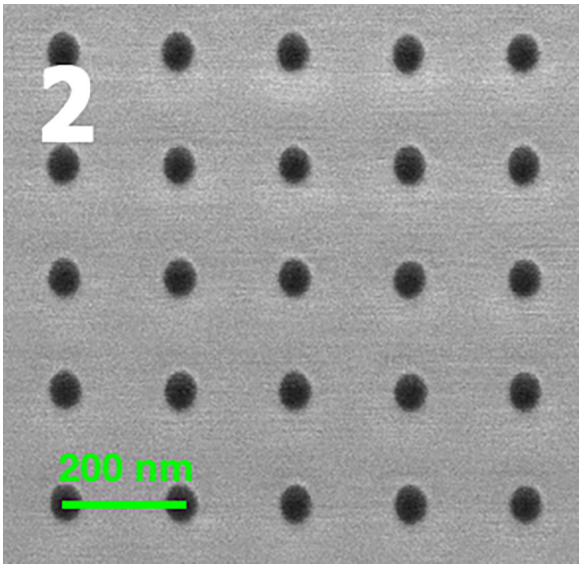

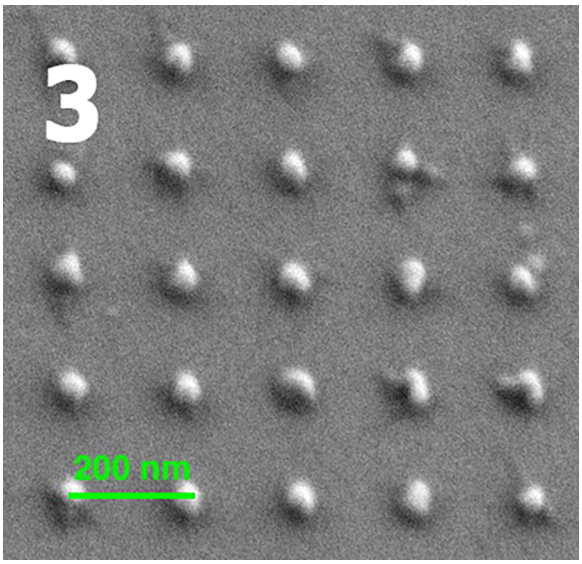

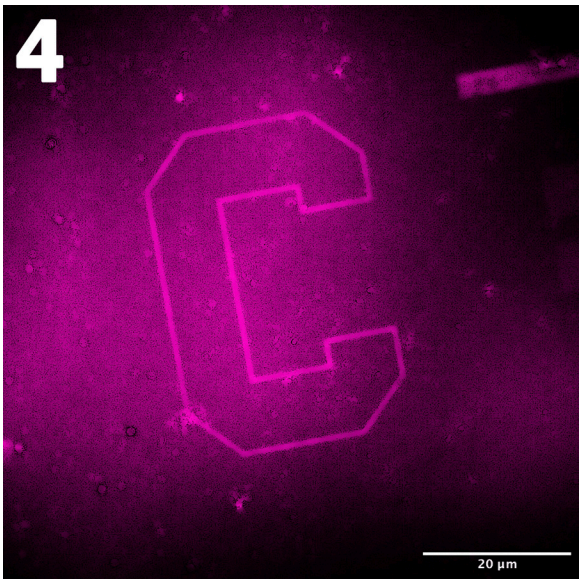

Figure 2, top: SEM of the patterned e-beam resist. Figure 3, middle: SEM of the patterned PBLG rod brushes. Figure 4, bottom: Florescence image of the rhodamine B functionalized patterned brushes.

Chemically Amplified Photoresists with Precise Molecular Structure

CNF Project Number: 1757-09

Principal Investigator(s): Christopher Kemper Ober

User(s): Florian Hermann Ulrich Kaefer

Affiliation(s): Department of Material Science and Engineering, Cornell University

Primary Source(s) of Research Funding: Intel

Contact: cko3@cornell.edu, hk28@cornell.edu

Website: https://ober.mse.cornell.edu/

Primary CNF Tools Used: ASML 300C DUV Stepper, AFM Bruker Icon, JEOL 6300 E-Beam, Woollam RC2, Zeiss Ultra SEM, YES HMDS Prime Oven

Abstract:

In most synthetic copolymers, monomer units are distributed randomly along the polymer chain. In sequence-controlled polymers such as peptides and peptoids, however, monomers are arranged in a specific, application-optimized order. Polypeptoids are thus attractive as a new category of photoresists for EUV lithography, as full control over the placement of individual functional groups yields in tunable properties with extremely low chemical, structural, and molar mass variability [1-3]. This report demonstrates the potential use of peptoids CAR resist using an electron-beam and deep-UV (DUV) lithography obtaining 36 nm line pattern.

Introduction:

Polymeric resists are typically based on random copolymers. These polymers are polydisperse and relatively large in size, with molar masses ranging from 5,000-15,000 g/mol [1]. Characteristics such as these can have a negative impact on resist performance, and therefore it is necessary to explore other architectures for new resist platforms. As a result, there has been research on using molecular glasses as photoresists due to their defined, repeatable structure, and low molecular weight compared to conventional polymeric photoresists. Like molecular glass, peptoids can be synthesized with a controlled sequence and chain length. Due to these properties, it is hypothesized that using peptoids as photoresist material may be the next promising path towards smaller feature sizes.

The goal of this project is to investigate and optimize the composition and sequence of the synthesized short peptoids to obtain resist with high resolution and good processibility, as the precise sequence of moieties is key to tuning the nano- and macro-scale characteristics of the resulting resists.

Results:

Peptoids with 10 repeat units were synthesized using a solid phase peptoid synthesis approach [3]. After activating the resin with bromoacetic acid for 30 min the first amine solution was added and the reaction was completed after 60 min. These steps were repeated until a peptoid with a total length of ten amines with a defined sequence was obtained, see Figure 1. Subsequently, the peptoid was cleaved from the resin under mild acetic conditions, purified and dried. Di-tert butyl decarbonate was used to protect the hydroxy groups to introduce solubility switching groups.

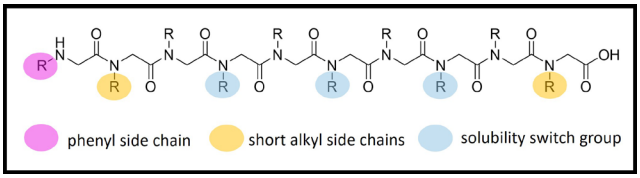

Figure 1: Peptoid 10mers used as positive tone chemically amplified resist (CAR).

The synthesized peptoids were characterized using matrix assisted laser desorption ionization (MALDI) time of flight (TOF) mass spectrometry, and differential-scanning calorimetry (DSC).

Resists with different sequences, composition, and hydrophobic side groups, were dissolved and spin coated on 4-inch silicon wafers. The resist film thickness was measured using a Woollam RC2 ellipsometer. The resist films were exposed using deep-UV (DUV) (ASML 300C stepper) and electron-beam (JEOL 6300). Sequence, composition, and the choice of hydrophobic side groups led to significantly changes in the solubility and performance.

The obtained patterns were characterized using scanning-electron microscopy (SEM) and atomic force microscopy (AFM Bruker Icon), see Figure 2. The micrographs of 24 nm-line pattern are demonstrating the potential of peptoids as new class of resists while the sequence, composition and total length are adjustable and are changing and affecting the lithographical performance. However, further research must be carried out to further improve the lithographical performance and demonstrate the potential of peptoids as a new generation of EUV resists.

Conclusions and Future Steps:

Sequence controlled peptoids were synthesized and successfully used as positive tone photoresist using the DUV and electron beam lithography. The obtained line patterns were characterized via SEM and atomic force microscopy, and proved the potential of peptoids as resists for electron and EUV lithography. However, further research on these new class of resists materials is required to optimize the properties of the resist as well as their performance.

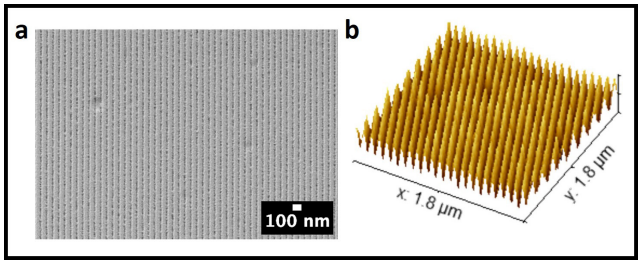

Figure 2: Line pattern by e-beam (a) SEM of line pattern 36 nm, (b) AFM 3D height profile.

References:

[1] Patterson, K.; Yamachika, M.; Hung, R.; Brodsky, C.; Yamada, S.; Somervell, M.; Osborn, B.; Hall, D.; Dukovic, G.; Byers, J.; Conley, W.; Willson, C. G., Polymers for 157-nm photoresist applications: a progress report. SPIE: 2000; Vol. 3999.

[2] Gangloff, N.; Ulbricht, J.; Lorson, T.; Schlaad, H.; Luxenhofer, R., Peptoids and Polypeptoids at the Frontier of Supra- and Macromolecular Engineering. Chemical Reviews 2016, 116 (4), 1753-1802.

[3] Culf, A. S.; Ouellette, R. J., Solid-phase synthesis of N-substituted glycine oligomers (alpha-peptoids) and derivatives. Molecules (Basel, Switzerland) 2010, 15 (8), 5282-5335.

Identifying the Occurrence and Sources of Per- and Polyfluoroalkyl Substances in Photolithography Wastewater

CNF Project Number: 2938-21

Principal Investigator(s): Damian Helbling, Christopher Kemper Ober

User(s): Paige Jacob

Affiliation(s): Civil and Environmental Engineering, Cornell University

Primary Source(s) of Research Funding: Semiconductor Research Corporation, National Science Foundation

Contact: deh262@cornell.edu, cko3@cornell.edu, pv7@cornell.edu
Website: https://helbling.research.engineering.cornell.edu/

Primary CNF Tools Used: DISCO Dicing Saw, Jelight 144AX UVO-Cleaner, FilMetrics F40

Abstract:

Per- and polyfluoroalkyl substances (PFASs) are contaminants of emerging concern to environmental and human health [1]. PFASs are present in chemical mixtures used during photolithography [2] and might undergo transformation reactions during the steps of photolithography. We acquired five photolithography materials and characterized the occurrence of PFASs in the native materials. We performed photolithography and collected the resulting wastewater samples to evaluate the chemical transformations. The goal of the project is to elucidate the sources of and mechanisms by which PFASs are introduced or generated during photolithography.

Summary of Research:

The occurrence of PFASs in wastewater and fresh water has emerged as a challenge for engineers [1]. A major obstacle for water quality managers and policy makers is that there are thousands of known PFASs, and countless others that may arise from transformation reactions during industrial processing, environmental transport, or water and wastewater treatment [3]. A variety of PFASs are used in photolithography and a recent study demonstrated that photolithography wastewater contains known and previously unknown PFASs [4]. Although it is known that perfluorobutane sulfonate (PFBS) is a widely used constituent of photoacid generators (PAGs) [2], the sources of nearly all of the other PFASs in photolithography wastewater remain unknown.

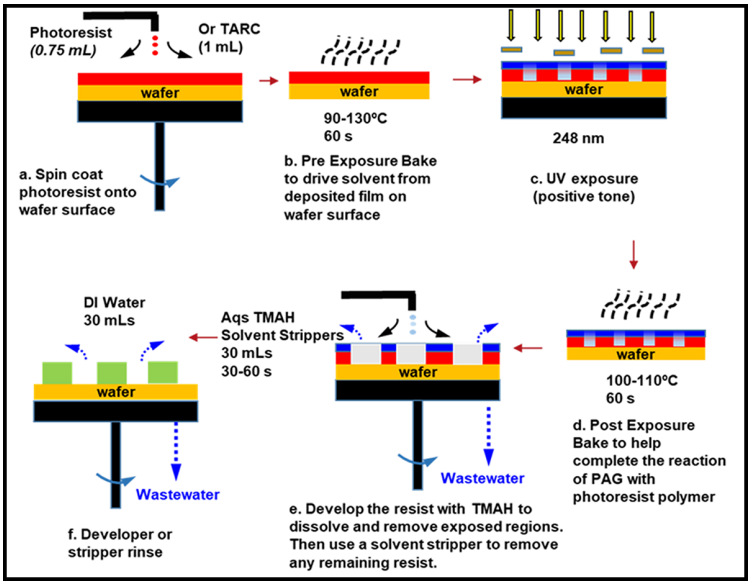

Figure 1: Process diagram of the photolithography workflow conducted at the CNF for each of the five native materials. In this figure, "DI water" = deionized water, and "TMAH" = tetramethylammonium hydroxide.

The complex materials are also subject to transformation reactions induced by the chemical conditions of photolithography. Photolithography requires the application of the photoresist through spin-coating followed by a soft bake, 248 nm exposure, a hard bake, development, and stripping [5]. These steps expose the materials to UV radiation and highly basic conditions. We hypothesize that many PFASs measured in photolithography wastewater are transformation products formed during photolithography.

The goal of the project is to elucidate the sources of and mechanisms by which PFASs are introduced or generated during photolithography. We also aim to study transformation pathways, as improved understanding of transformation pathways will lead to better predictions

Chemical	Measured TOF (g/L)
Photoresist A	1.65±0.14
Photoresist B	0.36±0.03
Photoresist C	1.31±0.04
TARC A	18.1±0.35
TARC B	4.62±0.08

Figure 2: Total organic fluorine measurements of each of the native photolithography mixtures.

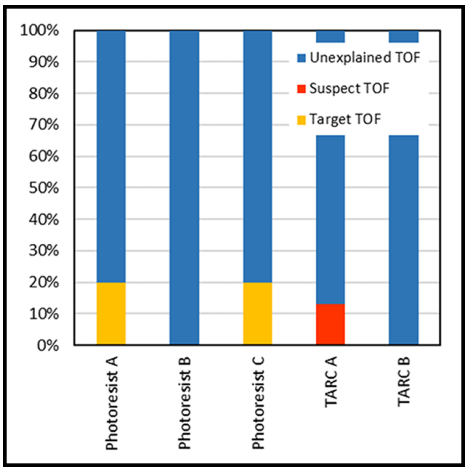

Figure 3: Percentage of total organic fluorine measurements that are accounted for by target or suspect PFASs in the native materials.

of how chemicals transform and inform the development of new photolithography chemicals.

First, we acquired five industrially relevant photolithography materials consisting of three photoresists (Photoresists A, B, and C) and two top antireflective coatings (TARCs A and B). We identified and quantified the PFASs in the materials with multiple analytical techniques, including two high resolution mass spectrometry (HRMS) analyses and a combustion ion chromatography (CIC) analysis. The HRMS analyses consisted of a target screening, where authentic standards of 35 target PFASs and isotope-labelled internal standards were used to quantify PFASs in the materials, and a suspect screening, where HRMS data was mined to gather qualitative information on a list of 171 PFASs that were previously identified in photolithography wastewater samples. The CIC analysis combusts all fluorinated compounds directly into hydrogen fluoride (HF) and the fluoride is then measured with IC to quantify the total organic fluorine (TOF) in the sample [3].

Next, at the CNF we manually performed the steps of photolithography and collected the wastewater from a single material after development and stripping to identify which step may be inducing transformations (Figure 1). We also performed photolithography on clean wafers and collected wastewater samples to characterize the background contamination of PFAS within the CNF and to determine which PFASs are derived from the native materials.

Then we performed target and suspect screenings on the wastewater samples to identify the PFASs present post-photolithography. In addition to collecting wastewater samples, the DISCO dicing saw to was used to cut wafers into pieces that would fit inside the combustion unit to measure the TOF of the wafer after each step of photolithography. Lastly, the FilMetrics F40 was used for thickness measurements of the wafers after each step of photolithography. These measurements will allow us to calculate a mass balance of the native materials on the wafer throughout photolithography.

Conclusions and Future Steps:

The results of the target screening of the five materials revealed the presence of only one target PFAS in two of the materials. Photoresists A and C contained PFBS, which is probably used as the PAG anion in these materials, at concentrations of 331 and 268 mg L-1, respectively. The suspect screening results revealed that suspect PFASs were only identified in TARC A. Photoresist B and TARC B did not contain any target or suspect PFASs.

Next, the samples were analyzed by means of CIC for TOF. The TOF measurements of each photolithography material were in the g L-1 range (Figure 2). We also found that TARCs have higher concentrations of TOF, sometimes an order of magnitude higher than photoresists. These measurements display a gap between the TOF accounted for with target and suspect compounds and the total TOF in the materials, leaving a fraction of the TOF unexplained (Figure 3).

After photolithography, we observed that PFBS was still the main target PFAS identified in post- photolithography wastewater samples and was present in the µg L-1 range. We identified a limited number of other target and suspect PFASs in the wastewater samples. We will next analyze the HRMS acquisitions of the wastewater for unexpected PFASs and measure the TOF of the wastewater and wafer samples.

After identifying the PFASs generated during photolithography, we aim to identify transformation reaction pathways for the fluorinated constituents in native materials to identify reactions occurring at each step and link parent chemicals to the products found in the wastewater from that step. Additionally, we are currently in the process of obtaining a 193 nm exposure tool and temporarily installing it within the CNF to perform the same workflow at 193 nm exposures.

References:

[1] Z. Wang, et al.; 10.1021/acs.est.6b04806.

[2] C. K. Ober, et al.; 10.1117/1.JMM.21.1.010901.

[3] C. A. McDonough, et al.; 10.1016/j.coesh.2018.08.005 (4) P. Jacob, et al.; 10.1021/acs.est.0c06690.

[4] D. Bratton, et al.; 10.1002/pat.662.

Intrinsically Switchable Gigahertz Ferroelectric ScAlN SAW Resonators

CNF Project Number: 1121-03
Principal Investigator(s): Amit Lal
User(s): Ved Gund

Affiliation(s): School of Electrical and Computer Engineering, Cornell University
Primary Source(s) of Research Funding: Defense Advanced Research Projects Agency (DARPA) Tunable Ferroelectric Nitrides (TUFEN)
Contact: amit.lal@cornell.edu, vvg3@cornell.edu
Website: http://www.sonicmems.ece.cornell.edu/
Primary CNF Tools Used: SÜSS MA-6 Contact Aligner, CVC SC-4500 Odd-Hour Evaporator, JEOL 6300 Electron-Beam Lithography, Zeiss SEM

Abstract:

This work details intrinsic switching of 1-3 gigahertz (GHz) ferroelectric scandium aluminum nitride (ScAlN) surface acoustic wave (SAW) resonators. Reversible switching is demonstrated for SAW devices fabricated on 22-30% ScAlN, with metal interdigitated transducers (IDTs) of widths 1 µm-400 nm patterned with a combination of contact and electron-beam lithography. Two-state switching of the resonator is demonstrated with single-sided pulses of ± 6 MV/cm, which demonstrates reversible on-off switching of piezoelectricity in ScAlN. The results show a method of programmable RF signal processing and sensing using ferroelectric ScAlN.

Summary of Research:

Aluminum nitride (AlN) is used in MEMS RF resonators due to its excellent piezoelectric properties and CMOS-compatible processing. Fundamental limits in the piezoelectric properties of AlN have necessitated the exploration of new materials with improved performance. One such material is scandium aluminum nitride ($Sc_xAl_{1-x}N$), which can increase the piezoelectric coefficient by up to ~ 4x with Sc-incorporation. More recently, the discovery of ferroelectric switching in high Sc-concentration $Sc_xAl_{1-x}N$ (x>0.22), has generated significant interest as the first III-V ferroelectric [1].

To demonstrate reconfigurable and adaptive filtering, it is desirable to achieve programmable piezoelectric coupling in ScAlN with ferroelectric switching, which can then be used to tune the filter frequency and transmission level. We have previously reported on the ferroelectric properties of various ScAlN compositions across a range of device sizes, templating electrodes, film stress, and frequency of switching with a goal of identifying reduced switching voltages, including a reduction in the coercive field by 37% with *in situ* ovenization [2,3]. This work builds on the materials characterization and development we have performed previously by demonstration intrinsic polarization switching in ScAlN resonators [4].

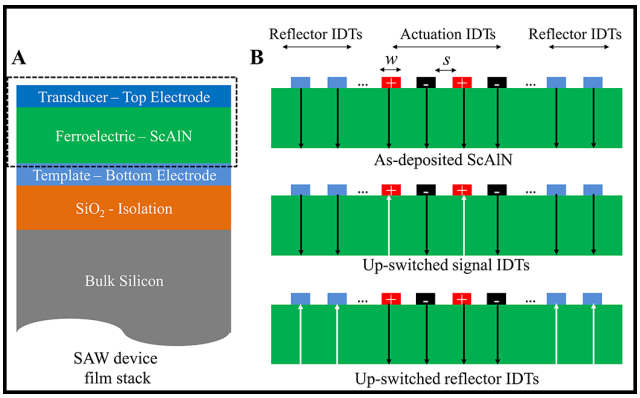

Figure 1: A) SAW device consisting of SiO_2 isolation, template bottom electrode, wurtzite ferroelectric ScAlN, and top electrodes for SAW actuation. B) Schematic of the transducer IDTs and ferroelectric ScAlN showing three distinct configurations of ScAlN polarization: as-deposited N-polar ScAlN with polarization pointing downward, up-switched ScAlN under signal IDTs to program piezoelectric coupling in the active region, up-switched ScAlN under reflector IDTs to program acoustic wave boundary conditions.

The film stack used to make the resonator comprises of a continuous bottom electrode which serves as the template for the ferroelectric, c-axis wurtzite ScAlN and the top electrode for patterning the SAW IDTs (Figure 1A). The IDTs with width *w* and spacing *s* enable lithographic definition of the resonance wavelength: $\lambda = 2(w+s)$. Passive reflectors enable energy confinement in the acoustic cavity defined by the IDTs. It is, hence, possible to switch the polarization of ScAlN under signal electrode IDTs, ground electrode IDTs, reflectors, or a combination of these for local tuning of the piezoelectric coupling, to program the resonator frequency and S_{11} reflection coefficient as shown in Figure 1B. 200 nm ScAlN films with 22% and 30% doping were deposited on continuous Pt and Mo bottom electrodes respectively by reactive co-sputtering (Sc) of scandium and aluminum (Al) in nitrogen at an external vendor. A double-layer lift-off process was used to evaporate 10 nm/100 nm Ti/Au metal electrodes in the odd-hour evaporator.

The contact pads, routing lines, and test capacitors were patterned using SÜSS MA-6 contact photolithography (smallest features = 3 µm), and the metal IDTs were patterned using JEOL 6300 electron-beam lithography. The IDT widths were designed to 1 µm-400 nm, corresponding SAW frequencies in the 1-3 GHz range.

Figure 2 shows a Zeiss scanning electron microscope (SEM) image and zoom-in of a ScAlN SAW device with 400 nm IDTs including a process simulation to verify high-fidelity contact with the 2-layer evaporation.

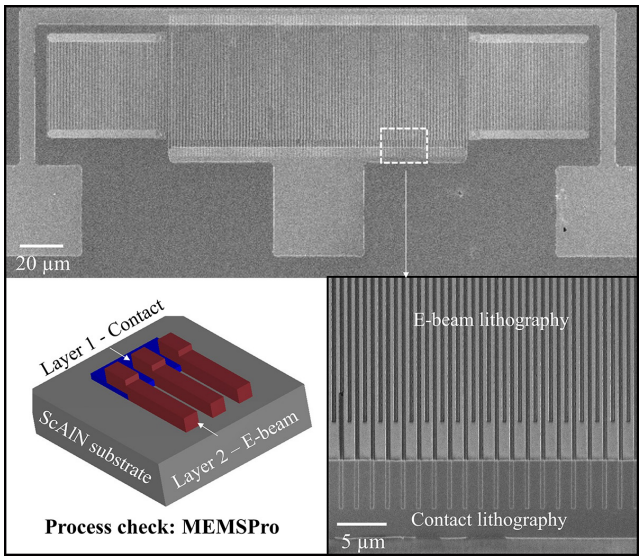

Figure 2: SEM image of a SAW device with 400 nm IDTs, including a zoom-in view of the overlapping metal layers patterned with e-beam and contact lithography. A 3D isometric view serves as a process check to confirm high-fidelity contact between the two layers.

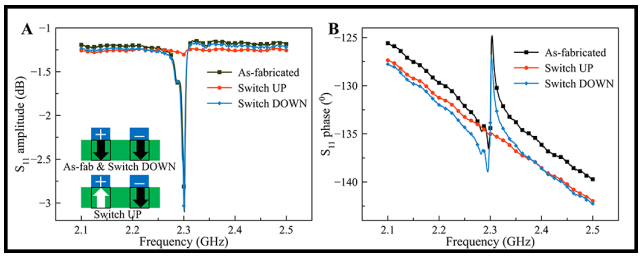

Figure 3: A) S11 amplitude (in dB) and B) phase (in 0) for a 2.3 GH 22% ScAlN SAW resonator showing two-state ScAlN programming. The as-fabricated, up-switched, and down-switched responses demonstrate reversible polarization switching, which enables turning off of the piezoelectric coupling and its full recovery to demonstrate a programmable resonator.

Results:

A setup with continuous wave positive-up-negative-down (PUND) was used for ferroelectric testing of $Sc_xAl_{1-x}N$ [2]. Single-sided triangular pulses of ± 6 MV/cm (larger than the coercive field), were applied to the SAW signal IDTs to sequentially up-switch and down-switch the ScAlN underneath them, followed by S_{11} measurements. Figure 3 shows S11 amplitude and phase responses of a 2.3 GHz 22% ScAlN SAW device for as-fabricated, up-switched and down-switched (±6MV/cm) pulses. The resonance vanishes with up-switching of ScAlN due to an ensemble switching off of the piezoelectricity, but can be fully recovered with down-switching. This process is repeatable over multiple cycles, demonstrating reversible switching of the resonator with minimal ScAlN degradation. The results show a pathway towards a CMOS-compatible filter with programmable frequency and amplitude control.

References:

[1] S. Fichtner, N. Wolff, F. Lofink, L. Kienle, and B. Wagner, "AlScN: A III-V semiconductor based ferroelectric," Journal of Applied Physics, 2019.

[2] V. Gund, et al., "Temperature-dependent Lowering of Coercive Field in 300 nm Sputtered Ferroelectric $Al_{0.70}Sc_{0.30}N$," IEEE ISAF, 2021.

[3] V. Gund, et al., "Towards Realizing the Low-Coercive Field Operation of Sputtered Ferroelectric $Sc_xAl_{1-x}N$," IEEE Transducers, 2021.

[4] V. Gund, K. Nomoto, H. G. Xing, D. Jena, and A. Lal, "Intrinsically Switchable GHz Ferroelectric ScAlN SAW Resonators," IEEE ISAF, 2022.

Si-SiO_2 Metamaterial Ultrasonic Lens for Fourier Ultrasonics

CNF Project Number: 1121-03

Principal Investigator(s): Amit Lal

User(s): Juneho Hwang

Affiliation(s): Department of Electrical and Computer Engineering, Cornell University

Primary Source(s) of Research Funding: Defense Advanced Research Projects Agency, Intelligence Advanced Research Projects Activity, National Science Foundation under Grant No. ECCS-1542081

Contact: amit.lal@cornell.edu, jh882@cornell.edu

Website: https://sonicmems.ece.cornell.edu/

Primary CNF Tools Used: ASML DUV Wafer Stepper, Oxford 81 Etcher, Unaxis 770 Deep Silicon Etcher, Plasma-Therm Deep Silicon Etcher, Thermal Oxidation Furnace

Abstract:

Modern signal processing and machine learning greatly depend on high-performance and power-efficient computation. Fourier transform is one of the most widely used mathematical algorithms in signal processing, speech recognition, and image processing. The complexity of the digital fast Fourier transforms scale in the order of $O(N^2 \log N)$, requiring significant computational resources for large data sets. It has been shown that ultrasonic waves can compute the Fourier transform with a planar lens at the focal length of the input. In this research, we fabricated a planar metamaterial lens that can bend the ultrasonic waves to form the Fourier transform at the lens's focal length.

Summary of Research:

The Fourier transform is a mathematical formula that transforms its time component into the frequency domain. Fourier transform is one of the most widely used algorithms with applications in signal processing, machine learning, and finance. Additionally, the computation power and efficiency of Fourier transform are needed to meet the exponential growth of data in both industries and science. Modern computation frameworks rely on transistor-based processing units. However, it became challenging to continue Moore's law and meet the need for power-efficient computation as the size of the transistor reduced. The Fourier transform using the ultrasonic wave is an alternative solution that can drastically reduce the computation time and power consumption [1-5].

The propagation of waves can be calculated by the Huygens-Fresnel principle. The Huygens-Fresnel principle could be computed from the Rayleigh-Sommerfeld diffraction formula and further simplified for the far-field as the Fraunhofer approximation. However, the Fraunhofer approximation contains an additional quadratic compared to the exact 2D Fourier transform.

In this work, we present a Fourier transform accelerator using the properties of waves. In order to obtain the exact Fourier transform at the receiver side, the accelerator requires a planar lens in front of the transmitter.

Numerous planar binary Fresnel lenses were presented in the past. They consist of binary phase shifts represented by the 2-step size of the lens. In this work, we present a metamaterial lens by fabricating a 4-step size lens and changing the fraction between silicon and SiO_2. This fabrication process only requires a single mask and yields a higher diffraction efficiency which is the ratio between the energy at the focal point and the incoming wave [1-3].

The lens is fabricated by establishing spatially varying SiO_2 pillars inside the silicon wafers that correspond to the different indices of refraction to the passing waves, as shown in Figure 1. The mask is analytically calculated and designed with python to generate the final GDS file. ASML DUV stepper is used for photolithography with pillar diameter of 500 nm - 1 μm. The silicon wafer is etched 16 μm with deep reactive ion etching (DRIE), as shown in Figure 1. SEM pictures are taken after the DRIE

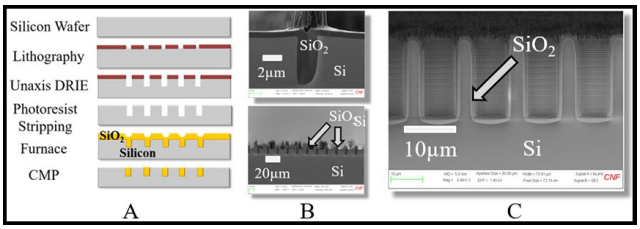

Figure 1: The process flow and SEM pictures after oxidation. A. is the process flow of the ultrasonic lens. B. and C. are the SEM picture after the wet furnace oxidation. The device SEM pictures show the filled trenches of SiO_2 on the silicon wafer [3].

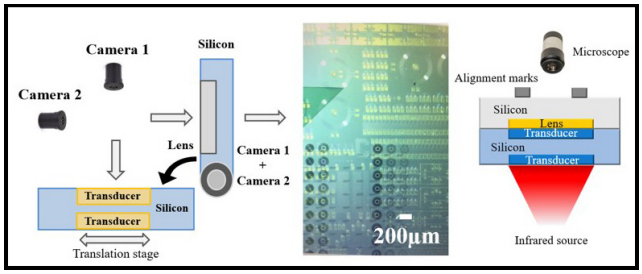

Figure 3: The final lens is bonded to the AlN transmitter using the Pico MA fine-placer. The flip-chip bonder shows the two devices on the same screen overlapping each other [3].

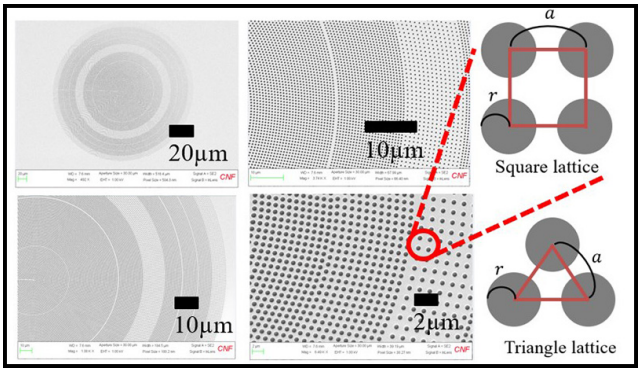

Figure 2: The top-side SEM images of the final device. The varying spatial distribution of the pillar corresponds to a different index of refraction for the acoustic waves. The size of the lens varies from 100 μm to 200 μm in diameter [3].

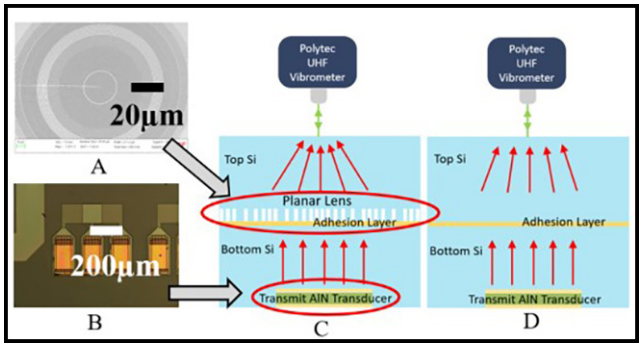

Figure 4: After bonding the lens with the AlN transmitter, the focusing effect is tested with the Polytec UHF [3].

to verify the exact etching rate of the DRIE. Then the trenches are filled with oxide by wet thermal oxidation at 1100°C for 100 minutes. Finally, the device is flattened by chemical mechanical polishing (CMP) and diced using the DISCO.

The final planar metamaterial lens is shown in Figure 2, where the different radii of the pillar spacing represent the different indices of refraction [2].

The final device consists of lenses with a focal length of 500 μm and 1 mm at 1.2 GHz, as shown in Figure 2. After the final fabrication, the device is bonded to the double-sided square transducer actuators fabricated from IME-ASTAR Foundry as shown in Figure 3. The flip chip bonder is used to align the lens and the AlN transmitter for the bonding. Additionally, the infrared microscope was used to verify the alignment after bonding. Finally, the bonded device was tested under Laser Doppler Vibrometry (LDV) to measure the lens's focusing power, as shown in Figure 4 [3].

Conclusions and Future Steps:

In this work, we presented a planar GHz lens that can focus the ultrasonic waves generated from a 100 μm × 100 μm AlN transducer. The lens consists of spatially varying SiO_2 pillars embedded in the silicon wafer to induce different indices of refraction for the incoming waves. The final device was tested using the Polytec UHF to show the focusing effect of the lens at 676 MHz and 1.016 GHz. The demonstrated lens is a preliminary result of the metamaterial lens necessary to make the Fourier transform accelerator.

References:

[1] J. Hwang, J. Kuo, and A. Lal, "Planar GHz Ultrasonic Lens for Fourier Ultrasonics," in IEEE International Ultrasonics Symposium, IUS, Oct. 2019, pp. 1735-1738.

[2] J. Hwang, B. Davaji, J. Kuo, and A. Lal, "Planar Lens for GHz Fourier Ultrasonics," in IEEE International Ultrasonics Symposium, IUS, Sep. 2020, pp. 1-4, doi: 10.1109/IUS46767.2020.9251614.

[3] J. Hwang, B. Davaji, J. Kuo, and A. Lal, "Focusing Profiles of Planar Si-SiO_2 Metamaterial GHz Frequency Ultrasonic Lens," in IEEE International Ultrasonics Symposium, IUS, 2021, pp. 1-4.

[4] M. Abdelmejeed et al., "Monolithic 180 nm CMOS Controlled GHz Ultrasonic Impedance Sensing and Imaging," in Technical Digest - International Electron Devices Meeting, IEDM, Dec. 2019, vol. 2019-December, doi: 10.1109/IEDM19573.2019.8993623.

[5] Y. Liu, J. Kuo, M. Abdelmejeed, and A. Lal, "Optical Measurement of Ultrasonic Fourier Transforms," in IEEE International Ultrasonics Symposium, IUS, Dec. 2018, vol. 2018-October, doi: 10.1109/ULTSYM.2018.8579938.

HZO-Based Ferro NEMS MAC for In-Memory Computing

CNF Project Number: 1121-03
Principal Investigator(s): Amit Lal
User(s): Shubham Jadhav, Ved Gund

Affiliation(s): School of Electrical and Computer Engineering, Cornell University
Primary Source(s) of Research Funding: Defense Advanced Research Projects Agency (DARPA), Tunable Ferroelectric Nitrides (TUFEN)
Contact: amit.lal@cornell.edu, saj96@cornell.edu
Website: http://www.sonicmems.ece.cornell.edu/
Primary CNF Tools Used: SÜSS MA-6 Contact Aligner, CVC SC-4500 Odd-Hour Evaporator, Zeiss SEM, OEM Endeavor M1, Plasma-Therm Takachi HDP-CVD, Arradiance ALD, AJA Sputter Deposition, Oxford PECVD, Oxford 81/82, Primaxx Vapour HF Etcher, UN770 Etcher, YES EcoClean Asher, Xactix Xenon Difluoride Etcher, AJA Ion Mill, Heidelberg Mask Writer-DWL2000, P7 Profilometer, Zygo Optical Profilometer, Flexus Film Stress Measurement

Abstract:

This work details the fabrication of a hafnium zirconium oxide (HZO)-based ferroelectric NEMS beam as the fundamental building block for very low-energy capacitive readout in-memory computing. The demonstration device consists of a 250 × 30 µm unimorph cantilever of 20 nm thick ferroelectric HZO on 1 µm SiO_2. The displacement of the piezoelectric unimorph was measured by actuating the device with different input voltages V_{in}. The resulting displacement was measured as a function of the ferroelectric programming voltage V_p. The beam displacement scale factor was measured to be 182.9 nm/V for -8V V_p and -90.5 nm/V for 8V V_p, demonstrating that the programming voltage can be used to change the direction of motion of the beam. The resultant output beam displacement from AC actuation is in the range of -15 to 18 nm and is a scaled product of the input voltage and programmed d_{31} (governed by the poling voltage). The multiplication function serves as the fundamental unit of MAC operations with the ferroelectric NEMS beam.

Summary of Research:

Neuromorphic computation is of great interest to computing theory and practical implementations due to the potential for low-power, high efficiency, and small form factor information processing with deep neural networks (DNN) [1,2]. With the ever-increasing number of variables required for neuromorphic computation with high accuracy, there is an urgent need to develop highly energy-efficient device architectures [2-4]. FET-based in-memory computation architectures are susceptible to large read and write energy consumption and high leakage currents in idle mode, particularly with gate dielectric thickness scaling down to < 5 nm [5]. NEMS switches and beams offer an alternate pathway to zero-leakage in-memory compute synaptic functionality, provided that the beam actuation has embedded programmable weights in the form of tunable capacitive or piezoelectric coupling.

While analog in-memory computing has been demonstrated using different architectures that use transistors or memristors, few prior works have used a NEMS-based approach that takes advantage of released beam structure to eliminate energy leakage in an idle state [6].

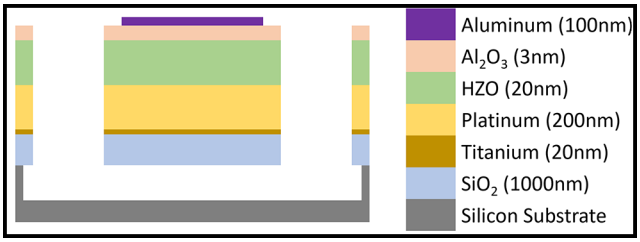

Figure 1: Schematic cross-section view of the ferroelectric beam.

In this work, we present a ferroelectric/piezoelectric beam transducer to enable the multiplication that can be read out capacitively eliminating any DC currents.

Figure 1 shows the cross-section view of the clamped-clamped unimorph ferroelectric beam used to

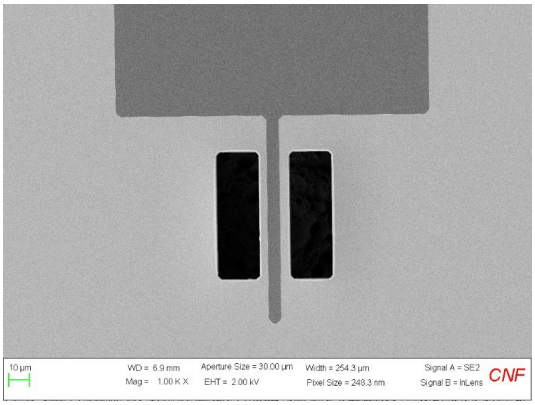

Figure 2: SEM of the beam showing the released structure.

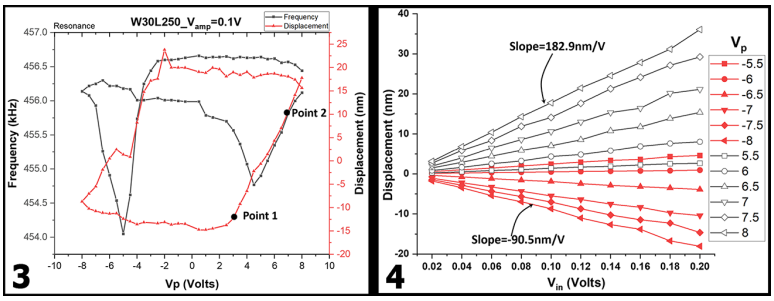

Figure 3, left: Central beam displacement δ_{max} and resonant frequency f_0 vs. poling voltage V_p. Figure 4, right: The displacement vs. V_{in} for different values of the V_p.

demonstrate piezoelectric coefficient programming. 1 µm thick thermal SiO_2 forms the passive elastic layer underneath the 20 nm ferroelectric HZO. The HZO is capped by 3 nm of alumina (Al_2O_3), followed by annealing at 400°C to crystallize the HZO in its ferroelectric orthorhombic phase. Then 200 nm platinum (Pt sputtering) and 100 nm Al (Al evaporation) were deposited to form the bottom and top metal electrode contacts for the HZO respectively. Pt was etched using AJA ion mill and the liftoff technique was used to pattern the Al electrode. The beam was released by isotropic etching of the silicon substrate using Xactix XeF_2.

A Zeiss scanning electron microscope image of the fabricated device is shown in Figure 2.

After release, the beams were observed to be buckled due to residual film stress generated during microfabrication. A 3D optical profilometer (Zygo™ system) was used to measure the beam buckling profile. The maximum displacement for a 250 × 30 µm was 4.98 µm.

Figure 3 shows the central beam displacement δ_{max} and resonant frequency f_0 vs. poling voltage V_p plot in the frequency range of 450 to 460 kHz for the nominal 250 × 30 µm ferroelectric clamped-clamped beam presented here. Peak displacement δ_{max} (red line) is modulated for different values of V_p and traces a hysteresis loop. The net effect of the number of upward and downward pointing dipoles that control the macroscopic polarization in the beam (induced due to V_p) also changes the beam stiffness resulting in resonance frequency modulation (black line), which presents a separate modality of memory storage in the beam. The two dips in f_0 correspond to the positive and negative coercive fields of the HZO film where the net polarization is almost zero.

To show the effect of V_{in} on δ_{max}, we swept V_{in} from 0.02V to 0.20V for different values of the V_p. Figure 4 shows a plot of δ_{max} vs. V_{in} at different values of V_p, which emulates the transfer characteristics of the analog multiplier. For constant poling voltages, if we sweep the inputs, we get a linear increase in displacement value. Similarly, for constant inputs, different poling voltages outputs different displacement values.

In conclusion, we have demonstrated an HZO-based NEMS multiplier weight storage functionality. The device was fabricated and characterized, showing the dependence of beam displacement on the poling voltage of the ferroelectric film. The frequency tunability was also demonstrated that can be further explored to realize unique features such as an electrically tunable filter. Future work will build on this demonstration for device scaling towards high device density.

References:

[1] C. Mead, "Neuromorphic electronic systems," Proc. IEEE, vol. 78, no. 10, pp. 1629-1636, 1990.

[2] A. Keshavarzi, K. Ni, W. Van Den Hoek, S. Datta, and A. Raychowdhury, "FerroElectronics for Edge Intelligence," IEEE Micro, vol. 40, no. 6, pp. 33-48, Nov. 2020.

[3] W. Haensch, T. Gokmen, and R. Puri, "The Next Generation of Deep Learning Hardware: Analog Computing," Proc. IEEE, vol. 107, no. 1, pp. 108-122, 2019.

[4] M. Horowitz, "Computing's Energy Problem (and what we can do about it)," pp. 10-14, 2014.

[5] S. S. Cheema, et al., "Enhanced ferroelectricity in ultrathin films grown directly on silicon," Nature, vol. 580, no. 7804, pp. 478-482, Apr. 2020.

[6] A. Sebastian, M. Le Gallo, R. Khaddam-Aljameh, and E. Eleftheriou, "Memory devices and applications for in-memory computing," Nat. Nanotechnol., vol. 15, no. 7, pp. 529-544, 2020.

HF Vapor Release Etch

CNF Project Number: 1611-07
Principal Investigator(s): Gregory L. Snider
User(s): Rene Celis-Cordova

Affiliation(s): Department of Electrical Engineering University of Notre Dame

Primary Source(s) of Research Funding: National Science Foundation

Contact: gsnider@nd.edu, rene.celiscordova.1@nd.edu

Primary CNF Tools Used: Primaxx Vapor HF Etcher

Abstract:

Reversible computing reduces the energy dissipation of a circuit by using logical reversibility and quasi-adiabatic transitions, introducing a trade-off between energy and speed. Adiabatic CMOS is the most developed implementation of reversible computing, but it is ultimately limited by passive power, the energy dissipation caused by leakage. New computing approaches try to eliminate the leakage current completely by using micro-electro-mechanical systems (MEMs) as relays to implement computing. Unlike CMOS circuits, the MEMs relays do not have a subthreshold current since they have no electrical contact when they are off. However, the relays will wear out over time primarily due to degradation of the current-carrying contacts. Adiabatic Capacitive Logic (ACL) was proposed by Pillonnet and Houri as a novel approach to reversible computing that eliminates leakage current and does not have make and break contacts therefore avoiding the degradation problem seen in relays. The fabrication of these nano-relays requires a release etch to free the MEMs structures. A wet etch process with critical-point drying gave a very low yield, so a vapor HF process at the Cornell NanoScale Facility (CNF) was used instead.

Summary of Research:

The basic structure is shown in the diagram of Figure 1 in cross section. A control voltage is applied between the plates on the left side which pulls down the upper plate, changing the capacitance of the output capacitor at the right. A key step in the process is a vapor hydrofluoric acid (HF) release etch, performed at CNF using the Primaxx Vapor HF Etcher, instead of the liquid HF followed by critical point drying that we used previously. This greatly increased the yield of process, since the critical point dryer was a very difficult process to control, and nearly all devices would stick to the surface during the drying process. With the vapor process the yield increased to about 50% in the first two runs. One disadvantage of the vapor HF process is that the vapor etches the TiN electrode layer more than in a liquid HF process. This resulted in an increased access resistance between the probe pads and the device that adversely impacted the capacitance measurements.

An SEM micrograph of the finished device is shown in Figure 2. There is still some residual stress in the polysilicon layer that causes the springs to bend out of plane. During the fabrication the samples are given a high-temperature treatment after the polysilicon deposition that is intended to relieve stress in the film, but this process needs further optimization. Initial measurements show that the devices operate correctly, and the characteristics of the devices are being measured. A pull-in voltage at an average of 22V is observed, in close agreement with COMSOL simulations.

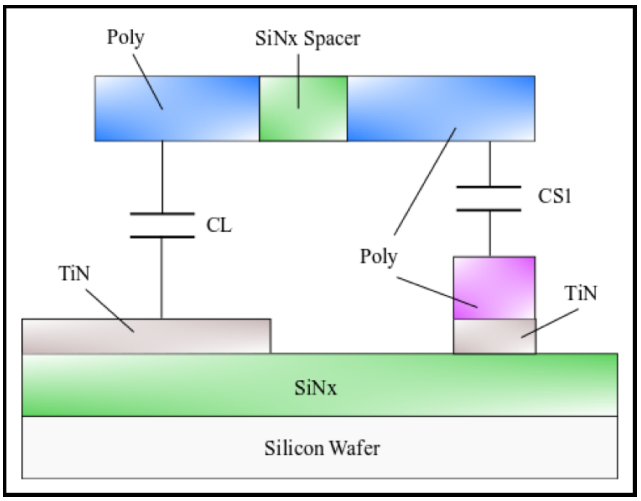

Figure 1: Voltage-controlled variable capacitor gap closing structure.

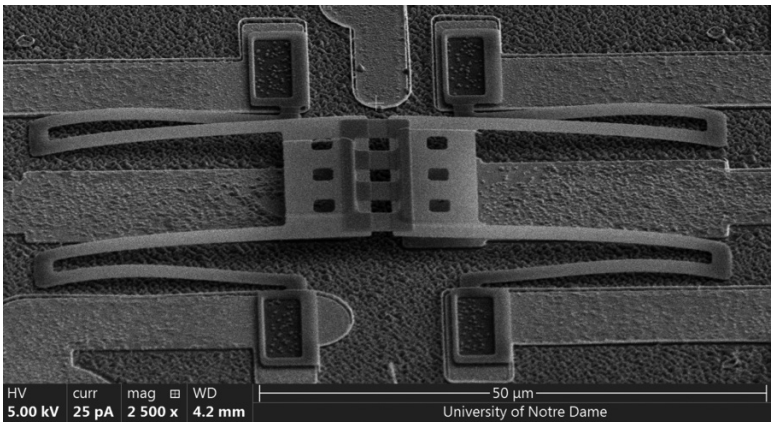

Figure 2: SEM micrograph of completed ACL variable capacitor.

MBE Grown AlScN/AlN/GaN High Electron Mobility Transistors with Regrown Contacts

CNF Project Number: 2438-16

Principal Investigator(s): Huili Grace Xing, Debdeep Jena

User(s): Kazuki Nomoto

Affiliation(s): School of Electrical and Computer Engineering, Cornell University

Primary Source(s) of Research Funding: DSSP/ASCE

Contact: grace.xing@cornell.edu, kn383@cornell.edu

Primary CNF Tools Used: Autostep i-line Stepper, Heidelberg Mask Writer - DWL2000, P7 Profilometer, FilMetrics, AFM Veeco Icon, Zeiss SEM, PT 770, Oxford 81, Oxford ALD / PECVD, SC4500 Evaporators, AJA Sputter Deposition, RTA AG610, JEOL 9500

Abstract:

We report the first observation of ferroelectric gating in AlScN barrier wide-bandgap nitride transistors. These FerroHEMT devices realized by direct epitaxial growth represent a new class of ferroelectric transistors in which the semiconductor is itself polar, and the crystalline ferroelectric barrier is lattice-matched to the substrate. The FerroHEMTs reported here use the thinnest nitride high-K and ferroelectric barriers to date to deliver a high on-currents at 1.34 A/mm, and highest speed AlScN transistors with f_{MAX} > 150 GHz observed in any ferroelectric transistor. The FerroHEMTs exhibit hysteretic I_d-V_{gs} loops with subthreshold slopes below the Boltzmann limit. A control AlN barrier HEMT exhibits neither hysteretic nor sub-Boltzmann behavior. While these results introduce the first epitaxial high-K and ferroelectric barrier technology to RF and mm-wave electronics, they are also of interest as a new material platform for combining memory and logic functionalities in digital electronics.

Summary of Research:

The GaN/$Al_{0.86}Sc_{0.14}N$/AlN/GaN HEMT structure consists of a 2 nm GaN cap layer, a 5 nm $Al_{0.86}Sc_{0.14}N$ barrier, a 2 nm AlN spacer (total barrier thickness: 9 nm), a 1000 nm unintentionally doped GaN channel, and AlN nucleation layer on a SiC substrate, grown by plasma assisted molecular beam epitaxy (PA-MBE). Room temperature Hall-effect measurements with In-dots prior to device fabrication showed a 2DEG sheet concentration of 2.99 × 10^{13}/cm^2 and electron mobility of 500 cm^2/V·s, corresponding to a sheet resistance of 417 Ω/sq.

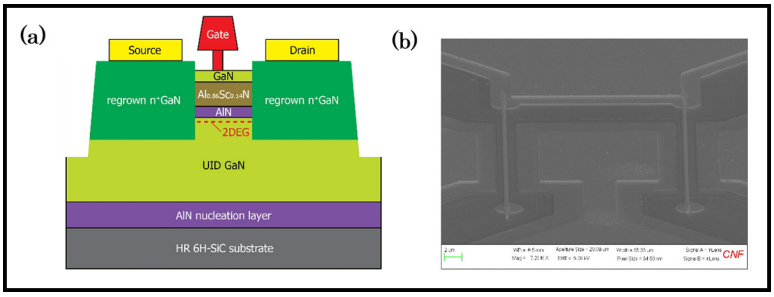

Figure 1: (a) Schematic cross-section and (b) SEM image of AlScN/AlN/GaN HEMTs on 6H-SiC with regrown n^+GaN contacts.

A schematic cross-section of the AlScN/AlN/GaN HEMT device with regrown n^+ GaN contacts is shown in Figure 1(a). The device fabrication process started with patterning of a SiO_2/Cr mask for n^+GaN ohmic regrowth by PA-MBE. The pre-regrowth etch depth into the HEMT structure was 40 nm, and regrown n^+GaN was 100 nm with a Si doping level of 7 × 10^{19}/cm^3. Non-alloyed ohmic contact of Ti/Au was deposited by e-beam evaporation. T-shaped Ni/Au (30/350 nm) gates were formed by e-beam lithography, followed by liftoff. TLM measurements yielded a contact resistance of 0.31 Ω·mm.

The device presented here has a regrown n^+GaN source-drain distance L_{SD} of 600 nm, a gate width of 2 × 25 µm, and a gate length L_G of 90 nm. An SEM image of completed AlScN/AlN/GaN HEMT is shown in Figure 1(b).

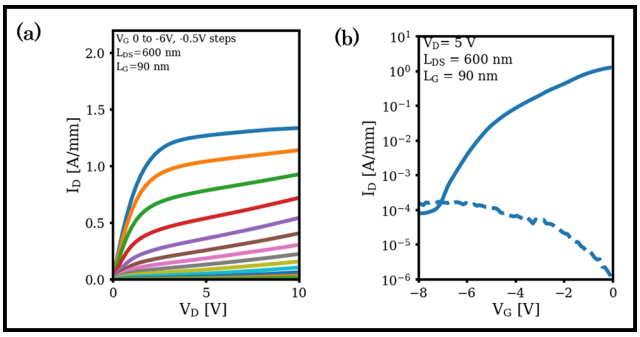

Figure 2: (a) Family I-V curves and (b) transfer characteristics of the device with L_G = 90 nm and L_{SD} = 600 nm.

Figure 2(a) shows the family I-V curves of the device, measured for V_{DS} = 0 to 10 V and V_{GS} = 0 to -6 V. The device has a saturation drain current I_{DSS} = 1.34 A/mm and an on-resistance R_{ON} = 1.4 Ω·mm extracted at V_{gs} = 1 V. The transfer curves are shown in Figure 2(b). A peak extrinsic transconductance g_m is 0.46 S/mm at V_{DS} = 5 V.

Figure 3(a) shows the current gain $|h_{21}|^2$ and unilateral gain U of the device as a function of frequency at the peak f_T bias condition, V_{DS} = 10 V, and V_{GS} = -1.4 V.

The extrapolation of both $|h_{21}|^2$ and U with -20 dB/dec slope gives the current gain cutoff frequency/maximum oscillation frequency f_T / f_{MAX} of 78/156 GHz after de-embedding. The f_T and f_{MAX} of the device are summarized in Figure 3(b), showing how the results of this device compare with the early state-of-art results of AlScN/GaN HEMTs on SiC substrates [1-3].

This work was supported by the DARPA DSSP program monitored by Dr. Tom Kazior. This work was also supported, in part, by NSF DMREF Grant No. 1534303, Cornell NanoScale Facility (Grant No. NNCI-2025233), AFOSR Grant No. FA9550-20-1-0148, NSF Grant No. DMR-1710298, and the CCMR Shared Facilities, which are supported through the NSF program.

References:

[1] T. E. Kazior, et al., 2019 IEEE/MTT-S International Microwave Symposium (2019).

[2] A. J. Green, et al., IEEE Electron Device Letters, Vol. 40, No. 7, July (2019).

[3] J. Cheng, et al., IEEE Transactions on Electron Devices, Vol. 68, No. 7, July (2021).

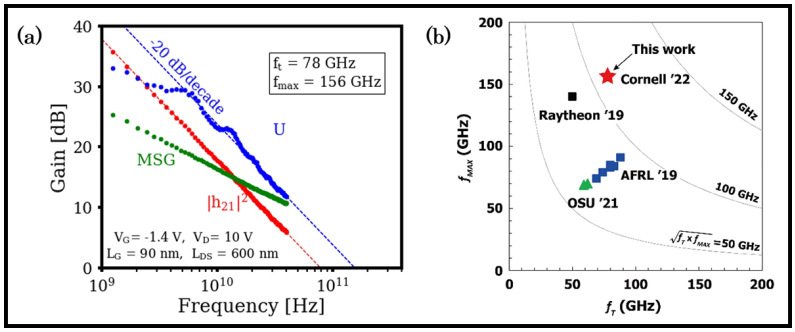

Figure 3: (a) Current gain and unilateral gain of the device with L_g = 90 nm, showing f_T / f_{MAX} = 78/156 GHz. (b) Comparison of the measured f_T and f_{MAX} of $Al_xSc_{1-x}N$/GaN HEMTs.

Fabrication and Manipulation of Micro-Scale Opto-Electrically Transduced Electrodes (MOTEs)

CNF Project Number: 2658-18 & 2836-19

Principal Investigator(s): Prof. Alyosha C. Molnar

User(s): Shahab Ghajari, Sunwoo Lee, Sanaz Sadeghi, Devesh Khilwani

Affiliation(s): Electrical and Computer Engineering, Cornell University
Primary Source(s) of Research Funding: National Institutes of Health
Contact: am699@cornell.edu, sg2367@cornell.edu, sl933@cornell.edu, ss3842@cornell.edu, dk842@cornell.edu
Website: https://molnargroup.ece.cornell.edu/
Primary CNF Tools Used: ABM Contact Aligner, AJA Sputter, Westbond 7400A Ultrasonic Wire Bonder, Oxford 81/82/100, Unaxis Deep Si Etcher, Oxford PECVD, Oxford ALD, Anatech, P7 Profilometer, Zeiss Ultra and Supra Scanning Electron Microscopes

Abstract:

Recording neural activity in live animals *in vivo* is critical in elucidating how the brain functions. However, such recording poses several challenges. Electrical techniques typically require electrodes to be tethered to the outside world directly via a wire, or indirectly via an RF coil [1], which is much larger than the electrodes themselves. Tethered implants suffer from the residual motions between electrodes and neurons as the brain moves, limiting our ability to measure from peripheral nerves in moving animals, especially in smaller organisms such as zebra fish or fruit flies. On the other hand, optical techniques, which are becoming increasingly potent, are often limited to subsets of neurons in any given organism, impeded by scattering of the excitation light and emitted fluorescence, and limited to low temporal resolution [2]. Here we present an untethered opto-electrical system on chip (SoC), Micro-scale Opto-electrically Transduced Electrodes (MOTEs), which are powered by, and communicating through, a microscale optical interface, combining many benefits of optical techniques with high temporal-resolution of electrical recording.

Summary of Research:

Our fabrication starts with about 5 mm × 5 mm, conventional 180 nm CMOS die, which contains the electronics for signal amplification, encoding, and transmission. The CMOS die is then integrated with AlGaAs diode, which acts as a photovoltaic (PV) as well as light emitting diode (LED), hence the diode is abbreviated as PVLED. The PVLED provides an optical link which powers the electronics and transmits encoded signals in optical pulses. The MOTE utilizes Pulse Position Modulation (PPM) for signal encoding for its high information-per-photon efficiency, where the spacing between the output pulses is proportional to the measured electric field of neuronal signals across the measurement electrodes. Figure 1 depicts a conceptual deployment and system description of such MOTE [3].

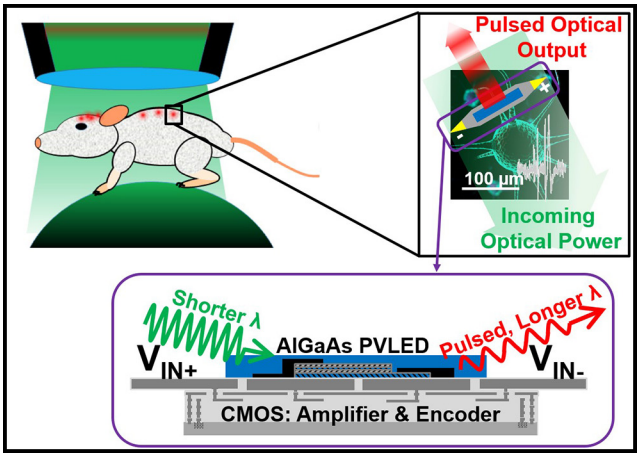

Figure 1: An exemplary implementation and system level description of the MOTEs in a mouse animal model [3].

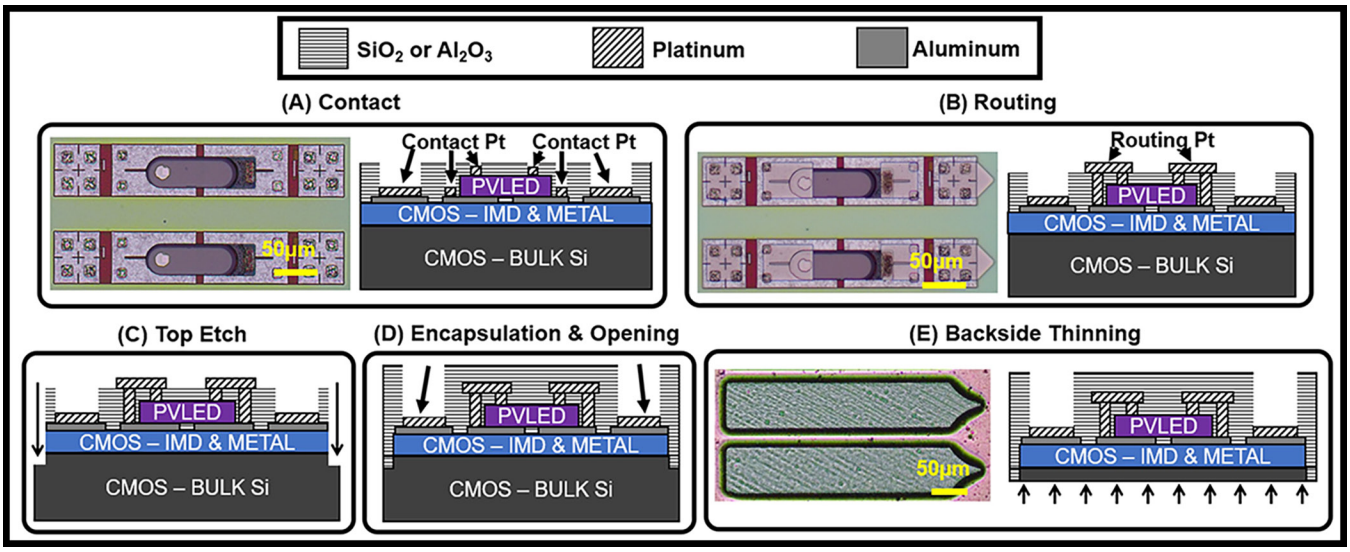

Figure 2: MOTE Fabrication Process. (A) An AlGaAs μLED (bullet-shaped) array is transferred on top of a CMOS chip containing an array of unit MOTE circuitry, and Pt is deposited over contact areas. (B) Routing Pt electrically connects each μLED with an underlying CMOS. (C) Each MOTE is segregated and (D) encapsulated with SiO_2 and Al_2O_3 except for the measurement electrodes area. (E) The backside Si is thinned so that total thickness is < 30 μm. Adapted from [4].

The AlGaAs diodes are first fabricated on a sapphire wafer, to be later released from the sapphire substrate with a sacrificial poly(methyl methacrylate) (PMMA) polymer. Once the PMMA-coated AlGaAs diodes are transferred onto the CMOS die, Oxford 81 plasma etcher is used to remove the sacrificial PMMA, leaving only the diodes array intact on the CMOS die. To establish the electrical contact between the PVLED and CMOS, we have used the CNF ABM Contact Aligner for photolithography with AZ nLof2020 UV photoresist for efficient lift-off process that ensues after metal deposition. After the contact fabrication, the contacts of CMOS and PVLED are connected via similar photo-lithography process, and to maximize the conformality of the metal routing, we employ AJA Sputter. Following the routing step, each MOTE is encapsulated using Oxford ALD and PECVD for SiO_2 and Si_3N_4 deposition, followed by dielectric etching using Oxford 100 and Unaxis deep reactive ion etch (DRIE) for release. Figure 2 described the fabrication sequence described herein.

It should be noted that before embarking on the nano/micro-fabrication flow, to confirm the functionality of each module (CMOS and the diode), we use Westbond 7400A Ultrasonic Wire Bonder for board-level test. ZEISS ultra and supra scanning electron microscopes (SEMs) are also used to inspect the fabricated MOTE for debugging purposes.

Conclusions and Future Steps:

MOTEs are the smallest electrophysiological sensor of its kind, and we are currently testing the MOTEs *in vivo* in mouse animal models. As we accumulate more data on our ongoing *in vivo* efforts, we plan to improve fabrication processes as well as surgical procedures for inserting the MOTEs into the mouse cortex. Moreover, we are aiming to design MOTEs for electrochemical applications.

References:

[1] Harrison RR, Watkins PT, Kier RJ, Lovejoy RO, Black DJ, Greger B, and Solzbacher F. A Low-Power Integrated Circuit for a Wireless 100-Electrode Neural Recording System. IEEE J. Solid-State Circuits. 2006 Dec 26;42(1): 123-133.

[2] Yang W and Yuste R. *In vivo* Imaging of Neural Activity. Nature Methods. 2017 Mar 31;14(4):349-359.

[3] Lee S, Cortese AJ, Trexel P, Agger ER, McEuen PL, and Molnar AC. A 330 μm × 90 μm Opto-Electronically Integrated Wireless System-on-Chip for Recording of Neural Activities. IEEE ISSCC. 2018 Feb.

[4] Lee S, Cortese A, Mok A, Wu C, Wang T, Park J, Smart C, Ghajari S, Khilwani D, Sadeghi S, Ji Y, Goldberg J, Xu C, McEuen P, and Molnar A. Fabrication of Injectable Micro-Scale Optoelectronically Transduced Electrodes (MOTEs) for Physiological Monitoring. IEEE JMEMS. 2020 June 12;29(5):720-726.

High Frequency Sensors and Actuators for Ultrasonic Imaging

CNF Project Number: 2876-20

Principal Investigator(s): Robert Scharf, Amit Lal

User(s): Brian Wu, Anuj Baskota, Justin Kuo, Scott Zimmerman

Affiliation(s): Geegah, Inc.

Primary Source(s) of Research Funding: DARPA, ARPA-E, DOE

Contact: rms248@cornell.edu, amit@geegah.com, brian@geegah.com, anuj@geegah.com, justin@geegah.com, scottez@geegah.com

Website: www.geegah.com

Primary CNF Tools Used: SÜSS MA6 Contact Aligner, PT740 Reactive Ion Etcher, E-Beam Evaporators, PECVD Deposition Tools

Abstract:

Geegah develops CMOS compatible ultrasonic imaging for fast and high-resolution environmental sensing; thanks to the high excitation frequencies (>1GHz) and lack of mechanical scanners that are typical to many commercial scanning acoustic microscopes. Using ultrasonic transducers made from aluminum nitride (AlN) deposited on top of CMOS, Geegah demonstrated imaging worms in soil, drying blood droplets, 3-D printed ink, fingerprints, and bacteria colony growth at frame rates more than 6Hz with 128 × 128 pixel arrays [1-3]. While the imaging chips are manufactured in a commercial CMOS foundry, early packaging of these systems were done in CNF.

For some applications that require imaging of soft materials or sensing over long distances in liquid, high acoustic impedance of AlN and large acoustic absorption due to high frequency of operation are not desired. To be used in this complementary set of applications, Geegah has been developing PVDF-TrFE spin-on piezoelectric films in CNF. These transducers are expected to operate at frequencies from 20 MHz to 600 MHz and are being fabricated using a three-mask process.

Summary of Research:

Planar ultrasonic transducers realized on silicon substrate emit ultrasonic waves through the piezoelectric effect. Amplitudes and nature of these waves are a function of the elastic properties of the transducer stackup as well as the frequency and amplitude of excitation. These ultrasonic waves can be used for imaging and sensing through pulse-echo operation where one transducer transmits and the other or the same transducer receives. Time-of-flight and amplitude of the received pulse in this process is used for sensing or imaging. Crystalline nature of the silicon substrate helps by providing a low acoustic loss medium as these waves propagate through the substrate.

The PVDF-TrFE is a much softer material than both silicon and AlN, and hence it is commonly used in biomedical sensing applications. Figure 1 shows the 3-mask process we developed to fabricate PVDF-TrFE transducers. The process starts with PECVD SiO_2 deposition on blank silicon wafer to serve as an insulation material. Then bottom electrode material, aluminum, is evaporated and patterned using the first mask and wet etching. Next, off-the shelf PVDF-TrFE powder is dissolved in a solvent and spun on the wafer to get thicknesses varying from 1.5 to 2.5 µm. The film thickness vs. spin-speed characterization curve is given in Figure 2. Following vacuum annealing and curing, the piezoelectric film is patterned using the second mask and an oxygen plasma etcher. Due to the reaction of standard photoresist removal solutions with the PVDF-TrFE film, a double exposure photoresist strip step is followed. Finally, a top metal layer is evaporated and patterned using the last mask.

Figure 3 shows the picture of a 200 µm diameter transducer after the lithography for the top electrode. Next steps involve dicing As for the high frequency imaging applications, Figure 4 illustrates a typical ultrasonic image acquired using Geegah's imaging chip, which was wirebonded and packaged in CNF. Here, the sample imaged is conductive ink printed directly on the surface of the imager for use in quality control of additive manufacturing [4].

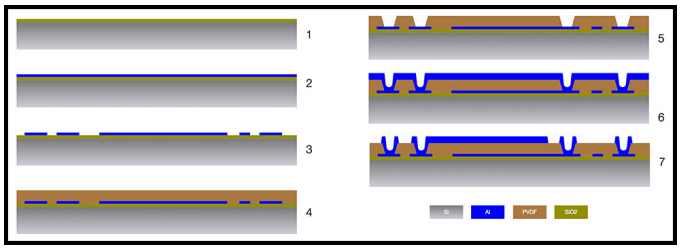

Figure 1: Process flow for the PVDF-TrFE ultrasonic transducer fabrication.

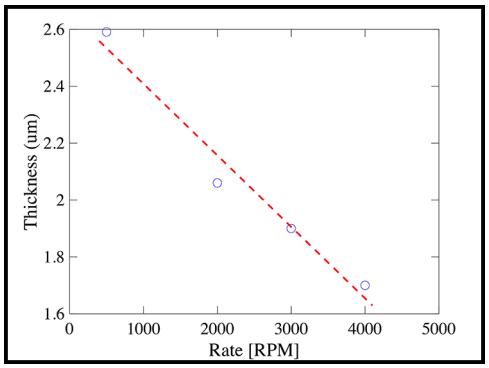

Figure 2: Characterization of the PVDF-TrFE thickness control using the spin-speed.

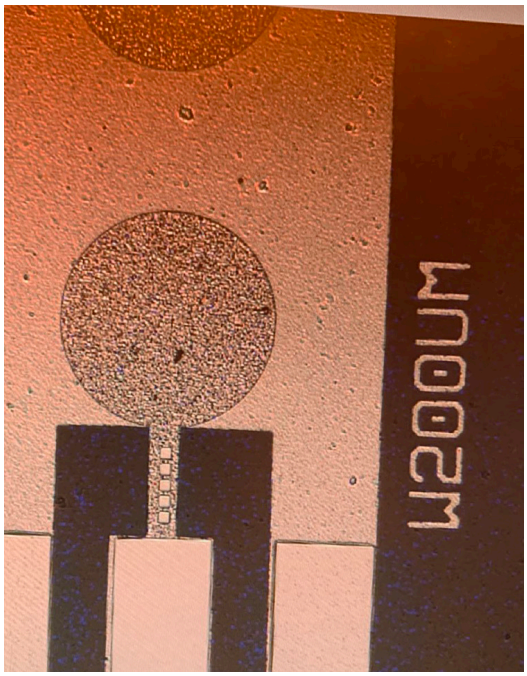

Figure 3: Picture of a fabricated 200 µm diameter device.

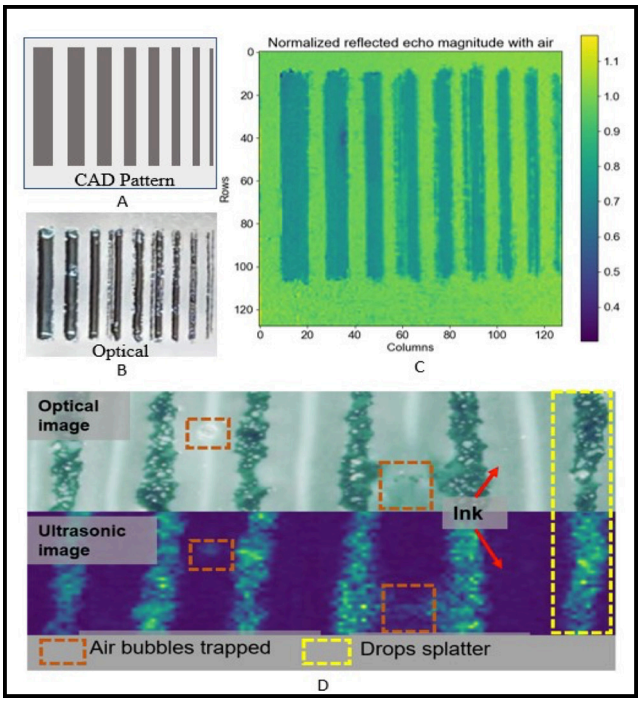

Figure 4: A) CAD pattern (grey area shows ink) for printed conductive ink lines. B) Optical image of the printed conductive ink on the imager surface. C) Ultrasonic image of the same ink patterns. D) Optical and ultrasonic images showing defects in the ink print pattern: air bubbles trapped within ink and tiny drops splattering between the ink lines [4].

In addition to imaging elastic properties, our results showed that the phase of the received echo carries signature of the temperature changes in the medium and sample.

Conclusions and Future Steps:

A PVDF-TrFE ultrasonic transducer is being developed to enhance imaging for materials with lower acoustic impedances or through longer fluidic coupling mediums. The three-mask process flow is close to completion and devices will be ready for testing following dicing and polarization. This process is expected to complement the high-frequency ultrasonic imaging capabilities and work with softer materials at lower excitation frequencies.

References:

[1] Kuo, J., Baskota, A., Zimmerman, S., Hay, F., Pethybridge, S. and Lal, A., 2021, September. Gigahertz Ultrasonic Imaging of Nematodes in Liquids, Soil, and Air. In 2021 IEEE International Ultrasonics Symposium (IUS) (pp. 1-4). IEEE.

[2] Baskota, Anuj, Justin Kuo, and Amit Lal. Real-time GHz Ultrasonic Imaging of Nematodes at Microscopic Resolution. Microscopy and Microanalysis 28.S1 (2022): 1594-1596.

[3] Baskota, A., Kuo, J. and Lal, A., 2022, January. Gigahertz Ultrasonic Multi-Imaging of Soil Temperature, Morphology, Moisture, and Nematodes. In 2022 IEEE 35th International Conference on MEMS (pp. 519-522). IEEE.

[4] Baskota, A., Ivy, L., Ospina, C., Kuo, J., Hwang, J., Gund, V., Davaji, B., Doerschuk, P. and Lal, A., *In-Situ* Ultrasonic Imaging of Printed Electronics Ink Deposition And Curing, researchgate.net.

General Electric Global Research Microfabrication Highlights 2022

CNF Project Number: 2993-21

Principal Investigator(s): Robert MacDonald

User(s): Robert MacDonald, Charles Szymanski, Timothy VandenBriel

Affiliation(s): General Electric Global Research

Primary Source(s) of Research Funding: General Electric, Corporate

Contact: robert.macdonald@ge.com, charles.szymanski@ge.com, timothy.vandenbriel@ge.com
Website: https://www.ge.com/research/electronics-sensing

Primary CNF Tools Used: SÜSS Bonder/Aligner, STPS uEtch HF Vapor Release, Schott IR Inspection Microscope

Abstract:

Developments in analog computing have led to an interest in mechanical computing elements. We are persuing research in this field using small resonators and switches built in silicon.

Summary of Research:

We are developing analog computing elements out of mechanical structures. The structures are fabricated in silicon, so called 'NEMS', or nano electromechanical systems. The structures consist of resonant elements where computation is mapped to phase, frequency or amplitude. We fabricated these structures at our facility in Niskayuna, New York. We use the CNF as a backup for certain tools. In addition, we plan on using CNF to extend our capabilities to build smaller structures than we are capable of building in our own facility. We have not yet published our results in this area, with publications expected in 2023.

Our work is based on our GE 'Polaris' process, a foundry process which we offer commercially. Polaris has been used to fabricate accelerometers and gyroscopes, with future projects slated for timing, pressure and strain sensing.

Conclusions and Future Steps:

We expect to publish results in 2023 on our mechanical computing devices, when we will have more data to report.

Design and Fabrication of Magnetic Elastomer-Based Soft Actuator

2022 CNF REU Intern: Rodolfo Cantu

Intern Affiliation: Mechanical Engineering, The University of Texas at Austin

CNF REU Principal Investigator: Dr. Amal El-Ghazaly, Electrical and Computer Engineering, Cornell
CNF REU Mentor: Ludovico Cestarollo, Electrical and Computer Engineering, Cornell University

CNF REU Project and Primary Source(s) of Research Funding: 2022 Cornell NanoScale Science & Technology Facility Research Experiences for Undergraduates (CNF REU) Program via the National Science Foundation under Grant No. NNCI-2025233

Contact: rodolfo.cantu@utexas.edu, ase63@cornell.edu, lc942@cornell.edu

Website: https://cnf.cornell.edu/education/reu/2022
Primary CNF Tools Used: ABM Contact Aligner, Heidelberg Mask Writer - DWL2000, AJA Ion Mill, Plasma-Therm 72, P7 Profilometer, AFM Bruker Icon

Abstract:

Technological advancements to date have primarily focused on stimulating only two of the five human senses: sight and hearing. Touch-based interactive technologies are still in their infancy. Haptic devices allow tactile interactions between humans and digital interfaces, assisting humans in industries such as healthcare, automotive and entertainment. Magnetorheological elastomers (MREs) based on nanoparticles constitute a promising candidate material for creating tactile interfaces [1] capable of creating high-resolution features on the micron scale [2]. These magneto-responsive elastomers must be integrated with magnetic micro-controls to create the local magnetic fields necessary to actuate deformations.

Summary of Research:

The future of touch-based haptic interfaces relies on the actuation of microscale thin films. Magnetoresponsive soft-actuators have the potential to create low-power, high-responsivity, and low-cost haptic interfaces. A process was developed to create a system of micromagnetic controls integrated into microscale beams made of an MRE. This project is structured into three main objectives: the fabrication and characterization of magnetic microcontrols, the fabrication of a micrometer thin MRE, and the integration of actuation controls and MRE.

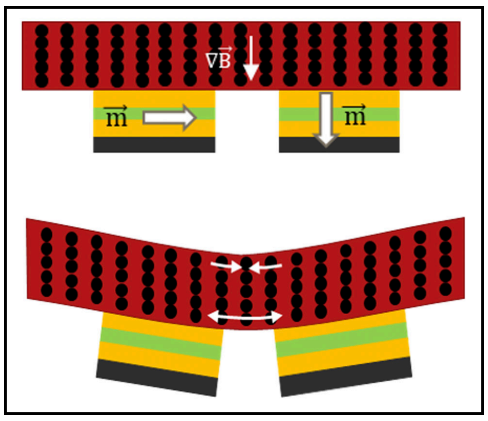

Figure 1: Device design of magnetorheological elastomer with two integrated magnetic micro controls.

The design concept involves two micromagnetic controls on the surface of an MRE thin film (see Figure 1). The MRE is constituted of a soft silicone rubber matrix and magnetic nanoparticles forming vertical chains in the thickness direction of the film. The micro controls are made of pillars with circular and elliptical base. The circular magnets (perpendicular magnetic anisotropy (PMA) magnets) are fabricated so that the magnetic moment lies preferentially in the direction perpendicular to their surface. The elliptical magnets (in-plane magnetic anisotropy (IMA) magnets) are deposited to be magnetized in the direction of the long axis. When the controls are embedded into the MRE, their magnetic fields will couple and interact with the elastomer in proximity of the gap between them, causing it to deflect.

The first step in the creation of this device is the fabrication of the magnets. Starting with a 4-inch clean silicon wafer, 350 nm of LOR3A and 450 nm of S1805 (positive) resist were spin coated, following with a soft bake at 180°C for five minutes for the former and at 115°C for one minute for the latter. The coated wafer was then exposed in an ABM contact aligner for 1.5 seconds and developed for 60 seconds using 726 MIF solvent. The patterned wafer was then descummed with oxygen plasma for 60 seconds

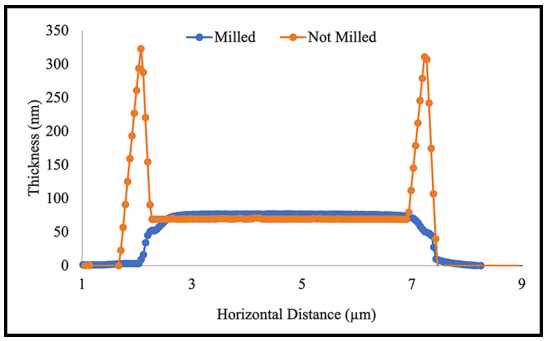

Figure 2: Ion milling to remove "rabbit ears" resulting from sputtering and lift-off.

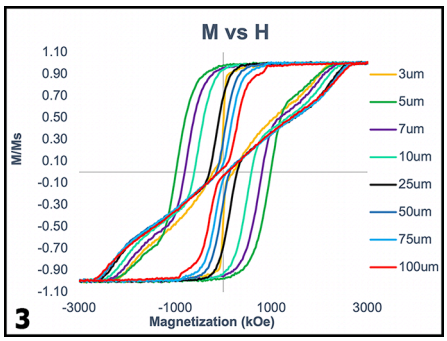

Figure 3: Magnetic hysteresis loops for PMA circles.

with oxygen flow of 30 sccm and 50 W of power. Then the magnets were deposited via sputtering.

The elliptical pillars were constituted of 3 nm of Ta, 5 nm of Pt, 58 nm of Co, and 5 nm of Pt. The circular pillars were sputtered with 19 alternating layers of Co (1 nm) and Pt (2 nm) and a final 1 nm layer of Co, using the same Ta/Pt underlayer and Pt capping layer as for the elliptical magnets. After sputtering, the wafer was soft baked at 115°C to facilitate the lift-off process, which was performed by first hitting the wafer with pressurized solvents at 1600 psi (C&D SmartProP9000), and submerging it in Remover 1165 for 20 minutes. Finally, an AJA milling tool was used at 600 V for 120 seconds with a 5° tilt to eliminate the "rabbit ears" caused by sputtering and lift-off (see Figure 2).

At this stage, the wafer was diced into 10 × 10 mm devices, each presenting specific geometry and dimensions. The magnetic properties of the deposited magnets were studied via vibrating sample magnetometry (VSM) and the optimal dimensions for both geometries were identified. The hysteresis loops obtained with VSM illustrate the magnetic properties of a magnetic sample, allowing to extract coercivity and remanent magnetization values. The circular pillars, with diameters ranging from 3 to 100 μm were tested for their magnetization in response to an out-of-plane applied magnetic field (see the hysteresis loops in Figure 3). The elliptical samples with in-plane magnetization were measured along both the short and long axes, as shown in Figure 4. The optimal magnetic properties were found in the 5 μm diameter circular magnet (maximum remanent magnetization and coercivity) and the 3 μm (short axis), 15 μm (long axis) elliptical magnet (largest difference between hysteresis loop measured along the two axes). Atomic force microscopy (AFM) was used to confirm the dimensions of the deposited geometries.

Finally, a system of micromagnets (one IMA and PMA magnet spaced apart 1, 1.5 and 2 μm) was ultimately designed to be integrated into cantilevers and simply supported beams made of a micrometer-thin MREs to create a magnetic soft actuator. the elastomer was composed of 95 wt% Sylgard 527 and 5 wt% Sylgard 184. After mixing the two elastomers using a vortex for a few seconds, 6 vol% of Fe nanoparticles were added and mixed for about 3 minutes. The dispersion was homogenized for 1 hour and 15 minutes using an ultrasonicating bath. Finally, the mix was spin coated on a wafer at 7500 rpm for 60s to achieve a thickness of 2-2.5 μm.

Conclusions and Future Steps:

We demonstrated the fabrication process of micro-magnets and discussed their optimal dimensions to achieve desired magnetic properties. Magnetic simulations carried out in our lab guided the choice of a reasonable spacing between the IMA and PMA magnets when integrated into the soft actuator. Next, the developed controls will need to be embedded into cantilevers and beams with the actuation performance assessed. We believe these results serve as a foundation for the fabrication of soft magnetorheological elastomers with integrated magnetic controls.

References:

[1] Böse, H., et al. Magnetorheological Elastomers - An Underestimated Class of Soft Actuator Materials. Journal of Intelligent Material Systems and Structures (2021).

[2] L. Cestarollo, et al. Nanoparticle-based magnetorheological elastomers with enhanced mechanical deflection for haptic displays, ACS Applied Materials and Interfaces 14 (2022),

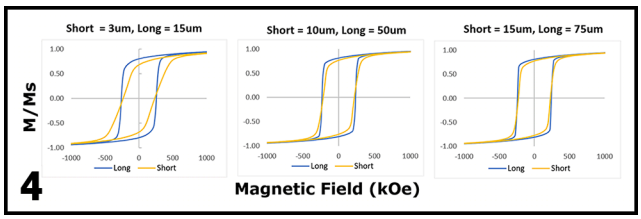

Figure 4, bottom: Magnetic hysteresis loops for short and long axis of IMA ellipses.

Investigating the Electrokinetic Behavior of Cement-Based and Alternative Cementitious Materials

2022 CNF REU Intern: Rachel Qian

Intern Affiliation: Chemical Engineering, Villanova University

CNF REU Principal Investigator: Dr. Sriramya Nair, Civil and Environmental Engineering, Cornell
CNF REU Mentor: Lyn Zemberekci, Civil and Environmental Engineering, Cornell University

CNF REU Project and Primary Source(s) of Research Funding: 2022 Cornell NanoScale Science & Technology Facility Research Experiences for Undergraduates (CNF REU) Program via the National Science Foundation under Grant No. NNCI-2025233
Contact: rqian@villanova.edu, sn599@cornell.edu, lz549@cornell.edu
Website: https://cnf.cornell.edu/education/reu/2022
Primary CNF Tools Used: Malvern Zetasizer, Scanning Electron Microscope

Abstract:

Portland cement production is a major contributor of carbon dioxide emissions, The need to incorporate large amounts of Supplementary Cementitious Materials (SCMs) to reduce the carbon footprint arises. Various SCMs were dispersed in diluted pore solutions that mimic native pore solutions of cement pastes characterized by their high pH and ionic nature. Chemical additives such as sodium glucoheptonate retarders and naphthalene sulfonate-based superplasticizers were employed to track their efficacy with the SCMs. Electrokinetic properties such as zeta potential was of primary interest in this study to ensure cement pastes have adequate rheological properties. Factors that influenced zeta potential such as electrical conductivity and pH were also measured in optimized particle solid concentrations. Stable zeta potentials have an absolute value measurement of 30 mV or above. Without the use of admixtures, it was found that majority of the particles were unstable and tended to aggregate in the pore solutions, with zeta potential values ranging from –3.13 mV to 11.5 mV. Silica flour displayed the most stable behavior in the diluted pore solution concentration, with a zeta potential around –22 mV. The use of chemical additives led to increases in the zeta potential values as compared to those of the neat particles, demonstrating that the additives are compatible with some of the particles and effective in improving the stability of the solution. Furthermore, scanning electron microscope imaging was used to view the shape and size of the cementitious particles as these factors also affect the rheology of the cementitious paste.

Summary of Research:

This research aimed at characterizing the electrokinetic behavior of Supplementary Cementitious Materials (SCMs), such as silica flour (SFL), class F fly ash (FAF), class C fly ash (FAC), metakaolin (MK) and ground granulated blast-furnace slag (SLAG) in DI water and pore solutions. Additionally, class H cement (CEM-H) was also analyzed as a baseline. To study the electrokinetic behavior, zeta potential values were tracked using a zetasizer, Malvern Instrument. 800 µL of these neat (in the absence of chemical additives) pore solutions was injected into a reusable cuvette, which was then placed into the zetasizer. The zetasizer measured the sample's electrophoretic mobility at six measurements per sample and used the Smoluchowski approach to calculate the zeta potential values.

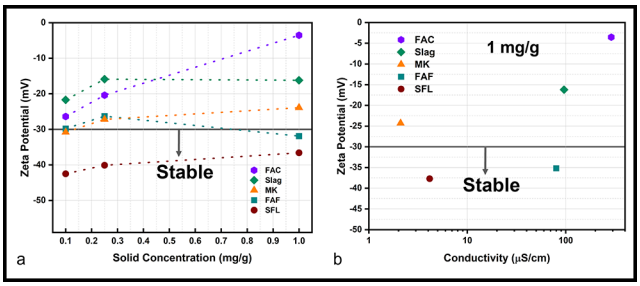

Figure 1: (a) Zeta potential values of various SCM particles with increasing solid concentration in deionized water, (b) Zeta potential vs. conductivity for one concentration.

We found that SFL had most stable behavior in DI water, with zeta potential values above 30 mV for all concentrations. FAC experienced aggregation, which was attributed to the pH and conductivity of the solution. After graphing zeta potential vs. conductivity, it was found that as conductivity increased, the zeta potential decreased, and solutions became less stable. These trends are summarized in Figure 1.

Then we used a synthesized pore solution made up of 0.6 g/L calcium sulfate dehydrate, 5.2 g/L sodium hydroxide, 17.9 g/L potassium hydroxide, and 2.4 g/L calcium hydroxide with a pH of 13.5 to test our SCMs and class H cement particles. Pore solution concentration used was 25 mL pore solution / 375 mL DI water. We mixed 100 mL of this diluted solvent with 100 mg particles through a 15-minute sonication.

Particle	Zeta Potential (mV)	pH	Conductivity (mS/cm)
Class H Cement (CEMH)	4.5	12.4	7.5
Silica Flour (SFL)	-22.0	12.2	7.2
Class F Fly Ash (FAF)	-3.1	12.1	6.9
Metakaolin (MK)	1.4	12.1	7.6
Class C Fly Ash (FAC)	2.2	12.1	6.8
Slag	12.0	12.2	8.0

Table 1: Electrokinetic behavior of various SCMs and class H cement in pore solution.

As shown in Table 1, it was found that majority of the particles became unstable and tended to aggregate in the pore solutions, with zeta potential values ranging from –3.13 mV to 11.5 mV. SFL displayed the most stable behavior in the diluted pore solution concentration, with a zeta potential around –22 mV. The use of chemical additives such as sodium glucoheptonate (SGH) and naphthalene-based superplasticizers led to increases in the zeta potential values of the CEM-H as compared to those without any additives, demonstrating that the additives are compatible and effective in improving the stability of the solution. However, these increases were bounded by certain concentrations of additives. This is illustrated in Figures 2 and 3.

Conclusions and Future Steps:

Zeta potential values of SCMs such as MK and FAF were similar to those found in literature [1-3], validating the procedure of this study. Majority of SCMs exhibited stable behavior when using deionized water as a solvent, apart from FAC.

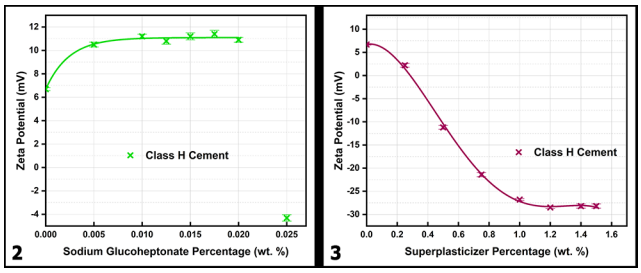

Figure 2, left: Zeta potential values of class H cement in pore solution with an increasing content of the retarder sodium glucoheptonate. Figure 3, right: Zeta potential values of class H cement in pore solution with an increasing content of the naphthalene-based superplasticizer.

Opposite was true when using pore solution as a solvent, except for SFL. CEM-H interactions with the retarding additive SGH in the pore solution indicated that this additive improves the stability of the solution to a certain point, after which increasing the SGH content results in aggregation. CEM-H in the presence of the superplasticizer additive showed that stability of the solution increased up to a saturation point, after which there is no significant effect.

To observe aggregation of particles, along with measuring zeta potential we will also measure the particle size of each of the SCMs. This will be achieved by adding an additional sieving and filtering process to limit particle sizes to 5 µm. We will also aim at conducting adsorption tests of polymer-based additives onto the SCM particles using an ultraviolet-visible (UV-vis) light device. In future experiments, there will be further optimization of pH and conductivity versus zeta potential.

References:

[1] Malta, J. O., Oliveira, L. V., Ueki, M. M., and Barreto, L. S. (2021). Characterization and stabilization of nano-metakaolin colloidal suspensions. Powder Technology, 383, 43-55.

[2] Malek, R. I., Khalil, Z. H., Imbaby, S. S., and Roy, D. M. (2005). The contribution of class-F fly ash to the strength of cementitious mixtures. Cement and concrete research, 35(6), 1152-1154.

[3] Wang, C., Kayali, O., and Liow, J. L. (2021). The effectiveness and mechanisms of superplasticisers in dispersing class F fly ash pastes. Powder Technology, 392, 81-92.

Access to Porous Substructure of Block Copolymer-Derived Nanomaterials via Reactive Ion Etching (RIE)

CNF Project Number: 1356-05

Principal Investigator(s): Ulrich Wiesner

User(s): Fei Yu

Affiliation(s): Department of Materials Science and Engineering, Cornell University

Primary Source(s) of Research Funding: U.S. Department of Energy (DOE), Office of Science (Basic Energy Sciences (DE-SC0010560)

Contact: ubw1@cornell.edu, fy84@cornell.edu

Website: http://wiesner.mse.cornell.edu/

Primary CNF Tools Used: Oxford 81 Etcher

Abstract:

The use of block copolymers (BCPs) as structure-directing agent offers a facile pathway toward nanomaterials with tunable mesostructures and functional properties. However, the surface energy often disrupts the thermodynamics of block copolymer self-assembly and results in a different surface morphology from the bulk substructure. In this report, we demonstrate the use of reactive ion etching (RIE) in the CNF cleanroom as a simple technique to access the substructure in block copolymer-derived carbon materials. RIE removes the dense capping layer on the surface so that we can make use of the internal structure with massive meso- and nano-porous surface areas. These carbon monoliths with open pore structures may be promising candidates for electrode materials in the design of 3D continuous electrochemical energy storage devices.

Summary of Research:

With high interfacial areas and a low areal footprint, three-dimensionally (3D) continuous nanostructured electrode materials have gained interest as the demand for increasingly efficient electrochemical energy storage devices grows. As a result, nanostructured carbon materials with 3D network architectures are under active investigation for routes to 3D functional composite materials, e.g., via straightforward backfilling, for the eventual incorporation into energy storage devices.

In our work, ultralarge molar mass diblock copolymers are employed as structure-directing agents for carbon precursors to prepare carbons with ultralarge pore sizes. The unfavorable interaction between the large blocks forces them to segregate from each other at the nanoscale and the carbon precursors preferentially mix with the more hydrophilic block. Upon heat treatment in the furnace to high temperatures of up to 1600°C, nonperiodically ordered co-continuous network structures are derived with an average pore sizes of around 100 nm (Figure 1).

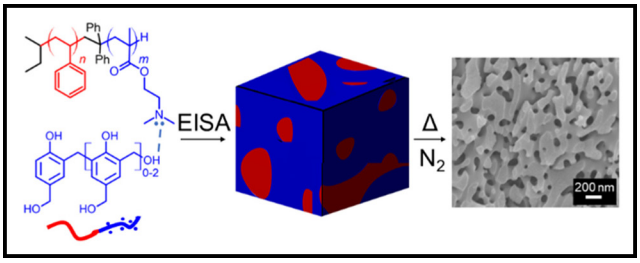

Figure 1: Schematic of the self-assembly of BCPs and carbon precursors (left) via evaporation-induced self-assembly (EISA) into mesostructured hybrids (middle) and the mesoporous carbon materials after high-temperature treatments (right). The SEM images show representative cross sections of the final monoliths.

After subsequent carbon activation processes, the porous carbons with continuous 3D network structures are a promising candidate as the cathode materials for the intercalation of lithium. However, since the self-assembled mesostructures are formed from a solution in

a dish, the solution-air and solution-container interfaces experience different thermodynamic driving forces for the microphase segregation of the BCPs. The scanning electron microscopy (SEM) image in Figure 2a shows that the surface of an as-made hybrid that has gone through the heat treatment is capped by a dense layer, which renders the porous understructure inaccessible.

In order to realize the potential of the porous 3D network structure, Oxford 81 Etcher was utilized with oxygen plasma. Each side of the as-made hybrid is subject to 30 min of oxygen plasma at 150 W forward power, 50 sccm flow rate, and 60 mTorr pressure. Figure 2b shows the carbon structure derived from heat treating the etched hybrid, whose underlying pores in the substructure are now fully accessible from the surface.

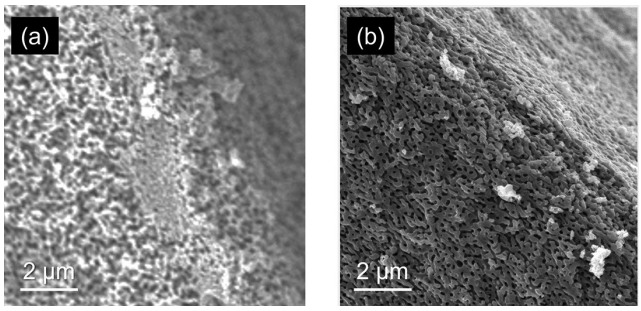

Figure 2: Scanning electron microscopy (SEM) images of carbon monoliths derived from heat treating BCP-carbon precursor hybrids (a) without and (b) with oxygen plasma etching.

Conclusions and Future Steps:

In summary, a one-pot route to co-continuous porous carbons is demonstrated via ultralarge molar mass block polymer self-assembly with carbon precursos. Aided by reactive ion etching (RIE), open and accessible 3D co-continuous pore network structures of carbon materials make them appealing for applications that require fast kinetics through the large 3D continuous pore network or backfilling processes, e.g., required for producing 3D nanoarchitecture-based energy storage devices.

References:

[1] Tait, W.R., Thedford, R.P., Chapman, D.V., Yu, F., Freidl, J.W., Sablina, E.S., Batsimm, G.M. and Wiesner, U.B. One-Pot Structure Direction of Large-Pore Co-Continuous Carbon Monoliths from Ultralarge Linear Diblock Copolymers. Chemistry of Materials 2021, 33(19), 7731-7742.

Autonomous High-Throughput Materials Discovery of Metal Oxide Thin Films via Laser Spike Annealing, Spatially Resolved X-Ray Diffraction, and Thin Film Device Characterization

CNF Project Number: 1400-05

Principal Investigator(s): R. Bruce van Dover

User(s): Duncan Ross Sutherland

Affiliation(s): Materials Science and Engineering, Cornell University

Primary Source(s) of Research Funding: Air Force Research Laboratory FA9550-18-1-0136, Cornell NanoScale and Science and Technology Facilities NNCI-2025233, Cornell High Energy Synchrotron Source DMR-1332208

Contact: vandover@cornell.edu, drs378@cornell.edu

Primary CNF Tools Used: CHA Thermal Evaporation, General Photolithography Equipment, Developing Tools, Mask Writers, Wafer Scale Tube Furnaces, Some Metrology Equipment

Abstract:

The study of complex oxides through combinatorial efforts would require a prohibitive amount of material resources and time if experiments were conducted using bulk techniques and at macroscopic length scales. We employ leading edge materials processing in conjunction with advanced micron-scale synchrotron characterization to enable these high-throughput studies and accelerate materials optimization and discovery. This research area is additionally enhanced by incorporating artificial intelligence and machine learning methods. Dimensionality reduction and reproducibility of the processing techniques requires a precision registration of the micron-scale x-ray characterization is essential for analytical autonomous research. We use the Cornell NanoScale and Science and Technology Facilities (CNF) in order to align each of the experimental elements with a primary goal of discovering novel materials. Thin film capacitor devices are constructed post material processing to allow electrical characterization of the properties of the materials synthesized.

Summary of Research:

The focus of the van Dover research group is combinatorial and autonomous materials exploration via thin film synthesis, processing, and characterization. The scale of possible material combinations becomes exponentially large for thin films with a composition spread spanning multiple degrees of chemical freedom, and processing adds even more dimensions of complexity. While exhaustive searching of a system may be impossible, strategically planned experiments can dramatically reduce the resources required to completely map composition/processing space. We collaborate with experts to develop and deploy state of the art artificial intelligence methods to accelerate the discovery of material systems [1,2].

Combinatorial thin film libraries are created by reactively sputtering atoms from one or more targets onto a 4-inch silicon wafer, followed by processing the as-deposited material with a thermal treatment technique called laser spike annealing (LSA) in collaboration with the Thompson group (Figure 1). Co-sputtering in an off-axis geometry with two or more targets produces a monotonic gradient in chemical makeup of the thin film across the

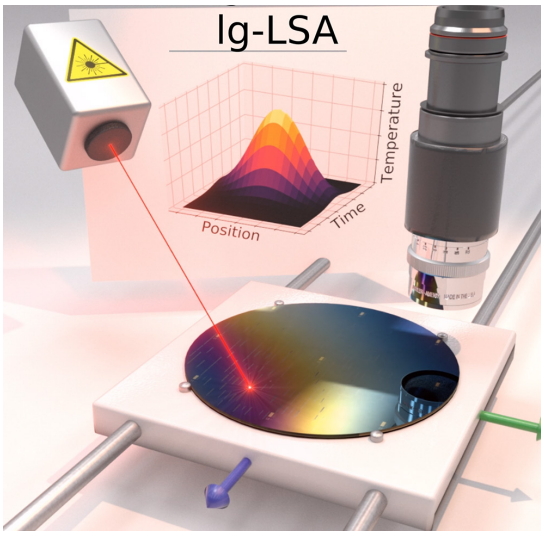

Figure 1: A rendering of the laser spike annealing experiment in relation to the as-deposited thin film and analytical methods.

substrate. Increasing the number of targets decreases the area on the film with unique composition; the trade-off of span in chemical space is the scarcity. LSA controls the peak temperature and duration at that temperature; i.e., the thermal history the material experiences. LSA can be localized to a 2 mm by 5 mm area on the wafer, allowing a regular gird of 616 independently chosen LSA conditions.

There are an additional nine locations photolithographically defined on the wafer that enable precise alignment among various spatially resolved techniques used to analyze the processed materials (e.g., optical microscopy, thin film reflectance spectroscopy, and spatially resolved x-ray diffraction characterization).

Figure 2 shows the layout of the annealed stripes on a composition spread and the total number of conditions for an example material system. To make the experimentation reproducible and precise (especially critical for automation and autonomous learning,) prior to thin film deposition every silicon wafer has the location grid and calibration marks lithographically patterned using CNF.

We successfully processed and characterized (see one example stripe in Figure 3) over 30 unique thin film metal oxide libraries at the Cornell High Energy Synchrotron Source in April 2022. Five of those libraries were used in successful active learning trials yielding a marked improvement in throughput of materials exploration and demonstrating integration of artificial intelligence into experimental materials research. Four of the other libraries were of interest for their electrical properties and further processed into a dense array of thin film capacitor devices which are currently being measured. The remainder of the combinatorial libraries are being analyzed and the most illuminating results are being prepared for publication. An example product from the x-ray characterization is the processing phase diagram in Figure 4.

Conclusions and Future Steps:

We have engineered an autonomous materials synthesis and characterization system for accelerating the discovery of novel materials. The reproducibility, reliability, and analytical requirements for automating the experimentation and incorporating the artificial intelligence was made possible by utilizing the CNF. Future research efforts will focus on improving the temporal and thermal calibration of the laser spike annealing method using lithographically patterned phase-change materials. One limitation of the post processed capacitor devices is the time required to exhaustively measure the properties each stripe of annealed material. We plan to employ artificial intelligence to optimally measure the minimum number of capacitors required to map structure/property relations by taking advantage of information derived from x-ray characterization. Developing this foundation will allow us to construct more complicated devices for assessing transport and carrier properties of the electronic materials.

References:

[1] Ament, S., et al. Sci. Adv. 7, eabg4930 2021.

[2] Sutherland, D., et al. ACS Combi. Sci. 2020, 22, 12, 887-894.

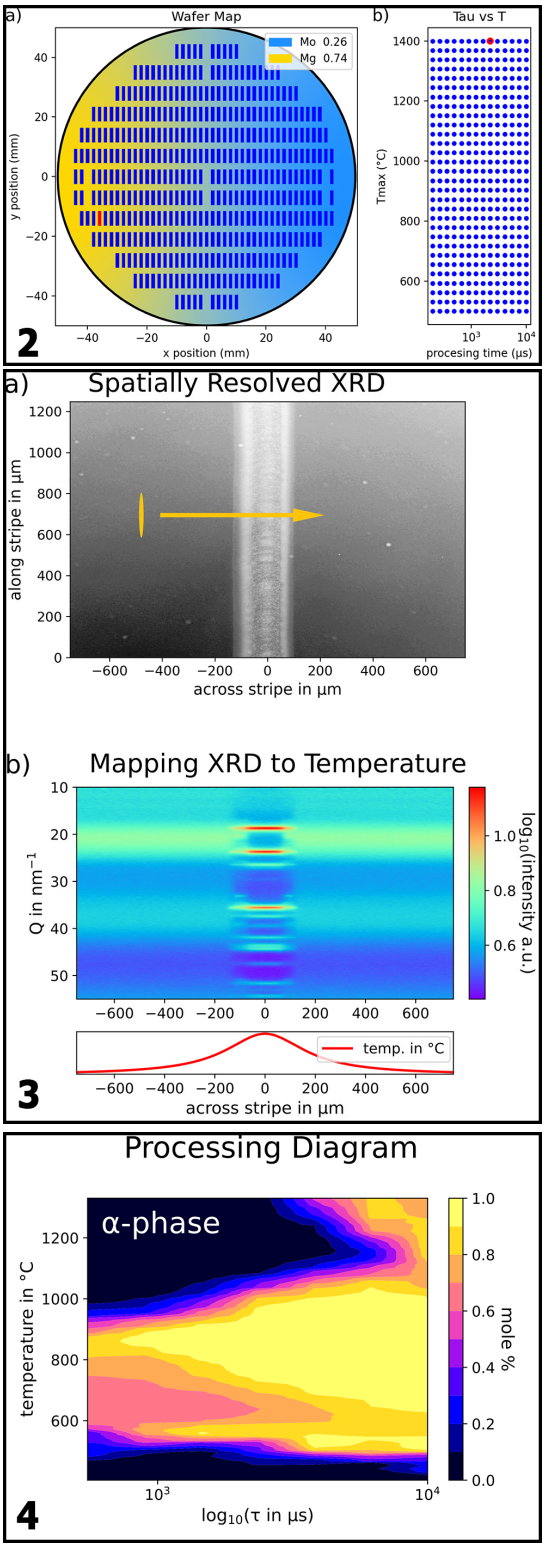

Figure 2, top: a) Cartoon description showing the distribution of laser spike annealing experiments over a 4" wafer with a pseudo binary composition spread of the cations Mg and Mo. b) Distribution of laser spike annealing conditions in the materials processing space. Figure 3, middle: a) Optical micrograph of a stripe of annealed material; yellow spot indicates the footprint and aspect ratio of the x-ray diffraction beam and arrow indicates direction of data collection. b) The spatially resolved x-ray diffraction heatmap comprised of the individual 1D diffraction patterns with the conversion of spatial extent to effective temp of annealing. Figure 4, bottom: A novel quantitative processing phase phase diagram for a laser spike annealed thin film oxide.

Low Loss Superconducting LC Resonator for Strong Coupling with Magnons

CNF Project Number: 2126-12

Principal Investigator(s): Gregory D. Fuchs

User(s): Qin Xu

Affiliation(s): Physics Department, Cornell University

Primary Source(s) of Research Funding: Center for Molecular Quantum Transduction (CMQT)

Contact: gdf9@cornell.edu, qx85@cornell.edu

Primary CNF Tools Used: AJA Sputter Deposition, Heidelberg Mask Writer - DWL2000, GCA 6300 DSW 5X g-line Wafer Stepper, YES Asher, AJA Ion Mill, P7 Profilometer, Zeiss Ultra SEM, DISCO Dicing Saw, Nabity Nanometer Pattern Generator System (NPGS), Westbond 7400A Ultrasonic Wire Bonder

Abstract:

We design, fabricate and study an on-chip superconducting LC resonator that is strongly coupled to a magnon mode of the molecular ferrimagnet vanadium tetracyanoethylene ($V[TCNE]_x$). We demonstrate a fully integrated, lithographically defined photon-magnon hybrid quantum system in the strong coupling limit where all elements have low damping.

Summary of Research:

The goal of this research is to study a strongly coupled hybrid quantum device composed of a superconducting microwave resonator and a magnon mode. A key figure-of-merit is the cooperativity $C = 4g^2/K_mK_r$ between magnons and resonator photons, where g is the coupling strength between magnons and photons, and K_m, K_r are damping rate for magnons and resonator respectively. The two systems are strongly coupled if $C > 1$.

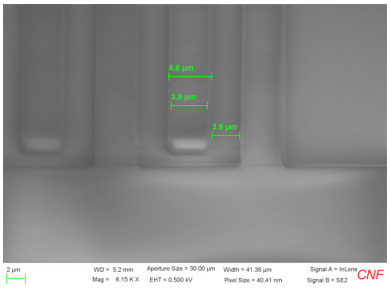

Figure 1: SEM image of the profile of resist after being exposed and developed.

We use $V[TCNE]_x$ as the magnetic material in this work because of its low Gilbert damping rate $\alpha \sim 10^{-4}$ and thus low K_m, and because it can be grown on most materials and patterned via electron beam lithography. To increase the coupling g, we design an LC resonator with a small inductance and a narrow inductor wire. We pattern the $V[TCNE]_x$ directly on the inductor wire of LC resonator.

We first designed the LC resonator based on a single layer of photolithography. We used KLayout to design the structure and ADS to simulate its microwave response. The simulation predicts a resonance frequency around 4.2 GHz. We then patterned the photomask with the Heidelberg Mask Writer - DWL2000.

The superconducting material for our device is niobium that we deposited on sapphire using the AJA Sputter Deposition (second tool) at 600°C. The resulting Nb thickness is around 60 nm measured with the P7 profilometer. It has a critical temperature (T_c) of 7.3 K. The high T_c of Nb and the low loss tangent of sapphire help limit the damping rate of the superconducting device.

We patterned the Nb using photolithography followed by dry etching. We spun LOR3a and then S1813 on the Nb with hotplate baking, exposed the resists in GCA 6300 DSW 5X g-line stepper, and then developed the resist in MIF 726. The profile of the patterned resists was checked in Zeiss Ultra SEM. Figure 1 shows the SEM image of the patterned resists which looks perfect.

Then we descummed the developed resists in YES Asher, etched the Nb not covered by resist in AJA ion mill, and then put the wafer into the solution 1165 to strip off all the resists on the wafer. We patterned around 50 resonators on a 2-inch wafer. Because of the dust on the wafer during photolithography, around 20 of the devices have defects on their patterns, but the remaining 30 looked perfect under the microscope.

Before $V[TCNE]_x$ deposition, we tested the resonator itself. For measurement setup, we cut the wafer and

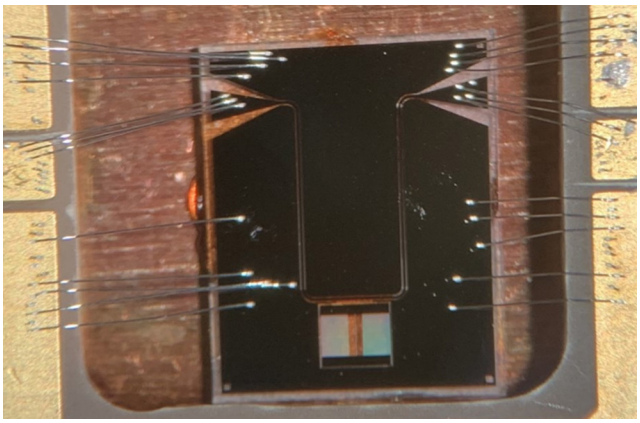

Figure 2: The LC resonator device bonded to a chip carrier.

separated those 50 devices using the DISCO dicing saw, glued one of the resonators on a PC board with varnish and then used the Westbond 7400A Wire Bonder to wire-bond the device for microwave measurement.

Figure 2 shows a microscope image of the device wire bonded on the PC board.

With a vector network analyzer (VNA), we tested the resonator device in a He-3 cryostat at base temperature 0.43 K. The transmission spectrum of the frequency scan shows the resonator has a quality factor of 5031.

We use an electron-beam lithography liftoff process to template the growth of $V[TCNE]_x$. We spun the e-beam resist on the resonator chip and then exposed the resist in Nabity Nanometer Pattern Generator System (NPGS). Figure 3 shows the device after being exposed in the NPGS, where vertical line of the T-shaped part is the inductor wire.

We then shipped the templated device to Ohio State University for collaborator Donley Cormode in Professor Ezekiel Johnston-Halperin's group for $V[TCNE]_x$ growth and liftoff. The dimension of the $V[TCNE]_x$ is 600 μm times 6 μm times 300 nm.

We studied the integrated hybrid device at 0.43 K. We measured the microwave transmission coefficient using a vector network analyzer.

Figure 4 shows the trans-mission spectrum as a function of magnetic field and frequency. The avoided level crossing characteristic of a strongly coupled hybrid device is observed. We find the coupling coefficient is g = 90.4 MHz, the resonator damping rate is K_r = 0.90 MHz and the magnon damping rate is K_m = 33.3 MHz. Using these values, we find the cooperativity $C = 4g^2/K_mK_r$ = 1091, which greatly exceeds 1.

Conclusions and Future Steps:

We have demonstrated the design and fabrication of a low loss superconducting on-chip LC resonator in the CNF cleanroom. Our device achieved strong coupling between $V[TCNE]_x$ magnons and resonator photons with a cooperativity greater than 1000. In this experiment the $V[TCNE]_x$ appeared inhomogeneously broadened (not limited by intrinsic damping). We may increase the cooperativity further by better understanding and controlling the mechanisms of $V[TCNE]_x$ linewidth at cryogenic temperatures.

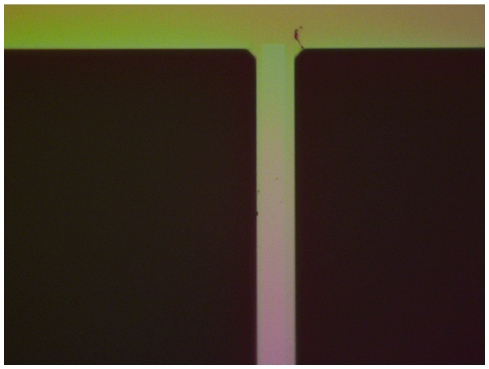

Figure 3: Microscope image of LC resonator device after being coated with e-beam resist and then being exposed in Nabity. The T-shaped part represents the superconducting film, and the lighted vertical rectangle on the vertical line of the T-shaped part represents the Nabity exposed area.

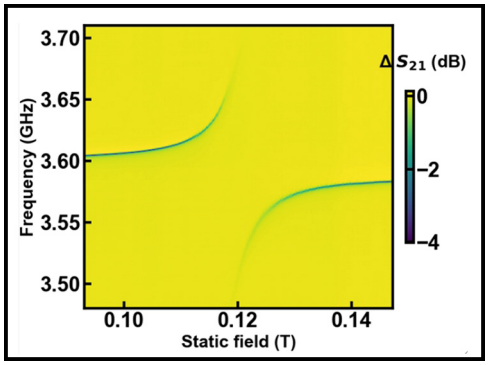

Figure 4: The transmission spectrum of field-frequency scan of the resonator-magnon system. The anti-crossing of the dip is the signature of coupling between resonator photons and $V[TCNE]_x$ magnons.

Encapsulation of Photocathodes in Two-Dimensional Materials

CNF Project Number: 2584-17

Principal Investigator(s): Melissa A. Hines

User(s): Qingyuan "Amy" Zhu, Dulanga Somaratne, Annabel Selino

Affiliation(s): Dept. of Chemistry and Chemical Biology, Cornell University

Primary Source(s) of Research Funding: Center for Bright Beams, an NSF Science and Technology Center

Contact: Melissa.Hines@cornell.edu, qz337@cornell.edu, dulanga.somaratne@cornell.edu, avs58@cornell.edu
Website: https://mahines.github.io/HinesLab/

Primary CNF Tools Used: SC4500 Odd-Hour Evaporator, Glen 1000 Resist Strip

Abstract:

We are developing a new technique for encapsulating highly reactive photocathodes in an atomically thin membrane that protects them from oxidation and degradation without affecting their photoemission properties or chemical purity.

Summary of Research:

Photocathodes are materials that eject electrons under illumination. By their very nature, high-performance photocathodes must be made from materials that lose electrons easily — in other words, materials that are easily oxidized. For example, many photocathodes are either coated with alkali metals (e.g., Cs/GaAs) or comprised of alkali metals (e.g., Cs_3Sb). This presents a technical challenge, as exposure to even trace amounts of O_2 or H_2O will destroy or degrade the photocathode. For highest performance, the photocathodes must also be atomically flat and extremely homogeneous.

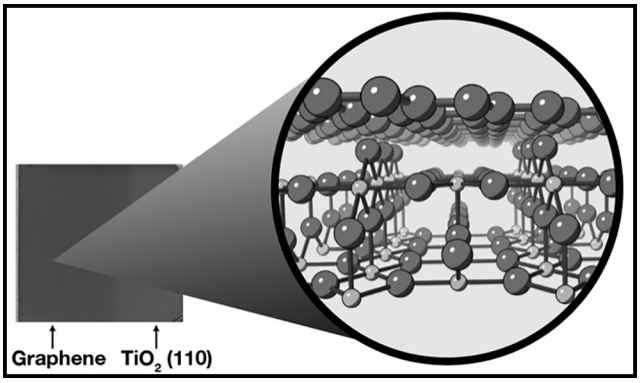

Figure 1: Optical image of TiO_2(110) with single-layer graphene on left side. The inset is a model of single-layer graphene on TiO_2(110).

To meet these challenges, we are developing a technique to produce photocathodes encapsulated in two-dimensional materials, such as graphene or hexagonal boron nitride. The key challenge in this project is ensuring that every step of the fabrication leaves no residue on the surface, as even monolayer levels of contamination could significantly reduce photoelectron transmission and beam brightness.

In the first step of fabrication, commercial two-dimensional materials, which are grown on a copper foil, are coated with a thin gold layer in the SC4500 thermal/e-beam evaporator. The two-dimensional material on the backside of the copper foil is then removed using 100W of oxygen plasma in the YES oxygen plasma asher. The copper foil is then removed with an aqueous etchant, allowing the graphene side of the gold-coated graphene to be adhered to a low energy substrate. The gold film is then removed by a second aqueous etch.

Fabricating Superconducting Microwave Resonators for On-Chip Electron Spin Resonance Spectroscopy

CNF Project Number: 2705-18

Principal Investigator(s): Farhan Rana

User(s): Arjan Singh

Affiliation(s): Electrical and Computer Engineering, Cornell University

Primary Source(s) of Research Funding: Air Force Research Lab (AFRL)
Grant No. FA9550-18-1-0529

Contact: farhan.rana@cornell.edu, as2995@cornell.edu

Primary CNF Tools Used: AJA Sputter Deposition Tool,
ABM Contact Aligner, PT770 Etcher, DISCO Dicing Saw

Abstract:

Electron spin resonance (ESR) spectroscopy has been a useful tool for measuring defect spins in semiconductors [1-6]. We are utilizing the robust capabilities of the Cornell NanoScale Facility (CNF) to develop an ESR spectrometer with the capability to measure defect spins in MBE-grown films as thin as 100 nm. Here, we demonstrate a planar microwave resonator, the principal device to be used in the spectrometer, fabricated using the superconducting metal niobium (Nb). The superconducting metal allows us to shrink the dimensions of our device by a hundred times, compared to a copper resonator, while avoiding any kind of resistive loss. This allows us to simultaneously benefit from a high quality-factor (*Q*-factor) and a small spatial extent of the microwave-spin interaction.

Summary of Research:

Electron spin resonance (ESR) spectroscopy is based on exploiting the Zeeman interaction between a magnetic field and a spin. Ever since it was proposed to study nuclear spins nearly a century ago [8], it has been a useful tool to study spins in materials (1-7).

A (non-oscillating) magnetic field splits degenerate spin states by an energy, $E = \gamma_S B$ (assuming spin-1/2 particles), where γ_S is the gyromagnetic ratio (the ratio between the magnetic moment of a particle to its angular momentum) and B is the applied magnetic field. The energy E for magnetic fields on the order of 1 T can easily be supplied by microwaves of frequencies, $f \sim$ 1-10 GHz.

Thus, the essential idea of ESR spectroscopy is that by supplying microwave radiation to semiconductor samples subject to a magnetic field, we can induce transitions between spin states of defects when the condition, $hf = \gamma_S B$ is met, where h is Planck's constant.

By observing these transitions, we can extract the gyromagnetic ratio, γ_S, associated with a defect-spin state, giving us insight into its electrical/magnetic properties. Figure 1 shows a schematic of such an ESR experiment.

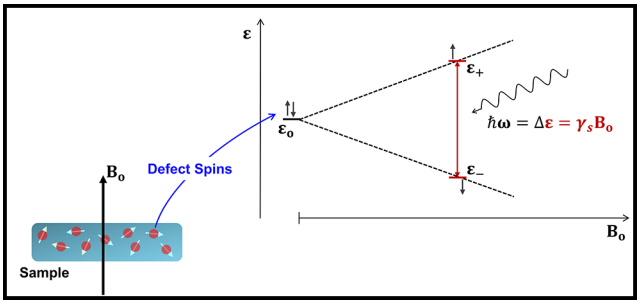

Figure 1: Schematic showing the basic principle of electron spin resonance (ESR) spectroscopy.

ESR spectrometers, by and large, use a 3-D microwave resonator to deliver microwaves to samples subject to a DC magnetic field. 3-D microwave resonators, owing to their large magnetic field mode volumes, are not sensitive to MBE grown thin films. Using a 2-D, planar microwave resonator we can minimize the magnetic field mode volume, and thus minimize the magnetic field fill factor (represents the fraction of magnetic field seen by the film being probed). A small magnetic fill factor (close to unity) will allow us to probe defect spins in

semiconductor films as thin as ~ 10 nm. The key to a high magnetic fill factor is shrinking the dimensions of the resonator. However, small dimensions also mean higher resistive losses in metals. We use the superconducting metal Nb, to overcome this trade-off, thus maintaining a high magnetic fill-factor and near-zero resistive loss [9]. The small mode volume of a 2-D planar resonator also means that much of the magnetic field is within the substrate on which the resonator is patterned. To minimize the dielectric loss resulting from this, we use a sapphire substrate, owing to sapphire's small loss-tangent and high dielectric constant.

Methods and Results:

We used the Cornell NanoScale Facility (CNF) to fabricate this superconducting 2D resonator. Figure 3a shows the fabrication procedure for our devices. We sputter deposit 100 nm of Nb. We measured the temperature dependent resistance of this film and found the superconducting transition temperature T_c, to be ~ 6 K. Since we will be conducting our experiments in a 4.2 K liquid He cryostat, this T_c will work well for our experiments. Figure 4 shows the critical dimensions of the fabricated device.

Conclusion and Future Steps:

The next step is to measure the transmission through the fabricated resonators and measure the *Q*-factor. This will be followed by an ESR measurement of MBE grown thin films of ultrawide-bandgap semiconductor β-Ga_2O_3.

Acknowledgements:

I would like to thank the CNF staff, without whom this work would not have been possible and will not be able to continue. I especially thank Tom Pennell, Chris Alpha, Aaron Windsor, Garry Bordonaro, and Jeremy Clark for their invaluable input and support.

References:

[1] M Baeumler, et al., J. Phys. C: Solid State Phys. 20 L963 (1987).

[2] W. E. Carlos, et al., Phys. Rev. B 48, 17878 (1993).

[3] J H N Loubser and J A van Wyk, Rep. Prog. Phys. 41 1201 (1978).

[4] W. V. Smith, et al., Phys. Rev. 115, 1546 (1959).

[5] B. E. Kananen, et al., Applied Physics Letters 110, 202104 (2017).

[6] Nguyen Tien Son, et al., Applied Physics Letters 117, 032101 (2020).

[7] Conrad Clauss, et al., J. Phys.: Conf. Ser. 592 012146 (2015).

[8] G. Breit and I. I. Rabi, Phys. Rev. 38, 2082 (1931).

[9] A. Bienfait, et al., Nature Nanotechnology, volume 11, pages 253–257 (2016).

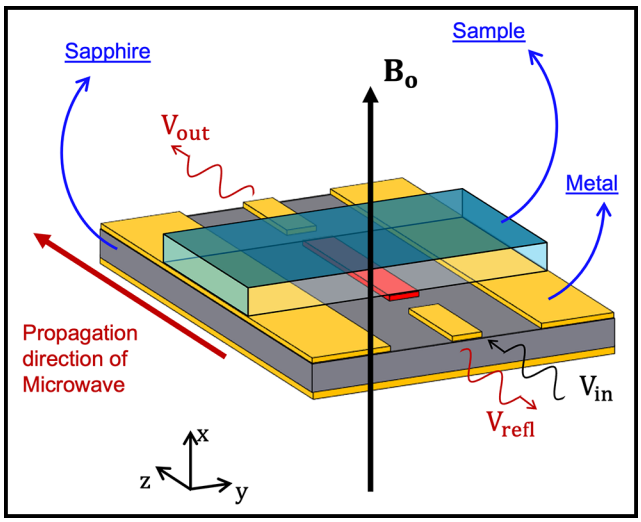

Figure 2: Basic layout of our ESR measurement. The planar microwave resonator lies at the heart of the setup and is fabricated at the Cornell NanoScale Facility (CNF).

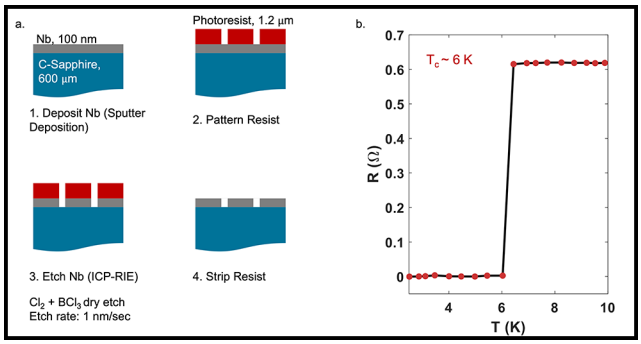

Figure 3: (a) Shows the schematic of the fabrication process used to fabricate our microwave resonator. (b) Shows Resistance vs. Temperature of our deposited Nb film.

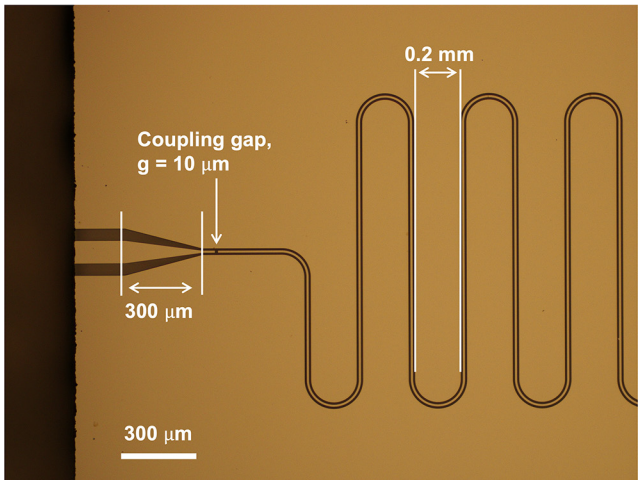

Figure 4: Key dimensions of the fabricated superconductor microwave resonator.

Investigation of Palladium Strains and Actuation in Gaseous Environments

CNF Project Number: 2736-18

Principal Investigator(s): Nicholas L. Abbott[1]

User(s): Hanyu (Alice) Zhang[2]

Affiliation(s): 1. Smith School of Chemical and Biomolecular Engineering,
2. School of Applied and Engineering Physics; Cornell University

Primary Source(s) of Research Funding: Cornell Center for Materials Research with funding from the National Science Foundation Materials Research Science and Engineering Centers program (DMR-1719875)

Contact: nla34@cornell.edu, hz496@cornell.edu

Primary CNF Tools Used: Heidelberg Mask Writer - DWL2000, ABM Contact Aligner, Oxford 81/82/100 Etchers, AJA Sputter Deposition Tool, AJA Ion Mill, Oxford PECVD, SC4500 Odd-Hour Evaporator, PT770 Etcher (Left Side), OEM Endeavor Aluminum Nitride Sputtering System, Leica CPD300 Critical Point Dryer, DISCO Dicing Saw

Abstract:

We are developing a palladium-based microactuator that is driven by hydrogen as a fuel. After an initial delay upon exposure to hydrogen, these actuators exhibit high strains within a short time period. In this report, we show the fabrication process of these devices, present the characterization of simple hinge structures, and discuss initial results.

Summary of Research:

We are interested in understanding palladium as a material that can be used to drive the actuation of microscopic hinges for use in micro robotics. Palladium is a metal known for its high hydrogen affinity, and the palladium hydride system is well-studied [1]. For this project, we are utilizing palladium's high affinity to hydrogen to obtain actuation on the microscale. By inducing an asymmetric strain across the thickness of a bimorph made with palladium and an inert material (currently using titanium), we have observed curling and bending in these devices.

To fabricate these devices, a sacrificial layer of aluminum nitride is initially sputtered onto a fused silica wafer with the OEM Endeavor tool and patterned. Then a layer of titanium sputtered, and a layer of palladium is evaporated onto the sample to create a Ti-Pd bimorph of various thicknesses. This bimorph is patterned and etched with the Ion Mill. To selectively control where the bimorph bends, silicon dioxide panels that are around 500nm thick are deposited with plasma enhanced chemical vapor deposition on the Oxford PECVD and etched with a mixture of trifluoromethane and oxygen plasma on the Oxford 100. We then soak the chips in 726 MIF developer to release the devices and use the Leica critical point dryer to dry the chips.

After the devices are made, we bring them into the lab to test inside a gas chamber.

Conclusions and Future Steps:

Figure 1 shows some example devices that we are currently testing. After an initial delay upon exposure to hydrogen, these devices respond rapidly and show high strain (Figure 2). We also observed that this process is reversible (Figure 3).

To understand palladium's interaction with hydrogen in our microactuators, we are planning various experiments in which critical dimensions of the palladium microactuators will be varied. We will also perform imaging of the deposited palladium before, during and after exposure to gaseous environments.

References:

[1] Dekura, S., Kobayashi, H., Kusada, K., and Kitagawa, H. (2019). Hydrogen in Palladium and Storage Properties of Related Nanomaterials: Size, Shape, Alloying, and Metal-Organic Framework Coating Effects. ChemPhysChem, 20(10), 1158-1176.

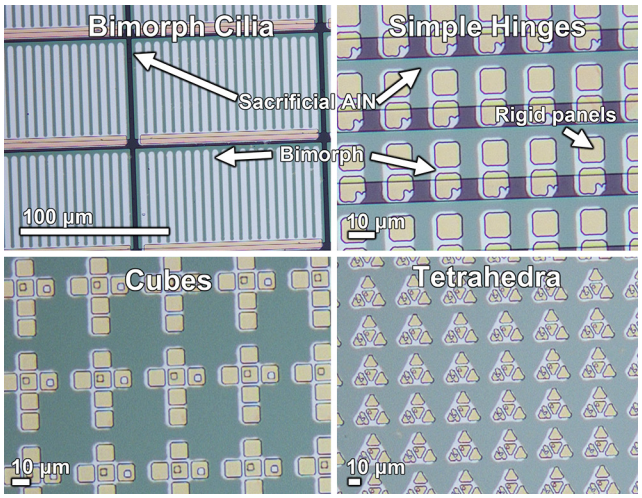

Figure 1: Example collection of devices pre-release.

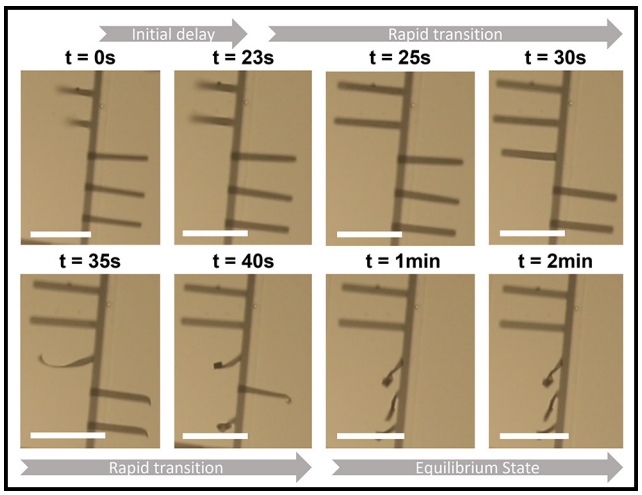

Figure 2: Time-lapse photos showing palladium's response to hydrogen using simple cilia-like microactuator devices. The microactuators consist of 3.5 nm of sputtered titanium and 7.6 nm of evaporated palladium, both deposited as a bilayer. Scale bars are 50 µm.

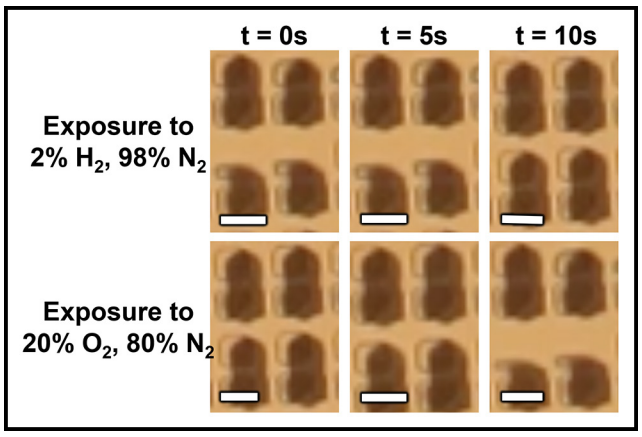

Figure 3: Time-lapse photos showing bilayer hinges exposed to a hydrogen environment and then air. Scale bars are 10 µm. The bilayer hinge consists of 10 nm of sputtered titanium and 20 nm of evaporated palladium. The panels are fabricated from 420 nm of SiO_2. A 20 nm layer of titanium is used to adhere the palladium and SiO_2 layers.

Scissionable Polymer Photoresist for Extreme Ultraviolet Lithography

CNF Project Number: 2751-18
Principal Investigator(s): Christopher Kemper Ober
User(s): Jingyuan Deng

Affiliation(s): Materials Science and Engineering, Cornell University

Primary Source(s) of Research Funding: INTEL Corporation

Contact: c.ober@cornell.edu, jd966@cornell.edu

Primary CNF Tools Used: ASML 300C DUV Stepper,
JEOL 6300 E-Beam Lithography, P10 Profilometer

Abstract:

Scissionable polymers are polymers that will depolymerize under different stimuli including acid, base, and free radicals. These polymers have been investigated in the development of photoresists and other degradable materials. This work focuses on the poly(phthalaldehyde), PPA, a family of scissionable polymers. The PPA backbone consists of acetal linkages that are very sensitive to acids. Upon exposure to acids, the polymer chain depolymerizes to its corresponding monomers. This depolymerization behavior makes PPAs excellent candidates as photoresist materials. Several new PPA photoresists are being explored in this work.

Summary of Research:

Poly(phthalaldehyde) (PPA) is a well-established depolymerizable photoresist developed by IBM in 1983 [1]. Monomer outgassing and absence of bench-stability resulted in the resist being abandoned in favor deprotection based resists. However, multiple groups have recently explored the potential of PPA under EUV exposure [2-4], but so far success has been elusive. In comparison with other depolymerizable systems, a very limited number possess the same depolymerization kinetics, and those that do suffer from poor sensitivity or outgassing.

The difficulty in simultaneously maximizing resolution, line edge roughness, and sensitivity is known as the RLS trade-off and is one of the foremost issues hampering EUV performance. One accepted technique to bypass the RLS trade-off is to employ high loadings of photoacid generator (PAG) and in the process diminish deleterious shot noise effects. Unfortunately, the popular ionic PAGs phase separate regularly at elevated concentrations, especially above 20 wt%. Non-ionic PAGs present a potential solution to this problem as they can remain miscible at significantly higher concentrations compared to ionic PAGs. These PAGs also possess advantages in dark loss and acid yield when exposed to e-beam.

Despite the potential of non-ionic PAGs, they are consistently inferior to ionic PAGs in terms of sensitivity, with few able to achieve the requisite EUV dose-to-clear under 20 mJ/cm^2. This challenge has been worsened by the dearth of mechanistic information available concerning the behavior of non-ionic PAGs under EUV exposure.

In this report, we describe the development and photolithographic performance of photoresists consisting of a PPA derivative and a non-ionic PAG. We found that many simultaneously possessed high stability and remarkable EUV sensitivity.

Results and Discussions:

Photoresist polymers (35 mg) and photoacid generators (7 mg) were dissolved in 1 mL propylene glycol methyl ether acetate (PGMEA). The resist was spin-coated onto a silicon wafer at 3000 rpm for 1 min. The coated silicon wafers were then exposed using ASML 300C DUV stepper. After exposure, the exposed film was baked and developed. The resulting line-space patterns were characterized using AFM shown in Figure 1.

As seen from these figures, the relatively rough line edge roughness was caused by the acid diffusion, which could be alleviated by changing the chemical structure of the photoacid generator.

We further investigated these resist materials under EUV exposure. By using these non-ionic PAGs, we were able to achieve dose to clear for as low as 12 mJ/cm^2.

Summary:

In summary, preliminary results were obtained with chain scissionable photoresists. With these results in hand, the lithographic performance of newly developed functionalized PPAs will be investigated.

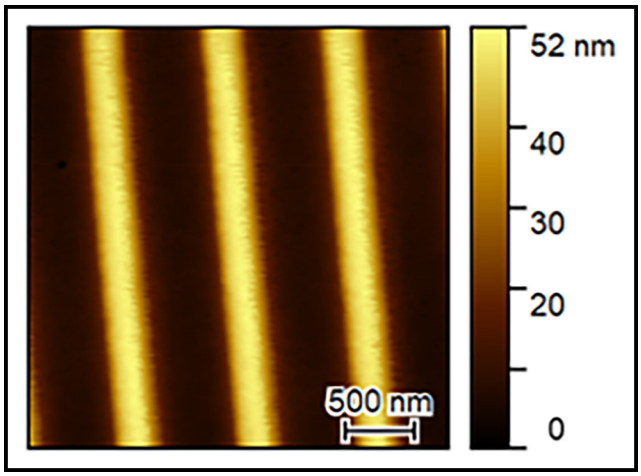

Figure 1: Line-space patterns characterized using AFM.

References:

[1] H. Ito, C. G. Willson, Polym. Eng. Sci., Chemical amplification in the design of dry developing resist materials, 1983, 23, 1012-1018.

[2] A. Rathore, I. Pollentier, S. S. Kumar, D. De Simone, S. De Gendt, J. Micro/Nanopattern. Mats. Metro., Feasibility of unzipping polymer polyphthalaldehyde for extreme ultraviolet lithography, 2021, 20, 034602.

[3] P. A. Kohl, A. Engler, C. Tobin, C. K. Lo, Journal of Materials Research, Influence of material and process parameters in the dry-development of positive-tone, polyaldehyde photoresist, 2020, 35, 2917-2924.

[4] J. Deng, F. Kaefer, S. Bailey, Y. Otsubo, Z. Meng, R. Segalman, C. K. Ober, J. Photopol. Sci. Technol., New Approaches to EUV Photoresists: Studies of Polyacetals and Polypeptoids to Expand the Photopolymer, 2021, 34, 71-74.

Design and Fabrication of Integrated Magnetic Elastomer-Based Soft Actuator

CNF Project Number: 2866-20

Principal Investigator(s): Amal El-Ghazaly[1]

User(s): Ludovico Cestarollo[2], Rodolfo Cantu[3], Karthik Srinivasan[1]

Affiliation(s): 1. Electrical and Computer Engineering, Cornell University; 2. Materials Science and Engineering, Cornell University; 3. Summer 2022 CNF REU Intern, Mechanical Engineering, The University of Texas at Austin

Primary Source(s) of Research Funding: National Science Foundation, 2022 CNF REU Program NSF Grant NNCI-2025233

Contact: ase63@cornell.edu, lc942@cornell.edu, rodolfo.cantu@utexas.edu, ks934@cornell.edu

Website: https://vesl.ece.cornell.edu

Primary CNF Tools Used: Heidelberg Mask Writer - DWL2000, ABM Contact Aligner, Hamatech Hot Pirana/Wafer Processor Develop, PT 72, C&D SmartProP9000, DISCO Dicing Saw, AFM - Veeco Icon, P7 Profilometer, RC2 Woollam Ellipsometer

Abstract:

Technological advancements to date have primarily focused on stimulating only two of the five human senses: sight and hearing. Touch-based interactive technologies can still be considered to be in their infancy. Haptic devices allow tactile interactions between humans and digital interfaces in many different arenas such as user interfaces for assisted and autonomous driving [1] and teleoperation [2]. Magnetorheological elastomers (MREs) based on nanoparticles constitute a promising candidate material for creating tactile interfaces capable of creating high-resolution features on the micron scale [3,4]. These magneto-responsive elastomers must be integrated with magnetic controls to create the local magnetic fields necessary to actuate deformations. Such a system composed of a magneto-responsive soft material and integrated magnetic controls has not been developed to date.

In order to highlight the potential for these devices, a process was developed to create a system of micromagnetic controls integrated into free-standing microscale cantilevers and beams. First, magnetic microscale circular and elliptical pillars were developed via sputtering and photolithography utilizing a lift-off process. These structures were utilized to create magnets with magnetic moments pointing respectively in the direction perpendicular and parallel to their surface. The magnetic properties of the deposited magnets were studied via vibrating sample magnetometry and the optimal dimensions for both geometries were identified. Based of simulation results, the optimally fabricated circles and ellipses were then deposited in pairs at different distances from each other. These systems of magnets were ultimately designed to be integrated into cantilevers and beams made of a micrometer thin nanoparticle-based MRE to create a magnetic soft actuator.

Summary of Research:

First, sets of micromagnets were fabricated with two geometries in order to preferentially set the anisotropy (direction of the magnetic moments) along two specific directions. Contact photolithography, sputtering, lift-off and argon ion milling (see Figures 1 and 2) were used to fabricate the magnets. Pillars with a circular base were developed to create magnets with perpendicular magnetic anisotropy (PMA), so with magnetic moments pointing in the thickness direction of the pillars. Pillars with an elliptical base were instead developed to create magnets with in-plane magnetic anisotropy (IMA), so with magnetic moments pointing in a direction lying on the base of the pillars. The effect of the size of the magnets on their magnetic properties was investigated by depositing sets of magnets of different sizes on a wafer and then cutting the wafer into dies, with each die having a set of magnets with specific geometry and dimensions. These dies were then tested in a vibrating sample magnetometer to record magnetic hysteresis loops (magnetization vs. magnetic field). For the PMA magnets, pillars having a circular base with 5 μm diameter were determined to be optimal, since they yield a remanent to saturation magnetization almost equal to 1 and a large coercivity of about 1000 Oe.

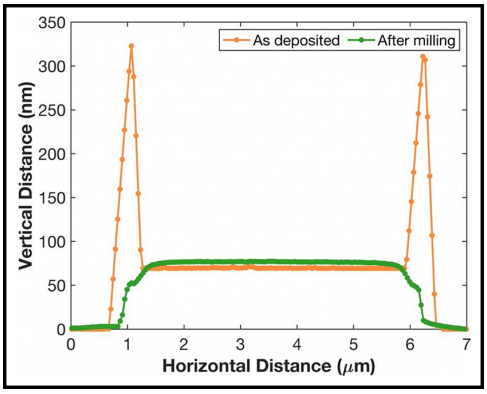

Figure 1: 2D AFM profile of 5 μm diameter circular pillar as deposited and after argon ion milling of the "rabbit ears".

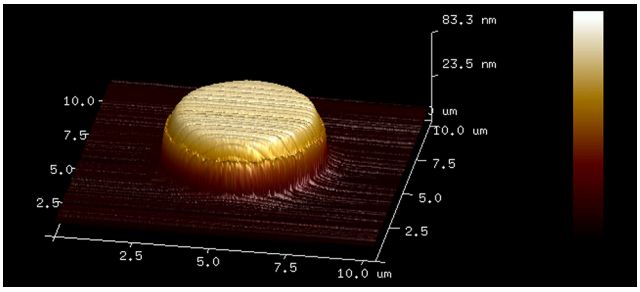

Figure 2: 3D AFM image of 5 μm diameter circular pillar after argon ion milling, showing smooth edges and absence of "rabbit ears" characteristic of lift-off process using deposition via sputtering.

For the IMA magnets, elliptical pillars with long and short axes dimensions of 3 and 15 μm were chosen as the optimal ones. This size allows to better tune the magnetic anisotropy in the direction of the long axis of the pillar (with larger sizes the difference between the loops recorded along the short and long axes of the pillars becomes less pronounced).

In order to obtain a soft magnetic elastomer with magnetic controls able to actuate deflections, we designed a system composed of a magnetorheological elastomer and the two optimally fabricated micromagnets described above (Figure 3 illustrates the device in the case of a simply supported beam). By having a PMA and an IMA magnet on the surface on a magnetoresponsive material, the two magnets can couple with each other with magnetic flux lines penetrating into the material. Based on magnetic simulations performed in COMSOL Multiphysics, the two magnets were spaced 1, 1.5 and 2 μm away from each other (Figure 4 shows the 1.5 μm spacing case). These spacings guarantee strong coupling between IMA and PMA magnets so that the flux generated by the IMA magnet closes into the PMA one, creating a strong field extending into the elastomer. This magnetic flux closure generates a magnetic field gradient in proximity of the gap between the two magnets, which in turn causes the magnetic particles embedded into the elastomer to move towards where the flux is stronger, forcing the magnetic elastomer to deform.

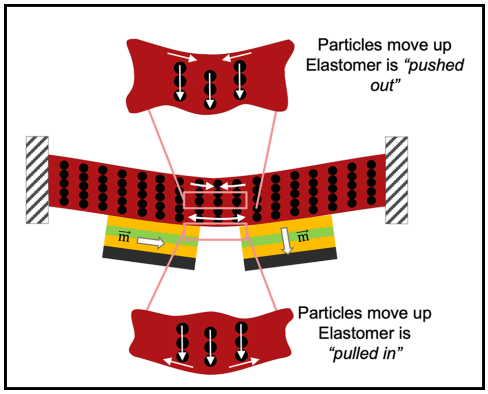

Figure 3: A magnetic soft actuator in the form of a simply supported beam. The two micromagnets generate the local fields that cause the deflection of the magnetic elastomer.

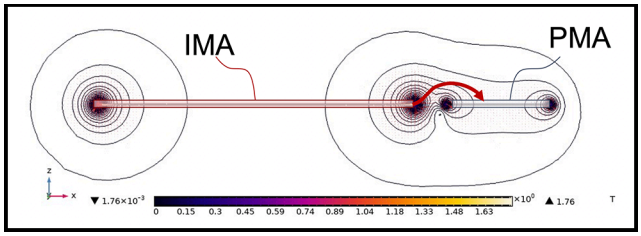

Figure 4: Magnetic simulation of IMA and PMA magnets spaced 1.5 μm away from each other. The contour lines show the change in magnitude of the magnetic flux density. The red arrow emphasizes the direction of magnetic flux closure from the IMA to the PMA magnet.

Conclusions and Future Steps:

We have successfully fabricated micro-sized magnets with perpendicular (PMA) and in-plane (IMA) magnetic anisotropy. In the case of PMA magnets, circular pillars were selected as the geometry of choice and an optimal diameter of 5 μm was determined. On the other hand, in the case of IMA magnets, elliptical pillars were selected as the geometry of choice and optimal long and short axes dimensions of 3 and 15 μm were selected.

PMA and IMA magnets were then fabricated on a wafer with spacings of 1, 1.5 and 2 μm between them. Simulations results indicated that such spacings allow the magnetic flux from the IMA magnet to couple with the PMA one. The next steps will require embedding these sets of micromagnets into a thin (2 μm thick) magnetic elastomer and shape this into beams to test their actuation performance.

References:

[1] Terken, J; Levy, P; Wang, C; Karjanto, J; Yusof, N; Ros, F; Zwaan, S; Advances in Human Factors and System Interactions; Nunes, I. L., Ed.; Springer International Publishing, 2017; pp 107-115.

[2] Hayward, V; Astley, O; Cruz-Hernandez, M; Grant, D; Robles-De-La-Torre, G; Sensor Review 2004, 24, 16-29.

[3] L. Cestarollo, S. Smolenski, A. El-Ghazaly; ACS AppMats and Interfaces 14 (2022) 19002-19011. doi:10.1021/acsami.2c05471

[4] Böse, H.; Gerlach, T.; Ehrlich, J. of Intelligent Material Systems and Structures 2021, 0, 1-15.

Fabrication of Microwells to Host Liquid Crystals (LCs) for Studies Aimed at Understanding the Coupling of Surfactant Concentration Gradients with LC Ordering

CNF Project Number: 2874-20

Principal Investigator(s): Nicholas L. Abbott

User(s): Soumita Maiti

Affiliation(s): Chemical and Biomolecular Engineering, Cornell University

Primary Source(s) of Research Funding: National Science Foundation (CBET-1803409 and EFMA1935252), Army Research Office through W911NF-15-1-0568 and W911NF-17-1-0575

Contact: nla34@cornell.edu, sm2766@cornell.edu

Website: https://nlabbottcornell.weebly.com/

Primary CNF Tools Used: Heidelberg Mask Writer, ABM Contact Aligner, DISCO Dicing Saw

Abstract:

We have used the CNF to fabricate microwells to host liquid crystals (LCs) in studies aimed at understanding how surfactant concentration gradients impact the LC ordering. Specifically, microwells with various shapes were fabricated by patterning SU-8 on glass surfaces using photolithography. LCs were dispensed into the microwells to create LC domains with diverse shapes. We have discovered that the optical responses of the LC films depend strongly on the LC domain shape.

Summary of Research:

We used photolithography to fabricate microwells with a depth of ~ 20 μm and lateral dimensions ranging from 50 μm to 500 μm. SU-8 25 was used as the photoresist. The ABM contact aligner was employed for UV exposure of the films of SU-8 on glass wafers through a chrome mask written using the Heidelberg Mask Writer - DWL2000. The wafers were cut in the shape of microscope slides (75 mm × 25 mm) using the dicing saw. After treating the microwells with octadecyltrichlorosilane, we dispensed thin films of nematic LCs (5CB; Figure 1a) in them and attached them to the floor of a milli-fluidic channel (Figure 1c; detailed elsewhere [1]). A gradient in surfactant concentration (sodium dodecyl sulfate (SDS; Figure 1b)) was generated within the milli-fluidic channel by pumping two aqueous solutions containing different concentrations of SDS through the channel inlets under conditions of laminar flow (Figure 1c).

In response to a given external gradient in concentration of SDS, we observed the LC films to exhibit bright shape-dependent optical responses as presented in Figure 2. Although Figure 2 reveals a qualitatively similar progression of LC interference colors in the y-direction (direction of predicted SDS gradient) across each sample, independent of the shape of the LC film, the maximum optical retardance of the LC films and the width of the optically dark (extinct) bands were noted to differ significantly with a change in shape of the LC films.

We made systematic changes to the shapes of the LC films (lateral to the external gradient), ranging from the initial rectangular shapes to triangular shapes. We found that a select set of shapes generated a strong optical response (higher optical retardance) as presented in Figure 3. An inverted triangular shape (Figure 3 k-n) appears to be the LC domain shape that generates the strongest optical response.

In addition, we used rectangular LC films (prepared in rectangular microwells) to investigate how the non-equilibrium ordering of LCs driven by external gradients in surfactant concentration leads to the formation of localized assemblies of microparticles (Figure 4). Specifically, silica microparticles (diameter 3 μm), initially present in the bulk 5CB, were driven to the aqueous-LC interface and formed localized chains at the middle of the interface when placed in a milli-fluidic channel containing a gradient in SDS concentration.

References:

[1] Roh, S.; Tsuei, M.; Abbott, N. L. Using Liquid Crystals for *in situ* Optical Mapping of Interfacial Mobility and Surfactant Concentrations at Flowing Aqueous-Oil Interfaces. Langmuir 2021, 37 (19), 5810–5822. https://doi.org/10.1021/acs.langmuir.1c00133.

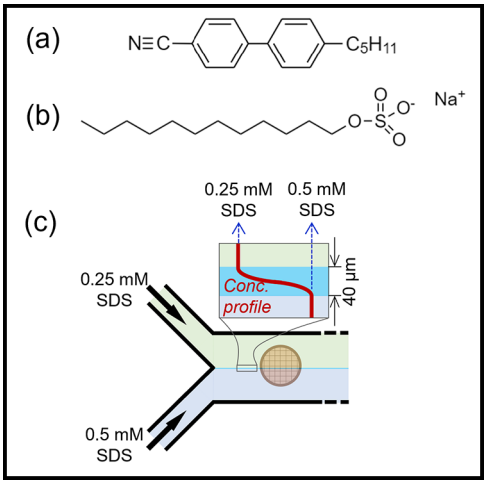

Figure 1: Molecular structure of (a) 4-Cyano-4'-pentylbiphenyl (5CB) and (b) Sodium dodecyl sulfate (SDS). (c) Aqueous solutions of SDS at 0.25 mM and 0.5 mM concentrations (color-coded as green and blue, respectively) are passed through two inlets of the milli-fluidic channel at a flow rate of 2 mL/min each. The concentration profile of SDS near the middle of the channel width is illustrated in the inset.

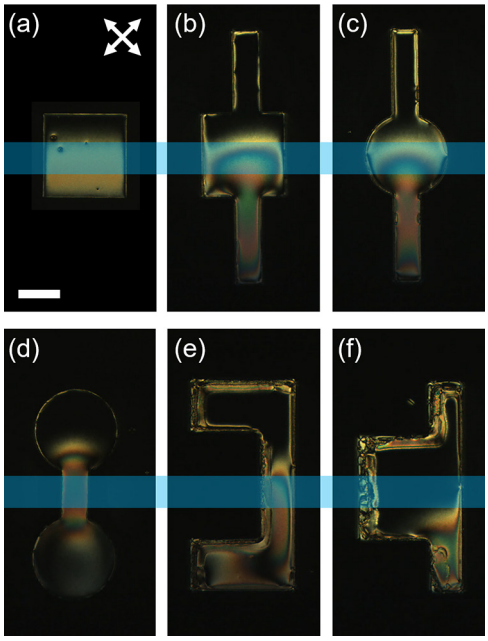

Figure 2: Optical response of 5CB confined in microwells of different shapes to a gradient in SDS concentration generated by pumping solutions of 0.5 mM and 0.25 mM SDS in 300 mM NaCl at a flow rate of 0.5 mL/min each. The blue bands passing through the middle of the films represent the position of the external gradient. Scale bar is 100 µm.

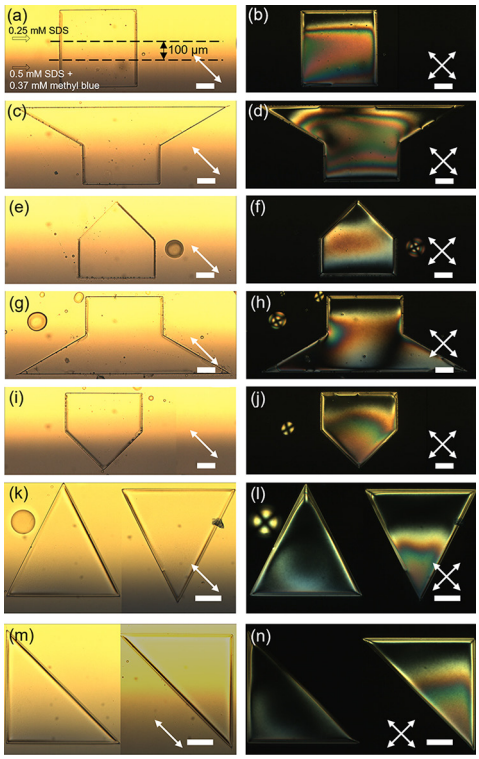

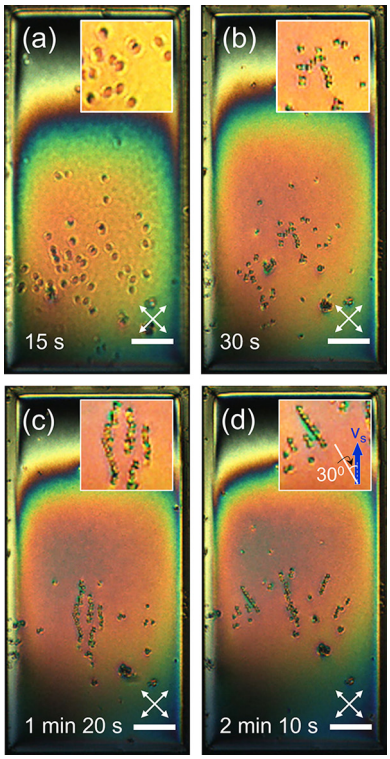

Figure 3, left: 0.25 mM SDS solution is pumped through one inlet and a solution containing 0.5 mM SDS and 0.37 mM methyl blue is pumped through the other inlet of the channel at a flow rate of 0.5 mL/min each. (a, c, e, g, i, k, m) Bright-field images of LC confined in microwells of different shapes. Black dotted lines in (a) represent the extent of the imposed gradients in the bulk aqueous solution. (b, d, f, h, j, l, n) Optical response of LC between cross polars. Scale bars are 100 µm. Figure 4, right: A film of 5CB with dispersed silica particles is placed inside a milli-fluidic channel containing a gradient in SDS concentration generated by pumping solutions of 0.5 mM and 0.25 mM SDS in 300 mM NaCl at a flow rate of 0.5 mL/min each. Insets show magnified views of the organizations of particles in the time series images. Scale bars are 50 µm.

Sizing Thermoresponsive Colloidal Particles with Dynamic Light Scattering

CNF Project Number: 2949-21
Principal Investigator(s): Jerome Fung
User(s): Jerome Fung, Emily Leach

Affiliation(s): Department of Physics and Astronomy, Ithaca College, Ithaca, NY
Primary Source(s) of Research Funding: American Chemical Society – Petroleum Research Fund
Contact: jfung@ithaca.edu, eleach@ithaca.edu
Primary CNF Tools Used: Malvern Zetasizer Nano

Abstract:

We are synthesizing transparent, thermoresponsive core-shell colloidal particles for use as a model system in studies of the glass transition. The particles consist of an optically- dense polystyrene core surrounded by a nearly-transparent poly-N-isopropylacrylamide shell. We use dynamic light scattering (DLS) to measure the size of the particles during and after their preparation. We also use DLS to examine the response of the core-shell particles to temperature changes.

Summary of Research:

Understanding the mechanical behavior of glasses, which have liquid-like structure but solid-like moduli, is an important open question in condensed matter physics. Colloidal suspensions are useful as model systems for studying condensed- matter phenomena like the glass transition. Specifically, colloidal particles can be used as "model atoms" that can be engineered to exhibit interactions similar to those in atomic systems, but are large enough to be directly visualized in real space using optical microscopy.

Recently, Perro and co-workers introduced a core-shell particle that could potentially be useful as a model system for studying glasses [1]. The particles consist of a small, optically-dense, mechanically-rigid core surrounded by a thermoresponsive, nearly-transparent, soft hydrogel shell (Figure 1). These particles are expected to have soft-sphere interactions, which may be more relevant to atomic systems than colloidal particles with hard-sphere interactions, which have been much more extensively studied. The particles reversibly deswell when heated above room temperature, which would allow the particle volume fraction, a key thermodynamic parameter, to be tuned *in situ*. Finally, since the shells are nearly refractive index-matched in water, it is possible to image deep within dense suspensions using techniques such as confocal microscopy. Our overall goal is to measure the interactions between these core-shell particles and how the interactions affect the rheology of dense suspensions of the particles.

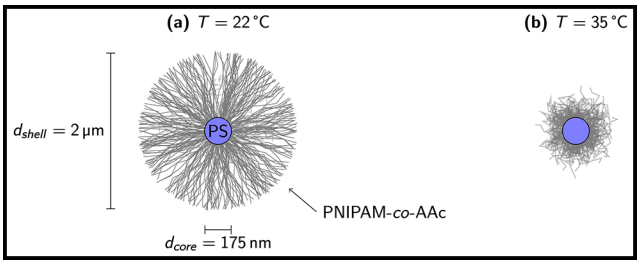

Figure 1: Schematic illustration of core-shell polymer particles characterized using dynamic light scattering. The particles consist of a polystyrene (PS) core surrounded by a thermoresponsive poly-N-isopropyl acrylamide/acrylic acid (PNIPAM-co-AAc) shell. At room temperature, the shells are highly swollen and nearly index-matched in water. At higher temperatures, the shells collapse.

First, however, we need to synthesize the particles since they cannot be purchased commercially. Measuring particle sizes with dynamic light scattering (DLS) using the Malvern Zetasizer Nano at CNF is important in the synthesis. We need to know both the size of the cores alone as well as the size of the completed core-shell particles. We also need to measure the temperature dependence of the shell size.

The Zetasizer is useful for these measurements for several reasons. DLS is particularly appropriate for sizing our particles: because our cores are smaller than the optical diffraction limit and the shells are nearly-index matched, sizing the particles by direct optical imaging would not be effective, and electron microscopy would most likely destroy them. In addition, the Zetasizer allows us to easily regulate the sample temperature over the relevant range (25-40°C). Finally, we can also use

the intensity autocorrelation functions measured in DLS to determine whether or not the particles are monodisperse.

Figure 2 shows two intensity autocorrelation functions, one for cores alone and one for completed core-shell particles. The autocorrelation functions exhibit an exponential decay characteristic of monodisperse suspensions. Notably, the longer decay time scale for the core-shell particles indicates that they are larger than the bare cores as expected. Moreover, fitting a refined model based on a cumulant expansion of the particle size distribution to the measured autocorrelation functions allows us to quantify the particle size as well as estimate the small but nonzero polydispersity index of the suspensions [2].

While the core-shell particles we have prepared thus far have not exhibited the expected thermoresponsive behavior, we are currently working to optimize the synthesis reaction parameters. We expect DLS measurements with the Zetasizer at CNF to remain an important part of our ongoing work.

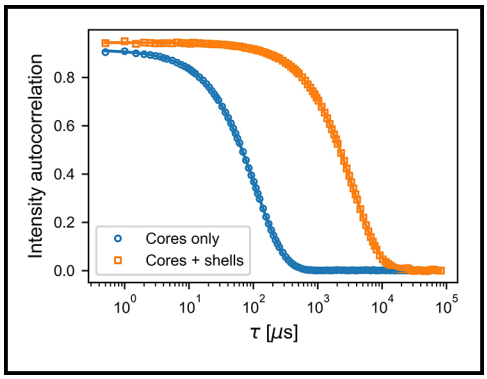

Figure 2: Intensity autocorrelation functions measured for cores only (blue circles) and core-shell particles (orange squares). Solid lines are fits to a second-order cumulant model for the particle size distribution [2]. The autocorrelation function for the core-shell particles decays over a longer time scale than the autocorrelation function for the cores only, indicating that the core-shell particles are larger than the cores alone as expected.

References:

[1] A. Perro, G. Meng, J. Fung, and V. N. Manoharan, "Design and synthesis of model transparent aqueous colloids with optimal scattering properties." Langmuir, 25 (19), 11295-11298 (2009).

[2] B. J. Frisken, "Revisiting the method of cumulants for the analysis of dynamic light-scattering data." Applied Optics, 40 (24), 4087-4091 (2001).

Measuring the Conductivities of Ionic and Metal Ligand Coordinated Polymers

CNF Project Number: 2952-21

Principal Investigator(s): Meredith Silberstein

User(s): Max Tepermeister

Affiliation(s): Sibley School of Mechanical and Aerospace Engineering, Cornell University

Primary Source(s) of Research Funding: Defense Advanced Research Projects Agency

Contact: meredith.silberstein@cornell.edu, mt845@cornell.edu
Website: silbersteinlab.com

Primary CNF Tools Used: SC4500 Evaporator, ABM Contact Aligner, Heidelberg Mask Writer

Abstract:

Ionic polymers are a new class of material that promise to enable deformable computers and biocompatible electronics. We developed a gold on glass experimental electrode setup with built-in spacers using photolithographic tools. We then used this setup to characterize a wide range of ionic polymers and discovered some unexpected trends in their behavior, including an increase in conductivity with ion size.

Summary of Research:

The primary goal of this research project is to discover circuit elements describing synthetic soft materials that utilize ionic transport. This work is funded through a Defense Advanced Research Projects Agency Young Faculty Award.

Circuit design to date has been primarily based upon metal and semiconductor substrates—inherently hard materials with features that have minimal similarity to or compatibility with biosystems. Biosystems have a diverse set of highly nonlinear and environmentally responsive features within underlying circuitry (e.g., neurons, membrane ion channels) that operate via ion transport and storage. While these systems have been extensively studied within biomechanical contexts, few reduced-order circuit models have been developed. Moreover, soft ionic conducting material development has primarily been focused on maximizing conductivity for use as electrochemical conversion and storage device membranes. As a result of the foregoing prevailing conditions, progress in wetware has been limited: hampered by the disparate knowledge bases.

As part of this broader effort, we are experimentally characterizing the ionic conductivity of a wide range of polymers. These electrochemical impedance spectroscopy and cyclic voltammetry experiments are conducted on a Gamry 3000AE in the Silberstein lab with either a 2-wire standard or 4-wire Kelvin measurement. It is critical for the accuracy and repeatability of these experiments that the electrodes be non-reactive and that the distance between electrodes and electrode area be set at a constant value.

Utilizing CNF tools, we built a gold on glass electrode using a liftoff process that meets all our requirements. We patterned S1800 series photoresist onto fused quartz 100 mm wafers, then deposited a 10 nm titanium adhesion layer followed by a 100 nm gold layer via electron-beam thermal evaporation. The photoresist and excess gold was then removed using the water-jet liftoff machine. We then photo-patterned 5 μm and 10 μm thick SU-8 spacers on the periphery of the electrodes.

Some of the materials we test are viscous liquids, so we designed the spacers in a sparse grid to allow for the test materials to flow out of the test cell. A diagram and image of these devices are shown in Figure 1 and 2 respectively. The SU-8 spacer can be seen in Figure 2 as the small lighter rectangles in a square around the central gold square.

In order to perform impedance spectroscopy measurements, sample material is dropped on one of these electrodes and a second electrode is clamped on top, rotated by 180°. The central 1 cm^2 squares of gold overlap and create a parallel plate capacitor. By applying

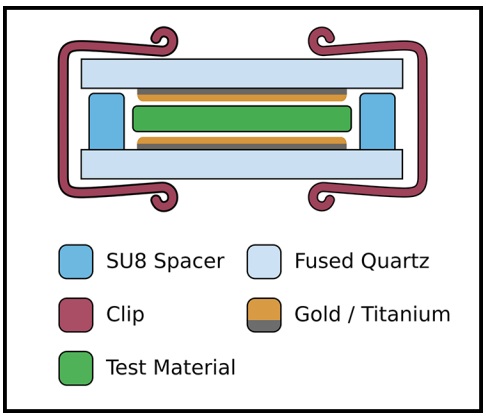

Figure 1: Diagram of experimental setup.

Figure 2: One electrode out of four on a wafer.

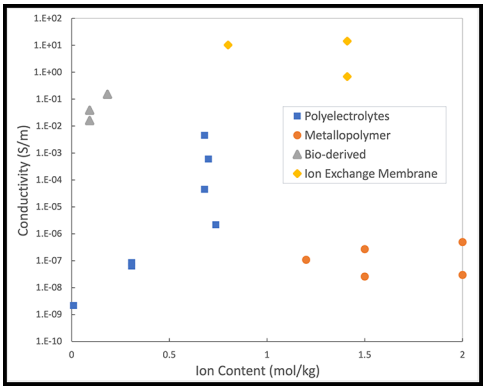

Figure 3: Conductivity vs. ion content for four material classes.

oscillating electric fields at various frequencies, we can precisely characterize the electrical response of our test material. This electrochemical testing fixture has been applied to testing metal ligand coordinated polymers, polyionic hydrogels, and ionomers swollen with ionic liquids. Figure 3 shows the ionic conductivity of a wide range of materials that we have characterized, mainly with this device.

With PDMS, we have found that the ionic conductivity of ligand functionalized PDMS with metal salts incorporated far exceeds the conductivity of unfunctionalized PDMS. Further, the conductivity of metallo-PDMS depends on both the type of anion and cation within the added salt and on the concentration of the salt. Interestingly, larger anions lead to higher conductivity despite expected size effects on their diffusivity because they associate less strongly with the metal cation. Advantageously, these larger anions are also able to be incorporated into the polymer at larger concentrations without precipitating into crystallites. We also found that by using more than one cation type, we could partially de-couple viscosity and conductivity. With the polyionic hydrogels and ionomers, we have used the test setup to characterize their basic electrical response, and are in the process of characterizing the properties of various material junctions. These junctions promise to give current rectifying behavior in a way similar to semiconductor diodes.

Conclusions and Future Steps:

The tools at the CNF were instrumental in creating a precise and repeatable experimental setup for our material characterization, leading us to surprising conclusions about the behavior of some ionic systems. In the coming year, we are interested in moving beyond single material characterization and towards device/junction characterization. Many proposed devices require length scales on the order of microns in order to function effectively. As such, one possible way to make these devices is by patterning positive and negative ionomers themselves using photolithographic techniques, which we hope to explore in the near future.

Magnetic Polymer-Grafted Nanoparticles

CNF Project Number: 2955-21
Principal Investigator(s): Christopher Kemper Ober
User(s): Chenyun Yuan

Affiliation(s): Department of Materials Science and Engineering, Cornell University
Primary Source(s) of Research Funding: About Air Force Office of Scientific Research
Contact: cko3@cornell.edu, cy479@cornell.edu
Primary CNF Tools Used: Malvern Nano ZS Zetasizer, DISCO Dicing Saw, Rame-Hart 500 Goniometer, Scanning Electron Microscope

Abstract:

In this project, polymer-grafted nanoparticles with various magnetic cores (Fe_3O_4, $CoFe_2O_4$, etc.) and different polymer canopies are synthesized. The magnetic interactions among cores and the chemical forces (hydrogen bond, ionic interactions, etc.) among polymer brushes are assumed to affect the self-assembly property of the nanoparticles. The self-assembly structures (monolayers, superlattices, etc.) of the particles are made on silicon wafers and other substrates for further study. The polymer canopies would not only modify the surface properties of the metal oxide nanocores to prevent them from aggregating, but also introducing tunable chemical forces into the polymer-graft nanoparticles self-assembly structures.

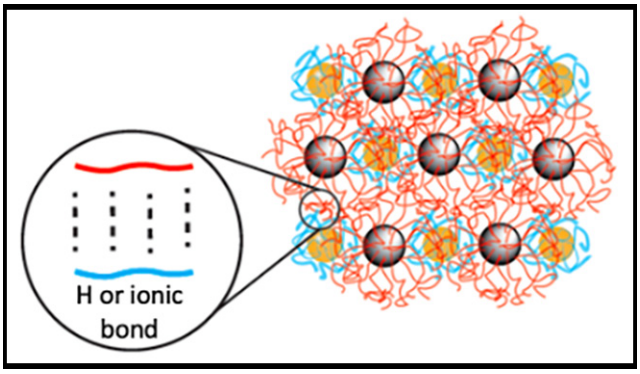

Figure 1: Demonstration of the inter-particle hydrogen bonding or ionic interactions.

Summary of Research:

Polymer-grafted nanoparticles (PGNs) have received increasing attention because they possess the advantages of both the grafted polymer and inorganic cores, and thus demonstrate superior optical, magnetic, electronic, and catalytic properties. One potential application for PGNs is the formation of self-assembly structures and as a building block for the development of photonic/optical/magnetic devices. Thus, PGNs with tailorable interparticle interactions, via either inorganic magnetic cores (magnetic interactions) or polymer brush chemistry (hydrogen bonds, ionic interactions, etc.) (Figure 1), are indispensable for the formation of a superlattice with a defined and ordered structure.

A combined approach of mini-emulsion polymerization and surface-initiated Atom Transfer Radical Polymerization will be used to make the PGNs [1]. To couple the initiator molecules and the metal oxide surface, a silane-based coupling agent is used. The surface-initiated Atom Transfer Radical Polymerization is carried out by adding appropriate combination of ligand, copper, monomer, reducing agent, and shuttling agent. The emulsion is prepared by Pluronic F-127, a non-ionic surfactant. The PGN self-assembly structures are fabricated using multiple techniques, including Langmuir-Blodgett method and simply drop-casting. The morphology of PGNs and order of the self-assembly structure are characterized by scanning electron microscope (SEM), transmitting electron microscope (TEM), scanning transmission electron microscopy (STEM), and atomic force microscope (AFM), and the magnetic properties are characterized using Physical Property Measurement System (PPMS). Besides these, many facilities in CNF would help this research project.

For example, the Malvern Nano ZS Zetasizer will be helpful for characterizing the size of synthesized particles. To study the magnetic properties of the particle self-assembly, we need to cut silicon wafers into 2 mm × 2 mm square pieces precisely, and the DISCO Dicing Saw can help us doing this. The polymer-grafted nanoparticles with different polymer canopies are mixed in the self-assembly structure, and the Energy-dispersive X-ray Spectrometer will help us see which polymer corona is around the particles. Also, we may

characterize the surface modified by those particles, so facilities like contact angle would be very helpful.

An example HAADF-STEM image of polymethyl methacrylate-grafted Fe3O4 nanoparticles is shown in Figure 2. The polymer chains are entangled together and form a thick shell around the particle cores. Because of the low electron scatter ability of the polymers, the polymer shell is transparent than the inorganic crystal cores.

In conclusion, polymer-grafted nanoparticles with various polymer chemistries and different magnetic core materials are synthesized using a grafting-from approach. The self-assembly structures of these PGNs are made using several techniques. While we are getting some promising initial results that are showing the potential of these magnetic PGNs for fabricating self-assembled structures, further research is still needed to optimize the inter-particle interactions and tune the self-assembling behaviors. In future, the effect of the size, the polymer composition, and graft density, etc., will be studied.

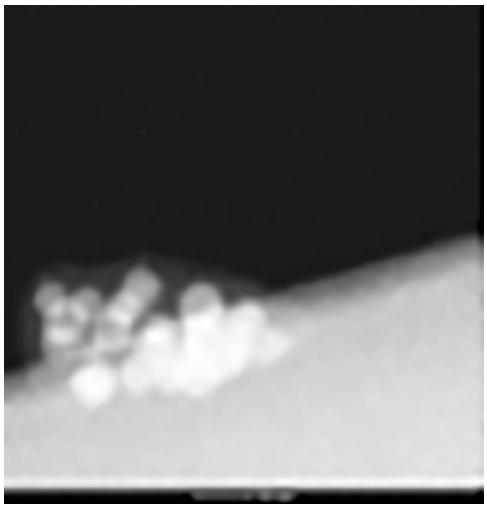

Figure 2: An example HAADF-STEM image of PMMA-grafted Fe_3O_4 cores.

References:

[1] Yuan, C., Käfer, F., and Ober, C. K. (2021). Polymer-Grafted Nanoparticles (PGNs) with Adjustable Graft-Density and Interparticle Hydrogen Bonding Interaction. Macromolecular Rapid Communications, 43(12), 2100629. https://doi.org/10.1002/marc.202100629.

[2] Oh, J. K., and Park, J. M. (2011). Iron oxide-based superparamagnetic polymeric nanomaterials: Design, preparation, and biomedical application. Progress in Polymer Science, 36(1), 168-189. https://doi.org/10.1016/j.progpolymsci.2010.08.005.

Tracking the TaS2 Charge Density Wave Transition with Electron Microscopy and Electric Biasing

CNF Project Number: 2967-21
Principal Investigator(s): Judy J. Cha
User(s): James L. Hart, Saif Siddique

Affiliation(s): Department of Materials Science and Engineering, Cornell University, Ithaca NY
Primary Source(s) of Research Funding: Gordon and Betty Moore Foundation
Contact: jc476@cornell.edu, jlh487@cornell.edu, ms2895@cornell.edu
Primary CNF Tools Used: Nabity Lithography System, Zeiss Supra SEM, CHA Thermal Evaporator

Abstract:

Our project's aim is to better understand the charge density wave (CDW) and associated metal to insulator transition (MIT) in 2-dimensional crystals of tantalum disulfide (TaS_2). We use *in situ* cryogenic scanning transmission electron microscopy (STEM) with *in situ* electric biasing to correlate changes in the CDW properties and sample resistance as a function of temperature. While this project is still on going, we have reached several milestones, including detecting the CDW and MIT with electrical resistance measurements, and developing a novel STEM strategy to track the CDW transition in real space. This project involves electron beam lithography and thin film deposition performed at the CNF.

Summary of Research:

Tantalum disulfide (TaS_2) crystals with the 1T crystal structure undergo a CDW transition at ~ 150 K from the so-called nearly commensurate (NC) to the fully commensurate (C) phases, and there is an associated MIT with a ~ 10-fold increase in resistance. Importantly, the transition can be driven via an electric pulse, which allows for the operation of 2-terminal devices for neuromorphic computing [1]. However, our understanding of how the CDW transition occurs in real space is very limited, both for transitions driven by thermal cycling and with electric pulses. To address this question, we use a novel variable temperature STEM holder, which allows for continuously variable temperature from ~ 100-1000 K, and also permits measurement of sample resistance *in situ* [2]. In principle, this approach will allow us to visualize changes in the CDW structure as a function of temperature, which we can then correlate with changes in the sample resistance. Moreover, we will be able to visualize the CDW during electric pulsing.

The first step towards this goal is to fabricate TaS_2 devices and measure the CDW / MIT *ex situ* (meaning outside of the STEM). To do so, we first exfoliated TaS_2 flakes onto a SiO_2 / Si substrate. We then used the Nabity electron lithography package on the Supra scanning electron microscope (SEM) to lithographically pattern electrodes onto the flake. Lastly, we used the CHA thermal evaporator to deposit Cr / Au electrodes. An example device is shown in Figure 1.

Electrical resistance versus temperature data is shown in Figure 2 for another device. The measurement was performed using a physical property measurement system. The thermally induced CDW transition is clearly observed.

Having successfully measured the CDW transition in flakes *ex situ*, our next goal was to observe the transition with *in situ* STEM. For these experiments, we used specialty SiNx substrates with pre-patterned electrodes and through-holes for STEM observation. Figure 3 shows a TaS_2 flake which we transferred onto the pre-patterned electrodes. Note the hole underneath the flake, which is used for STEM imaging. We then studied this device within the STEM. Figure 4 shows a STEM image of the same flake, and the inset shows an electron diffraction pattern, which encodes information related to the CDW structure. By analyzing the diffraction data, we are able to determine the nature of the CDW phase.

Conclusions and Future Steps:

In this project we have fabricated TaS_2 electronic devices, and observed the CDW transition using electrical measurements. We have also developed a STEM method to observe the CDW transition in real space with nanoscale spatial resolution. Next steps for this project will include imaging the CDW phase with STEM, both as a function of temperature and applied electric field.

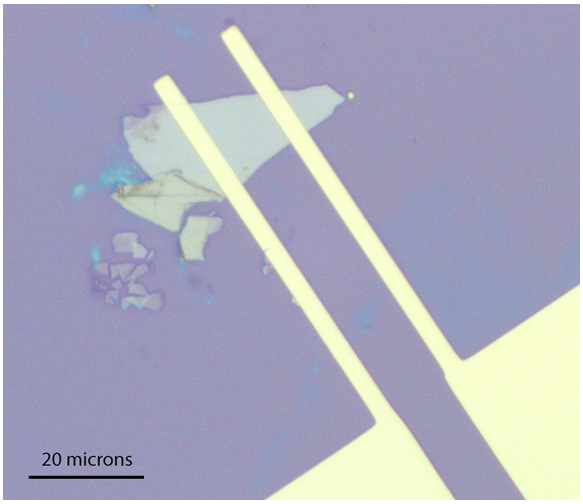

Figure 1: Optical image of a TaS_2 flake exfoliated onto SiO_2/ Si, with Cr / Au electrodes patterned on top of the flake.

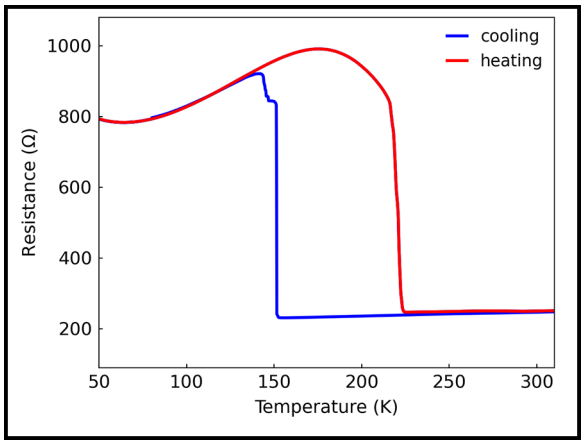

Figure 2: Resistance versus temperature data for a 2-terminal TaS_2 device.

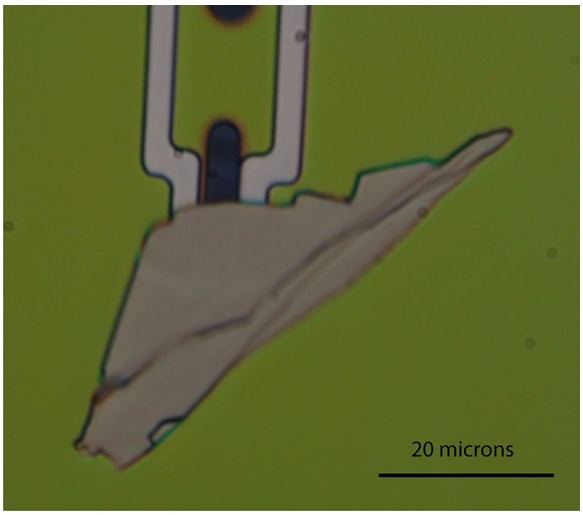

Figure 3: Exfoliated TaS_2 transferred to a chip that allows for in situ *STEM measurements. The dark hole beneath the flake allows for STEM observation, and the electrodes allow for* in situ *biasing.*

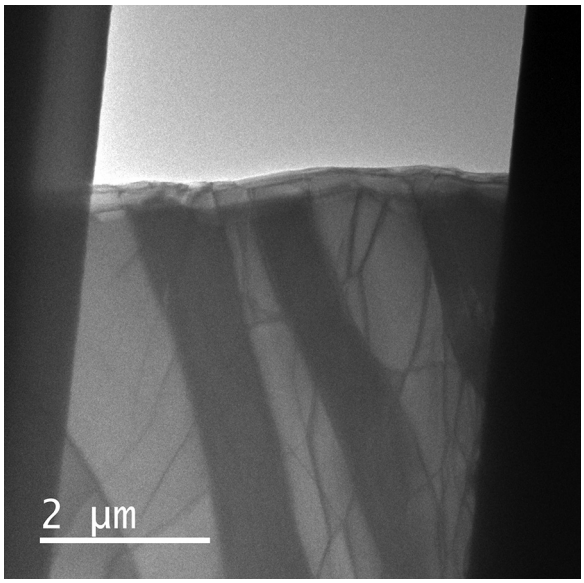

Figure 4: Same TaS_2 flake shown in Figure 3, but imaged within the STEM. The dark bands on the left and right hand sides of the image are the electrodes, and the empty region at the top of the image is the through-hole. The inset shows an electron diffraction pattern, and the weaker spots correspond to the CDW.

References:

[1] Hollander, M. J.; Liu, Y.; Lu, W.-J.; Li, L.-J.; Sun, Y.-P.; Robinson, J. A.; Datta, S. Electrically Driven Reversible Insulator-Metal Phase Transition in 1T-TaS_2. Nano Lett. 2015, 15 (3), 1861-1866.

[2] Goodge, B. H.; Bianco, E.; Schnitzer, N.; Zandbergen, H. W.; Kourkoutis, L. F. Atomic-Resolution Cryo-STEM Across Continuously Variable Temperatures. Microsc. Microanal. 2020, 26 (3), 439-446.

Photolithographic Patterning of Alignment Fiducials for X-Ray Nano-Diffraction

CNF Project Number: 2989-21

Principal Investigator(s): Andrej Singer

User(s): Aileen Luo

Affiliation(s): Materials Science and Engineering, Cornell University
Primary Source(s) of Research Funding: National Science Foundation, Department of Energy
Contact: asinger@cornell.edu, al2493@cornell.edu
Primary CNF Tools Used: Heidelberg Mask Writer – DWL 2000,
Hamatech Mask Chrome Etch, ABM Contact Aligner

Abstract:

Alkaline fuel cells and electrolyzer cells are promising alternative forms of energy conversion and storage devices due to their potential for eliminating the need for precious-metal catalysts. Epitaxially grown transition metal oxide thin films have demonstrated promising activity for the oxygen reduction reaction [1], the rate-limiting step for catalysis in alkaline fuel cells. To better understand localized structural and electronic changes in the catalyst under operating conditions, we aim to study them using x-ray nano-diffraction and x- ray absorption near-edge structure at the hard x-ray nanoprobe beamline at the National Synchrotron Light Source II.

Summary of Research:

Focusing of x-rays to a 25 nm spot on a sample requires alignment fiducial markers with sharp edges of less than half a micron in width. Using the computer-aided design software L-Edit and the Heidelberg Mask Writer – DWL2000, we designed and wrote a 5-inch photomask with multiple configurations of the pattern shown in Figure 1. Using S1800 series positive tone photoresist and the ABM Contact Aligner, we transferred the pattern onto samples of sizes 5 mm × 5 mm and 10 mm × 10 mm. DC magnetron sputtering (Cornell Center for Materials Research) was used to deposit 10 nm of titanium and 50 nm of copper metal onto the samples. Sonication in acetone was used to lift off the excess metal and complete the process.

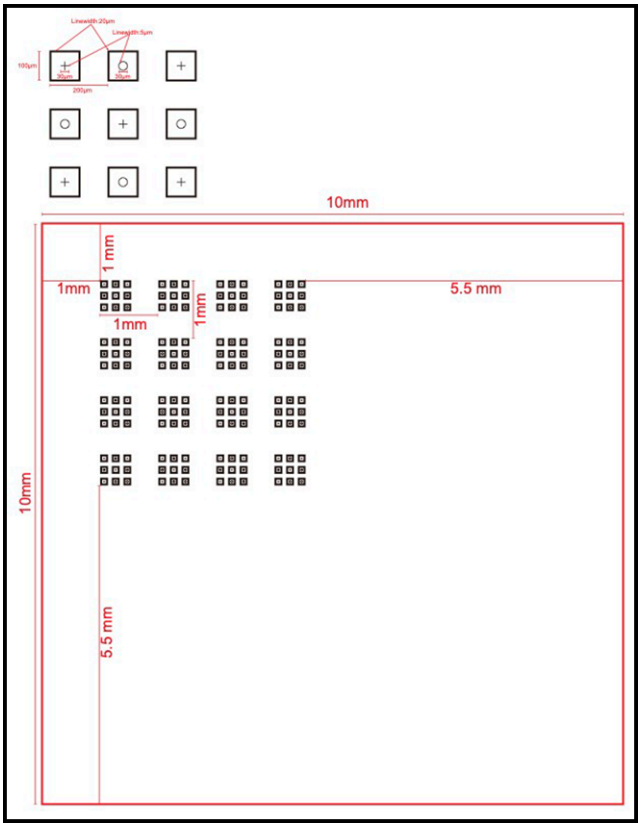

Figure 1: Schematic credit to Dr. Ludi Miao. Arrays of circles and crosses contained in larger squares.

Conclusions and Future Steps:

The fabrication of alignment features was completed successfully and tested at the hard x-ray nanoprobe beamline. For future measurements, we will design and make proof-of-concept devices at the Cornell NanoScale Facility for a three-electrode electrochemical cell compatible with the limitations of the beamline.

References:

[1] Y. Yang, et al. J. Am. Chem. Soc. 2019, 141, 1463-1466.

Magnetically Tunable Optical Metamaterials and Diffractive Robotics

CNF Project Number: 900-00

Principal Investigator(s): Paul L. McEuen[1,2]

User(s): Conrad L. Smart[1], Tanner G. Pearson[3], Zexi Liang[1,2], Melody Lim[1,2]

Affiliation(s): 1. Laboratory of Atomic and Solid-State Physics, 2. Kavli Institute for Nanoscale Science, 3. School of Applied and Engineering Physics; Cornell University

Primary Source(s) of Research Funding: NSF grant DMR-1921567, Air Force Office of Scientific Research (AFSOR) grant FA2386-13-1-4118, CCMR through NSF MRSEC program (DMR-1719875), and the Kavli Institute at Cornell for Nanoscale Science

Contact: plm23@cornell.edu, cs2239@cornell.edu, tgp34@cornell.edu, zl467@cornell.edu, mxl3@cornell.edu

Primary CNF Tools Used: Oxford FlexAL ALD, ASML DUV Stepper, JEOL 6300, CVC E-Beam Evaporators, Oxford 81/82/100 Etchers, PT770/PT740 Etchers, Anatech Asher, Zeiss SEMs, Veeco AFM, Tencor P7 Profilometer, Filmetrics UV, AJA Sputterer

Abstract:

We integrate ultra-flexible, five nanometer thick atomic layer deposition glass hinges with rigid magnetically programmed panels to create untethered, magnetically tunable optical metamaterials and robots at the diffraction limit. We first present a simple walking magnetic microbot consisting of two panels that form a simple mountain-valley fold in an external magnetic field. Next, we fabricate several larger optical metamaterials with magnetically tunable periodicities using this same mountain-valley motif. These structures form the basis for a new class of untethered, microscale optical robots that dynamically interact with the local surroundings (locomotion) and incident light (diffraction).

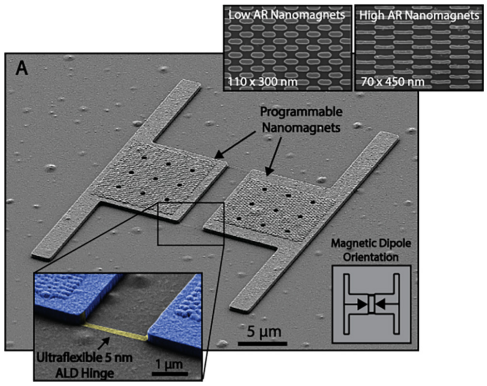

Figure 1: (A) SEM of magnetic microbot. (top-right inset). Arrays of low/high AR nanomagnets used to program the microbot. (bottom-right inset) Final magnetization of the microbot (lower-left zoom). False-color SEM of ALD hinge.

Summary of Research:

Figure 1 shows a microbot at the diffraction limit capable of magnetically controlled locomotion. We first fabricate arrays of single-domain cobalt nanomagnets (top inset) ~ 100 nm on a side with varying aspect ratios (ARs) that form magnetic dipoles along the long axis of the magnets. The coercive fields and magnetic dipole directions of these nanomagnet arrays are tied to the shape anisotropy; since moments prefer to align along the long axis of the magnet, higher shape anisotropy (higher AR) magnets require higher coercive fields. For example, the nanomagnets in Figure 1 (top inset) have coercive fields of 90 mT and 150 mT for the low AR and high AR magnets, respectively. We sequentially magnetize these arrays of nanomagnets with disparate coercive fields to program the magnetic control mechanism of the microbot [1]. The final magnetization directions of the microbot are shown in the bottom-right inset of Fig.1.

We embed these nanomagnets in rigid glass panels and connect the glass panels together with nanometer thick atomic layer deposition (ALD) glass hinges (lower left, Figure 1) that form a kind of fascia strong enough to hold together the body of the microbot but flexible enough to bend under an external torque [2]. We apply a uniform out-of-plane external field to torque both panels up or down, demonstrating the basic mountain-valley fold essential for origami-inspired metamaterials.

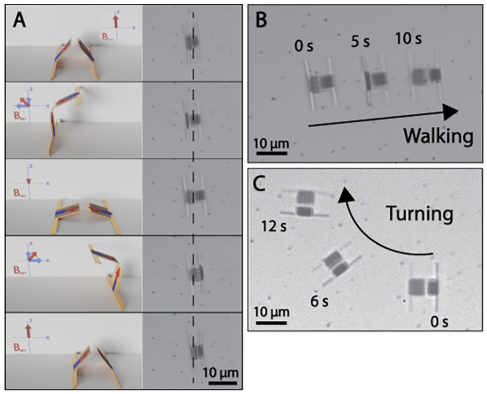

Figure 2: (A) Step motion of the magnetic microbot controlled by sinusoidal external magnetic torque. (B-C) Locomotion of the inchworm with a combination of a 1 Hz sinusoidal z-axis and x-axis magnetic field out-of-phase by 90 degrees. (C) Controlled turning locomotion.

Moreover, we demonstrate a crawling motion that mimics an inchworm by applying a combination of sinusoidal in-plane and out-of-plane magnetic fields out-of-phase by 90 degrees. The stepwise motion of the crawl is depicted in Figure 2A. The main mechanism of walking relies on the extension/contraction of the front/back armature as the microbot pivots out-of-plane. Each step moves the microbot about one-half body length; Figure 2B shows a timelapse of the microbot moving across the substrate with a 1 Hz sinusoidal field over 10 seconds moving at 0.5 body-lengths/second. Faster walking speeds are achieved by increasing the frequency of the control fields. Directional motion and turning (Figure 2C) of the microbot is achieved by adjusting the parity of the in-plane fields.

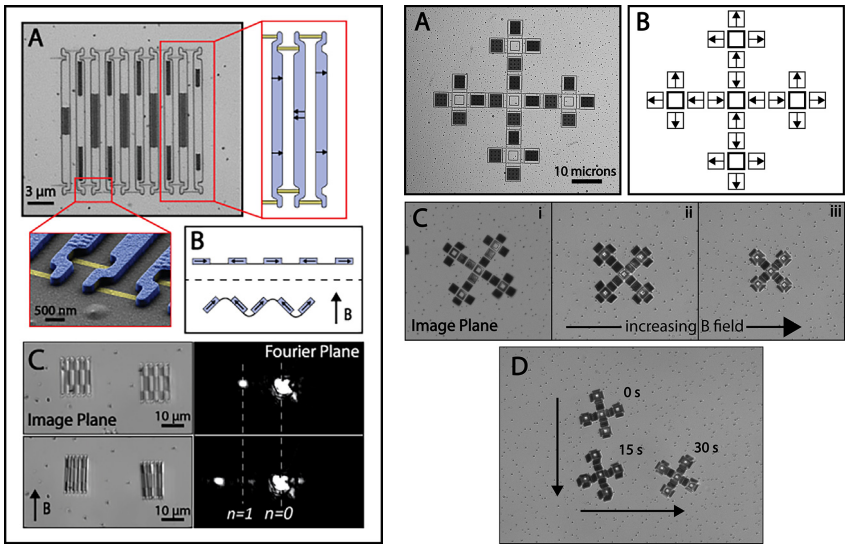

Figure 3, above left: (A) Diffraction grating with magnetically tunable periodicity. (B) Schematic of grating mountain-valley fold. (C) Image (left) and diffraction image (right) of the grating before and after actuation. Figure 4, abive right: (A) Micrograph of optical metamaterial with magnetic armature. (B) Programmed magnetic dipole directions. (C) Actuation of the microbot with an increasing out-of-plane external magnetic field from left to right, and (D) locomotion of the microbot, including a 90-degree change of direction.

The simple mountain-valley motif of the microbot is extended to an array of mountain-valley folds to create magnetically tunable optical metamaterials.

For example, Figure 3A shows a linear diffraction grating with a line spacing of 0.5 lines/micron that consists of an array of rigid panels with alternating magnetic dipole orientations (Figure 3A, top-right inset) held together by ALD hinges (Figure 3A, bottom inset). An external out-of-plane field of < 5 mT torques the panels out-of-plane (Figure 3B), and the ALD hinges bend elastically to accommodate this motion contracting and reducing the periodicity of the grating (Figure 3C, left). This contraction can be seen clearly by examining the diffraction peaks in the Fourier plane (Figure 3C, right) when illuminating the gratings with a laser. The first-order diffractive peak (n=1) moves away from the central peak as the periodicity of the grating decreases when compressed.

Finally, we apply this same mountain-valley motif to larger, less periodic structures. Figure 4A shows a micrograph of a microbot 50 μm on a side consisting of 25 panels, 20 magnetized panels, 4 magnetization directions, all held together by nanometer-thick ALD hinges [3]. The armature structure consists of four arms extending outward from a central panel, with three panels at the end of each arm forming a claw. The dipole orientations are shown in Figure 4B. An external out-of-plane field torques the panels out-of-plane, and the entire structure contracts in two-dimensions (Figure 4C). Finally, we can walk the microbot along the surface using the same crawling motion depicted in Figure 2A. Figure 4D shows a time lapse of the microbot walking along the surface, including a 90-degree turn.

Conclusions and Future Steps:

The combination of magnetic tunability and ultra-flexible hinges enable a new class of optical metamaterials and microbots at the diffraction limit that provide a new method to actively shape and control incident light using external magnetic fields. Future designs of these optical metamaterials will take the control of light a step further by fabricating optical meta-atoms, subwavelength dielectric optical elements that form the basis of metasurfaces, onto the surface of the microbots. We anticipate incredible potential in numerous fields from local Raman spectroscopy to medical imaging.

Acknowledgements:

This work was performed in part at the Cornell NanoScale Facility (CNF), a member of the NNCI, which is supported by the National Science Foundation (Grant NNCI-2025233).

References:

[1] J. Cui, et al., Nature 2019, 575, 164.

[2] K. J. Dorsey, et al., Adv. Mater. 2019, 31, 1901944.

[3] Kim, Y, et al., Nature 558.7709 (2018): 274-279.

Characterizing Diamond Thin-Film Bulk Acoustic Resonators for Quantum Control

CNF Project Number: 2126-12

Principal Investigator(s): Gregory Fuchs[1]

User(s): Johnathan Kuan[2], Anthony D'Addario[2]

Affiliation(s): 1. Department of Applied and Engineering Physics, Cornell University;
2. Department of Physics, Cornell University

Primary Source(s) of Research Funding: Defense Advanced Research Projects Agency - DARPA DRINQS program (Cooperative Agreement #D18AC00024)

Contact: gdf9@cornell.edu, jk2788@cornell.edu, ajd344@cornell.edu
Website: https://fuchs.research.engineering.cornell.edu/

Primary CNF Tools Used: OEM Endeavor M1, Westbond 7400A Ultrasonic Wire Bonder

Abstract:

Electro-mechanical resonators have been used to coherently control electron spins in solid-state defect centers such as the nitrogen-vacancy center in diamond. These resonators introduce strain into the diamond lattice, which can be used to drive magnetically-forbidden transitions of the defect center. Strong AC stain driving with these resonators can enhance the spin coherence of the electron spins. To achieve strong AC strain driving, we fabricate a diamond thin-film bulk acoustic resonator and characterize its electromechanical performance. In addition, we use x-ray diffraction to image the ac strain produced by our device, to better understand the device performance.

Summary of Research:

The diamond nitrogen-vacancy (NV) center is a point defect center in the diamond lattice that consists of a substitutional nitrogen atom adjacent to a lattice vacancy. The NV center has been demonstrated to couple to external fields, making it an excellent platform for quantum sensing (e.g., magnetometry, thermometry, strain). In previous experiments, it has been demonstrated that ac lattice strain is an effective mechanism for manipulating the electron spin of the nitrogen-vacancy center. Oscillating lattice strain has been used to coherently drive the electron spin between magnetically forbidden transitions [1,2], which can dynamically decouple the NV center from magnetic noise to enhance its spin coherence [3]. To achieve this dynamical decoupling in a variety of NV center applications, we require strong ac strain driving, which we implement using a diamond thin-film bulk acoustic resonator.

We fabricate a thin-film bulk acoustic resonator (FBAR) on single crystal diamond (Figure 1). The FBAR consists of a transducer stack of AlN (1.5 μm) that is sandwiched between a bottom and top Pt electrode. This transducer sits on a 10 μm optical-grade diamond membrane that is thinned through reactive-ion etching. The AlN film is deposited with the OEM Endeavor M1 tool at CNF.

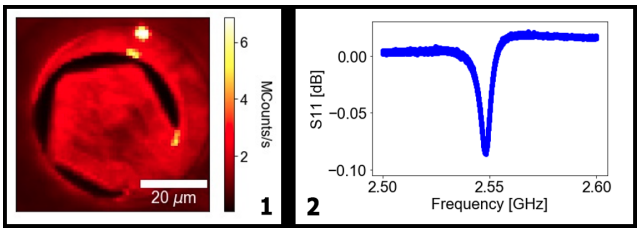

Figure 1, left: Photoluminescence image of the diamond FBAR. The FBAR sits on top of a pentagonal diamond membrane (10 μm) and consists of a Pt bottom electrode, AlN film (1.5 μm), and a top Al electrode. Figure 2, right: S11 measurement of the 2.54 GHz acoustic mode of the AlN FBAR.

In addition, we fabricate an antenna surrounding the FBAR, which allows for magnetic control of the NV center spins in the diamond membrane.

We characterize the electromechanical properties of the FBAR device by measuring the S11 response with a vector network analyzer. We measure a resonance mode at 2.54 GHz, which has a quality factor of 200 (Figure 2). To demonstrate coherent strain driving of a mechanically-forbidden double quantum transition (m_s=-1 to m_s=+1), we first perform spectroscopy to identify the resonant external magnetic field. We sweep the external field,

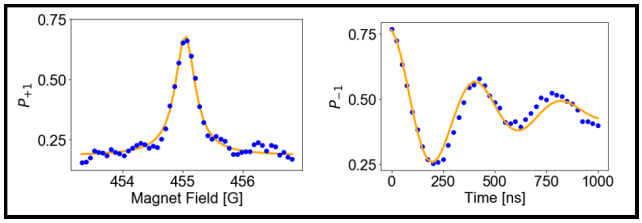

Figure 3: Spectroscopy of the magnetically-forbidden double quantum transition and coherent Rabi driving of the double quantum transition. The spectroscopy sweeps the external magnetic field to tune the Zeeman splitting between m = -1 and m = +1 to be resonant with the FBAR mode. Rabi oscillations are measured at this field with a Rabi frequency of 2.5 MHz.

which tunes the Zeeman splitting between m_s = -1 and m_s = +1, while driving the FBAR mode. At this resonant field, we use the FBAR to drive Rabi oscillations between the m = -1 and m = +1 transition (Figure 3). For this mode, we achieve a Rabi frequency of 2.5 MHz.

We use the Advanced Photon Source at Argonne National Laboratory to measure the strain in the bulk of our FBARs directly with x-rays. We measure the x-ray diffraction of the diamond device using pulsed synchrotron x-rays. We quantify the static strain created during fabrication by comparing the collected diffraction patterns on and off the FBAR region. We can also measure the dynamic ac strain while actively driving the transducer. We collect throughout the entire bulk of the diamond with the X-ray diffraction, which has two full oscillations of the strain wave due to the diamond thickness and mode frequency. As we change the phase of the driving voltage, we observe a peak separate and recombine in the detector images, which quantifies the stroboscopic strain within the device. Figure 4 shows the mode confinement at the center of the FBAR, which is found by computing the lateral variance subtracted from a reference image for each phase value

Conclusions and Future Steps:

We fabricate and characterize an electro-mechanical mode an AlN diamond thin-film acoustic resonator. We perform spectroscopy to tune double quantum transition of the NV center to be resonant with the FBAR mode and demonstrate coherent strain driving with a Rabi frequency of 1.7 MHz. In addition, to understand the spatial distribution of strain in the FBAR device, we image the FBAR mode with X-ray diffraction and show mode confinement. To improve the performance of our device, we are increasing the size of the device to improve the quality factor and impedance matching.

References:

[1] E. R. MacQuarrie, T. A. Gosavi, N. R. Jungwirth, S. A. Bhave, and G. D. Fuchs, Mechanical spin control of nitrogen-vacancy centers in diamond, Phys. Rev. Lett. 111, 227602 (2013).

[2] E. R. MacQuarrie, T. A. Gosavi, A. M. Moehle, N. R. Jungwirth, S. A. Bhave, and G. D. Fuchs, Coherent control of a nitrogen-vacancy center spin ensemble with a diamond mechanical resonator, Optica 2, 233 (2015).

[3] E. R. MacQuarrie, T. A. Gosavi, S. A. Bhave, and G. D. Fuchs, Continuous dynamical decoupling of a single diamond nitrogen-vacancy center spin with a mechanical resonator, Phys. Rev. B 92, 224419 (2015).

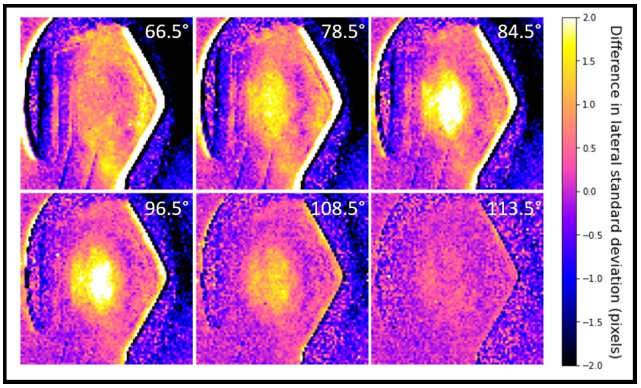

Figure 4: X-ray diffraction imaging of the FBAR. At each pixel of these two-dimensional images, there is a detector image. The standard deviation of the data in the lateral dimension is calculated. Each of the images are taken at various phases of the driving voltage to the transducer. The images are subtracted from a reference image at another phase value at 125.5°. These difference images show the mode confinement in the center of the FBAR region that appears as we introduce strain through the bulk of the diamond.

Electrochemical Thin Film Actuator Enabled Microrobots and Micromachines for Fluid Manipulation, Shape Morphing and Neural Probing

CNF Project Number: 2416-16

Principal Investigator(s): Itai Cohen, Paul L. McEuen

User(s): Qingkun Liu, Wei Wang, Jacob T. Pelster

Affiliation(s): Kavli Institute at Cornell for Nanoscale Science, Applied and Engineering Physics, Laboratory of Atomic and Solid-State Physics, Department of Physics; Cornell University

Primary Source(s) of Research Funding: National Science Foundation, Contract DMR-1719875; EFMA-1935252, Army Research Office, Contract W911NF-18-1-0032; National Institutes of Health, Grant 1R21EY033080-01

Contact: itai.cohen@cornell.edu, plm23@cornell.edu, ql59@cornell.edu, ww459@cornell.edu, jtp246@cornell.edu

Primary CNF Tools Used: Oxford ALD FlexAL, Arradiance ALD Gemstar-6, Oxford 81/100 Etchers, ABM Contact Aligner, SC 4500 Odd-Hour, AJA Sputter Depostition, AJA Ion Mill, Oxford Cobra ICP Etcher, Heidelberg DWL2000, Oxford Endeavor, Oxford PECVD

Abstract:

The ability to efficiently actuate structures at the micro- and nanoscale is an essential technology for the development of microbots and micromachines. Our team is developing a class of electrochemically driven thin film bending actuators with low voltage input and high energy density. These actuators are compatible with complementary metal-oxide-semiconductor (CMOS) technologies, which we use to interface with controlling integrated circuits. We use these actuators for three novel devices: artificial cilia that can manipulate microscale fluid fields, metamaterial robots with the ability to change shape and locomote, and a novel minimally invasive neural probe.

Summary of Research:

We developed bilayered thin film actuators that can bend in response to an electrical voltage signal [1,2]. These thin film actuators are composed of a passive layer, and an active layer, which generates strain in response to certain electrochemical reactions. Upon the application of a voltage to the active layer, the resulting strain in the active layer generates differential stresses between the two layers, triggering the actuation of bending. These actuators work in an aqueous environment and are programmable with low-voltage signals. Here we demonstrate three different applications of the actuators for developing artificial cilia [3], metamaterial robots, and neural probes.

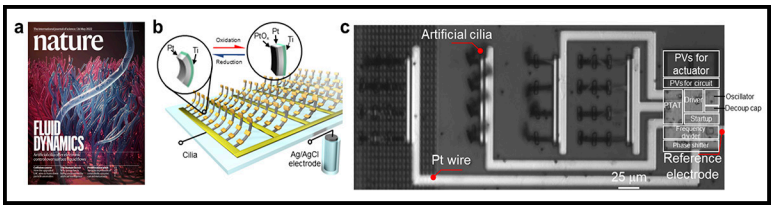

Figure 1: Current and proposed artificial cilia platforms. a) Electronically actuated artificial cilia featured in the May 26th issue of Nature*. b) Electrochemical mechanism of cilia. c) Phase delayed actuation of CMOS circuit integrated cilia arrays.*

Cilia Metasurfaces for Electronically Programmable Microfluidic Manipulation. Cilial pumping is a powerful strategy many microorganisms use to control and manipulate fluids at the microscale. However, the development of an efficient artificial cilial platform that can functionally manipulate fluids remained elusive. Utilizing the thin film electrochemical actuators, we have developed a new class of electrically controlled artificial cilia that can programmably control micro- and nanoscale flow fields (Figure 1a). These cilia are comprised of nm thin films of Pt capped on one side by Ti. By oxidizing and reducing the platinum thin film, the induced expansion and contraction with respect to the inactive capping layer drives cilial beating, and generates a surface flow (Figureure 1b). These cilia were used to create an active cilia metasurface that can generate

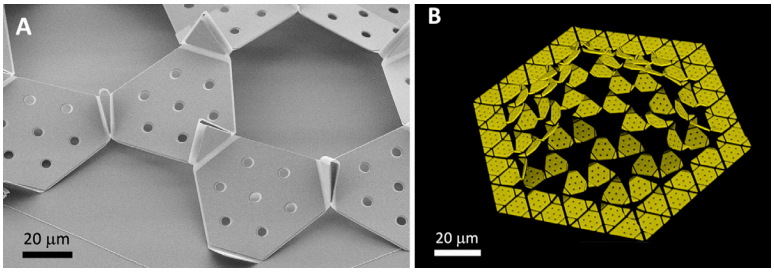

Figure 2: (a) SEM image of the active origami-inspired hinges connecting passive SiO panels. (b) Confocal image of a metarobot that transform into dome shape.

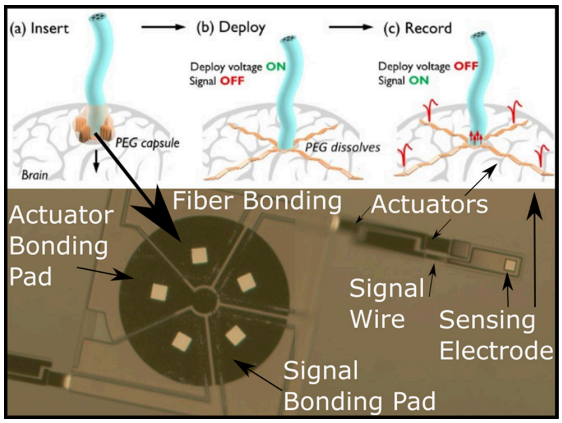

Figure 3: (Top) Schematics of the proposed probe working principle with low invasiveness. (Bottom) Structure of the prototype probe.

and switch between any desired surface flow patterns. We also integrated the cilia with a light-powered CMOS clock circuit (Figure 1c) to demonstrate wireless operation. As such, we envision numerous applications of cilia metasurfaces for fluidic manipulation with solar-powered lightweight devices in the near future.

Metamaterial-Based Microrobots. We demonstrate electrically programmable, micrometer-sized meta-material-based robots (metarobots) that can form three-dimensional (3D) surfaces from two-dimensional patterns, cycle among different shapes, and locomote in a biocompatible solvent. These metarobots have a hierarchical structure: the repeating panels are linked by origami-based splay hinges, which are controlled by applying voltage to atomically thin surface electrochemical actuators (Figure 2A). The actuator consists of a 7 nm thick platinum layer capped on one side by a 2 nm titanium layer. Under application of potentials in the range of 1 volt, ions oxidize the platinum, create a differential in stress between the two sides, and cause the structure to bend. The splay hinge contains a single mountain and two valley folds, which convert the out-of-plane bending of the nanoactuator into in-plane rotation of the panels. When we apply a voltage, the local expansions of the unit cells alter the local Gaussian curvature of the metarobots, allowing it to reconfigure into a 3D surface. We used confocal optical microscopy to image the 3D structures of the metarobots (Figure 2B). The Gaussian and mean curvatures are then calculated from the experimental 3D images. We show that the metarobots can transform into a rich class of 3D shapes by locally actuating different subsets of the splay hinges. As a demonstration, if the inner region of the sheet is activated, the metarobot morphs into a dome shape, whereas if the outer region is activated, it transforms into a saddle shape. Furthermore, by applying a phase delay between the actuation signals of different parts of the metarobot, we break both the spatial and temporal symmetry, and drive the metarobots to locomote in a biocompatible solution.

Extendable Neural Probes. Neural probes have cemented themselves in the minds of researchers and medical practitioners as a valuable instrument with multiple applications ranging from early detection of chronic disease, to brain stimulation and prosthetic interfaces. However, conventional probes are fabricated as thin, long structures inserted perpendicular to the surface of the brain. If transverse measurement is desired, multiple probes must be inserted as an array, requiring the removal of the skull over the entire recording area. One approach to minimizing the area of skull removed is to develop a deployable probe, which actuates after insertion to increase the area of transverse measurement. Such an approach requires the use of actuators that can generate enough force to achieve transverse motion through biological tissues. We developed such an actuator based on a bilayer structure of palladium and titanium, which can now be combined with a series of 120 µm wide fiber probes, signal wires, and rigid panels to create a deployable probe. Our vision is that the entire device will be released from the substrate, and inserted into the brain in one hole only slightly larger than the (contracted, 150 µm) probe. The device will then expand transversely into the brain, allowing a much larger measurement area than the invasive area (Figure 3 top).

References:

[1] Miskin, M. Z.; Cortese, A. J.; Dorsey, K.; Esposito, E. P.; Reynolds, M. F.; Liu, Q.; Cao, M.; Muller, D. A.; McEuen, P. L.; Cohen, I., Electronically integrated, mass-manufactured, microscopic robots. Nature 2020, 584 (7822), 557-561.

[2] Liu, Q.; Wang, W.; Reynolds, M. F.; Cao, M. C.; Miskin, M. Z.; Arias, T. A.; Muller, D. A.; McEuen, P. L.; Cohen, I., Micrometer-sized electrically programmable shape-memory actuators for low-power microrobotics. Science Robotics 2021, 6 (52), eabe6663.

[3] Wang, W.; Liu, Q.; Tanasijevic, I.; Reynolds, M. F.; Cortese, A. J.; Miskin, M. Z.; Cao, M. C.; Muller, D. A.; Molnar, A. C.; Lauga, E., Cilia metasurfaces for electronically programmable microfluidic manipulation. Nature 2022, 605 (7911), 681-686.

Synchronization and Bistability in Coupled Opto-Thermal MEMS Limit Cycle Oscillators

CNF Project Number: 2732-18

Principal Investigator(s): Prof. Alan T. Zehnder

User(s): Aditya Bhaskar

Affiliation(s): Sibley School of Mechanical and Aerospace Engineering, Cornell University

Primary Source(s) of Research Funding: NSF United States, grant number CMMI-1634664

Contact: atz2@cornell.edu, ab2823@cornell.edu

Primary CNF Tools Used: Heidelberg Mask Writer - DWL2000, Hamatech Hot Piranha, DISCO Dicing Saw, GCA 6300 DSW 5X g-line Wafer Stepper, Unaxis 770 Deep Si Etcher, Anatech Plasma Asher, Leica CPD300 Critical Point Dryer, Zygo Optical Profilometer, Zeiss Supra SEM

Abstract:

In this work, we study the nonlinear dynamics of pairs of mechanically coupled, opto-thermally driven, MEMS limit cycle oscillators. We vary three key parameters in the system — frequency detuning, coupling strength, and laser power, to map the device response. The coupled oscillators exhibit states such as the self-synchronized state, quasi-periodic state, drift state, and bistability. Specifically, we show that the laser power can be used to change the effective frequency detuning between the oscillators and at high laser powers the system shows irregular oscillations due to the existence of bistable states and sensitive dependence on system parameters.

Summary of Research:

Coupled oscillators at the microscale exhibit strong nonlinearities owing to the large deformations relative to the device dimensions [1]. This makes them suitable as experimental testbeds to study nonlinear dynamics. We study clamped-clamped beams that are nominally 40 μm long, 3 μm wide and 205 nm thick. Frequency detuning is introduced in the system by varying the lengths of adjacent oscillators and coupling is affected by short bridges between the devices as well as elastic overhangs near the anchor points. The bridges are spaced apart by 3 μm and are simultaneously excited into limit cycle oscillations using a single continuous wave laser beam at a wavelength of 633 nm. The resonator structure forms a Fabry-Perot interferometer where the absorbance and reflectance are modulated with the cavity gap. The interference setup allows for the driving and detection of oscillations [2]. A top-view of a sample device with the edges outlined and the laser beam aligned is shown in Figure 1.

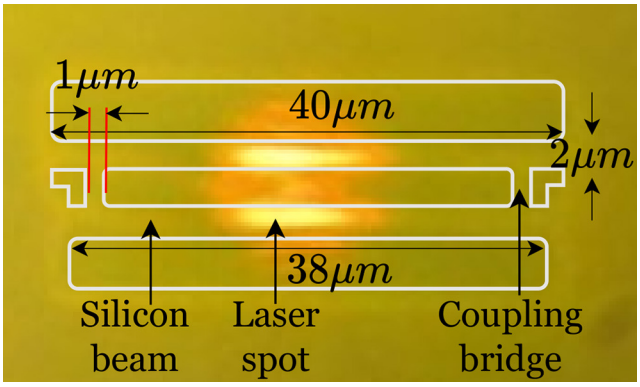

Figure 1: Optical microscope image of a sample device with the beams outlined and key dimensions labelled. The silicon device layer thickness is 205 nm. The laser spot aimed at the center of the device is used to drive and detect oscillations.

For plotting the synchronization region, the laser power was kept constant at approximately 1.3 mW striking the devices. The spectral responses were recorded for 25 different devices. These consisted of pairs of oscillators at five different coupling and five detuning levels. In all 25 devices, the reference oscillator was of length 38 microns. The other oscillators in the pair were of length {42, 40, 38, 36, 34} microns corresponding to a minimally coupled frequency detuning percentage of {−18%, −10%, 0%, +10%, +14%} respectively. A heat map of the difference in frequencies between the two oscillators for the 25 different devices is shown in the 5 × 5 grid in Figure 2. The plot shows a region of synchronization with boundaries marked in white. The spectra corresponding to three different dynamical states are also shown.

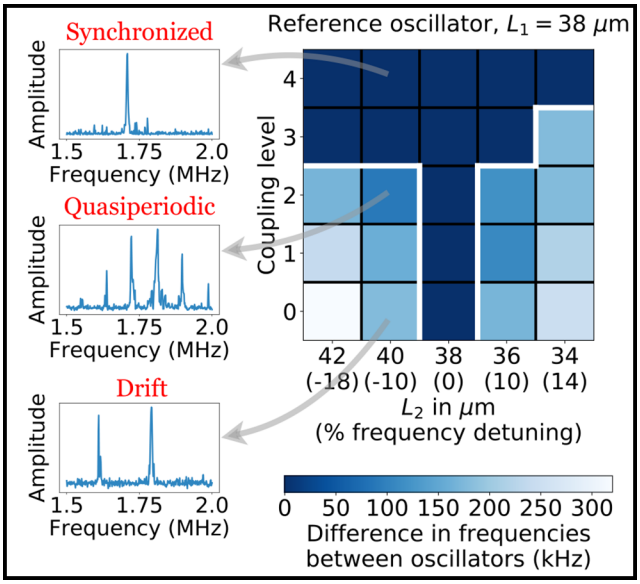

Figure 2: Experimental results showing the difference in limit cycle frequencies between pairs of oscillators in the frequency detuning vs. coupling strength space forming an Arnold tongue region of synchronization. The spectra of the system show drift, quasi-periodic, and synchronization states.

At low coupling, the oscillators are drifting with two prominent peaks in the spectrum. At moderate coupling strengths, the system shows quasi-periodic behavior with multiple sidebands in the spectrum in addition to two prominent peaks. This is the result of amplitude modulation of the oscillators due to the coupling.

At higher coupling strengths, inside the Arnold tongue region, the oscillators synchronize and the spectra collapses to a single prominent peak corresponding to the frequency of locking.

We also studied the device response at a fixed frequency detuning of −10% and by varying the coupling strength and laser power [3]. The resulting map in shown in Figure 3.

At minimal coupling, the devices exhibit a drift response for all laser powers. We note that the limit cycle frequencies decrease with an increase in laser power due

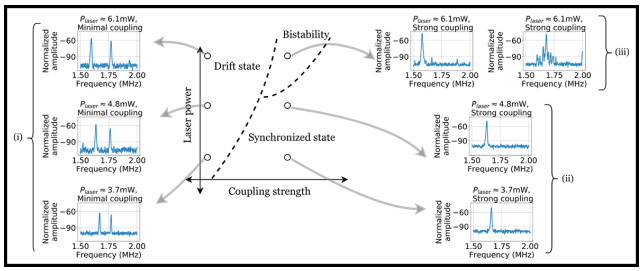

Figure 3: A map of the experimentally recorded dynamics of a pair of coupled MEMS oscillators (i) drift state at minimal coupling strengths, (ii) synchronized state in the presence of strong coupling at low laser powers, and (iii) co-existence of two stable states, i.e. synchronized oscillations and quasi-periodic oscillations in the presence of strong coupling at high laser powers.

to the strong amplitude softening behavior of the post-buckled beams, but the frequency detuning between the oscillators increases with an increase in laser power. This implies that the frequency detuning between the oscillators can be varied using the continuously varying laser power parameter.

At strong coupling, the oscillators show synchronized oscillations at low and moderate laser powers. At high laser powers, the system shows irregular oscillations with the system switching between two stable states: the synchronized state and the quasiperiodic state rapidly, due to the presence of noise in the system such as an unstable laser source. The system switching between the two states and exhibiting a broadband spectrum in the intermediate time is shown in Figure 4.

Conclusions and Future Steps:

In this work, we charted the behavior of pairs of coupled opto- thermally driven oscillators in the coupling, detuning, and laser power parameter space. The rich dynamics exhibited by such devices furthers our understanding of nonlinear oscillations and may have utility in devices such as sensors, filters, oscillator-based computers, and time-keeping devices.

References:

[1] S. Tiwari and R. N. Candler, "Using flexural MEMS to study and exploit nonlinearities: A review," Journal of Micromechanics and Microengineering, vol. 29, no. 8, Aug. 2019, Art. no. 083002.

[2] Blocher, David. "Optically driven limit cycle oscillations in MEMS." Cornell Thesis, https://hdl.handle.net/1813/31202 (2012).

[3] A. Bhaskar, M. Walth, R. H. Rand, and A. T. Zehnder, "Bistability in coupled opto-thermal micro-oscillators," Journal of Microelectromechanical Systems, (to appear) 2022.

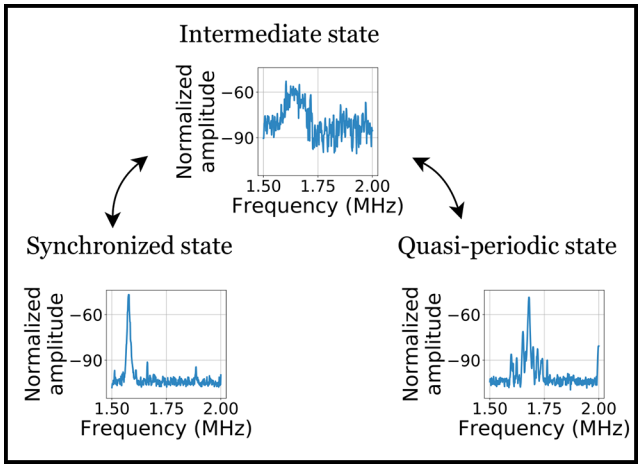

Figure 4: Bistability manifests as a broad-band spectral response in strongly coupled oscillators in the experiments (center). The oscillators rapidly switch between the synchronized state (left) with a single prominent peak in the spectrum, and the quasi-periodic state (right) with multiple satellite peaks, due to sensitive dependence of the system on the dynamical variables.

Reconfigurable Waterbomb Antenna

CNF Project Number: 2851-19
Principal Investigator(s): Robert Shepherd
User(s): Hyeon Seok An

Affiliation(s): Mechanical and Aerospace Engineering, Cornell University

Primary Source(s) of Research Funding:

Contact: rfpshepherd@gmail.com, ha259@cornell.edu

Primary CNF Tools Used: AJA Sputter Deposition

Abstract:

Up to this point, our research has focused on the materials and mechanisms for dynamic actuation of waterbomb antenna structures. Specifically, we focused on the selection of materials for foldable liquid metal (LM) joints to maintain conductivity between faces. Due to the demand for integrating multiple wireless standards into a single wireless platform, a reconfigurable antenna, also known as a tunable antenna, is attracting much attention. In mechanically reconfigurable antennas, the antenna structures consist of movable parts. In order to enable the electrical operation and mechanical reconfiguration, the antenna pieces are connected by foldable joints. In this project, an elastomer joint filled with LM was used to connect the waterbomb antenna pieces (see Figure 1a and 1b).

Summary of Research:

LMs such as gallium (Ga), eutectic gallium-indium alloy (EGaIn), or gallium-indium-tin alloy (Galinstan) are intrinsically stretchable (Dickey et al., 2008). However, Ga atoms from EGain spontaneously penetrate from the EGaIn to the region of the metal pad of the antenna. Moreover, it decreases the conductivity of the metal. It is possible to prevent penetration by using a thin metal layer that serves as a sacrificial layer.

The sacrificial layer absorbs the Ga atoms from EGaIn and traps them within. Ga atoms cannot transfer to the next metal layer (the thick copper layer of the antenna), preventing it from being damaged.

We used a sputtered 100 nm Au layer (sacrificial layer) above a 20 nm Cr layer (adhesion layer) to provide penetration protection. To investigate the durability against repetitive folding and releasing, the resistance of the joint was measured during cyclic bending (1,000 cycles of 45° bending angle) (see Figure 1c). The resistance remains almost constant throughout this test.

Mechanically reconfigurable waterbomb antennas were demonstrated by connecting eight waterbomb antenna pieces using eight foldable joints. An external force can control the folding angle of the waterbomb antenna, and the structure is tunable (see Figure 1d).

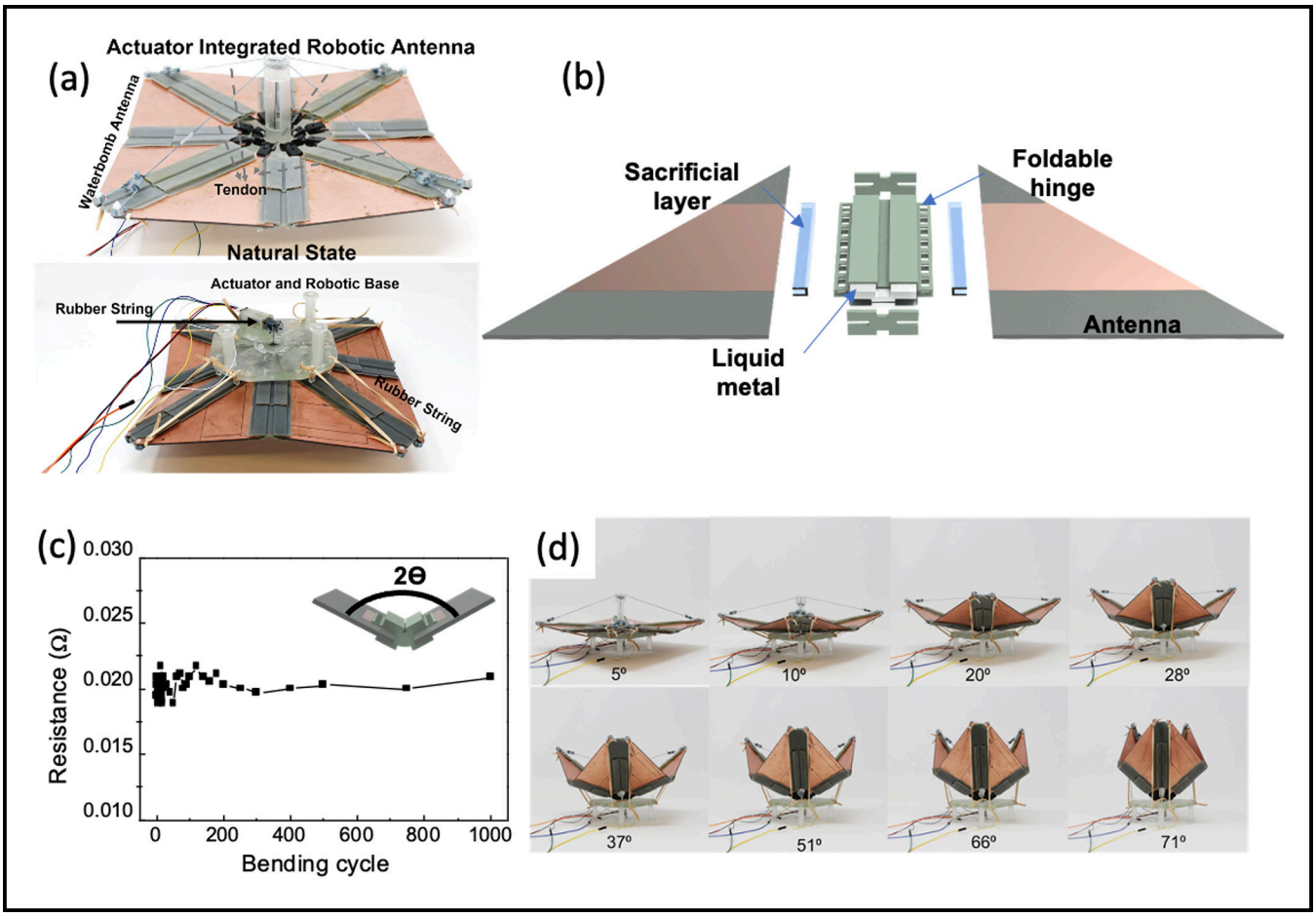

Figure 1: (a) Photograph of the waterbomb antenna. (b) Schematic image of two waterbomb pieces and a foldable joint. (c) Bending cyclic test (bending angle: 45°). (d) Photographs of the waterbomb antenna with the different folded states.

Fabrication of Micro Scale Triboelectric Generator

CNF Project Number: 2929-21
Principal Investigator(s): Shahrzad Towfighian
User(s): Mohammad Alzgool

Affiliation(s): Mechanical Engineering, Binghamton University
Primary Source(s) of Research Funding: National Science Foundation Grant #1919608
Contact: stowfigh@binghamton.edu, malzgoo1@binghamton.edu, mmalzgool14@gmail.com
Primary CNF Tools Used: YES Asher, AJA Sputter Deposition, Heidelberg DWL-2000 Mask Writer, Oxford PECVD, Oxford 81 Etcher, PT770 Etcher, DISCO Dicing Saw, SÜSS MA6-BA6 Contact Aligner, YES Polyimide Curing Oven, Primaxx Vapor Etcher

Abstract:

Energy harvesting became of extreme importance as advances on internet of things are made. Although triboelectric generators (TEGs) are extensively researched in meso-scale as devices to harvest mechanical energy, research on downsizing TEGs to micro-scale is scarce [1]. In this project, we created and investigated the performance of a micro-scale TEG operating in contact-separation mode. The fabricated device was used as an accelerometer for accelerations in the range of 1-3 g.

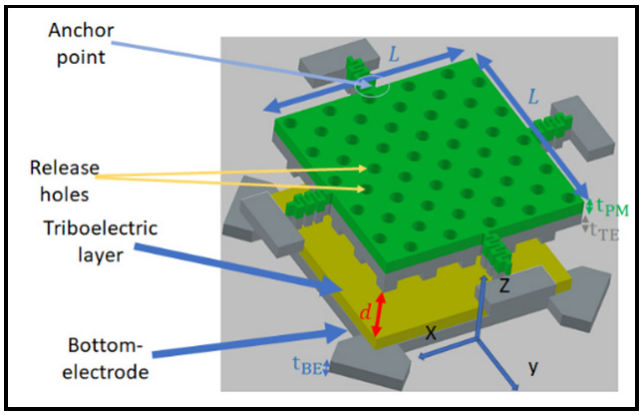

Figure 1: Micro triboelectric generator schematic.

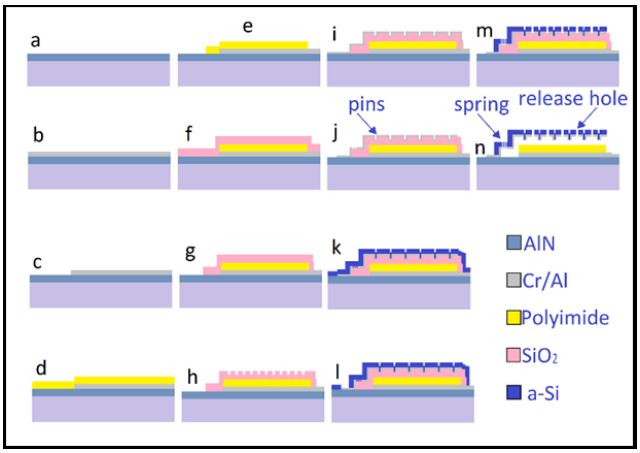

Figure 2: Micro triboelectric generator fabrication process flowchart.

Research Summary:

Triboelectric generators (TEGs) are researched nowadays because of their advantages over piezoelectric generators such as low cost, flexibility, and their high output. The triboelectric generator operating in contact-separation mode typically has three layers, two layers of which forms a triboelectric pair, and the third layer is a conductive layer that hits the substrate as shock is applied (Figure 1). Once the conductive electrode contacts the dielectric material, both layers in contact will gain\lose electrons which creates potential difference when these layers are separated. In our work, the triboelectric pair is made of polyimide (using HD microsystems PI2574 precursor) and aluminum, and the top electrode is made of aluminum too [2].

Fabrication:

The fabrication process started with sputtering 200 nm chrome/ aluminum on 1.5 µm aluminum nitride insulating layer (Figure 2 a, b). Then the chrome/ aluminum layer is patterned using PT770 etcher (Figure 2 c). Then polyimide layer was formed by spin-coating the precursor and baking it on a hot plate for 1 min followed by oven curing in the YES polyimide oven for 1.5 hours (Figure 2d). Then the polyimide was patterned using Oxford 81 etcher with CF_4/O_2 recipe (Figure 2e) [3]. This process was followed by PECVD film of SiO_2 deposited to create a gap (Figure 2f). This film was etched twice using Oxford 81 with different masks to create ditches on the top (Figure 2g,h). Then, another sputtered chrome/ aluminum film of 120 nm

was deposited on top of the oxide layer (Figure 2i), this film will have pins when it fills the ditches created on the oxide layer. This layer was etched to form top layer and springs (Figure 2j). Then, a-Si layer is deposited on top to create a proof-mass and a structural layer on top of the chrome/ aluminum (Figure 2k).

Parameters for a-Si deposition were chosen such that the resulted film stress of a-Si and chrome/ aluminum is tensile and less than 180 MPa to avoid breakage in the serpentine springs. Then, a-Si on contact pads is etched using Oxford 81 (Figure 2l), and both a-Si and chrome/ aluminum are etched to form release holes for vapor hydrofluoric acid etching (Figure 2m). Finally, dicing and releasing of the chips with vapor HF etching to remove the oxide layer was done to create micro-scale triboelectric generator (Figure 2n).

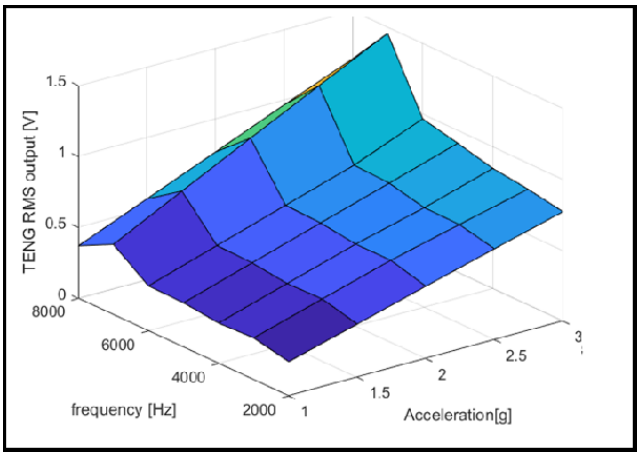

Figure 3: The relation between frequency, acceleration, and generated voltage.

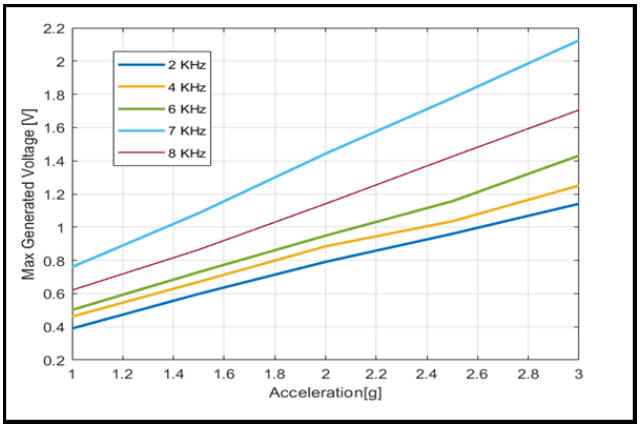

Figure 4: Generated output against acceleration with different input frequencies.

Results:

The fabricated device was mounted on a mini-shaker (B&K 4810) and an accelerometer was attached to the stage to measure the acceleration. Then the shaker was excited sinusoidally with acceleration in the range of 1-3 g. The output of the micro triboelectric generator as a function of acceleration and input frequency is shown in Figure 3. The generated voltage is noticed to be linear against acceleration at any given frequency as show in Figure 4. The sensitivity of the fabricated TENG varies as frequency is changed from ~0.4 V/g to ~0.65 V/g, which is higher than the sensitivity of the commercial accelerometer used. The highest sensitivity value is seen at the frequency of 7 KHz.

Conclusions and Future Steps:

There are plenty of parameters that could be optimized in this work. For instance, the polyimide was used here because it can withstand the 300-400°C temperature of the PECVD process while other materials like PDMS would evaporate, the output voltage might improve if we found a way to use PDMS instead of polyimide. Also, the amorphous silicon film was used here because the stress can be tuned to overcome the compressive stress of the chrome/ aluminum sputtered film. If we could swap the a-Si with a thicker conductive material and get neutralized film stress, it is possible to get higher voltage output from the reported device.

References:

[1] H. A. Hamid, Z. Celik-Butler, Design and optimization of a mems triboelectric energy harvester for nano-sensor applications, in: 2019 IEEE Sensors Applications Symposium (SAS), IEEE, 2019, pp. 1-6.

[2] H. Zhang, L. Quan, J. Chen, C. Xu, C. Zhang, S. Dong, C. Lu, and J. Luo, A general optimization approach for contact-separation triboelectric nanogenerator, Nano energy, vol. 56, pp. 700-707, 2019.

[3] G. Turban, M. Rapeaux, Dry etching of polyimide in o 2-cf 4 and o 2-sf 6 plasmas, Journal of the Electrochemical Society 130 (11) (1983) 2231.

Programmable Microscopic Magnetic Self-Assembly

CNF Project Number: 2964-21

Principal Investigator(s): Itai Cohen, Paul L. McEuen

User(s): Zexi Liang, Melody Xuan Lim, Tanner Pearson, Conrad Smart

Affiliation(s): Kavli Institute at Cornell for Nanoscale Science, School of Applied and Engineering Physics, Laboratory of Atomic and Solid-State Physics, Department of Physics, Cornell University; School of Engineering and Applied Sciences, Harvard University.

Primary Source(s) of Research Funding: This work was supported by NSF grant DMR-1921567, Sloan Foundation-Contract G-2021-14198

Contact: itai.cohen@cornell.edu, plm23@cornell.edu, brenner@seas.harvard.edu, zl467@cornell.edu, mxl3@cornell.edu, tgp34@cornell.edu, cs2239@cornell.edu

Primary CNF Tools Used: Oxford 81/82 Etcher, Oxford 100 Etcher, ASML DUV Stepper, JEOL 6300 EBL, SC 4500 Odd-Hour Evaporator, AJA Sputter, Oxford PECVD, Heidelberg Mask Writer - DWL2000, PT770 Etcher, Unaxis DRIE, Plasma-Therm DRIE, Zeiss SEM, Veeco AFM

Abstract:

We are developing a microscopic self-assembly system with programmable magnetic interactions. In order to encode specific magnetic lock-and-key interactions between pairs of micron-scale particles, we embed nanoscale single-domain magnets along their perimeters, and program their magnetic configurations. When these non-equilibrium particles are magnetically and hydrodynamically driven to explore their configuration space, they self-assemble into complex structures, as encoded by the embedded magnetic information.

Summary of Research:

Self-assembly refers to a group of ubiquitous processes that turns a disordered system of dispersed building blocks into organized structures or patterns via local interactions between the building blocks with minimal external guidance. Among various kinds of local interactions that can lead to self-assembly, the magnetic interaction is unique for its scalability across multiple scales from sub-micrometer to macroscopic. Previously, we have shown that macroscopic polymer particles with embedded permanent magnets can self-assemble via programmable magnetic interactions into 1D polymers, 2D square lattices and even 3D cage structures [1]. Based on the scalable nature of magnetic interactions, we are now developing magnetically programmable particles with information encoded in the magnetic patterns to achieve self-assembly in a controlled manner at the microscale.

We have fabricated microscale panels with magnetic patterns embedded in silicon oxide thin films as building blocks for programmable magnetic self-assembly (Figure 1a,b). Sub micrometer single-domain nanomagnets that are pill shaped and have various aspect ratios are patterned via electron beam lithography followed by metallization of cobalt and liftoff. Since the nanomagnet coercivity is directly controlled by its aspect ratio, we can fabricate domains with small and large magnetic coercivity which allows us to control the domain magnetization through sequential application of large followed by smaller magnetic fields [2]. For instance, in order to have opposite magnetic dipoles in both x and y directions, we pattern two types of nanomagnets with different aspect ratios and coercivities.

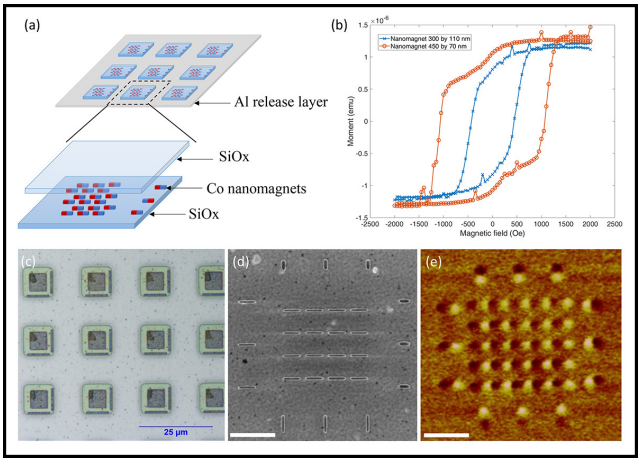

Figure 1: Magnetically programmable self-assembly at water-air interface. (a-b) schematics and optical image of the magnetic panels. (c-d) SEM and MFM images of the magnetic panels. Scale bar: 1 μm.

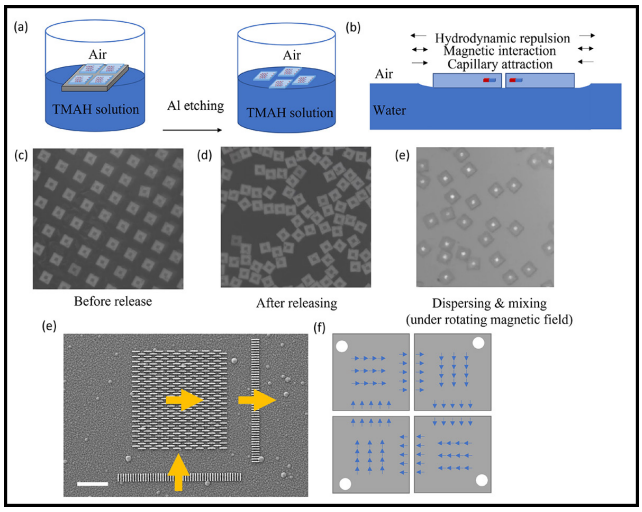

Figure 2: (a) Schematics of magnetic panels released and assembled at water-air interface. (b-e) Magnetic panels float at the water-air interface before/after releasing and mixing. (f) SEM of nanomagnets pattern for self-limiting assembly. Scale bar: 2 μm. (g) Schematic of a tetramer assembled from four identical magnetic panels.

All the magnets are first magnetized (in both x and y directions) using a magnetic field higher than the coercive fields for both domains. Subsequently, the shorter domains are magnetized in the opposite directions using a coercive field whose intensity is high enough to flip the short domains but too weak to flip the long domains. In this way, we produce near-field interactions between adjacent magnetic panels with programmable selectivity.

By introducing lock and key pairs of magnetic handshake patterns into the design of patterns, we aim to generate specificity in magnetic bindings [1,3]. Utilizing the specificity of magnetic bindings, we could further design more complex self-assembled structures such as polymers with unique properties and functionalities and even self-assembled magnetic micromachines. Finally, in addition to these near-field interactions, we control the panel far-field interactions by patterning a large central array of magnets (see Figure 1a). This central array of magnets also provides a means to actuate the magnetic panels with an external magnetic field.

The panels are fabricated on a suspended thin sacrificial layer made of aluminum. We release the panels for self-assembly by floating the panels and sacrificial layer on top of a tetramethylammonium hydroxide (TMAH) solution. The TMAH etches the aluminium layer, leaving the magnetic panels free-floating in a single layer, on an effectively frictionless two-dimensional surface (Figure 2a). We design the shape and size of the magnetic panels so as to minimize the distortion of the liquid interface caused by the panels, thus isolating the forces driving assembly to the magnetic patterns on the panel edge.

The very low friction environment of the liquid interface enables us to visualize the effect of small magnetic forces, as well as to introduce out-of-equilibrium driving.

In particular, to allow the panels to effectively explore their configuration space, we spin the panels using a rotating external magnetic field. As the particles spin, the fluid around them is also forced to flow in a vortex. As the spinning speed increases, this rotating flow leads to chaotic trajectories between individual magnetic panels, so that panels “mix” and weak structures break (Figure 2b-d). For sufficiently large rotation rates (more than 10 Hz), the magnetic panels explore their configuration space until they bind in their strongest configuration (Figure 2e).

As the first proof of concept, we demonstrate that a single type of magnetically patterned square panel self-assembles into self-limiting clusters. The magnetic patterns consist of a large central magnet array as the handle for external field manipulation and mixing, and two arrays of magnets near the two adjacent edges of the panels (Figure 2f,g). When the correct binding forms, four panels will be assembled into a tetramer, with each panel rotated 90° from the adjacent one (Figure 2g).

In addition to self-assembly at the water-air interface for 2D structures, we also developed an acoustic approach that could effectively agitate the micrometer-sized particles in 3D (Figure 3a,b). We utilize surface acoustic wave (SAW) devices to generate standing surface acoustic wave (SSAW) on a lithium niobate piezoelectric substrate and then couple the wave into the microfluidic well where the magnetic particles are released (Figure 3a). The particles are manipulated by acoustic radiation force and acoustic streaming. To effectively mix the particles, we further modulate the phase of the voltage signal applied to the interdigital transducers and randomized the distribution of the pressure nodes of the SSAW. We envision that this acoustic agitation approach could be adopted in future self-assembly experiments for programmable 3D assembly of magnetic particles.

References:

[1] R. Niu, C. X. Du, E. Esposito, J. Ng, M. P. Brenner, P. L. McEuen, I. Cohen, Proceedings of the National Academy of Sciences 2019, 116, 24402.

[2] J. Cui, T.-Y. Huang, Z. Luo, P. Testa, H. Gu, X.-Z. Chen, B. J. Nelson, L. J. Heyderman, Nature 2019, 575, 164.

[3] C. X. Du, H. A. Zhang, T. Pearson, J. Ng, P. McEuen, I. Cohen, M. P. Brenner, arXiv preprint arXiv:2112.02614 2021.

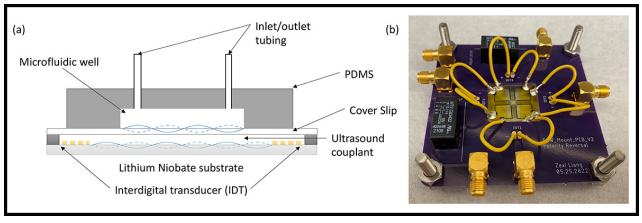

Figure 3: (a) Schematic of the surface acoustic wave setup for magnetic particle agitation in microfluidics. (b) Photo of the surface acoustic device bonded to the driving circuit board.

Superconducting Coplanar Microwave Resonator

2022 CNF REU Intern: Sean C. Anderson, Jr.

Intern Affiliation: Electrical and Computer Engineering, Morgan State University

CNF REU Principal Investigator: Prof. Farhan Rana, Department of Electrical and Computer Engineering, Cornell University
CNF REU Mentor: Arjan Singh, Electrical and Computer Engineering, Cornell University

CNF REU Project and Primary Source(s) of Research Funding: 2022 Cornell NanoScale Science & Technology Facility Research Experiences for Undergraduates (CNF REU) Program via the National Science Foundation under Grant No. NNCI-2025233

Contact: seandl@morgan.edu, fr37@comell.edu, as2995@cornell.edu

Website: https://cnf.cornell.edu/education/reu/2022
Primary CNF Tools Used: AJA Sputter Deposition, ABM Contact Aligner, Hamatech Wafer Processor

Abstract:

We are trying to make on-chip superconducting microwave resonators which are capable of driving spins in semiconductors by using the superconducting metal niobium (Nb). These microwave resonators will work mainly in two ways; Sensing magnetic defects and magnetic order in thin films of new materials; Manipulating and measuring the quantum state of a collection of spin defects for use in quantum technologies. This will aid in the optimization of optics and optoelectronics. In the past, the Rana research group did a similar project with the coplanar microwave waveguide resonator, however, in that experiment, the smaller the dimensions of the metal of the deposited metal, which in that case was copper, then the smaller the extent the magnetic field will radiate outward and there will be greater conductive losses. This is the reason we chose to go with a superconductor, which minimizes conductive losses.

Summary of Research:

This summer research project focused on getting familiar with the cleanroom, learning about what a coplanar microwave resonator is, and aiding in the process of developing one that is superconducting.

The tools we used the most with this project were the AJA sputter deposition system to deposit niobium on a sapphire wafer, along with the ABM contact aligner for the UV exposure to the sapphire wafer, and then development with the Hematech development tool, which makes the pattern on the sapphire wafer visible using the 726 MlF solution for 60 seconds.

The working principles behind why the device will be resonant at certain frequencies has to do with the transmission lines on the device. A simple analogy can be made with the length of a string where its resonant frequency is directly related to its length by the equation f_o = velocity/ 2Length, which are considered standing waves.

The same is true of our transmission lines except that in AC electronics, we must consider the voltage and current waves and the rise and collapse of these waves, which will in turn give us a better idea of their resonant frequencies. The inductive and capacitive properties of the superconducting coplanar

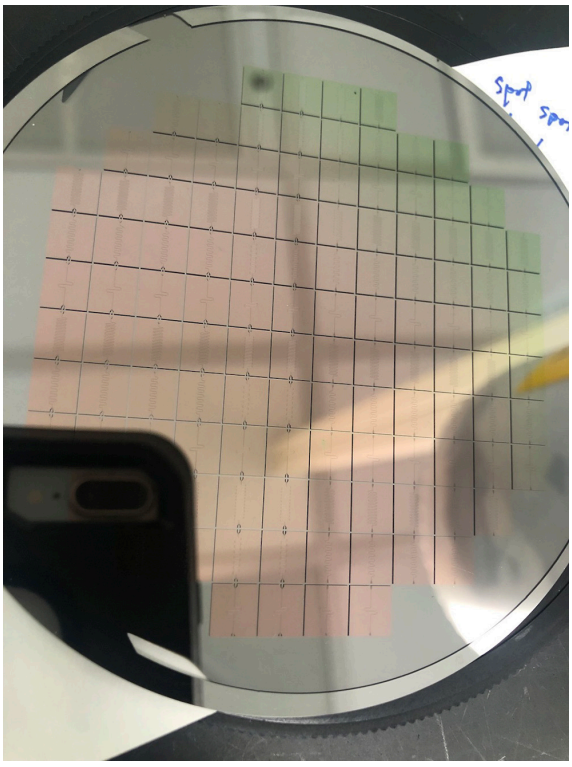

Figure 1: We designed three devices on the sapphire wafer.

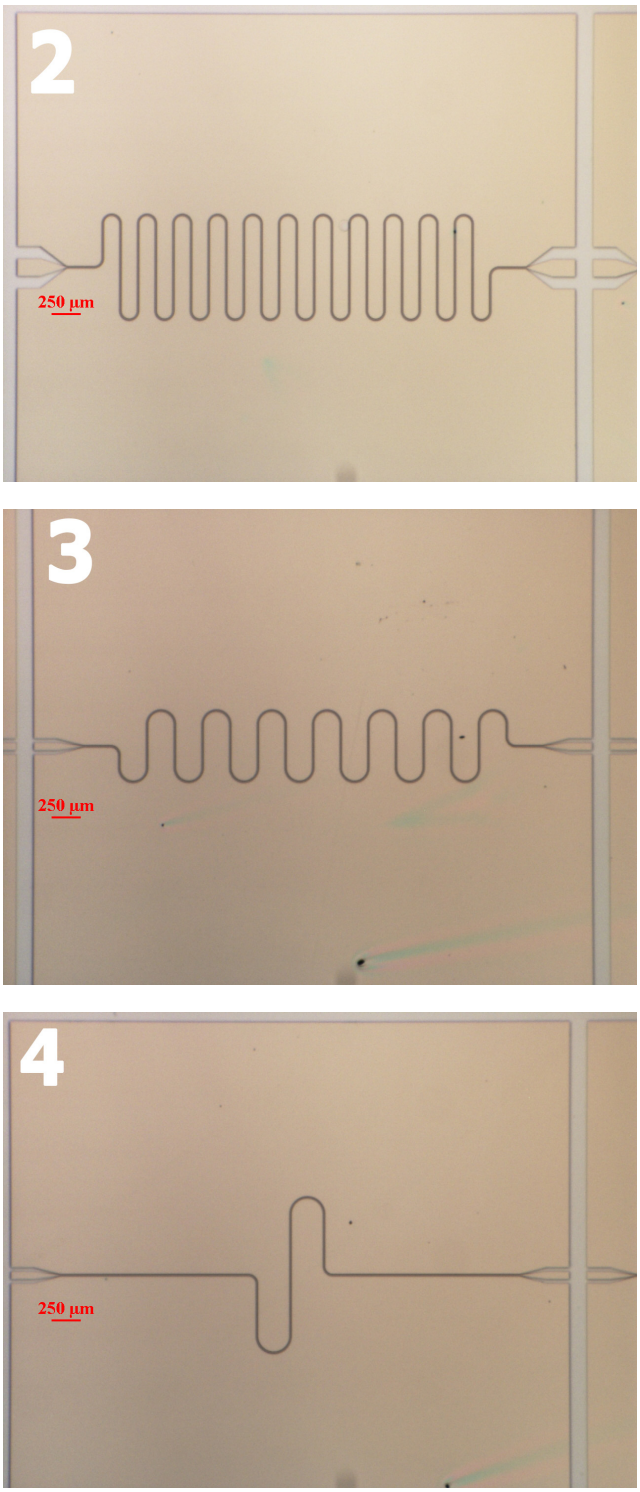

Figure 2-4: The respective resonant frequencies of each device are shown in an array on the sapphire wafer and are 2GHz at 29.62 mm (Figure 2 top), 4.l GHz at 14.61 mm (Figure 3 middle), and 8 GHz at 7.5 mm (Figure 4 bottom).

microwave resonator also gives rise to the resonant frequencies at which the device will operate. Given those two things, transmission line length and the reactive AC components of the device will determine the resonance at which the device operates.

We designed three devices on the sapphire wafer (Figure 1). The respective resonant frequencies of each device are shown in an array on the sapphire wafer and are 2GHz at 29.62 mm (Figure 2), 4.l GHz at 14.61 mm (Figure 3), and 8 GHz at 7.5 mm (Figure 4).

The idea was to sample materials using the super-conducting coplanar microwave resonator, which entailed probing the resonator with a DC power source to get a static magnetic field that shoots out perpendicular to the coplanar microwave resonator's surface, and probing the device with a microwave frequency to be sent inside of the device, which created our oscillating magnetic field.

At microwave frequencies, the spin-states of the electrons will split into two even but opposite energies of El = +1/2gµBB and E2 = -1/2gµBB where ~ E = El - E2.

From there we could observe the electron's spin behaviors from the bode plot that was characterized from the material we sampled and which will be the future work to be performed on this device.

Conclusions and Future Steps:

The device is now ready for characterization, which means that we will next take a look at the transmission characteristics and see where our device is resonant at. Resonance will occur at microwave frequencies where $\hbar(\omega) = g\,\mu_B$.

References:

[1] Standing Waves and Resonance, Chapter 14 - Transmission Lines, Electronics Textbook (allaboutcircuits.com).

[2] Coplanar waveguide resonators for circuit quantum electrodynamics, Journal of Applied Physics 104, 113904 (2008); https://doi.org/10.1063/1.3010859; M. Göppl, A. Fragner, M. Baur, R. Bianchetti, S. Filipp, J. M. Fink, P. J. Leek, G. Puebla, L. Steffen, and A. Wallraff.

Microscale Broadband Optical Upconverter

CNF Project Number: 900-00

Principal Investigator(s): Paul L. McEuen[1,2,4]

User(s): Yanxin Ji[3], Alejandro J. Cortese[4], Conrad L. Smart[1]

Affiliation(s): 1. Laboratory of Atomic and Solid State Physics, Cornell University;
2. Kavli Institute at Cornell for Nanoscale Science, Cornell University;
3. Electrical and Computer Engineering, Cornell University; 4. OWiC Technologies

Primary Source(s) of Research Funding: Cornell Center for Materials Research (DMR1719875), Air Force Office of Scientific Research (MURI: FA9550-16-1-0031), New Frontier Grants from the Cornell College of Arts & Sciences, Cornell IGNITE Innovation Acceleration Program

Contact: plm23@cornell.edu, yj323@cornell.edu, cs2239@cornell.edu

Primary CNF Tools Used: Odd Hour Evaporator, ABM Contact Aligner, Oxford 81 Etcher, AJA Sputter Deposition Tool, Hot Press, Heidelberg Mask Writer DWL2000, Oxford Cobra ICP Etcher, PT770 Etcher

Abstract:

Optoelectrical materials/devices that convert long-wavelength light into shorter wavelengths have gained increasing interest in fields like bio-sensing and infrared imaging [1]. Here we present a microscale optical upconverter made by heterogeneously integrating Si photovoltaics (PVs) and GaN light emitting diodes (LEDs). Previous research on photon upconversion mainly focused on upconversion nanoparticles (by nonlinear anti-Stokes emission) [2]. This kind of upconversion is limited by the materials and has a narrow band of excitation/emission wavelength. In contrast, our optical upconverter can be excited by a wide range of light wavelengths: from visible to infrared light. The emission wavelength can reach blue or even shorter wavelengths which are determined by the LED's emission.

Summary of Research:

The broadband optical upconverter is made by fabricating silicon (Si) PVs and gallium nitride (GaN) LEDs separately and then integrating them together.

To fabricate Si PVs, we start from n-type doped SOI wafers and utilize phosphosilicate glass to dope the top layer, creating a vertical PN junction. The PVs' contacts and interconnect are Pt/Ti and are deposited through AJA sputtering tool. The PVs are isolated by inductively coupled plasma (ICP) etching (Cobra ICP etcher).

To fabricate GaN LEDs, we start from GaN heterostructure wafers (from a commercial vendor). The n-contacts and p-contacts are Au/Pd and Ti/Au respectively, which are deposited through e-beam evaporation. The LEDs are outlined by ICP dry etch via PT770 etcher.

After the PVs and LEDs are fabricated on their native substrates, we integrate them together through a transfer method developed by our group. We spin ~ 6 μm PMMA onto the LEDs as the protection layer. By using a thermoplastic polymer (polypropylene carbonate), we bond the LED substrate to a sapphire carrier wafer through Hot Press. Afterward, the LEDs' native substrate is removed by laser lift-off. In the end, the LEDs are aligned and transferred to the PV substrate via ABM contact aligner alignment and Hot Press bonding. The carrier wafer is removed through thermal slide. The polymer residue is cleaned in acetone.

Our upconverters are powered by long-wavelength light and emit short-wavelength light. The optical energy is firstly converted into electrical energy and then converted back to optical energy, which is an optical-electrical-optical (O-E-O) process. Si PVs carry out the optical-electrical conversion. Si's narrow bandgap (~1.1eV) enables a broad range of excitation photon energies. GaN LED performs the electrical-optical conversion. The efficiency of our upconverter is determined by the product of two efficiencies: Si PV's conversion efficiency (~20%) and GaN LED's light-emitting efficiency (~2%). Therefore, overall power efficiency can reach ~ 0.4%, which is comparable to the upconversion nanoparticles (~0.01%-1%) [3].

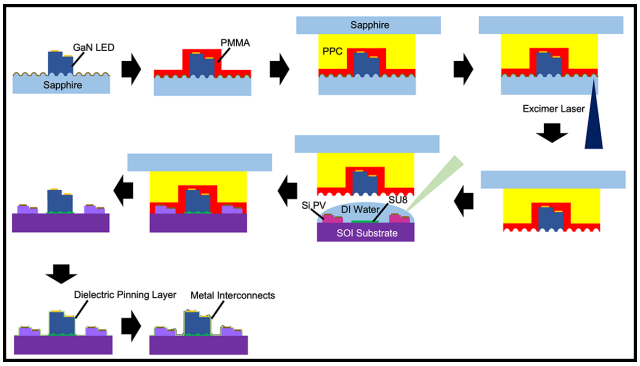

Figure 1: Schematic illustration of the upconverter integration process.

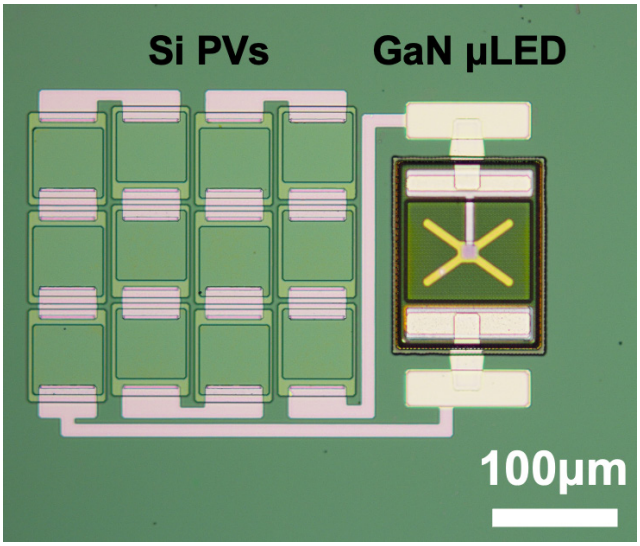

Figure 2: Optical image of an upconverter.

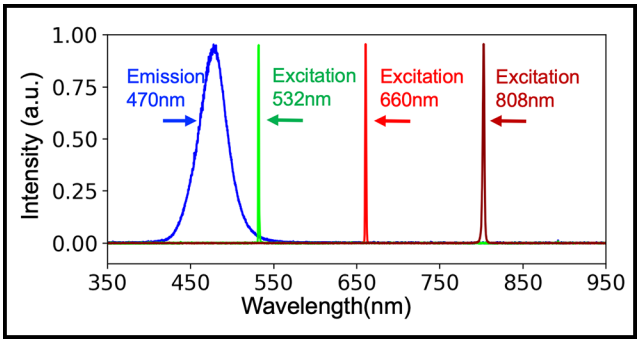

Figure 3: Spectra of the excitation source (532 nm, 660 nm, and 808 nm laser) and the upconverter's emission with a peak at 470 nm.

Conclusions and Future Steps:

Here we present a platform that enables microscale broadband optical upconverters made by heterogeneous integration of Si based PVs and III-V materials-based LEDs. This heterogeneous integration technique allows the fabrication of thousands of optical upconverters in parallel per wafer. The efficiency of the upconverter is ~ 0.4%, which is comparable to the best upconversion nanoparticles. Our next step is to make devices with more sophisticated functions based on this platform. It will be integrating CMOS circuits with III-V materials based optical devices.

References:

[1] Zhou, B., Shi, B., Jin, D. and Liu, X. Controlling upconversion nanocrystals for emerging applications. Nat. Nanotechnol. 10, 924-936 (2015).

[2] Auzel, F. Upconversion and anti-Stokes processes with f and d ions in solids. Chem. Rev. 104, 139-173 (2004).

[3] Algar, W. R. et al. Photoluminescent Nanoparticles for Chemical and Biological Analysis and Imaging. Chem. Rev. 121, 9243-9358 (2021).

Microscopic Optically Powered Bubble Rockets

CNF Project Number: 900-00
Principal Investigator(s): Paul L. McEuen
User(s): Samantha L. Norris, Michael F. Reynolds

Affiliation(s): Physics, Cornell University

Primary Source(s) of Research Funding: Cornell Center for Materials Research (DMR-1719875)

Contact: plm23@cornell.edu, sn588@cornell.edu, mfr74@cornell.edu

Primary CNF Tools Used: ABM Contact Aligner, Oxford Cobra/81/82/100 Etchers, Oxford ALD/PECVD, Heidelberg Mask Writer - DWL2000

Abstract:

Bubble propulsion as a swimming mechanism for artificial microswimmers has been of significant interest recently, especially for biomedical applications. We demonstrate hundred-micron-scale bubble-propelled microswimmers that produce bubbles via voltage-induced water electrolysis, allowing operation in any aqueous solution, including physiological saline. These bubble rockets are powered by onboard photodiodes, allowing individual addressability limited only by the power and divergence of the light beam. We also demonstrate the ability to design microswimmers with different trajectories based on device geometry, and show integration with thin-film magnets for *in situ* steering. Finally, we present a novel method for locomotion on a solid-liquid interface.

Summary of Research:

We present hundred-micron-scale bubble rockets that consist of onboard photodiodes used to convert incident light into a voltage and current for water electrolysis. A diagram of a microswimmer is shown in Figure 1a. Each device consists of multiple silicon P-N junctions wired in series with two platinum electrodes roughly shaped like a tapered hollow cylinder with a rectangular cross section. Each photodiode has an open-circuit voltage of roughly 0.65V with a responsivity of ~ 0.3 A/W under Hg lamp illumination and operates in a light intensity of 1 kW/m^2, roughly that of a sunny day. The entire device is encapsulated in silicon dioxide except for the interior of the hollow electrodes.

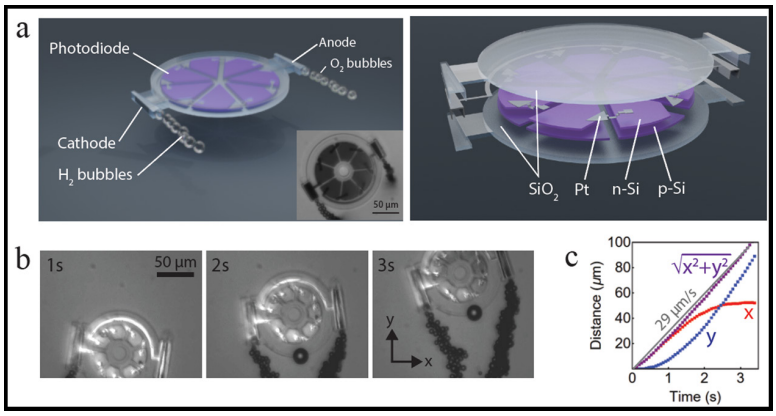

Figure 1: Diagrams and optical micrographs of optically powered microswimmer and time lapse of swimming behavior. a) Diagrams of optically powered microswimmer showing encapsulated photodiodes, hollow platinum electrodes, and bubble production. Inset: microswimmer operating on glass-water interface in 10 mM PBS solution under Hg lamp illumination. b) Time lapse of a device swimming under mercury lamp illumination at an air-water interface in 10 mM PBS solution. c) Displacement vs. time for the swimming device shown in b.

Under standard microscope illumination, the onboard photodiodes apply a voltage between the two electrodes sufficiently high to split water, producing hydrogen and oxygen gas at the cathode and anode respectively. The capillary force on these bubbles in the tapered cylinder forces them to be ejected from the tube, propelling the microswimmer forward.

A time lapse of a device swimming in 10 mM PBS is shown in Figure 1b, with a displacement vs. time curve in Figure 1c. This bubble rocket is swimming at roughly 30 µm/s at an air-water interface. Due to the stoichiometric ratio of hydrogen to oxygen produced during water splitting, the instantaneous velocity of the hydrogen-producing cathode is twice that of the oxygen-producing anode, resulting in a circular trajectory.

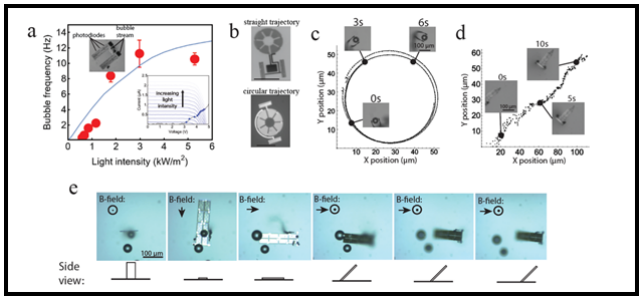

Figure 2: Description of microswimmer behavior. a) Measured bubble frequency as a function of incident light intensity for stationary microswimmer device (red) with expected bubble frequency from operating points in inset (blue). b) Micrographs of devices with circular and straight swimming trajectory showing wiring and electrode geometry. c) Time lapse and corresponding circular trajectory of a microswimmer with separate anodic and cathodic rockets on a solid-liquid interface. d) Time lapse and corresponding straight trajectory of a microswimmer with each rocket containing both anode and cathode on a liquid-liquid interface. e) Microswimmer on a solid-liquid interface with thin film magnets rotating in three dimensions and locomoting with an attack angle of 45 degrees to reduce friction.

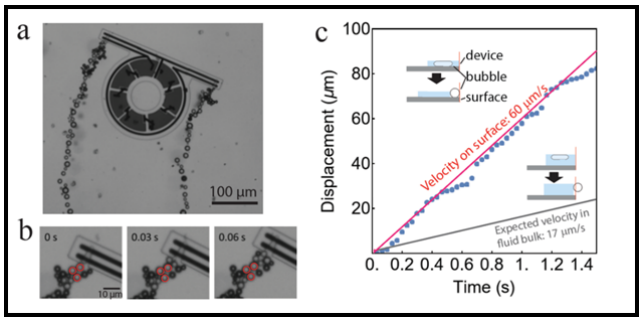

Figure 3: Utilizing bubble surface adhesion for increased surface swimming velocity. a) Micrograph of microswimmer locomoting on glass-water interface by pushing off ejected bubbles attached to the surface. b) Time lapse of microswimmer shown in (a) moving by approximately one bubble diameter with each bubble expulsion. c) Displacement as a function of time for device shown in (a) compared to maximum expected velocity using traditional bubble-propelled motion. Insets: diagrams showing mechanism of bubble propulsion for devices without (top) and with (bottom) a bottom on the rockets.

The relationship between bubble ejection frequency and incident light intensity can be understood by considering separately the current-voltage characteristics of the photodiodes and on-chip rocket-shaped electrodes. The bubble ejection frequency for a microswimmer is shown in Figure 2a; the frequency increases with input light intensity until the photodiodes become voltage limited. The I-V curves of the photodiodes and on-chip electrodes are shown in the inset.

In addition, we demonstrate the ability to control microswimmer trajectory both by controlling electrode geometry and by integrating onboard thin film magnets for steering in a uniform magnetic field. The current required for bubble nucleation on an electrode depends on the confinement of the produced gas. Although both anode and cathode of the microswimmer must be exposed to fluid for current to flow, the placement and geometry of the electrodes can be designed to allow different swimming trajectories, as shown in Figure 2b. Circular and linear trajectories are shown for microswimmers in Figure 2c-d. By fabricating Co magnets onboard the microswimmers and performing experiments in a three-axis solenoid, the microswimmers can also be rotated and steered in three dimensions as shown in Figure 2e.

We have also shown the ability to engineer the microswimmer/substrate interface for more effective locomotion on a flat surface, as shown in Figure 3. By removing the bottom of the tube-shaped electrode, bubbles are able to attach to the surface and remain stationary while the capillary force of bubble growth propels the microswimmer forward. As such, the swimmer moves forward roughly one bubble diameter with each bubble expulsion, leaving the bubbles behind as shown in Figure 3a. A time lapse of the rocket movement is shown in Figure 3b. Each rocket contains both anode and cathode, such that the overall device moves forward in a straight line, with its trajectory shown in Figure 3c.

In conclusion, we have demonstrated a truly microscale bubble-propelled swimmer that can swim in physiological solutions with a long lifetime, paving the way for intelligent bubble-propelled microrobots to be used in applications from drug delivery, to manipulation, to *in vivo* monitoring. These bubble rockets can be fabricated to swim with a circular or linear trajectory and can also be integrated with thin-film magnets for steering in a uniform magnetic field. Finally, we have shown a novel method for bubble-propelled locomotion on a solid-liquid interface.

Microwave-Rate Soliton Microcombs on a Monolithic $LiNbO_3$ Platform

CNF Project Number: 1997-11
Principal Investigator(s): Qiang Lin
User(s): Yang He, Mingxiao Li, Shixin Xue

Affiliation(s): Department of Electrical and Computer Engineering, University of Rochester

Primary Source(s) of Research Funding: Defense Threat Reduction Agency (HDTRA11810047)

Contact: qiang.lin@rochester.edu, yhe26@ur.rochester.edu,
mingxiao.li@rochester.edu, sxue4@ur.rochester.edu

Primary CNF Tools Used: JEOL JBX9500FS Electron-Beam Lithography System, AJA Ion Mill, SEM

Abstract:

We report microwave-rate soliton microcombs on a chip-scale lithium niobate platform.

Summary of Research:

Coherent microwaves play an important role in many applications, such as wireless communication, radar, imaging, and clocks. Among various approaches, soliton microcombs exhibit great potential for coherent microwave generation due to their good coherence properties in combination with chip-scale design. So far, radio-frequency-rate and microwave-rate soliton microcombs were produced only in silica and silicon nitride platforms [1-4]. Here we report microwave-rate soliton microcombs produced on a chip-scale lithium niobate platform, with repetition rate down to 13.5 GHz.

The devices are fabricated on the 610 nm Z-cut lithium niobate (LN) on insulator wafer. The etching thickness is about 420 nm and the waveguide width of the ring resonator is about 2.2 μm (Figure 1(a) insets). The group velocity dispersion is about -0.037 ps^2/m for the fundamental TE mode family, which is suitable for the soliton generation.

To tune the microwave frequency, we integrate an electro-optic modulator directly onto the comb resonator, as shown in Figure 1(a). Lithium niobate exhibits strong electro-optic Pockels effect, which is ideal for this purpose. For the z-cut comb resonator, we utilize the r_{31} EO term of lithium niobate to tune the quasi-TE comb modes of the resonator. The electrodes are deposited along the ring resonator waveguide with an electrode-waveguide spacing of about 4 μm so as to maintain the high optical Q of the resonator as well as good electro-optic tuning efficiency.

The repetition rate of the soliton microcombs, corresponding to the frequency of the microwave, is determined by the resonator size. By changing the radius of the ring resonator from 100 μm to 1500 μm, we are able to produce soliton microcombs with rep rate from 200 GHz to 13.5 GHz, as shown in Figure 1(b),(c),(d), and (g). As an example, Figure 1(d) and (g) show the spectra of the detected microwave at 19.8 and 13.5 GHz, respectively, which exhibit a signal-to-noise ratio of above 70 dB. The corresponding phase noise spectra are shown in Figure 1(f) and (i), respectively. For the 19.8 GHz signal (Figure 1(e)), the phase noise is about -40 dBc/Hz at 1 kHz, reaches -110 dBc/Hz at 10 kHz, and finally goes below -130 dBc/Hz at 3 MHz. The phase noise for the 13.5 GHz signal (Figure 1(h)) exhibits a similar phase noise level. The low phase noise indicates the high coherence of LN solitons, which is crucial for their applications in microwave photonics.

References:

[1] X. Yi, et al., "Soliton frequency comb at microwave rates in a high-Q silica microresonator," Optica 2, 1078 (2015).

[2] M. Suh and K. Vahala, "Gigahertz-repetition-rate soliton microcombs," Optica 5, 65 (2018).

[3] J. Liu, et al., "Photonic microwave generation in the X-and K-band using integrated soliton microcombs," Nature Photon. 14, 486 (2020).

[4] T. J. Kippenberg, et al., "Dissipative Kerr solitons in optical microresonators," Science 361, 567 (2018).

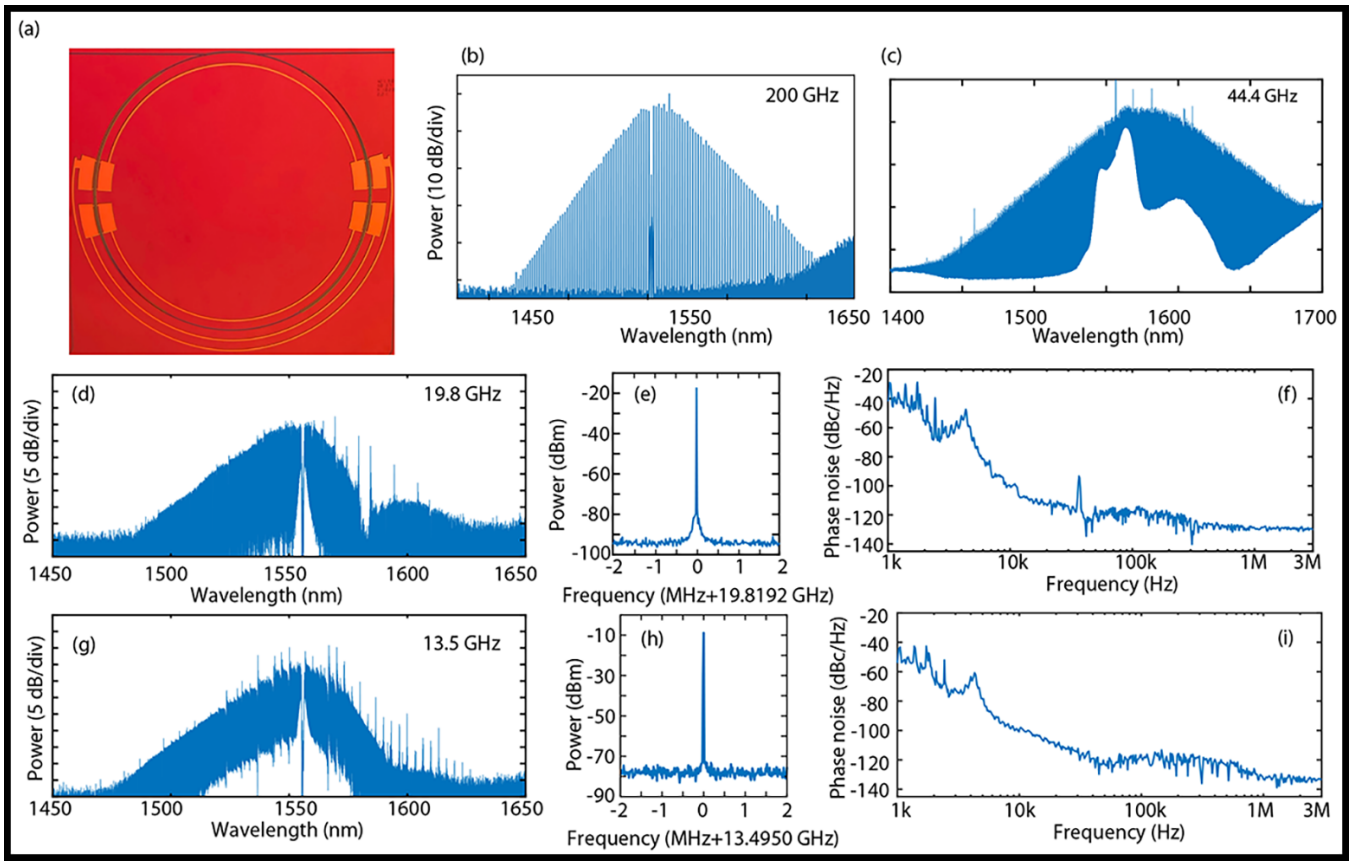

Figure 1: (a) Image of a ring resonator integrated with electrodes. Soliton spectra for LN ring resonators with radii of about 100 μm (b), 450 μm (c), 1020 μm (d), and 1500 μm (g). (e) ((h)) RF signal generated from soliton microcombs in (d) ((g)), and the RBW is 200 Hz. (f) ((i)) Measured phase noise of the RF signal in (e) ((h)).

Lithium Niobate Nanophotonic Resonators for Quantum Simulations

CNF Project Number: 1997-11

Principal Investigator(s): Qiang Lin[1,2]

User(s): Usman A. Javid[1]

Affiliation(s): 1. Institute of Optics, University of Rochester, Rochester NY.; 2. Department of Electrical and Computer Engineering, University of Rochester, Rochester NY.

Primary Source(s) of Research Funding: National Science Foundation (Grants No. EFMA-1641099, ECCS-1810169, and ECCS-1842691); Defense Threat Reduction Agency, Joint Scient and Technology Office for Chemical and Biological defense Grant No. HDTRA11810047; Defense Advanced Research Projects Agency (DARPA) Agreement No. HR00112090012

Contact: qiang.lin@rochester.edu, usman.javid@rochester.edu

Primary CNF Tools Used: JEOL 9500, AJA Ion Mill, SC4500 Evaporator

Abstract:

Integrated photonic devices have enabled momentous progress in development of scalable quantum computing and information processing technologies. These devices are designed to control quantum states of light confined within nanophotonic structures to implement computing protocols. To that end, we demonstrate a frequency domain analog quantum simulator that can simulate a two-dimensional lattice of atoms on the thin-film lithium niobate platform. The device is fabricated at the Cornell NanoScale Facility (CNF).

Summary of Research:

Quantum simulation is one of the primary computational tasks that a quantum computer can perform much more efficiently than a classical computer. Over the past two decades, significant efforts have been made for efficient simulation of condensed matter systems [1]. Integrated photonic devices are well-suited for these applications due to their inherent scalability that can help build large-scale simulation and perform computational tasks [2]. One of the most promising techniques for quantum simulation with light involves photons in distinct frequency modes. Here, we demonstrate frequency domain simulation of the tight-binding model. This model describes a chain of atoms that have nearest neighbor coupling. We implement this by coupling adjacent frequency modes of an optical resonator with electro-optic modulation done using on-chip electrodes. With this system, we demonstrate simulation of a two-dimensional quantum random walk and simulation Bloch oscillations of an electron in the presence of an eternal electric field.

The device used for these simulations is a nanophotonic racetrack resonator fabricated on 600-nm X-cut lithium niobate on insulator (LNOI) wafer. The ring has a width of 1.5 μm and an etch depth of 300 nm. The device is patterned on the wafer using electron-beam-lithography on the JEOL 9500 machine using ZEP520A as the resist mask. After development, the device is etched using argon ion milling on the AJA ion mill achieving a 50% (300 nm) etching depth. The resist is then stripped using standard resist remover chemistry and the chip is prepared for a second electron-beam exposure. This is to pattern electrodes on both sides of the resonator as previously stated. The material is coated with PMMA resist and exposed again to pattern the electrodes. After development, the chip is deposited with a 400 nm layer of gold using an evaporator (SC4500). The electrode pattern is subsequently created by a resist liftoff process in acetone. Figure 1 shows an optical microscope image of a fabricated device at different magnifications.

The simulations are run on the temporal evolution of entangled photon pairs inside the resonator. These photons are also generated within the resonator using spontaneous parametric down conversion (SPDC), a process in which a laser photon annihilates to generate a photon pair [3]. Figure 2 shows evolution of a quantum random walk of the photon pairs. Each pixel in the images represent a resonator mode pair. Photons in one mode of the resonator can scatter to its two adjacent modes using the on-chip electro-optic modulator driven at a microwave frequency matching the resonators mode spacing. This implements a coin toss experiment

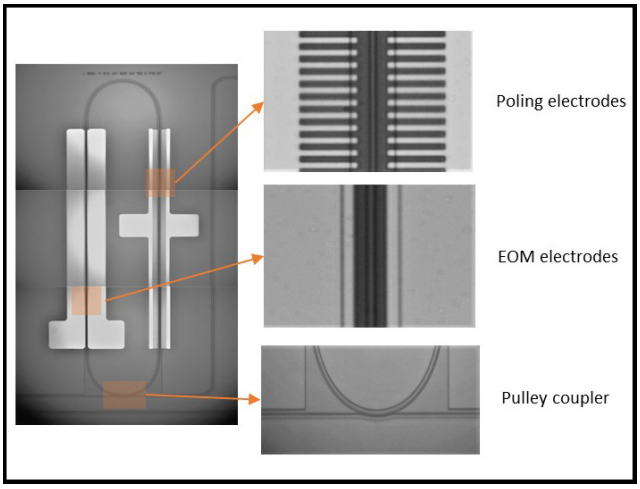

Figure 1: Microscope image of a fabricated device showing different sections of the device. These are: a ring resonator, an evanescently coupled waveguide to couple light into and out of the resonator, and electrodes patterned around the resonator.

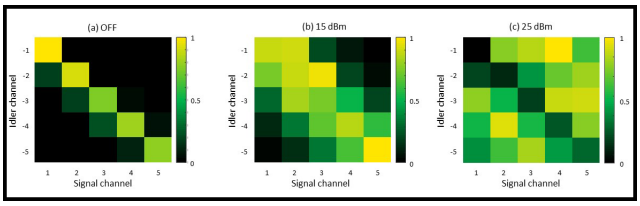

Figure 2: Quantum random walk of the frequency correlation of the photon pairs with (a) no modulation signal, (b) Microwave signal amplitude at 15 dBm and (c) at 25 dBm. The axes indicate the mode number of the resonator and the colormap shows the strength of the correlation at each mode pair. The spread of the correlation with increasing modulation amplitude is a signature of a random walk.

at each mode implementing the random walk. The spread of the random walk increases by increasing the mode coupling using a stronger microwave signal as shown in Figure 2. Another simulation we perform is motion of an electron under an influence of a constant electric field inside a crystal lattice. The electric field is simulated by detuning the microwave signal away from the resonator's mode spacing. This imparts a Bloch-like phase on the coupling [4]. Figure 3 shows the temporal correlation of the photon pairs. We see the correlation turns oscillatory when the microwave signal detuning is introduced with a frequency matching the detuning. These are Bloch oscillations simulated on the temporal correlation of the photon pairs.

Conclusions:

To conclude, we have designed and fabricated an optical quantum simulator based on thin-film lithium niobate. We have demonstrated simulation of quantum random walk and Bloch oscillations. Although these are simple simulations, they demonstrate the ability of this platform for frequency domain computational and simulation tasks. Furthermore, we envision that this demonstration will motivate experiments in quantum simulation on chip-scale architectures.

References:

[1] Reviews of Modern Physics 86.1 (2014): 153.

[2] Science 360.6386 (2018): 285-291.

[3] Reports on Progress in Physics 66.6 (2003): 1009.

[4] Optica 3.9 (2016): 1014-1018.

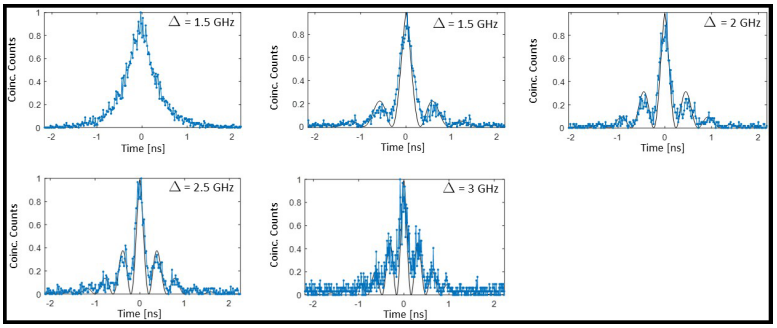

Figure 3: Temporal correlation of the photon pairs at different modulation detunings D. The oscillations occurring at non-zero detuning values are an analog of Bloch oscillations of an electron in the presence of a constant electric field.

Self-Injection-Locked Second-Harmonic Integrated Source

CNF Project Number: 1997-11

Principal Investigator(s): Qiang Lin[1,2]

User(s): Jingwei Ling[1], Jeremy Staffa[2]

Affiliation(s): 1. Department of Electrical and Computer Engineering, University of Rochester, Rochester NY.; 2. Institute of Optics, University of Rochester, Rochester NY

Primary Source(s) of Research Funding: Defense Advanced Research Projects Agency (DARPA) LUMOS program under Agreement No. HR001-20-2-0044, the Defense Threat Reduction Agency-Joint Science and Technology Office for Chemical and Biological Defense (grant No. HDTRA11810047), National Science Foundation (NSF) (ECCS-1810169, ECCS-1842691 and OMA-2138174)

Contact: qiang.lin@rochester.edu, jling8@ur.rochester.edu, jstaffa@ur.rochester.edu

Primary CNF Tools Used: JEOL 9500, AJA Ion Mill, CVC SC4500 Odd-Hour Evaporator, DISCO Dicing Saw

Abstract:

High coherence laser sources are centrally important to the operation of advanced position/navigation/timing systems [1] as well as classical/quantum sensing systems [2]. However, the complexity and size of these bench-top lasers impedes their transition beyond the laboratory. Here, a system on-a-chip that emits high-coherence visible and near-visible light is demonstrated. The devices use a new approach wherein wavelength conversion and coherence increase by self-injection-locking are combined within in a single nonlinear resonator.

Summary of Research:

Optical frequency conversion based upon a quadratic optical nonlinearity is a powerful technology to transfer high coherence laser radiation to new frequencies [3]. Recently, the development of nonlinear photonic integrated circuits (PICs), particularly the on-chip lithium niobate-on-insulator (LNOI) platform [4-8], have boosted nonlinear conversion efficiency while enabling photonic integration with active and passive waveguide elements. However, to achieve high coherence in these systems bench top source lasers have been used.

Here we demonstrate for the first time a hybridly-integrated laser that produces efficient and ultra-coherent near-visible light. The device combines second harmonic generation (SHG) in an LNOI microresonator that also functions to line narrow a DFB pumping laser through self-injection locking (SIL) [9].

The high-*Q* lithium niobate (LN) microresonator and distributed-feedback (DFB) diode laser are facet-to-facet coupled as shown in Figure 1a and b. The LN resonator provides both resonantly-enhanced SHG and feedback to line narrow the DFB pump. For SHG, it is periodically poled to quasi-phase match the resonant pump and up-converted modes. For line narrowing, the high-*Q* mode introduces weak backscattering into the DFB laser to achieve SIL. The pump coherence is readily transferred to the up-converted light, resulting in linewidth narrowing of the frequency-doubled light.

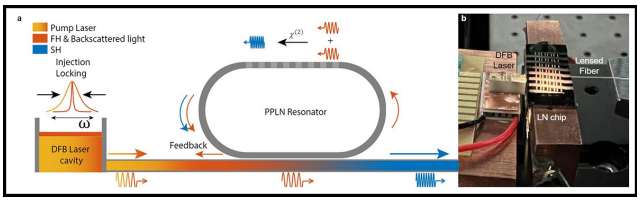

Figure 1: (a) Conceptual diagram of the self-injection locking and second-harmonic generation process. (b) Optical image of the self-injection-locked frequency-doubling chip system.

The race-track LN microresonator device is fabricated on congruent x-cut thin film lithium-niobate-on-insulator (LNOI), with 600 nm LN sitting upon a 4.7 μm silica layer. ZEP-520A resist is used for a first e-beam lithography step (JEOL 9500), followed by 300 nm Ar-ion milling (AJA ion mill) to define the devices. A second e-beam writing step is performed on PMMA resist, and 400 nm electrodes are created using a gold evaporation and lift-off process (CVC SC4500 odd-hour evaporator).

The poling process is similar to previously reported methods [6], but the poling is done after the etching process. The poling uniformity can be observed in Figure 2b. We target SHG of a 1560 nm pump to a near-infrared wavelength near 780 nm.

Maximum conversion occurs at the pump wavelength of 1559.5 nm. By fixing the laser wavelength at this

resonance the SHG output power versus coupled power is measured in Figure 3.

Maximum SHG power is 11.3 mW at a pump power of 44.6 mW, corresponding to a conversion efficiency of about 25%. This conversion efficiency is among the highest reported to date for on-chip LN devices [4,5,7,8]. The measurements are in good agreement with the theory (solid curves), which predicts a maximum conversion efficiency of 28%.

The frequency noise of the self-injection locked pump laser is characterized with a self-heterodyne approach [10] while the noise of SHG light is measured with a conventional homodyne detection setup with quadrature-point locking [11]. The results are shown in Figure 4. The high-offset-frequency pump noise is significantly reduced compared to the free-running DFB laser by over 20 dB, demonstrating the effect of the SIL process. The SHG noise reaches a level of 1600 Hz^2 Hz^{-1} at around 3 MHz offset frequency. These data place the SHG short-term linewidth in the range of 10-30 kHz. Because the SHG frequency noise is fundamentally proportional to the square of the doubled pump noise, the SHG frequency noise must therefore be 4× larger (6 dB) than the pump frequency noise.

Conclusions and Future Steps:

We have demonstrated a highly-efficient, chip-scale laser that produces high-coherence light by combining SIL and SHG within a single high-*Q* nonlinear resonator. A SH linewidth as narrow as 10 kHz is achieved by suppression of pump frequency noise. On-chip converted power over 2 mW is obtained in a hybrid-integrated design. An external pump laser yields a maximum conversion efficiency over 25% and maximum SHG power of 11.3 mW. These measurements suggest much higher integrated device performance will be possible by replacing this hybrid design with a heterogeneously-integrated device that features low pump to LN resonator coupling loss. This approach can be applied to other optical frequency conversion processes such as optical parametric oscillation for frequency down-conversion, and third-harmonic generation. Moreover, the on-chip LN platform enables integration with electro-optic components for further functional enhancement.

Acknowledgements:

Thank you to Heming Wang, Boqiang Shen, Lue Wu, Zhiquan Yuan, and Bohan Li from Professor Kerry J. Vahala's group Caltech and to Lin Chang from John E. Bower's group at UCSB for their essential collaborative work on this project, as well as to Usman A. Javid, Raymond Lopez-Rios, Mingxiao Li, and Yang He from Qiang Lin's group.

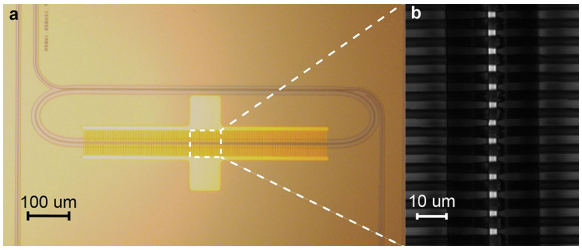

Figure 2: (a) Optical image of the PPLN racetrack resonator. Dashed box gives region of grating imaged in panel b. (b) 2nd-harmonic confocal microscope image of the periodically poled waveguide section showing the uniformity of periodic poling.

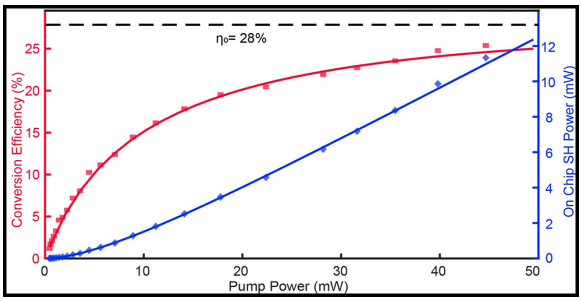

Figure 3: SHG power (blue diamonds) and conversion efficiency (red squares) as a function of the pump power on chip.

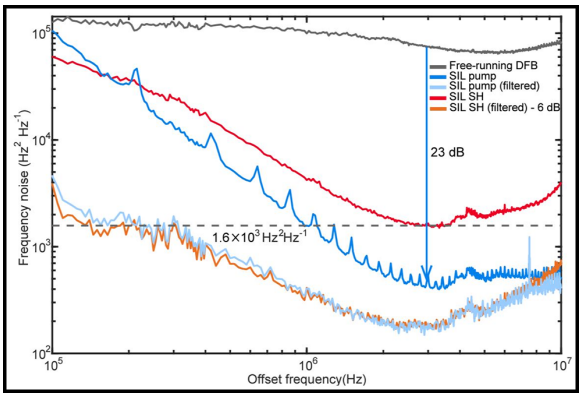

Figure 4: Recorded frequency noise spectrum. Grey, blue and red traces show the frequency noise spectrum of the free-running DFB laser, SIL pump laser, and SIL frequency-doubled light, respectively. The light blue trace and the orange traces show the frequency noise of the pump light and 6 dB down-shifted SHG light when frequency jumping noise is removed from data.

References:

[1] 2014 ISISS, 1-4 (IEEE, 2014).
[2] Reviews of modern physics 89, 035002 (2017).
[3] Physics today 47, 25-33 (1994).
[4] Optica 5, 1438-1441 (2018).
[5] Optica 6, 1455-1460 (2019).
[6] Optics Express 28, 19669-19682 (2020).
[7] arXiv:2102.05617 (2021).
[8] Laser & Photonics Reviews 15, 2100091 (2021).
[9] Optics letters 12, 876-878 (1987).
[10] Journal of Lightwave Technology 26, 30483055 (2008).
[11] Nature Photonics 6, 369-373 (2012).
[12] https://arxiv.org/abs/2207.03071.

Two-Dimensional TMD as a Single Photon Source and a Quantum Sensor

CNF Project Number: 2126-12

Principal Investigator(s): Gregory Fuchs, David Muller

User(s): Jaehong Choi

Affiliation(s): Applied and Engineering Physics, Cornell University

Primary Source(s) of Research Funding: Air Force Office of Scientific Research Multidisciplinary Research Program of the University Research Initiative (AFOSR MURI)

Contact: gdf9@cornell.edu, jc3452@cornell.edu

Primary CNF Tools Used: JEOL 6300, Oxford COBRA, 5X g-line Stepper, Wire Bonder, DISCO Dicing Saw, SC4500 Odd-Hour Evaporator, AFM – Veeco Icon, Zeiss Supra SEM, Zeiss Ultra SEM

Abstract:

Electronic and optical properties of two-dimensional transition metal dichalcogenides (2D TMDs) are readily tuned by strain and external fields due to their atomic thickness. Tensile strain is known to confine excitons and create single photon emitters in 2D TMDs. We are working toward using electron microscopy to directly measure the strain to better understand the strain confinement of excitons. Also, the exciton emission energy in TMDs can be tuned with an external field and we tried using an interlayer exciton in homobilayer tungsten diselenide (WSe_2) as a quantum sensor for the polarization change in ferroelectric materials in vicinity.

Summary of Research:

Single photon emitters with high brightness and purity are key components for quantum communication and information technologies. Monolayer transition metal dichalcogenides (TMDs) have been established as promising sources of single photon emitters, and a recent study showed that the hybridization of strain-localized excitonic state and localized defect state induces single photon emission in monolayer WSe_2 [1]. To better understand the interplay among strain, exciton, and defect, it is crucial to have a clear picture of strain localization of excitons.

Electron microscopy is promising for the direct measurement and quantification of strain responsible for single photon emission in monolayer WSe_2. We were able to create single photon emitters by stacking monolayer WSe_2 on top of a nanorod-gap array. Monolayer WSe_2 is folded into nanogaps (90 nm) between nanorods, and the high strain point at the wrinkle confines excitons to create single photon emitters with high purity (Fig.1).

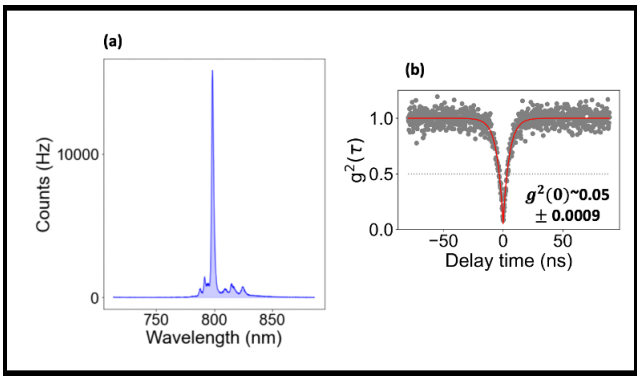

Figure 1: (a) Spectrum from the fold at the nanogap site. We observed an emission peak with a narrow linewidth, which implies a strong exciton confinement. (b) Time correlation measurement of the emitter created at the nanogap. We observed the antibunching with $g^2(0)$ value ~ 0.05, which unambiguously shows the high purity of the single photon emitter.

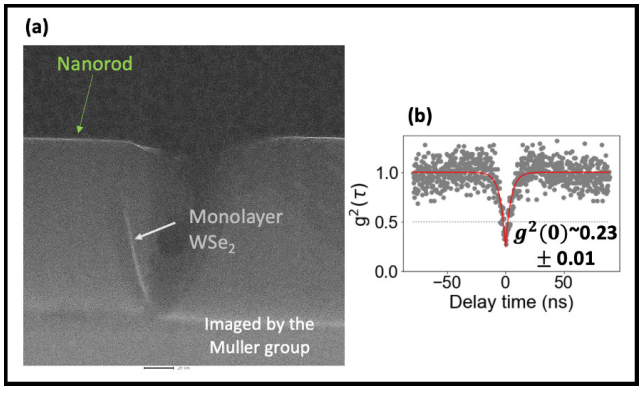

Figure 2: (a) TEM image of a nanogap site with the sharply folded monolayer WSe_2. (b) Time correlation measurement of a quantum emitter created at the sharp fold in (a). $g^2(0)$ is 0.23, which shows a single photon nature of the emitter.

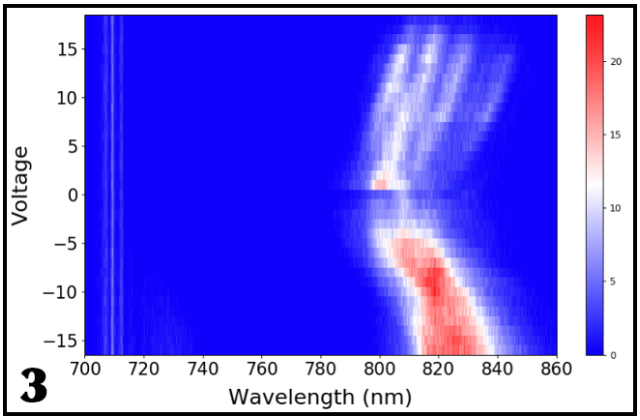

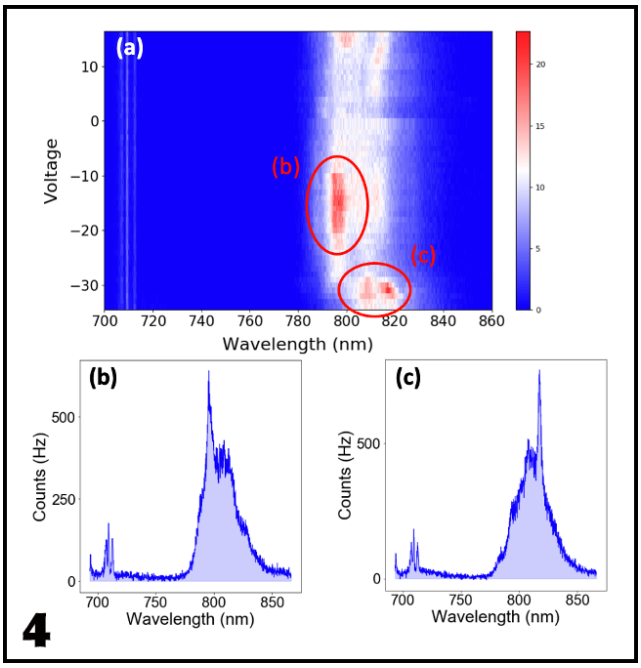

Figure 3, top: Photoluminescence modulated by V_{gb}. V_{tg} is adjacent to 2L-WSe_2, and it directly pumps charge carriers into 2L-WSe. We can see a clear doping effect. Figure 4, bottom: (a) Photoluminescence modulated by V_{tg}. V_{tg} is adjacent to BTO, and it switches the polarization in BTO. (b) and (c) show the change in population proportion of Λ – K and Λ – Γ indirect excitons under the polarization switching in BTO.

To better understand the strain confinement of excitons at the wrinkle apex, Transmission electron microscopy (TEM) imaging was attempted on the nanogap sites in collaboration with the Muller group at Cornell University. By TEM imaging, we confirmed that the high strain achieves a strong confinement of a single exciton. Anti-bunched quantum emitters were observed at sharp folds (Figure 2). At relatively flat and gradual folds, the strain was expected to be small. This resulted in creation of multiple emitters.

One of the pre-requisites for the strain analysis is that the atom columns in the material should be aligned with the beam axis. However, monolayer WSe_2 is thin and flimsy. We were unable to align the beam axis with the atom columns in WSe_2. To allow the strain analysis, it is important to have a support layer that gives a structural support so that the curvature of wrinkle is uniform throughout a monolayer WSe_2.

The next step is using a thick support layer underneath monolayer WSe_2 which will enable the strain analysis.

2D TMDs can be used as quantum sensors as well due to their sensitivity to their immediate environment. In homobilayer (2L) WSe_2, the Bloch states of valleys at each point in the momentum space have different orbital compositions, and this makes wavefunctions reside at different positions in real space and form interlayer exciton (2). Due to the spatial distance between an electron and a hole, interlayer excitons possess a dipole moment in an out-of-plane direction. This dipole moment can be modulated by an external field (2-4), so an interlayer exciton can be used to sense a polarization-induced field in ferroelectric materials in vicinity (4,5).

We studied the optical property change in 2L-WSe_2 in response to the polarization change in ferroelectric BTO in 2L-WSe_2/BTO hybrid heterostructure. A gate voltage was applied to modulate the polarization in BTO *in situ*. We observed that the spectral change in response to the polarization switching. When the bottom gate (V_{bg}), which is adjacent to 2L-WSe, was modulated, we observed a clear doping effect (Figure 3). When we modulated the top gate (V_{tg}), which is adjacent to BTO, the population proportion of indirect Λ – *K* and Λ – Γ excitons was changed at different voltage values (Figure 4). We wanted to see the hysteresis, but BTO started leaking at higher voltages, so the higher range voltage sweep was not possible. Next step is using a much thicker BTO membrane to minimize the leaking and study the photoluminescence change in WSe_2 when the polarization switches in BTO.

Conclusions and Future Steps:

Deterministic activation of single photon emitters is crucial for quantum technology application, and a better understanding of exciton confinement that leads to single photon emission is required. Electron microscopy on the strained monolayer WSe_2 will enable us to directly measure and quantify the strain responsible for single photon emission. Homobilayer WSe_2 was used to sense the polarization change in ferroelectric BTO. Interlayer exciton emission energy and spectral composition are expected to be modulated by the polarization-induced field in ferroelectric BTO. Thick BTO will be used to minimize the leaking and allow a wide range of voltage sweep.

References:

[1] Linhart, L., et al, Phy. Rev. Lett. 123, 146401 (2019).
[2] Huang, Z., et al, Phy. Rev. Lett. B 105, L041409 (2022).
[3] Altaiary, M., et al, Nano Lett. 22, 5, 1829-1835 (2022).
[4] Wang, Z., et al, Nano Lett. 18, 1, 137-143 (2018).
[5] Li, T., et al., Nano Lett. 17, 922.927 (2017).
[6] Li, P., et al., Adv. Funct. Mater. 2201359 (2022).

Sputtered Oxide Integrated Photonics

CNF Project Number: 2297-14
Principal Investigator(s): Amy Foster
User(s): Neil MacFarlane, David Irvine, Aaron Schreyer-Miller

Affiliation(s): Electrical and Computer Engineering Department, Johns Hopkins University

Primary Source(s) of Research Funding: Viavi Solutions, Inc.

Contact: amy.foster@jhu.edu, nmacfar2@jhu.edu, dirvine4@jhu.edu, aschrey1@jh.edu

Primary CNF Tools Used: Oxford 100 Etcher, Oxford PECVD, PT770 Etcher, Zeiss SEM, JEOL 6300

Abstract:

Niobium tantalum dioxide (NbTaOx) is a material developed by collaborator Viavi Solutions. NbTaOx films are deposited using low temperature pulsed DC magnetron sputtering. We have been investigating NbTaOx as a new platform for both linear and nonlinear integrated photonics. We have fabricated ring resonators with quality factors as high as 858,000 corresponding to propagation losses as low as 0.47 dB/cm. Using these high-quality ring resonators, we have also investigated the nonlinear capabilities of the NbTaOx platform and demonstrated optical parametric oscillation.

Summary of Research:

NbTaOx is a high linear refractive index material, with a linear refractive index that is about 10% higher than that of silicon nitride at a wavelength of 1550 nm. This high refractive index results in a high index contrast with respect to the typical silicon dioxide (SiO_2) cladding material. The higher contrast produces highly confined waveguide modes, allows for tighter waveguide bending radii, and enhanced nonlinear interactions.

Our waveguides were dispersion engineered for broadband nonlinear interactions, which require anomalous dispersion. Through design and simulation, it was found that the required film thickness for anomalous waveguide dispersion at C-band wavelengths was about 800 nm. Because these films are deposited using a sputtering deposition technique, depositing 800 nm thick films does not come with the same challenges associated with depositing thick Si_3N_4 films like stress induced film cracking. The waveguide devices were patterned using electron-beam lithography. We used a chromium etch mask was dry etched using the CNF PT770 etcher. The NbTaOx film was then etched using the CNF Oxford 100 etcher. The devices were clad with SiO_2 and diced into individual chips. SEM images of waveguide cross section and side wall are shown in Figure 1.

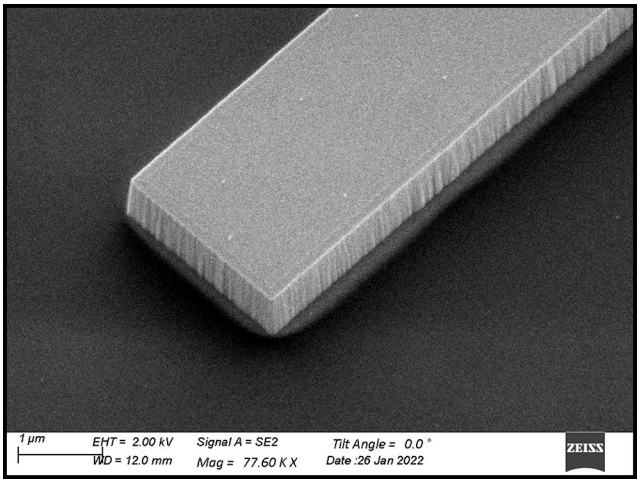

Figure 1: SEM image of NbTaOx waveguide sidewall.

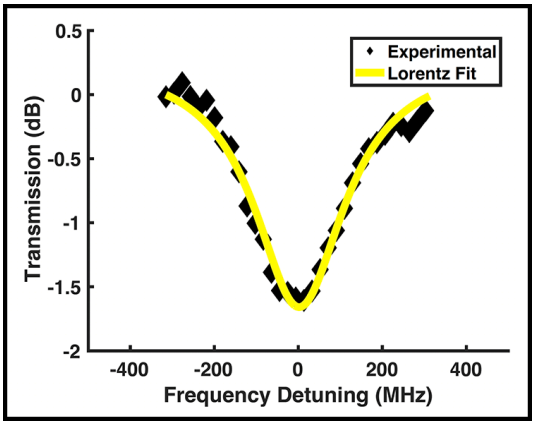

Figure 2: Individual resonance fit to a Lorentzian function.

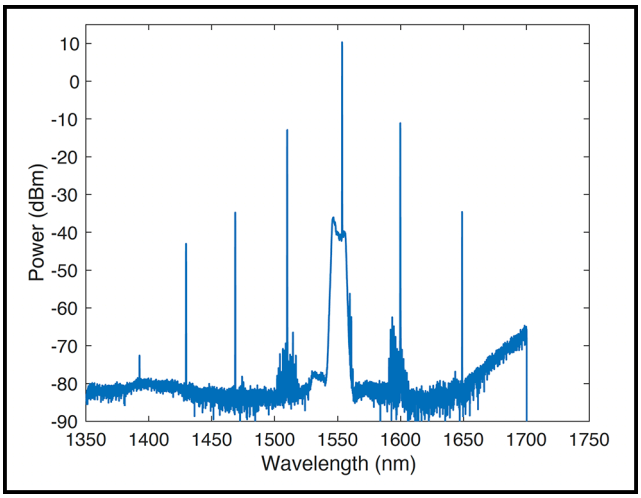

Figure 3: a) Spectrum of optical parametric oscillator generated in NbTaOx ring resonator.

The linear transmission of the waveguides was measured as a function of propagation length ranging from 0.6 cm to 2.8 cm. The losses varied from 0.56 dB/cm to 0.99 dB/cm for waveguide widths of 3.5, 2.5, and 1.5 µm.

We also extracted propagation losses by measuring the spectrum of high-quality ring resonators. The resonator spectrum for the 2.5 µm waveguide width are shown in Figure 2. The highest quality factor resonance was found to be 858,000, which corresponds to linear propagation losses of 0.47 dB/cm.

Using the high-quality ring resonator, we investigated the nonlinear capabilities of the NbTaOx films by generating optical parametric oscillation. The spectrum of the frequency comb is shown in Figure 3. We couple a high-power pump on-chip and slowly tune its wavelength to one of the resonance wavelengths of the device. Once the round-trip optical parametric gain via four-wave mixing within the ring exceeds the round-trip losses, the four-wave mixing process spontaneously generates single and idler sidebands of an optical parametric oscillator shown in Figure 3.

Conclusions and Future Work:

Our initial investigation into the NbTaOx films indicated that they are a high-quality platform for both linear and nonlinear integrated photonics. These results are the first demonstration of frequency comb generation in this material platform. Some of our immediate future work is to lower the oscillation threshold and to fill in more comb lines of the Kerr frequency comb. This will be done through a combination of fabrication optimization as well as decreasing the size of the ring resonators. In addition to this, we plan to investigate the minimum bending radius capabilities of this platform and use this information to demonstrate dense and complex linear integrated photonic circuits.

Development of Single and Double Layer Anti-Reflective Coatings for Astronomical Instruments

CNF Project Number: 2458-16

Principal Investigator(s): Gordon Stacey[1]

User(s): Bugao Zou[2]

Affiliation(s): 1. Department of Astronomy,
2. Department of Applied and Engineering Physics, Cornell University

Primary Source(s) of Research Funding: NASA Grant NNX16AC72G

Contact: stacey@cornell.edu, bz332@cornell.edu

Primary CNF Tools Used: Oxford Plasma Enhanced Chemical Vapor Deposition, Anatech Resist Strip, Oxford 81/82/100 Etchers, Manual Resist Spinners, Resist Hot Strip Bath, Plasma-Therm Deep Silicon Etcher, ASML 300C DUV Stepper, JEOL JBX 9500FS Electron-Beam Lithography System

Abstract:

The Epoch of Reionization Spectrometer (EoR-Spec) is one of the instrument modules to be installed in the Prime-Cam receiver of the Fred Young Submillimeter Telescope (FYST). This six-meter aperture telescope will be built on Cerro Chajnantor in the Atacama Desert in Chile. EoR-Spec is designed to probe early star-forming regions by measuring the [CII] fine-structure lines between redshift z = 3.5 and z = 8 using the line intensity mapping technique. The module is equipped with a scanning Fabry-Perot interferometer (FPI) to achieve the spectral resolving power of about RP = 100. The FPI consists of two parallel and identical, highly reflective mirrors, forming a resonating cavity called etalon. The mirrors are silicon-based and patterned with double-layer metamaterial anti-reflection coatings (ARC) on one side and metal mesh reflectors on the other. The double-layer ARCs ensure a low reflectance at one substrate surface and help tailor the reflectance profile over the FPI bandwidth. Here we present the design and fabrication processes of silicon mirrors for the FPI.

Summary of Research:

The goal of the project is to develop microfabricated, silicon-substrate-based mirrors for use in cryogenic Fabry-Perot Interferometers for astronomical instruments in the mid-infrared to sub-mm/mm wavelength regimes. The mirrors consist of high-purity, float-zone, 500-µm-thick silicon wafers that are lithographically patterned with frequency-selective, gold mesh reflectors. Due to the high index of refraction of silicon, the other side of the mirror must be patterned with an ARC to achieve the broadband capability and mitigate contaminating resonances from the silicon surface [1,2].

The deep reactive-ion etching (DRIE) technique was employed to etch bulk silicon. It involves the Bosch processes which use alternate SF_6 and C_4F_8 gas exposures to produce near-vertical sidewalls and high aspect ratio features [3]. The fabrication recipe of the double-layer ARC structure is outlined in Figure 1.

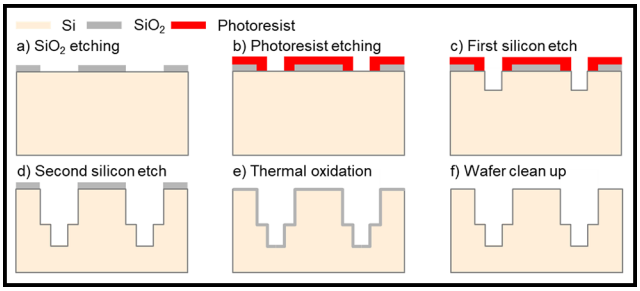

Figure 1: Key fabrication processes of the double-layer ARC structure.

Before performing DRIE silicon etches, we patterned SiO_2 and photoresist grids as two silicon etch masks, defining the upper and lower geometry. Process (a) comprises three individual steps.

The SiO_2 layer was first deposited onto the wafer by an Oxford plasma-enhanced chemical vapor deposition (PECVD) machine. Another layer of UV photoresist was then printed above the SiO_2 using an ASML PAS 5500/300C DUV Wafer Stepper with a resolution of 0.2 μm, serving as the oxide etch mask. A final oxide etch in an Oxford inductively coupled plasma (ICP) dielectric etcher with O_2 and CHF_3 gases transferred the grid pattern from the photoresist to the SiO_2 layer. The photoresist residue was removed further in an O_2 asher. The other photoresist silicon etch mask was then spun and exposed by the same stepper mentioned before, shown in process (b).

After a short descum and seasoning process, we proceeded to do the first silicon etch using a Plasma-Therm DRIE deep silicon etcher. When the target depth was reached, the wafer was cleaned with an O_2 plasma for half an hour at 3000 W to remove the photoresist and C_4F_8 related passivation residue. Then the second silicon etch was carried out, which constructed the upper ARC layer and pushed the lower ARC layer further down to the designated depths.

To further improve the morphology of the etched surfaces, we adopted a thermal oxidation and a clean-up process. We grew a sacrificial layer of thermal SiO_2 of about 1.1 μm thickness using water vapors at 1200°C for 100 mins in a furnace and then removed it by a hydrofluoric acid (HF) bath. The growth of the thermal SiO_2 layer and undercuts caused by previous etching processes widened the hole structure on both layers. Therefore, we shrank the dimensions on the mask designs by 1 to 2 μm accordingly to compensate for it. A scanning electron microscope (SEM) images of the double-layer ARC structure are shown in Figure 2.

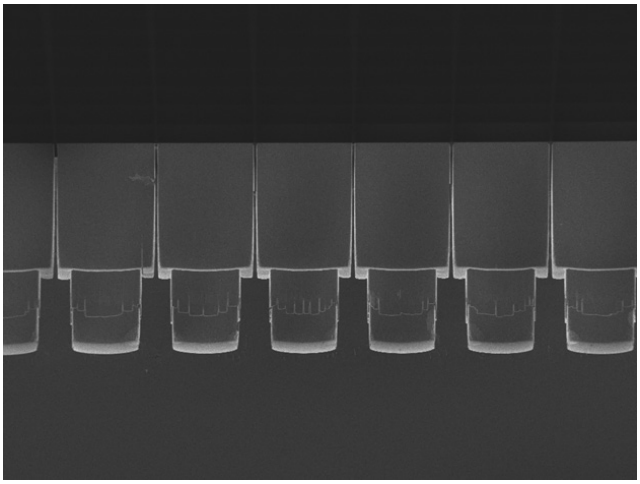

Figure 2: An SEM image showing the two-layer structure of anti-reflection coatings.

After constructing the double-layer ARC structure on one side of the silicon wafer, a layer of 2 μm photoresist was spun and baked on top of it to protect it from scratches and dust. Standard electron beam lithography, metal evaporation, and lift-off technologies were used to pattern the metal mesh structure on the other side. We coated the standard electron beam resist PMMA on the wafer and exposed it in a JEOL JBX 9500FS electron-beam lithography system with a maximum resolution of 6 nm. The wafer was then descumed and mounted inside a CVC SC4500 e-gun evaporation system where a 10 nm chromium adhesion layer and a 100 nm gold layer were evaporated. Afterward, we soaked the wafer into a Microposit 1165 remover bath heated to 80°C to lift the gold-coated PMMA layer off.

Conclusions and Future Steps:

In the past year, we have refined our past recipes with electron-beam lithography to achieve better resolution. We have demonstrated our ability to fabricate double-layer ARCs for different wavelengths and metal meshes with different feature sizes. We also published a new paper [4] about the design and characterization of the silicon mirrors in SPIE.

Our next steps are to better characterize our etched geometries and improve our metamaterial ARCs using Fourier transform spectrometers, and then use the results to iterate on our fabrication design.

References:

[1] Cothard, N., Choi, S., Duell, C., et al. The Design of the CCAT-prime Epoch of Reionization Spectrometer Instrument. J Low Temp Phys (2020). https://doi.org/10.1007/s10909-019-02297-1.

[2] N.F. Cothard, M. Abe, T. Nikola, G.J. Stacey, G. Cortes-Medellin, P.A. Gallardo, B.J. Koopman, M.D. Niemack, S.C. Parshley, E.M. Vavagiakis, K. Vetter, "Optimizing the efficiency of Fabry-Perot interferometers with silicon-substrate mirrors," Advances in Optical and Mechanical Technologies for Telescopes and Instrumentation III (2018).

[3] Chattopadhyay G, Reck T, Lee C, et al. Micromachined packaging for terahertz systems [J]. Proceedings of the IEEE, 2017, 105(6): 1139-1150.

[4] Zou B, Choi S K, Cothard N F, et al. CCAT-prime: The Design and Characterization of the Silicon Mirrors for the Fabry-Perot Interferometer in the Epoch of Reionization Spectrometer [J]. arXiv preprint arXiv:2207.08318, 2022.

Fabrication Strategy for Large-Area Meta-Optic Elements Exceeding the Exposure Size Limits of Lithography Tools

CNF Project Number: 2471-16

Principal Investigator(s): Professor Federico Capasso

User(s): Joon-Suh Park

Affiliation(s): John A. Paulson School of Engineering and Applied Sciences, Harvard University

Primary Source(s) of Research Funding: Defense Advanced Research Projects Agency (Grant no. HR00111810001)

Contact: capasso@seas.harvard.edu, parkj@g.harvard.edu
Website: https://www.seas.harvard.edu/capasso

Primary CNF Tools Used: Heidelberg Mask Writer - DWL2000, HamaTech Mask Chrome Etch 1, ASML 300C DUV Stepper, Gamma Automatic Coat-Develop Tool, CHA Mark 50 E-beam Evaporator, Plasma-Therm Dual Chamber 770, Oxford 81, Oxford 82, Oxford 100, P10 Profilometer, Disco Dicing Saw, Zeiss Ultra SEM

Abstract:

We show a fabrication path for creating a mass-producible metalens that works at visible wavelength, exceeding the inherent exposure size limit of the currently available lithography tools. We use the rotational symmetry of the metalens to save the number of required photomasks (reticles) for cost-efficiency, and therefore create a 10 cm diameter metalens from seven reticles with 2 cm × 2 cm exposure areas at wafer-scale, respectively.

Summary of Research:

For imaging at low-light conditions, one needs to increase the imaging optic's diameter to take in more light. However, simply increasing the diameter of an imaging lens faces two important tradeoffs in their application: the increase in aberration and the weight of the optic itself.

For applications in aerial drones or satellite imaging systems, where the payload is one of the primary concerns, simply increasing the lens diameter is therefore not a desirable option.

Here, we show our process development in creating a 10 cm diameter, ultrathin metasurface lens (metalens) consisting of 18.7 billion nanostructures with DUV projection lithography, which is more than 40 times thinner and 16.5 times lighter than a refractive lens with similar optical power.

A metasurface optical element consists of sub-wavelength spaced structures on a two-dimensional surface that alters the incoming light and produce a designed outgoing wavefront. Each subwavelength structure in the metasurface locally change the transmitted light's amplitude, phase, polarization, or wavenumber in a way that one can design the combined wavefront to create optical functions, such as metasurface lenses (metalenses) [1], orbital angular momentum beam generators [2], polarization-dependent holograms [3], or Jones-matrix holograms [4].

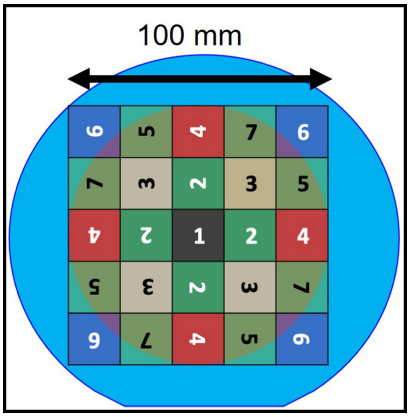

Figure 1: 10 cm diameter metalens fabrication strategy: The metalens is divided into 25 sections of 20 mm × 20 mm area, respectively. Only seven reticles are needed to expose the whole metalens by exploiting the rotational symmetry of the metalens.

For a metasurface optical element to function at a visible wavelength, the constituent sub-wavelength structures are required be in the order of few tens to hundreds of nanometers to avoid efficiency losses by high-order diffraction. Fabrication of such a metasurface therefore requires high-resolution lithography process such as electron-beam lithography or DUV lithography to be able to resolve such features. In the recent years, we have shown that a mass-production of metalenses with 1 cm in diameter and diffraction-limited performing at visible wavelength is possible with DUV lithography [5].

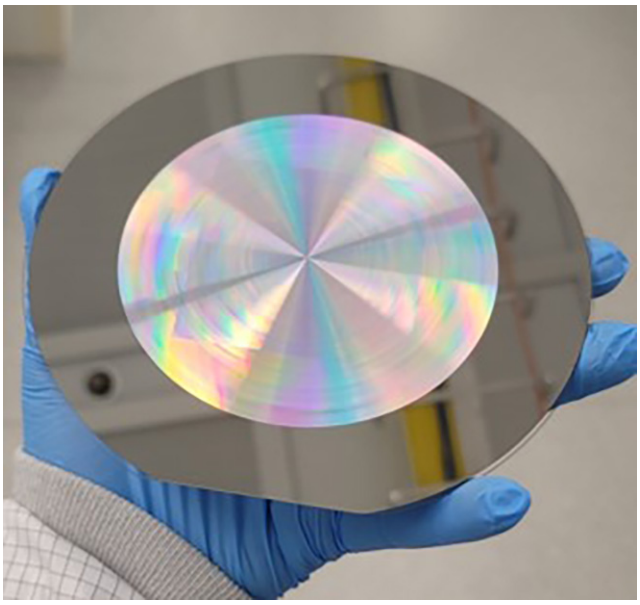

Figure 2: Photograph of the 10 cm diameter metalens' photoresist pattern on an aluminum coated 150 mm fused silica wafer.

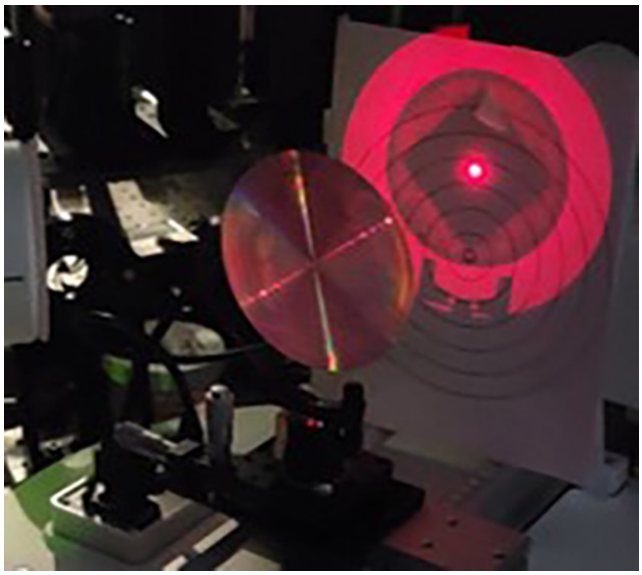

Figure 3: Photograph of the 10 cm diameter metalens focusing collimated He-Ne laser (633 nm).

To create a 10 cm diameter metalens, however, one faces size limitations restricted by the fabrication methods. With the conventional stepper lithography tools having maximum exposure area of 32 mm × 22 mm on a wafer per die, the stepper restricts the maximum diameter of a circular aperture metalens to 22 mm. To overcome such limitations, we divide the metalens into 25 sections, each consisting of 20 mm × 20 mm area.

For cost-effective fabrication, we use the rotation symmetry of the metalens to reduce the number of required reticles (Figure 1). As the metalens is rotationally symmetric, we can expose the whole 10 cm metalens with only seven reticles, instead of 25, if we rotate the wafer 90, 180, 270 degrees to expose each section, respectively, with global alignment process that has alignment error less than an order of magnitude smaller than the metalens' target wavelength. Figure 2 shows the result of DUV (248 nm, KrF) projection lithography of 10 cm diameter metalens on an aluminum coated 150 mm fused silica wafer. DUV lithography was performed with DUV-24P ARC layer and UVN2300 negative DUV resist.

Figure 3 shows the fabricated 10 cm diameter, all-glass metalens, focusing a collimated visible (λ = 633 nm) beam. The reticles for the central section (sections 1, 2, and 3 in Figure 1) were fabricated by an industry-grade photomask company, and outer sections 4-7 were fabricated with CNF tools (Heidelberg Mask Writer - DWL2000). As the reticles are of different quality, one can see the diffraction efficiency difference between the fields visible in the transmitted collimated beam at the focal plane of the metalens. Such difference can be resolved if all reticles are fabricated from the same source.

As the whole lens is fabricated with CMOS foundry compatible process, the shown metalens is mass-producible by IC chip companies. Detailed results and analysis are being prepared for peer-reviewed publication.

Conclusions and Future Steps:

We demonstrated a proof-of-concept fabrication of mass-manufacturable, all-glass 10 cm diameter metalens, capable of focusing monochromatic visible wavelength. We are further investigating on finding a path toward a broadband, achromatic, and large diameter metalens.

References:

[1] M. Khorasaninejad, W.T. Chen, R.C. Devlin, J. Oh, A.Y. Zhu, and F. Capasso, "Metalenses at visible wavelengths: Diffraction-limited focusing and subwavelength resolution imaging," Science 352, 1190 (2016).

[2] H. Sroor, Y.-W. Huang, B. Sephton, D. Naidoo, A. Valles, V. Ginis, C.-W. Qiu, A. Ambrosio, F. Capasso, and A. Forbes, "High-purity orbital angular momentum states from a visible metasurface laser," Nature Photonics 14, pp. 498-503 (2020).

[3] J. P. Balthasar Mueller, N.A. Rubin, R.C. Devlin, B. Groever, and F. Capasso, "Metasurface Polarization Optics: Independent Phase Control of Arbitrary Orthogonal States of Polarization," Physical Review Letters 118, 11, pp. 113901 (2017).

[4] N.A. Rubin, A. Zaidi, A.H. Dorrah, Z. Shi, and F. Capasso, "Jones matrix holography with metasurfaces." Science Advances 7, 33, eabg7488 (2021).

[5] J.-S. Park, S. Zhang, A. She, W.T. Chen, P. Lin, K.M.A. Yousef, J.-X. Cheng, and F. Capasso, "All-Glass, Large Metalens at Visible Wavelength Using Deep-Ultraviolet Projection Lithography," Nano Letters 19, 12, 8673-8682 (2019).

Prototype Photolithography for Multilayer Diffractive Lenses

CNF Project Number: 2472-16

Principal Investigator(s): Gennady Shvets

User(s): Giovanni Sartorello

Affiliation(s): School of Applied and Engineering Physics, Cornell University

Primary Source(s) of Research Funding: National Cancer Institute (award number R21 CA251052), National Institute of General Medical Sciences (award number R21 GM138947) of the National Institutes of Health

Contact: gs656@cornell.edu, gs664@cornell.edu

Primary CNF Tools Used: Heidelberg Mask Writer - DWL2000, SÜSS MicroTec Gamma Cluster Tool, ASML PAS 5500/300C DUV Stepper, Oxford PlasmaLab 100 ICP Etcher

Abstract:

We test a photolithography process to be used to fabricate large scale multilevel diffractive optics for use in thin optical systems.

Summary of Research:

Conventional optical systems, based on refractive lenses, must be of a certain thickness to perform their function. Optical requirements sometimes make such system impractically large and heavy. Solutions for some applications have included Fresnel lenses and gradient-index optics, and newer and intensively studied approaches include negative-index metamaterials, resonator-based metalenses and multilevel diffractive optics. The latter are ultrathin (few-wavelength) optical elements that use diffraction of radially symmetric elements, rings of various heights, to bend light. They can have the same imaging performance as metalenses while not being much thicker, and being faster and cheaper to fabricate [1]. Multilevel optics can be fabricated by repeated photolithography and etching steps with a sequence of patterns on the same wafer, whose superposition produces the final multilevel structure. After N steps, the MLD device has 2^N levels [2].

As a proof of concept, single-level samples to explore this process were fabricated at CNF on a silica wafer using the ASML DUV stepper with masks made with the Heidelberg Mask Writer - DWL2000. Each sample is about 1.5 mm across and contains circular features ranging from several dozen micrometers down to less than a micrometer. The wafer was coated in antireflective coating (ARC) and UV210 resist, exposed, processed

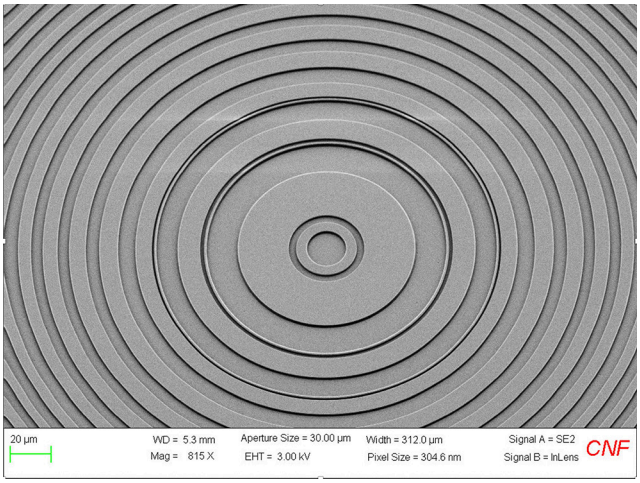

Figure 1: 35° SEM view of the center of one of the fabricated structures.

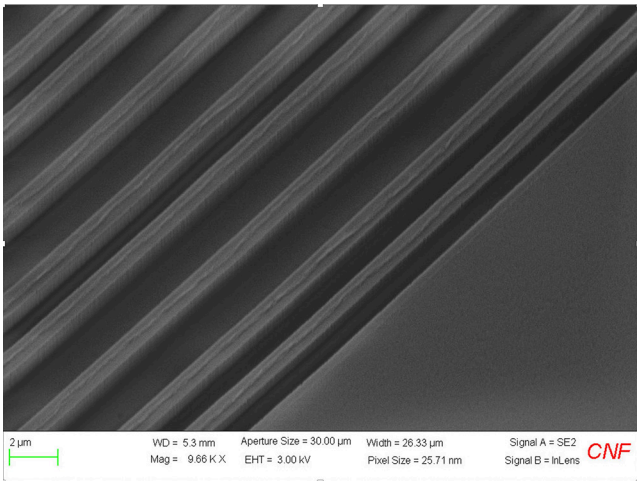

Figure 2: 35° SEM view of the edge of one of the fabricated structures.

in the Gamma tool and, after ARC removal, etched in the Oxford 100 etcher with a slow, consistent etching recipe. The resulting samples have well-defined edges both near the center, where features are largest (Figure 1), and near the edges, where they are finest (Figure 2), although the smallest (sub-micron) features are shallower than the design. By using a photolithographic process, the individual samples can be large (eventually, only limited by wafer size) and dozens can be made on a single wafer with little increase in overall fabrication time.

Conclusions and Future Steps:

The process has been proven suitable for the first step in the fabrication of a MLD system. Future tests would involve the fabrication of the remaining levels by repeating the process for 2-7 steps with a different exposed pattern each, using markers for alignment between layers. Tweaking the resist type and deposition method will be necessary to prevent pooling as the levels become deeper, and the etching method must be refined to achieve uniform depth even for the smallest features.

References:

[1] Banerji, S., Meem, M., Majumder, A., Vasquez, F. G., Sensale-Rodriguez, B., and Menon, R. (2019). Imaging with flat optics: metalenses or diffractive lenses? Optica, 6(6), 805. https://doi.org/10.1364/optica.6.000805.

[2] Saha, S. C., Li, C., Ma, Y., Grant, J. P., and Cumming, D. R. S. (2013). Fabrication of Multilevel Silicon Diffractive Lens at Terahertz Frequency. IEEE Transactions on Terahertz Science and Technology, 3(4), 479-485. https://doi.org/10.1109/TTHZ.2013.2251929.

Integrated Optical Gyroscope with Inverse Weak Value Amplification

CNF Project Number: 2524-17

Principal Investigator(s): Jaime Cardenas

User(s): Meiting Song

Affiliation(s): The Institute of Optics, University of Rochester

Primary Source(s) of Research Funding: Leonardo DRS
Center for Emerging and Innovative Science (CEIS)

Contact: jaime.cardenas@rochester.edu, msong17@ur.rochester.edu
Website: https://www.hajim.rochester.edu/optics/cardenas/

Primary CNF Tools Used: ASML Stepper, Oxford 100 Etcher,
Oxford PECVD, LPCVD Nitride, DISCO Dicing Saw, XeF_2 Etcher

Abstract:

Weak value amplification has been demonstrated to enhance interferometric signals. We apply inverse weak value amplification to an integrated Sagnac interferometer gyroscope and demonstrate rotation measurement with the weak value gyroscope.

Summary of Research:

Gyroscopes are key elements for systems such as motion sensing and navigation. Optical gyroscopes using Sagnac effect are being widely adopted for their high sensitivity and reliability. Recently, micro optical resonators have been used for integrated optical gyroscopes [1,2], which are compact and robust for field applications. However, Sagnac phase scales with size and quality factor of the ring. Due to the small area and shorter lifetime in the cavity, micro ring resonator gyroscopes are generally less sensitive than optical fiber gyroscopes. Therefore, we apply integrated weak value amplification device to a Sagnac interferometer with ring resonator to increase its signal-to-noise ratio and sensitivity without increasing the size of the ring. This combined weak value gyroscope paves the way for more applications of integrated gyroscopes in fields that require high sensitivity and stability.

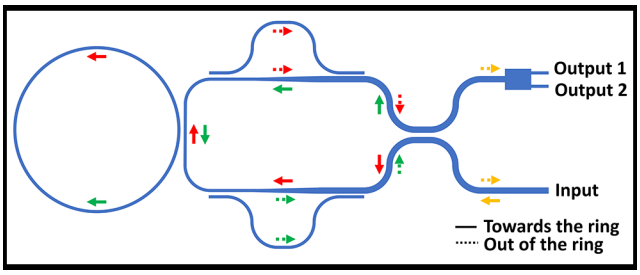

Figure 1: Schematic of integrated gyroscope with inverse weak value amplification (not to scale).

Weak value amplification can enhance interferometric signal-to-noise ratio [3], which optical gyroscopes rely on to increase sensitivity. Weak value amplification is a technique that takes a small amount of the dataset in a slightly perturbed system to enhance the signal without increasing the noise floor. For example, in the dark port of a balanced interferometer, ideally there is no light output. However, by introducing a small phase front tilt to the beam, a light beam appears at the dark port and the path-dependent phase shifts can be converted to location shift of the beam. This beam location shift, determined by a location-sensitive detector, yields to a larger signal than a traditional interferometer. In the meantime, it does not add additional noise compared to the traditional interferometers. Therefore, it can also be applied to optical gyroscopes, whose main component is Sagnac interferometer.

We use our integrated weak value device to detect interferometric signals from a ring resonator to measure rotation as a gyroscope. In a regular Sagnac interferometer, rotation is transferred to a phase difference between the clockwise and counterclockwise propagating light. In our weak value gyroscope, we use integrated weak value device to determine the phase difference between the two paths. The light is sent in through the bright port of the weak value device and gets split into two paths (Figure 1). The two paths

couple to the ring resonator in different directions and accumulate Sagnac. Then they become the two inputs of the weak value device. They both go through a phase front tilter and interfere at the multimode directional coupler. The final beam location shift can also be interpreted as a phase front tilt. Therefore, at the dark port of the interferometer, we use a MMI (multimode interferometer) to determine the amount of phase front tilt of the light, which contains the information of rotation-dependent phase shift.

The device is fabricated with silicon nitride platform and CMOS compatible processes. We deposit 300 nm thick silicon nitride on 4 μm of silicon dioxide and pattern the interferometer. Then we etch the silicon nitride layer and deposit another layer of 2 μm silicon dioxide on top with PECVD (plasma enhanced chemical vapor deposition). All waveguides are patterned with DUV photolithography and etched by ICP-RIE (inductively coupled plasma reactive ion etching).

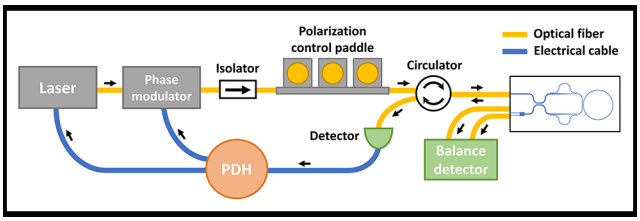

Figure 2: Testing setup of weak value gyroscope with PDH laser stabilization.

To characterize the performance of our weak value gyroscope, we mount the chip onto a motorized rotation stage and measure its angular velocity (Figure 2). We fuse a ribbon fiber with CO_2 laser to couple light around 1550 nm wavelength in and out of the device [4]. The light from the two dark port waveguides is sent to a balanced detector to get the power difference between them. The bright port is sent to a PDH system to lock the laser frequency to the resonance of the ring. The rotation phase in the bright port is in the TE1 mode and it is filtered out with a waveguide taper. We rotate the gyroscope back and forth in 1-sec steps while monitoring the balanced detector reading.

The gyroscope signal increases with rotation speed. The signal is calculated over 20 steps. Each step is averaged over 0.8 sec to avoid acceleration and deceleration. The gyroscope signal follows the rotation pattern of 1-sec rectangle waves as shown in Figure 3. The averaged signal shows linear relationship to the rotation rate up to 8°/sec (Figure 4). The loss of linearity could be due to the laser stabilization running out of tunability for long time operation. It can be improved by optimizing the PDH system settings.

Conclusions and Future Steps:

Integration of weak value amplification device with gyroscope can increase its sensitivity and enjoy the advantage of compactness and low noise. By adding weak value technique into micro ring gyroscopes, the sensitivity could be brought up one magnitude higher, which makes it more practical for field applications. The sensitivity can be improved with better quality factor of the ring resonator.

References:

[1] Y.-H. Lai, M.-G. Suh, Y.-K. Lu, B. Shen, Q.-F. Yang, H. Wang, J. Li, S. H. Lee, K. Y. Yang, and K. Vahala, "Earth rotation measured by a chip-scale ring laser gyroscope," Nature Photonics 14, 345-349 (2020).

[2] W. Liang, V. S. Ilchenko, A. A. Savchenkov, E. Dale, D. Eliyahu, A. B. Matsko, and L. Maleki, "Resonant microphotonic gyroscope," Optica, OPTICA 4, 114-117 (2017).

[3] M. Song, J. Steinmetz, Y. Zhang, J. Nauriyal, K. Lyons, A. N. Jordan, and J. Cardenas, "Enhanced on-chip phase measurement by inverse weak value amplification," Nat Commun 12, 6247 (2021).

[4] J. Nauriyal, M. Song, R. Yu, and J. Cardenas, "Fiber-to-chip fusion splicing for low-loss photonic packaging," Optica, OPTICA 6, 549-552 (2019).

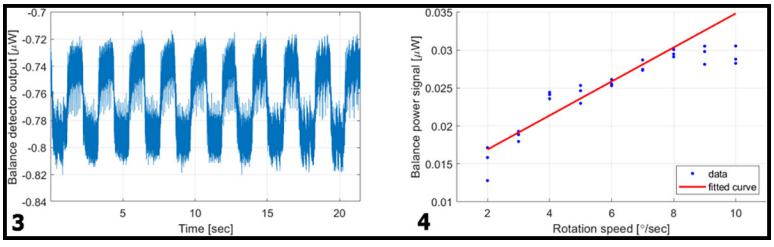

Figure 3, left: Balanced detector output of 5°/sec rotation, 1 sec time step. Figure 4, right: Weak value gyroscope signal vs. rotation speed.

Monolithic Multispectral Color Filter Array

CNF Project Number: 2524-17

Principal Investigator(s): Jaime Cardenas

User(s): Jiewei Xiang

Affiliation(s): The Institute of Optics, University of Rochester

Primary Source(s) of Research Funding: National Science Foundation

Contact: jaime.cardenas@rochester.edu, jxiang6@ur.rochester.edu
Website: https://www.hajim.rochester.edu/optics/cardenas/

Primary CNF Tools Used: ASML Stepper, Oxford 100 ICP-RIE, YES EcoClean Asher, Oxford PECVD, Furnace, JEOL 9500, Heidelberg Mask Writer - DWL2000, ABM Contact Aligner, Oxford Cobra ICP Etcher, Woollam RC2 Spectroscopic Ellipsometer, Oxford ALD FlexAL, Logitech Orbis CMP, AJA Sputter System

Abstract:

We introduce subwavelength grating and selective suppression to a Fabry-Perot cavity. We demonstrate a miniaturized monolithic broadband multispectral color filter with more than 40% transmission and less 30 nm full width at half maximum (FWHM).

Summary of Research:

A CMOS compatible multispectral color filter array with miniatured size is desired for the application in displays, image sensors and multispectral imaging. Many conventional multispectral imaging systems consist of a dispersive element (prism or grating) to separate the wavelengths, which makes the system challenging to further miniaturize [1]. Many transmissive color filters based on surface plasmon resonance and dielectric metasurfaces have been demonstrated to have high spatial resolution and small pixels. However, due to large FWHM (>50nm), low transmission (<40%) and high angular sensitivity, it is challenging to apply them to multispectral imaging.

People propose to combine multiple thin-film color filters based on Fabry-Perot (FP) resonators for high-quality MSFA [2]. Compared to a color filter based on diffraction, an FP resonator is polarization insensitive and relatively angular insensitive. It also has a high transmission and a narrow FWHM. The transmission peaks are tuned by changing the thickness of the cavity with lithography and etching. Due to the increasing steps of fabrication, it is challenging to have many detection channels. To overcome this challenge, people propose to introduce a 2D subwavelength grating structure inside the resonance cavity to manipulate the optical path length and control the transmission peak [3]. However, due to the properties of FP resonators, there will be multiple resonance peaks which constrain the free spectral range (FSR). Also, due to the limitation of fabrication, the fill ratio of the subwavelength grating structure cannot be too high which would result in a small spectral tuning range.

We demonstrate a broadband multispectral FP color filter array based on two-dimensional subwavelength gratings and selective suppression [4], which can cover from red to near-infrared (630nm-960nm) with narrow bandwidths (<30nm). Our thin-film color filter stack consists of two DBR mirrors and a cavity with two layers of subwavelength gratings sandwiching a thin metal layer (Figure 1). To achieve a large tuning range, we apply a combination of mesh and grating structures (Figure 2) and use the second-order resonance of the FP resonator with selective suppression. We change the effective index of the cavity to tune the location of the transmission peak. Instead of using the first-order transmission peak, we choose the second-order transmission peak for its smaller reflection phase. Also, the second-order transmission peak has a narrower linewidth compared to the first-order transmission peak due to a larger optical path length in the cavity, which makes the FWHM of our filters smaller than 30 nm. By inserting a metal layer in the middle of the cavity, the odd-order transmission peaks will be largely suppressed, which allows the second-order resonance to have a comparable FSR with the first-order resonance.

There are mainly six steps for the fabrication of our color filter array (Figure 1). We use polysilicon as the high index material for both DBR and cavity. Polysilicon

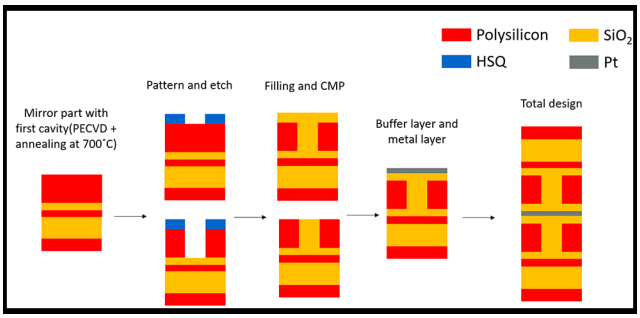

Figure 1: Schematic of the stack structure of the color filter and the main fabrication steps.

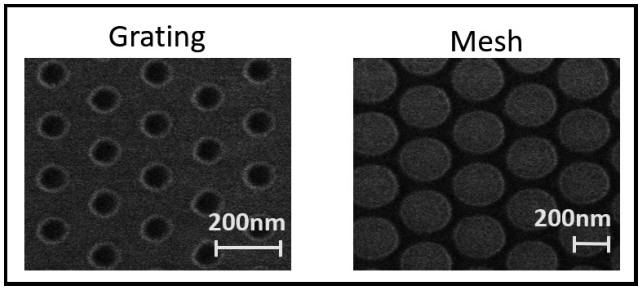

Figure 2: SEM of the mesh and grating structure. The dark part is the HSQ after e-beam lithography and developing. The gray part is polysilicon underneath the HSQ.

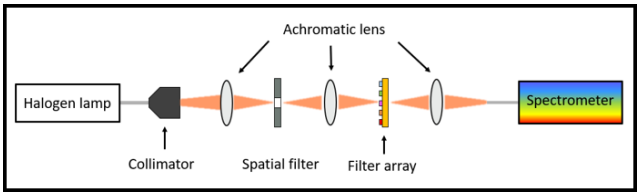

Figure 3: Schematic of the measurement setup.

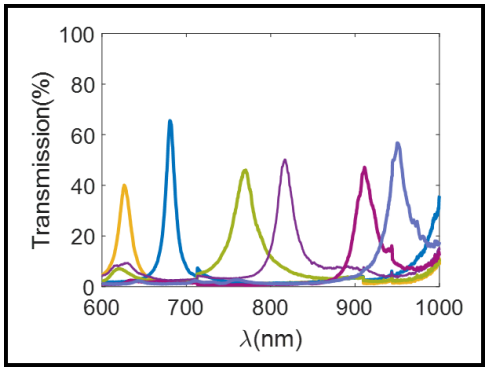

Figure 4: The relative transmission of different color filters based on measurement.

is deposited by plasma-enhanced chemical vapor deposition (PECVD) and anneal it at 700°C for two hours to make it crystalize. We use JEOL 9500 and negative resist hydrogen silsesquioxane (HSQ) to pattern the cavity and use inductively coupled plasma reactive ion etching with HBr to transfer the pattern from HSQ to polysilicon. We fill the gap by atomic layer deposition (ALD) with SiO_2 and polish the surface with chemical mechanical polishing (CMP).

We demonstrate a multispectral color filter array covering from 630 nm to 960 nm with transmissions over 40% and FWHM less than 30 nm. We use a halogen lamp (HL-2000-LL) to generate a broadband light source that covers 400-1700 nm (Figure 3). A collimator and an achromatic lens are used to focus the light on the filter which is 50 μm × 50 μm. We deposit 100 nm Pt above the sample and open a 40 μm × 40 μm aperture on the filter. A blank fused silica wafer with the same apertures is used as the reference. The transmitted light is collected and focused on the spectrometer (Ocean Insight FLAME-S-VIS-NIR-ES). The relative transmission is acquired by comparing the transmission of filters with the reference wafer. From the measurement (Figure 4), the filter array can cover the spectrum from 630 nm to 960 nm with transmission above 40%. The FWHM of all measured transmission peaks is smaller than 30 nm. The transmission and FWHM can be improved by refining the fabrication process to decrease the asymmetry between the two cavities.

Conclusions and Future Steps:

We show that using the sub-wavelength grating, broadband and narrow linewidth color filter array with the same layer structure can be created, which enables monolithic integration of filter banks with imaging sensors. This design can be transferred to visible or infrared wavelength by changing the high index material and optimizing the thickness and lattice structure. This has the promise of a monolithic broadband multispectral color filter array and paves the way for one-shot multi-spectral imaging.

References:

[1] Lapray, P.-J., Wang, X., Thomas, J.-B., and Gouton, P. Multispectral Filter Arrays: Recent Advances and Practical Implementation. Sensors 14, 21626-21659 (2014).

[2] McClung, A., Samudrala, S., Torfeh, M., Mansouree, M., and Arbabi, A. Snapshot spectral imaging with parallel metasystems. Sci. Adv. 6, eabc7646 (2020).

[3] Horie, Y., Arbabi, A., Arbabi, E., Kamali, S. M., and Faraon, A. Wide bandwidth and high resolution planar filter array based on DBR-metasurface-DBR structures. Opt. Express 24, 11677 (2016).

[4] Lee, K.-T., Han, S. Y., Li, Z., Baac, H. W., and Park, H. J. Flexible High-Color-Purity Structural Color Filters Based on a Higher-Order Optical Resonance Suppression. Sci Rep 9, 14917 (2019).

Engineered Second-Order Nonlinearity in Silicon Nitride

CNF Project Number: 2524-17

Principal Investigator(s): Jaime Cardenas

User(s): Yi Zhang

Affiliation(s): The Institute of Optics, University of Rochester

Primary Source(s) of Research Funding: National Science Foundation

Contact: jaime.cardenas@rochester.edu, yzh239@ur.rochester.edu
Website: https://www.hajim.rochester.edu/optics/cardenas/

Primary CNF Tools Used: JEOL 9500, ASML PAS 5500/300C DUV Stepper, Oxford PECVD, AJA Sputter Deposition, LPCVD Furnace, Oxford 100 Etcher, Unaxis 770 Deep Silicon Etcher, Xactix Xenon Difluoride Etcher

Abstract:

We induce a permanent second order nonlinearity of 0.24 pm/V in silicon nitride via electrical poling at a high temperature. We demonstrate electro-optic response usable for modulation in the engineered silicon nitride device up to 15 GHz.

Summary of Research:

Silicon nitride (Si_3N_4) is as a high-performance platform for versatile on-chip photonic devices [1,2] because of its low propagation loss, broad transparency window (400-6700 nm [3]) and good compatibility with complementary metal-oxide semiconductor (CMOS) processing. However, Si_3N_4 lacks an intrinsic second-order nonlinearity ($\chi^{(2)}$) due to its centrosymmetric structure [4]. Building an intrinsic $\chi^{(2)}$ that allows high-speed (gigahertz level) EO response in Si_3N_4 will create a new photonic platform with great potential in integrated photonics.

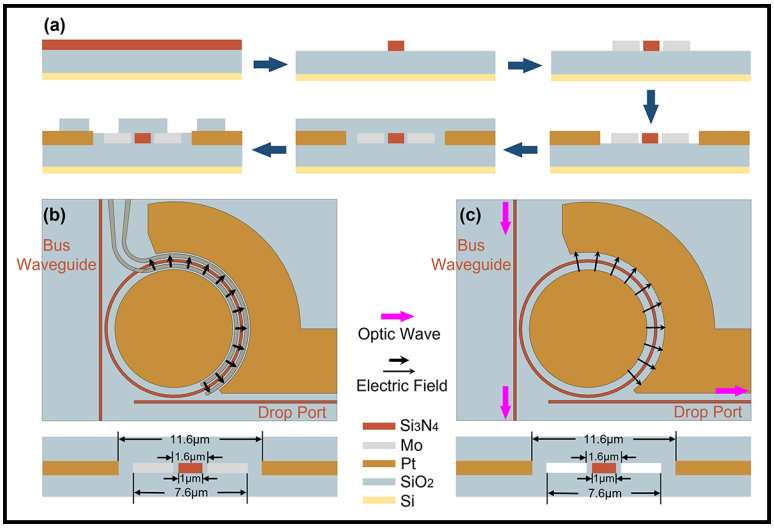

Figure 1: (a) Fabrication procedures of our device. (b) Ring resonator under poling. (c) Ring resonator under high-speed test (Mo removed).

We demonstrate induction of a second-order nonlinearity in Si_3N_4 by electrically poling the film and aligning the Si-N bonds. Khurgin, et al. [5] hypothesized that the Si-N bonds in Si_3N_4 possess a second-order hyperpolarizability comparable to Ga-As bonds in GaAs, whose $\chi^{(2)}$ is as large as 300 pm/V. The centrosymmetric orientation of the Si-N bonds causes their contribution to cancel each other and leads to a bulk $\chi^{(2)}$ of zero. However, by aligning these bonds and breaking the symmetry, even slightly, a non-trivial intrinsic $\chi^{(2)}$ will naturally emerge and thus induce a high-speed EO response in Si_3N_4.

We use an Si_3N_4 ring resonator (1μm*300nm) with electrodes to study the EO response in poled and non-poled Si_3N_4. Fabrication procedures are shown in Figure 1(a). We deposit 300 nm LPCVD nitride over 4 μm thermally-grown oxide on a silicon wafer. The waveguide is patterned using e-beam lithography and etched using reactive-ion etching (RIE). We then pattern a pair of Mo electrodes using DUV lithography and deposit the metal through sputter-liftoff process. This pair of electrodes is placed 300 nm away from the waveguide (edge to edge) to generate a strong electric field to pole the Si_3N_4 ring (Figure 1(b)).

We choose Mo as the material since it can be removed using XeF_2 after poling to eliminate the huge loss it introduces to the ring, which we need for characterization of the EO response, which has a high selectivity to all the other materials used in the device.

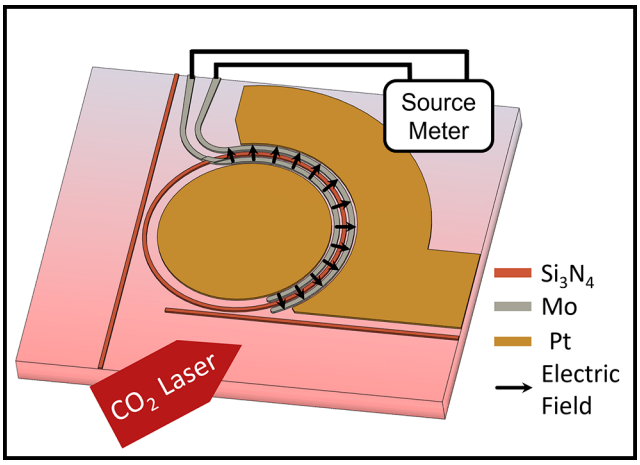

Figure 2: Poling of Si_3N_4 ring resonator heated by CO_2 laser beam.

Another pair of platinum (Pt) electrodes is then patterned and deposited in the same way outside the Mo ones for EO modulation after the removal of Mo (Figure 1(c)). Afterwards, we clad the waveguide and electrodes with 2 µm PECVD oxide and open vias for probe contact and XeF_2 etching.

We heat up the device to facilitate the poling process [6] by focusing a 10W CO_2 laser beam beside the ring (Figure 2). We limit the heating to 700°C as we observe rapid dropping of the arcing threshold between the electrodes, which limits the field strength we can apply, when going to higher temperature. After reaching this desired temperature, we apply a high voltage to the Mo electrodes for poling. The maximum voltage we manage to apply without arcing is 160V and it corresponds to a horizontal poling field of 0.68 MV/cm in Si_3N_4 according to simulation. The device sinks in the high temperature poling for five minutes before we disable the heating laser. The poling field is maintained until the device cools down to room temperature (in a few seconds). Such rapid cooling helps to freeze the aligned bonds in their new positions and prevent them from rolling back (as the poling field still remains).

We quantitively characterize the r_{33} and r_{31} EO coefficients of the Si_3N_4 resonator (Figure 3(a)). The measured values at different working frequencies for the poled device (red lines, various time after poling) and non-poled reference (green line) are shown in Figure 3 (b-c). We observe that the poled device demonstrates an enhancement of the r_{33} component to 30 fm/V (effective $\chi^{(2)}$ 240 fm/V [4]). After the poling the speed of the measured EO response increases. The reference device shows a 3dB cutoff frequency of 3 GHz (data points at high frequencies have their lower error bar set to zero since they are hardly distinguishable from the background noise), while this number improves to at least 15 GHz for the poled device, for both r_{33} and r_{31} component. The *slow response* measured in the non-poled device is a result of carrier-related effects in Si_3N_4 as previously reported [7], which has a speed limit of approximately 1 GHz [8]. The *fast response* of the poled device, on the other hand, confirms our induction of a second-order nonlinearity in the poled Si_3N_4 as no other mechanism can enable EO response of such high speed. We track the EO response in the poled device for one week and observe no significant decay, suggesting our induction is long-lasting and permanent.

Conclusions and Future Steps:

In conclusion, we demonstrate a permanent second-order nonlinearity of 0.24 pm/V and corresponding electro-optic response as fast as 15 GHz built in silicon nitride through electrical poling. This work paves the way to enabling high-speed active functions on the Si_3N_4 platform, substantially expanding its potential applications.

References:

[1] D. J. Blumenthal, R. Heideman, D. Geuzebroek, A. Leinse, and C. Roeloffzen, Proceedings of the IEEE 106, 2209-2231 (2018).

[2] P. Muñoz, et al. Sensors 17, 2088 (2017).

[3] R. Soref, Nature Photon 4, 495-497 (2010).

[4] R. W. Boyd, Nonlinear Optics (Academic Press, 2020).

[5] J. B. Khurgin, T. H. Stievater, M. W. Pruessner, and W. S. Rabinovich, J. Opt. Soc. Am. B 32, 2494 (2015).

[6] R. A. Myers, N. Mukherjee, and S. R. J. Brueck, Opt. Lett. 16, 1732 (1991).

[7] S. Sharif Azadeh, F. Merget, M. P. Nezhad, and J. Witzens, Opt. Lett. 40, 1877 (2015).

[8] M. Borghi, et al. Opt. Lett. 40, 5287 (2015).

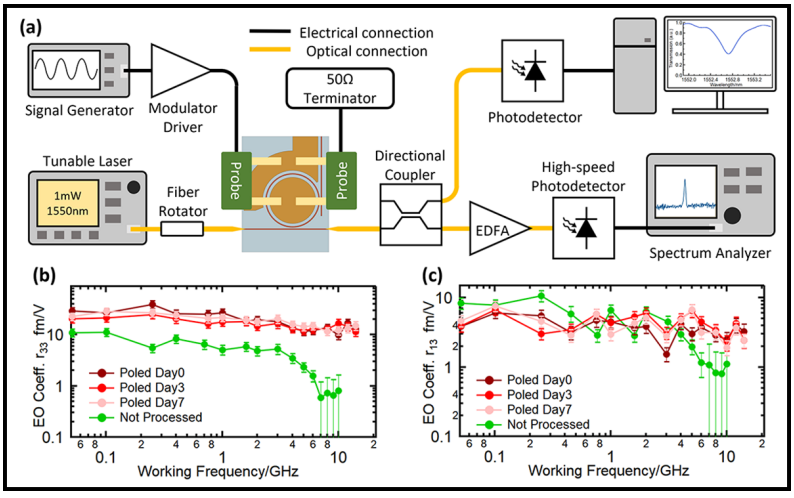

Figure 3: (a) Schematic of apparatus of EO response characterization. (b-c) Measured EO coefficient r_{33}(b) and r_{13}(b) at various frequencies of both poled and non-poled device.

A Low SWaP, Robust, High Performance Hyperspectral Sensor for Land and Atmospheric Remote Sensing

CNF Project Number: 2661-18

Principal Investigator & User: Lori Lepak

Affiliation(s): Phoebus Optoelectronics LLC
Primary Source(s) of Research Funding: National Aeronautics and Space Administration (NASA)
Contact: llepak@phoebusopto.com
Website: www.phoebusopto.com
Primary CNF Tools Used: ASML DUV Stepper, Oxford 81 Etcher, Logitech CMP, Supra SEM

Abstract:

Since 2003, Phoebus Optoelectronics LLC has enabled custom R&D solutions in the fields of Plasmonics, Metamaterials, Antennas, and Sensors. We work closely with our customers throughout device development, from simulation and design, to prototype realization, testing, and small volume manufacturing. Our R&D portfolio spans the spectral ranges of visible light, infrared, terahertz, and microwave radiation, for applications in high resolution imaging systems, wavelength and polarization filtering, tunable optical components, beam forming and steering, solar cells, renewable energy devices, and chemical and biological toxin sensors. We routinely partner with large, industry-leading businesses to develop products in all of these areas, jointly performing advanced testing and working together to scale up to medium- and large-volume manufacturing.

Our agile team makes extensive use of the resources at the CNF for our nano/micro fabrication and testing, to provide cost efficiency and rapid turnaround.

In the present report, we discuss the ongoing development of a metamaterial-based hyperspectral imaging filter.

Summary of Research:

Phoebus Optoelectronics uses the resources of the CNF to fabricate plasmonic chips patterned with a metamaterial surface to enable Extraordinary Optical Transmission (EOT), a phenomenon unique to metastructures in which light is transmitted through apertures much smaller than the incident wavelength, at anomalously large intensities relative to the predictions of conventional aperture theory. EOT was first observed by T.W. Ebbesen in 1998 [1]. Since its founding in 2003, Phoebus has successfully harnessed EOT by incorporating metasurfaces into devices used to perform light filtering [2,3], photon sorting [4,5], polarimetric detection [6], high speed optical detection [7], and SPR plasmonic sensor chips [8].

In our current project, we are developing a hyperspectral imaging system, shown schematically in Figure 1. Our technology (Figure 1b) uses a metasurface to precisely target very narrow spectral bands of interest, enabling a significant reduction in the size and number of optical components relative to current state-of-the-art imaging systems (Figure 1a), which in turn will enable the integration of our high-performance sensor onto weight-sensitive platforms (i.e., satellites) far more readily than existing systems. Our initial goal is to detect and image trace gases in the Earth's atmosphere in the midwave infrared (MWIR), defined as 3-5 μm

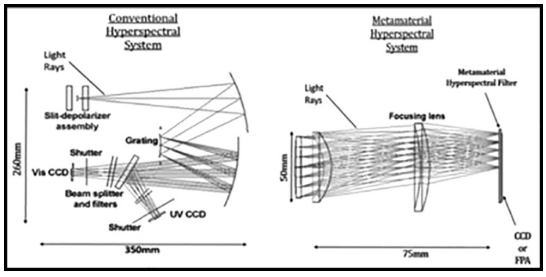

Figure 1: Phoebus's Metamaterial Spectrometer (MS) technology (right) eliminates much of the size and weight of conventional hyperspectral spectrometer technologies (left). Note the significant difference in scale of the two images.

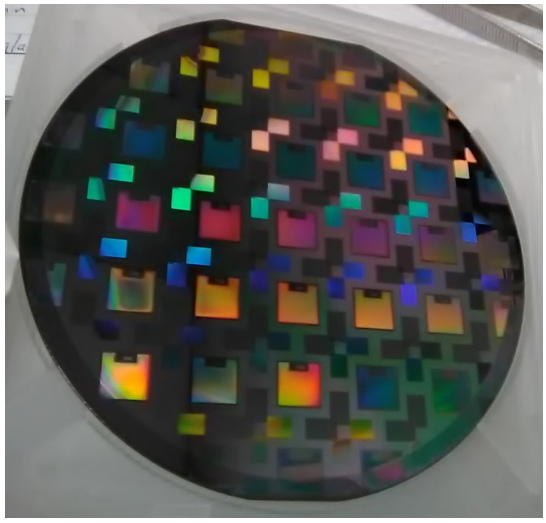

Figure 2: Wafer lithographically patterned with optical metastructures, using the ASML DUV stepper.

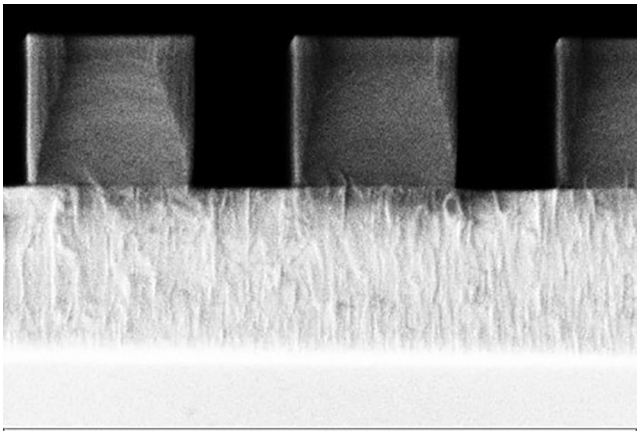

Figure 3: SEM image (cross section) of etched pillars with near-vertical sidewalls. Imaged at ~ 90 kX in the Supra SEM, the grain structure of the etch stop layer is clearly visible.

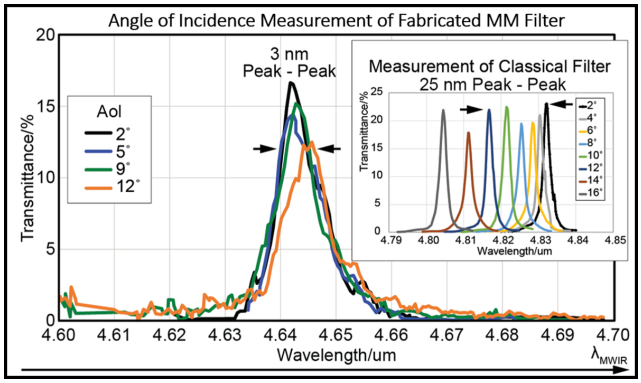

Figure 4: Measured optical performance of fabricated metamaterial filter showing the angle of incidence independence up to a cone of 12° (f/2.4). (Inset) Same measurement performed on a classical Fabry-Pérot filter. Reproduced from reference 9.

wavelength, while minimizing dependence on the Angle of Incidence (AoI) of light upon the sensor, up to an angle of 12° off-normal.

Using the ASML DUV stepper, entire wafers can rapidly be lithographically patterned with highly uniform, large-area arrays of metastructures, as shown in Figure 2. In general, the optimal feature size and period of these metastructures depends primarily upon the desired wavelength of operation and the refractive indices of the constituent materials. In the MWIR, typical feature sizes are on the order of ~ 1 μm. Equally critical for minimizing optical losses in photonics applications, the relatively narrow spaces between features can be etched to form high-aspect-ratio structures with nearly vertical sidewalls, as shown in Figure 3.

Conclusions and Future Steps:

With strong, ongoing support from the National Aeronautics and Space Administration (NASA), we have successfully tested our second generation MWIR devices. As shown in Figure 4, they demonstrated the desired AoI insensitivity up to 12°. Having identified a few key areas for process improvements, we are currently fabricating a third generation, to fully optimize and pixelate our MWIR device. In addition, we are adapting our metasurface technology to other spectral ranges, from the visible to the microwave, by substituting appropriate materials, and scaling feature sizes as appropriate to the imaging wavelength.

In particular, we developing a second generation of a visible/NIR-wavelength counterpart of the current technology. The NIR/vis devices are fabricated using all of the same tools as the MWIR project, plus the Oxford PECVD and AJA sputter tool to deposit thin films. Thus, the extensive resources of the CNF are enabling us to rapidly develop our Metamaterial Spectrometer technology for a broad range of imaging and sensing applications.

References:

[1] Ebbesen, T.W., et al., "Extraordinary optical transmission through sub-wavelength hole arrays." Nature, (1998). 391(6668): p. 667-669.

[2] Crouse, D. "Numerical modeling and electromagnetic resonant modes in complex grating structures and optoelectronic device applications." Electron Devices, IEEE Transactions on 52.11 (2005): 2365-2373.

[3] Crouse, D., and Keshavareddy, P. "Polarization independent enhanced optical transmission in one-dimensional gratings and device applications." Optics Express 15.4 (2007): 1415-1427.

[4] Lansey, E., Crouse, D., et al. "Light localization, photon sorting, and enhanced absorption in subwavelength cavity arrays." Optics Express 20.22 (2012): 24226-24236.

[5] Jung, Y.U; Bendoym, I.; Golovin, A.B.; and Crouse, D.T. "Dual-band photon sorting plasmonic MIM metamaterial sensor." Proc. SPIE 9070, Infrared Technology and Applications XL, 90702X (June 24, 2014); doi:10.1117/12.2050620.

[6] Crouse, D., and Keshavareddy, P. "A method for designing electromagnetic resonance enhanced silicon-on-insulator metal–semiconductor–metal photodetectors." Journal of Optics A: Pure and Applied Optics 8.2 (2006): 175.

[7] Mandel, I.; Gollub, J.; Bendoym, I; Crouse, D. Theory and Design of A Novel Integrated Polarimetric Sensor Utilizing a Light Sorting Metamaterial Grating. Sensors Journal, IEEE, (2012): Vol. PP, 99.

[8] Lepak, L., et al. "Handheld chem/biosensor using extreme conformational changes in designed binding proteins to enhance surface plasmon resonance (SPR)" Proc. SPIE 9862, Advanced Environmental, Chemical, and Biological Sensing Technologies XIII, 9862-7 (April 17, 2016); doi:10.1117/12.2222305.

[9] Bendoym, I., Lepak, L., Leitch, J., Applegate, J., Crouse, D. "Low SWaP-C hyperspectral metamaterial spectrometer (MMS) for narrow-band, wide angle-of-incidence MWIR atmospheric sensing," Proc. SPIE 12091, Image Sensing Technologies: Materials, Devices, Systems, and Applications IX, 120910J (30 May 2022); https://doi.org/10.1117/12.2632794.

OWiC microLINKs: Microscopic Optical Smart Tags for Connecting Digital Content to the Physical World

CNF Project Number: 2909-20

Principal Investigator(s): Alejandro Cortese[1], Paul L. McEuen[1], Alyosha Molnar[1], Robert Scharf[2]

User(s): Alejandro Cortese

Affiliation(s): 1. OWiC Technologies, Inc.; 2. Praxis Center for Venture Development

Primary Source(s) of Research Funding: NSF SBIR Phase I Award Number 2014984

Contact: alejandro@owictech.com, pmceuen@gmail.com, amolnar@owictech.com, rms248@cornell.edu

Primary CNF Tools Used: Heidelberg Mask Writer - DWL2000, ABM Contact Aligner, Zeiss SEMs, Oxford 100 ICP Etcher, Oxford 81 Etcher, Oxford Cobra Etcher, PT770 Etcher, AJA Sputter Deposition, Oxford PECVD, SC4500 Evaporator, Oxford ALD

Abstract:

OWiC Technologies is a Cornell spinout startup commercializing a new class of unique ID tags called microLINKs to securely, intelligently, and wirelessly connect the physical and digital worlds. The microLINKs tags are based on the core technology of Optical Wireless Integrated Circuits (OWiCs), that are effectively in-visible, intelligent, and integrated with a built-in optical power and communication system made of photovoltaics/ microLED. A microLINK tag functions in a way analogous to an RFID tag but uses light for power and communication instead of RF. When light is directed toward a microLINK, it will blink out a unique 64-bit ID that can be read out with a handheld reader. The code, in conjunction with a cloud database of tags and links, connects to digital content on a smartphone, tablet, or, in the future, smart glasses. We use a wide range of tools in the Cornell NanoScale Facility (CNF) to produce these microLINK tags.

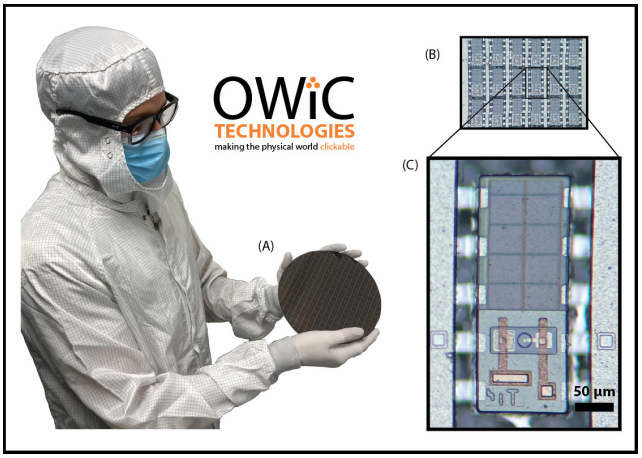

Figure 1: (A) An 8-inch wafer of microLINK integrated circuits from a commercial foundry. (B) An array of integrated microLINK tags. (C) An integrated microLINK tag prior to removal from the substrate. This microLINK tag design is approximately 100 × 300 microns.

Summary of Research:

The entire microLINK device is approximately 100 × 300 microns in size and is composed of photovoltaics, a circuit for on board digital logic, and a microLED. The photovoltaics and integrated circuit are designed in a 180 nm silicon-on-insulator (SOI) complementary metal-oxide-semiconductor (CMOS) process available from a commercial foundry. The circuit creates a series of electrical pulses that encode a unique identification code that are used to drive the microLED, producing the output light. These circuits are received from the commercial foundry as a wafer shown in Figure 1(A).

Separately, we produce light emitting elements in the CNF primarily out of gallium arsenide heterostructures. These two components — the CMOS components and microLED — are then integrated using heterogenous integration methods. Methods for producing these devices are detailed in references below [1-4].

Figure 1 A shows an array of integrated microLINK devices before being removed from the substrate is shown in Figure 1 (B) as well as a zoomed in image of a single device, Figure 1 (C).

References:

[1] A. C. Molnar, S. Lee, A. Cortese, P. McEuen, S. Sadeghi, S. Ghajari, in 2021 IEEE Custom Integrated Circuits Conference (CICC) (2021), pp. 1-6.

[2] S. Lee, A. J. Cortese, A. P. Gandhi, E. R. Agger, P. L. McEuen, A. C. Molnar, A 250 μm × 57 μm Microscale Opto-electronically Transduced Electrodes (MOTEs) for Neural Recording. IEEE Trans. Biomed. Circuits Syst. 12, 1256-1266 (2018).

[3] S. Lee, A. J. Cortese, A. Mok, C. Wu, T. Wang, J. U. Park, C. Smart, S. Ghajari, D. Khilwani, S. Sadeghi, Y. Ji, J. H. Goldberg, C. Xu, P. L. McEuen, A. C. Molnar, Fabrication of Injectable Micro-Scale Opto-Electronically Transduced Electrodes (MOTEs) for Physiological Monitoring. J. Microelectromechanical Syst. 29, 720-726 (2020).

[4] A. J. Cortese, C. L. Smart, T. Wang, M. F. Reynolds, S. L. Norris, Y. Ji, S. Lee, A. Mok, C. Wu, F. Xia, N. I. Ellis, A. C. Molnar, C. Xu, P. L. McEuen, Microscopic sensors using optical wireless integrated circuits. Proc. Natl. Acad. Sci. 117, 9173-9179 (2020).

Electrical and Optical Characterization of Thin Film Silicon-Rich Nitride

CNF Project Number: 2971-21

Principal Investigator(s): Peter McMahon[1,2]

User(s): Tatsuhiro Onodera[1,3], Martin Stein[1,3]

Affiliation(s): 1. School of Applied and Engineering Physics, Cornell University, Ithaca, NY 14853, USA; 2. Kavli Institute at Cornell for Nanoscale Science, Cornell University, Ithaca, NY; 3. NTT Physics and Informatics Laboratories, NTT Research, Inc., Sunnyvale, CA, USA

Primary Source(s) of Research Funding: National Science Foundation (award CCF-1918549), David and Lucile Packard Foundation Fellowship, NTT Research

Contact: pmcmahon@cornell.edu, to232@cornell.edu, ms3452@cornell.edu

Primary CNF Tools Used: Oxford 100 PECVD, E-Beam Evaporator, Woollam RC2 Spectroscopic Ellipsometer, Metricon 2010/M Prism Coupler

Abstract:

Silicon-rich silicon nitride (SRN) has recently attracted attention for its promise to enable high-power nonlinear optical information processing. The same qualities that make SRN promising for this application—a large optical nonlinearity and high dielectric strength—also make SRN a promising material for programmable integrated photonics. To demonstrate this potential, we fabricated low loss SRN films with a large electro-optic effect and show that the material's electrical properties are extremely versatile and can be optically controlled.

Summary of Research:

We characterized electrical and optical properties of thin silicon-rich silicon nitride (SRN) PECVD films with different silicon and nitrogen contents. SRN is a class of materials with a bandgap ranging between that of stoichiometric silicon nitride (SiN) and amorphous silicon. This makes SRN generally more electrically insulating than silicon but more conductive than SiN. Its optical properties similarly range between those of silicon and SiN, with a refractive index from about 2 to 3.5 at 1550 nm, increasing with higher silicon content, and a large Kerr nonlinearity.

We measured the electrical conductivity of different SRN films by measuring the I-V characteristics under different conditions and we measured the propagation loss of light at 1550 nm in SRN slab waveguides using prism coupling, as well as the electro-optic effect at 1550 nm.

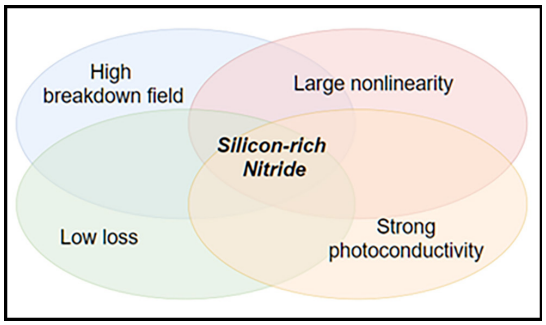

Figure 1: Silicon-rich nitride combines several desirable material properties for programmable photonic circuits. The combination of a high breakdown field [2] and large nonlinear coefficients allows large refractive index modulations [1,3]. A strong photoconductivity allows modulating the electro-optic effect with visible light while low losses [4] are a prerequisite for deep photonic circuitry.

Electrical Conductivity. To measure the electrical conductivity, we deposited around 500 nm thick SRN layers of different silicon content using PECVD on strongly p-type Si wafers. The gas flow ratios for the different materials were varied from 40 sccm SiH_4, 10 sccm NH_3 and 1425 sccm N_2 for the material closest to SiN (lowest refractive index and lowest conductivity) to 25 sccm SiH_4 and no NH_3 or N_2 for the material closest too amorphous silicon (highest index and most conductive). We then deposited 15 nm titanium and 15 nm gold electrodes on top of the SRN layer. We inferred the conductivity from the current flowing when applying a negative bias to the gold electrode and keeping the substrate at ground. We repeated the measured while illuminating the chips with approximately 100 mW/cm^2 at 530 nm.

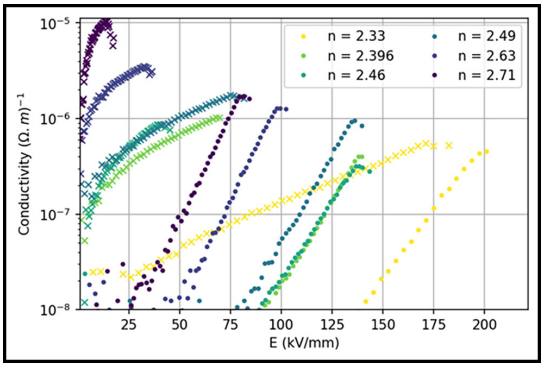

Figure 2: Conductivity of different silicon-rich nitrides as a function of electric field and illumination. Different colors correspond to different gas flow rates of SiH_4 and NH_3, ranging from 4:1 (n=2.33) to >10:1 (n=2.71). Different markers correspond to different illuminations: Dots mark the conductivity in the dark state, "x"s mark the conductivity in the bright state under approximately 100 mW/cm^2 of 530 nm light. The saturation at the top of each conductivity curve is an artifact from the compliance current of our high voltage amplifier.

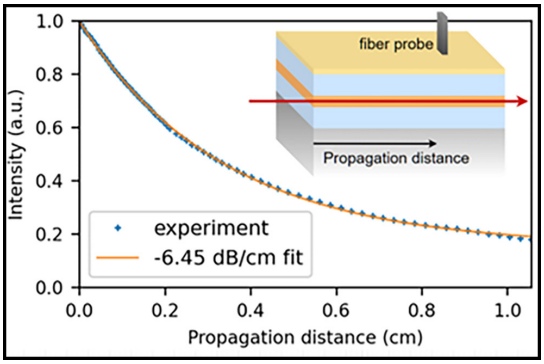

Figure 3: Measurement of optical propagation loss in SRN slab waveguide. The waveguide consists of a 500 nm thick SRN core with refractive index of 2.45 at 1550 nm (SiH_4:NH_3 gas ratio of 6) and 700 nm thick SiO_2 claddings on each side. The loss is estimated by measuring scattered light on top of the waveguide as a function of propagation distance using the Metricon 2010/M prism coupler. An exponential fit yields a loss of 6.45 dB/cm.

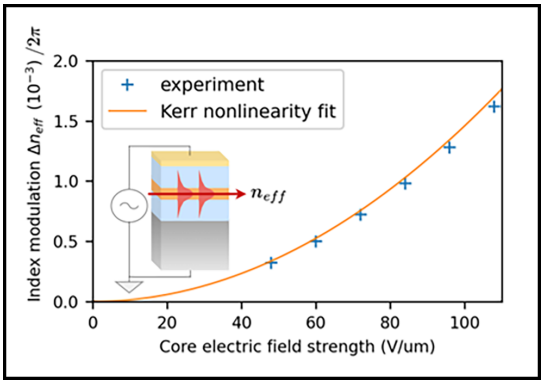

Figure 4: Measurement of the electro-optic response of the SRN waveguide from Figure 3 at 1550 nm. We applied a 10 Hz AC voltage across the waveguide stack. The electric field strength in the core was estimated using the conductivity measurements from Figure 2. The refractive index modulations were measured using an interferometer. A part of the 1550 nm beam was splitted off before entering the waveguide, routed around the waveguide and then recombined with the beam going through the waveguide. We established the refractive index modulations of the waveguide from the resulting interference fringes. The measured index modulations are consistent with a Kerr nonlinearity.

The results are shown in Figure 2. SRN is generally very resistive with conductivities ranging from 10.8 to 10.5Ω cm, but the conductivity is very sensitive to the silicon content (as evident from the refractive index), applied voltage, and can change more than three orders of magnitude from bright to dark state.

Optical Properties. We measured the refractive index of SRNs with different silicon content. Representatively shown in Figure 3 is a measurement of the optical propagation loss of a 1550 nm beam in a 500 nm thick slab of SRN with 700 nm SiO_2 claddings. The loss was much higher than expected from ellipsometer measurements of the extinction coefficient, so we believe the loss is largely due to surface roughness. We also observed a photo-induced loss of yet unknown origin when illuminating the waveguide with visible light. This loss is about 3 dB/cm and might be due to the photoconductivity shown in Figure 2.

We measured the electro-optic modulation by measuring the change in effective refractive index when applying an electric field across the waveguide. As seen in Figure 4, the relation between refractive index and applied field is quadratic, suggesting a Kerr nonlinearity.

Conclusions and Outlook:

We have characterized silicon-rich silicon nitride films for its applications as a controllable electro-optic material. While lower losses (e.g. [4]) and stronger optical nonlinearities (e.g. [3]) in SRN have been demonstrated before, we also show strong photoconductivity. Although our work is preliminary and should not be treated as definitive, we believe SRN is a promising material for optically programmable photonics.

Acknowledgements:

PLM gratefully acknowledges financial support from a David and Lucile Packard Foundation Fellowship. The authors wish to thank NTT Research for their financial and technical support, and the National Science Foundation (award CCF-1918549). This work was performed in part at the Cornell NanoScale Facility, a member of the National Nanotechnology Coordinated Infrastructure (NNCI), which is supported by the National Science Foundation (Grant NNCI-2025233).

References:

[1] Tan, D. T. H., K. J. A. Ooi, and D. K. T. Ng. "Nonlinear optics on silicon-rich nitride—a high nonlinear figure of merit CMOS platform." Photonics Research 6.5 (2018): B50-B66.

[2] Piccirillo, A., and A. L. Gobbi. "Physical-electrical properties of silicon nitride deposited by PECVD on III–V semiconductors." Journal of The Electrochemical Society 137.12 (1990): 3910.m.

[3] Friedman, Alex, et al. "Demonstration of the DC-Kerr effect in silicon-rich nitride." Optics Letters 46.17 (2021): 4236-4239.

[4] Lacava, Cosimo, et al. "Si-rich silicon nitride for nonlinear signal processing applications." Scientific reports 7.1 (2017): 1-13.

Visible-Light Metasurfaces Based on Silicon-Rich Silicon Nitride

CNF Project Number: 2979-21

Principal Investigator(s): Gennady Shvets

User(s): Melissa Bosch

Affiliation(s): School of Applied and Engineering Physics, Department of Physics; Cornell University

Primary Source(s) of Research Funding: Office of Naval Research (ONR), National Science Foundation (NSF)

Contact: gs656@cornell.edu, mb2583@cornell.edu
Website: http://shvets.aep.cornell.edu

Primary CNF Tools Used: JEOL 9500, Zeiss Ultra SEM, Oxford 100 Etcher, Oxford PECVD, Woollam RC2 Ellipsometer

Abstract:

Optical metasurfaces, consisting of planar arrangements of lithographically-defined subwavelength scatterers, offer a highly compact and scalable alternative to conventional freespace refractive optical elements. We report on the fabrication 500 nm thick silicon-rich silicon nitride (SRN) metasurfaces exhibiting tunable optical resonances, fit for various photonic applications requiring visible light modulation. For example, we integrate SRN-metasurfaces with liquid crystals (LCs) to demonstrate voltage-controlled zoom lenses operating at red/green/blue (RGB) wavelengths. Their scalability, ultrathin-profile, and CMOS-compatibility renders SRN-metalenses uniquely poised to benefit RGB imaging technologies such as augmented reality and depth perception devices.

Summary of Research:

I. Silicon-Rich Silicon Nitride (SRN) Metasurfaces. Metasurfaces have drawn considerable interest over the past decade owing to their widespread potential applications. Semiconductor and dielectric metasurfaces are especially promising platforms for efficient light modulation owing to their low Ohmic losses and support of localized Mie-type resonance modes which are spectrally-sensitive to the permittivity of the media adjacent to the metasurface array [1]. Typically, metasurfaces working at visible wavelengths are composed of GaP or TiO_2, requiring costly and time-consuming deposition processes (i.e., metal-organic chemical vapor deposition and atomic layer deposition) [2,3]. Our project focuses on the PECVD-based fabrication of SiN_x metasurfaces with sub-100 nm feature sizes and moderate (1:4) aspect ratios. Our ellipsometric characterization of PECVD-deposited SiN_x thin films shows flexible control over the films' refractive index and extinction coefficient through variations in the SiH_4:NH_3 gas ratio (Figure 1). Several gas ratios yield SRN films exhibiting low extinction coefficients and acceptable refractive indices at RGB wavelengths: fit for use as the constituent material of visible-light metasurfaces. A scanning electron microscope (SEM) image of a representative SRN metasurface is shown in Figure 2, consisting of an array of rectangular SRN resonators on a silica substrate, where the spacing between neighboring resonators governs the bandwidth of the optical resonance. The SRN devices are fabricated using plasma-enhanced chemical vapor deposition (Oxford PECVD) of SRN onto a fused silica substrate; HSQ 6% spin-coat, baking, and e-beam exposure at 7.5 mC/cm^2 (JEOL 9500FS); development in TMAH/NaCl (0.25/0.7N) salty solution; and pattern transfer to the SRN layer through reactive ion etching (Oxford 100). The fabricated samples were characterized with a scanning electron microscope (Zeiss Ultra), showing good accuracy of geometric dimensions.

II. Tunable-Focus Lens Using a Liquid-Crystal-Embedded SRN-Metasurface. In one application, we utilize PECVD SRN films to create a SRN-metalens behaving as a visible-light lens with voltage-actuated zoom. Metalenses with tunable focal lengths offer many advantages to contemporary vision and imaging systems; however, most metalenses have static focal lengths after fabrication. Our previous work used amorphous silicon metasurfaces infiltrated with liquid crystals (LCs) to demonstrate a varifocal metalens with voltage-actuated focal length in the infrared [2].

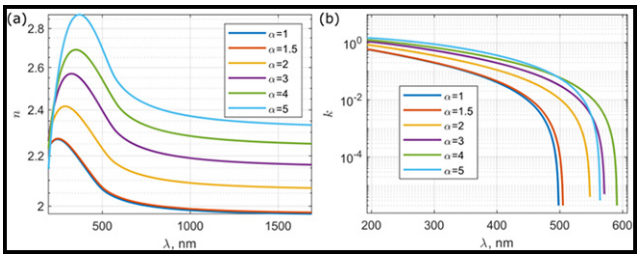

Figure 1: (a) Refractive index n and (b) extinction coefficient k of PECVD-deposited SRN films as a function of the SiH_4:NH_3 gas ratio α and wavelength λ.

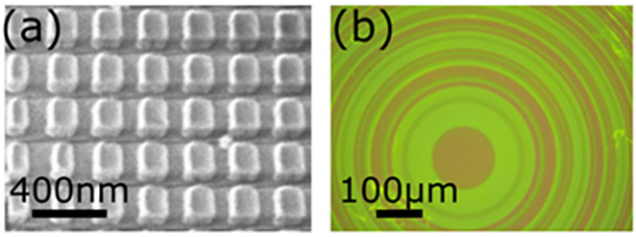

Figure 2: (a) A scanning electron microscopy (SEM) image of a representative SRN-metasurface, consisting of a periodic array of rectangular SRN pillars on a silica substrate. (b) Optical microscope image of the fabricated 1.5-mm-diameter spherical SRN-metalens. The different colors of the concentric rings of the metalens correspond to unique metasurface pillar geometries.

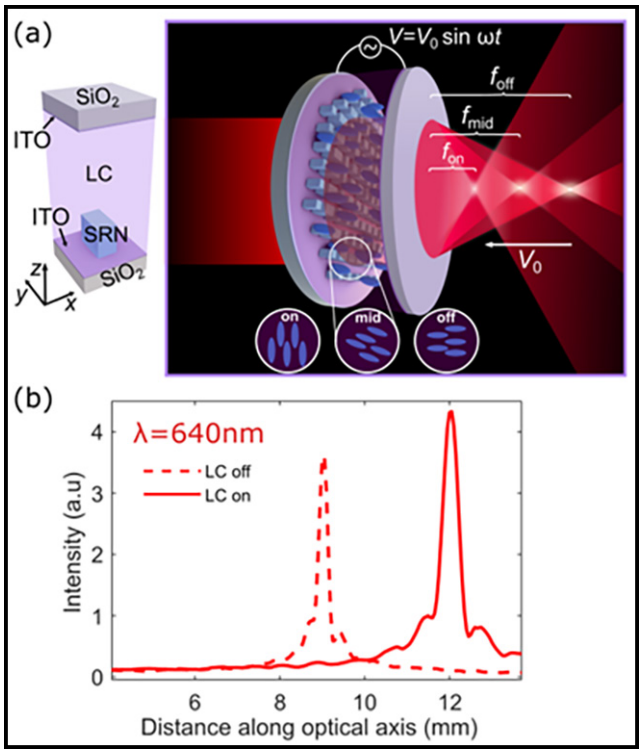

Figure 3: Left: The metasurface unit cell, consisting of a rectangular SRN meta-atom embedded in a LC and sandwiched between two transparent conducting indium-tin-oxide (ITO)-coated silica plates. Right: An AC voltage applied across electrodes modulates the LC molecule orientation and resulting focal length of the metalens. (b) Simulated intensity of transmitted light along the optical axis of the SRN-metalens for λ = 640 nm. The lens acts as a converging lens with a 9 mm focal length in the absence of an external electric field (dashed red line) and a 11 mm focal length in the presence of an external electric field (solid red line).

We merge this design strategy with SRN thin film engineering to design and fabricate SRN-based resonant LC-metalenses (Figure 2b) that enables switchable-focus at visible wavelengths. The metasurface unit cell is a rectangular SRN pillar embedded in a nematic LC and sandwiched between two conductive plates, as shown in Figure 3a. The local phase response of the SRN meta-atoms are modulated by means of the field-dependent LC, resulting in continuous and reversible modulations of the metalens focal length. In one design for red light meta-atom geometries are optimized to impart phase shifts that approximate the ideal focusing phase profile for a converging lens with focal distance $f = f_{off}$ in the LC "off" state, while simultaneously engineered to impart the phase profile of a converging lens with $f = f_{on}$ in the LC "on" state. To validate the approach, we fabricated a 1.5-mm-diameter spherical metalens that facilitates voltage-actuated switching between two distinct focal distances of f_{off} = 9 mm and f_{on} = 11 mm at a wavelength of 640 nm. Our simulations at predict high-contrast switching between focal spots in response to the "off"-to-"on" permittivity modulation of the LC, as shown in Figure 3b.

References:

[1] Genevet, Patrice, et al. "Recent advances in planar optics: from plasmonic to dielectric metasurfaces." Optica 4.1 (2017): 139-152.

[2] Devlin, Robert C., et al. "Broadband high-efficiency dielectric metasurfaces for the visible spectrum." Proceedings of the National Academy of Sciences 113.38 (2016): 10473-10478.

[3] Grinblat, Gustavo, et al. "Efficient ultrafast all-optical modulation in a nonlinear crystalline gallium phosphide nanodisk at the anapole excitation." Science advances 6.34 (2020).

[4] Bosch, Melissa, et al. "Electrically actuated varifocal lens based on liquid-crystal-embedded dielectric metasurfaces." Nano Letters 21.9 (2021): 3849-3856.

Development of Visible Light/IR Diffractive Optical Elements for Beam Shaping Using Nanoimprint Lithography

CNF Project Number: 3024-22

Principal Investigator(s): Keiko Munechika

User(s): Kaito Yamada

Affiliation(s): HighRI Optics, Inc., Oakland, California, USA

Primary Source(s) of Research Funding: HighRI Optics, Inc.

Contact: km@highrioptics.com, kaitoy@highrioptics.com
Website: https://highrioptics.com

Primary CNF Tools Used: Nanonex NX-2500

Abstract:

The development process in nanoimprint lithography is a key piece of technology for optical device fabrications, such as Diffractive Optical Elements. Our developed UV curable resins with refractive indices of 1.8-2.0 have now been successfully imprinted without any defects. This technology will not only improve the device performance, but also expand the applications of nanoimprint lithography for use with an array of optical devices.

Summary of Research:

Many fields have begun looking to the development of nanofabrication technologies to achieve better resolution, improved variation of critical dimensions, and improved placement accuracy in their technology. Nanoimprint lithography has shown to be a promising avenue from which to accomplish these goals at a low cost, for a wide variety of consumer applications [1]. However, the development process can be quite challenging since the optimized conditions vary depending on the mold design and chosen materials.

Applications for Diffractive Optical Elements (DOEs) have attracted a lot of attention, as they can implement versatile functionalities such as beam shaping and phase encoding [2]. For such applications, high refractive index materials are highly sought after to improve the performance of these devices. HighRI Optics is developing a series of high refractive index nanoimprint resins with the refractive index n ~ 1.8-2.0, representing one of the highest commercially available RI values [3]. Here we report on the successful fabrication of DOEs using our developed materials with a refractive index of up to 2.0.

Silicon or fused silica wafers were spin-coated with the high refractive index materials, and nanoimprint lithography was performed using Nanonex NX-2500 as shown in Figure 1. Following UV exposure, the master mold was demolded from the UV resin layer to achieve the desired replicated patterns. Figure 2 shows an image

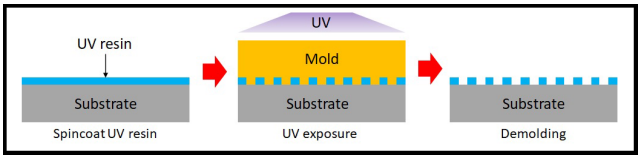

Figure 1: A schematic of nanoimprint lithography.

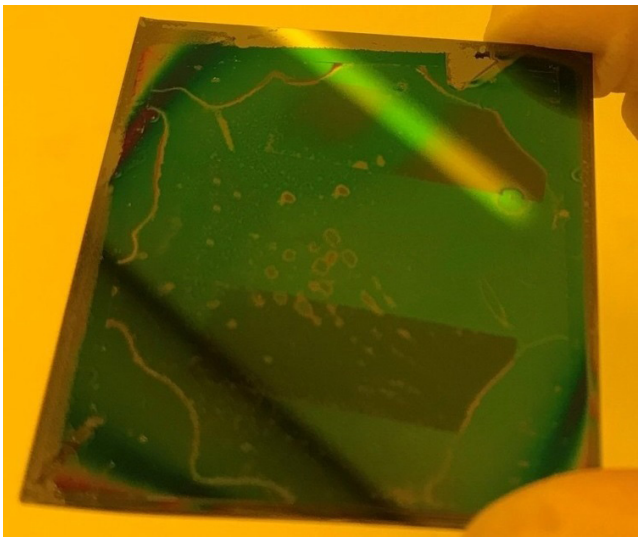

Figure 2: Imprinted patterns in the high refractive index polymer with many defects.

of the imprinted patterns fabricated in our facility, and Figure 3 displays an image of the same patterns fabricated at CNF. The results clearly show an increase in the quality of the imprinted patterns, and no defects were observed on the device.

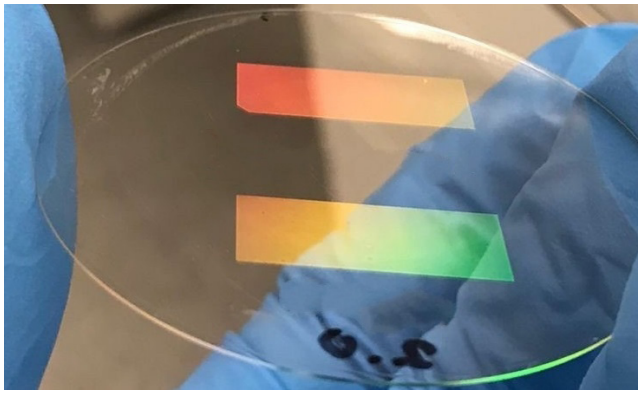

Figure 3: Imprinted patterns in the high refractive index polymer with no defects.

Conclusions and Future Steps:

By optimizing the imprint conditions, our developed materials with high refractive index have been successfully imprinted with the necessary patterns for DOE applications. This technology is expected to greatly improve the performance of DOEs for versatile applications such as augmented reality and virtual reality devices. Our next steps are to continue optimizing the fabrication process to suit more complex designs, as well as to further increase the refractive index of the materials.

References:

[1] S. Chou, P. R. Krauss, and P. J. Renstrom, Science, 272, 5258, 85 (1996).

[2] A. Siemion, Sensors, 21, 100 (2021).

[3] C. Pina-Hernandez, et al., Scientific Reports, 7, 17645 (2017).

Development of Functional Gas Diffusion Layers for use in CO_2 Reduction Reactors via Microscale Printing

2022 CNF REU Intern: Zeinab Ismail

Intern Affiliation: Physics, St. John's University

CNF REU Principal Investigator: Dr. Sadaf Sobhani, Mechanical and Aerospace Engineering, Cornell
CNF REU Mentor: Giancarlo D'Orazio, Mechanical and Aerospace Engineering, Cornell University

CNF REU Project and Primary Source(s) of Research Funding: 2022 Cornell NanoScale Science & Technology Facility Research Experiences for Undergraduates (CNF REU) Program via the National Science Foundation under Grant No. NNCI-2025233

Contact: z_nab01@hotmail.com, sobhani@cornell.edu, gd373@cornell.edu

Website: https://cnf.cornell.edu/education/reu/2022
Primary CNF Tools Used: NanoScribe GT2, Objet 30 Printer, AJA Sputter Deposition, Zeiss Ultra SEM

Abstract:

In a world reliant on the burning of fossil fuels to run some of its major industries, there is concern as to how we dispose of the carbon dioxide (CO_2) waste produced. One approach is to reprocess the CO_2 into simple hydrocarbons using a CO_2 Reduction Reactor (CO_2RR). A CO_2RR's ability to produce useful products relies heavily on its gas diffusion electrodes (GDEs), which consist of porous membranes called gas diffusion layers (GDLs) coated in a metal catalyst. GDLs act as a barrier against unwanted liquids, letting only gasses pass through.

A conventional GDE, consisting of PTFE and copper covered carbon paper, typically operates for a few hours before its efficiency begins to drop and it floods. Printing GDLs using a 3D printer would allow for optimization of the layer through the customization of the pore size, structure, and density of the layer.

Summary of Research:

The CO_2RR used consisted of three SLA-printed compartments: gas, anolyte, and catholyte compartments. The anode, ion-exchange membrane, and cathode used in the reactor were respectively a platinum mesh, nafion ion exchange membrane, and 3D printed GDL created using the NanoScribe GT2, attached to an adapter made by the Objet 30 printer, and sputtered in copper. The reactor was constantly being pumped with carbon dioxide gas and electrolytic solution, consisting of water and potassium bicarbonate. The process of creating functional GDLs was broken into three parts: designing a GDL, creating the gas diffusion electrode, and assembling the reactor and testing it.

The NanoScribe GT2 sweeps a femtosecond near IR laser across resin, curing sections with two-photon polymerization. The two resins experimented with to produce the GDLs were the IP-S and IP-Q resins. The general workflow for the NanoScribe consisted of creating a CAD model and generating an STL, slicing the STL using DeScribe, prepping the resist on a silicon wafer, loading the wafer into the printer, and printing, unloading, and developing the sample. The first design attempt to generate the full-scale layer of 10.095 mm × 10.095 mm × 400 µm thickness was too computationally intensive. The NanoScribe slicer, DeScribe, can work with files up to two gigabytes, but the full-scale GDL, in its lowest quality, was six gigabytes.

The next design created an STL out of 1/16 of the full-scale layer, one block, and used a for-loop of arrays and an overlap of 5 µm to build the full layer. The layer printed using this design began to deteriorate and peel off the silicon wafer after development. The final GDL design made and used was a 2 × 2 array of 5 mm × 5 mm × 100 µm each block, layered on top of each other four times, to create a thickness of 400 µm.

Using the IP-S resin and 2 × 2 array design, a second GDL print was made. After development, the GDL layers began to fall apart, and the layer began to peel off the wafer. At this point, the suitability of the IP-S resin was put in question.

The IP-S resin was initially chosen because it was not sensitive to overdevelopment and was the freshest resin available. It was only after printing the third gas diffusion using IP-Q resin instead that the layer turned out better than previous prints, with the IP-Q resin layer having no visible discoloration, excess uncured resin, or separation of layers from each other or off the wafer (see Figure 1).

After developing the layer in PGMEA for 45 minutes and IPA for 30 min, it was soaked for another 30 minutes in IPA. Next, it was sonicated for 10 minutes at 21°C, then placed on a hot plate of 90°C for 20 seconds and moved onto a cool plate. After doing this twice, the layer popped off the wafer.

Then the layer was glued to an adapter printed on the Objet 30 and cured using UV light. Afterwards, the glued pieces were sputtered with a 254 nm layer of copper, using the AJA sputter deposition tool (see Figure 2). Finally, the CO_2RR was assembled, and the finished gas diffusion electrode was incorporated into it (see Figure 3).

The CO_2RR was connected to a power source, potentiostat, and peristaltic pump. However, the gas chromatograph, a machine that would collect and quantify the gas products, was not working. The IR drop was collected and was found to be similar to an IR drop of a conventional GDL on the market. Then a cyclic voltammetry (CV) scan, which measures the change in current as different potentials are applied, was generated. Ideally, the plot should have multiple peaks, each peak representing the reduction/oxidation process. However, as shown in Figure 4, there's no current in the cell until about -1.2 V of potential is applied. This conclusion informs us that there is an electrochemical reaction taking place. However, there is another issue preventing a proper CV scan from being generated.

When the GDL was taken out of the cell, it was discovered that the copper wasn't adhering well to the GDL. A possible solution to try down the line would be to coat the layer initially with another metal, like chromium, then coat it with copper.

Conclusion and Future Steps:

Through the lengthy process of designing the gas diffusion layer, 3D printing it, and running it in a CO_2RR, we were able to produce a GDL that has a similar IR Drop to a conventional market GDL. More importantly, the GDL did not flood during the process of running the cell, showing the potential of using microscale manufacturing in producing optimized GDLs. The next steps would be to try coating the printed GDLs with a hydrophobic coating, as well sputtering it with chromium and copper. Afterwards, it would be tested in the CO_2RR when the gas chromatograph is working.

References:

[1] Energy Environ. Sci., 2021, 14, 3064 Wakerley, D., Lamaison, S., Wicks, J. et al. Gas diffusion electrodes, reactor designs and key metrics of low-temperature CO_2 electrolysers. Nat Energy 7, 130-143 (2022). https://doi.org/10.1038/s41560-021-00973-9.

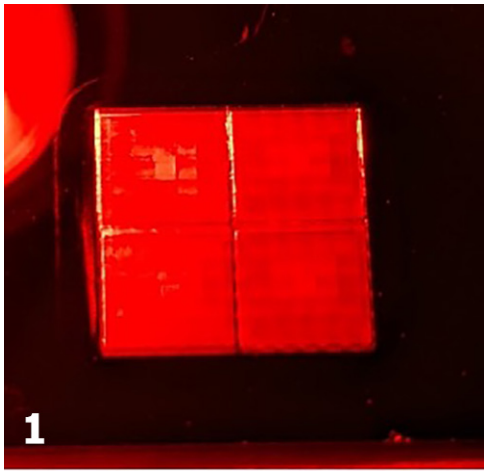

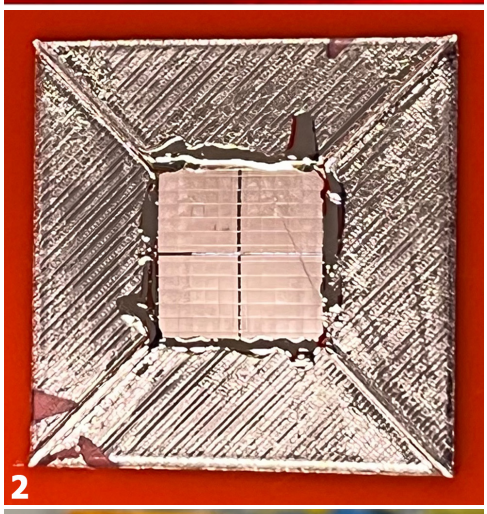

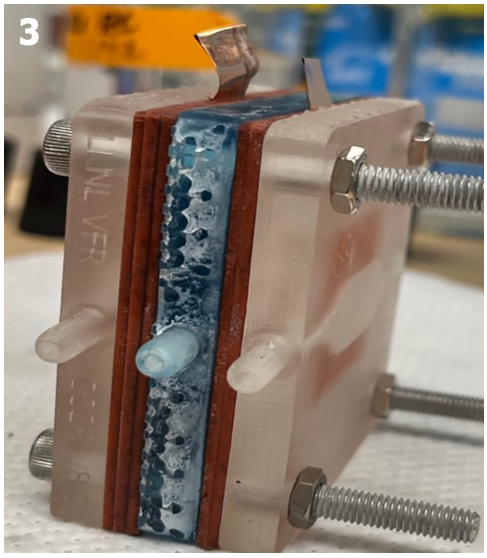

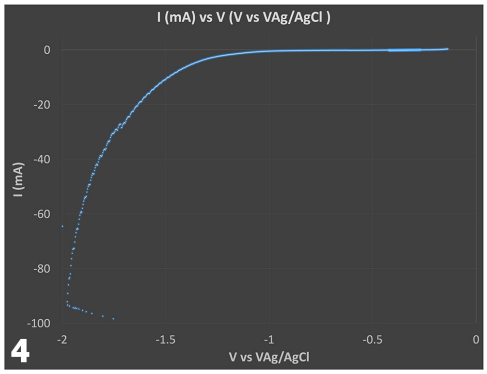

Figure 1, top: IP-Q resin layer with no visible discoloration, excess uncured resin, or separation of layers from each other or off the wafer. Figure 2, second from top: A 254 nm layer of copper was added using AJA sputter deposition. Figure 3, third from top: Assembled CO_2RR with gas diffusion electrode incorporated. Figure 4, bottom: Electrochemical reaction.

Anisotropic Gigahertz Antiferromagnetic Resonances of the Easy-Axis van der Waals Antiferromagnet CrSBr

CNF Project Number: 598-96

Principal Investigator: Daniel C. Ralph

User: Thow Min Jerald Cham

Affiliation: Laboratory of Atomic and Solid State Physics, Cornell University

Primary Source of Research Funding: National Science Foundation/Division of Materials Research, Air Force Office of Scientific Research, Agency for Science Technology and Research (Singapore)

Contact: dcr14@cornell.edu, tc676@cornell.edu

Primary CNF Tools Used: Supra SEM, Nabity Nanometer Pattern Generator, AJA Sputter Deposition, Even-Hour Evaporator

Abstract:

We report measurements of antiferromagnetic resonances in the van der Waals easy-axis antiferromagnet CrSBr. The spectra show good agreement with a Landau-Lifshitz model for two antiferromagnetically-coupled sublattices, accounting for inter-layer exchange and triaxial magnetic anisotropy. Fits allow us to quantify the parameters governing the magnetic dynamics: at 5K, the interlayer exchange field is $\mu_0 H_E$ = 0.395(2) T, and the hard and intermediate-axis anisotropy parameters are $\mu_0 H_c$ = 1.30(2) T and $\mu_0 H_a$ = 0.383(7) T [1].

Summary of Research:

Chromium bromide (CrSBr) is an A-type antiferromagnetic vdW semi-conductor with intralayer ferromagnetic coupling and interlayer antiferromagnetic coupling [2-4]. It has a bulk Néel temperature (T_N) of 132K and an intermediate ferromagnetic phase with Curie temperature (T_C) in the range of 164-185 K as measured using transport and optical methods [2,5,4]. Each vdW layer consists of two buckled rectangular planes of Cr and S atoms sandwiched between Br atoms. The layers are stacked along the *c*-axis through vdW interactions to form an orthorhombic structure (space group *Pmmn*). We investigate the antiferromagnetic resonances of CrSBr by placing the crystal on a coplanar waveguide and measuring the microwave absorption spectrum using a two-port vector network analyzer.

We align the crystal with its long axis perpendicular to the waveguide, such that the Néel axis is perpendicular to the in-plane RF field (H_{RF}). An external DC magnetic field is swept in-plane, either perpendicular, parallel, or at intermediate angles to the Néel axis. Representative transmission spectra as a function of applied field at 5K are shown in Figure 1. Dark green features represent

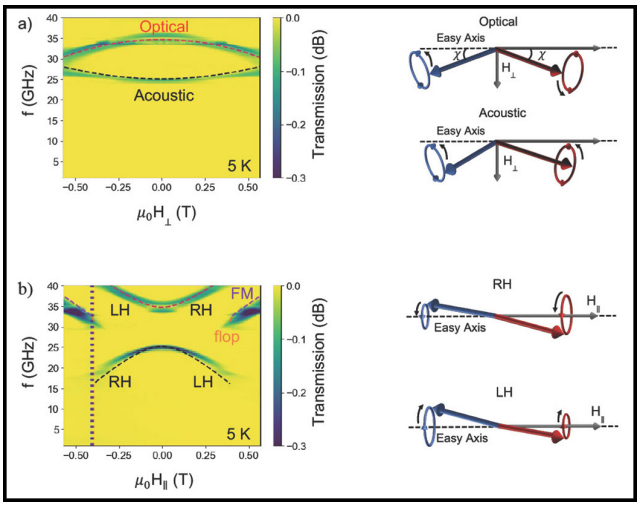

Figure 1: (a) Microwave transmission (S_{21}) signal as a function of $H_\perp$, magnetic field applied along the crystal a *axis. (b) The corresponding spectra as a function of H∥, magnetic field applied along the crystal* b *axis. S_{21} values are shown relative to a field-independent subtracted background. Dashed lines show a fit to the results of the L-L model. Diagrams on the right illustrate the form of some of the resonant modes.*

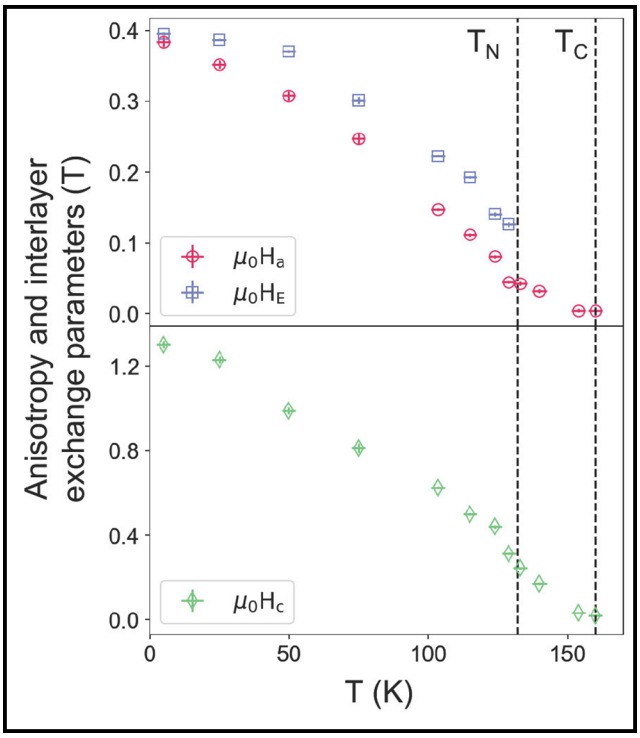

Figure 2: (a) Temperature dependence of the interlayer exchange H_E (blue squares) and the in-plane easy-axis anisotropy parameter H_a (red circles). (b) Temperature dependence of out-of-plane anisotropy parameter H_c. The black dashed lines indicate the estimated Néel temperature $T_N \approx 132$ K and the Curie temperature $T_c \approx 160$ K, previously measured in magnetometry and magnetotransport measurements.

strong microwave absorption due to resonance modes. We observe two resonance modes in the $H_\perp$ configuration and show their dependence on magnetic field in Figure 2a up to the maximum applied field of ± 0.57 T. We identify the two resonances in Figure 1a as acoustic and optical modes originating from an initial spin-flop configuration in which the two spin sublattices are canted away from the easy axis. In the $H_\parallel$ case (Figure 1b), two resonance features are also observed, but with opposite signs of concavity compared to Figure 1a.

Next, we investigate the evolution of the resonant modes with temperature. We observe qualitatively similar resonance features over the temperature range from 5 to 100 K. With increasing temperature, the modes shift to lower frequency and the magnetic field scales decrease for both the value of $H_\perp$ where the two modes become degenerate and for the value of $H_\parallel$ corresponding to the discontinuous transition. These observations can be attributed to decreasing values of all of the exchange and anisotropy parameters H_E, H_a and H_c with increasing temperature. Figure 2 plots the values of the parameters for a series of temperatures from 5 to 128K. We observe a monotonic decrease in all three parameters.

Conclusion and Future Steps:

In summary, we report measurements of gigahertz-frequency antiferromagnetic resonance modes in the van der Waals antiferromagnet CrSBr that are anisotropic with regard to the angle of applied magnetic field relative to the crystal axes. The modes are well described by two coupled Landau-Lifshitz equations for modeling the spin sublattices, when one accounts for interlayer exchange and triaxial magnetic anisotropy present in CrSBr. Our characterization of antiferromagnetic resonances in an easily-accessible frequency range, and the understanding of how the resonances can be tuned between uncoupled and strongly-coupled by adjusting magnetic field, sets the stage for future experiments regarding manipulation of the modes and the development of capabilities like antiferromagnetic spin-torque nano-oscillators.

References:

[1] Thow Min Jerald Cham, Saba Karimeddiny, Avalon H. Dismukes, Xavier Roy, Daniel C. Ralph, and Yunqiu Kelly Luo. Anisotropic gigahertz antiferromagnetic resonances of the easy-axis van der waals antiferromagnet crsbr. Nano Letters, 22(16):6716-6723, 2022. PMID: 35925774.

[2] Evan J. Telford, Avalon H. Dismukes, Kihong Lee, Minghao Cheng, Andrew Wieteska, Amymarie K. Bartholomew, Yu-Sheng Chen, Xiaodong Xu, Abhay N. Pasupathy, Xiaoyang Zhu, Cory R. Dean, and Xavier Roy. Layered antiferromagnetism induces large negative magnetoresistance in the van der waals semiconductor CrSBr. Advanced Materials, 32(37):2003240, 2020.

[3] Ke Yang, Guangyu Wang, Lu Liu, Di Lu, and Hua Wu. Triaxial magnetic anisotropy in the two-dimensional ferromagnetic semiconductor crsbr. Physical Review B, 104:144416, Oct 2021.

[4] Evan J Telford, Avalon H Dismukes, Raymond L Dudley, Ren A Wiscons, Kihong Lee, Daniel G Chica, Michael E Ziebel, Myung-Geun Han, Jessica Yu, Sara Shabani, Allen Scheie, Kenji Watanabe, Takashi Taniguchi, Di Xiao, Yimei Zhu, Abhay N Pasupathy, Colin Nuckolls, Xiaoyang Zhu, Cory R Dean, and Xavier Roy. Coupling between magnetic order and charge transport in a two-dimensional magnetic semi.conductor. Nature Materials, 21(7):754-760, 2022.

[5] Kihong Lee, Avalon H. Dismukes, Evan J. Telford, Ren A. Wiscons, Jue Wang, Xiaodong Xu, Colin Nuckolls, Cory R. Dean, Xavier Roy, and Xiaoyang Zhu. Magnetic Order and Symmetry in the 2D Semiconductor CrSBr. Nano Letters, 21(8):3511-3517, 2021.

Gate-Tunable Anomalous Hall Effect in a 3D Topological Insulator/2D Magnet van der Waals Heterostructure

CNF Project Number: 598-96

Principal Investigator(s): Daniel C. Ralph

User(s): Rakshit Jain, Vishakha Gupta

Affiliation(s): Physics Department, Cornell University

Primary Source(s) of Research Funding: Air Force Office of Scientific Research, Department of Energy

Contact: dcr14@cornell.edu, rj372@cornell.edu, vg264@cornell.edu

Primary CNF Tools Used: Zeiss Supra SEM, Nabity Nanometer Pattern Generator, AJA Sputter Deposition, CVC SC4500 Even-Hour Evaporator

Abstract:

We demonstrate advantages of samples made by mechanical stacking of exfoliated van der Waals materials for controlling the topological surface state of a 3-dimensional topological insulator (TI) via interaction with an adjacent magnet layer. We assemble bilayers with pristine interfaces using exfoliated flakes of the TI $BiSbTeSe_2$ and the magnet $Cr_2Ge_2Te_6$, thereby avoiding problems caused by interdiffusion that can affect interfaces made by top-down deposition methods. The samples exhibit an anomalous Hall effect (AHE) with abrupt hysteretic switching. For the first time in samples composed of a TI and a separate ferromagnetic layer, we demonstrate that the amplitude of the AHE can be tuned via gate voltage with a strong peak near the Dirac point. This is the signature expected for the AHE due to Berry curvature associated with an exchange gap induced by interaction between the topological surface state and an out-of-plane-oriented magnet.

Summary of Research:

Interactions between three-dimension topological insulators (TIs) and magnets can induce exotic topological phases like the quantum anomalous Hall or axion insulator states, and might be used to harness the properties of topological-insulator surface states in spintronic devices [1]. We study TI/magnet bilayers using an all-van der Waals (vdW) heterostructure, by stacking together in a glovebox exfoliated flakes of the TI $BiSbTeSe_2$ and the insulating magnet $Cr_2Ge_2Te_6$ [2].

In contrast to previous work on TI/magnet samples grown by top-down deposition methods, or made by assembling exfoliated flakes with air exposure, the use of a glovebox-assembled vdW structure ensures a defect- and diffusion-free atomically-flat interface. Further, our use of a thin insulating vdW magnet enables both spatially-uniform magnetic coupling to the topological surface state and large tunability of the electron chemical potential using electrostatic gating (see Figure 1 for device structure and gating geometry). We measure the anomalous Hall response while continuously controlling the contribution of the surface state by gating.

The out-of-plane magnetization of the CGT is expected to break time-reversal symmetry in the BSTS surface through proximity coupling and result in the opening of an exchange gap (Δ) in the adjacent Dirac surface state, as described by the following 2D Dirac Hamiltonian:

$$H(k) = \hbar v_F(k_x\sigma_y - k_y\sigma_x) + \Delta\sigma_z$$

where $\sigma_{x,y,z}$ are the Pauli spin matrices, k_x and k_y are in-plane wave vectors, and v_F is the Fermi velocity. States in the vicinity of the gap have non-zero Berry curvature, with equal and opposite values on opposite sides of the gap. Therefore when states on opposite sides of the gap have unequal occupations, the result is a nonzero Hall conductance, σ_{xy}. The peak value of the Hall conductance, when the electron chemical potential lies in the gap, should be $e^2/2h$ in the low temperature limit (3). Consequently, a peak of the Hall resistivity ($\rho_{xy} = \sigma_{xy}/(\sigma^2_{xx} + \sigma^2_{xy})$), where σ_{xx} is the longitudinal conductivity) should be found when the chemical potential is tuned through the gap.

In Figure 2a, we show the Hall resistance (R_{xy}) after subtraction of the ordinary Hall background for the measurement done at top gate voltage V_{tg} = 0V. The measurements are performed at 4.4K and under a constant bias current, with the bottom-gate voltage V_{bg} fixed at 0V. The current flows primarily through the BSTS layers since CGT is insulating at this temperature. We observe hysteretic step-like changes in V_{xy} corresponding to an anomalous Hall effect (AHE), indicative of a strong perpendicular anisotropy for the magnetism in CGT that is coupled to the BSTS surfaces.

As the chemical potential of the top surface is tuned by varying the V_{tg}, we observe a modulation in the observed AHE signal. The amplitude of the AHE response is maximum at V_{tg} = 0.55V and becomes smaller as the gate voltage is tuned on either side of this maximum.

In Figure 2b, we plot the extracted signal size of the anomalous Hall resistance response as a function of V_{tg} (black trace). This trend tracks approximately with the gating behaviour of the longitudinal resistance R_{xx} shown by the dotted blue trace. We therefore identify the maximum in the AHE response as due to tuning of the electron chemical potential within the exchange gap, as expected from the Berry curvature picture.

Conclusions and Future Directions:

We have demonstrated that the use of mechanical assembly of van der Waals materials to form a pristine interface provides a strategy that avoids materials challenges which have inhibited research progress in studying topological insulator/magnet heterostructures grown by molecular beam epitaxy or other deposition techniques. The high quality of mechanically-assembled van der Waals structures provides a platform for future studies of the quantum anomalous Hall and axion insulator states, and the rich phenomenology of topological magneto-electric phenomena predicted for these states.

References:

[1] Tokura, Y., Yasuda, K., and Tsukazaki, A. Magnetic topological insulators. Nature Reviews Physics 1, 126–143 (2019).

[2] Gupta, V., et al. Gate-tunable anomalous Hall effect in a 3D topological insulator/2D magnet van der Waals heterostructure. Nano Letters URL https://doi.org/10.1021/acs.nanolett.2c02440.

[3] Xiao, D., Chang, M.-C. and Niu, Q. Berry phase effects on electronic properties. Rev. Mod. Phys. 82, 1959 (2010).

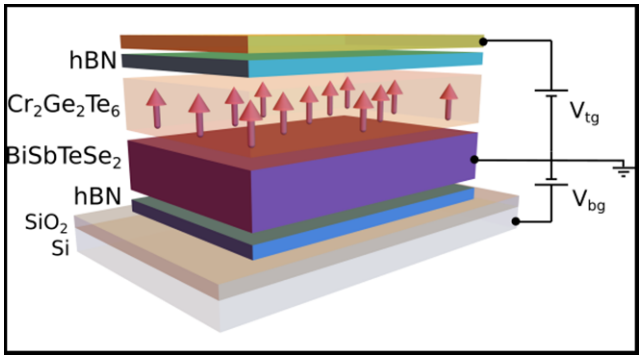

Figure 1: Schematic of the device geometry and electrostatic gating geometry. TI and 2D magnet flakes with few-layer thickness are double-encapsulated between h-BN layers on a Si/SiO_2 substrate.

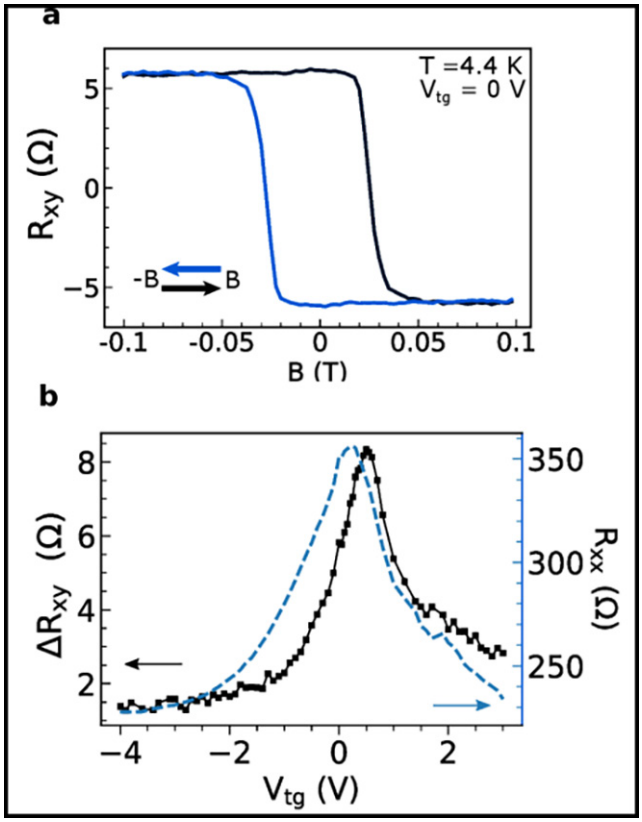

Figure 2: (a) AHE contribution to R_{xy} at V_{tg} = 0 after subtraction of linear background. (b) Size of AHE signal (black solid line) ΔR_{xy} as a function of top-gate voltage. The trend matches closely with the observed top-gate dependence of R_{xx} (blue dashed line) measured at zero magnetic field.

Fabricating Micron-Sized Devices for Measuring Magnetic Properties

CNF Project Number: 598-96

Principal Investigator(s): Daniel C. Ralph

User(s): Maciej Olszewski

Affiliation(s): Laboratory of Atomic and Solid State Physics (LASSP), Cornell University

Primary Source(s) of Research Funding: Defense Advanced Research Projects Agency (DARPA), National Science Foundation (NSF)

Contact: dcr14@cornell.edu, mwo34@cornell.edu
Website: https://ralphgroup.lassp.cornell.edu/

Primary CNF Tools Used: Zeiss Supra SEM, Nabity Nanometer Pattern Generator System, SC4500 Odd-Hour / Even-Hour Evaporator, Oxford 81 Etcher, AFM – Veeco Icon

Abstract:

We present various methods for improving the removal of residual polymethyl methacrylate (PMMA) resist in electron beam lithography (EBL) processes. We explore various methods of PMMA removal, including furnace annealing, plasma cleaning, solvent stripping, and atomic force microscope (AFM) tip cleaning. We compare the various removal procedures by measuring the average roughness of the region using AFM. We report that the best method for removing polymer residue is a combination of solvent stripping and AFM tip cleaning.

Summary of Research:

Van der Waals material heterostructures fabricated from exfoliated crystals have atomically smooth layers, forming pristine interfaces between various materials [1]. This allows for studying new and exotic states of matter as well as improving the understanding of physics in the quantum mechanics regime. One drawback of this technique is the different shapes and sizes of the exfoliated flakes, which compose the heterostructures. Especially in the case of geometrically sensitive measurements, such as Hall conductance, we require a very precise device geometry.

This issue can be resolved by a combination of lithography, etching and metal deposition, however these techniques usually involve various polymers which can contaminate the pristine nature of the interfaces, reduce the electrical mobility in the materials, and introduce noise in the measurements. To try and maintain a pristine nature of the interfaces we explore a various combination of methods that can help clean the residual resist from the materials. We explore various methods presented in literature, including furnace annealing [2], plasma cleaning [3], various solvent stripping [4,5], and AFM tip cleaning [6].

Initially, we tried using various forms of vacuum furnace annealing and plasma cleaning to remove the remainder polymer residue. These tests however an increase of black spots on the devices which has be reported to be residual amorphous carbon atoms [2,3]. We then turned to trying various wet solvent stripping methods using various combinations of acetone, dichloromethane, glacial acetic acid, and Allresist AR700-61.

For each process we ran the same e-beam lithography process on the Nabity Nanometer Pattern Generator System (NPGS) using a polymethyl methacrylate (PMMA) bilayer resist, after developing we either etched the devices using the Oxford 81 Etcher or deposited metal using the SC4500 Odd-Hour Evaporator. After the etching and/or metal deposition the devices were soaked in various solvents for varying amounts of

Process Type	RMS Roughness (pm)	Mean Roughness (pm)
Allresist	367.05	303.23
DCM and Acetone	632.43	426.76
Toluene	3047.25	2237.50
Acetone	649.40	524.50
Acetic Acid	1150.23	900.01

Figure 1: Table of the surface roughness of the device region after stripping in various resists. The values are obtained by measuring the roughness across many devices.

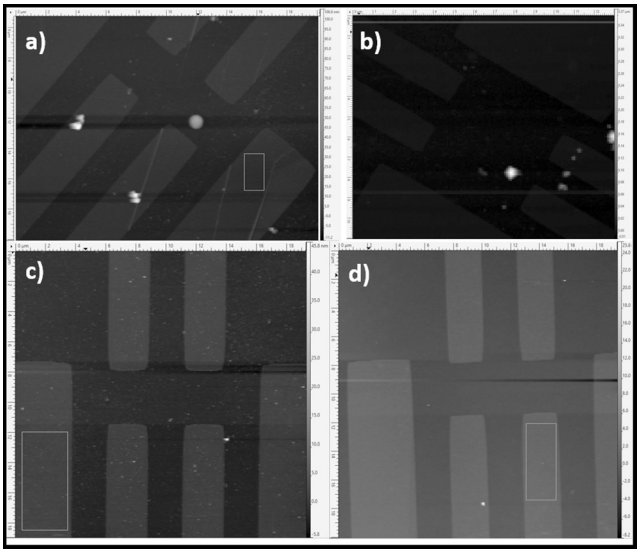

Figure 2: An AFM topography scan of a sample device after a) acetone stripping, b) acetone/dichloromethane stripping, c) acetic acid stripping, d) acetone/Allresist stripping.

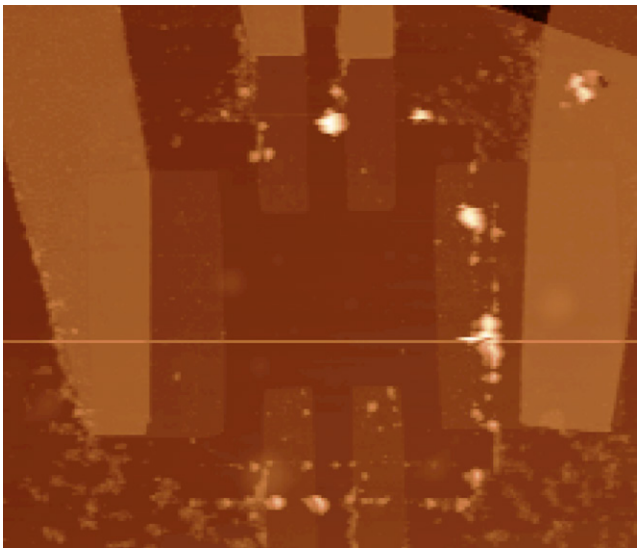

Figure 3: An AFM topography scan of a sample device after the AFM tip cleaning procedure done after acetone stripping.

time. The roughness of the devices was then measured using tapping mode AFM, sample scans for various solvents are shown in Figure 1. Further we analyzed the roughness for various regions and complied the average roughness value for different solvent methods in Figure 2. We were able to conclude that soaking in Allresist was the best solvent at removing PMMA residue from the device areas.

Finally, we attempted to clean the devices using an AFM tip. This was done by taking an AFM tip in contact mode and dragging it over the surface of the device moving the PMMA residue around. As shown in Figure 3 this causes the PMMA residue to move around however it does not remove the resist but simply relocates it to a different region on the chip. This process proved to be by far the best, often yielding roughness of less than 300 pm.

In summary, we showed that using various solvents for stripping can improve the removal of residual PMMA, however AFM tip cleaning is by far the most efficient method of removing the polymer.

This research allowed us to determine the most optimal method of removing the residue from our devices and improving the interfaces in the heterostructures.

References:

[1] Castellanos-Gomez, A., Duan, X., Fei, Z. et al. Van der Waals heterostructures. Nat Rev Methods Primers 2, 58 (2022).

[2] Wang, X., et al. Direct Observation of Poly (Methyl Methacrylate) Removal from a Graphene Surface. Chem Mater 29, 5 (2017).

[3] Cunge, G., et al. Dry efficient cleaning of poly-methyl-methacrylate residues from graphene with high density H_2 and H_2-N_2 plasmas. Journal of Applied Physics 118, 12 (2015).

[4] Honghwi P., et al. Optimized poly (methyl methacrylate)-mediated graphene-transfer process for fabrication of high-quality graphene layer. Nanotechnology 29, 415303 (2018).

[5] Tyagi, A., et al. Ultra-clean high-mobility graphene on technologically relevant substrates. Nanoscale, 14, 2167 (2022).

[6] Chen, S., et al. Tip-Based Cleaning and Smoothing Improves Performance in Monolayer MoS_2 Devices. ACS Omega 6, 5 (2021).

Nanofabricated Superconducting Devices for Vortex Dynamics and Qubits

CNF Project Number: 1314-05

Principal Investigator(s): Britton L.T. Plourde

User(s): Brad Cole, Kenneth Dodge, Jaseung Ku, Clayton Larson, Yebin Liu, Eric Yelton

Affiliation(s): Department of Physics, Syracuse University

Primary Source of Research Funding: Army Research Office

Contact: bplourde@syr.edu, bgcole@syr.edu, krdodgej@syr.edu, jku102@syr.edu, cllarson@syr.edu, yliu166@syr.edu, epyelton@syr.edu
Website: https://bplourde.expressions.syr.edu/

Primary CNF Tools Used: ASML Photostepper, JEOL 6300, Plasma-Therm 770

Abstract:

We fabricate superconducting microwave devices for studying the dynamics of vortices at low temperatures and for forming novel qubits. Vortices are quantized bundles of magnetic flux that thread many different superconductors over a particular range of applied magnetic field. By using disordered superconducting thin films to form high kinetic inductance wires combined with novel arrays of Josephson junctions, we are able to build structures that can lead to qubits that are protected against decoherence. With charge-sensitive superconducting qubits, we are able to probe sources of correlated errors in quantum processors.

Summary of Research:

Superconducting microwave circuits play an important role in quantum information processing. Circuits composed of Josephson junctions and capacitors with superconducting electrodes can serve as qubits, the fundamental element of a quantum computing architecture. Various loss mechanisms limit the ultimate performance of these devices, including trapped magnetic flux vortices. Vortices can be trapped in the superconducting electrodes when background magnetic fields are present and contribute dissipation when driven with microwave currents [1]. Thus, techniques for controlling the trapping of vortices are critical to the development of large-scale quantum information processors with superconducting circuits.

By arranging nanoscale Al-AlO_x-Al Josephson tunnel junctions in novel arrays, it is possible to implement new qubit designs that are protected against decoherence [2-4]. We are also able to use such Al-AlO_x-Al tunnel

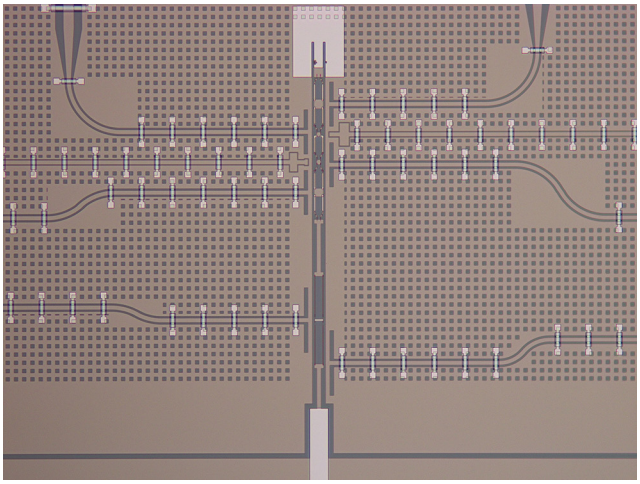

Figure 1: Optical micrograph of plaquette structures formed from arrays of Al-AlO_x-Al Josephson junctions for protected qubit design with Nb ground plane and flux-and charge-bias lines along with Al/SiO_x ground straps.

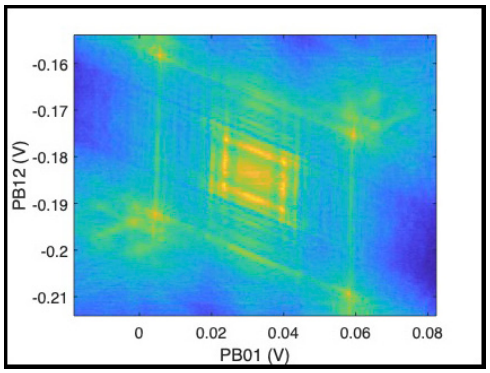

Figure 2: Microwave transmission through feedline coupled to readout cavity with capacitive coupling to plaquette-chain structure as a function of the magnetic flux bias using two of the on-chip bias lines.

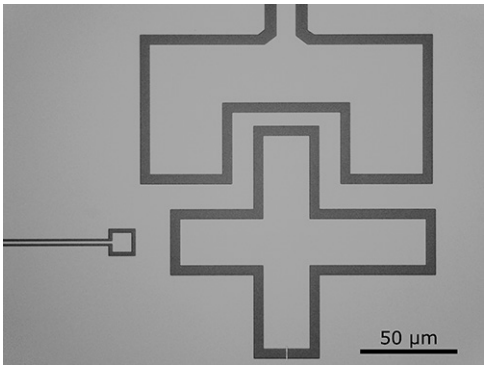

Figure 3: Optical micrograph of charge-sensitive transmon qubit with Al-AlO$_x$-Al tunnel junction for measurement of phonon-mediated quasiparticle poisoning.

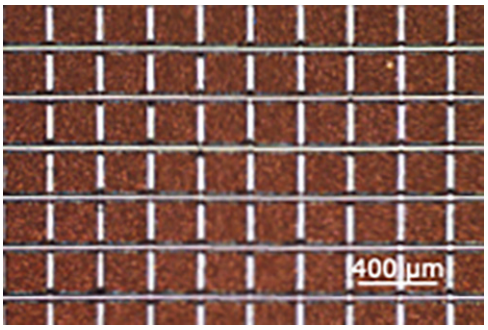

Figure 4: Optical micrograph of electroplated Cu islands on the back side of Si chip for downconversion of high energy phonons, with transmon qubits on the device layer.

junctions in superconducting qubits to probe poisoning effects from nonequilibrium quasiparticles, which are a source of correlated errors in quantum processors. We can mitigate this quasiparticle poisoning through the use of electroplated Cu metallic reservoirs for downconversion of high energy phonons [5].

We fabricate our microwave resonators from various superconducting films, including aluminum and niobium, deposited onto silicon wafers in vacuum systems at Syracuse University. We define the patterns on the ASML stepper and transfer them into the films with a combination of reactive ion etching and liftoff processing. For defining Josephson junctions, we use the JEOL 6300 along with a dedicated deposition system at Syracuse University. We measure these circuits at temperatures of 100 mK and below in our lab at Syracuse University.

References:

[1] Song, C., Heitmann, T.W., DeFeo, M.P., Yu, K., McDermott, R., Neeley, M., Martinis, John M., Plourde, B.L.T.; "Microwave response of vortices in superconducting thin films of Re and Al"; Physical Review B 79, 174512 (2009).

[2] Doucot, B., Ioffe, L.; "Physical implementation of protected qubits"; Reports on Progress in Physics 75, 072001 (2012).

[3] Liu, Y., Dodge, K., Cole, B., Ku, Shearrow, A., Snyder, M., Brann, E., Klots, A., Faoro, L., Ioffe, L.B., McDermott, R., Plourde, B.; "Charge-parity qubits based on concatenation of p-periodic Josephson elements: Part 1"; Bull. Am. Phys. Soc. 2022, https://meetings.aps.org/Meeting/MAR22/Session/S41.6

[4] Dodge, K., Liu, Y., Cole, B., Ku, Shearrow, A., Snyder, M., Brann, E., Klots, A., Faoro, L., Ioffe, L.B., McDermott, R., Plourde, B.; "Charge-parity qubits based on concatenation of p-periodic Josephson elements: Part 2"; Bull. Am. Phys. Soc. 2022, https://meetings.aps.org/Meeting/MAR22/Session/S41.5

[5] Iaia, V., Ku, J., Ballard, A., Larson, C.P., Yelton, E., Liu, C.H., Patel, S., McDermott, R., Plourde, B.L.T.; "Phonon downconversion to suppress correlated errors in superconducting qubits"; arxiv:2203.06586 (2022).

Fabrication of Nanoscale Josephson Junctions for Quantum Coherent Superconducting Circuits

CNF Project Number: 1735-08

Principal Investigator(s): Britton L.T. Plourde

User(s): Brad Cole, Tianna McBroom, JT Paustian, Michael Senatore

Affiliation(s): Department of Physics, Syracuse University

Primary Source(s) of Research Funding: Air Force Research Lab,
Air Force Office of Scientific Research

Contact: bplourde@syr.edu, bgcole@syr.edu, tamcbroo@syr.edu,
jtpausti@syr.edu, masenato@syr.edu
Website: https://bplourde.expressions.syr.edu/

Primary CNF Tools Used: ASML Photostepper, JEOL 6300, Plasma-Therm 770

Abstract:

We fabricate nanoscale superconductor tunnel junctions and other structures for experiments involving quantum coherent circuits. Such circuits have shown great promise in recent years for explorations of quantum mechanics at the scale of circuits on a chip and for forming qubits, the foundational elements of a quantum computer. The quantum state of these superconducting qubits can be manipulated with microwave radiation at low temperatures. We are currently developing superconducting metamaterial structures with novel microwave mode spectra for coupling to superconducting qubits.

Summary of Research:

The unique properties of nanoscale Josephson junctions enable a wide range of novel superconducting circuits for investigations in many diverse areas. In recent years, circuits composed of such junctions have emerged as promising candidates for the element of a quantum computer, due to the low intrinsic dissipation from the superconducting electrodes and the possibility of scaling to many such qubits on a chip [1]. The quantum coherent properties of the circuits are measured at temperatures below 50 mK with manipulation of the qubit state through microwave excitation.

We are developing multimode microwave resonators using combinations of superconducting lumped-circuit elements to engineer metamaterial transmission lines, including metamaterial ring resonator devices. These structures exhibit novel mode structures characteristic of left-handed materials [2]. We are fabricating such metamaterial transmission lines from Al and Nb films on Si and characterizing these at low temperatures [2]. We are working on experiments to couple these left-handed lines and ring resonators to superconducting qubits for experiments involving the exchange of microwave photons [2-4].

We pattern these circuits at the CNF with nanoscale structures defined with electron-beam lithography on the JEOL 6300 integrated with photolithographically defined large-scale features. The junctions are fabricated using the standard double-angle shadow evaporation technique, in which a resist bilayer of copolymer and PMMA is used to produce a narrow PMMA airbridge suspended above the substrate. Evaporation of aluminum from two different angles with an oxidation step in between forms a small Al-AlO_x-Al tunnel junction from the deposition shadow of the airbridge. We have developed a process for defining these junctions with electron-beam lithography and we perform the aluminum evaporations in a dedicated chamber at Syracuse. We pattern large-scale features using the ASML stepper, with electron-beam evaporation of Al and sputter-deposition of Nb. Measurements of these circuits are performed in cryogenic systems at Syracuse University, including dilution refrigerators for achieving temperatures below 30 mK.

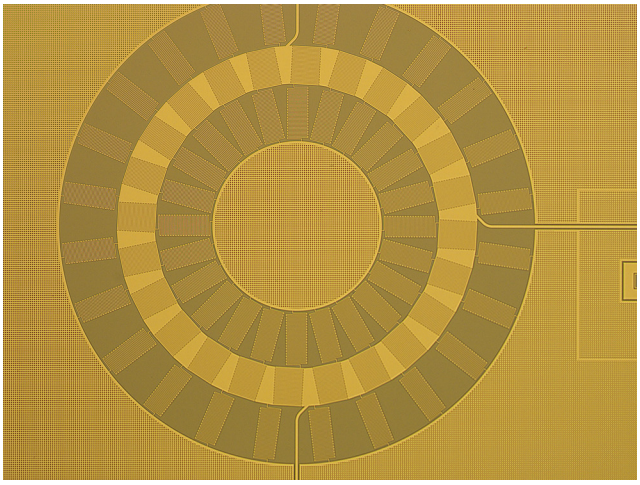

Figure 1: Optical micrograph of left-handed metamaterial ring resonator fabricated from Nb on Si.

Figure 2: Zoomed-in optical micrograph of transmon qubit coupled to metamaterial ring resonator.

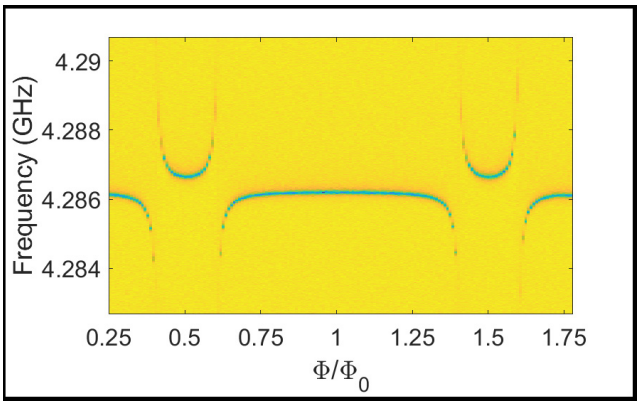

Figure 3: Measurement of microwave transmission through feedline coupled to metamaterial ring resonator as a function of the magnetic flux bias to the transmon qubit. Vacuum Rabi splittings in spectrum are characteristic of quantum mechanical coupling between qubit and ring resonator.

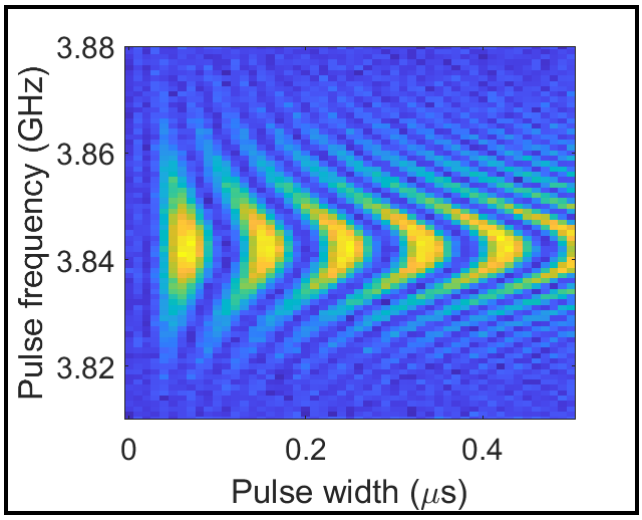

Figure 4: Measurement of Rabi oscillations of transmon qubit coupled to metamaterial ring resonator as a function of microwave drive frequency and pulse duration.

References:

[1] Clarke, J. and Wilhelm, F.K.; "Superconducting quantum bits"; Nature, 453, 1031 (2008).

[2] Wang, H., Zhuravel, A., Indrajeet, S., Taketani, B., Hutchings, M., Hao, Y., Rouxinol, F., Wilhelm,F., LaHaye, M.D., Ustinov, A., Plourde, B.; "Mode Structure in Superconducting Metamaterial Transmission Line Resonators"; Physical Review Applied 11, 054062 (2019).

[3] Indrajeet, S., Wang, H., Hutchings, M.D., Taketani, B.G., Wilhelm, F.K., LaHaye, M.D., Plourde, B.L.T.; "Coupling a Superconducting Qubit to a Left-Handed Metamaterial Resonator"; Physical Review Applied 14, 064033 (2020).

[4] McBroom, T.A., Ku, J., Cole, B.G., Plourde, B.; "Characterization of left-handed metamaterial ring resonator coupled to transmon qubits"; Bull. Am. Phys. Soc. 2022, http://meetings.aps.org/Meeting/MAR22/Session/Q37.3.

Probing Nanoscale Magnetism in 2D van der Waals Ferromagnet $Fe5GeTe_2$ with Magneto-Thermal Microscopy

CNF Project Number: 2091-11

Principal Investigator(s): Gregory D. Fuchs

User(s): Eegene (Clara) Chung

Affiliation(s): Department of Physics, School of Applied and Engineering Physics; Cornell University

Primary Source(s) of Research Funding: Air Force Office of Scientific Research (AFOSR) Multidisciplinary Research Program of the University Research Initiative (MURI) Grant (FA9550-18-1-0480)

Contact: gdf9@cornell.edu, ec893@cornell.edu

Primary CNF Tools Used: GCA 6300 DSW 5X g-line Wafer Stepper, AJA Orion Sputtering Systems, DISCO Dicing Saw, Heidelberg Mask Writer – DWL2000, Westbond 7400A Ultrasonic Wire Bonder

Abstract:

The relevant length and time scales of magnetic phenomena are typified by the width of domain walls, ranging over 10-1000 nm, and the time scale of ferromagnetic resonance and spin waves, ranging over 10-1000 ps. Currently, synchrotron x-ray techniques are the only reliable methods capable of simultaneously resolving both spatial and temporal scales. However, they are facility techniques that impose a limit on its accessibility and throughput. Here, we present a table-top method called magneto-thermal microscopy [1], to study magnetism with a spatial resolution of 650 nm (≤ 100 nm with near-field methods [2]) and a temporal resolution of 10-100 ps. This technique is based on the magneto-thermoelectric anomalous Nernst effect for conducting magnetic materials. The spatial resolution is limited only by the area of the thermal excitation, and it possesses no fundamental limit due to diffraction. We present a study of the recently discovered two-dimensional ferromagnetic van der Waals metal Fe_5GeTe_2 [3] using magneto-thermal microscopy to image the static magnetization at low temperatures. This work is part of an ongoing effort using magneto-thermal interactions to probe the competition between spin and charge ordered phases of this material, along with associated changes in band structure [4].

Summary of Research:

Two-dimensional (2D) magnets are interesting for applications in spintronics, in part because of their low-energy switching of spin states through various gating methods and ability to create heterostructures with engineered properties [5]. They are also interesting for their exotic quantum phenomena such as topological states, anomalous Hall effect, quantum spin hall effect, and skyrmions [5]. However, most 2D ferromagnetic materials have Curie temperatures well below room temperature, which limits their commercial applications.

A new material, Fe_5GeTe_2 (F5GT), has recently emerged [3] with a Curie temperature as high as 332 K in bulk [6] and 280K in exfoliated thin flakes (10 nm) [3]. Unlike most other 2D ferromagnets, F5GT has magnetic easy-plane anisotropy, and the magnetization vs. temperature plots across many different studies exhibit exotic phase transitions [3-4, 6-7]. In particular, it shows a ferro- to ferri-magnetic transition at 275 K [6], suspected competition between spin and charge order at 180 K, and a transition caused by the fading of charge order at 110 K [4] (the exact transition temperatures depends on the experiment).

Our research utilizes a unique experimental technique called "magneto-thermal microscopy" [1] to study the magnetic behaviors of thin F5GT flakes (Figure 1). We can determine the in-plane local magnetic moment $\vec{M}$ of a material via the anomalous Nernst effect (ANE) by applying an out-of-plane thermal gradient $\vec{\nabla}T$, as given by the equation $\vec{E}_{ANE} = -N\vec{M} \times \vec{\nabla}T$, and measuring the anomalous Nernst voltage V_{ANE} created by the ANE electric field $\vec{E}_{ANE}$. A schematic is shown in Figure 2.

A spatially localized and short-lived thermal gradient creates an $\vec{E}_{ANE}$ that is also spatially localized and short-lived, hence the spatial resolution depends only on the size of the thermal excitation and is not inherently

limited (e.g., by diffraction). The temporal resolution depends on how long it takes the thermal gradient to equilibrize. With this, we obtain a sub-micron spatial resolution of 0.65 μm and a temporal resolution of typically < 30 ps.

Fabrication:

The F5GT nanoflake, provided by our collaborator, was placed on top of electrical contact pads fabricated via photolithography at CNF. The photomask was created with the Heidelberg Mask Writer – DWL2000, and the substrate was exposed using the GCA 6300 DSW 5X g-line Wafer Stepper. Ti/Pt was sputtered using AJA Orion Sputtering Systems to form conducting pads. The resulting wafer was diced into 5 mm × 5 mm pieces using the DISCO Dicing Saw.

To take electrical measurements (i.e., V_{ANE}), the Westbond 7400A Ultrasonic Wire Bonder was used to wirebond the contact pads to an electrical circuit component.

Conclusions and Future Steps:

While magneto-thermal microscopy has been used in the past to study various ferromagnetic and antiferromagnetic metals and insulators, this study is the first to apply it to 2D materials. Our preliminary results confirm that we can use magneto-thermal microscopy to study and image magnetization of 2D ferromagnets as shown in Figure 3. Magnetic domains are visible at an applied field of 67 G at 77 K, and we can characterize its magnetic properties by varying the field and temperature, alongside taking magnetic hysteresis measurements. With this, we would like to further investigate the exotic phase transitions at 180K and 110K, which Wu, et al. (2021) proposed is due to the competing charge and spin orders [4]. We would like to expand upon this topic by probing the magnetization vs. temperature behavior at different field cooling to help elucidate the energy barriers between the competing orders, as well as magnetic imaging to illustrate the spatial extent of the different phases. In addition, our magneto-thermal microscopy can not only measure magnetization via ANE, but it is also capable of current imaging, which can give different signatures of the charge and spin order.

References:

[1] J. M. Bartell, D. H. Ngai, Z. Leng, G. D. Fuchs, Nat. Commun., 6, 8460 (2015).

[2] C. Zhang, J. M. Bartell, J. C. Karsch, I. Gray, and G. D. Fuchs, Nano Lett., 21, 4966-4972 (2021).

[3] A. F. May, et al., ACS nano, 13, 4436-4442 (2019).

[4] X. Wu, et al., Phys. Rev. B., 104, 165101 (2021).

[5] K. S. Burch, D. Mandrus, and J.-G. Park, Nature, 563, 47-52 (2018).

[6] L. Alahmed, et al., 2D Mater. 8, 045030 (2021).

[7] H. Zhang, et al., Phys. Rev. B., 102, 064417 (2020).

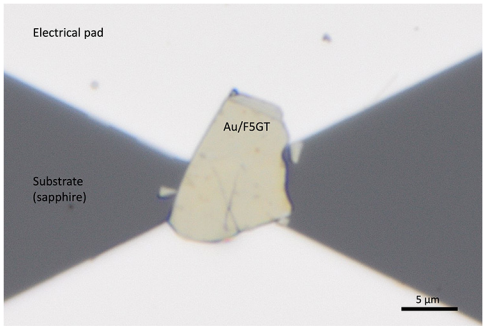

Figure 1: Optical image of a F5GT sample, Au coated to prevent degradation.

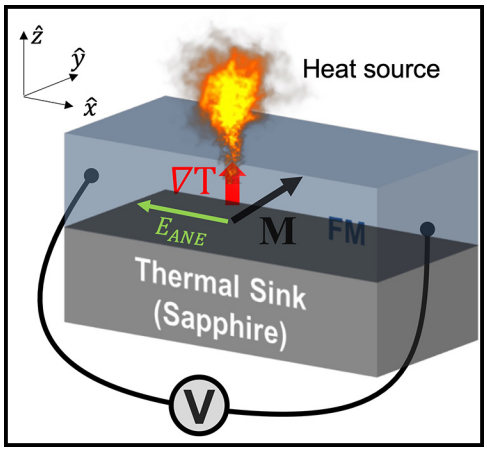

Figure 2: Schematic of the magneto-thermal microscopy technique, which exploits the anomalous Nernst effect to extract the local magnetic moment of a material.

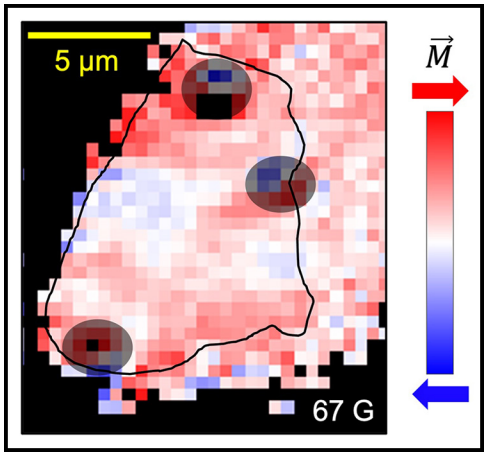

Figure 3: Magnetization image of F5GT sample shown in Figure 1 (outlined here) taken with magneto-thermal microscopy. The sample was cooled to 77 K then an external field of 67 G was applied. Magnetic domains are visible. Highly noisy parts are blacked out or shaded.

Magnetic Field Sensor Based on Spin-Hall Nano-Oscillators

CNF Project Number: 2091-11
Principal Investigator(s): Gregory D. Fuchs
User(s): Yanyou Xie

Affiliation(s): Applied and Engineering Physics, Cornell University

Primary Source(s) of Research Funding: Cornell Center for Materials Research

Contact: gdf9@cornell.edu, yx322@cornell.edu

Primary CNF Tools Used: JEOL 9500, SÜSS MA6 Contact Aligner

Abstract:

Spin-Hall nano-oscillators (SHNOs) are magnetic bilayer devices that convert DC charge current to microwave frequency magnetic oscillations under external magnetic field. The oscillation frequency of a SHNO is linearly dependent on the external magnetic field strength, and thus SHNOs can be used as bias magnetic field sensors. We demonstrate the ability of our SHNO sensor to sense small AC magnetic field with a detectivity of less than 1 $\mu T/\sqrt{Hz}$ for AC magnetic field frequency > 20-100 Hz, despite having small effective sensing area ranging from 0.32 μm² tp 0.071 μm².

Summary of Research:

The spin Hall effect (SHE) is the generation of transverse spin currents by electric currents. In a non-magnetic material (NM), this leads to the accumulation of spins with opposite polarization at opposite edges of the NM [1,2]. By placing a nonmagnetic film on top of a ferromagnetic film, the spin current generated in the NM can diffuse into the ferromagnet (FM), providing spin transfer torque (STT) to the FM [1]. Under suitable conditions, the STT is able to compensate the damping of magnetic precession, leading to steady precession of magnetization [3]. With this principle, spin-Hall nano-oscillators (SHNOs) are developed as a bilayer system consisting of NM and FM, patterned as nanowires or nanoconstrictions.

In our study we fabricated arrays of four $Ni_{81}Fe_{19}$ (5 nm)/ $Au_{0.25}Pt_{0.75}$ (5 nm) constriction-based SHNOs on 20.5 μm × 4 μm wires. Devices included both single w = 150 nm constriction and arrays of four w = 150 nm constrictions separated by a = 350 nm, with a lateral shift along -30° from the x axis, perpendicular to the magnetic field direction (Figure 1). This shifted design is to maximize the overlap between spin wave modes, as spin wave emission is perpendicular to magnetic field [4]. We used JEOL 9500 for the e-beam patterning of the SHNOs, and SÜSS MA6 contact aligner and evaporator for depositing contact pads for electrical measurements.

We use a home-built spectrum analyzer (Figure 1) to perform auto-oscillation measurements and sensing. The device is placed in an electromagnet which applies a magnetic field H = 400 Oe. A DC charge current I_{dc} is

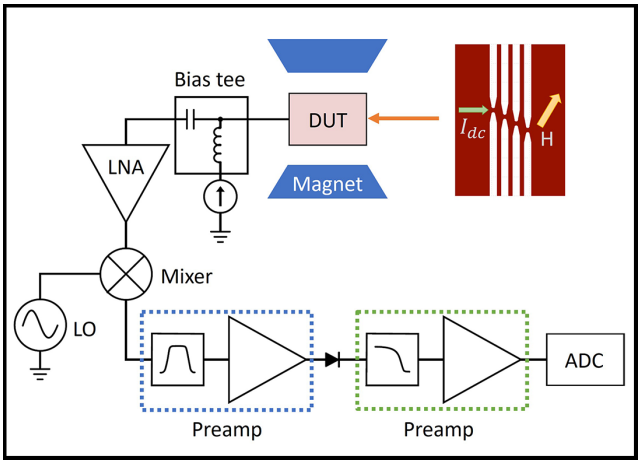

Figure 1: Schematic of measurement circuit and device under test.

applied to the device to excite auto-oscillation. The output gigahertz signal is then amplified and down-convert to megahertz (MHz) frequency by mixing it with the output from a local oscillator (LO). The output MHz signal then goes through a preamplifier before being converted to voltage signal by a RF diode. This voltage signal then goes through another preamplifier and is finally converted to a digital signal.

As we scan the frequency of LO, when the frequency of LO matches the auto-oscillation frequency from SHNO device, a peak shows up. To operate the SHNO device as a sensor, we keep the frequency of LO at the steepest slope on the peak and monitor the output voltage. As

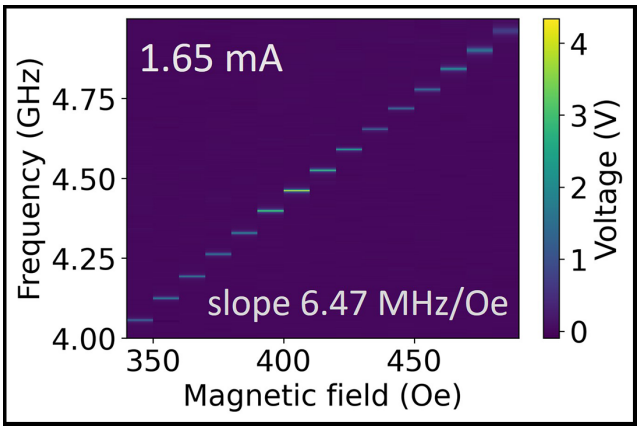

Figure 2: Auto-oscillation frequency dependence on external magnetic field under charge current I_{dc} = 1.65 mA.

the external magnetic field slightly deviates, the output voltage changes and thus we are able to measure the change in the external magnetic field.

Figure 2 shows the linear dependence of oscillation frequency on the array device under an external magnetic field at I_{dc} = 1.65 mA, with a slope df/dH = 6.47 × 10^{-3} GHz/Oe. Averaging 3000 scans over the same frequency range yields a linewidth of 6.4 MHz and a maximum dV/df = 312 V/GHz, corresponding to a sensor sensitivity $S = dV/dH$ = 2.02 V/Oe.

The detectivity of sensor is characterized by measuring the linear spectral density and dividing by the sensitivity at the optimal operating conditions. For this sensor, the detectivity goes below 1 $\mu T/\sqrt{Hz}$ for AC magnetic field frequency > 20 Hz, shown in Figure 3. The noise floor of our SHNO sensor is close to $1/\sqrt{f}$ line, indicating the noise in our sensor is dominated by the pink noise. Note that the effective sensing area is the constriction region, which is less than 0.32 μm².

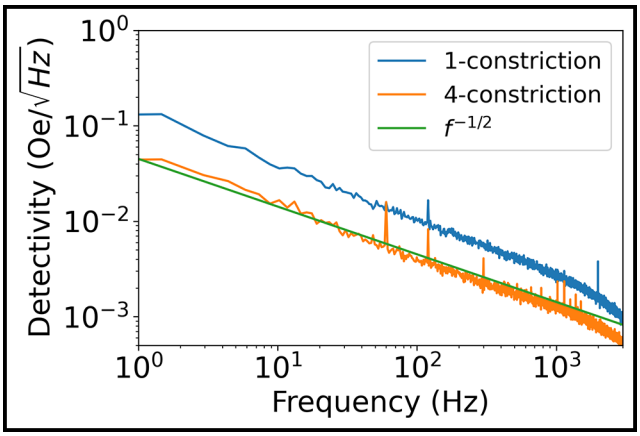

Figure 3: Noise floor of SHNO sensor at optimal operating conditions in comparison to $1/\sqrt{f}$ line.

We also fabricated a 1-constriction device with constriction width w = 150 nm for comparison. For the 1-constriction device, the detectivity goes below 1 $\mu T/\sqrt{Hz}$ for AC magnetic field frequency > 100 Hz (Figure 3), but the effective sensing area is reduced to 0.071 μm².

To demonstrate the ability to sense small magnetic variation, we place the 4-constriction array in an AC modulating field with a rms value of 0.153 Oe, and measure the output from the senor and from a Gaussmeter with its probe near the sensor. From Figure 4, the output from our sensor agrees well with the Gaussmeter.

Conclusions and Future Steps:

We developed a bias magnetic field sensor based on spin-Hall nano-oscillators to sense small variation in magnetic field within a nanoscale area, which has a detectivity of less than 1 $\mu T/\sqrt{Hz}$ for AC magnetic field frequency > 20 Hz. We have characterized quasi-DC sensing for up to kilohertz-scale frequencies. We plan to extend the measurement range up to MHz based on sideband modulation.

References:

[1] J. Sinova, et al., "Spin Hall effects," Reviews of Modern Physics, vol. 87, no. 4, p. 1213, 2015.

[2] M. D'yakonov and V. Perel, "Possibility of orienting electron spins with current," Soviet Journal of Experimental and Theoretical Physics Letters, vol. 13, p. 467, 1971.

[3] D. C. Ralph and M. D. Stiles, "Spin transfer torques," Journal of Magnetism and Magnetic Materials, vol. 320, no. 7, pp. 1190-1216, 2008.

[4] T. Kendziorczyk and T. Kuhn. "Mutual synchronization of nanoconstriction-based spin Hall nano-oscillators through evanescent and propagating spin waves," Physical Review B, vol. 93, no. 13, p.134413, 2016.

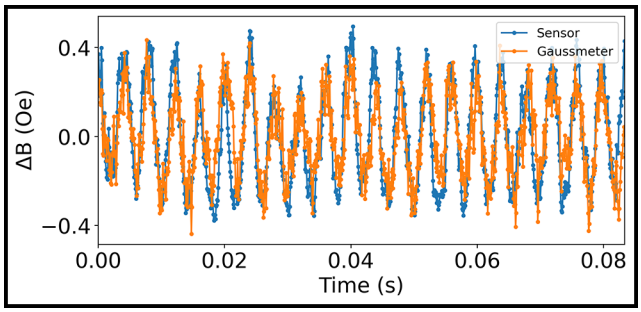

Figure 4: Comparison of measurements of a 251 Hz modulation field with a rms 0.153 Oe from the 4-constriction SHNO sensor and the Gaussmeter.

Towards Building a Bright Single-Photon Source with h-BN Defect Emitters

CNF Project Number: 2126-12

Principal Investigator(s): Gregory D. Fuchs[1]

User(s): Jialun Luo[2]

Affiliation(s): 1. Applied and Engineering Physics, 2. Department of Physics; Cornell University

Primary Source(s) of Research Funding: National Science Foundation (ECCS-1839196)

Contact: gdf9@cornell.edu, jl3562@cornell.edu
Website: http://fuchs.research.engineering.cornell.edu

Primary CNF Tools Used: AJA Sputtering System, OEM Endeavor AlN Sputtering System, JEOL 9500, JEOL 6300, PT770 Etcher, AJA Ion Mill, P-7 Profilometer, GCA 5x Stepper

Abstract:

Single-photons are essential in realizing photon-based quantum technologies [1]. Defect emitters in hexagonal boron nitride (h-BN) have been found to be bright and photostable, making them good candidates for implementing single-photon sources. We developed a fabrication process for an inverse-design cavity device from AlN for efficient photon-extraction from the defect emitters. We present an update on our work-in-progress on the fabrication and characterization of the device.

Summary of Research:

Single-photon sources are important pillars in quantum technologies such as quantum communication protocols [1,2], precision metrology [3], and quantum sensing. Building a single-photon source involves two parts: 1) a single-photon emitter and 2) a photon-extraction method. Hexagonal boron nitride (h-BN) hosts atomic defects that, upon optical excitation, emit bright and photostable fluorescence [5,6]. The zero-phonon line fluorescence from carbon-related h-BN defects falls near 585 nm [6]. Previous publications suggest that carbon ion-implantation can deterministically create these defect emitters [7]. Since h-BN is a van der Waals material that can be prepared into flakes thinner than a tenth of the fluorescence wavelengths, photons emitted from defects hosted within naturally suffer less from total internal reflection. However, the far-field radiation power from these defect emitters typically concentrates at higher angles, which means a high numerical aperture microscope objective is necessary to collect the light.

Our collaborator from the Rodriguez group then calculated a nanostructure to aid the photon collection [8]. The nanostructure shortens a dipole emitter's lifetime when one is placed at the center high field region due to the Purcell effect, and it modifies the near-field dielectric environment of the dipole emitter so that more photons are emitted into a smaller cone for lower numerical aperture lenses to collect (Figure 1).

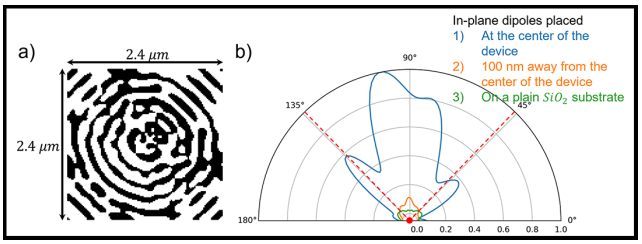

Figure 1: a) Top-down view of an optimized structure pattern for an in-plane dipole emitter. The thickness is 300 nm. b) Far-field radiation patterns comparison among dipole emitters placed at the center of the device, 100 nm shifted away from the center of the device, and placed on a plain SiO_2 substrate. The red dashline indicates the maximum collection angle of a 0.7 NA microscope objective.

In this work, we attempt to build a h-BN defect emitter-based single-photon source integrated with a nanostructure to efficiently extract the single photons.

We fabricated the current generation devices on Si wafer, which allows us to cleave the sample and inspect the cross section. The devices are made from AlN sputtered by the OEM Endeaver M1 AlN sputter system. We chose hydrogen silsesquioxane (HSQ) as our resist layer due to its 10 nm spatial resolution with electron-beam (e-beam) lithography. The nanostructure is patterned by the JEOL 9500 e-beam lithography system. The pattern is transferred to a hard mask layer made of

Ni by ion milling. Then, the devices are etched by reactive ion etch with chlorine/oxygen plasma. While reactive ion etch has high directionality, the device aspect ratio is as high as 5 to 1, so we faced the problem of angled sidewalls. We optimized the etch recipe and reached a sidewall angle of 82 degrees (Figure 2). According to the calculation, such a device can still enhance the photon collection by 7-to-10-fold.

Following the Aharonovich group result [7], we send exfoliated h-BN flakes with thicknesses ranging from tens to hundreds of nm for carbon ion-implantation process. However, the resulting flakes contain mostly short-lived emitters with broad emission spectra (Figure 3), rendering h-BN flakes not suitable for single-photon sources. We also found that the thin h-BN flakes become much harder, if not impossible, to pick up with our 2D material transfer techniques.

We tried characterizing the inverse-design cavity nanostructures by transferring a 100-nm sized h-BN flake over (Figure 4), however, the fluorescence and the collected spectra showed no enhancement, likely because the h-BN flake drastically changed the dielectric environment and broke the nanostructure design assumption that only a thin layer of h-BN is placed on it.

Future Work:

We are trying to characterize the inverse-design cavity nanostructures with commercially available CdSe quantum dots which are of 10 nm in size. The characterization result can provide guidance for the next steps.

Acknowledgements:

We would like to thank members of the Rodriguez Group on the discussion on and their designs of the inverse-design cavity nanostructures.

References:

[1] Bennett, C. H., and Brassard, G. Quantum cryptography: Public key distribution and coin tossing. Theoretical Computer Science 560, 7-11 (2014).

[2] Waks, E., Inoue, K., Santori, C., Fattal, D., Vuckovic, J., Solomon, G. S. and Y. Yamamoto, "Quantum cryptography with a photon turnstile," Nature 420, 762 (2002).

[3] Giovannetti, V. Lloyd, S. and Maccone, L., Quantum-enhanced measurements: Beating the standard quantum limits, Science 306, 1330 (2004).

[4] Thiel, C., Bastin, T., Zanthier J. von and G. S. Agarwal, Sub-Rayleigh quantum imaging using single photon soucres, J. Lightwave Technol. 20, 2154 (2002).

[5] Aharonovich, I., Englund, D., and Toth, M. Solid-state single-photon emitters. Nature Photonics 10, 631-641 (2016).

[6] Jungwirth, N. R., and Fuchs, G. D. Optical Absorption and Emission Mechanisms of Single Defects in Hexagonal Boron Nitride. Phys. Rev. Lett. 119, 057401 (2017).

[7] Mendelson, N., et al. Identifying carbon as the source of visible single-photon emission from hexagonal boron nitride. Nat. Mater. 20, 321-328 (2021).

[8] Molesky, S., et al. Inverse design in nanophotonics. Nature Photonics 12, 659-670 (2018).

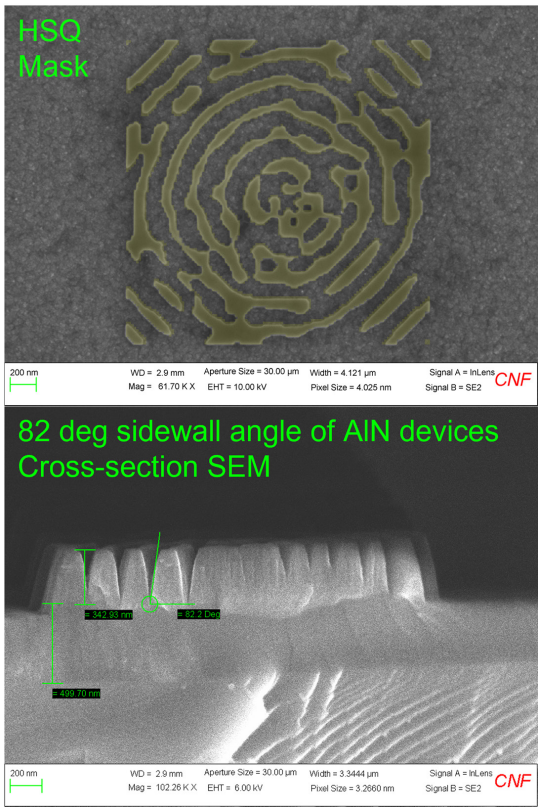

Figure 2: Upper: Developed HSQ mask overlayed with the design pattern (in yellow) Lower: The cross-section SEM of etched AlN devices showing an 82-degree sidewall angle.

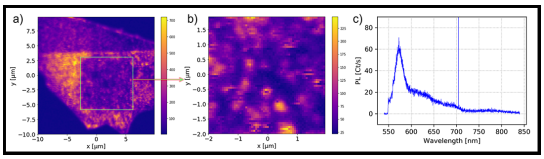

Figure 3: a) A typical fluorescence map under 532-nm laser excitation. b) A finer fluorescence map zoomed into the boxed region in a), there are point-like emitters in general. c) Typical spectrum of the point-like emitters. While the zero-phonon line centers around 585 nm, the linewidth is broad (~20 nm).

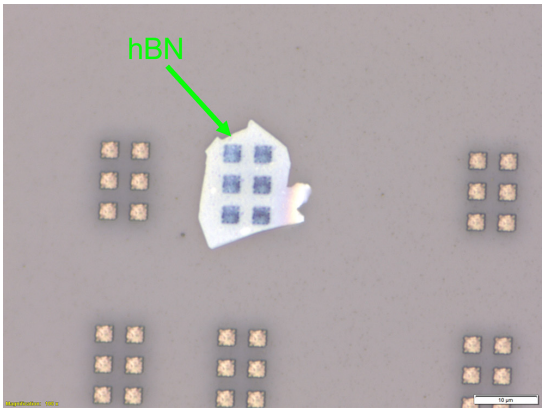

Figure 4: An optical image of a 100 nm thick h-BN flake placed over six inverse-design cavity devices.

Quantifying NV Center Spectral Diffusion by Symmetry

CNF Project Number: 2126-12

Principal Investigator(s): Gregory D. Fuchs

User(s): Brendan Andrew McCullian

Affiliation(s): School of Applied and Engineering Physics, Cornell University

Primary Source(s) of Research Funding: DARPA Driven and Nonequilibrium Quantum Systems (DRINQS) Program, Department of Energy Office of Basic Energy Sciences, Office of Naval Research

Contact: gdf9@cornell.edu, bam327@cornell.edu

Primary CNF Tools Used: GCA 6300 DSW 5X g-line Wafer Stepper, Heidelberg Mask Writer – DWL2000, AJA Sputter Deposition, Westbond 7400A Ultrasonic Wire Bonder

Abstract:

The spectrally narrow, spin-dependent optical transitions of nitrogen vacancy (NV) center defects in diamond can be harnessed for quantum networking applications. Two challenges limit scalability: defect-to-defect variations of the optical transition frequencies caused by local strain variation, and spectral diffusion of the optical frequencies on repeated measurement caused by photoexcitation of nearby charge traps. We quantify spectral diffusion and strain, decomposing each into components of specific symmetry, and investigate correlations between spectral diffusion, strain, and depth from surface. Our correlation study reveals that ideal NV centers are likely found to have large transverse strain and are at depths which balance surface charge trap effects with laser focal aberration effects.

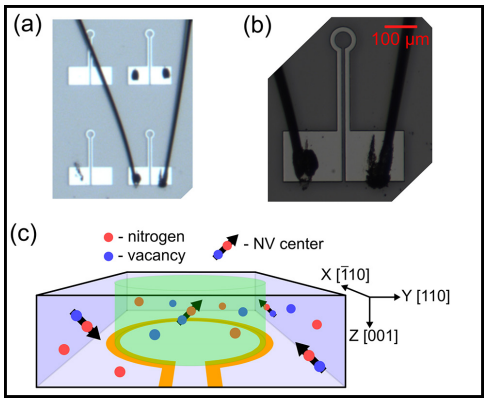

Figure 1: (a, b) Optical micrographs of litho-graphically defined loop antennas grown on diamond surface and wire bonds to microwave source. (c) Schematic of diamond sample with spatially isolated single NV centers and nearby bulk charge traps.

Summary of Research:

NV centers in diamond exhibit narrow, spin-preserving optical transitions at cryogenic temperatures that can be harnessed for quantum networking applications [1]. Such applications are limited by two key factors: spectral diffusion of the optical transition frequencies on repeated measurement [2] and defect-to-defect variation in optical transition frequencies resulting from strain [3]. Though there has been significant progress toward quantum networking with NV centers [4], only carefully chosen defects are able to be incorporated into such devices.

We quantify spectral diffusion and investigate how spectral diffusion correlates with other physical parameters of NV centers. We quantify both the spectral diffusion and the static strain for 16 individual bulk NV centers, breaking each into components of a given Jahn-Teller symmetry. We then calculate the correlation and significance (p-value) between the different components of spectral diffusion, components of strain, and depth from the diamond surface.

Our sample (Figure 1) is a type IIa diamond with individually addressable single NV centers formed via electron irradiation and subsequent annealing. We patterned a microwave loop antenna for spin control on the diamond surface, using the Heidelberg Mask Writer – DWL2000 to make the mask, the GCA 6300 DSW 5X g-line stepper to write the pattern,

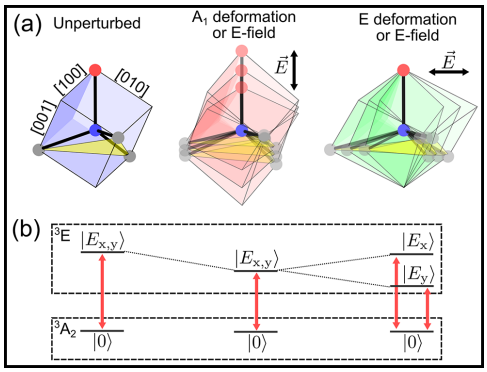

Figure 2: (a) An unperturbed NV center has C_{3v} symmetry and can undergo either A_1-symmetric (longitudinal) or E-symmetric (transverse) perturbation from strain or electric field. (b) Longitudinal perturbations globally shift the optical transition frequencies, while transverse perturbations split the excited-state orbital doublet into two branches.

the AJA sputter deposition system to deposit 25 nm of Ti and 225 nm of Pt. After lift-off the device was wire bonded to our cryostat microwave feed lines using the Westbond 7400A Ultrasonic Wire Bonder.

We perform photoluminescence excitation (PLE) spectroscopy measurements by tuning a red laser (~637.2nm) across the resonant optical transitions of the NV center while counting photons emitted into the phonon sideband. The spin-preserving optical transitions are from orbital singlet, spin triplet ground states to orbital doublet, spin triplet excited states. All measurements are carried out in a helium flow cryostat at 10 K.

An unperturbed NV center has C_{3v} point-group symmetry and two degenerate spin-0 optical transition energies (Figure 2) [5]. Longitudinal (A_1) perturbations shift the excited states together, while transverse perturbations (E) split the orbital branches.

We characterize the strain components for each NV center by applying 637.2 nm and 532 nm laser pulses while tuning the red laser frequency. The 532 nm laser ensures that the defects is always in spin-0. As shown in Figure 3, by measuring the splitting of the two optical transitions, the rotation of the optical dipole [6], and the absolute center frequency of the PLE peaks we fully quantify the strain components for each NV center.

We then characterize the spectral diffusion. We apply a single green laser pulse followed by a full red laser sweep and repeat 125 times on each defect. These spectra are summed, and the changes in splitting and center frequency are recorded for each of the sweeps in a histogram. By extracting the width of these histograms via fitting with a Gaussian response we can quantify the longitudinal and transverse components of spectral diffusion.

We calculate the correlations and p-values of each component of spectral diffusion, static strain, as well as the measured depth from surface. These correlations reveal that both strain and spectral diffusion are dominated by longitudinal perturbations. Also, NV centers with larger transverse strain are more protected from orthogonal and transverse spectral diffusion. Last, for bulk NV centers the spectral diffusion increases with depth due to laser aberration.

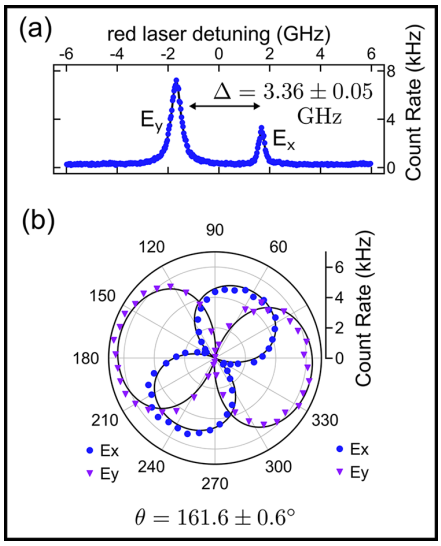

Figure 3: (a) PLE frequency sweep and extracted strain splitting Δ from two Lorentzian fits. (b) PLE laser polarization rotation and extracted dipole rotation θ.

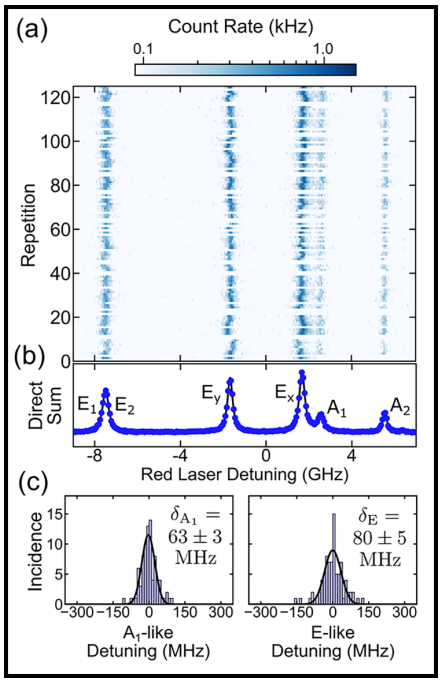

Figure 4: (a) 125 repetitions of frequency-swept PLE showing spectral diffusion on repeated measurement. (b) Direct sum of repeated PLE response. (c) Histogram of longitudinal and transverse spectral diffusion components including Gaussian fits to quantify degree of each symmetry of spectral diffusion.

Conclusions and Future Steps:

Our results indicate that NV centers with large transverse strain will on average have reduced spectral diffusion. This can provide a quick means of searching for good candidate defects for quantum networking. Also, defects should be located at a depth which balances the spectral diffusion known to occur from near-surface charge traps [7] with the depth-related spectral diffusion we uncovered. Future work will investigate how NV centers driven with mechanical resonators can be made robust to spectral diffusion.

Our manuscript is under review, and a preprint is available on arXiv [8].

References:

[1] L. Childress, et al., Phys. Rev. A 72, 052330 (2005).
[2] K. M. C. Fu, et al., Phys. Rev. Lett. 103, 256404 (2009).
[3] F. Grazioso, et al., App. Phys. Lett. 103, 101905 (2013).
[4] S. L. N. Hermans, et al., Nature 605, 663 (2022).
[5] J. R. Maze, et al., New J. Phys. 13, 025025 (2011).
[6] K. W. Lee, et al., Phys. Rev. Appl. 6, 034005 (2011).
[7] M. Ruf, et al., Nano Lett. 19, 3987 (2019).
[8] B. A. McCullian, et al., arXiv:2206.11362 (2022).

Building van der Waals Pi Josephson Junctions

CNF Project Number: 2633-18

Principal Investigator(s): Jie Shan, Kin Fai Mak

User(s): Kaifei Kang

Affiliation(s): Laboratory of Atomic and Solid State Physics,
School of Applied and Engineering Physics; Cornell University

Primary Source(s) of Research Funding: United States Army Research Office

Contact: jie.shan@cornell.edu, kinfai.mak@cornell.edu, kk726@cornell.edu

Primary CNF Tools Used: Autostep i-line Stepper, Hamatech Wafer Processor Develop,
Heidelberg Mask Writer - DWL2000, Photolithography Spinners,
SC4500 Odd/Even-Hour Evaporator, DISCO Dicing Saw

Abstract:

At the interfaces of superconductors (SC) and ferromagnets (FM), exotic Cooper pairs with finite center-of-mass momentum can be realized [1]. Here we build van der Waals ferromagnetic Josephson junctions using atomically thin $NbSe_2$ and $Cr_2Ge_2Te_6$ (CGT) flakes. We observe a damped-oscillatory dependence of the Josephson critical current density on the CGT barrier thickness, which is the definitive evidence for a thickness-driven 0 to π transition. Near the transition, we observe 0 – π Josephson junctions with zero critical current at zero magnetic field. Our work demonstrates the thickness-driven 0 to π transition in van der Waals Josephson junctions and 0 – π Josephson junctions with uniform barrier thickness.

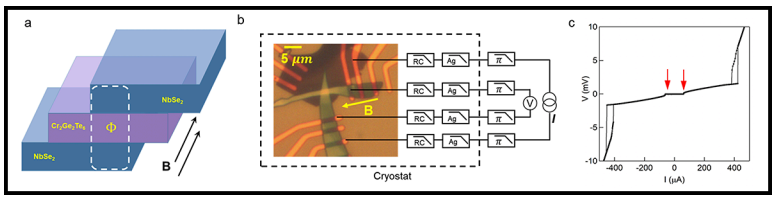

Figure 1: $NbSe_2/Cr_2Ge_2Te_6/NbSe_2$ Josephson Junctions. a, Schematics of the device structure. The magnetic field is applied to the in-plane direction, which produces a magnetic flux through the cross-sectional area of the device (marked by the white dashed rectangle). b, Schematics for the electrical measurements. All electrical lines are filtered by π, silver-epoxy, and low-temperature RC filters. c, I-V *characteristic of a device with a CGT barrier thickness of about 3.6 nm.*

Summary of Research:

The recent discovery of two-dimensional (2D) layered superconducting and magnetic materials provides a new platform to realize π Josephson junctions (JJs) with atomically uniform thickness and sharp interfaces via van der Waals stacking [2,3]. In this project, we fabricate JJs using van der Waals superconductor $NbSe_2$ and semiconducting ferromagnet $Cr_2Ge_2Te_2$ (CGT) (Figure 1a).

Figure 1b shows the schematics for the electrical measurements. The JJs are current-biased, and the voltage drop across the JJs is measured. Radiation with frequencies above 30 kHz is filtered to avoid unwanted quasiparticle excitations. Figure 1c shows the current-voltage characterization of a JJ with a 3.6-nm CGT barrier. The voltage drop V across the JJ vanishes when the bias current I is smaller than the Josephson critical current of $I_c \approx 63$ μA (marked by the red arrows). At a large bias current of $I \sim 500$ μA, a second voltage jump of about 3 mV is observed, corresponding to the superconducting critical current of the $NbSe_2$ flakes.

We study the thickness dependence of the Josephson critical voltage $V_c = I_c R_n$. Here R_n is the resistance of the JJs when $I > I_c$. Figure 2 shows V_c as a function of the CGT thickness, d. As d increases, V_c first decreases for $d <$ 8.4 nm, increases for 8.4 nm $< d <$ 9.9 nm, and then vanishes when $d \approx 12.3$ nm. Such a thickness dependence of V_c is consistent with the thickness-driven 0 to π transition with a critical barrier thickness of $d_c = 8.4$ nm.

We also examine the magnetic interference patterns in JJs with different barrier thicknesses. Figures 3a-3d show the sample differential resistance as a function of magnetic field (B) and bias current in JJs with selected CGT barrier thickness of 5.2, 7.7, 9.1, and 9.9 nm. For JJs with CGT thicknesses away from the critical thickness (Figure 3a and Figure 3d), regular Fraunhofer patterns are observed with pronounced central lobes near B = 0 T. However, for JJs with CGT barrier with just one layer thinner (Figure 3b) or one layer thicker (Figure 3c) than the critical thickness d_c, we observe zero critical current near B = 0 T, which signifies the formation of 0 – π JJs. The observation of the 0 – π JJs with uniform barrier thickness is attributed to the inhomogeneous magnetization induced by the magnetic domain walls in CGT, which is reported by a recent Lorentz TEM study [4].

In conclusion, we have fabricated high-quality van der Waals ferromagnetic Josephson junctions. By varying the thickness of the ferromagnetic barrier, we observe a damped oscillatory behavior for the JJ critical current density and thus a thickness-driven 0 to π transition. Near the transition, we identify 0 – π JJs with zero critical current near zero magnetic field and uniform barrier thickness.

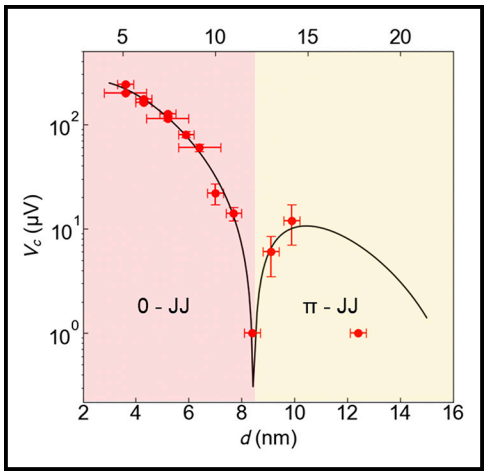

Figure 2: Thickness-driven 0 to π transition. Critical voltage V_c as a function of CGT barrier thickness. JJs have zero phase difference in red dashed region and π phase difference in the orange region.

References:

[1] Buzdin, A. I. Proximity effects in superconductor-ferromagnet heterostructures. Rev. Mod. Phys.77, 935 (2005).

[2] Saito, Y. et al. Superconductivity protected by spin-valley locking in ion-gated MoS_2. Nat. Phys. 12, 144-149 (2016).

[3] Mak, K. F., Shan, J. and Ralph, D. C., Probing and controlling magnetic states in 2D layered magnetic materials. Nat. Rev. Phys.1, 646-661 (2019).

[4] Idzuchi, H. et al., Unconventional supercurrent phase in Ising superconductor JJ with atomically thin magnetic insulator. Nat. Comm.12, 5332 (2021).

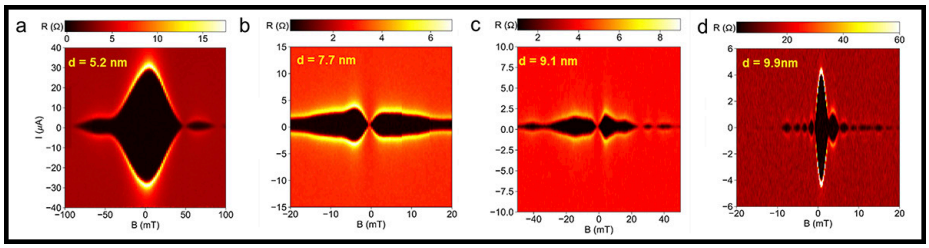

Figure 3: Magnetic interference pattern of the Josephson supercurrent. a – d, Magnetic interference pattern of the supercurrent in JJs with barrier thickness of 5.2 nm (a), 7.7 nm (b), 9.1 nm (c), and 9.9 nm (d). The magnetic field is scanned in the forward direction.

Strongly Correlated Excitonic Insulator in Atomic Double Layers

CNF Project Number: 2633-18

Principal Investigator(s): Jie Shan, Kin Fai Mak

User(s): Liguo Ma, Phuong X. Nguyen

Affiliation(s): Laboratory of Atomic and Solid State Physics,
School of Applied and Engineering Physics; Cornell University

Primary Source(s) of Research Funding: The US Department of Energy (DOE)

Contact: jie.shan@cornell.edu, kinfai.mak@cornell.edu, lm837@cornell.edu, pxn2@cornell.edu

Primary CNF Tools Used: Autostep i-line Stepper, Hamatech Wafer Processor Develop, Heidelberg Mask Writer - DWL2000, Photolithography Spinners, SC4500 Odd/Even-Hour Evaporator, DISCO Dicing Saw, Zeiss Supra SEM, Nabity Nanometer Pattern Generator System (NPGS)

Abstract:

Excitonic insulators (EIs) arise from the formation of bound electron-hole pairs (excitons) in semiconductors and provide a solid-state platform for quantum many-boson physics. Here, we demonstrate a strongly correlated two-dimensional (2D) EI ground state formed in transition metal dichalcogenide (TMD) semiconductor double layers, where spatially indirect excitons form. We construct an exciton phase diagram that reveals both the exciton Mott transition and interaction-stabilized quasi-condensation through a quantum capacitance measurement.

Summary of Research:

In bulk materials, excitonic insulators (EIs) can occur in small band gap semiconductors and small band overlap semimetals [1]. In the semiconductor limit, EIs occur when the electron-hole binding energy of an exciton exceeds the charge band gap. The ground state exciton population is determined by balancing the negative exciton formation energy against the mean exciton-exciton repulsion energy.

Although the concept has been understood for a long time, establishing distinct experimental signatures of the EIs has remained challenging.

In this experiment, we employ the atomic double layer structure to establish electrical control of the chemical potential of interlayer excitons (by making separate electrical contacts to isolated electron and hole layers). Since the electron and hole wavefunctions do not interfere, macroscopic phase coherence is spontaneous, allowing exciton superfluidity.

The dipolar nature of the interlayer excitons and the reduced dielectric screening in our devices also favor strong exciton-exciton repulsion.

Figure 1 shows the device schematics and optical image of a typical device. The device is made of a $WSe_2/MoSe_2$ bilayer separated by a thin hexagonal boron nitride (h-BN) spacer. It is also encapsulated by two gates made of h-BN and graphite. Atomically thin samples of WSe_2, $MoSe_2$, h-BN and graphite were first exfoliated from their bulk crystals onto silicon substrates. Selected thin flakes of appropriate thickness and geometry were picked up one-by-one by a stamp consisting of a thin layer of polycarbonate on polydimethylsiloxane (PDMS). The complete heterostructure was then deposited onto the substrates with pre-patterned Pt electrodes.

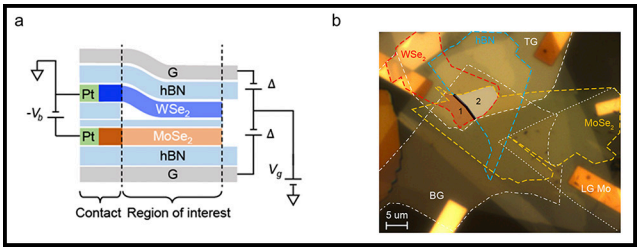

Figure 1: a, Device schematics. b, Optical microscope image of a dual-gated device. Scale bar is 5 μm.

Figure 2 (top row) shows schematics of the penetration (a) and interlayer (b) capacitance measurements. A commercial high electron mobility transistor is used

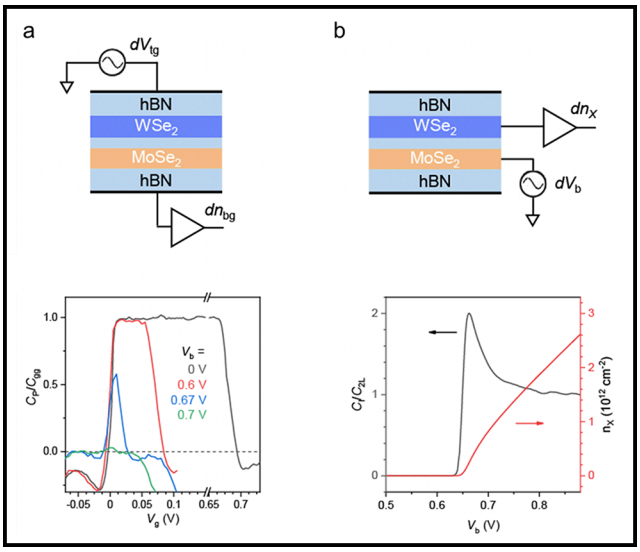

Figure 2: a, Normalized penetration capacitance as a function of gate voltage for representative bias voltages. b, Normalized interlayer capacitance (left axis) and exciton density extracted from the interlayer capacitance (right axis) as a function of bias voltage. Top row shows the schematics of the corresponding capacitance measurements.

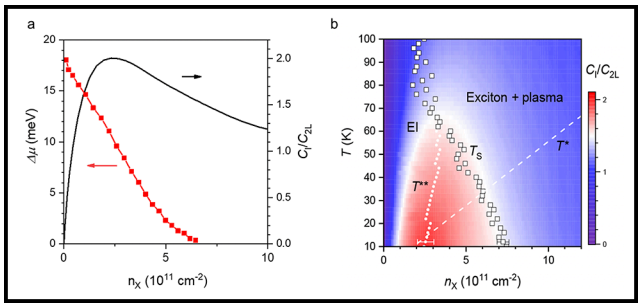

Figure 3: a, Charge gap and exciton compressibility as a function of exciton density at 15 K. b, Exciton compressibility as a function of temperature and exciton density.

as the first-stage amplifier to effectively reduce the parasitic capacitance from cabling [2]. To obtain the penetration capacitance, we apply an AC voltage (5 mV in amplitude) to the top gate and collected the signal from the bottom gate. For the interlayer capacitance, we apply an AC voltage (5 mV in amplitude) to the $MoSe_2$ layer and collected the signal from the WSe_2 layer. The measured penetration capacitance signal (Figure 2a) tracks changes in the charge gap when a bias is applied between WSe_2 and $MoSe_2$. The interlayer capacitance signal directly measures the formation of electron-hole pairs, or exciton compressibility, from which the exciton density can be obtained by integration with respect to bias voltage (Figure 2b).

We obtained exciton phase diagram in Figure 3 by combining the two measurements. The charge gap under various electron-hole pair density is measured by penetration capacitance (Figure 3a). Nonzero gap at finite density indicates that the electron-hole pairs are in the EI phase. With increasing density, the charge gap decreases to zero gradually at a critical density (the Mott density), at which the excitons are dissociated into electron-hole plasma [3]. Figure 3b shows the constructed exciton phase diagram from the measured exciton compressibility as a function of temperature and density.

The density dependence of the exciton compressibility in Figure 3 indicates the importance of exciton-exciton interactions. We consider an interacting Bose gas model [4] below the exciton ionization temperature T_s. The effective interaction strength extracted from our result is an order of magnitude larger than in other systems such as cold atoms and helium. The strong correlation is expected to suppress exciton density fluctuations [5] and enhance the effective degeneracy temperature from the degeneracy temperature T^* for non-interacting bosons to T^{**}. The region bound by T^{**} and T_s represents a degenerate exciton fluid with suppressed density fluctuations (i.e., a quasi-condensate). The strong correlation is also expected to suppress phase fluctuations and enhance the exciton superfluid transition temperature.

Our experiment paves the path for realizing the exotic quantum phases of excitons, as well as multi-terminal exciton circuitry for applications.

References:

[1] Jérome, D., Rice, T.M., and Kohn, W. Excitonic Insulator. Physical Review 158, 462-475 (1967).

[2] Ashoori, R. C., et al. Sigle-Electron Capacitance Spectroscopy of Discrete Quantum Levels. Phys. Rev. Lett. 68, 3088-3091 (1992).

[3] Mott, N.F. The transition to the metallic state. The Philosophical Magazine: A Journal of Theoretical Experimental and Applied Physics 6, 287-309 (1961).

[4] Wu, F.-C., Xue, F., and MacDonald, A.H. Theory of two-dimensional spatially indirect equilibrium exciton condensates. Physical Review B 92, 165121 (2015).

[5] Kagan, Y., Kashurnikov, V.A., Krasavin, A.V., Prokof'ev, N.V., and Svistunov, B.V. Quasicondensation in a two-dimensional interacting Bose gas. Physical Review A 61, 043608 (2000).

Superconducting Thin Film Growth, Process Development, Defects Investigation, and Device Fabrication for Radio-Frequency Accelerating Cavities

CNF Project Number: 2779-19

Principal Investigator(s): Matthias Liepe

User(s): Zeming Sun

Affiliation(s): Cornell Laboratory for Accelerator-based Sciences and Education, Cornell University

Primary Source(s) of Research Funding: the U.S. National Science Foundation under Award PHY-1549132, the Center for Bright Beams

Contact: mul2@cornell.edu, zs253@cornell.edu
Website: https://physics.cornell.edu/matthias-liepe

Primary CNF Tools Used: Thermal / E-Gun Evaporation System, Oxford FlexAL Atomic Layer Deposition System, Jelight 144AX UV Ozone Generator, Arradiance Gemstar-6 Atomic Layer Deposition System, Chemical Vapor Deposition System, Woollam Spectroscopic Ellipsometer, Zygo Optical Profilometer, P10 Profilometer

Abstract:

Superconducting radio-frequency (SRF) cavities are the key component for particle accelerators that have broad applications such as synchrotron X-ray, high-energy colliders, and extreme-UV lithography. Our research is to search for the next-generation SRF materials and surfaces beyond the industry-standard niobium (Nb). Niobium-tin (Nb_3Sn), niobium-zirconium (NbZr), Nb with a processed/designed surface, niobium titanium nitride (NbTiN), and vanadium silicate (V_3Si) are of our interest. By using facilities at the CNF, we mainly focus on SRF thin film growth, sample preparation for material characterization, post treatment to improve RF properties, and device fabrication to fundamentally understand the SRF physics. We highlight our recent success on a NbZr alloyed cavity, which is the first experimental demonstration for such cavities and shows better RF performance than a reference Nb cavity [1-3].

Summary of Research:

(1) We demonstrated a high-performance NbZr alloyed SRF cavity [1-3]. In the sample-scale study, we deposited the initial Zr films using the e-beam evaporator at CNF, and achieved different Zr surface profiles after thermal annealing. Figure 1 shows the surface morphology of the annealed samples. We found the critical temperature of these samples are improved due to the NbZr alloying. We further developed an electrochemical deposition process to scale up the alloying process to a Cornell sample test cavity, and we observed the reduction of surface resistance owing to the increased critical temperature of NbZr alloys.

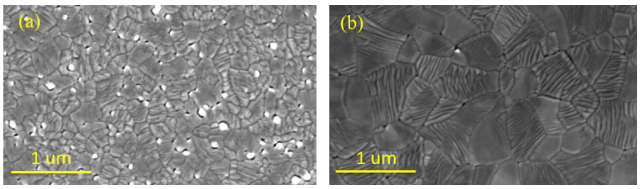

Figure 1: Surface morphology of the annealed NbZr samples with different initial Zr film thicknesses: (a) 40 nm and (b) 20 nm.

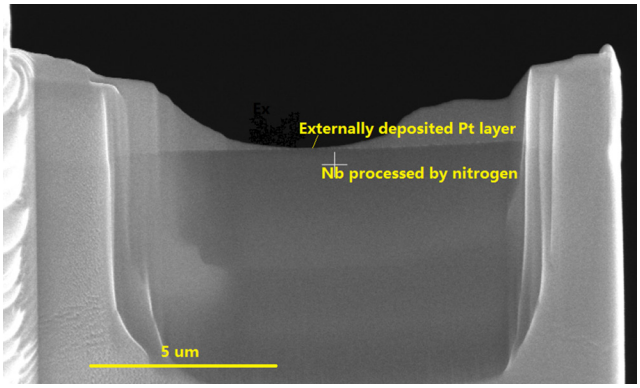

Figure 2: Cross-sectional image of a nitrogen-doped Nb specimen coated with the Pt protective layer used for scanning transmission electron microscopy.

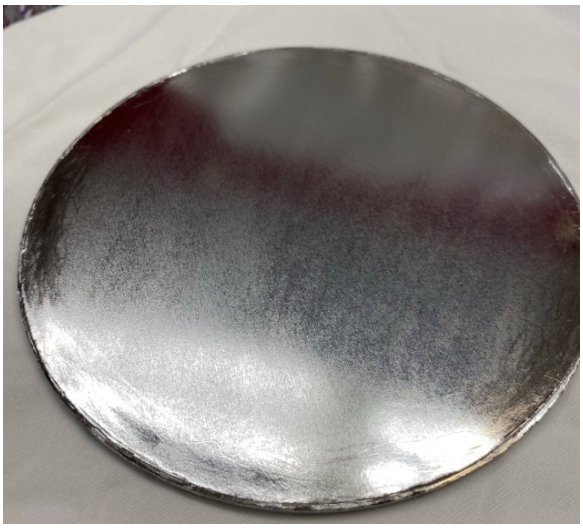

Figure 3: Picture of a Cornell sample test SRF cavity (the testing plate) with the artificially controlled surface.

(2) We demonstrated electrochemically-made Nb_3Sn thin films with extremely low surface roughness and an improved stoichiometry. Zhaslan Baraissov and Prof. David Muller's research group at Cornell Applied Physics are working on atomic analysis of these high quality Nb_3Sn films together with Nb samples processed under different treatments. To overcome the sample preparation issues before atomic imaging, we deposited an external Pt layer, at CNF, to protect the sample surface which is the most critical region for SRF applications (Figure 2).

(3) We fabricated SRF devices using the e-beam evaporator and Oxford FlexAL atomic layer deposition system at CNF to fundamentally understand the RF surface design. This year, we scaled up the artificial control process of a Nb surface to the Cornell sample test cavity. Preliminary results showed positive RF results owing to our rational surface design.

References:

[1] Z. Sun, et al., "Materials investigation and surface design of superconducting radio-frequency accelerating cavities at Cornell University", presented at the 2022 MRS Spring Meeting, Honolulu, HI, May 2022.

[2] N. S. Sitaraman, "Theory results on novel surface preparations for superconducting radio-frequency cavities", presented at the 2022 MRS Spring Meeting, Honolulu, HI, May 2022.

[3] Z. Sun, et al., "First demonstration of a ZrNb alloyed surface for superconducting radio-frequency cavities", presented at the North American Particle Accelerator Conference (NAPAC'22), Albuquerque, NM, August 2022.

Development of Fabrication Process on Strainable Polyimide Substrate

CNF Project Number: 2790-19

Principal Investigator(s): Katja Nowack

User(s): Ruiheng (Rex) Bai

Affiliation(s): Lab of Atomic of Solid State Physics, Cornell University

Primary Source(s) of Research Funding: National Science Foundation

Contact: katja.nowack@cornell.edu, rb873@cornell.edu
Website: https://nowack.lassp.cornell.edu/

Primary CNF Tools Used: Heidelberg Mask Writer - DWL2000, GCA 6300 DSW 5X g-line Wafer Stepper, Nabity System for Supra SEM, SC4500 Evaporator, Trion Etcher

Abstract:

In this project, we make bilayer graphene devices with a metal gate and electrical contacts on strainable polyimide substrates. We developed a procedure for doing photolithography with the resolution of 2.5 μm on polyimide substrate and using electron beam lithography along with etcher to pattern devices. Currently, we have achieved about 1% of strain on a graphene device and over 1% of strain on bare chip.

Summary of Research:

Theoretical calculation has shown that net orbital magnetization would appear in uniaxially strained bilayer graphene with broken inversion symmetry and current bias [1]. Similar magnetization has been observed in exfoliated single layer MoS_2 device [2].

To induce orbital magnetization in bilayer graphene, the device has to be dual gated, strained, and have electrical contact. We chose strainable polyimide substrate and used photolithography to pattern the prepattern, which includes a bottom gate, metal contacts to the device and a meander strain gauge. A picture of the prepattern is shown in the figure section. Then we transfer a boron nitride (BN) flake to the prepattern and pattern the flake so that it covers the bottom gate with electron beam (e-beam) lithography and reactive ion etching (RIE). Lastly, we transfer the rest of the stack on the chip with the conventional dry transfer technique. The polyimide substrate is soft and often has a curvature, making lithography difficult. It also has a non-negligible thermal expansion rate, making baking resist tricky.

By using nLOF negative tone photo resist, instead of bilayer photo resist, we managed to reduce the effect of substrate curvature on uniformity of resist thickness. Then we experimented with both a contact aligner and a stepper and found that a stepper gives better resolution. The substrate curvature making it hard for the mask to have uniform contact with the substrate. By the end, we were able to achieve 2.5 μm resolution with over 90% yield rate.

The difficulty we encountered when doing e-beam lithography is mostly related to baking resist (PMMA 495 A4 495). Since the substrate expand and shrink as temperature changes, the BN flake on it often gets wrinkles after baking, resulting in defective devices. We figured that by baking at a lower temperature (90°C) with longer time (20 min), we managed to reach our resolution requirements without making the BN flake wrinkle.

With the improved fabrication process, we have made several single gated devices. They could be strained to 0.5-0.7%, confirmed with Raman spectroscopy. We could induce an even larger strain on the substrate (over 1%) but could not transfer this strain onto the device. The strain on substrate is confirmed by both optical image and resistance measurements of the strain gauge.

Conclusions and Future Steps:

As we have successfully strained single gated bilayer graphene device, our next step would be to fabricate dual gated devices, which has an extra layer of graphite on top of the stack compared to our current stack. We also plan to try to increase clamping force on our device. Our current devices start to lose strain at 0.5-0.7% and we hope to increase the maximum strain we can induce on the device. One possible improvement we plan to try is to evaporate a layer of metal on the contact region on top of the device, thus clamping the device from both top and bottom.

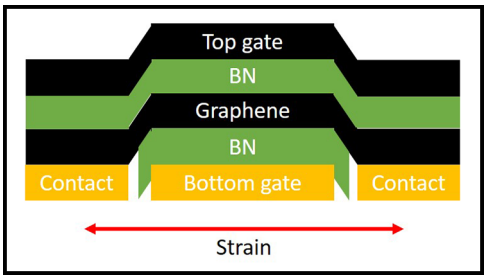

Figure 1: Cartoon picture of the structure of our final device. The red double headed arrow indicated the orientation of strain. We rely on the adhesion between the metal contact and graphene to transfer the strain from substrate to graphene. Currently, we have fabricated and strained several devices without the top graphite gate layer.

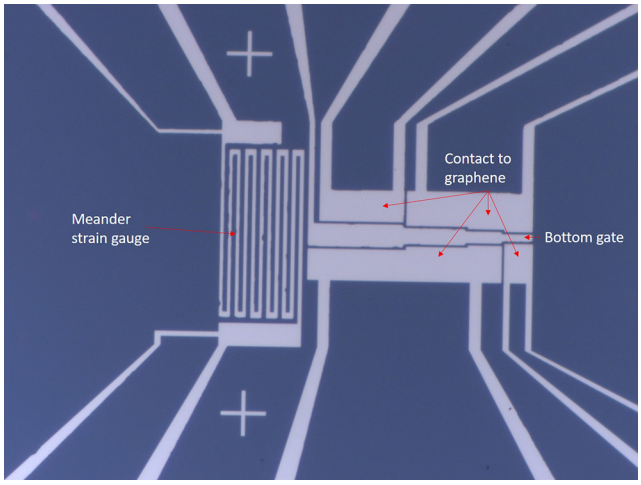

Figure 2: Prepattern that was made with photolithography and metal evaporation.

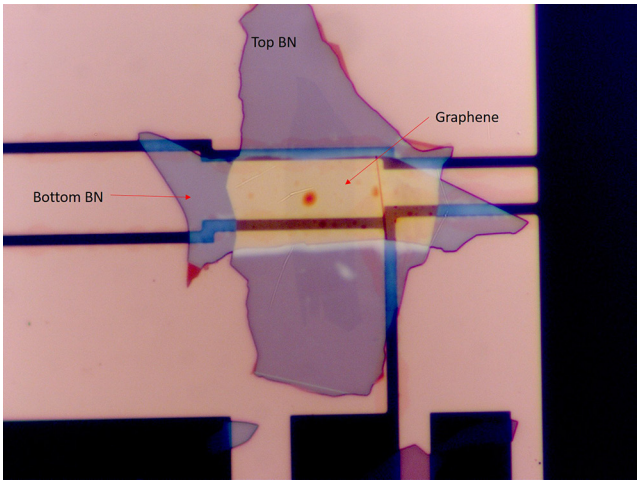

Figure 3: Fabricated device. This device does not go through the e-beam pattern step because the BN flake has the same width as the bottom, not requiring any patterning.

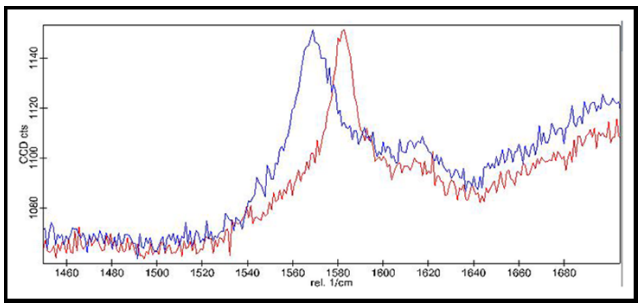

Figure 4: Raman spectrum of the device in Figure 3. The red spectrum was taken when the substrate was not strained and the blue spectrum was taken when the substrate was strained. The shift of the peak in the spectrum indicate that we have achieved ~0.7% of strain on graphene.

References:

[1] B. Schaefer, Phys. Rev. B. 103, 224426 (2021)

[2] Lee, J., Wang, Z., Xie, H., et al. Valley magnetoelectricity in single-layer MoS2. Nature Mater 16, 887-891 (2017).

Development of Engineered Gas Diffusion Layers Via Two-Photon Polymerization

CNF Project Number: 2924-21

Principal Investigator(s): Sadaf Sobhani

User(s): Giancarlo D'Orazio

Affiliation(s): Department of Mechanical and Aerospace Engineering, Cornell University

Primary Source(s) of Research Funding: Cornell University Lab Startup Grant

Contact: sobhani@cornell.edu, gd373@cornell.edu
Website: www.sobhanilab.com

Primary CNF Tools Used: NanoScribe Photonic Professional GT2

Abstract:

The need for low carbon and carbon-neutral energy sources has become increasingly clear as CO_2 emissions have continued to increase at an impressive rate. Efforts to sequester carbon show some promise, though storage remains a major issue. Utilizing this captured CO_2 in electrochemical reduction reactors can yield valuable products, such as ethanol, propanol, formic and acetic acids, among others.

As these reactors generate these products, however, the gas diffusion layer (GDL) separating the carbon dioxide gas from the cell's electrolyte begins to wet and subsequently flood with the change in product concentration; this flooding behavior severely limits operational lifespan and cell efficiency. In this work, micro-scale additive manufacturing via two-photon polymerization enables the printing of microfluidic devices. These devices were dynamically tested for flow properties via in operando testing and analysis by means of high energy X-ray imaging. The impact of architected geometry with variable surface texturing is explored, as well as the effects of electrolyte composition and surface coatings. The results of this analysis are further used in computational fluid dynamic models to better optimize GDL design to minimize flooding in subsequent designs.

Summary of Research:

In order to manufacture gas diffusion layers, the NanoScribe Photonic Professional GT2 two-photon polymerization printer was used. The high-resolution (< 1 µm voxel size) enabled by this machine allows printed porous structures with pore sizes similar to those of conventional GDLs [1,2]. The GDL designs were comprised of triply periodic minimal surfaces, a type of cubic, repeating lattice structure which is entirely formula driven. nTopology 3D modelling software was used to generate slices of these complex lattices and subsequently assembled in NanoScribe DeScribe slicing software to create a single piece while minimizing processing overhead in DeScribe.

Additively manufactured substrates were designed to serve as an interface between the printed samples and microfluidic fittings to connect the experimental setup to a micropump. These substrates were printed via stereolithography (SLA) in a resin compatible with that used by the NanoScribe GT2 to ensure bonding between printed samples and substrate. Substrates were polished to 3 µm surface finish, enabling consistent results with manual interface finding in NanoWrite.

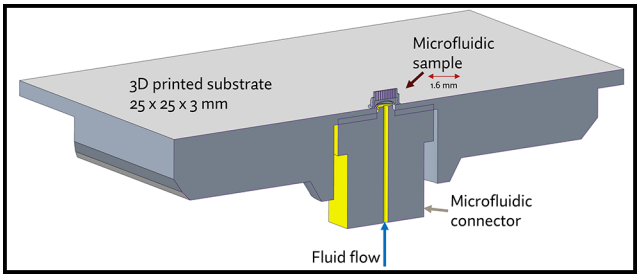

Figure 1: Section view of the microfluidic sample as mounted on the additively manufactured substrate.

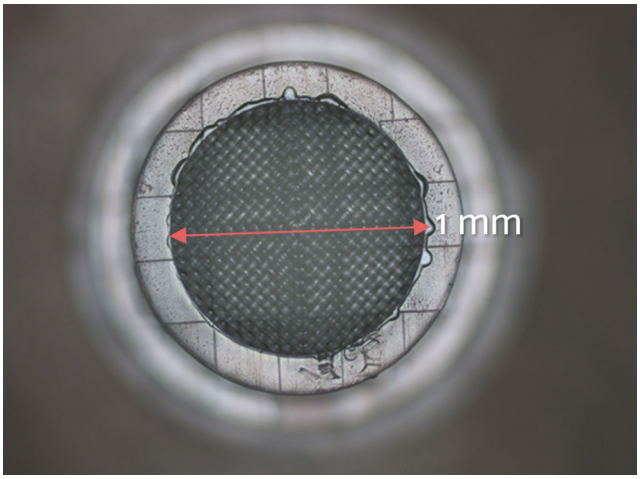

Figure 2: Top view of an as-printed sample. The internal GDL section is 1 mm in diameter with a support structure that is 1.6 mm in diameter.

Engineered GDL samples were printed in two parts on the NanoScribe GT2. First, a lower quality base layer was printed to form a support structure for the gas diffusion layer. This layer used the 25X Medium Feature Swift Mode to decrease printing time. Once this support structure was printed, the GDL was printed with the 25X objective Medium Feature Solid Mode for maximum part strength and resolution. The substrate pore directly below the samples, seen in Figure 1, enabled short development times in propylene glycol monomethyl ether acetate (PGMEA) by enhancing transport of uncured resin from the structure. Samples were developed for 30 to 60 minutes in PGMEA then 15 to 30 minutes in isopropyl alcohol (IPA). Prior work with samples printed flush to the substrate required in excess of 36 hours of development time in PGMEA and 12 hours in IPA. A finished sample, shown in Figure 2, is illustrative of the type of lattice structures developed for this experiment. After air drying, half of the samples were sent for perfluoroalkoxy alkane (PFA) coating, with the remainder uncoated for comparison purposes.

Samples were tested at Argonne National Lab's Advanced Photon Source using the 2-BM beamline. A 2 mm by 1 mm field of view was maintained while capturing at 400 frames per second in order to capture dynamic fluid flow throughout the structure. Samples were tested with pressure-driven water flow to determine flooding behavior. Pressure was ramped from 0 to 200 mBar in most cases, resulting in flow rates of approximately 2 µL/min. After data capture, XCT data was reconstructed with Tomopy and Tomocupy [3,4]. The pressure and flow rate were compared to the flooding behavior of each design.

Preliminary results validate the expected effect of the hydrophobic coating, with significantly decreased flooding compared to uncoated samples. Figure 3 demonstrates the clear difference in flooding behavior in coated versus uncoated samples, validating the coating process.

Further work is ongoing to determine the impact of lattice morphology on GDL flooding.

References:

[1] D. Corral, et al., "Advanced manufacturing for electrosynthesis of fuels and chemicals from CO_2," Energy Environ. Sci., vol. 14, no. 5, pp. 3064-3074, May 2021, doi: 10.1039/D0EE03679J.

[2] Y.-R. Lin, et al., "Vapor-Fed Electrolyzers for Carbon Dioxide Reduction Using Tandem Electrocatalysts: Cuprous Oxide Coupled with Nickel-Coordinated Nitrogen-Doped Carbon," Advanced Functional Materials, vol. 32, no. 28, May 2022, doi: 10.1002/adfm.202113252.

[3] D. Paganin, S. C. Mayo, T. E. Gureyev, P. R. Miller, and S. W. Wilkins, "Simultaneous phase and amplitude extraction from a single defocused image of a homogeneous object," J Microsc, vol. 206, no. Pt 1, pp. 33-40, Apr. 2002, doi: 10.1046/j.1365-2818.2002.01010.x.

[4] D. Gürsoy, F. De Carlo, X. Xiao, and C. Jacobsen, "TomoPy: a framework for the analysis of synchrotron tomographic data," J Synchrotron Radiat, vol. 21, no. Pt 5, pp. 1188-1193, Aug. 2014, doi: 10.1107/S1600577514013939.

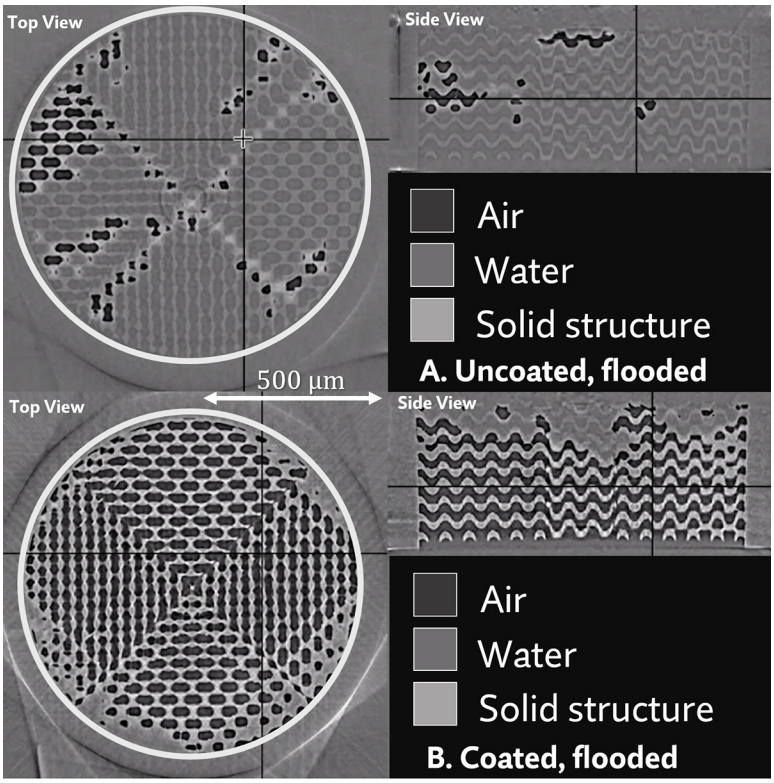

Figure 3: Real-time XCT reconstruction of an uncoated sample (top) and a PFA coated sample (bottom) during in operando *testing with water. Flooding is significant in the uncoated sample.*

Design of Porous Substrates for Enhanced Development of Microfluidic Devices

CNF Project Number: CNF Fellowship

Principal Investigator(s): Christopher Kemper Ober[1]

User (s): Giancarlo D'Orazio[2]

Affiliation(s): 1. Cornell NanoScale Science and Technology Facility (CNF),
2. Department of Mechanical and Aerospace Engineering; Cornell University

Primary Source(s) of Research Funding: Cornell NanoScale Science and Technology Facility (CNF)

Contact: ober@cnf.cornell.edu, gd373@cornell.edu

Website: https://cnf.cornell.edu/

Primary CNF Tools Used: NanoScribe Photonic Professional GT2

Abstract:

Production of micro-scale devices, particularly for microfluidic applications, commonly require high aspect-ratio channels. The sub-micron resolution of the NanoScribe Photonic Professional GT2 allows arbitrarily complex channel designs to be fabricated with relative ease. However, these complex microfluidic channels present significant challenge in terms of post-print part development due to transport limitations of the developer. In this work, custom substrates were designed to increase developer transport, minimizing overall development time and increasing part quality due to decreased exposure to development chemicals. Additionally, through selection of compatible substrate materials it is possible to print directly to a matching material, resulting in a solid bond between the part and substrate.

Summary of Research:

Devices printed on the NanoScribe Photonic Professional GT2 require, at times, a lengthy development process consisting of soaking parts in propylene glycol methyl ether acetate (PGMEA) and isopropyl alcohol (IPA). In this process, PGMEA dissolves the bulk of the uncured acrylate resin left by the printing process, followed by a wash with IPA which removes the remaining PGMEA and resin. In high aspect ratio channels, this process is transport limited due in large part to the high viscosity of the liquid resin (>13,000 mPas at ambient temperature), which flows very slowly and mixes poorly with PGMEA without agitation. Increasing transport therefore will have a significant impact on decreasing development time. This will also help maintain the structural integrity of printed parts by minimizing swelling and ensuring overdevelopment does not occur.

Device design plays a large part in ensuring proper development; minimizing channel length and other bottlenecks in the design is critical. However, altering the substrate from the conventional silicon or borosilicate glass can yield significant dividends. Printing a device atop an open pore in the substrate offers a direct path for PGMEA development, of particular use for certain part orientations and designs. This can also reduce print time, as supports may no longer be required to raise a print from the surface or orient the part on its side. Figure 1 illustrates one such design, where a microfluidic structure is raised to allow for PGMEA transport via a set of supports which are later removed. By printing directly on a pore, this support structure is obviated and removes flow restrictions from below the structure.

A 25 mm × 25 mm × 4 mm substrate with integrated 1 mm diameter pore and microfluidic connector mount was designed, shown in Figures 2 and 3. The design for this substrate is available on the NanoScribe GT2 tool wiki, hosted by CNF under the section "Printing on Porous Substrates" [1]. Substrates were printed on three different resin-based printing systems: an Elegoo Mars 2 Pro with Elegoo Standard Transparent Resin, a low cost stereolithography (SLA) printer; a FormLabs Form 3 SLA printer with FormLabs Clear Resin, and a Carbon digital light synthesis (DLS) printer with Loctite 3D IND405 Clear Resin. In all cases, an acrylate resin was used to ensure compatibility with the printing process and subsequent development as the swelling may cause cracks to form in the substrate and device after the developers have evaporated. Additionally, the same 3D model was utilized, with print orientation varied based on the requirements of the printer.

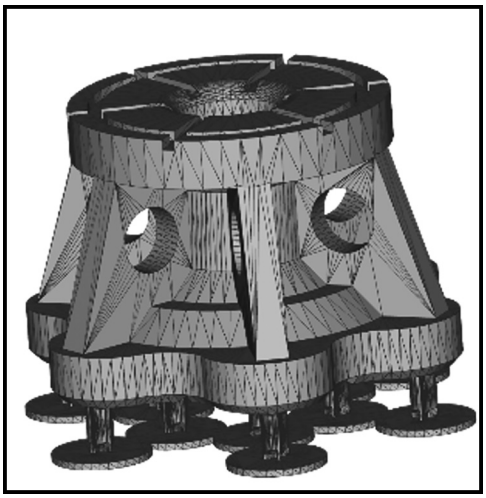

Figure 1: Original microfluidic device with standoffs for enhanced transport.

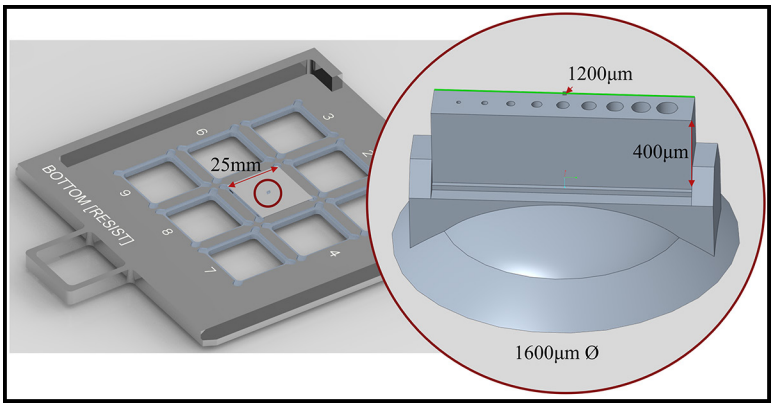

Figure 2: Model of substrate with 1 mm pore.

Figure 3: Model of printed microfluidic design on custom substrate.

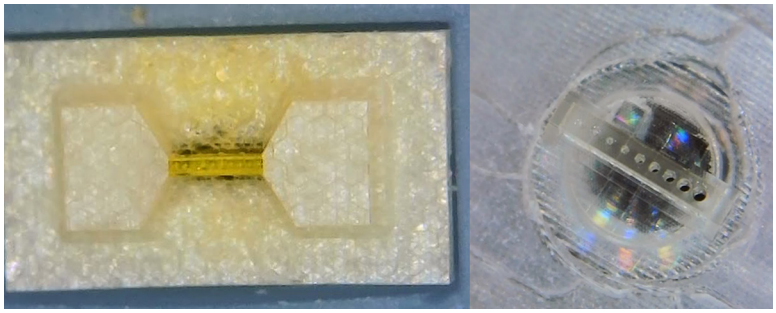

Figure 4: Two prints of a similar channel design illustrating overdevelopment of the old design (left) versus the well-developed porous substrate design.

After printing, the substrates were polished to a 3 µm surface finish then sonicated in IPA before use in the NanoScribe printer. The Elegoo Standard Transparent Resin had experienced minimal swelling and produced no defects due to the development process. The FormLabs Clear Resin swelled little and was acceptable for this process. The Loctite resin exhibited the most swelling during development with notable warping and is not suitable for fine parts, particularly if there are other printing options available.

Samples were printed with the 25x Medium Feature objective and IP-S resin. A microfluidic sample was developed in its standard configuration, then a modified version was reprinted on the porous substrate.

The standard sample required nearly 48 hours of development in PGMEA to attain clear channels, while experiencing massive structural issues due to PGMEA infiltration and swelling of the structure. The white, pillowy texture is characteristic of overdevelopment as the supporting shell-and-scaffold structure experienced significant PGMEA intrusion. The reprint on porous substrate was developed in one hour in PGMEA and 15 minutes in IPA. Due to this significantly shorter development time, device structure did not noticeably swell or overdevelop. A comparison of the two prints shows significant improvements in part quality, as seen in Figure 4. Further, this modification reduced print time from between 6 and 10 hours to just two hours since supports were no longer necessary and the part required less supporting structure for the same strength. Devices were subsequently pressure tested with both deionized water and 99% IPA with pressures of up to 345 mBar without leakage in the new design. Additional details regarding the use of these substrates is available to all users on the CNF User Wiki for Two-Photon Lithography.

References:

[1] "Two-photon Lithography - CNF User Wiki - Dashboard." https://confluence.cornell.edu/display/CNFUserWiki/Two-photon+Lithography.

You Will Ru(e) the Day: Developing Area-Selective Processes to Enable Ru-Based Interconnect at the 2 nm Node and Beyond

2022 CNF REU Intern: Elisa Simoni

Intern Affiliation: Engineering Physics and Electrical Engineering, Rose-Hulman Institute of Technology

CNF REU Principal Investigator: Prof. James Engstrom, Chemical and Biomolecular Engineering, Cornell University
CNF REU Mentor: Jay Vishnu Swarup, Chemical and Biomolecular Engineering, Cornell University

CNF REU Project and Primary Source(s) of Research Funding: 2022 Cornell NanoScale Science & Technology Facility Research Experiences for Undergraduates (CNF REU) Program via the National Science Foundation under Grant No. NNCI-2025233

Contact: simoniev@rose-hulman.edu, jre7@cornell.edu, jvs64@cornell.edu
Website: https://cnf.cornell.edu/education/reu/2022

Primary CNF Tools Used: Veeco Savannah, Oxford ALD FlexAL, Oxidation Furnace, Heidelberg Mask Writer - DWL2000, SC4500 Evaporator

Abstract:

For many years, scientists have used photolithography to layer patterns onto wafers. However, the minimum size of the features on the patterns is limited by the wavelength of the light used. Now, as the electronics industry seeks to create single digit nanometer features, photolithography is reaching the limits of its capabilities; a new method for patterning substrates is needed. One such way is through selective deposition of materials in which deposition is determined by the surface chemistry. In atomic layer deposition (ALD), a film is typically grown using half reactions in an AB cycle. First, the precursor (A) binds the substrate. Then, the co-reactant (B) reacts on the surface with the precursor to grow the desired film. Each AB cycle results in a film growth thickness of approximately one angstrom [1]. Because the user controls the number of cycle repetitions, thickness can be tailored with high precision. For area-selective ALD, if a chemical (co-adsorbate) is introduced before and alongside the precursor, the co-adsorbate can attach to certain surfaces and block film growth in order to achieve selectivity [2]. Additionally, the typical material used for electrical interconnects is copper. However, for single digit nanometer features, ruthenium is a better conductor. Overall, the purpose of this project is to create different sized line-and-space patterns of alternating ruthenium and dielectrics (Al_2O_3 and SiO_2) using a lift-off process. These patterns can then be used to test which co-adsorbates provide the best selectivity given the metals and dielectrics used in the patterns.

Summary of Research:

Ten 100 mm silicon wafers were utilized to create the patterns. First, all wafers were cleaned using an RCA clean. A 200 nm film of SiO_2 was thermally grown on five of the wafers using an oxidation furnace. A 50 nm film of Al_2O_3 was deposited via ALD on the other wafers using the Veeco Savannah and the Oxford ALD FlexAL. The negative photoresist nLOF2020 was spun on each wafer at 3000 rpm for one minute, followed by a one-minute bake. A GDSII file containing line-and-space patterns of 100, 30, 10, 3, and 1 μm was created using the gdstk python library and then used along with the Heidelberg Mask Writer - DWL2000 to create the mask pattern.

Each wafer was then exposed using the ABM contact aligner, baked on a hotplate for one minute, and developed in the Hamatech wafer processor.

The SC4500 evaporator was used to deposit the metals. Five nm of titanium was first deposited to help the ruthenium stick to the wafer. Then, 20 nm of ruthenium was deposited. After stripping the photoresist, the pattern was then examined using atomic force microscopy (the AFM).

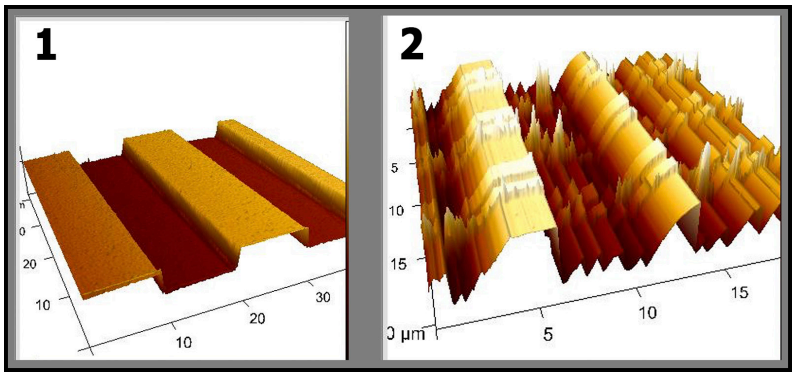

Figure 1, left: 10 µm line-and-space pattern. Figure 2, right: 3 µm line-and-space pattern.

Overall, the 100, 30, and 10 µm lines had good coverage and little surface roughness. However, there were holes and significantly more roughness in the 3 and 1 µm lines. This can be seen in the AFM images of the 10 µm and 3 µm lines as shown in Figures 1 and 2. This is likely due to the wafer not being clean enough before undergoing the photolithography process. Therefore, the 100, 30, and 10 µm lines can now be utilized for area-selective depositions.

References:

[1] S. M. George, "Atomic Layer Deposition: An Overview," ACS Publications, Nov. 2009. https://pubs.acs.org/doi/pdf/10.1021/cr900056b (accessed Aug. 13, 2022).

[2] T. Suh, et al., "Competitive Adsorption as a Route to Area-Selective Deposition," ACS Appl. Mater. Interfaces, vol. 12, no. 8, pp. 9989–9999, Feb. 2020, doi: 10.1021/acsami.9b22065.

Inkjet Printing of Epitaxially Connected Nanocrystal Superlattices

CNF Project Number: 1645-08

Principal Investigator(s): Tobias Hanrath

User(s): Daniel M. Balazs, N. Deniz Erkan, Michelle Quien

Affiliation(s): School of Chemical and Biomolecular Engineering, Cornell University

Primary Source(s) of Research Funding: Department of Energy – Basic Energy Sciences (DE-SC0018026), National Science Foundation (DMR-1719875) for the use of Cornell Center for Materials Research tools

Contact: tobias.hanrath@cornell.edu, daniel.balazs@cornell.edu, nde26@cornell.edu, mq65@cornell.edu

Primary CNF Tools Used: Dimatix Printer

Abstract:

Access to a growing library of colloidal nanomaterials provides building blocks for complex assembled materials. The journey to bring these prospects to fruition stand to benefit from the application of advanced processing methods. Epitaxially connected nanocrystal (or quantum dot) superlattices present a captivating model system for mesocrystals with intriguing emergent properties. The conventional processing approach to create these materials involves assembling and attaching the constituent colloidal nanocrystals at the interface between two immiscible fluids. Processing small liquid volumes of the colloidal nanocrystal solution involves several complexities arising from the concurrent spreading, evaporation, assembly and attachment. The ability of inkjet printers to deliver small (typically picoliter) liquid volumes with precise positioning is attractive to advance fundamental insights into the processing science, and thereby potentially enable new routes to incorporate the epitaxially connected superlattices into technology platforms. This project identified the processing window of opportunity, including nanocrystal ink formulation and printing approach to enable delivery of colloidal nanocrystals from an inkjet nozzle onto the surface of a sessile droplet of the immiscible subphase. We demonstrate how inkjet printing can be scaled-down to enable the fabrication of epitaxially connected superlattices on patterned sub-millimeter droplets. We anticipate that insights from this work will spur on future advances to enable more mechanistic insights into the assembly processes and new avenues to create high-fidelity superlattices.

Summary of Research:

Bringing the heralded prospects of nanocrystal (NC) assemblies to fruition is contingent on better understanding of and control over the formation mechanism and the emerging structure-property relationships; both of these tasks rely critically on access to high-fidelity superlattices. Recent interfacial assembly and attachment studies point towards the need for more advanced processing methods to provide refined control over the delivery of the NC solution to the fluid interface. The volume of the deposited solution is a key consideration in the process of creating a liquid thin film from which NCs assemble on the surface of the sessile liquid subphase and attach to form epitaxially connected superlattices. Considering a typical NC colloidal concentration in the range of ~ 2-300 mg/ml, the formation of a monolayer NC film requires deposition of an ink film thickness of a least 100 nm. In the case of microliter droplets deposited from a conventional micro-pipettor, this film thickness requires spreading across an interface area of ~ 10^2 cm^2 [1]. Translating processing insights from earlier studies with cm2 scale surfaces to smaller interfaces in which dynamic processes can be better controlled therefore requires the ability to deposit smaller solution volumes. In this context, the ability of inkjet printers to deliver small (typically picoliter) liquid volumes with precise positioning is very attractive for both scientific and technological reasons. For example, Minemawari, et al. [2], successfully demonstrated inkjet printing of single crystals of organic semiconductors on the surface of micrometer-sized antisolvent droplet. Beyond providing an experimental testbed to refine our mechanistic understanding of the assembly and

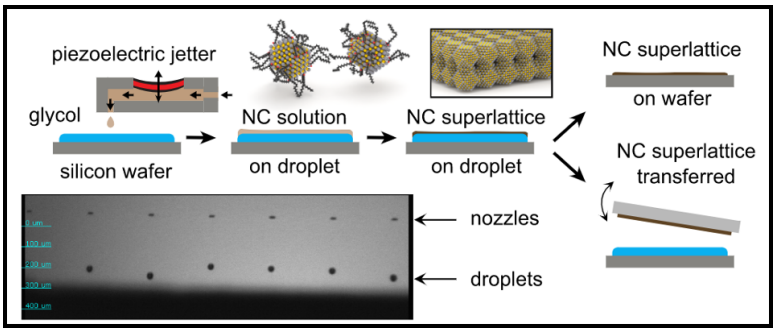

Figure 1: Sketch of the experimental setup. A colloidal NC ink is jetted on to of a sessile droplet of an immiscible subphase. NCs in the thin liquid film then assemble and attach to form an epitaxially connected superlattice (epi-SL) which can subsequently be transferred to a solid substrate.

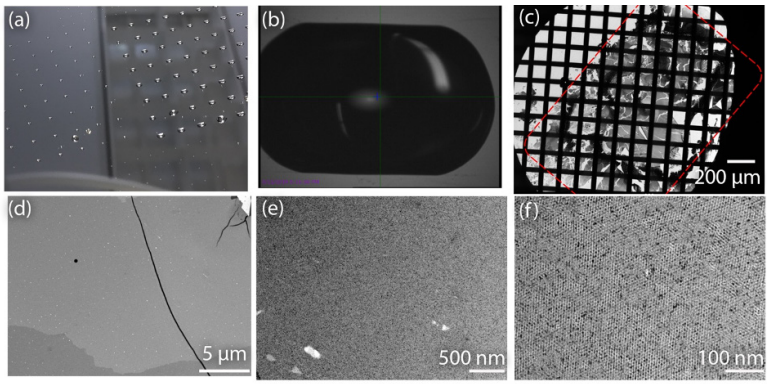

Figure 2: Multi-scale analysis of NC printed on patterned droplet. a) Optical image of droplets formed by spreading ethylene glycol on a patterned-fluorinated substrate; b) optical micrograph image of such a droplet; c) TEM image of a ~ 3 monolayer thick NC film prepared on a 1-by-1.5 mm droplet by inkjet printing; the shape of the droplet is marked showing complete spreading and coverage; d-f) the local homogeneity and superlattice structure are similar to those of samples prepared on larger scale.

attachment, inkjet printing of NC assemblies at fluid interfaces also has notable technological implications as this fabrication strategy could enable creation of epi-SLs in more complex geometries required for device integration. Inspired by these prospects, we set out to translate this approach to enable the delivery of colloidal NCs on top of an immiscible fluid interface.

In this project, we sought to build on these insights to identify a window of opportunities (including ink formulation and printing approach) to enable delivery of colloidal NCs onto the surface of a sessile droplet. Basic aspects of the processing workflow are summarized in Figure 1. We identified critical considerations for the NC ink formulation including NC solute concentration and NC surface ligand coverage, choice of solvent (with regards to NC solubility, vapor pressure and viscosity). The processing window of opportunity for stable inkjet printing is constrained by several factors. We examined inkjet printing of NC inks in the parameter space defined by the Reynold and Weber numbers. We established the basic relationship between fluid dynamic conditions during inkjet printing and the structural fidelity of the NC superlattice. We analyzed the structure of NC films formed on a geometrically contained droplet. The results of this project were recently published in Nano Research [3]. We anticipate that insights from this work will spur on future advances to enable more mechanistic insights into the assembly processes and new avenues to create high-fidelity superlattices.

References:

[1] Balazs, D. M.; Dunbar, T. A.; Smilgies, D.-M.; Hanrath, T., Coupled Dynamics of Colloidal Nanoparticle Spreading and Self-Assembly at a Fluid-Fluid Interface. Langmuir 2020, 36 (22), 6106-6115. doi:10.1021/acs.langmuir.0c00524.

[2] Minemawari, H.; Yamada, T.; Matsui, H.; Tsutsumi, J.; Haas, S.; Hasegawa, T., Inkjet printing of single-crystal films. Nature 2011, 475, 364. doi:10.1038/nature10313.

[3] Balazs, D. M.; Erkan, N. D.; Quien, M.; Hanrath, T., Inkjet printing of epitaxially connected nanocrystal superlattices. Nano Research 2021, 15 (5), 4536-4543. doi:10.1007/s12274-021-4022-7.

Genetically Encoded Platform for Mucin-Induced Extracellular Vesicle Production

CNF Project Number: 2272-14

Principal Investigator(s): Dr. Matthew Paszek

User(s): Erik Chow

Affiliation(s): Department of Biomedical Engineering, Cornell University

Primary Source(s) of Research Funding: National Science Foundation Graduate Research Fellowship

Contact: paszek@cornell.edu, ec829@cornell.edu

Primary CNF Tools Used: Malvern NS300 Nanosight

Abstract:

Extracellular vesicles (EVs) are critical in mediating intercellular communication. Because of the diverse nature of their cargoes — which include DNA, coding and noncoding RNA, and proteins — and their innate biocompatibility, EVs have quickly become a prominent focus in numerous biomedical engineering applications, including diagnostics, drug delivery, and targeted therapies. One largely unexplored area is the significance of the glycocalyx in EV biogenesis and function. Specifically, the capacity to rationally manipulate the glycocalyx to produce vesicular materials for biomedical applications remains poorly understood. We have previously demonstrated that overexpressing the mucin glycoprotein MUC1 in the glycocalyx leads to a dramatic increase in the production of EVs [1]. Here we summarize our recent efforts to develop and characterize a genetically encoded platform for the production of these so-called mucin-induced EVs (MUC-EVs).

Summary of Research:

Extracellular vesicles (EVs) have been shown to carry a wide range of cargoes, including DNA, coding and non-coding RNAs, and proteins. Because of the diverse nature of their cargoes, and their innate biocompatibility, EVs have quickly gained traction in numerous areas of biomedical engineering research, including disease pathogenesis, diagnostics, drug delivery, and targeted therapies. The glycocalyx is a polymer meshwork of proteins, nucleic acids, and glycans which dictates numerous intercellular interactions. However, the capacity for the production of rationally designed EVs through engineering of the glycocalyx remains poorly understood. It has been previously shown that engineering the glycocalyx via the overexpression of mucin can result in membrane morphologies which are favorable for the formation of EVs [1]. This report summarizes research from the last year characterizing a genetically encoded platform for increased generation of so-called "mucin-induced" EVs with tunable size characteristics and surface coatings.

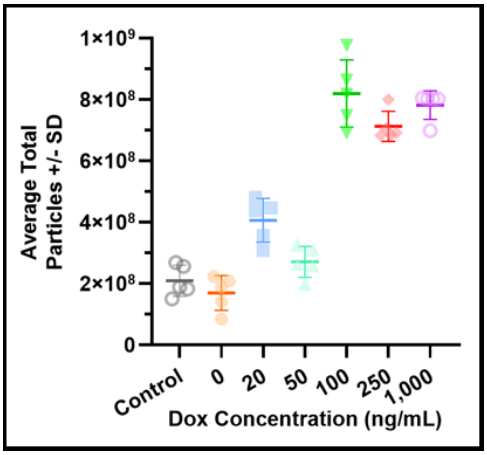

Figure 1: Tunable mucin-induced EV production. EV particle concentrations measured by NTA from MCF10A-rtTA cells (Control) and MCF10A-1E7 cells induced with a ranged of Dox concentrations. Plotted are the average reported total particle concentrations +/-SD from five video recordings.

To engineer the glycocalyx, MCF10A cells were genetically engineered to overexpress a MUC1-mOxGFP construct on the cell membrane. A single clone was expanded and used as a workhorse cell line for this

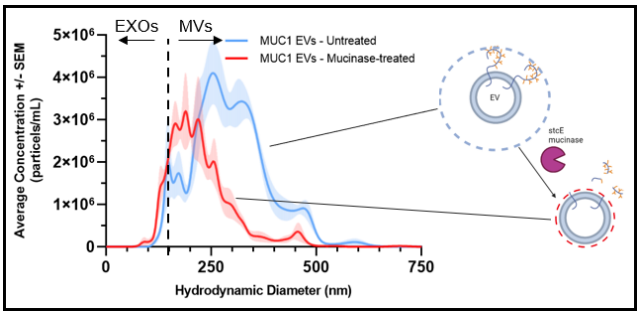

Figure 2: Mucin-induced EVs have removable mucin coatings. EV size distributions measured by NTA from MCF10A-1E7 derived EVs either untreated (Control) or treated with 100nM stcE mucinase. Histograms represent the average reported size from five video recordings.

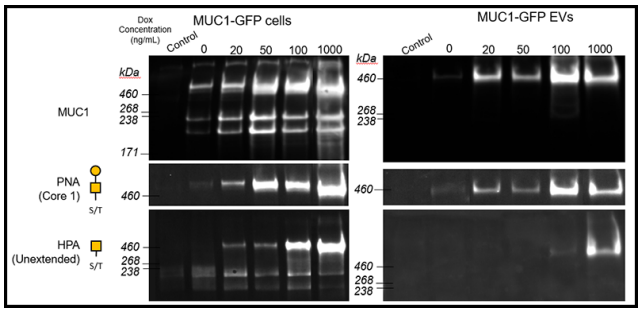

Figure 3: EVs from MCF10A-1E7 cells have similar mucin coating characteristics to their parent cells. Lectin blots comparing MUC1 glycosylation patterns in mucin-induced EVs and the cells from which they were derived.

research, hereafter referred to as MCF10A-1E7 cells. Expression of MUC1-mOxGFP in MCF10A-1E7s was tied to a tetracycline-inducible promoter, and cells were treated with doxycycline (Dox) for 24 h at a concentration of either 0.1 µg/mL or 1 µg/mL to induce MUC1-mOxGFP overexpression. MCF10A cells engineered with only the promoter but no MUC1-mOxGFP construct, hereafter referred to as MCF10A-rtTA cells, were used as a negative control. After Dox treatment, the cells were switched to serum-free media and cultured at 37°, 5% CO_2 for 15 h to 18 h. EV-containing media was harvested, and the EVs were isolated by PEG-enrichment [2]. EV mucin coatings were optionally removed by treatment with stcE mucinase [3], and EV sizes and concentrations were measured by nanoparticle tracking analysis (NTA) using the Malvern NS300 Nanosight.

Figure 1 illustrates the dose-dependent production of mucin-induced EVs based Dox titration. These data illustrate that tunable EV production in MCF10A-1E7 cells is achieved using our genetically encoded platform. Additionally, mucin-induced EVs were found to carry their own mucin coatings, as supported by Figure 2. Treatment of mucin-induced EVs with mucinase resulted in an overall decrease in EV size, consistent with the cleavage of MUC1 from the EV surface.

Figure 3 shows lectin staining of the mucins isolated from mucin-induced EVs. The EV-derived mucins show both similar expression and glycosylation patterns to cell-surface mucins from MCF10A-1E7 cells, suggesting that glycocalyx engineering at the cellular level can be used to tune mucin-induced EV coatings.

Conclusions and Future Steps:

Altogether, these data demonstrate that EV production and properties can be controlled by engineering the glycocalyx of cells. Further experiments are needed to explore the applications of engineered EV mucin coatings. Additionally, future experiments will strive to reliably segregate exosomes and microvesicles in order to more precisely study the exosome and microvesicle characteristics.

References:

[1] Shurer, C. R., Kuo, J. C.-H., Roberts, L. D. M., Gandhi, J. G., Colville, M. J., Enoki, T. A., Pan, H., Su, J., Noble, J. M., Hollander, M. J., O'Donnell, J. P., Yin, R., Pedram, K., Möckl, L., Kourkoutis, L. F., Moerner, W. E., Bertozzi, C. R., Feigenson, G. W., Reesink,

H. L., and Paszek, M. J. (2019). Physical Principles of Membrane Shape Regulation by the Glycocalyx. Cell, 177(7), 1757–1770. https://doi.org/10.1016/j.cell.2019.04.017

[2] Rider, M., Hurwitz, S. and Meckes, D. ExtraPEG: A Polyethylene Glycol-Based Method for Enrichment of Extracellular Vesicles. Sci Rep 6, 23978 (2016).

Fabrication and Characterization Support for CCMR

CNF Project Number: 2974-21
Principal Investigator(s): Jonathan Shu
User(s): Philip Carubia

Affiliation(s): Cornell Center for Materials Research (CCMR), Cornell University

Primary Source(s) of Research Funding: National Science Foundation

Contact: jbs24@cornell.edu, pmc228@cornell.edu
Website: www.ccmr.cornell.edu

Primary CNF Tools Used: Universal Laser Systems VersaLaser VLS3.50

Abstract:

Over the last year, the Cornell NanoScale Facility (CNF) has been accessed three times on project number 2974-21. Once for training on the Universal Laser Systems VersaLaser VLS3.50, and twice for laser cutting 20 mm, 25 mm, and 40 mm discs from PSA backed grinding papers to be used with the DHR3 shear rheometer located in the Cornell Center for Materials Research (CCMR).

Summary of Research:

CNF Project 2974-21 was established for facilities staff from the Cornell Center for Materials Research (CCMR) to access basic instrumentation within the Cornell NanoScale Facility (CNF) for purposes of sample preparation and fabrication of accessories for CCMR instrumentation. The initial project proposal was started to gain access to the Universal Laser Systems VersaLaser VLS3.50 by the bard materials facility for cutting 20 mm, 25 mm, and 40 mm discs from PSA backed grinding papers to be used with our DHR3 shear Rheometer. These discs are used to increase the friction between stiffer samples and the instrument to reduce artifacts related to sample slippage.

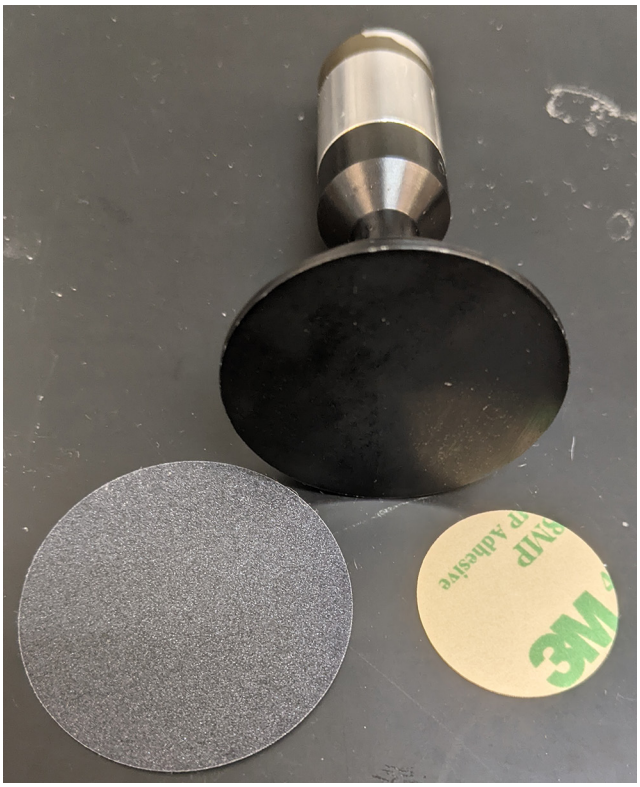

Figure 1: 40 mm upper parallel plate geometry with 40 mm disc front and 25 mm disc back.

Conclusions and Future Steps:

Access to this laser cutter has allowed us to test tougher hydrogels and viscoelastic materials at higher strains than previously available. It is likely that we will be using the Universal Laser Systems VersaLaser VLS3.50 in the future as we use up our existing stock.

Current Progress in Superconducting Device Fabrication

CNF Project Number: 2998-22
Principal Investigator(s): Valla Fatemi
User(s): Luojia Zhang, Haoran Lu

Affiliation(s): School of Applied and Engineering Physics, Cornell University

Primary Source(s) of Research Funding: Lab start-up account

Contact: vf82@cornell.edu, lz282@cornell.edu, hl2396@cornell.edu
Website: https://fatemilab.aep.cornell.edu/

Primary CNF Tools Used: Heidelberg Mask Writer - DWL2000, ABM Contact Aligner, AJA Sputterer, AJA Ion Mill, Glen 1000

Abstract:

The Fatemi Lab is mainly interested in the intersection of low dimensional materials and quantum circuits. The current ongoing project is transport and microwave spectroscopy on graphene Josephson junction, and the main cleanroom activities are fabrication and packaging of those superconducting Josephson devices. So far, our efforts have been towards the deposition and measurement of base-layer superconducting niobium films.

Summary of Research:

The users from our lab have completed the cleanroom orientation and obtained the access in March this year. Later, Luojia got trained and started using the AFM to measure the thickness of boron nitride for our 2D materials stack. The majority of the fab work started in this summer. Haoran was trained on the wire bonder and used it to package preliminary resonator devices.Luojia started making devices with sputter deposition, photolithography, and RIE etching. The first contact mask was made using the Heidelberg DWL2000 mask writer. Later, the AJA sputterer was used to deposit a layer of niobium on top of a silicon wafer. The sputtered wafer was then patterned using photolithography. For that, we used the ABM contact aligner with AZ nLoF photoresist. After determining the optimal spin coating recipe and dose, we used the AJA ion mill to etch away the metal, and Glen 1000 to descum the wafer.

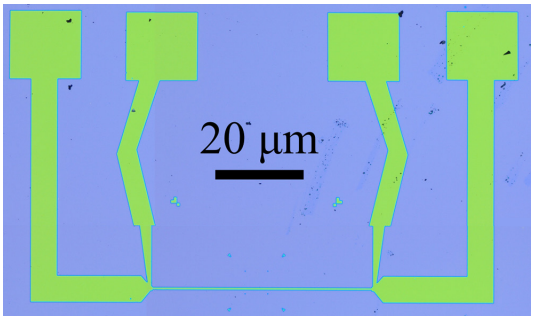

Figure 1: Image of etched niobium film patterned into a four-probe device structure for testing residual resistance ratio and the superconducting critical temperature.

Conclusions and Future Steps:

So far, we have made good first steps towards super-conducting niobium layers for use in Josephson and other superconducting devices. Next steps include:

(1) Determining the sputtering recipe to produce good quality nNB film with critical temperature larger than 9K.

(2) Print and use a stepper reticle for microwave resonators.

(3) Use E-beam lithography to make superconducting contacts with hBN-graphene-hBN stacks.

(4) Perform RIE side contacts on the 2D materials van der Waal stack, test the quality of the superconducting contacts.

INDEX

Reports by CNF Project Number

A

B

C

D

E

F

G

H

I

J

K

L

M

N

O

P

Q

R

S

T

V

W

X

Y

Z

The 2021-2022
Cornell NanoScale Facility
Research Accomplishments
are online in full color PDFs,

http://cnf.cornell.edu/publications/research_accomplishments

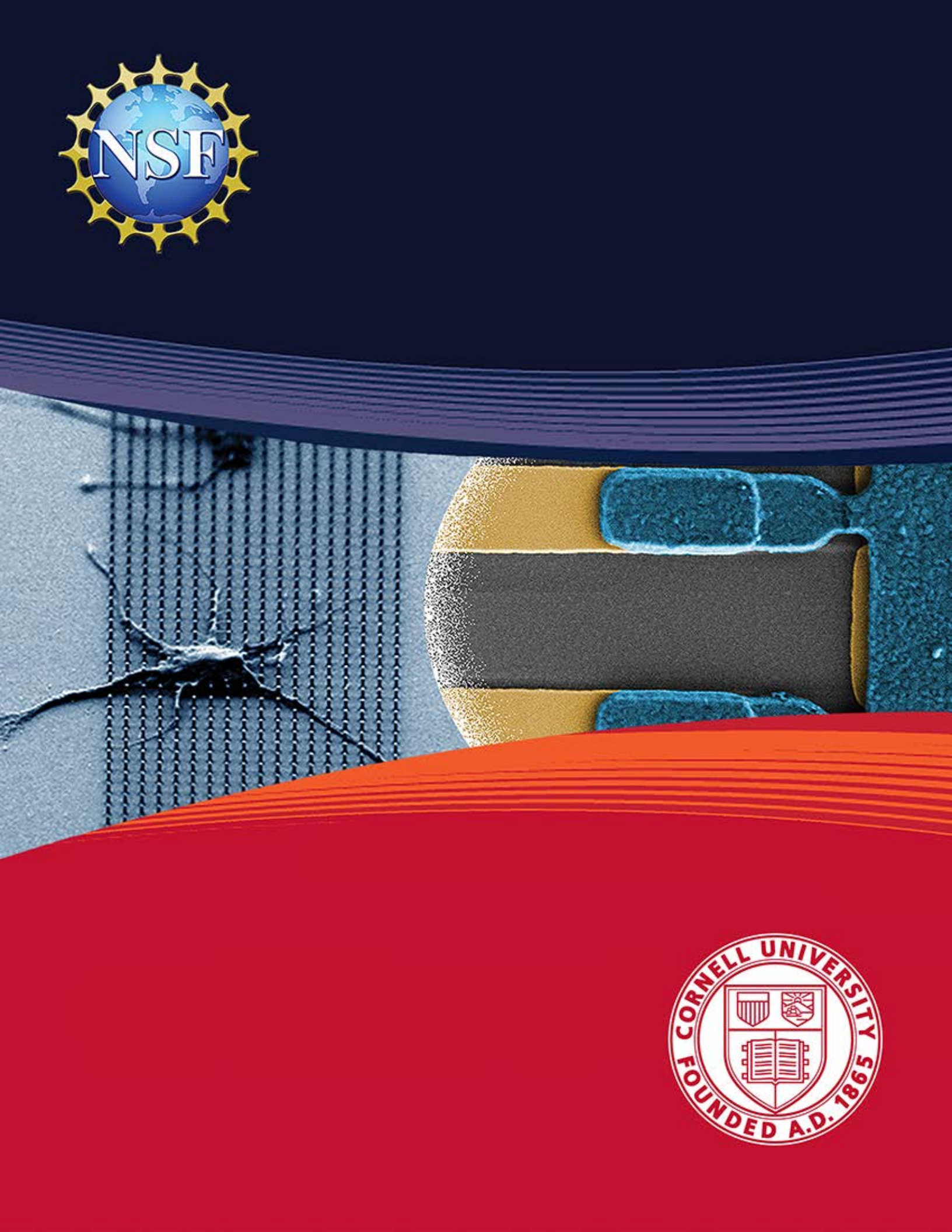
NSF
CORNELL UNIVERSITY
FOUNDED A.D. 1865